Photo-Bioreactor Modelling And Development Of Methods For The Optimisation Of Micro-algal Biodiesel Production

By

Krys Bangert

BSc Honours, Sheffield Hallam University, UK

Thesis submitted in part fulfilment of the requirement for the degree of Doctor of Philosophy

Department of Molecular Biology and Biotechnology
Department of Chemical & Biological Engineering.

The University of Sheffield, UK

November 2013

Abstract

This research project investigated the bottlenecks for microalgal growth within current photo-bioreactor designs. Mass transfer limitations including light, CO_2, and O_2 have been investigated, along with the effects of fluid flow. These variables were assessed to find the overall impact on the lipid production and growth of the algal species *Dunaliella salina* CCAP19-30 and *Dunaliella salina* CCAP19-18. A number of techniques to measure lipid production by *D. salina* were developed including Nile Red staining, direct trans-esterification and NMR.

The study was divided into two main areas, based around laboratory experimental work and computer simulation. Initially, small lab scale algal growth experiments were performed to gather basic growth data and establish assessment procedures. These were then followed by small (100ml) and larger (3 litre) photo-bioreactor experiments, which included the use of a patented micro-bubble technology developed in the laboratory of Prof. Will Zimmerman (Department of Chemical and Biological Engineering). The data from these experiments, along with existing published work, provided the basis for a series of further computer simulations.

The majority of the simulation work was conducted using COMSOL multi-physics, in which models of media flow and mixing within prototype 100 ml and 3 L photo-bioreactor designs were produced. During the later stages of the project, this combination of empirical and theoretical work was used to highlight the areas in which significant improvements can be made within existing algal growth systems. The hypothesis that the integration of micro-bubble sparging in a system, can increase the productivity of standard bioreactor designs was tested as a part of this work.

In addition, the effects of photo-bioreactor light ingress and utilisation were also considered for the development of a novel passive "smart skin" coating, which was tested to see if ambient light could be shifted into the algal photosynthetically active region.

Acknowledgements

Throughout the course of this research project I have been fortunate enough to meet and work with many kind hearted people who have given their time, knowledge, help to support to me in my studies. I would like to take this opportunity to acknowledge how truly grateful I am to every one of you.

Firstly, I would like to thank my two supervisors; Dr Jim Gilmour for his resolute faith in my abilities, endless patience and calm resolve, which have helped keep me on track all of the way through this challenging and diverse project. Dr Steve Wilkinson for his seemingly limitless technical knowledge and open ear to my engineering woes. I am eternally grateful to you both for helping to put together this amazing multi-disciplinary project and enabling me to study science and engineering again.

I would also like to thank all of the technicians in the University that have helped me along the way, in particular; Andy Patrick andMike Omeara in CBE for their help in designing and building the photo-bioreactor systems (and letting me get my hands dirty), Ralph Moyles in MBB for his help with the electrical work and helping me to cobble together my rather 'Heath Robinson' apparatus, Greg Nicholson in APS for help modifying equipment in the upper annex, Glass blower Daniel Jackson in Chemistry for help with rig modifications and photo-bioreactor construction (along with sharing 'most excellent' guitar music) and Simon Thorpe, also in Chemistry, for tuition and assistance in all aspects of mass spectroscopy.

From the academic side, I would like to give thanks to; Prof. Will Zimmerman in CBE for the use of his fluidic oscillator design and COMSOL software, along with the guidance he provided with those. Prof. Mike Williamson in MBB for his help in processing and interpreting a huge range of NMR algal samples. Prof. Keith Cooksey and Dr Robert Gardner for informative their email discussions on the subject of Nile Red fluorescence methodology. Dr Alan Dunbar for his assistance in the 'smart skin' aspects of the project and the loan of his light measurement equipment. Members of the Wilkinson, Zimmerman and Gilmour research groups for their time and assistance, with a particular mention to Kezhen Ying for his collaboration on the 'smart skin' and micro bubble aspects of my work.

I am also very grateful to the many project students have aided me, not just in term of knowledge but also in mentorship and tuition experience. Most notable amongst them are the contributions from Stephen Marshall and David Hosking.

I am indebted to Prof. Tony West, Dr Neil Lowrie, the EPSRC and everyone involved in the E-Futures DTC program for giving me this opportunity to help contribute to human understanding, it has been one of my life's ambitions realised to do so.

Finally, I would like to thank my supportive parents, who have been behind me every step of the way through my educational adventures in life. All my friends and former mentors that have helped me reach this point in my life. And last, but certainly not least, my long suffering partner Samantha who has kept me sane and grounded through all the highs and lows a PhD has to offer, without her love and understanding I would never have made it this far.

I thank you all.

Table of Contents

1 Literature Review

1.1 Climate Change and UK targets

Since the mid part of the 20th century, there has been a growing body of scientific evidence that indicates humankind is having a detrimental impact on our planet's natural greenhouse gas (GHG) system. The seminal works of climatologist Hubert Lamb in the late 1960s (Lamb, 1966) and other prominent climate researchers in the subsequent decades, demonstrated that levels of atmospheric CO_2, CH_4 and N_2O have increased rapidly since around 1750, the start of the industrial revolution, see Figure 1.1 below(IPCC, 2007; IPCC, 2013). This evidence, when it was compared with atmospheric data for the previous thousand years (using ice-core measurement techniques), showed a clear correlation between GHG emissions, man's technological activity and a steady rise in the temperature of the global climatic system(Petit, et al., 1999).

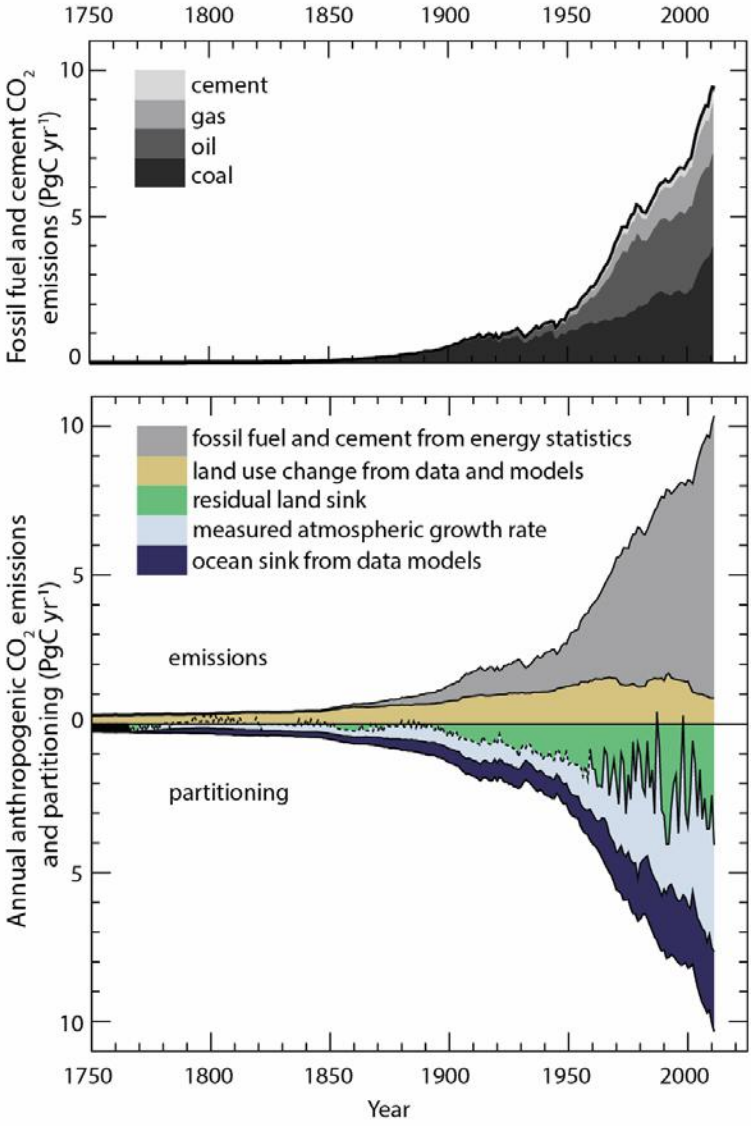

Figure 1.1 - Annual anthropogenic CO_2emissions and their partitioning among the atmosphere, land and ocean (PgC yr^{-1}) from 1750 to 2011.

(Top) Fossil fuel and cement CO_2 emissions by category, estimated by the Carbon Dioxide Information Analysis Center (CDIAC).

(Bottom) Fossil fuel and cement CO_2emissions as above. CO_2emissions from net land use change, mainly deforestation, are based on land cover change data.

The atmospheric CO_2growth rate prior to 1959 is based on a spline fit to ice core observations and a synthesis of atmospheric measurements from 1959.

(IPCC, 2013)

A prolonged period of stringent peer-review and experimental validation ensued in the following years, culminating with a broad scientific consensus that man made global warming is now “unequivocal” (IPCC, 2007). However, the time scale of these temperature changes is still the topic of intense debate within the relevant bodies. A number of scenarios have been put forward to date, based on complex computer simulations. The worst of which, predicts a global surface temperature rise of 2.4 - 6.4˚C and a corresponding sea level rise of 0.26 - 0.59m by the end of the century (relative to 1980-1999 levels) (IPCC, 2007). Alarmingly, even if one of the best scenarios was to take place, where GHG concentrations were reduced back to 2000 levels, the temperature would still increase by approximately 0.3 - 0.9˚C, due to an increasing global population and the increased use of fossil fuels in developing nations (IPCC, 2007). It is clear that GHGs will need to be reduced quickly to avoid the most extreme cases affecting future generations, but unfortunately, some of those impacts will be felt regardless due to the emissions already present in the atmosphere. Some studies have already shown evidence of this, with a “significant change in many physical and biological systems” and rapid changes to polar ice formation, currently underway (IPCC, 2007). For the rest of this century it seems it is now a question of damage limitation.

In the light of these stark predictions, national political and governing bodies are starting to react to the problem. The last decade has seen a radical political shift towards the production of energy in various forms from renewable sources with low or zero carbon emissions. This has been partially motivated by warnings from senior economists (as well as scientists), stating that the financial and physical repercussions of inaction will make the situation harder to deal with in the longer term (Stern, 2007). Recent global climate summits such as Kyoto and Copenhagen have also helped this motivation, by facilitating the establishment of increasingly tough international caps on GHG emissions and penalties for non-compliance (UNFCCC, 1998; UNFCCC, 2009). Unfortunately though, negotiations to establish a multinational timetable of action have thus far failed to produce a truly unified agreement, due to many countries adopting individual strategies based on their own national interests. This situation has been also been exacerbated in recent years by the global financial slow down and subsequent need for budgetary austerity.

In November 2008, the UK government passed the ‘Climate Change Act 2008’ through parliament, thusbecoming the first country in the world, to sign up to a long-term legally binding strategy to address climate change. The act set a target of reducing the country’s Kyoto GHGs by 80% relative to 1990 levels, with the aim of trying to limit average global temperature changes to below 2˚C (DECC, 2009). To implement this, the UK government adopted a multi-pronged strategy, looking at all aspects of power generation, usage, and

related policy, including fiscal incentives to help in decarbonisation (DECC, 2011b). One of the key areas targeted by this legislation is transport. Surface vehicles currently account for 19% of total UK GHG emissions and 22% of CO_2 emissions (CCC, 2010). Under the medium abatement scenario set by the Committee on Climate Change (CCC), a reduction of 44% of surface transport emissions relative to 2008 levels will need to be achieved by 2020 if the Climate Change act reduction target is to be met. UK aviation emissions are also a major contributor, according to predictions by the Department for Transport air travel emissions are expected to increase from 37.5 $MtCO_2$ (in 2005) to around 60 $MtCO_2$ by 2030 (CCC, 2010). But surprisingly, given this situation, international aviation and shipping emissions have thus far not been formally included in the 2008 act. These emissions will instead be included in the governments total 2050 reduction target (80% below 1990 levels) to allow other sector emission reductions to compensate (DECC, 2012). Current data from the CCC shows that some progress is been made with domestic transport CO_2 emissions falling by 1.2% in 2011 and again slightly in 2012 (with aviation reduced by 4.5% and domestic shipping by 3.2% in 2011), but there is some way to go yet to meet the major milestones (CCC, 2013).

Another motivating factor for rapid decarbonisation, especially in transport is resource depletion, specifically relating to crude oil. The vast majority of current energy/transport infrastructure relies on this single fossil resource for the production of fuels and lubricants (IEA, 2013). In recent years there has been increased speculation in the energy market that the availability of crude oil may be coming to a peak in production (de Almeida and Silva, 2009). Indeed, some researchers have suggested that the peak may already have been reached, due to the lack of new oil field discoveries and decreases in certain production areas (Aleklett, et al., 2010). Others however, believe that the peak will not occur until the middle of the century (Kjarstad and Johnsson, 2009). In either case, oil extraction is becoming increasingly difficult due to the lack of traditional easily obtainable reserves. This has led to the pursuit of highly technical approaches to extract oil from unconventional sources such as oil sands, bitumen and oil shale which due to the complexities involved have a much lower energy return on investment (EROI) (Brandt, Englander and Bharadwaj, 2013).

In the long term, the fact still remains that fossil fuels are a finite resource, and thus an alternative will need to be found quickly to maintain our transport infrastructure and meet the climate targets. To do this, the government has agreed that a combination of increased market penetration of Electric/Hydrogen vehicles, biofuels and sustainable public transport will be needed(CCC, 2013; DECC, 2011a).

1.2 Biofuels Overview

Biofuels derived from renewable plant biomass have a attracted significant interest from governmental bodies and legislators in recent years due to their ability to potentially provide an alternative fuel source to oil with net carbon neutrality (Durrett, Benning and Ohlrogge, 2008; Mathews, 2008). Liquid biofuel variants, such as bio-diesel and bio-ethanol have been of special interest to the transport and manufacturing sectors due to their capability of directly replacing most existing fossil fuels whilst maintaining significant parts of the original infrastructure (Basha, Gopal and Jebaraj, 2009). This factor is a major advantage over other types of renewable fuel sources, such as hydrogen that would need large investment in resources and a new distribution network before it could be commercially viable (Crabtree, Dresselhaus and Buchanan, 2004; Dunn, 2002). Current liquid biofuel penetration (sourced from 'first generation' fuel crops and re-cycled oils and fats) for the road transport in the UK stands at 3.1% by volume (2012), with an objective of reaching 8% by 2020 (CCC, 2013). However, if this target is to be reached in time further production capacity needs to be put in place and better productivity needs to be achieved, whilst not creating ethical problems due to constrained resources (i.e. land and nutrients) and maintaining carbon neutrality.

'First generation' fuel crops, based on plants such as corn and soybean require considerable amounts of land to grow in the required quantities to be able to produce a commercially scalable product.This is problematic because the process of farming these crops can then incentivise the planting of fuel crops over food crops in poorer regions, due to the lack of fertile land(RFA, 2008). This can lead to food shortages in the affected communities (Bioethics, 2011;Smith, et al., 2010). Also, these crops are also unlikely to provide a total replacement for conventional fuel generation, due to the lack of agricultural land in the first place. For example, just to meet 50% of the transport fuel needs of the United States alone, corn and soybean crops would have to be planted on 846% and 326% of the existing U.S. cropping areas respectively (Chisti, 2007), which is quite clearly unfeasible. Even with the development of faster growing more energy dense,'second generation' crops such as *Miscanthus* and Switchgrass(with others that can grow on marginal land), the area needed for growth would still be considerable; *Miscanthus* could provide 260% more bioethanol per hectare than corn grain (Heaton, Dohleman and Long, 2008). This performance turns out to be only marginally better than some of the better 'first generation crops' such as oil palm, which needs 24% (Chisti, 2007) compared to 11.6 - 23.3% for *Miscanthus giganteus* (Heaton, Dohleman and Long, 2008). Realistically, it is only 'third generation' fuel crops, such as micro/macro algae that have the potential to provide the quantities of biofuels required, while simultaneously avoiding the 'food vs fuel' conundrum (Chisti, 2013). For the purposes of this work only micro-

algae will be discussed in detail, however, it is worth mentioning that macroalgae (common seaweeds) such as *Euchema spp* that synthesise polysaccharides with much greater productivity than terrestrial plants (per unit area) also have great potential for production of fuels like bioethanol (Goh and Lee, 2010; IPCC, 2011; Jung, et al., 2013).

Microalgae as a biofuel resource, have many desirable attributes; high oil content to biomass ratio, with some strains exceeding 80% lipid to dry weight biomass compared to less than 5% for most 'first generation' fuel crops (Chisti, 2007; Metting, 1996; Spolaore, et al., 2006). Reduced area needed for growth, 1.1 - 2.5% cropping area compared to 'first' and 'second generation' crops (Chisti, 2007). The ability to be grown on marginal or non fertile land (Hu, et al., 2008) and some algae species also have better efficiencies than terrestrial plants in converting sunlight to biochemical energy (Stephenson, et al., 2011). Aside from the production of algal oils, which can be used for producing transportation fuels such as diesel, petrol and kerosene (Lestari, et al., 2009), many strains are also capable of producing fuels in other different forms (Figure 1.2), including;biomethane (via anaerobic digestion) (Markou, Angelidaki and Georgakakis, 2013; Sialve, Bernet and Bernard, 2009), biohydrogen (Kosourov, et al., 2005;Timmins, et al., 2009) and bioethanol (Ho, et al., 2013). However, the most versatile and applicable to the current transport infrastructure are the algal oil (or lipids) based fuel types, which is why the majority of commercial start-ups are focusing their R&D efforts in this area (Chisti, 2013). Of the different algal oil products available, this study will primarily focus on biodiesel as this form of fuel is already in circulation under the UK's Renewable Transport Fuel Obligation (DoT, 2012).

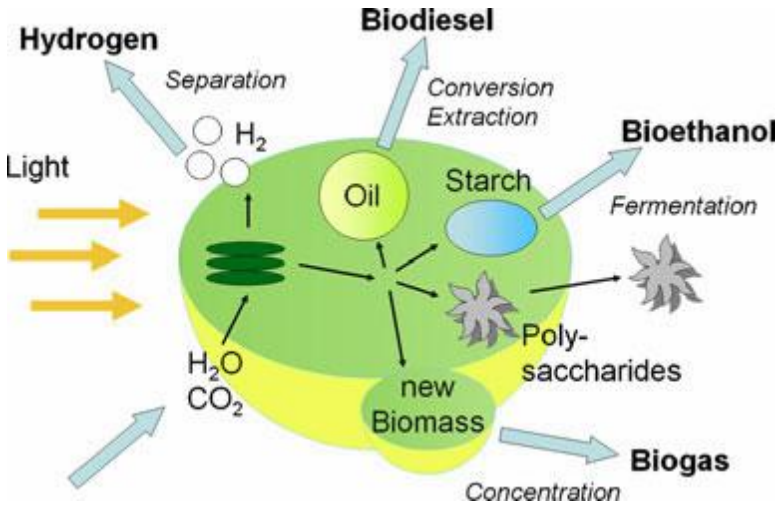

Figure 1.2. Diagram of algal inputs and potential products (Morweiser, et al., 2010)

1.3 What are Algae?

Algae are broadly defined as organisms thatare non-vascular in nature, lacking a differentiated root, stem and leaf system, that contain the photosynthetic pigment *chlorophyll a*(Richmond, 2004). They can be split into two major categories; the macroalgae (such as the seaweeds) and the microscopic sized microalgae (Lundquist, et al., 2010). Algae have been classified using many different systems over the last century, typically based on the coloured pigmentations, storage products and cell wall composition of the various strains. However, in recent years, due to the inconsistencies this approach can generate, phycologists have started to include additional criteria, taking into consideration cytological, morphological and genetic characteristics making the classification process more specific, culminating with the current classification system, see Table 1.1 below (Hoek, Jahns and Mann, 1995; Richmond, 2004).

Table 1.1. Current classification system of algae

Kingdom	Division (Phylum)	Class
Prokaryota	Cyanophyta (Cyanobacteria) – *Blue-green algae*	Cyanophyceae
	Prochlorophyta (Chloroxybacteria)	Prochlorophyceae
Eukaryota	Glaucophyta	Glaucophyceae
	Rhodophyta – *Red algae*	Bangiophyceae, Florideophyceae
	Heterokontophyta	Chrysophyceae – *Golden algae*, Parmophyceae, Sarcinochrysidophyceae, Xanthrophyceae, Eustigmatophyceae, Bacillariophyceae, Raphidophyceae, Dictyochophyceae, Phaeophyceae – *Brown algae*, Oömycetes
	Haptophyta	Haptophyceae
	Cryptophyta	Cryptophyceae
	Dinophyta	Dinophyceae
	Euglenophyta	Euglenophyceae
	Chlorarachniophyta	Chlorarachniophyceae
	Chlorophyta – *Green algae*	Prasinophyceae, Chlorophyceae, Ulvophyceae, Cladophorophyceae, Bryopsidophyceae, Zygnematophyceae, Trentepohliophyceae, Klebsormidiophyceae, Charophyceae

Microalgae have broadly evolved into three major forms of cell organisation; unicellular, colonial and filamentous. Each morphological form has different adaptations, such as flagella for motility. They are capable of rapid growth with typical doubling rates of 24 h for green algae, 17 h for Cyanobacteria (blue-green algae) and other taxa around 18 h, but due to large interspecies variations doubling rates of between 7-8 hours are possible (Griffiths and Harrison, 2009).Microalgae also have the ability to grow in a multitude of 'extreme' conditions such as varying salinity, pH, temperature etc, due to the simplicity of their structures (Richmond, 2004). Over 30,000 species have been discovered and analysed to date, with new species been found regularly via the process of ‘bioprospecting’ for desirable qualities

(Mutanda, et al., 2011; Richmond, 2004). Currently, the main focus of this research is based around oleaginous algal species, which can accumulate large quantities of neutral lipids that have similar properties to oils produced by first and second generation fuel crops (Chisti, 2007).

1.4 Algal Growth Requirements

Micro algae, like any other organism, require a particular set of conditions in which to flourish. The more optimised/similar the conditions are to the alga's natural evolved habitat, the higher the growth rate and productivity they can achieve as a crop. To enable this a number of factors need to be controlled or supplied:

- **Nutrients** - The major nutritional macro-elements required by microalgae are; C, N, P, K, Mg, Ca, the micronutrients required areCo, S, Fe, Cu, Mn, Mo, Si and Zn (Chen, et al., 2011). Certain species also require vitamins such as vitamin B_{12} (cobalamin), B_1 (thiamine) and B_7 (biotin) (Croft, Warren and Smith, 2006a). These nutrients are typically supplied as dissolved inorganic or organic salts in the culture medium or added separately, but in some cases co-culturing can also provide nutrients (Kazamia, Aldridge and Smith, 2012). Different species have greater need of different elements based on their metabolism and composition. The optimisation of the ratios of these nutrients provides a number of benefits, improved cell integrity, lipid storage capacity and proliferation rate of the cells (Danquah, et al., 2010). However, it is also known that the deficiency of a certain key nutrients can induce a radical change in cell metabolism that can be beneficial for biotechnological purposes, i.e. low nitrates often trigger lipid accrual in algae (Chen, et al., 2011). The will be discussed in detail later.

- **Light** - Photosynthetic microalgae require radiative energy (light) to perform the act of photosynthesis (see Figure 1.3). In brief, this process occurs when photons are absorbed by the chlorophyll pigment molecules, which leads to charge separation and the production of electrons. These electrons then dissociate water to make protons and oxygen. These products are used to reduce CO_2 to form various types of biomass with O_2 as a waste product. Stoichiometrically giving:

$$2H_2O + CO_2 \rightarrow [CH_2O] + O_2 + H_2O$$

Overall this process is split into two sets of reactions, which operate on radically different time scales, with light factoring in only one:

  - Light-dependent: $2H_2O \rightarrow 4[H] + O_2 + energy$ (10^{-3}-10^{-15} secs)

- Light-independent: $4[H] + CO_2 \rightarrow [CH_2O] + H_2O$ (secs-hours)

This difference in time scales can lead to inefficiencies if the algae are subjected to varying environmental conditions such as temperature and light radiance (Williams and Laurens, 2010). Photoinhibition due to high intensity light can also lead to the build up of toxic photo products such as H_2O_2, O_2^-, OH and triplet chlorophyll, which can lead to damage of the Photosystem II reaction centre (Figure 1.3). However, at the other extreme, too little light intensity can lead to growth retardation (Xu, et al., 2009).

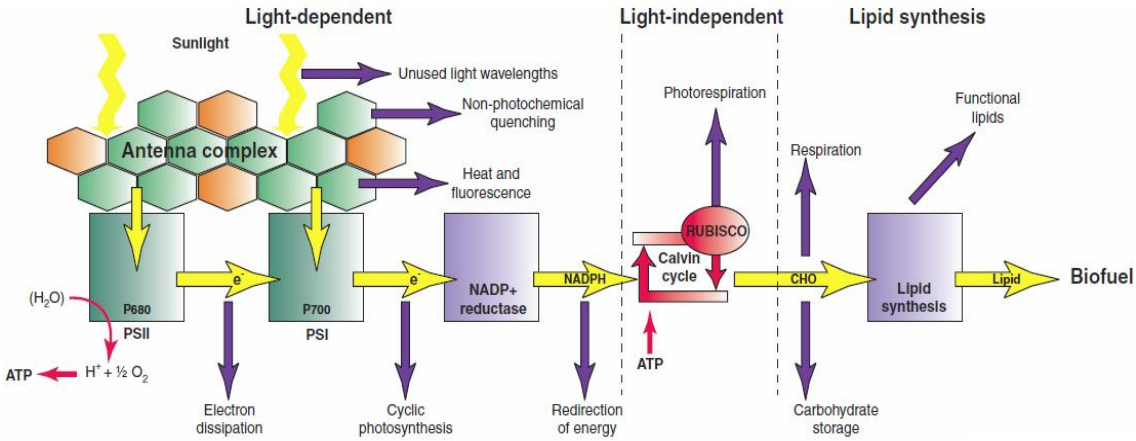

Figure 1.3 - Algal photosynthetic solar energy conversion (Stephenson, et al., 2011)

- **Carbon dioxide, Oxygen& pH regulation** - The availability of a source of carbon is essential for photosynthesis to take place (see the stoichiometry above). Without it an algal cell would not have the fundamental building blocks to manufacture products like carbohydrates (via glucose), fatty acids and amino acids via the Calvin-Benson cycle (Williams and Laurens, 2010). The amount of total inorganic carbon available is directly linked to the pH of the algal growth medium via a series of acid-base equilibria. When CO_2 dissolves into the algal medium it undergoes a series of reactions to form carbonic acid (H_2CO_3), bicarbonate ions (HCO_3^-) and carbonate ions (CO_3^{2-}), with the amount of freely dissolved CO_2 interrelated between the equilibrium concentration of all three types and the solution pH (Figure 1.4) (Zosel, et al., 2011). Certain species of algae are more tolerant to varying values of pH than others and some can also process different types of bicarbonates and ions to use them as an additional carbon source alongside dissolved CO_2. The acidophile *Dunaliella acidophila* (pH 0.7-1.5) and alkalphilic cyanobacteria such as *Spirulina* (pH 9.9-10.4) are extreme examples of algae with this ability, most other species are adapted to the narrow range around neutral pH 7 (Ben-Amotz, E.W. Polle and Subba

Rao, 2009; Chi, O'Fallon and Chen, 2011). To ensure good growth the pH must be regulated and the amount of carbon available to the algae must remain above a certain threshold, both these feats can be achieved by careful monitoring of pH levels and selectively sparging with CO_2. Another factor that needs regulation for continuous growth, is the amount of O_2 present as a by product of photosynthesis. High O_2 concentrations over 400% (~2 nM) can completely stop photosynthesis due to the competing oxygenase activity of the RuBisCO (ribulose bisphosphate carboxylase oxygenase) enzyme (Figure 1.3) (Williams and Laurens, 2010). To prevent this cultures can be purged with other gases or mixed to remove the excess O_2 gas.

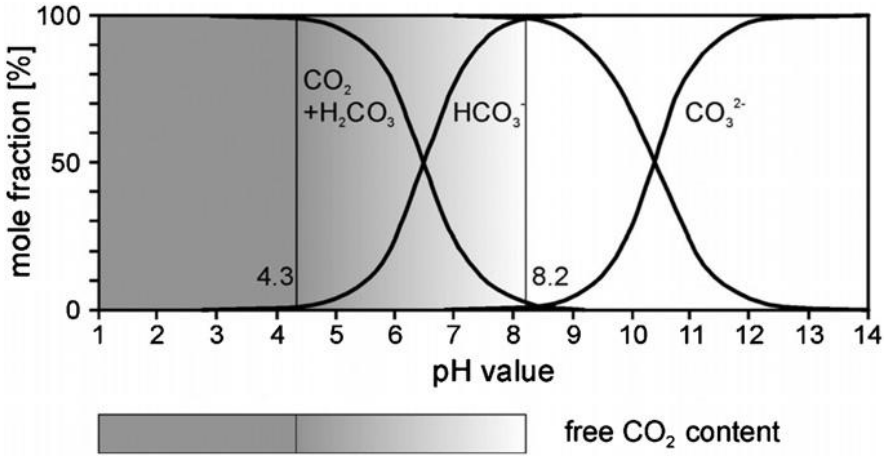

Fig 1.4 - pH carbonate molarity relationship (Zosel, et al., 2011)

- **Temperature -** The regulation of temperature is important to all of the factors previously mentioned. Extremes of temperature can inhibit the photosynthetic pathways, modify the solubility of the algal medium to gases and thus affect the homeostasis of the cultures and overall productivity (Vonshak, et al., 2001).

1.5 Historical Perspectives

The harvesting of microalgae for useful products (including fuel) is not a new concept. Certain species of algae have been collected or 'farmed' for centuries by humans to provide a viable food source. The cyanobacterium *Arthrospira platensis* (*Spirulina*) is one such example that is still collected by the native people living around Lake Chad in Africa (Lundquist, et al., 2010). However, modern biotechnological research into the mass cultures of microalgae began in earnest from 1948, when research teams at Stanford (USA), Essen (Germany) and Toyko (Japan) began to perform initial studies looking at microalgae applicability to food and fuel production (Burlew, 1953b). The first real successful commercial venture to come from this

research was the large scale culture of Nihon Chlorella by the Japanese in the early 1960s for food production (Spolaore, et al., 2006). This was followed by similar projects elsewhere in the 1970s and 1980s cultivating *Spirulina* again for food and *Dunaliella salina* for nutraceuticals (specifically β-carotene) (Borowitzka, 1999). However, it was in the 1970s that the R&D focus was shifted to microalgae as a potential source of renewable fuel as a result of the first Middle East oil crisis (Spolaore, et al., 2006). This situation prompted the U.S. National Renewable Energy Laboratory (NREL) to form the Aquatic Species Program (ASP), a dedicated R&D programme to look at renewable fuels, including biodiesel from microalgae(Sheehan, et al., 1998). The ASP looked at the biochemistry and physiology of lipid production in oleaginous microalgae and ran outdoor test facilities including high-rate open ponds in Roswell, New Mexico (Weissman and Goebel, 1987). The programme also looked at lipid variability between strains using flow cytometry and explored the possibility of using algal viruses as genetic vectors to modify the algae. However unfortunately, due to decreasing interest in renewable fuels because of the recurrent cheap price of oil, the programme's funding was cut which led to it closing in 1995. Sadly, the ASP work never progressed beyond the preliminary stages, but from their data it was concluded that the low cost production of biodiesel using microalgae was technically feasible, but required considerablymore R&D work(Sheehan, et al., 1998). With recent concerns over climate change, oil price volatility and national energy security, there has been a renewed interest in microalgal biofuels and products, leading to the establishment of ASP style programs internationally (US-DOE, 2013) and the creation of various new microalgal companies (Chisti, 2013).

1.6 Microalgal Bottlenecks and Current Developments

Since the resurgence of interest in algal biofuels and products in the last decade, great progress has been made toward commercialisation, however thus far large scale production has remained out of reach due to a number of factors which are summarised below, along with proposed possible future solutions.

Carbon dioxide supply restriction

To grow microalgae at maximal production rates, carbon dioxide must be provided in sufficient quantities to not be a source of resource limitation. Although many species of algae have natural adaptations that can concentrate CO_2 from the surrounding growth medium and get it into the cell (Meyer and Griffiths, 2013), the amount of CO_2 provided by atmospheric air (~0.039%) is insufficient (using all current methods) to enable growth at high productivity rates (Kumar, et al., 2010). Therefore, algal culture for fuel production is only possible if there is a

source of enriched CO_2 available, such as the flue gases produced by burning fossil fuels or from industrial processes like cement production. However, as useful as this method is for sequestration purposes (Pokoo-Aikins, et al., 2010), in the long term this approach is environmentally flawed for fuel production as "no oil can be produced unless fossil fuels are burned" (Chisti, 2013). Purchasing enriched CO_2 is another possible approach but the economics are not favourable; per ton of algal biomass 1.83 tons of CO_2 is needed, which would mean ~50% of product expenditure would be on gas supply alone, thus mass production is not feasible unless the CO_2 is available for free (Chisti, 2007). There are some avenues showing progress in this regard; current organic and inorganic Carbon Capture and Storage (CCS) technology is improving constantly, once the price is reduced this could potentially provide a steady stream of enriched CO_2(Figueroa, et al., 2008; Savile and Lalonde, 2011). Also, rather than using enriched gas, certain species of algae can metabolise bicarbonates depending on pH, this potentially could reduce operational costs because it bypasses the carbonate regeneration step (Chi, O'Fallon and Chen, 2011). There is also a great deal of interest currently in growing algae under hetrotrophic/mixotrophic growth conditions using the organically fixed carbon sources from terrestrial plants/waste (Inc, 2013; Liang, 2013). However, the renewable benefits of these approaches are dubious in the long term as there are more steps required to reach a final product ('indirect photosynthesis') and mixotrophic production is prone to serious contamination problems with bacteria using the same carbon source (Chisti, 2013).

Availability of Nitrates and Phosphates

Algal growth is also constrained by the availability of nitrogen and phosphorus. Most nitrogen based fertiliser is produced utilising fossil fuels and the highly energy intensive Haber-Bosch process, which is far from sustainable (Galloway, et al., 2013). Phosphorus is a finite resource which is mined in limited locations worldwide and is currently recycled on a very small scale, availability of it in the near future is seen to be a significant upcoming problem (Scholz, et al., 2013). Large quantities of both nutrients would be needed in the commercialisation of algal biofuels, for example; to produce 82 million tons of algal biomass (enough to cover 9 days of US petrol consumption), 44% of the US annual production of nitrogen would be required (Chisti, 2013). The same biomass would also require 1.1 million tons of phosphorus. Based on this, the supply of both of these nutrients using current methods would not be of sufficient scale to enable the mass production of algal biofuels alongside that of terrestrial plants (Chisti, 2013). Thus far there seems to be a few limited options to combat these problems; the first is using the products of anaerobic digestion (AD) to recycle the nutrients (see below), but the

quantities produced would not be able to fulfil the entire requirement (Chisti, 2008a). The second is genetically engineering the algae to fix nitrogen or co-culture them with cyanobacterial species which naturally perform this process, but there is still a great deal of research that needs to be performed to make this a reality (Ortiz-Marquez, et al., 2013; Pfreundt, et al., 2012).

Lipid productivity

In the previous work of the ASP and other research of the time, two main strategies were typically pursued towards creating biofuels from algae; the first was to isolate, screen and catalogue high lipid producing strains. The second was to identify rate limiting enzymes for the production of lipids and modify the promising organisms genetically to produce a better yield (Sheehan, et al., 1998). Unfortunately, although they identified many promising species, the project was terminated while work on the second objective was just starting. The most common approach today to increase the lipid productivity of a high lipid accruing strain (such as the ones isolated in the ASP) is to apply some type of physiological stress, such as nitrate deprivation to induce a metabolic 'stress' response (note, this approach will be discussed later in greater detail). However, this method has a cost in terms of reduced growth rates (and production of other useful cell products) while the lipids are produced in greater quantities in the 'stressed' cells, so overall biomass productivity can be affected (Williams and Laurens, 2010). Recent work has tried to avoid this problem by using genetic modification to enhance lipid biosynthetic pathways using new novel approaches such as transcriptomics, proteomics and protein interaction studies coupled with directed mutagenesis and protein design (Figure 1.5). These methods have been used to over express rate limiting enzymes (essentially carrying out the work the ASP started), to modify the enzymes themselves and to alter gene expression to make the biochemical algal lipid profiles more suitable for fuel production (Blatti, Michaud and Burkart, 2013; Khozin-Goldberg and Cohen, 2011; Liu and Benning, 2013). Work on engineering certain species to excrete lipids is also being pursued with good data arising (Liu, Sheng and Curtiss, 2011). However, even considering all of these recent advancements, there is still a long way to go before a commercially viable 'model' alga is available as these techniques are in their infancy. The first important step will be the mapping of the entire lipid pathway in algae and finding out how it is regulated, only then can it be modified to suit biofuel production purposes (Liu and Benning, 2013).

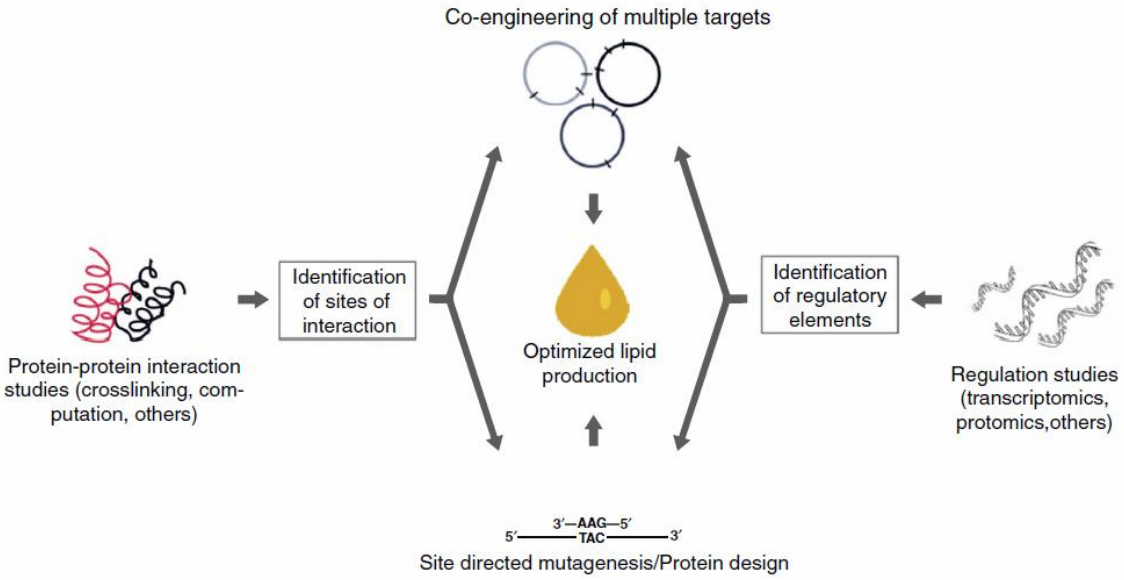

Figure 1.5 - New approaches for genetic engineering in microalgae and cyanobacteria, including the study of protein–protein interactions and regulatory networks with co-engineering of codependent proteins, site-directed mutagenesis, and protein design. (Blatti, Michaud and Burkart, 2013)

Light limitation

The amount of light that microalgal cells receive is critical to their photosynthetic efficiency and overall productivity, as mentioned in the previous section. In current growth systems, maximal productivity cannot be attained due to various degrees of light limitation. This is typically caused by two mechanisms; when the cultures become densely populated with cells it begins to self shade, so light cannot reach a proportion of the cells (Figure 1.6). The second is caused by photoinhibition, this can occur if the light level is as little as 10% of peak midday sunlight in a tropical region (Chisti, 2013). One potential solution is by controlling the mixing rates so that the algae are re-circulated in such a way that the cells experience a rapid light-dark exposure cycle (Grobbelaar, Nedbal and Tichy, 1996; Sforza, et al., 2012). This enables the cells to get a more even exposure to the light without saturation and if timed correctly achieve greater efficiency due to sympathetic timings aligned with the 'light/dark' reactions during photosynthesis (Yago, et al., 2012). However, the extra mixing required can increase energy costs and the turbulence can potentially damage cells (Silva, Cortinas and Ertola, 1987). Another approach is to increase the photosynthetic efficiency of the algae via genetic engineering . However, potential solutions in this area are made difficult by the algae's natural adaptations. When overexposed to high irradiances, the algae adapt by reducing the size of the light harvesting antennae to reduce the number of photons getting to the photosystem to avoid damage. Unfortunately this adaptation takes much longer than the rate of photosynthesis to occur and relies on the algae been exposed to the same irradiance from 10-60 minutes (Williams and Laurens, 2010). As cultured algal cells are constantly been moved in

growth systems, this means that constant exposure is not achievable. To further complicate matters, the algae also will revert back and elongate the antennae if removed from high light again, so an entire culture can be in different states of photosensitivity. Current genetic work is looking at the possibility of reducing the algal antenna to a fixed short size, so high light can be used with mixing to maximise productivity, as the irradiance would be able to penetrate deeper into the culture (Figure 1.6) (Melis, 2009). There has been some success in this area so far, but issues with algal cells producing other pigments to compensate and knock-on metabolic consequences still need to be addressed (Blankenship and Chen, 2013). Another approach is to engineer the algae to make use of wavelengths outside of the typically utilised photosynthetically active radiation (PAR) region (400-700 nm). Certain types of algae like the cyanbacterium *Acaryochloris marina* absorb light in the 700-750 nm region using the less common chlorophyll d pigment, if the genes required to produce this pigment could be expressed in 'typical' marine algae with basic chlorophyll a & b pigments the photosynthetic efficiency could potentially also be increased (Blankenship and Chen, 2013). Overexpression of the photosystems and engineering enzymes such as RuBisCo are other avenues for improving light harvesting efficiency, this and details of the other genetic methods are summarised in the review by (Stephenson, et al., 2011).

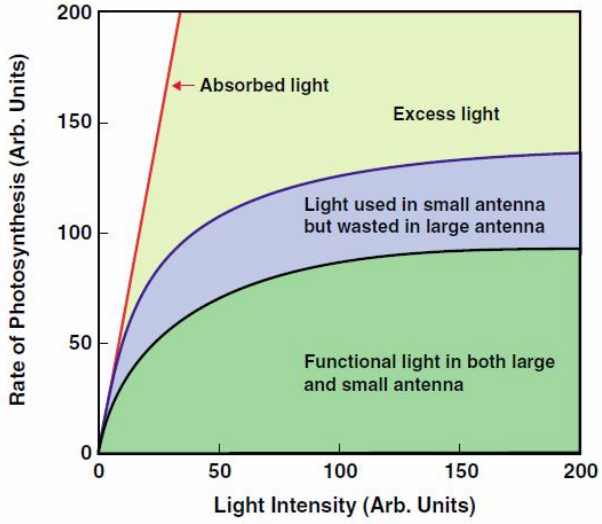

Figure 1.6. - Schematic light response curve for photosynthesis, where:

Black line: *saturation curve of the rate of photosynthesis versus light intensity.*
Red line: *absorption of light, which is linear with intensity.*
Blue line: *predicted light response curve for an antenna-reduced organism*
Green area: *functional light which drives photosynthesis*
Light green area plus blue area: *excess light, which is absorbed but cannot be used to drive photosynthesis.*

(Blankenship and Chen, 2013)

Biomass Recycling& Anaerobic Digestion

For the mass production of algae to be economic and sustainable it is widely acknowledged that there must be a high degree of process integration (Gebreslassie, Waymire and You, 2013). This suggested approach includes the recapture of nutrients by recycling the spent biomass, then anaerobically digesting the rest to produce biogas that can be used to provide power to the overall system. However, there is a major limitation with this process; any salt

present in the system could potentially kill the AD microbesand the products of the AD would also be unsuitable for further processing (use as fertiliser) (Liu and Boone, 1991). This situation is likely to be a problem because marine algae are currently the most suitable for the large scale production of biomass (Chisti, 2013). The salts can be removed by cleaning with fresh water, but as this is a scarce resource its inclusion in any biofuel production system would be very unsustainable (hence the recommended use of marine species). There is also very little information available on the AD performance of algal biomass that has had the oil extracted already, compared to whole cell digestion, which has been previously been studied in detail (Rashid, Rehman and Han, 2013). To tackle the AD problems, the use of halophilic methanogens has been suggested (Riffat and Krongthamchat, 2007), but these microbes are currently untested in commercial AD systems, so further development work is required (Chisti, 2013). Another option that has received considerable attention of late is hydrothermal liquefaction, this method can turn moist biomass into crude fuel and combustible gas simultaneously, completely replacing the traditional oil extraction and anaerobic digestion steps (Barreiro, et al., 2013). However, this method (and other similar variants) still require further developments to become technically feasible and carbon neutral (Biller, Friedman and Ross, 2013; Khoo, et al., 2013).

Wastewater treatment

This area of process integration has also received renewed interest recently for biofuels production. Waste water is a rich source of nitrogen and phosphorus, which if utilised could be extremely useful for the growth of algae in an integrated manner. This concept has been around since the 1960s and the advent of the ASP (Sheehan, et al., 1998). When coupled with modern high rate algal ponds designs (HRAP), there are potential for a number of benefits, including; energy efficient tertiary level wastewater treatment, reduced costs for algal production (capital and operational), lower cost harvesting (when coupled with bioflocculation), nutrient recovery and green house gas abatement (Craggs, Sutherland and Campbell, 2012; Craggs, et al., 2011). This integrated concept has been shown using financial models to be the only current concept, when coupled with flue gas, with a "favourable outcome for near-term, large-scale biofuels production from microalgae" (Batten, et al., 2013). However, the potential yields for fuel generated by this system are again restricted by fundamental resource availability, CO_2 (as discussed previously) and nutrient availability from the waste water, thus in an optimal case only 1% of the petrol demand in a large US city has been met (Chisti, 2013).

Water usage

The availability of water is of great importance worldwide as it is the basic resource for life, agriculture and industrial production. Unlike oil, water is part of a closed hydrological cycle so it will not be completely diminished over time. However, the availability of fresh water, which only constitutes 2.5% of the total water on earth (most of this is stored in glaciers or deep underground), can fluctuate greatly regionally over time (Oki and Kanae, 2006). This variation, coupled with an increasing global population and the effects of climate change (acceleration of the water cycle, extreme weather), mean that this resource will be at a premium in the coming decades (IPCC, 2013). This is one of the key reasons that mass production of algae is only sustainable using marine based strains, as seawater is abundant in many locations at any period of time. However, even using halophilic species (marine algae and possibly methanogens for AD), there would still be a need, albeit reduced, for fresh water. This arises from two major factors; the need to replace evaporative water losses in open pond cultivation to ensure that the salinity level stays within algal tolerance levels and fresh water is also needed for removal of salt from the harvested biomass (Chisti, 2013). Even when taking this into consideration the water footprint of marine micro algae is much better than terrestrial crops, but still much higher than petroleum extraction and refinement (Yang, et al., 2011). The only foreseeable solution to this water usage, would be the development of more efficient water recycling methods, the use of more extremophilic algae (such as *D. salina*) which would cope with greater NaCl variation or providing renewably powered de-salination for use at the growth plant (Baten and Stummeyer, 2013; Ben-Amotz, E.W. Polle and Subba Rao, 2009; Pate, Klise and Wu, 2011).

Limitations in production technologies

Current culturing methods using basic photo-bioreactors and open race way ponds have not changed radically from those first pioneered in the ASP back in the 1980s (Sheehan, et al., 1998). While these methods are robust and established, the productivities have been shown to be much lower that the theoretical maximum due a combination of light limitation, gas transfer (both mentioned previously) and energy inefficiency (Weyer, et al., 2010). "Novel biomass production methods that rely on sunlight, achieve high productivity and biomass concentration in the broth, and are inexpensive and energy efficient, are needed" (Chisti, 2013). The various systems currently available and potential improvements are discussed later in detail.

Overview

In order for algal biofuels to be an overall success commercially and climatologically, the end product must be produced at a net energetically favourable ratio. i.e. the energy in the algal oil product must be greater than the fossil derived equivalent (Chisti, 2008b). This feat also needs to be achieved with a minimal carbon footprint, that is, less greenhouse gases are produced net than with the comparable traditional manufacture and use of petroleum (Zamboni, et al., 2011). Thus far the performance of predictive models looking at both factors show mixed conclusions, due to inconsistencies in methodological approach and a lack of experimental evidence (Chisti, 2013). This variation has also led to estimates of biodiesel cost varying quite considerably; from $0.42 to >$75 per litre depending on the overall choice of processing. When these figures are compared with the latest figures from the US Energy Information Administration for fossil diesel at $1.046 per litre (as of Sept 2013), it is clear that only the figures at the lower end of the range will enable algal biodiesel to be commercially competitive (EIA, 2013; Nagarajan, et al., 2013). Another major hurdle that must be overcome is one of public perception, based on current estimates the only way that algal biofuels can become truly competitive in the longer term is with some form of genetic modification (GM) (previously discussed). Resistance to GM crops is very strong in some countries (such as the UK), so assurances need to be made that transgenic algae cannot proliferate in natural habitats and these need to be accepted by the public and governmental bodies (Borowitzka and Moheimani, 2013; RFA, 2008). As the most favourable figures discussed tend to be based on overly favourable scenarios in terms of algal production efficiency, it is clear that a great deal of further work needs to be performed to solve the technical bottlenecks mentioned here before 3rd generation biofuels can become a reality.

1.7 Strains of Interest

When bio-prospecting for suitable algal biofuel strains there are a number of desirable characteristics that are typically looked for, see Table 1.2 compiled by (Griffiths and Harrison, 2009).

Table 1.2. Desirable biofuel strain characteristics

Characteristic	Advantages	Reference
Rapid growth rate	Competitive advantage over competing species; reduces culture area required	(Borowitzka, 1992)
High product content	Higher value of biomass. (Note: use of metabolic energy to generate product usually leads to slower growth)	(Borowitzka, 1992)
Growth in extreme environment	Reduces contamination and predation. (Note: Limited number of species can grow in extreme environments. Can be difficult to maintain conditions)	(Borowitzka, 1992)
Large cell size, colonial or filamentous morphology	Reduces harvesting and downstream processing costs	(Borowitzka, 1992)
Wide tolerance of environmental conditions	Less control of culture conditions required. Growth over range of seasons and ambient weather conditions	(Borowitzka, 1992) (Grobbelaar, 2000)
CO_2tolerance and uptake	Greater potential for CO_2sequestration and use of waste CO_2	(Grobbelaar, 2000)
Tolerance of shear force	Allows cheaper pumping and mixing methods to be used	(Borowitzka, 1992)
Tolerance of contaminants	Potential growth in polluted water and on flue gases containing high CO_2, $NO_x$and SO_x	(Phycological Society Of, 1995)
No excretion of autoinhibitors	Reduces autoinhibition of growth at high biomass densities	(Grobbelaar, 2000)

Based on the criteria in Table 1.2, the research bottle necks previously mentioned and current commercial ability, three promising marine algal strains were selected for use in this study. Note, genetic engineering was not included in the selection criteria as this was not deemed to be possible in the project time scale alongside the chemical engineering aspects of the simulation and growth system design.Details of the strains and their attributes are provided in the following sections.

1.7.1 *Tetrasemlis suecica*

Tetraselmis suecica CCAP 66/4 is a member of the *Chlorophyta* (green algae) and is found in the *Chlorodendrales* group within the class *Prasinophyceae* (Figure 1.8). Strain CCAP 66/4 was isolated 10 miles off the coast south of La Spezia, Italy(CCAP, 2013d). It is typically grown commercially as an aquaculture feedstock in various types of photo-bioreactor systems (Day and Fenwick, 1993; Naumann, et al., 2013). It is considered to be an optimal source of long-chain PUFAs which are essential for filter feeders grown in aquaculture systems(Fabregas, et al., 2001). It has been demonstrated that the cultivation

Figure 1.8. *Tetraselmis suecica* CCAP 66/4

conditions it is exposed to can have a dramatic impact on its overall lipid production profile, because of this it is an excellent prospect as a potential biofuel feedstock as it can be 'stressed' to over produce useful lipids (Sanchez-Garcia, et al., 2013). The types of fatty acids it produces are predominantly C16:0 and C18:1 which are good for biodiesel production (Mendoza Guzman, et al., 2010). Its lipid content per % dry weight biomass is modest (8.5-23) but it has a high lipid productivity (Griffiths and Harrison, 2009; Mata, Martins and Caetano, 2010). One negative for mass culture *ofT. suecica* is the presence of a cell wall, which would need to be broken for lipid extraction. Due to its proven track record in commercial production using photo-bioreactors and lipid potential it was included in this work as a growth reference alga.

1.7.2 *Nannochloropsis oculata*

Nannochloropsis oculata CCAP 849/1 (Figure 1.9) is a member of the *Heterokontophyta,* specifically within the class*Eustigmatophyceae.* Strain CCAP 849/1 originated from Skate Point, Isle of Cumbrae, Scotland (CCAP, 2013c).This species, like *Tetraselmis,* is again widely utilised in marine aquaculture due to its production of the essential PUFA eicosapentaenoic acid (C20:5) (Sukenik, Zmora and Carmeli, 1993). *Nannochloropsis* has also been put forward as a potential source of nutritional PUFAs for human consumption(Zittelli, Pastorelli and Tredici, 2000).Due to the strains high natural productivity of mono-unsaturated C16:1 its has also been of interest for biofuels production (Chiu, et al., 2009b). This ability is also coupled with very useful shifts in lipid profile in response to nitrate deprivation, light saturation and salinity, where longer exposure times lead to a reduction in large PUFAs (such as C20:5) and an increase in C16:0, C16:1 and C18:1 fatty acids making it an ideal candidate for good quality biodiesel production (Pal, et al., 2011; Van Vooren, et al., 2012). Its lipid content per % dry weight biomass is also very high at (22.7-29.7) with a high lipid productivity (Griffiths and Harrison, 2009;Mata, Martins and Caetano, 2010). Also like *Tetraselmis* the alga has robust cell wall which is very strong due to its smaller size and more spherical shape, this fact is a negative for biofuel production (Chen, Sommerfeld and Hu, 2011).Again due to its proven track record in commercial operations and excellent lipid potential it was included in this work as a growth reference alga.

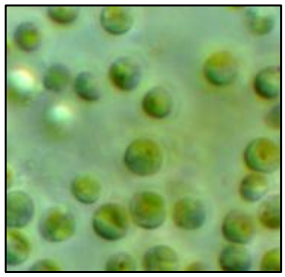

Figure1.9.*Nannochloropsis oculata* CCAP 849/1 from (CCAP, 2013c)

1.7.3 *Dunaliella salina*

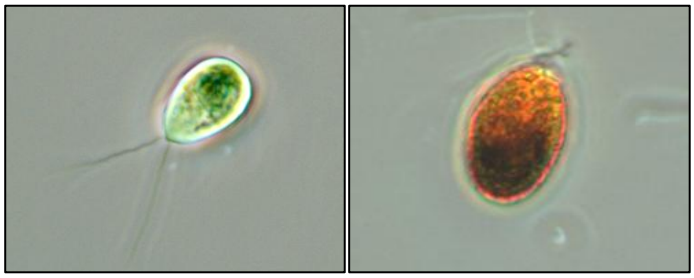

Figure 1.10 - *D. salina 19/30*, with standard green algal pigments (left), *D. salina 19/18*, with overproduction of β- carotene (right)

The two main strains of interest in this work both belong to the genus *Dunaliella*(Figure 1.10), *D.salina* CCAP 19/18 is a member of the green algae (*Chlorophyta*) of the group *Volvocales* within the class *Chlorophyceae*.CCAP 19/18 strainwas isolated from the hypersaline brine at Hutt Lagoon, Western Australia (CCAP, 2013a) *D.salina* CCAP 19/30 is a of the same lineage but isolated fromtheBardawil lagoon, North Sinai, Israel (CCAP, 2013b). Both strains have almost identical 18S rDNA sequences, but their phenotypes show one key difference, the 19/18 strain overproduces the β-carotene pigment ,which can be clearly seen as an orange colouration in Figure 1.10,) whereas the 19/30 strain does not. There is a great deal of confusion in the literature regarding the designation of the different *Dunaliella* species based around this pigmentation difference, the designation *D.bardawil* appearing in some cases to represent either or both pigment variants (Olmos, et al., 2009). For the sake of clarity in this study, *D. salina* 19/18 will be associated with the β-carotene overproducing variant and *D. salina* 19/30 with the 'regular' type exhibiting a standard balance of the photosynthetic pigments chlorophyll a and b. Alongside the production of pigments, *D. salina* also has other unique attributes; the ability to grow in a range of extreme salinities (up to 5 M NaCl), a wide tolerance to heavy metals and pesticides and, unlike many other algal species no cell wall (Borowitzka and Siva, 2007). These properties led to the development of *D. salina* as one of the first major successful commercial algal crops in the 1970s, as its high salinity tolerance allowed the alga to be cultured in outdoor ponds at scale without fear of contamination (Ben-Amotz, E.W. Polle and Subba Rao, 2009). This feature, along with the overproduction of the financially lucrative β-carotene (used as a nutraceutical) and no cell wall (cheaper harvesting) provided an economically viable model that is still in operation by a small group of companies today (Raja, Hemaiswarya and Rengasamy, 2007).

Given this well established history of successful mass production and favourable attributes, *D. salina* has good potential to be successful as a biofuel crop. However, the lipid productivity of the strain in the literature has shown large amounts of variance; 10-35%lipid content per dry weight biomass, but with relatively high overall biomass yields (Griffiths and Harrison, 2009).Intraspecific variants of *D. salina* have also been shown to have a lipid profile high in

C16:0, C18:0 saturated fatty acids and PUFA C18:3, which can be detrimental for biodiesel production (see section 1.9)(Guzman, et al., 2012). However, it has also been observed that a reduction in PUFA and a increase in C18:1 fatty acids could be linked to high levels of β-carotene production, which would mean overproducing strains like 19/18 could be more favourable (Mendoza, et al., 1999). A similar shift in fatty acid content has also been observed in certain NaCl 'stress' experiments (Xu and Beardall, 1997). Recent work by the Zimmerman research group at Sheffield university has also shown that *D. salina* is an excellent candidate for growth using industrial flue gas in custom made photo-bioreactors (Zimmerman, et al., 2010b). So, regardless of the slightly underwhelming previous lipid performance, this species of algae has a range of other attributes that give it merit as a biofuel crop (salt tolerance, ease of oil extraction etc). As these factors have a very large impact on the energy/water balance of the overall production process, *Dunaliella* is well worth consideration in biofuel research (Chisti, 2013).

1.7.4 Bacterial Symbiosis

As *D. salina* is the main strain of interest in this work its special relationship with bacteria is worthy of note as it is typically cultured commercially in non-axenic conditions. It has been hypothesised that*D. salina* has a relationship with certain types of halophilic bacteria and archaea due to availability of glycerol in saltern crystallizer pond ecosystems, where the strain originates (Bardavid, Khristo and Oren, 2008). *D. salina* produces significant quantities (6-7 M) of intracellular glycerol to serve as a compatible solute, which allows the cells to survive and function in the harsh high salt environments (Ben-Amotz, E.W. Polle and Subba Rao, 2009). It is assumed that this glycerol produced by the algae is one of the main carbon and energy sources for heterotrophic microbes in the saltern environment (Borowitzka, 1981). The mechanism of how the glycerol becomes available in the environment is thought to be due to leakage through the membrane of viable cells or when they lyse and it is released. In either case, the precise mechanism appears to be highly strain specific (Fujii and Hellebust, 1992; Hard and Gilmour, 1991; Wegmann, Benamotz and Avron, 1980). It has been shown in other research that bacteria can perform symbiotic roles within algal communities by producing certain vitamins and other products that are beneficial to the algae (Kazamia, Aldridge and Smith, 2012). Although there is no current evidence that *D. salina* needs vitamins produced by bacteria (Croft, Warren and Smith, 2006b), there has been research that has shown the bacterium *Halomonas* can improve the growth of the strain under iron deficient conditions potentially by the production of bacterial siderophores (Butler, 1998; Keshtacherliebson, Hadar and Chen, 1995). As members of this species can use glycerol as a carbon source (along

with sucrose, mannose and cellobiose) and are aerobes with similar physical tolerances to *Dunaliella* (pH 5-9, up to 20% NaCl and temp 4-45^{o}C), it is very possible a symbiotic relationship exists(Vreeland, Anderson and Murray, 1984; Vreeland, et al., 1980). Based on this reasoning, axenic culturing of *D. salina*is not needed and could possibly be detrimental to the health of the strain under certain conditions.

1.8 Lipids and Stress

1.8.1 Algal Lipids

A lipid can be classified as any biological molecule that is soluble in some form of organic solvent, as such it covers a large range of different types and structures (Halim, Danquah and Webley, 2012). The lipid type that is of most direct consequence to biodiesel production is the fatty acid (FA) and its variants. A fatty acid molecule consists of a hydrophilic carboxylate group (RCOO-) that is attached to one end of a hydrophobic hydrocarbon chain. They are classified using a number of different systems, which designate them based on the total number of carbon atoms and the number of double bondsin the FA chain (Blaha, et al., 1987; Nelson and Cox, 2004). Saturated FAs have no double bonds present, whereas unsaturated FAs have at least one. When a FA has more than one double bond present it can be classified as poly-unsaturated or a PUFA.

Lipid molecules can have a charge and thus they can be classified as either net polar or neutral. Thus when the carboxylate end of the fatty acid molecule bonds to an uncharged head group (such as glycerol), a lipid molecule is formed with a neutral change, such as triacylglycerol (which has three FAs) or a singular free fatty acid (FFA). Alternatively, if the FA bonds to a charged group head, such as a glycerol and phosphate complex a polar lipid molecule is formed such as a phospholipid. Neutrally charged lipids are predominantly used as a form of energy storage in microalgalcells, whereas polar lipids are combined to form phospholipid cell membranes. There are also othertypes of neutral lipids that do not contain FAs, such as hydrocarbons (HC), sterols (ST), ketones (K), pigments (carotenes and chlorophylls), but they are not convertible to biodiesel(Halim, Danquah and Webley, 2012).

As discussed previously the amount of total microalgal lipid content varies radically from one species to another in terms of dry biomass, from 5 to 77 wt.% (Chisti, 2007). The types of lipid within this figure also can vary widely between species, with some having more of an affinity for biodiesel production due to a greater proportion of neutral lipids (Zhukova and Aizdaicher, 1995). This matter is further complicated by the stage of the microalgal growth cycle and the

environment the algae are exposed to such as the medium composition, temperature, illumination intensity, ratio of light/dark cycle, and aeration rate, all of which can alter the types of FA produced(Mendoza Guzman, et al., 2010). Microalgae typically have larger amounts of polar lipids in the log growth phase compared to the stationary phase (Lv, et al., 2010). Nutrient starvation and other environmental 'stress' effects can also have a major effect on lipid composition, see section 1.8.3 (Solovchenko, 2012). Due to this variation, the suitability of algal lipids for biodiesel production needs to be assessed on a strain/condition/time basis. Neutral acylglycerol lipid classes are more sought-after for two reasons; acylglycerols typically have a lower amount of unsaturation in their structure than the polar type lipids, and can produce biodiesel with higher oxidation stability. Secondly, existing industrial-scale alkaline-catalyzed transesterification processes (see section 1.8.4)are optimised to process acylglycerols and have limited efficiencies at processing other lipid fractions, such as polar lipids and free fatty acids (Lang, et al., 2001).

On average oleaginous green algae have a total lipid content of 25.5% DCW, which can double or triple when the cells are put under 'stress' conditions (Hu, et al., 2008). Lipid accumulation also occurs when cells come to the end of their life cycle. In either case, the lipid increase comes primarily in the form of the neutral acylglycerols. This is due to a shift in lipidmetabolism from membrane lipid synthesis to the storage of neutral lipids as cell division is no longer a priority(Hu, et al., 2008). *De novo* (from the beginning) biosynthesis and conversion of certain existing membrane polar lipids into triacylglycerols are thought to contribute to this increase(Tonon, et al., 2002).Algae synthesize FAs as the first building blocks in the formation of a range of lipids, which typically range from 12 to 22 carbons in length and can be either saturated or unsaturated. However, the number of double bonds in the FA chains, never exceeds 6 and almost all of the unsaturated fatty acids are cis isomers (Medina, et al., 1998). The most common chain lengths are C16 to C18, similar to that of higher plants(Ohlrogge and Browse, 1995).Of these FAs, the saturated and mono-unsaturated variants occur the most in algae (Borowitzka, 1988). A list of the major types of FAs and PUFAs produced by each classification of algae is shown in Table 1.3. A comparison of the major groups of FAs produced by microalgae and cyanobacteria to those produced by plants (first generation biofuel crops is shown in Figure 1.11. It is clear that a wider range of fatty acid types are found in the microalgae/cyanobacteria groups.

Table 1.3 - Main lipid types found in different algae classes (Basova, 2005;Cobelas and Lechado, 1989;Hu, et al., 2008)

Algal class	Fatty acids	PUFAs
Bacillariophyceae	C16:0, C16:1	C20:5ω3, C22:6ω3
Chlorophyceae	C16:0, C18:1	C18:2, C18:3ω3
Euglenophyceae	C16:0, C18:1	C18:2, C18:3ω3
Chrysophyceae	C16:0, C16:1, C18:1	C20:5, C22:5, C22:6
Cryptophyceae	C16:0, C20:1	C18:3ω3, C18:4, C20:5
Eustigmatophyceae	C16:0, C18:1	C20:3, C20:4ω3
Prasinophyceae	C16:0, C18:1	C18: 3ω3, C20:5
Dinophyceae	C16:0	C18:5ω3, C22:6ω3
Prymnesiophyceae	C16:0, C16:1, C18:1	C18:2, C18:3ω3, C22:6ω3
Rhodophyceae	C16:0	C18:2, C20:5
Xanthophyceae	C14:0, C16:0, C16:1	C16:3, C20:5
Cyanobacteria	C16:0, C16:1, C18:1	C16:0, C18:2, C18:3ω3

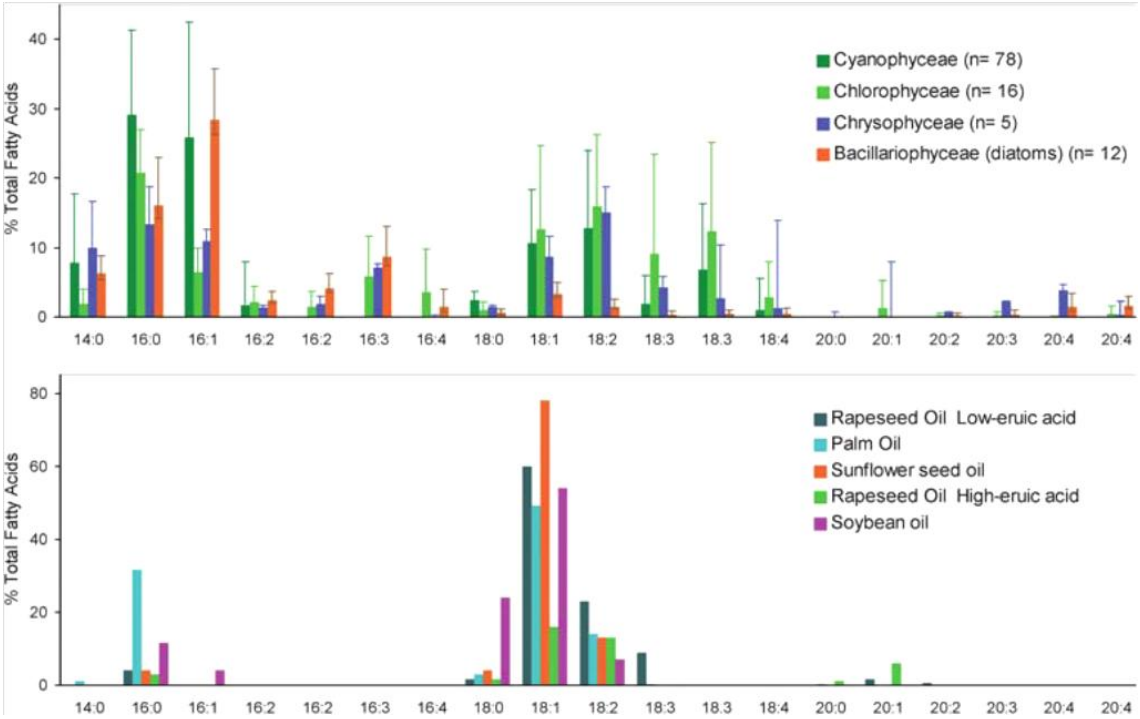

Figure 1.11 (a): Mean fatty acid composition of various eukaryotic algal groups and Cyanobacteria. n= numbers of analyses data derived from. Error bars are standard deviations. (b): Higher plant fatty acids (Williams and Laurens, 2010)

1.8.2 Biosynthesis of fatty acids

Lipid metabolism and the biosynthetic pathways of FAs have been poorly studied in algae compared with higher plants such as *Arabidopsis*(Liu and Benning, 2013).Current understanding of algal pathways is based upon shared biochemical characteristics of a range of genes and enzymes isolated from algae (typically *Chlamydomonas reinhardtii* as this is most well studied species genetically) and selected higher plants(Hu, et al., 2008). As such, there are

many broad generalisations made, which could potentially be wrong. Work is ongoing to compare the pathways between plants and microalgae, the current understanding is summarised in Figures 1.12 to 1.14, detailed information can be found in the work by (Hu, et al., 2008). The synthesis of fatty acids takes place primarily in the chloroplast (Figure 1.12), where glycolysis and pyruvate kinase (PK) catalyze pyruvate to form phosphoenolpyruvate (PEP), which is subsequently converted to acetyl co-enzyme A (CoA). The *de novo* synthesis pathway creates C16 and/or C18 FAs (Figure1.13).The first step is when ACCase catalyzes the formation of malonyl CoA from acetyl CoA and CO_2.These 'precursor' FAs are then used for the synthesis of chloroplast and other cellular membranes as well as for the synthesis of neutral storage lipids, such as TAG (Figure 1.14).

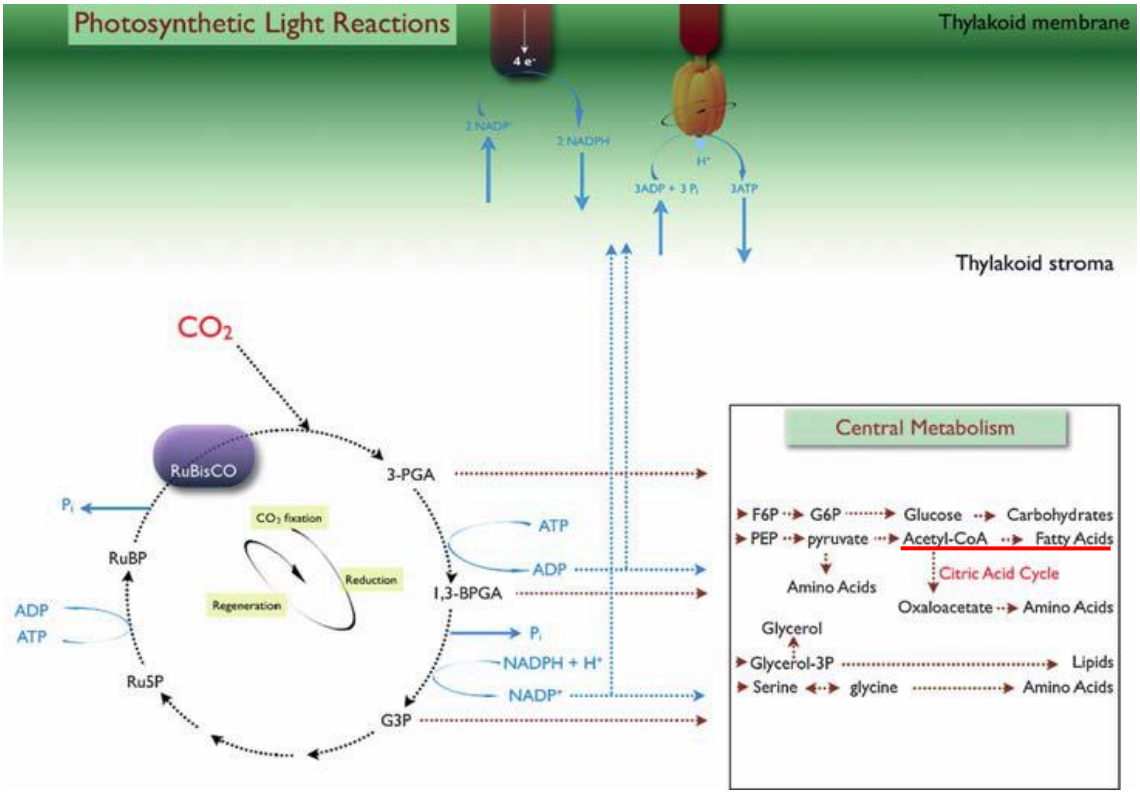

Figure 1.12. Schematic simplified representation of the Calvin-Benson cycle in three parts, (i) CO_2 fixation, (ii) reduction and (iii) regeneration. The average cycling time of one 'round' of CO_2 assimilation is 100 to 500 ms. The necessary energy (ATP) and reductant ($NADPH^+ + H^+$) (not shown stoichiometrically) are originating from the photosynthetic light reactions. RuBisCO: ribulose bisphosphate carboxylase/oxygenase; RuBP: ribulose-1,5- bisphosphate; 3-PGA: 3-phosphoglycerate; 1,3-BPGA: 1,3 bis-phosphoglycerate; G3P: glyceraldehyde-3-phosphate; F6P: fructose-6-phosphate; G6P: glucose-6-phosphate; PEP: phosphoenolpyruvate. Red underlined section linked to Figure 1.13(Williams and Laurens, 2010)

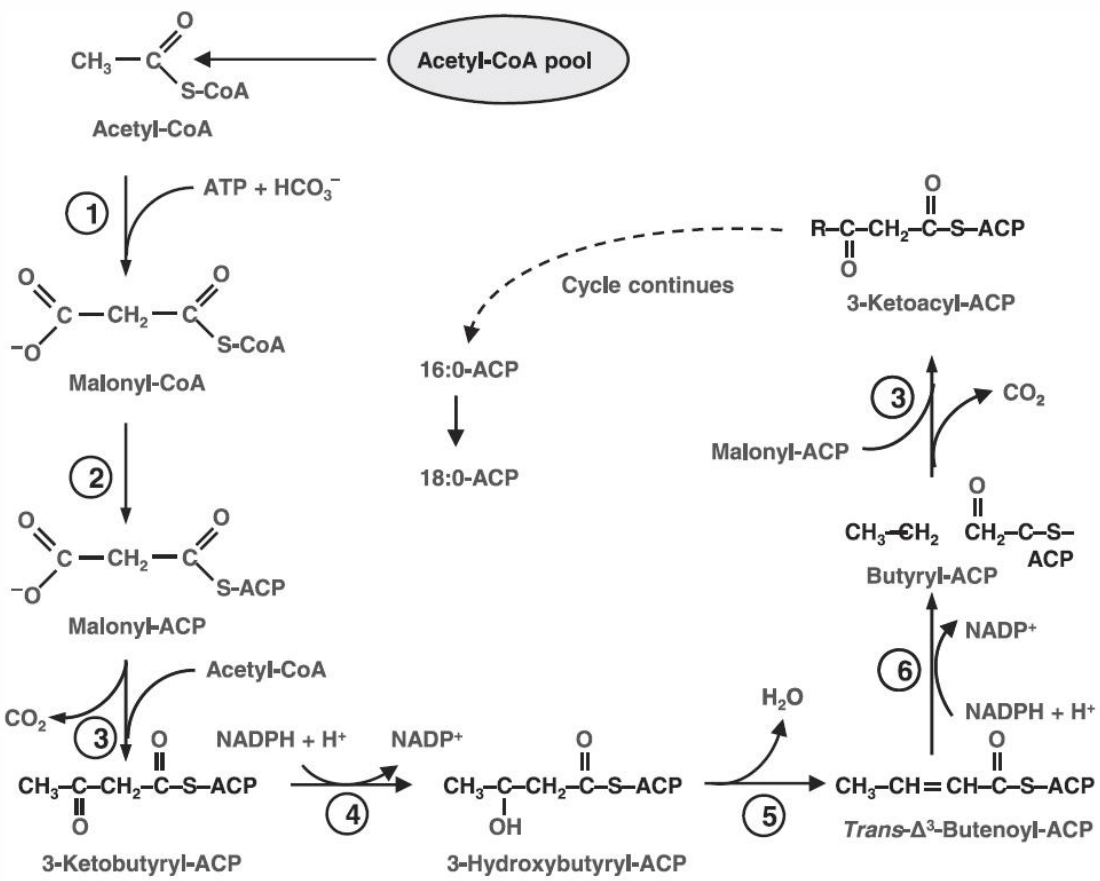

Figure 1.13 Fatty acid *de novo* synthesis pathway in the chloroplast

Acetyl CoA enters the pathway as a substrate for acetyl CoA carboxylase (Reaction 1) as well as a substrate for the initial condensation reaction (Reaction 3). Reaction 2, which is catalyzed by malonyl CoA:ACP transferase and transfers malonyl from CoA to form malonyl ACP. Malonyl ACP is the carbon donor for subsequent elongation reactions. After subsequent condensations, the 3-ketoacyl ACP product is reduced (Reaction 4), dehydrated (Reaction 5) and reduced again (Reaction 6), by 3-ketoacyl ACP reductase, 3-hydroxyacyl ACP dehydrase and enoyl ACP reductase, respectively (Hu, et al., 2008).

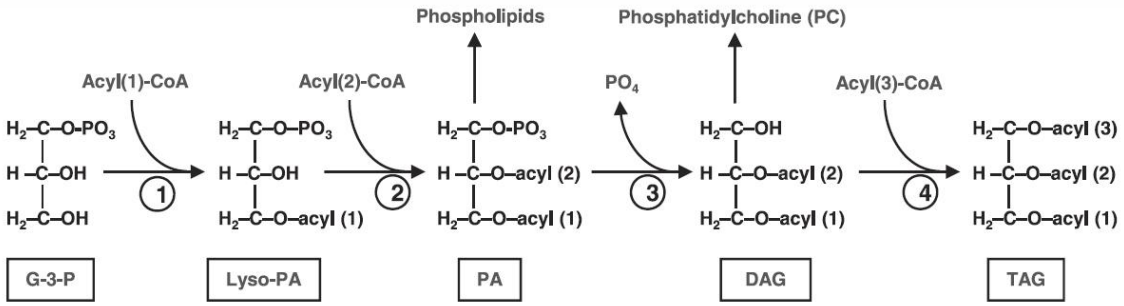

Figure 1.14.Triacylglycerol biosynthesis pathway. **(1) Cytosolic glycerol-3-phosphate acyl transferase, (2) lyso-phosphatidic acid acyl transferase, (3) phosphatidic acid phosphatase, and (4) diacylglycerol acyl transferase. Adapted fromRoessler et al. 1994b**

1.8.3 Algal stress factors

When oleaginous algae areexposed to detrimental 'stress' conditions imposed by chemical or physical environmental stimuli (or combinations of the two), it has been shown to trigger the synthesis and accumulation of large amounts of neutral TAG and alters the overall lipid composition in the culture(Hu, et al., 2008).Typically, when all elements needed for culture growth are available in medium, and no physical 'stress' factors are present, microalgal cells divide rapidly and synthesize mainly membrane lipids and chloroplast lipids. However, if this scenario changes and a 'stress' factor comes into play (such as nitrate deficiency), but photosynthetic fixation of carbon dioxide continues (Solovchenko, 2012), this triggers a 'lipogenic phase', which is characterized by a slowdown or cessation of cell division, often accompanied by a reduction in structure of the photosynthetic apparatus, and an accumulation of neutral TAG and nonpolar carotenoids (Leman, 1997). As a result of this response, the carbon to nitrogen (C/N) ratio in the cells increases dramatically (Mayzaud, Chanut and Ackman, 1989).When this occurs, ATP, reducing equivalents, and carbohydrates that are produced as a result of the photosynthesis processes are utilized predominantly for the biosynthesis of nitrogen free compounds, like TAG. Following *de novo* synthesis (previous section) the TAG is transported and stored in cytoplasmic oil bodies (OB)(Solovchenko, 2012).In some algae, lipid globules are also formed in the interthylakoid space in the chloroplast, carotenogenic algae such as *D. salina* also store globules of β-carotene and TAG in the same location(Lemoine and Schoefs, 2010; Ye, Jiang and Wu, 2008). A range of different 'stress' lipid triggers have been described in the literature over the last half century. The major chemical stresses that have been examined include various forms of nutrient starvation, and changes in salinity or pHof the growth-medium. The major physical stimuli covered are mainly

related to changes in temperature and light intensity. A selection of stress examples are shown in Table 1.4.

Table 1.4. Examples of algal 'stress' inducement experiments

'Stress' factor	Organism	Reference
Nitrogen deprivation	*Nannochloropsis*	(Rodolfi, et al., 2009)
NaCl concentration	*D. tertiolecta*	(Takagi, Karseno and Yoshida, 2006)
Temperature	Multiple	(Roleda, et al., 2013)
Light saturation	*Tetraselmis*	(Meseck, Alix and Wikfors, 2005)
CO_2 saturation	Multiple	(Bilanovic, et al., 2009)
Phosphorus limitation	*Monodus subterraneus*	(Khozin-Goldberg and Cohen, 2006)
Sulphur deprivation	*Chlamydomonas reinhardtii*	(Kosourov, et al., 2005)
Iron concentration	*Botryococcus*spp.	(Yeesang and Cheirsilp, 2011)
pH concentration	*Phaeodactylum tricornutum*	(Mus, et al., 2013)
Fatty acid growth inhibitors	*Monodus subterraneus*	(Bosma, et al., 2008)
Silicon deprivation	*Cyclotella cryptica*	(Roessler, 1988)

The effect of nitrogen starvation on cultures is the most heavily researched form of ‘stress’ stimuli related to algae, due to the large impact it has on certain species lipid yields(Hu, et al., 2008). For example, the work by Rodolfi, et al. (2009) demonstrated that the alga *Nannochloropsis* can achieve up to 60% lipid content after nitrogen starvation, along with high productivity. However, many other forms of 'stress' have equivalent potential, but the research thus far has been either contradictory or not carried out in depth due to the techniques that were available at the time.

Regarding the species *Dunaliella*, many methods of 'stress' inducement have previously been studied, including; nitrate depletion (Jiang, Yoshida and Quigg, 2012), nutrient deprivation (Roleda, et al., 2013), temperature variation (Thompson, 1996), light exposure (Park, Lee and Jin, 2013) and various combinations of the previous stresses (Mixson and Burkholder, 2012). However, NaCl stress in *Dunaliella* has, surprisingly given its halophilic nature, only been studied a few times in the past three decades and the data/findings have been highly fragmented and contradictory due to the different sub strains used (probably due to incorrect identification)(Olmos, et al., 2009;Oren, 2005). Given this situation and the ease of performing this type of 'stressing', NaCl 'stress' is one of the focal points in the current research (see Chapter 4 for further background).

Currently, whichever form of lipid triggering is used with external stimuli , there is always some form of trade off as the 'stress' effects will always cause a cessation of cell division (often accompanied by some form of structural damage). Until genetic tools can break the mutual exclusivity of growth versus high lipid productivity, a compromise will always need to be reached (Rodolfi, et al., 2009; Sheehan, et al., 1998). Whether this is growing cultures, until stationary phase with maximum biomass then stressing them, or putting them under 'mild stress' from inoculation, the approach and its effectiveness is dependent on the strain and a whole host of other variables (Chen, et al., 2011). A great deal of further research is needed in this area, to precisely model the metabolic effects of these different approaches to find the most effective strategy (Khozin-Goldberg and Cohen, 2011).

1.8.4 Algal Harvest & Lipid Extraction

Once a selected algal culture has been grown to a sufficient biomass yield and has the required lipids, it needs to be harvested and the lipids extracted. This downstream processing is of great significance to the overall energy balance and financial feasibility of the algal biofuel production endeavour (Chisti, 2013). As such, there is a great deal of research and funding going into this area both academically and commercially, the review by Kim, et al. (2013) gives an excellent summary of the current state of the art.

The most widely adopted forms of harvest are based on technologies that were developed for water purification and treatment; namely centrifugation, filtration and flotation (Kim, et al., 2013). However, these processes are not tailored to algal physiology and can be inherently energy intensive (see Table 1.5). Current research is looking at alternative methods or improving the efficiency of the existing infrastructure.

Lipid extraction methodologies have traditionally been based around mechanical disruption means coupled with solvent fractionation, but these approaches are relatively slow and wasteful of biomass (see Table 1.6). Newer methods such as electroporation, which have higher throughputs and are energy efficient are showing great promise (Halim, Danquah and Webley, 2012).

As this area is not of primary importance to the current study, only key highlights and references have been included in Tables 1.5 and 1.6. Further information on lipid extraction and measurement is included in section 1.10.

Table 1.5. Algal harvesting techniques, with pros and cons

Method	Description	Pros/Cons	Ref
Centrifugation	Recovering biomass from dilute suspension using centrifugal force	Good harvest efficiency and short time. Intensive energy consumption.	(Beach, et al., 2012)
Flocculation	Flocculating algal cells to enable separation. Including addition of metal salts, organic polymers, aminoclays, extracellular polymeric substances and potential auto-flocculation.	Low energy costs. Slow process, less effective on marine algae and expensive flocculants.	(Banerjee, et al., 2012;Farooq, et al., 2013;Vandamme, et al., 2012;Zhang and Hu, 2012;Zheng, et al., 2012)
Filtration	Membrane filtration through a porous mesh using passive or active means.	High separation efficiency, simple and continuous. Suffers from bio-fouling.	(Ahmad, et al., 2012;Zhang, et al., 2010)
Flotation	Cells are captured by gas bubbles rising and held in a vacuole layer at the medium surface.	High efficiency dependant on bubble size. Can be high energy costs, but this is dramatically reduced with fluidic oscillation.	(Garg, et al., 2012;Hanotu, Bandulasena and Zimmerman, 2012;Henderson, Parsons and Jefferson, 2010)
Magnetic separation	Magnetic particles bind to the micro algal surface, then the culture is harvested by magnetic fields.	Fast harvest time, recycling of magnetic particles. Expense of chemicals and recycling process.	(Lim, et al., 2012b; Toh, et al., 2012)
Electrolysis	Polyvalent cations are dissolved in the media forming hydroxides which bind to the algae and induce electro-coagulation.	High efficiency extraction over a wide range of pH. Poor medium recycling.	(Gao, et al., 2010;Kim, et al., 2012)
Ultrasound	Low frequency ultrasound forces cells to aggregate.	Can be used to break cells as well as aggregate. High energy input and low separation efficiency.	(Bosma, et al., 2003;Zhang, Zhang and Fan, 2009)
Immobilization	Cells are grown in a matrix to begin with, such as alginate, which be easily harvested.	Very low power requirements. Limited biomass potential, higher setup costs.	(Gonzalez and Bashan, 2000;Lam and Lee, 2012;Zhang and Hu, 2012)

Note: Combinations of the techniques above have also been found to give large efficiency gains, see: (Bilad, et al., 2012; Hanotu, Bandulasena and Zimmerman, 2012; Henderson, Parsons and Jefferson, 2010; Kim, et al., 2011; Lee, et al., 2012; Salim, Vermue and Wijffels, 2012; Zhang, Zhang and Fan, 2009).

Table 1.6. Algal lipid extraction techniques, with pros and cons

Method	Type	Description	Pros/Cons	Ref
Mechanical disruption	Microwave	Microwave radiation (2450 MHz) heats cell envelopes and breaks down hydrogen bonds.	Quick penetration into biomass and rapid disruption. High power required.	(Balasubramanian, et al., 2011;Prabakaran and Ravindran, 2011)
	Ultra-sonication	Ultrasound creates bubble cavitations which lyse the algae.	Most thorough form of cell disruption. High energy consumption, poor scale up.	(Adam, et al., 2012;Marrone, et al.)
	Bead beating	Container filled with culture is disrupted by collision or friction of bead interaction	Simple and rapid treatment. Lower efficiency extraction. Poor scaling potential.	(Sheng, Vannela and Rittmann, 2012;Zheng, et al., 2011)
	High pressure homogeniz-ation (HPH)	Hydraulic shear force compresses culture until breakage.	Simple and good extraction efficiency. Slow operation and high energy costs.	(Halim, et al., 2012;Zheng, et al., 2011)
	Electro-poration	Electromagnetic fields are used to disrupt algal cell envelope due to an interaction with dipole moments.	Simple with high energy efficiency. Limited data. Process currently in commercial trials with OriginOil.	(Halim, Danquah and Webley, 2012;Sheng, Vannela and Rittmann, 2011)
Chemical disruption	Chemical treatment	Acids, alkalis, various chemicals and detergents induce lysis.	Good disruption performance. Expensive chemicals, increased wear rates.	(Sathish and Sims, 2012;Vaara, 1992)
	Osmotic shock	Sudden increase or decrease in salinity ruptures cells through change in osmotic pressure.	Simple and cheap. Low efficiencies and water wastage.	(Prabakaran and Ravindran, 2011;Yoo, et al., 2012)
Biological disruption		Degradation of cell envelope using enzymes induces rupture.	Effective disruption. Enzyme cost can be high for tailored solution.	(Jin, et al., 2012)
Soxhlet extraction		A solvent is evaporated, re-condensed and combined with the sample continuously.	Widely known process. Slow and energy inefficient. Poor scale up.	(Halim, et al., 2012;Kanda and Li, 2011)
Direct transesterification		Combines extraction and biodiesel conversion.	Simple industrial procedure. Requires further processing to remove by-products.	(Patil, et al., 2011;Ranjan, Patil and Moholkar, 2010)
Milking		Target products are extracted from algae without the need of harvesting or killing cells.	Low extraction efficiencies currently. Further research required.	(Kleinegris, et al., 2010;Wijffels and Barbosa, 2010)

1.9 Biodiesel

1.9.1 Making Biodiesel

Following the lipid extraction process, the crude total lipids (typically containing a mix of acylgycerols, polar lipids, free FAs, pigments etc, mentioned previously) are typically fractionated (or separated using another method), as only acylgycerols are suitable for biodiesel production (Medina, et al., 1998). Once the lipids are purified they can be converted into biodiesel via the process of transesterification (Figure 1.15).

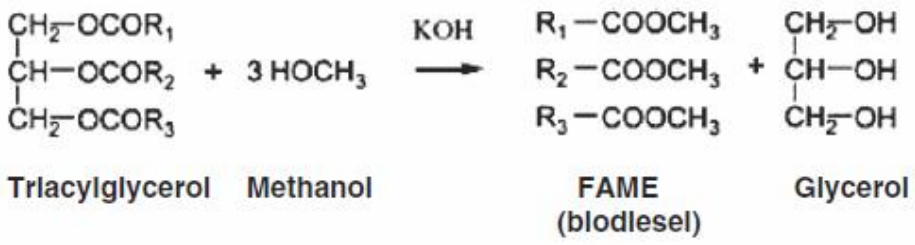

Figure 1.15.Transesterification reaction using an alkali KOH catalyst (Halim, Danquah and Webley, 2012)

The transesterifiction (or alcoholysis) reaction occurs when the acylgycerols (tri, di and mono varieties) are reacted with an alcohol (such as methanol) in the presence of a catalyst to produce fatty acid methyl esters (FAME) or biodiesel and glycerol as a by-product. The reaction can be catalysed by many different acids, alkalis (such as KOH above) or lipase enzymes, each providing their own advantages and disadvantages to the overall process(Fukuda, Kondo and Noda, 2001; Kim, et al., 2013; Xiao, Mathew and Obbard, 2009). Alkali catalysts are typically used in the chemical industry for the conversion of plant and animal lipids due to their superior reaction rates and conversion efficiencies compared to the acid catalysts (Huang, et al., 2010). Once the reaction is completed, the products undergo purification to remove the glycerol, catalyst and excess solvents, which typically involves some form of bi-phasic fractionation separation (Griffiths, van Hille and Harrison, 2010). The composition of the FAMEs is then checked using a gas chromatography (GC) system equipped with a lipid specific column (Laurens, et al., 2012). A number of factors affect the overall efficiency of the FAME conversion process, including; the molar ratio of acylglycerol to catalyst and acylglycerol to methanol, the reaction temperature and exposure time and the water content of the crude lipid extract. Monoacylglycerols can also react with water form FFAs, which can in turn react with alkali catalysts to form soaps. Alkali catalysts also have limited efficiencies converting non-acylglycerol fatty-acid-containing lipid fractions, such as polar lipids, hence neutral lipid feedstocks are better commercially (Halim, Danquah and Webley, 2012).

1.9.2 Fuel requirements

In contrast to other existing first and second generation biofuel crops (using higher plants), algae have a much greater variation in FA composition (see Figure 1.11 in section 1.8.1). This property can be of great benefit for the production of other useful compounds such as nutraceuticals, but of detriment for the production of biodiesel, in some cases (Spolaore, et al., 2006). The quality and viability of biodiesel is determined by the structure and composition of its FAME feedstock (Knothe, 2005). FAMEs derived from *cis*-unsaturated FAs produce fuel with advantageous cold flow properties (such as a low cloud and pour point). Whereas saturated FAMEs produce a biodiesel with superior oxidative stability and a higher cetane number, but poor low-temperature properties(Halim, Danquah and Webley, 2012).This is because saturated chains pack closely together with a temperature decrease to form tight semi-crystalline structures that gel.*Cis*-unsaturated FAMEs on the other hand, are prevented from molecular packing due to the bends imposed by the *cis* double bonds and thus consequentially freeze at a much lower temperature(Lang, et al., 2001). FAME produced from highly PUFAs also have good cold-flow properties, but are particularly susceptible to oxidation and have poor volatility. This can lead to instability problems during prolonged storage such as gum formation (Lang, et al., 2001; Ramos, et al., 2009). These reactions are why, as a feedstock, acylglycerols are more suitable for FAME production because they generally have a lower degree of unsaturation than polar lipids (C18:1 rather than C18:3, C18:4). However, it is worth noting that other less suitable algal lipids can also be used for the biodiesel process, but they require further processing steps, such as catalytic hydrogenation (BSI, 2009; Chisti, 2007; Dijkstra, 2006; Jang, Jung and Min, 2005).

To ensure quality of the biodiesel end product, given the inherent variability in the lipid production of the algal feedstock (lipid structure profile and volume), standardization is required to guarantee satisfactory engine performance(Balat and Balat, 2010; Lin, et al., 2011). The current properties and qualities that biodiesel must adhere to are the American Standards for Testing Materials (ASTM 6751-3) or the European Union (EN 14214) Standards for biodiesel fuel. However, othersexist such as the German (DIN 51606), Austrian (ON) and Czech Republic (CSN) standards (Lin, et al., 2011). Tables 1.7 and 1.8 show the list of properties on which the standards are assessed and their relevance. All data are quoted directly from the excellent review by Atabani, et al. (2012), the algal FAMES used for comparison were sourced from the species *Chlorella vulgaris.*

Table 1.7. Biodiesel fuel assessment criteria(Atabani, et al., 2012)

Property	Description
Kinematic viscosity	Viscosity indicates the ability of a material to flow. It therefore affects the operation of the fuel injection equipment and spray auto-atomization, particularly at low temperatures when the increase in viscosity affects the fluidity of the fuel. This is because of its large molecular mass and large chemical structure. In some cases at low temperatures biodiesel can becomes very viscous or even solidified. At low temperature it may even compromise the mechanical integrity of the injection pump drive systems.
Density and relative density	Density is the weight per unit volume. Oils that are denser contain more energy. Relative density is the density of the component compared to the density of water. The relative density of biodiesel is needed to make mass to volume conversions, calculate flow and viscosity properties, and is used to judge the homogeneity of biodiesel tanks.
Flash point (FP)	Flash point of a fuel is the temperature at which it will ignite when exposed to a flame or a spark. Flash point varies inversely with the fuel's volatility. The flash point of biodiesel is higher than the prescribed limit of diesel fossil fuel, which is safe for transport, handling and storage purpose.
Cloud point (CP)	The cloud point is the temperature at which wax crystals first becomes visible when the fuel is cooled. This is because partial or full solidification of the fuel may cause blockage of the fuel lines and filters, leading to fuel starvation, problems of starting, driving and engine damage due to inadequate lubrication.
Pour point (PP)	Pour point is the temperature at which the amount of wax out of solution is sufficient to gel the fuel, thus it is the lowest temperature at which the fuel can flow
Cold filter plugging point (CFPP)	CFPP refers to the temperature at which the test filter starts to plug due to fuel components that have started to gel or crystallize. It is a commonly used as indicator of low temperature operability of fuels and reflects their cold weather performance. At low operating temperature fuel may thicken and might not flow properly affecting the performance of fuel lines, fuel pumps and injectors. CFPP defines the fuels limit of filterability, having a better correlation than cloud point for biodiesel as well as diesel
Titer	Titer is the temperature at which oil changes from solid to liquid. Titer is important because the transesterification process is fundamentally a liquid process, and oils with high titer may require heating, which increase the energy requirements and production costs for a biodiesel plant.
Cetane number (CN)	The cetane number (CN) is the indication of ignition characteristics or ability of fuel to auto-ignite quickly after being injected. Better ignition quality of the fuel is always associated with higher CN value. Cetane number increases with increasing chain length of fatty acids and increasing saturation.
Oxidation stability (OS)	Oxidation stability is an indication of the degree of oxidation, potential reactivity with air, and can determine the need for antioxidants. Oxidation occurs due to the presence of unsaturated fatty acid chains and the double bond in the parent molecule, which immediately react with the oxygen as soon as it is being exposed to air.
Lubrication properties	Lapuerta, Armas and Rodriguez-Fernandez, (2009) reported that fatty acid alkyl esters (biodiesel) have improved lubrication characteristics, but they can contribute to the formation of deposits, plugging of filters, depending mainly on degradability, glycerol (and other impurities) content, cold flow properties, etc. Demirbas (2008) stated that biodiesel provides significant lubricity improvement over diesel fuel. Xue, Grift and Hansen (2011) shows that high lubricity of biodiesel might result in the reduced friction loss and thus improve the brake effective power.
Acid value	Acid number or neutralization number is a measure of free fatty acids contained in a fresh fuel sample. Higher amount of free fatty acids leads to higher acid value. Higher acid content can cause severe corrosion in fuel supply system of an engine.
Heating value, heat of combustion	Heating value, heat of combustion is the amount of heating energy released by the combustion of a unit value of fuels. One of the most important determinants of heating value is the moisture content of the feedstock oil

Property	Description
Free glycerol	Free glycerol refers to the amount of glycerol that is left in the finished biodiesel. The content of free glycerol in biodiesel is dependent on the production process. The high yield of glycerol in biodiesel may resultfrom insufficient separation during washing of the ester product. Free glycerol may remain either as suspended droplets or as the very small amount that is dissolved in the biodiesel. High free glycerol can cause injector coking and damage to the fuel injection.
Total glycerol	Total glycerol is a measurement of how much triglyceride remains unconverted into methyl esters. Total glycerol is calculated from the amount of free glycerol, monoglycerides, diglycerides, and triglycerides. The glycerol portion of these compounds is referred to as bound glycerol. When the bound glycerol is added to the free glycerol, the sum is known as the total glycerol. Fuels that do not meet these specifications are prone to coking; thus, may cause the formation of deposits on the injector nozzles, pistons and valves.
Water content and sediment	Water can present in two forms, either as dissolved water or as suspended water droplets. Sediment may consist of suspended rust and dirt particles or it may originate from the fuel as insoluble compounds formed during fuel oxidation. Water in the fuel generally causes two problems. First, it can cause corrosion of engine fuel system components. The most direct form of corrosion is rust, but water can become acidic with time and the resulting acid corrosion can attack fuel storage tanks. Water contamination can contribute to microbial growth. The species of yeast, fungi, and bacteria can grow at the interface between the fuel and water at the bottom of a storage tank. The organisms produce sludges and slimes that can cause filter plugging. Some of the organisms can convert the sulphur to sulphuric acid which can corrode metal fuel tanks. Moreover, high water contents can also contribute to hydrolysis reaction that is responsible for converting biodiesel to free fatty acids which is also linked to fuel filter blockage.
Carbon residue	Carbon residue of the fuel is indicative of carbon depositing tendencies of the fuel after combustion. Conradsons carbon residue for biodiesel is more important than that in diesel fuel because it shows a high correlation with presence of free fatty acids, glycerides, soaps, polymers, higher unsaturated fatty acids and inorganic impurities.
Copper strip corrosion	The copper corrosion test measures the corrosion tendency of fuel when used with copper, brass, or bronze parts. Corrosion resulting from biodiesel might be induced by some sulphur compounds by acids; hence this parameter is correlated with acid number.
Cold soak filtration	The cold soak filtration test is done to determine if crystals form at low temperatures and do not redissolve when the biodiesel returns to a higher temperature.
Phosphorus, calcium, and magnesium	The specifications from ASTM D6751 state that phosphorus content in biodiesel must be less than 10 ppm, and calcium and magnesium combined must be less than 5 ppm. Phosphorus was determined using ASTM D4951, calcium and magnesium were determined using EN Standard 14538.
Moisture contents	Moisture is the amount of water which cannot be converted to biodiesel. Moisture can react with the catalyst during transesterification which can lead to soap formation and emulsions.

Table 1.8. A comparison of fossil and algal derived diesel international standards(Atabani, et al., 2012)

Fuel properties	Diesel fuel - ASTM D975	Biodiesel ASTM D6751	Biodiesel DIN 14214	Microalgal 1 FAME	Microalgal 2 FAME	Test method ASTM	Test method DIN
Density 15 ◦C (kg/m3)	850	880	880	-	-	*D1298*	*EN ISO 3675/12185*
Viscosity at 40 ◦C (cSt)	2.6	1.9-6.0	3.5-5.0	4.519	4.624g	*D-445*	*EN ISO 3104*
Cetane number	40-55	Min. 47	Min. 51	-	-	*D-613*	*EN ISO 5165*
Iodine number	38.3	-	Max. 120	-	-	-	*EN 14111*
Calorific value (MJ/kg)	42-46	-	35	-	-	-	*EN 14214*
Acid (neutralization) value (mg KOH/g)	0.062	Max. 0.5	Max. 0.5	0.022	0.003	*D-664*	*EN 14104*
Pour point (◦C)	-35	-15 to -16	-	-	-	*D-97*	-
Flash point (◦C)	60-80	Min. 100-170	>120	>160	>160	*D-93*	*ISO DIS 3679*
Cloud point (◦C)	-20	-3 to -12	-	-5.2	3.9	*D-2500*	-
Cold filter plugging point (◦C)	-25	19	Max. +5	-7	2	*D-6371*	*EN 14214*
Copper strip corrosion (3 h at 50 ◦C)	1	Max. 3	Min.1	1a	1a	*D-130*	*EN ISO 2160*
Carbon (wt%)	84-87	77	-	-	-	-	-
Hydrogen (wt%)	12-16	12	-	-	-	-	-
Oxygen (wt%)	0-0.31	11	-	-	-	-	-
Methanol content % (m/m)	-	-	Max. 0.20	-	-	-	*EN 14110*
Water and sediment content (vol%)	0.05	Max. 0.05	Max. 500b	<0.005	<0.005	*D2709*	*EN ISO 12937*
Ash content % (w/w)	0.01	0.02	0.02	-	-	-	*EN 14214*
Sulphur % (m/m)	0.05	Max. 0.05	10b	5.1a	0.6a	*D5453*	*EN ISO 20846*
Sulphated ash % (m/m)	-	Max. 0.02	Max. 0.02	<0.005	<0.005	*D-874*	*EN ISO 3987*
Phosphorus content	-	Max. 0.001	10b	<0.1a	<0.1a	*D-4951*	*EN 14107*
Free glycerol % (m/m)	-	Max. 0.02	Max. 0.02	0.009	0.014	*D-6584*	*EN 4105/14106*
Total glycerol % (m/m)	-	Max. 0.24	0.25	0.091	0.102	*D-6584*	*EN 14105*
Monoglyceride % (m/m)	-	0.52	0.8	0.265	0.292	-	*EN 14105*
Diglyceride % (m/m)	-	-	0.2	0.078	0.07	-	*EN 14105*
Triglyceride % (m/m)	-	-	0.2	0.02	0.019	-	*EN 14105*
CCR 100% (mass%)	0.17(0.1)d	Max. 0.05	Max. 0.03	0.007	0.042	*D-4530*	*EN ISO10370*
Distillation temperature (%)	-	Max. 360ºC	-	-	-	*D-1160*	-
Oxidation stability (h, 110 ◦C)	-	3 min	6 min	8.5 min	11 min	*D-675*	*EN 14112*
Lubricity (HFRR; _m)	685	314	-	-	-	-	-

Where:a = ppm, b = mg/kg, c = determined at 25ºC, d = wt.%m, e = kJ/kg, f = determined at 20ºC, g = mm^2/s. h = g/cm^3. i = determined at 313 K. j = $K.kg\ g^{-1}$.

1.10 Algal Lipid Detection and Quantification

Given the strict tolerances for biodiesel production and the variability of the algal lipid feedstock depending on the conditions it has been cultured in and its age, it is imperative that the lipid testing techniques employed (at whatever scale) be as accurate and reliable as possible. To that end, there are many different methodologies available for determining the concentration and composition of lipids in fluids. This differentiation has been driven by advances in biomedical technology for use in the diagnostic process (Lam and Shui, 2013). However, in the last few decades, lipid analysis at the same scale (mass screening) has started to be directed toward non-medical applications such as the production of fuel crops like microalgae (Mutanda, et al., 2011).

One of the most prevalent methods for calculating lipid yield in microalgae (and many other species) are the gravimetric solvent extraction techniques developed by Bligh and Dyer (1959), Smedes and Askland (1999) and Folch, Lees and Stanley (1957), due to their simple methodologies and effective results. However, as simple as these processes are, they are very time consuming to perform and can be inaccurate due to the number of transfer and estimation steps involved. They also cannot differentiate between the neutral and polar lipid fractions in the biomass (just giving total or crude lipid values), which means additional processing steps are needed, such as liquid chromatography to screen if the correct lipids are present to produce high quality biodiesel (Ichihara and Fukubayashi, 2010).

Since the advent of the gravimetric techniques, a plethora of different methods have been developed, each with different advantages and disadvantages related to specificity, accuracy and processing time. But unfortunately, due to the sheer number of options available in the literature, no singular method of measure that has come to be seen as a 'standard', which can make comparative assessments of lipid production difficult (Griffiths and Harrison, 2009). An overview of the current different lab scale methods and their merits is compiled in Table 1.9. It is worth mentioning there are also other larger scale/industrial combined methods for the extraction and quantification of lipids based around supercritical fluids and hydrothermal liquefaction, but they are out of the scope of this project (Biller and Ross, 2011; Halim, Danquah and Webley, 2012).

Table 1.9. Comparison of current lipid methods

Analysis method:	Lipid Specificity:	Time total (h):	Outlay:	Quantification:	Sample size needed:	Reference:
Micro Gravimetric	Total Lipids only	72	Basic solvents	Difficult, highly variable. Large biomass needed.	Large >10mg BM	(Bligh and Dyer, 1959;Folch, Lees and Stanley, 1957)
Colorimetric (Sulfophosphovanillin)	Total Lipids only	48	Basic solvents + cheap reagent, std micro-plates	Difficult and variable.	Large >10mg BM	(Cheng, Zheng and VanderGheynst, 2011;Vanhandel, 1985)
Thin layer chromatography (TLC) + GC	Entire Composition	48	Basic solvents, silica cartridges and vials. Standards and machine time expensive.	Very precise and consistent (depending on column).	Large >10mg BM	(Yongmanitchai and Ward, 1992)
Nile Red/ BODIPY Staining – Fluorometer	Polar & Neutral (depending on signal overlap)	3-4	Expensive dye, standards and filters. Std micro-plates.	Standard comparison very difficult. Relative values good.	Very low $1x10^6$ cells	(Alonzo and Mayzaud, 1999;Cooksey, et al., 1987) (Chen, et al., 2009) (Govender, et al., 2012)
Nile Red/ BODIPY Staining - Flow cytometry	Polar & Neutral (depending on signal overlap). Can select productive cells.	24	Expensive dye, standards and filters. Machine time expensive.	Standard comparison very difficult. Relative values good.	Very low $1x10^6$ cells	(Guzman, et al., 2011) (Govender, et al., 2012)
Fourier transfer infra-red (FTIR)	Entire Composition (limited groups due to signal overlap)	1-2	Standards only.	Very difficult and variable due to machine.	Medium 5-10mg BM	(Dean, et al., 2010;Laurens and Wolfrum, 2011)
Soxhlet + GC	Entire Composition	24	Basic solvents and vials. Standards and machine time expensive.	Very precise and consistent	Large >10mg BM	(McNichol, et al., 2012)
Density equilibrium	Total Lipids plus certain fractions	1	Basic chemicals, sucrose etc	Reliable but limited precision	Medium 5-10mg BM	(Eroglu and Melis, 2009)
Triethanolamine–copper salts (TEA–Cu) spectroscopy	Total Lipids only	24	Basic solvents and standards	Very precise and consistent	Very low $1x10^6$ cells	(Chen and Vaidyanathan, 2012)
Direct Trans-esterification + MS-GC	Entire Composition	24-48	Basic solvents and vials. Standards and machine time expensive.	Very precise and consistent (depending on column).	Med-Large ~10mg BM	(Griffiths, van Hille and Harrison, 2010;Laurens, et al., 2012)
Nuclear magnetic resonance (NMR)	Entire Composition (limited groups due to signal overlap)	48	Basic solvents, reasonable machine time costs.	Generalised assumptions made, but very consistent.	Medium 2-10mg BM	N/A - In house
High Performance Liquid Chromatography (HPLC)+GC	Entire Composition	48	Basic solvents, silica cartridges and vials. Standards and machine time expensive.	Very precise and consistent (depending on column).	Large >10mg BM	(Jones, et al., 2012)
Single Cell Raman Spectroscopy	Entire Composition (limited groups due to signal overlap)	1-2	Basic solvents and vials. Machine time expensive.	Excellent quantification of general lipid groups	Single cell (non-disruptive)	(Wu, et al., 2011)

1.11 Systems for Algal Growth

1.11.1 General Overview

Algal growth systems need to fulfil certain basic criteria to allow an algalcrop to grow effectively;adequate exposure of lightto enable photosynthesis, the facilitation of mass transfer of CO_2& O_2 for photosynthesis/respiration (Molina Grima, et al., 1999), the provision of water for intracellular solutions, maintenance of inorganic salts required for osmotic gradients and a stable temperature range (typically 20-30°C)(Chiu, et al., 2009b). The growth medium also needs to be maintained and provide all of the elements required for cell replication, including nitrogen, phosphorus, iron and other trace elements and be kept free of predators and not allowed to stagnate (Richmond, 2004). In addition to providing all of these requirements (discussed in more detail in section 1.4), the fluid dynamics of the growth systems need to be considered. Cultures need to be mixed to enable sufficient light exposure for the cells, gas exchange and the avoidance of stratification (and the formation of dead flow zones) which can lead to stagnation and predation (Becker, 1994), whilst also maintaining a minimum usage of energy for economical operation and avoiding shear damage to the algal cells (Kawase and Mooyoung, 1990). The interrelation of these various aspects is complex (Figure 1.16) and the balance of optimum conditions can be difficult to achieve. The design of a growth system with these aspects in mind is therefore of paramount importance in ensuring the highest productivity possible.

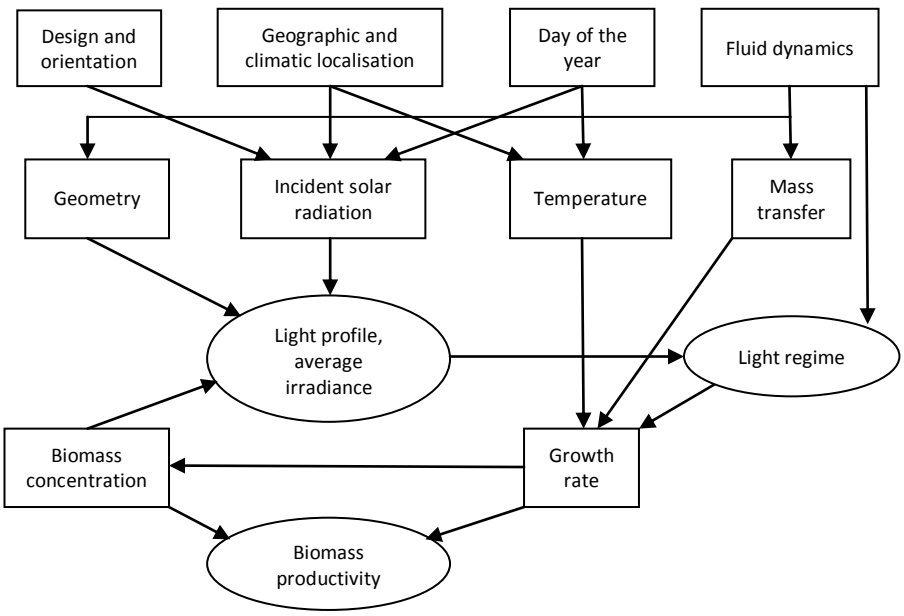

Figure 1.16. The relationship between major factors influencing biomass productivity in microalgal mass culture systems, modified from Fernandez, Sevilla and Grima(2013)

Algae are typically cultivated in two types of system; closed and open photo-bioreactors. Both systems have distinct advantages and disadvantages, see Table 1.10 below.

Table 1.10. The main design features of openand closed growth systems from Carvalho, Meireles and Malcata (2006)

Feature	Open system	Closed systems
area-to-volume ratio	large (4-10 times higher than closed counterpart)	small
algal species	restricted	flexible
main criteria for species selection	growth competition	shear-resistance
population density	low	high
harvesting efficiency	low	high
cultivation period	limited	extended
contamination	possible	unlikely
water loss through evaporation	possible	prevented
light utilization efficiency	poor/fair	fair/excellent
gas transfer	poor	fair/high
temperature control	none	excellent
most costly parameters	mixing	oxygen control, temperature control
capital investment	small	high

Given the trade offs between the two types of system, a combination of both is seen as the logical choice for cost-effective biofuel production (Schenk, et al., 2008). The best approach is thought to be using a closed system to produce a high concentration axenic algal inoculum that is transferred to an open system (such as a raceway pond) to be grown at scale. Using this method the primary culture could establish itself more rapidly before possible contamination issues would arise (Huntley and Redalje, 2007).

1.11.2 Algal ponds

Open and raceway pond photobioreactor systems have been commercially established since the 1970s (Borowitzka and Borowitzka, 1988; Terry and Raymond, 1985). Their designs typically consist of a series of closed loop flow channels (or a single 'pond') that are open to the air. The algal culture is circulated around the pond or raceway circuit by a pump or paddlewheel to avoid algal flocs forming on the liquid surface and to also provide enhanced aeration of the culture. The depth of the designs is normally around 0.2 - 0.3 meters, to enable the light to penetrate to the bottom of the culture. The areas covered can range from 0.5 to 200 hectares, depending on the crop (Greenwell, et al., 2010). Due to the large production capability, and established technology, of the different types of open systems (Figure 1.17) the

high rate algal pond (HRAP) type design is currently the favoured method of mass scale production of biofuels (using the hybrid system approach), see Figure 1.18 (Craggs, Sutherland and Campbell, 2012). However, these designs still have issues, with contamination, evaporation and mixing/mass transfer. Current research is looking at the prospect of improving the HRAP designs using buoyancy induced mixing and aeration with sparging (Ketheesan and Nirmalakhandan, 2011). Computational Fluid Dynamics (CFD) has also been used to optimise flow and reduce dead zones in current designs (Hadiyanto, et al., 2013).

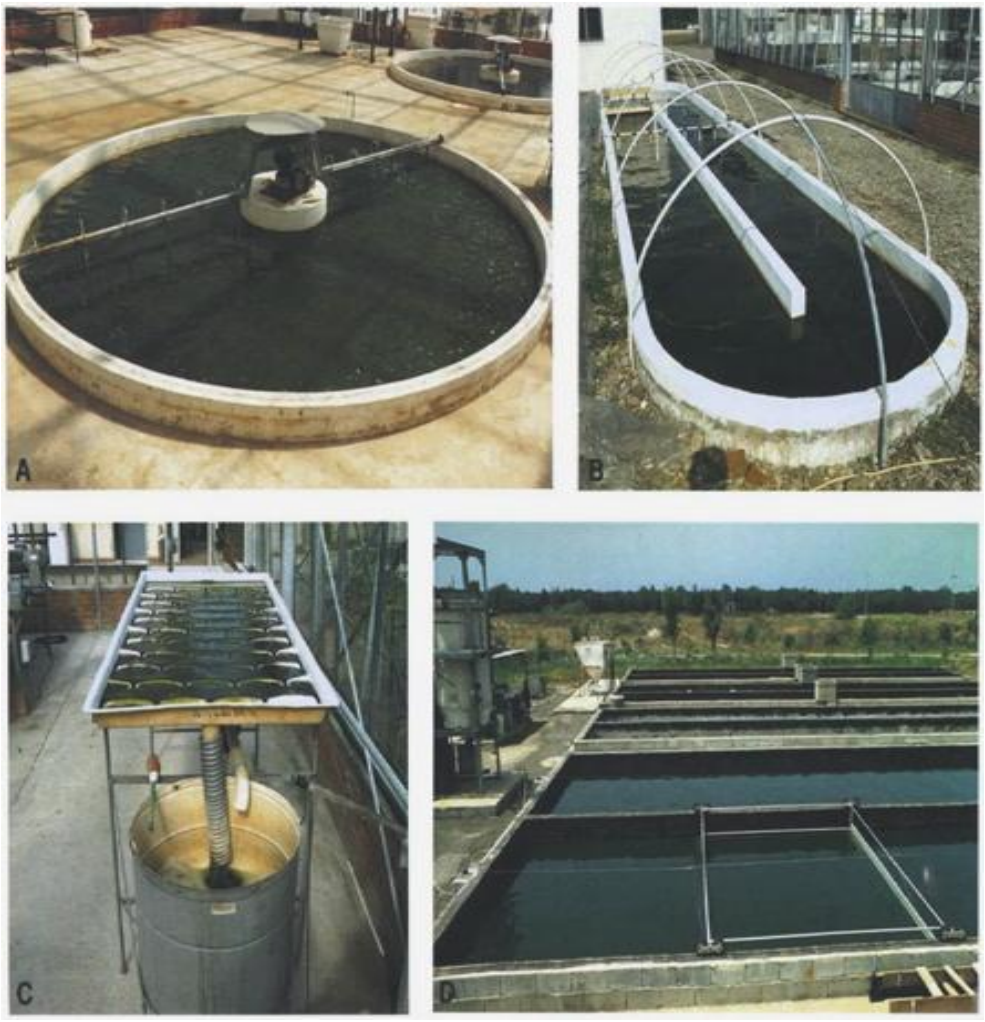

Figure 1.17. Different open photo-bioreactors used at the Centro di studio dei Microrganismi Autotrofi of Florence. Where; A: circular pond, B: 'raceway' pond, C: inclined trapezoidal pond and D: rectangular 'mixing board' pond. (Tredici and Materassi, 1992)

Figure 1.18 - Photograph of HRAPs in Christchurch New Zealand run by the National Institute of Water and Atmospheric Research Ltd (NIWA) (Craggs, Sutherland and Campbell, 2012)

1.11.3 Photo-bioreactors

Due to scalability and lab space issues the emphasis in this project is on culturing using closed photo-bioreactors systems (to be referred to hereon in as just photo-bioreactors). This type of reactor is defined as a system that does not allow direct exchange of gasses and liquids with the atmosphere. The main advantage of this system is that pure mono-cultures can be grown easily in high cell densities, as there is very little chance of competition from other species. However, these systems are highly complex, requiring careful pH, gas and temperature monitoring to make them viable, which also makes them expensive (Chisti, 2007). They also have smaller (net) yields compared to pond systems, which currently restricts their commercial applications to niche high value products, such as astaxanthin production (Schenk, et al., 2008). There have been many different types of photo-bioreactor designs over the last 50 years (Carvalho, Meireles and Malcata, 2006), the most successful of which are of the tubular, plate and bubble column variants (see Figure 1.19 below).

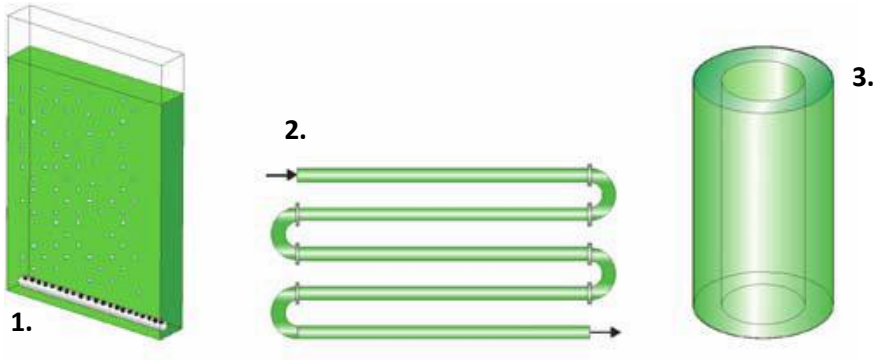

Figure 1.19. The three main types of photo-bioreactor design.
1 - Flat plate, 2 - Tubular, 3 - Bubble column. (Schenk, et al., 2008)

Flat plate photo-bioreactors

Flat plate photo-bioreactors are designed to have a high area-volume ratio based geometry, which can lead to high productivity due to the uniform distribution of light (via reduced self shading, see section 1.6). Designs typically consist of flat plastic/glass panels that have been bonded to plates, sizes can vary but heights up to 1.5 m with widths of 0.1 m are recommended to avoid the use of more expensive structural materials (Fernandez, Sevilla and Grima, 2013). The thickness of the sheet material is also of importance, thinner types enable a shorter light path which can increase the optimal cell density and thus increase biomass productivity (Hu, Guterman and Richmond, 1996; Zou and Richmond, 1999). However, this comes as a trade off in terms of greater temperature fluctuation, light saturation, oxygen build-up and difficulties in cleaning (Wang, Lan and Horsman, 2012). One major advantage of the design is due to its geometry it can be tilted and angled to maximise incidental light from the sun and gain productivity, which helps with seasonal variations in yield (Fernandez, Sevilla and Grima, 2013). Flat panel systems can be categorised by the type of mixing employed; pump driven, where fluid flow turbulence provides direct mixing and airlift where aeration provides buoyancy driven mixing. The first designs date back to the 1950s with the work by Burlew (1953a), but early designs were expensive. This concept was later improved by Tredici and Materassi(1992)with the addition of a rigid alveolar panel, which reduced costs and improved performance. Subsequent modern designs have taken this concept even further with the inclusion of moulded in baffles that induce constant horizontal vortices in the fluid, which induce the flashing light effect to increase productivity (see section 1.6), however this comes at a price of parasitic fluid energy loss (Degen, et al., 2001). Current work utilising this type of design is focussed on cost reduction and trying to achieve similar productivities and effects using disposable plastic variants, whilst reducing oxygen inhibition (Bergmann, et al., 2013; Morweiser, et al., 2010; Rodolfi, et al., 2009), see Figure 1.20.

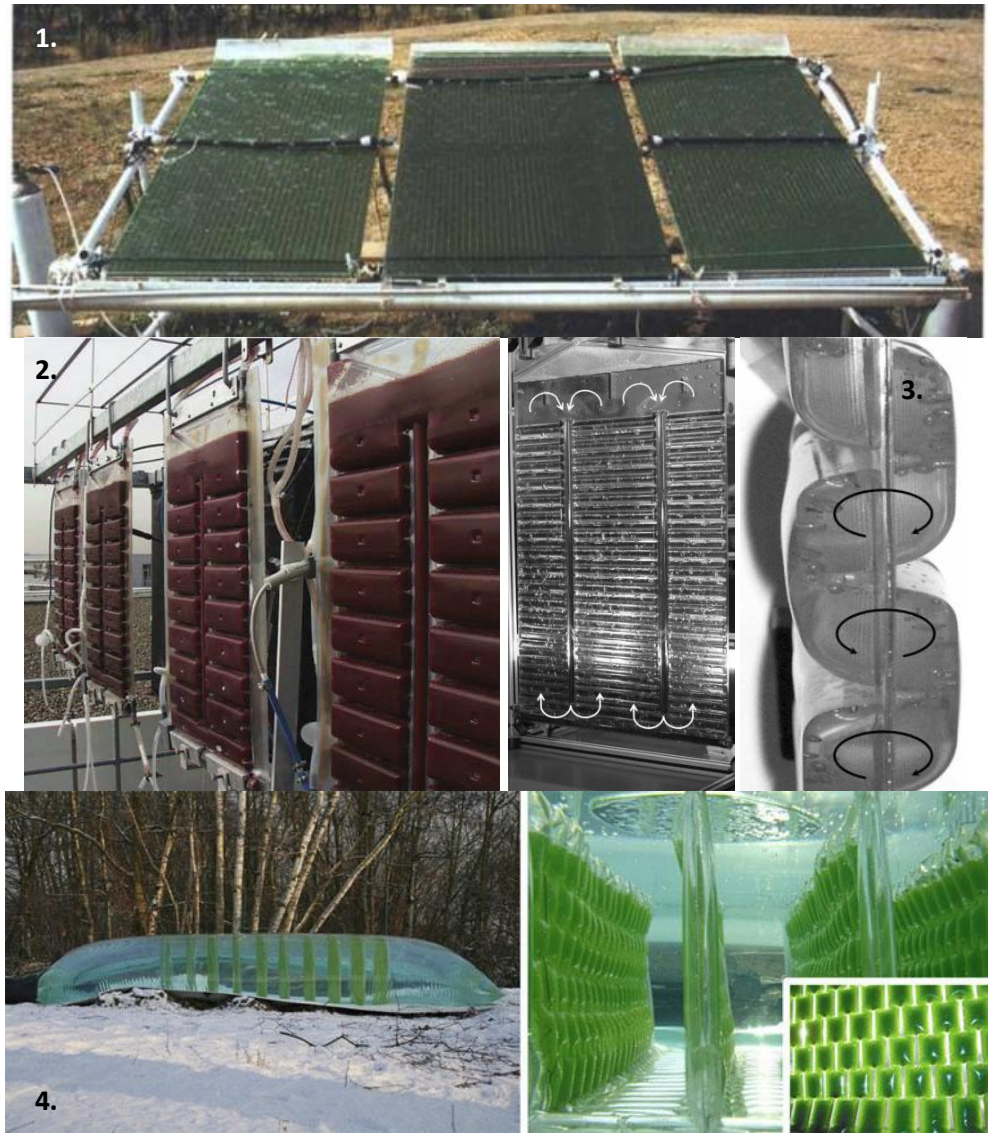

Figure 1.20. 1: Vertical alveolar panels used in Florence for the mass cultivation of *Spirulina*and other cyanobacteria (Tredici and Materassi, 1992). 2: Flat panel airlift from Subitec with usage of the flashing light effect (Schenk, et al., 2008). 3: Improved disposable flat panel design, with circular (horizontal) flow induced by the incorporated static mixers illustrated. (Bergmann, et al., 2013). 4 & 5: Low cost pilot reactor from Proviron, Belgium, all support and temperature control from surrounding water (Morweiser, et al., 2010).

Tubular photo-bioreactors

Tubular systems typically consisting of arrays of transparent conduits made from plastic or glass built in different formations (straight, curved, spiral) with different orientations (horizontal, inclined or vertical), in which the algae (suspended in a medium) flow around and are harvested at regular intervals(Chisti, 2007). The diameter is normally no greater than 0.1m in diameter to allow sunlight to penetrate through to the algal culture within. The algal broth is pumped around the reactor circuit and through a degassing section, that allows the medium to be temperature regulated (in certain designs), aerated with CO_2 and the excess $O_2$to be

removed (Molina, et al., 2000). Horizontal tube arrays can provide a greater surface area than their vertical counterparts, due to the ability to decrease the tube diameter without compromising structural integrity, they also have a greater exposure to sunlight due to the solar angle of incidence (Wang, Lan and Horsman, 2012). However this benefit comes at the cost of greater temperature variance, and increased oxygen build-up (Watanabe and Hall, 1995). Temperature control has been moderated using a number of different approaches including; using covers, submerging the array in water, spraying with water and using heat exchangers (Wang, Lan and Horsman, 2012). Mixing is typically provided by pumping or using the airlift effect, static mixers have also been employed in some cases to promote better mass transfer (Ugwu, Ogbonna and Tanaka, 2002). However, the turbulence needs to be maintained at low enough levels not to induce cell damage due to the formation of micro eddies (Fernandez, Sevilla and Grima, 2013). Tubular reactor systems have been used extensively at pilot scale and commercially in Spain, Germany and Hawaii for the production of food and pharmaceuticals (see Figure 1.21). However, as effective as these systems are, they have been proven to be too expensive and require too much auxiliary energy to be cost effective for mass biofuel production (Morweiser, et al., 2010). A comparison of various tubular reactor types and attributes is included in Table 1.11.

Table 1.11. Comparison of the performance of various types of tubular photo-bioreactors(Carvalho, Meireles and Malcata, 2006)

Reactor type	Light harvesting efficiency	Degree of control	Land area required	Scale-up	Productivity (g L^{-1} d^{-1}); species
Bubble column	medium	medium	medium	possible	0.5; *P. cruentum*
Horizontal tubular	good	medium	poor	possible	0.25; *S. platensis.* 0.7; *Nannochloropsis sp.*
Helical	medium	good	excellent	easy	0.4; S. *platensis*
α-shaped	excellent	good	poor	Very difficult	-
Flat-plate	excellent	medium	good	possible	0.85; *Nannochloropsis* sp. 2.15; *S. platensis*
Fermenter type	poor	excellent	excellent	difficult	0.03-0.05; several

Figure 1.21. (above)The world's largest closed tubular photo-bioreactor in Klötze, near Wolfsburg, Germany. 700 m^3 of culture is distributed in 500 km of tubes and produce up to 100t algae biomass per year. (Schenk, et al., 2008). (Below) Schematic diagram of a typical tubular photo-bioreactor system (Wang, Lan and Horsman, 2012).

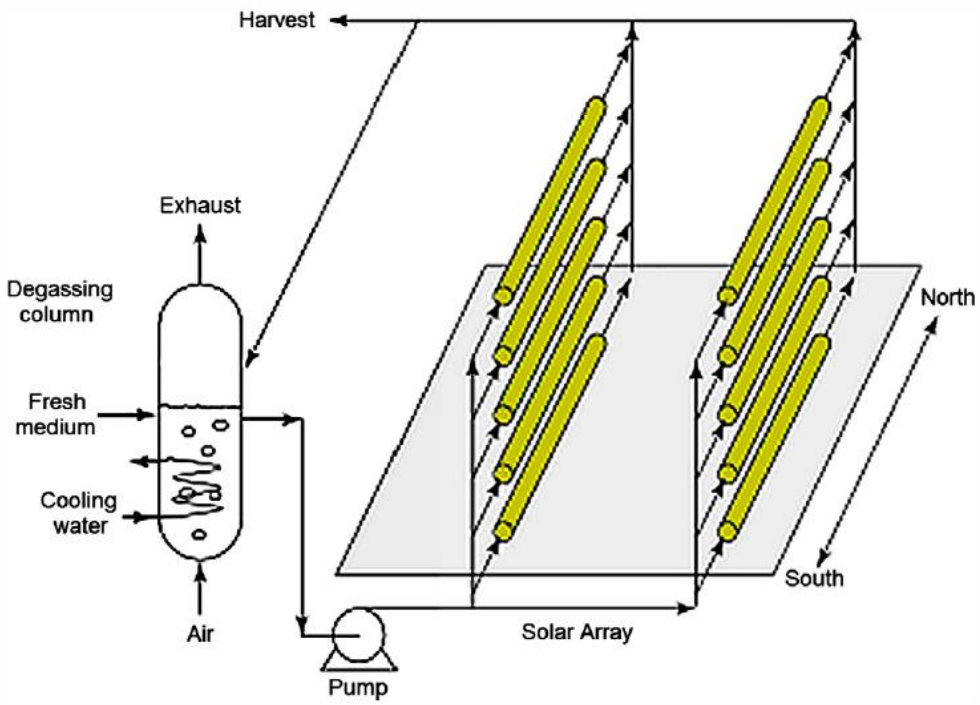

Bubble column photo-bioreactors

The third and simplest version of the photo-bioreactor systems is the bubble column bioreactor. They typically consist of cylinders made of glass or plastic, with radii and heights of up to 0.2 m and 4 m respectively (Wang, Lan and Horsman, 2012). The height limitation is due to two factors; the structural integrity of the materials and the mass transfer. If the column is any taller than 4 m, CO_2 gradients can form and also O_2 removal is reduced, both of which can inhibit culture growth (Xu, et al., 2009). As with the other designs, the smaller diameter enables a large surface to volume ratio which enables good light penetration. In addition, the

face to volume ratio of the column designs also require less cooling than their tubular counterparts (Miron, et al., 1999). Bubble column reactors also have excellent gas transfer coefficients and the constant motion of the bubbles causes mixing in the culture that is typically gentle with very little shear stress affecting the algae compared to impeller and pump driven systems (Miron, et al., 2002). However, extreme superficial gas velocities will still cause damage (Barbosa, Hadiyanto and Wijffels, 2004). There are four typical variants of the bubble column design (see Figure 1.22):

A. **Bubble column**- Comprised of a column with an air sparger located at the bottom.Gas rises in a freeboard regime to the top of the reactor then leaves at the gas/liquid interface.Mixing occurs due to the turbulence generated by the air bubbles rising due to buoyancy forces.
B. **Internal airlift loop reactor** -Consists of a transparent column, an internal 'draft tube' column, and a gas sparger at the bottom(Krichnavaruk, Powtongsook and Pavasant, 2007).When gas is introduced at the bottom of the draft tube it rises in the same way as it does in the bubble column variant. However, due to the gas hold-up (the gas/liquid ratio in a defined volume) in the draft tube being larger than that of theliquid outside of it, an upward flow of the liquid/gas mixture is induced in the draft tube, while a downward flow of degassed liquid is generated outside of it. This airlift loop effect provides excellent mixing and exposure of the algal cells to light even if the diameter of column is large and there is a high cell density. The design also has benefits in terms of its simplicity (cheaper manufacturing) andserviceability.
C. **Split column airlift reactor** - This design is akin to an airlift flat plate style reactor. A dividing panel is used to split the bubble column into two zones; the riser (the same as the inner volume of a draft tube) and the downcomer regions (for the returning de-gassed fluid) (Chiu, et al., 2009a). When gas is introduced at the bottom of the riser region, the airlift loop effect occurs in the same way as in the internal airlift loop reactor design. One drawback of this configuration is that serviceability is slightly reduced as the dividing panel is fixed.
D. **External loop airlift reactor** - In this concept, degassing occurs in the same way as the other designsat the gas/liquid interface at the top of the column, but this time the airlift loop is formed when the degassed liquid returns down an external circulation column.

Comparisons of the performance of each photo-bioreactor type have been carried out extensively in the literature (Miron, et al., 2002; Oncel and Sukan, 2008). These studies highlight the superiority of the airlift loop effect on growth performance versus the simple bubble column designs. Interestingly, it was also shown that there was little difference in

performance between the reactors exploiting the airlift loop effect. Current work is looking how to optimise and improve the performance of the airlift type reactors using modern CFD software packages (Xu, et al., 2012). Preliminary designs that have altered geometry of the draft tube section to induce controlled turbulence (which can simulate the flashing light effect) show promise, as does work reducing the aeration bubble size for increased levels of mass transfer (Wang and You, 2013; Zimmerman, et al., 2010a). However, as good as the systems become, it is unlikely they will be applicable for use in large scale culturing (other than inoculum generation), as the energy needed for circulation is much greater than bubble movement alone can provide in both large tubular and flat plate reactors systems (Xu, et al., 2009).

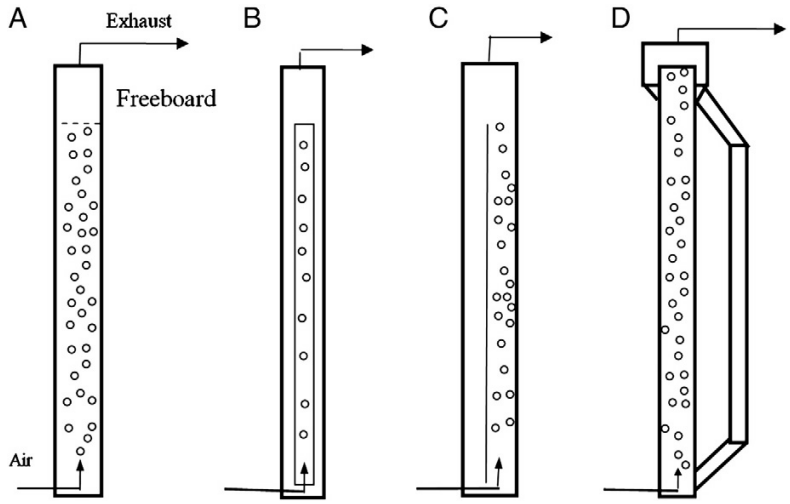

Figure 1.22. Schematic diagrams of various bubble column variants:

A: bubble column, B: internal-loop (draft-tube) airlift, C: split-column airlift and D: external-loop airlift.

(Wang, Lan and Horsman, 2012)

1.12 Mass Transfer and Aeration Systems

The rate of mass transfer of CO_2 and O_2 to and from an algal culture is of paramount importance to the overall productivity of any growth system. Too little CO_2 and the culture will be carbon limited, too much and the pH will be inhibitory, excess O_2 build up can also halt photosynthesis (see section 1.4). As such, the method of aeration selected can directly impact on the efficiency (and viability) of the culture process. In the case of airlift photo-bioreactors, the method selected is of even greater significance, as it not only provides gas exchange, but mixing too. In this section different sparging systems will be discussed alongside the impact of bubble size and the effects of fluidic oscillation.

1.12.1 Spargers, bubble size and coalescence

The first aspect of any aeration system is the creation of gas bubbles in the liquid medium. The number and size distribution of the bubbles is dictated by a range of interacting factors, including; the type of sparger (or diffuser) that the gas is pumped through, the gas flow rate used and the properties of the liquid phase (Kazakis, Mouza and Paras, 2008). Various types of sparger systems can be used for gas injection, the most common are the perforated metal, membrane and fine pore plates, see Figure 1.23 (Jha, et al., 2008; Luo, et al., 2011; Tchobanoglous, et al., 2003). Of those sparger types, the porous plate is considered to be the most effective as it typically produces smaller bubbles which have a better interfacial area for gas exchange (Mouza, Dalakoglou and Paras, 2005).

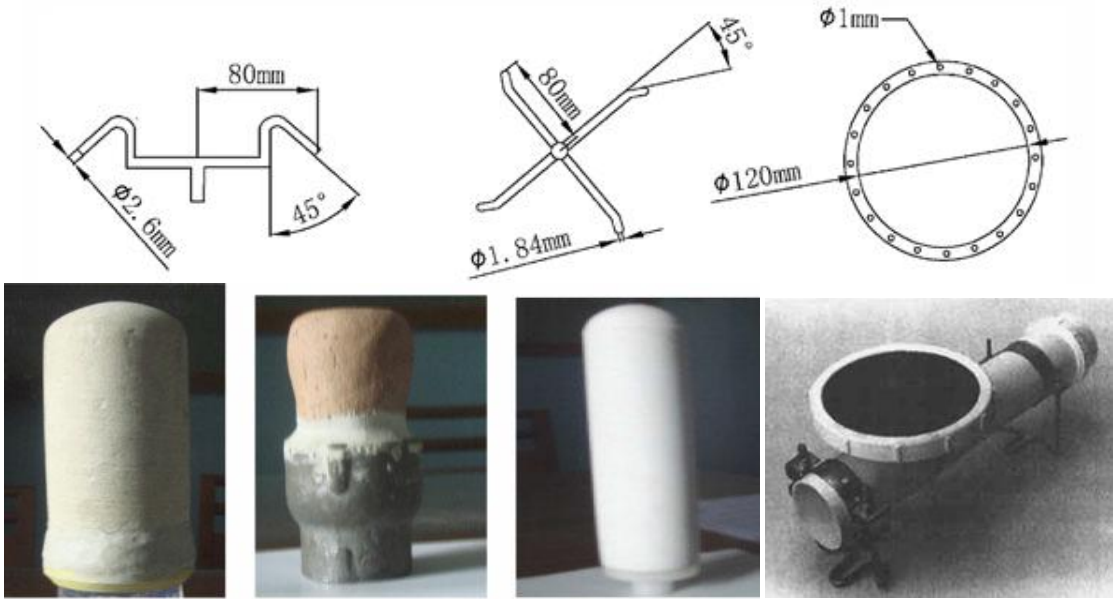

Figure 1.23. (top) Perforated metal spargers (Luo, et al., 2011) , (bottom left) various ceramic porous diffusers (Jha, et al., 2008), (bottom right) membrane diffuser (Tchobanoglous, et al., 2003)

A limited number of studies have been performed looking at the effects of other factors alongside the porous type diffusers. The work by Parthasarathy and Ahmed(1996) looked at the effects that liquids with different coalescence inducing behaviours have on average bubble sizes generated by fine pore spargers.Zahradnik, et al. (1997) investigated the combined effects of bubble column geometry, sparger type and liquid properties on the gas/liquid flow regime and gas holdup. Studies by Camarasa, et al. (1999), Mouza, Dalakoglou and Paras (2005) investigated further into the influence of the liquid properties and of the gas sparging methods using water-alcohol solutions to affect coalescence (Figure 1.24). Parthasarathy and

Ahmed (1996) also looked at bubble size distribution using various porous spargers with a range of pore diameters 5–400µm (Table 1.12). Other recent studies have also looked into the application of predictive formulas based on pore size and liquid characteristics (Kazakis, Mouza and Paras, 2008; Kazakis, Papadopoulos and Mouza, 2007). The conclusions from the literature demonstrate that gas flow rate, sparger pore size and a high liquid viscosity can promote the usage of more pores resulting in a greater density of smaller bubbles. However, the same effect can also be obtained from the use of a low-surface tension liquid, as the bubble attachment force at the surface of the sparger reduces. Visual observations have also demonstrated that bubble formation with porous spargers, is typically governed by a cluster of pores contributing to a single bubble (Kazakis, Mouza and Paras, 2008). Further research is needed in this area of chemical engineering as the precise mechanism of bubble growth at a sparger surface is still not fully understood.

Table 1.12. Influence of pore size on bubble size in non-coalescing water + 50ppm v/v methyl isobutyl carbinol with a superficial gas velocity of 1 mm/sec(Parthasarathy and Ahmed, 1996)

Sparger pore size (µm)	dmin (mm)	dmax (mm)	davg (mm)	Std dev (mm)
150-250	0.87	3.59	1.66	0.48
100-120	0.34	1.49	0.7	0.23
40-60	0.27	1.23	0.48	0.14
20-30	0.14	1	0.39	0.11
5-15	0.2	1.06	0.44	0.15

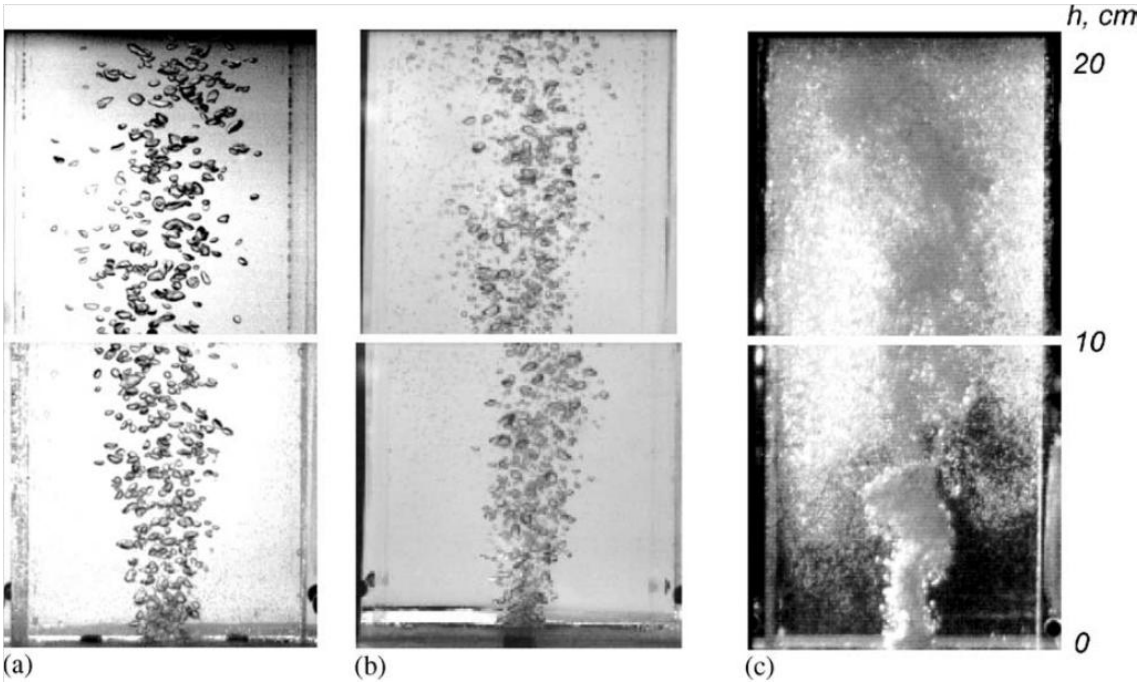

Figure 1.24. Photographs of the homogeneous regime for liquids with different coalescence inducing properties: (a) water, (b) glycerol 50% and (c) butanol 1.5%. Flow rate:1.5 ×10^{-5}m^3/s. Sparger pore size: 40 µm.(Mouza, Dalakoglou and Paras, 2005)

1.12.2 Benefits of small bubbles

Small bubbles are much sought after in a variety of fields and processes due to their superior interfacial surface area properties. A larger surface area to volume ratio enables enhanced mass transfer rates between gases and liquids in a reactor system (see section 1.12.4), which can dramatically increase culture productivity (Figure 1.25).

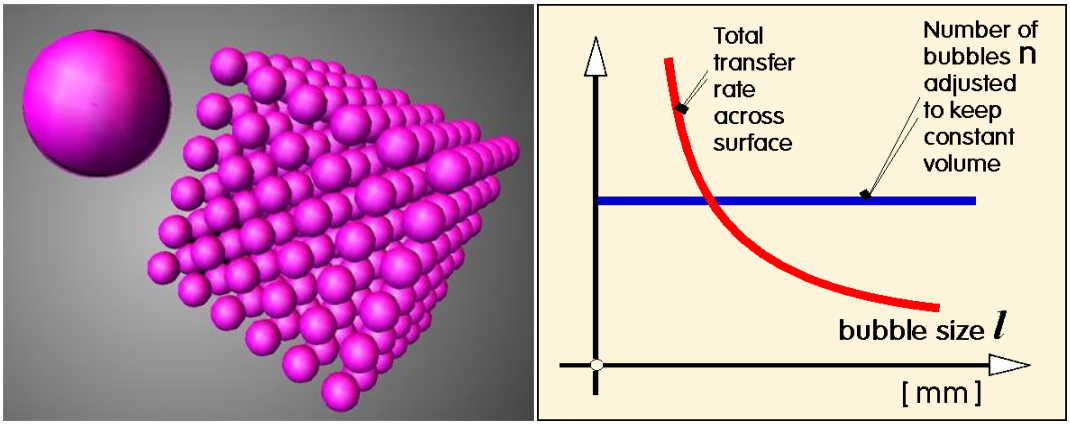

Figure 1.25. The mass transfer potential of small bubbles. (1): Visual representation of surface area increase with same volume for smaller bubbles. (2): Transfer rate increase with decrease in bubble size (Zimmerman, et al., 2007).

These benefits also extend to other transport processes too, including heat and momentum transfer. The latter is also of great interest in the performance of photo-bioreactors. Using the Hadamard–Rybczynski bubble rise velocity equation (accurate for bubbles smaller than 1 mm) for reference(Nguyen, et al., 2012; Parkinson, et al., 2008); $V = \frac{D^2 \delta g}{12\mu}$, where$\delta$, μ and g describe the liquid density and viscosity, and gravity acceleration. It can be seen that the residence time of the bubbles increases with a smaller size, due to a slower rise rate (Figure 1.26). Therefore, the bubbles have longer to transfer their momentum to the surrounding fluid via the shear stress across their respective surface areas. This enables the smaller bubbles to induce movement in the fluid more efficiently, which is of great benefit to air lift reactor designs as mixing can be achieved with lower volumetric flow rates (Zimmerman, et al., 2010a).

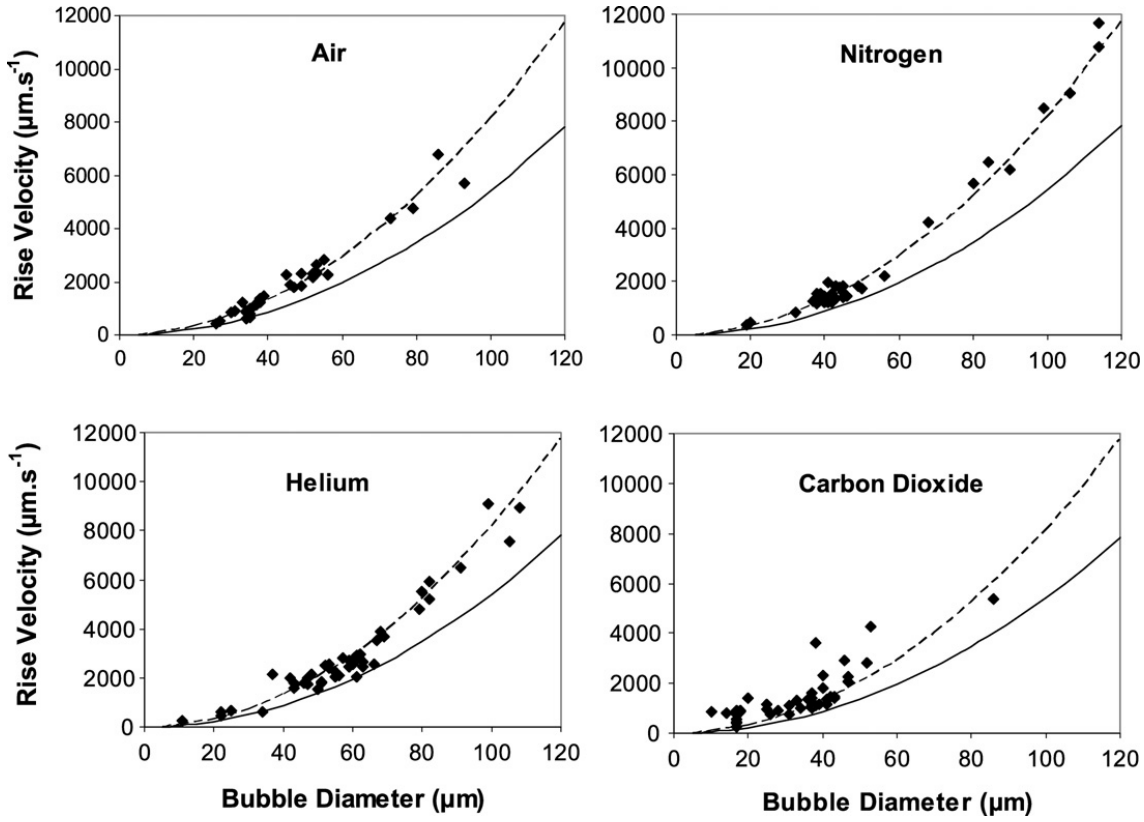

Figure 1.26.Terminal rise velocity versus bubble diameter plots for air, N_2, He and CO_2bubbles in pure water. Comparisons with Stokes rise law (solid lines, —) and the Hadamard–Rybczynski modification (broken lines, - - -) terminal velocity predictions are shown. Data points represent single bubbles (Parkinson, et al., 2008).

1.12.3 Microbubble generation and fluidic oscillation

With the properties of small bubbles being so desirable, there has been considerable interest in generating them in recent decades. A number of methods have successfully demonstrated the production of micro-bubbles, that is bubbles within the size range of 1-999 µm as opposed to fine bubbles with sizes in the range 1-2 mm (Zimmerman, Tesar and Bandulasena, 2011). The excellent recent review paper by Parmar and Majumder (2013) summarises each method in detail. As the production of algal biomass is highly energy critical (in order to maintain carbon neutrality), the use of microbubble generation is only applicable when the net gains in productivity outweigh the input energy costs. Even with current 'low power generation' techniques such as; capillary flow focusing (Ganan-Calvo and Gordillo, 2001), micro channel production (Yasuno, et al., 2004), shear flow pipes (Hasegawa, Nagasaka and Kataoka, 2008), and rotating plates (Fujikawa, et al., 2003), the energy/productivity balance would be tenuous. However, a recent innovationat the University of Sheffield has shown the potential to make low energy micro-bubble generation viable. A team of researchers led by Professor Will Zimmerman have demonstrated that micro-bubbles can be produced using the combination of a micro-porous sparger setup coupled with a unique fluidic oscillator device (Zimmerman, et al., 2010a). This fluidic oscillator design (patent: UK0621561) is novel due its lack of any moving parts and use of the Coanda effect to operate (Zimmerman and Tesar, 2006). The design consists of a stack of PMMA plastic plates with laser-cut cavities which are bolted together (Figure 1.27).

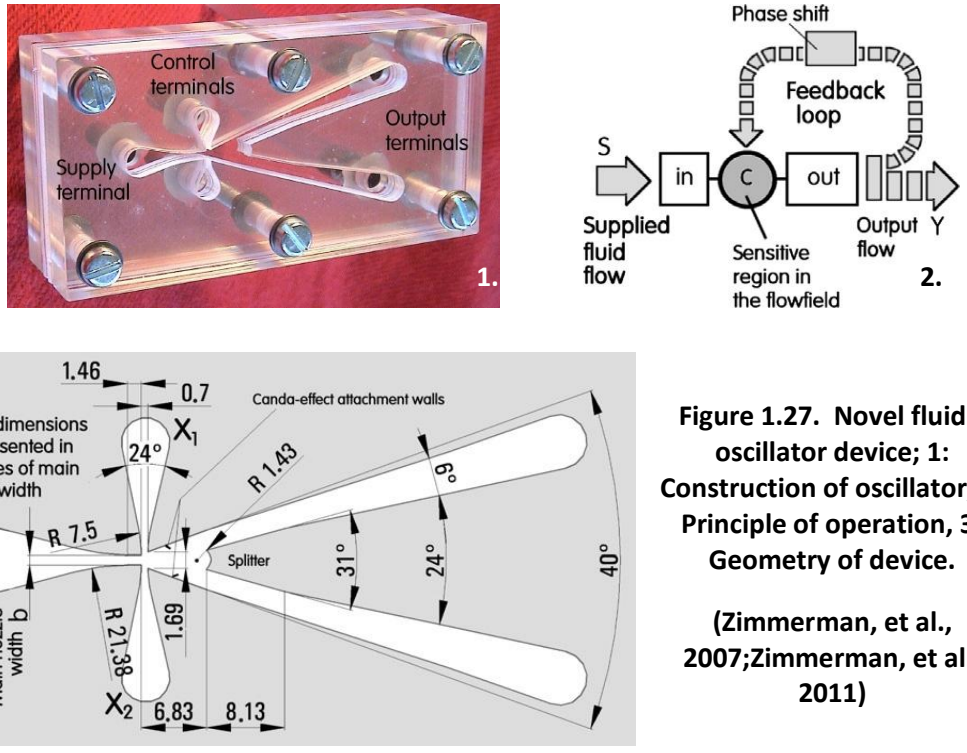

Figure 1.27. Novel fluidic oscillator device; 1: Construction of oscillator, 2: Principle of operation, 3: Geometry of device.

(Zimmerman, et al., 2007;Zimmerman, et al., 2011)

The oscillator operates when a steady fluid flow (of a gas such as air) is passed through the fixed geometry (Figure 1.27) of the device. When the fluid enters it is accelerated by the shrinking geometry towards the splitter region of the device. Due to the Coanda effect (Reba, 1966) the fluid jet attaches to one of the two walls, leading to one of the two output vents. The attachment is stabilised by a trapped vortex flow in the bicuspid shaped sensitive region in the flow field (Figure 1.27). However, this attachment is temporary due to the destabilising effect of the control feedback loop attached to the control terminals (Figure 1.28). Within the feedback loop tubing a pressure difference is created by the attachment of the fluid jet to one of the outputs (Figure 1.28). This pressure change induces a flow within the tube, which in turn causes a destabilisation of the sensitive region in the flow field and the attachment of the fluid jet to the other output wall. This process produces a constant oscillation as the fluid attaches to one side of the oscillator geometry or the other, which produces a pulsed output of fluid at either of the two output ports. Due to the way that the feedback mechanism works, the 'frequency' of the oscillation effect can be controlled by shortening or extending the feedback loop tube.

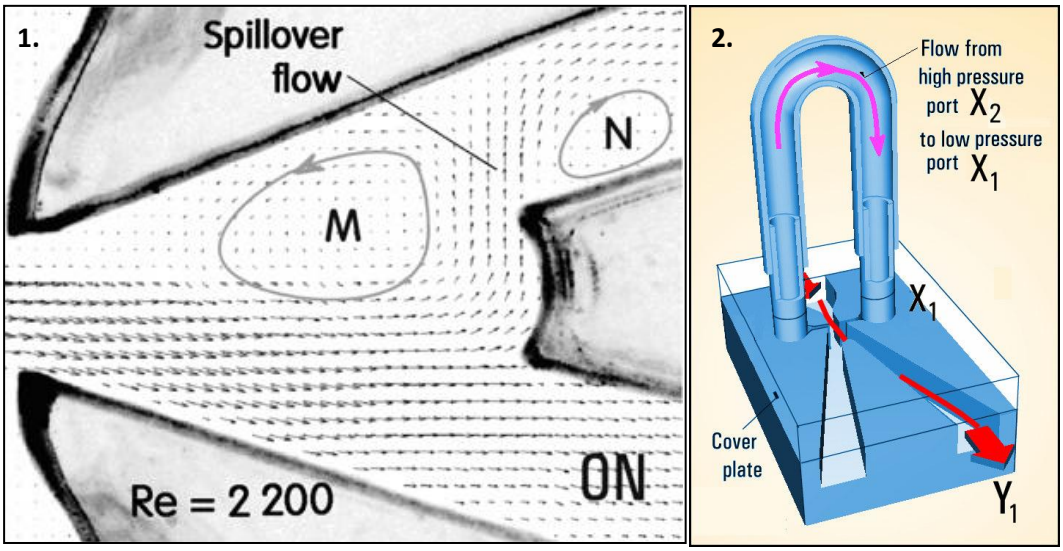

Figure 1.28. 1: Particle image velocimetry of the flowfield in the splitter region showing the stabilising feedback vortex (M) and the OFF diffuser entrance blocking vortex N. 2: The effect of the feedback loop on the oscillator function. (Zimmerman, et al., 2007;Zimmerman, et al., 2011)

Due to this behaviour the Zimmerman design has a number of inherent benefits, including simplicity, reliability, no electrical parts needed and low production costs. But the key aspect in terms of this work is its applicability to aid the production of small/micro-bubbles.

As mentioned previously, bubble size is heavily influenced by size of pore used in a sparger system and the coalescing properties of the fluid. Even in the best scenarios with non-coalescing media and smaller pores, the bubble sizes produced are typically an order of magnitude bigger than the original pore size (Table 1.12). Although the smaller pores can still produce net smaller bubbles (taking into consideration formation expansion), the overall process comes at an energetic cost. As the pores get smaller, with a continuous gas flow rate the friction forces increases proportionately. This effect leads to head loss in the pumping process due to increased hydraulic resistance and a net energy loss for the production of smaller bubbles (Zimmerman, et al., 2010a). The use of fluidic oscillation has been shown to negate this compromise in pilot scale trials of the device at a wastewater treatment site. The data from the test showed an 18% reduction of electricity using a steady flow with the same volumetric flow rate, whilst increasing overall mass transfer rates (Mahmood, et al., 2011; Medley, 2009). The source of this energy saving is thought to be a combination of two factors (Zimmerman, et al., 2010a): Firstly, in this trial the oscillator was acting as a splitter, feeding air two separate water tanks (one attached to each output). It is thought that due to the application of the Coanda effect in its operation, the oscillator output split produced less frictional resistance than a traditional T-junction. Secondly, the pulsing action of the oscillated air is thought to reduce frictional losses in the pipework as it could disrupt the formation of boundary layers which increase friction.

The increase in mass transfer rates is caused by another beneficial effect of fluidic oscillation; production of bubbles at the same scale as the pore itself. Typically, when bubbles form they grow in size until the buoyancy force (due to the increased volume of gas) exceeds the attachment force to the sparger surface, enabling disengagement of the bubble and it to rise in the medium (Wang, et al., 2010). The attachment force is influenced by the type of material the sparger is made from, with hydrophobic material giving a stronger attraction and a hydrophilic material the opposite. However, regardless of what type of material is employed, due to the interaction of forces the bubble size is normally an order of magnitude bigger than the pore it was formed from. This effect has another negative effect in the production of an even distribution of bubbles; when a bubble grows beyond the hemispherical shape, according to the Young-Laplace law of surface tension, the pressure force needed to create the bubble decreases rapidly. When this happens within the sparger, the gas follows the path of least resistance and preferentially forms bubbles from that pore, at the expense of other pores in the vicinity (Zimmerman, et al., 2007). This leads to uneven bubble formation at the sparger surface and a distribution of rise rates in the bubble plume and which can increase the chances of coalescence. Fluidic oscillation has been shown to combat these effects as bubble growth is halted at the end of each oscillation period, hence no bubble can keep growing in one pore at

the expense of another and there is a more even bubble distribution (Zimmerman, et al., 2007). Also, when coupled with a hydrophilic sparger material, the pulsing action of the oscillation causes the bubbles to "shoot out like bullets", so the size of the bubble is dictated by the period of the pulse and not purely by the relationship between attachment and buoyancy forces (Zimmerman, Tesar and Bandulasena, 2011).

Recently, pilot algal growth trials were conducted using a fluidic oscillator with a custom built airlift photo-bioreactor. The reactor was equipped with 50 µm pore size hydrophilic spargers and CO_2 was provided from the flue gases of a local steel works. Even under less than optimal ambient sunlight, the test showed remarkably positive data, including; the stripping of O_2 from the algal media, which it is thought resulted in super-exponential biomass growth, all $CO_2$was consistently delivered faster than algal uptake and observations also indicated there was 100% algal survivability(Zimmerman, et al., 2011).

1.12.4 Mass transfer and thin film theory

System wide mass transfer is affected by the complex interaction of molecular motion and convectional currents. Due to the turbulent nature of the fluids and gases involved, it is almost impossible to calculate the exact interaction of forces in place. However, many empirical and semi-empirical approximations exist that can provide a valid solution. When this approach is combined with state of the art computer programs based on CFD, rapid simulations and experimental validations can be performed. This section summarises how these approximations are typically made and how they can be used to assess photo-bioreactor mass transfer performance. Much of the following is taken from the compilation work by Garcia-Ochoa and Gomez (2009) and Doran (1995).

Diffusion theory

In systems with two components (binary mixtures, such as CO_2 and water), the rate of mass transfer can be calculated using Fick's first law of diffusion:

$$J_A = \frac{N_A}{a} = -D_{AB}\frac{dC_A}{dy}$$

Where; J_A = the mass flux component A, N_A = the rate of mass transfer of A, a = the cross sectional area that mass transfer occurs, D_{AB} = the binary diffusion coefficient (diffusivity) of A in mixture A & B, C_A = the concentration of A, y = the distance. Thus; $\frac{dC_A}{dy}$ = is the concentration gradient (or the concentration change of A over distance). The negative sign ensures that the direction of transfer is always from a high concentration to a low.

This law demonstrates that mass flux is proportional to a concentration gradient, where the unit of area is perpendicular to the direction of movement. From this it can be deduced that mass transfer can be improved by increasing the surface area for mass transfer (such as discussed previously with small bubbles), the concentration gradient in the system and magnitude of the diffusion coefficient.

The diffusivity (D_{AB}) depends on the nature of the components of the mixture and the temperature. Gas diffusivity (and liquid to a minor extent) is also dependant on the partial pressure within the system.

Bio-processing considerations and film theory

In large scale mass transfer applications, such as the ones used in industry, diffusion plays an important role alongside bulk fluid (convectional) flow. Within turbulent systems, bulk fluid mixing is significantly reduced in the scale below the smallest eddies sizes. In this domain mixing is predominantly performed by diffusion alone due to the streamline flows with these regimes. Diffusion is also important between the phases of the different substances due to these contact zones having such low fluid velocities. Two-film theory is the one of the simplest and most effective methods of approximating the mass transfer within these zones. Because of its relative simplicity, it allows a complete model of mass transfer to be computed when incorporated in fluid simulations (such as CFD packages) because of the low processing requirements.

Two-film theory models the mass transfer from one phase to another via a phase boundary. The theory is based on the idea that a fluid film (or mass transfer boundary) forms wherever there is contact between two phases.

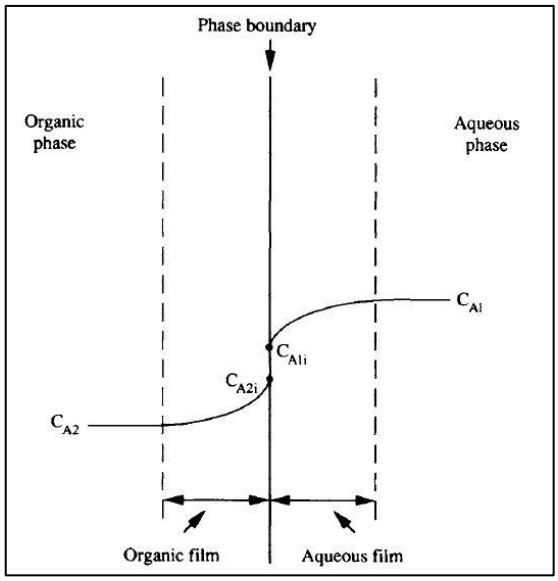

Figure 1.29. Mass transfer through a film (Doran, 1995)

Example:

If substance A was to be transferred across the phase interface (Figure 1.29) and we assume that both of the phases were immiscible (like oil and water). If initially A was at a higher concentration in the aqueous phase and each phase is well mixed within the turbulent regime. The concentration of A in bulk aqueous phase would be (C_{A1}) and the same in the organic phase would be (C_{A2}). Because the fluid velocity is thought to be negligible at the phase boundary, it is assumed that mass

transfer through this film is thought to be purely governed by molecular diffusion (governed by Fick's law). The concentration of A thus changes as it approaches the phase boundary, culminating with C_{A1i} as the interfacial concentration of A in and the aqueous phase and C_{A2i} in the organic phase. It is assumed that there is very little resistance to molecular transport at the interface point, the theory effectively assumes that both phases are in equilibrium at this point. The difference between C_{A1i}&C_{A2i} at the interface incorporates the notion that A may be more soluble in one phase than another.

Convective mass transfer & Gas liquid mass transfer

The rate of mass transfer is directly proportional to the driving force for transfer multiplied by the transfer area. This can be expressed with the proportionality coefficient, k, to give the formula:

$$Transfer\ rate = k \times transfer\ area \times driving\ force \qquad (1)$$

If this equation is adapted to represent the fluids at either side of a phase boundary, the driving force can be expressed in terms of concentration difference:

$$N_A = ka\Delta C_A = ka(C_{Ao} - C_{Ai}) \qquad (2)$$

Where; N_A= rate of mass transfer of A, k = the mass-transfer coefficient, a = the area available for mass transfer, C_{Ao} = the bulk transfer of A away from the phase boundary and C_{Ai} = the concentration of A at the interface.

To calculate k, the flow velocity, geometry of the system and fluid properties, such as viscosity and diffusivity all need to be considered. This is very difficult to do manually and accurately using equations alone, so typically this value is estimated from empirical data. However, certain CFD software packages such as COMSOL and FLUENT can incorporate these variables into their simulations, but this comes at the expense of increased processing time.

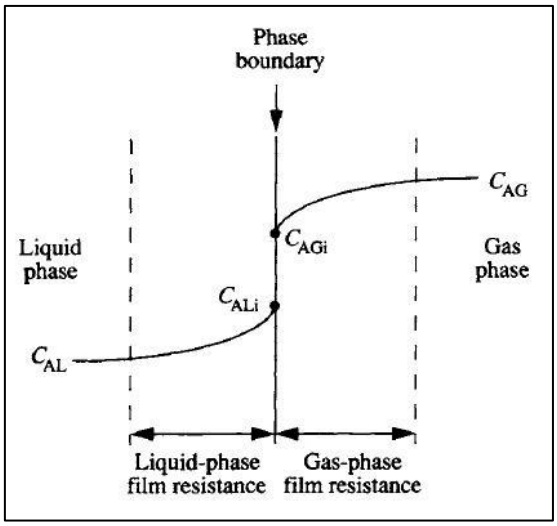

Figure 1.30. Mass transfer from gas to liquid (Doran, 1995)

To model the mass transfer within algal cultures, the mass transfer equation needs to be optimised for gas to liquid transfer.

If A is transferred from the gas into the liquid, the concentration of A in the bulk liquid is C_{AL} and C_{ALi} at the interface. The corresponding concentrations for A in the gas are C_{AG} and C_{AGi} respectively (Figure 1.30).

The rate of mass transfer of A through the gas boundary layer is:

$$N_{AG} = k_G a(C_{AG} - C_{AGi}) \qquad (3)$$

The rate of mass transfer of A through the liquid boundary layer is:

$$N_{AL} = k_L a(C_{ALi} - C_{AL}) \qquad (4)$$

Where k_G and k_L are the gas-phase mass-transfer and liquid-phase mass-transfer coefficients respectively.

The equations can be rearranged if it is assumed that an equilibrium of concentrations exists at the film central interface, i.e. $C_{ALi} = C_{AGi}$. This is described by the distribution law, which states: "At equilibrium, the ratio of solute concentrations in the two phases is given by the distribution coefficient or partition coefficient, m". This law is only valid when both of the solvents are immiscible and there is no chemical reaction taking place.

If there is a linear correlation between the equilibrium concentration in gas and liquid phases the equation can be rearranged to:

$$C_{AGi} = mC_{ALi} \text{ or } (5)$$

$$C_{ALi} = \frac{C_{AGi}}{m} \qquad (6)$$

$$\text{or } m = \frac{C_{AGi}}{C_{ALi}} \qquad (7)$$

If it is also assumed that the mass transfer reaction is in steady state, that is, elements in bulk gas are leaving the gas and entering the liquid at the same rate either side of the phase boundary. It can be assumed that; $N_{AG} = N_{AL}$. Which can be simplified to N_A, thus the prior equations can be changed to:

$$\frac{N_A}{k_G a} = C_{AG} - C_{AGi} \text{ for the gas mass transport and} \qquad (8)$$

$$\frac{N_A}{k_L a} = C_{ALi} - C_{AL} \text{ for the liquid mass transfer.} \qquad (9)$$

If the distribution coefficient (m) equations are then substituted in, the equations become:

$$\frac{N_A}{k_G a} = C_{AG} - mC_{ALi} \text{ for the gas and} \qquad (10)$$

$$\frac{N_A}{k_L a} = \frac{C_{AGi}}{m} - C_{AL} \text{ for the liquid mass transfers respectively.} \qquad (11)$$

If the two prior equations are then multiplied and divided by m:

$$\frac{N_A}{k_L a} = C_{ALi} - C_{AL} \quad \text{Becomes} \quad \frac{mN_A}{k_L a} = mC_{ALi} - mC_{AL} \& \qquad (12)$$

$$\frac{N_A}{k_G a} = C_{AG} - C_{AGi} \quad \text{Becomes} \quad \frac{N_A}{mk_G a} = \frac{C_{AG}}{m} - \frac{C_{AGi}}{m} \qquad (13)$$

And the four equations are added together (10+12 & 11+13), then the interfacial-concentration terms (mC_{ALi}&$\frac{C_{AGi}}{m}$) can be cancelled out, giving:

$$N_A\left(\frac{1}{k_G a} + \frac{m}{k_L a}\right) = C_{AG} - mC_{AL} \quad \text{for gas transfer \&} \qquad (14)$$

$$N_A\left(\frac{1}{mk_G a} + \frac{1}{k_L a}\right) = \frac{C_{AG}}{m} - C_{AL} \text{ for liquid.} \qquad (15)$$

The bracketed part of the previous equations can then be used to define the overall mass transfer coefficients; K_G = The overall gas-phase mass transfer coefficient and K_L = The overall liquid -phase mass transfer coefficient. Using the following formulas:

$$\frac{1}{K_G a} = \left(\frac{1}{k_G a} + \frac{m}{k_L a}\right) \text{ and} \qquad (16)$$

$$\frac{1}{K_L a} = \left(\frac{1}{mk_G a} + \frac{1}{k_L a}\right) \qquad (17)$$

The rate of mass transfer between the gas and liquid can then be summarised as:

$$N_A = K_G a(C_{AG} - mC_{AL}) \text{ and } N_A = K_L a\left(\frac{C_{AG}}{m} - C_{AL}\right) \qquad (18)$$

Where; $mC_{AL} = C_{AG}^*$, the gas-phase concentration of A in equilibrium with C_{AL} and $\frac{C_{AG}}{m} = C_{AL}^*$, the liquid-phase concentration of A in equilibrium with C_{AG}. Thus the equations become:

$$N_A = K_G a(C_{AG} - C_{AG}^*) \text{ and } N_A = K_L a(C_{AL}^* - C_{AL}) \qquad (19)$$

These equations can be further simplified depending on the where the most resistance to transfer occurs. If A was extremely soluble in the liquid phase (like ammonia in water), the liquid phase film would provide less resistance than that of the gas. Therefore, the $k_l a$, would be a large value, making $K_G a$ almost equal to $k_G a$. If this effect is applied to the to the gas side equation above, we get: $N_A = k_G a(C_{AG} - C_{AG}^*)$ (20)

If the opposite occurs, i.e. A is not very soluble in the liquid phase (e.g. oxygen in a liquid). Then, the equation can become: $N_A = k_L a(C_{AL}^* - C_{AL})$ (21)

When aeration is supplied by bubbles the interfacial area depends on the size and number of bubbles in the liquid. This is also dependant on other factors such as the medium composition, fluid velocity and the gas flow rates (in and out of the system). Typically to take into account

this variability, the mass transfer coefficients are estimated using empirical correlations or defined experimentally.

Gas transfer from bubble to cell

Photoautotrophic algae take up carbon dioxide from the liquid medium around them and expel oxygen. The rates at which these metabolic reactions and thus mass transfer takes place is dependent on many factors (discussed previously). The cultures can be grown in two main configurations, batch and continuous. Due to equipment limitations, the entirety of this study uses the batch configuration, so only this mode of culture will be discussed. In a batch system the CO_2 and O_2 vary with time due to the nutrients been consumed by the algal cells at different rates with periodic replenishment. As the cell biomass increases, the rate of CO_2 uptake and O_2 expulsion increases accordingly. The respiration rates of the individual cells also changes depending on the growth phase and whatever stress factors as in effect. The uptake rate can be calculated using the following simple equation:

$$Q_{CO2} = q_{CO2}x \qquad (22)$$

Where; x = the cell concentration, Q_{CO2} = the CO_2 uptake rate (g $l^{-1}s^{-1}$) and q_{CO2} = the specific CO_2 uptake rate (g $g^{-1}s^{-1}$).

If the dissolved CO_2 concentration (C_{AL}) is consumed and falls below the critical CO_2 concentration (C_{crit}), the q_{CO2} becomes dependant on C_{AL}in the liquid in a linear fashion. If the C_{AL} is maintained above the C_{crit} value then q_{CO2} is independent of the C_{AL} level and can be maximised. To maintain optimal growth rates for the culture and avoid limitation, C_{AL} must be maintained above C_{crit} everywhere in the growth vessel.

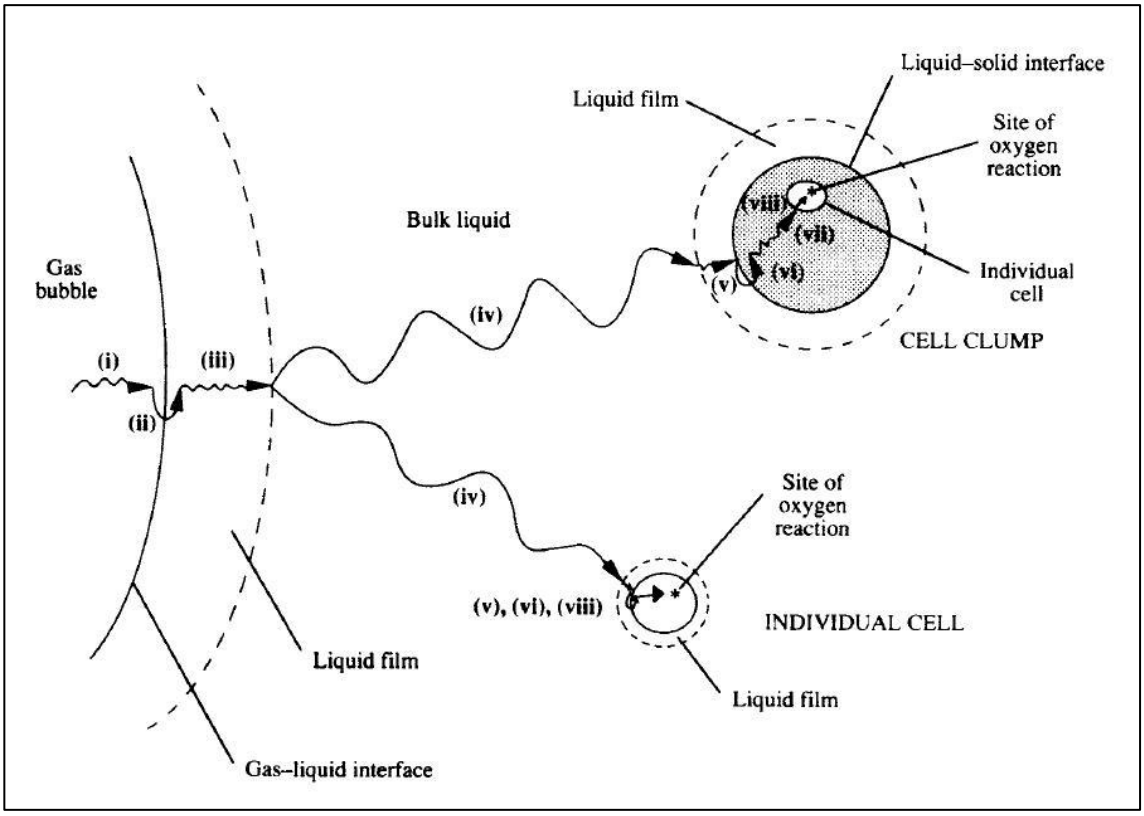

Figure 1.31. Mass transfer resistances from gas bubble to cell (Doran, 1995)

All mass transfer resistances need to be taken into consideration if a system is to be modelled effectively. This means that all eight steps as the gas transfers from the air bubbles to the cells need to be included, along with the various resistances depending on reactor conditions. For most bioreactors the following assumptions are valid (Figure 1.31):

i. Transfer from the interior of the bubble to the gas-liquid interface (relatively fast).
ii. Movement across the gas-liquid interface (negligible resistance).
iii. Diffusion through the liquid film surrounding the bubble (large resistance).
iv. Transport through the bulk liquid (if well mixed, small resistance).
v. Diffusion through the liquid film surrounding the cells (if single cells very small resistance, clumps/flocks can provide significant resistance).
vi. Movement across the liquid-cell interface (very small resistance).
vii. If the cells are in a floc, clump or solid particle, diffusion through the solid to the individual cell (resistance can be significant) [Note: if the cells are free floating within the media this step is redundant].
viii. Transport through the cell cytoplasm to the site of reaction. (very small resistance).

Assuming that the cultures are well mixed and free of clumps, the biggest resistance to mass transfer is that of the liquid film surrounding the gas bubbles. This factor is the rate limiting

point in the overall process, because points i-ii & iv-viii offer such small resistances they can effectively be removed from consideration. If this is the case, the previously derived equation (below) can be used to calculate mass transfer for part iii:

$$N_A = k_L a(C_{AL}^* - C_{AL}) \qquad (23)$$

With the following units; N_A = rate of CO_2 transfer per unit volume of fluid (gmol m^{-3} s^{-1}), k_L = the liquid phase mass transfer coefficient (m s^{-1}), a = gas-fluid interfacial area per unit volume of fluid (m^2 m^{-3}), C_{AL} = CO_2 concentration in the medium (gmol m^{-3}), C_{AL}^* = the equilibrium concentration or solubility of CO_2 in the medium. The difference between C_{AL} and C_{AL}^* represents the concentration-difference driving force for mass transfer.

If it is assumed that reactor is in steady state (no accumulation of gas in any location), the rate of CO_2 transfer from the bubbles must be equal to the consumption of the cells, thus:

$$N_A = Q_O = k_L a(C_{AL}^* - C_{AL}) = q_O x \qquad (24)$$

The $k_L a$ value then shows the mass transfer capability of the reactor. Changes in its value can indicate different scenarios and allow predictions to be made.

The maximum cell concentration that can be supported by the reactors mass transfer system is one useful parameter than can be predicted. If the maximum gas transfer occurs when the concentration driving force is at its highest, i.e. in; $(C_{AL}^* - C_{AL})$ when the value of C_{AL} is approximately zero. The maximum cell concentration (x_{max}) that can be supported is governed by the following equation:

$$x_{max} = \frac{k_L a C_{AL}^*}{q_O} \qquad (25)$$

From this it can be seen that if the cell concentration is lower than expected, the mass transfer ($k_L a$) needs to be improved.

The other important prediction that can be performed is calculating the minimum $k_L a$ required to keep the reactor gas concentration above the critical growth rate limiting value. This can be performed with this equation:

$$(k_L a)_{crit} = \frac{q_O x}{(C_{AL}^* - C_{AL})} \qquad (26)$$

The effect of bubble size

As has been shown previously, the efficiency of mass transfer within a reactor is heavily influenced by the interface characteristics of the bubbles within the medium. The interfacial area of the bubble (governed by its size) and its boundary layer have a large impact on the $k_L a$. The size of the bubbles is often the most important factor relating to reactor efficiency. For the same volume of gas, smaller bubbles provide a greater interfacial area for diffusion than large ones. Small bubbles also have other advantages; due to their buoyancy they have slower rising velocities in free liquid than their larger counterparts. This has the added benefit of allowing more time for mass transfer as they move through the medium (as well as creating greater mixing efficiencies, mentioned previously). This ability is defined by the gas hold-up, or the fraction of the fluid volume in a reactor that is occupied by gas. This is governed by the following equation:

$$\epsilon = \frac{V_G}{V_L + V_G} \qquad (27)$$

Where; ϵ = the gas hold-up, V_G = the volume of gas bubbles in the reactor and V_L = the volume of the liquid.

The level of gas hold-up is a very important parameter because the gas interfacial area is dependent on it, along with the bubble geometry.

The bubble sizes can also have an effect on the value of k_L in the system. If the bubble diameter is less than 2-3 mm, surface tension effects dictate the behaviour of the bubble surface. This leads to bubbles with high stability, immobile surfaces and have no internal gas circulation. This type of bubble gives a low k_L value, typically the k_L decreases with size below this size. Inversely, bubble with sizes greater than 3 mm have very flexible surfaces that can deform easily depending on the liquid flow characteristics and have internal circulation of gases. This has a beneficial effect on the k_L value and mass transfer.

Temperature

The temperature of the culture medium affects the solubility of gases into the medium, which in turn influences the k_L. An increase in temperature causes the C_{AL}^* to drop, which in-turn reduces the driving force for mass transfer due to the relation: $(C_{AL}^* - C_{AL})$. However, due to the increased energy within the system, the diffusivity of gases through the bubble liquid film is increased, which can also increase the k_L value. The net result of the two effects depends on the type of gas in the medium as well as the temperature range considered.

1.13 Fluid dynamics

The interaction and modelling of fluids in bubble column reactors is one of the most highly complex subject areas in the field of chemical engineering. Bubble dynamics and flow regimes indirectly influence all aspects of performance in airlift photo-bioreactor design (Figure 1.32).

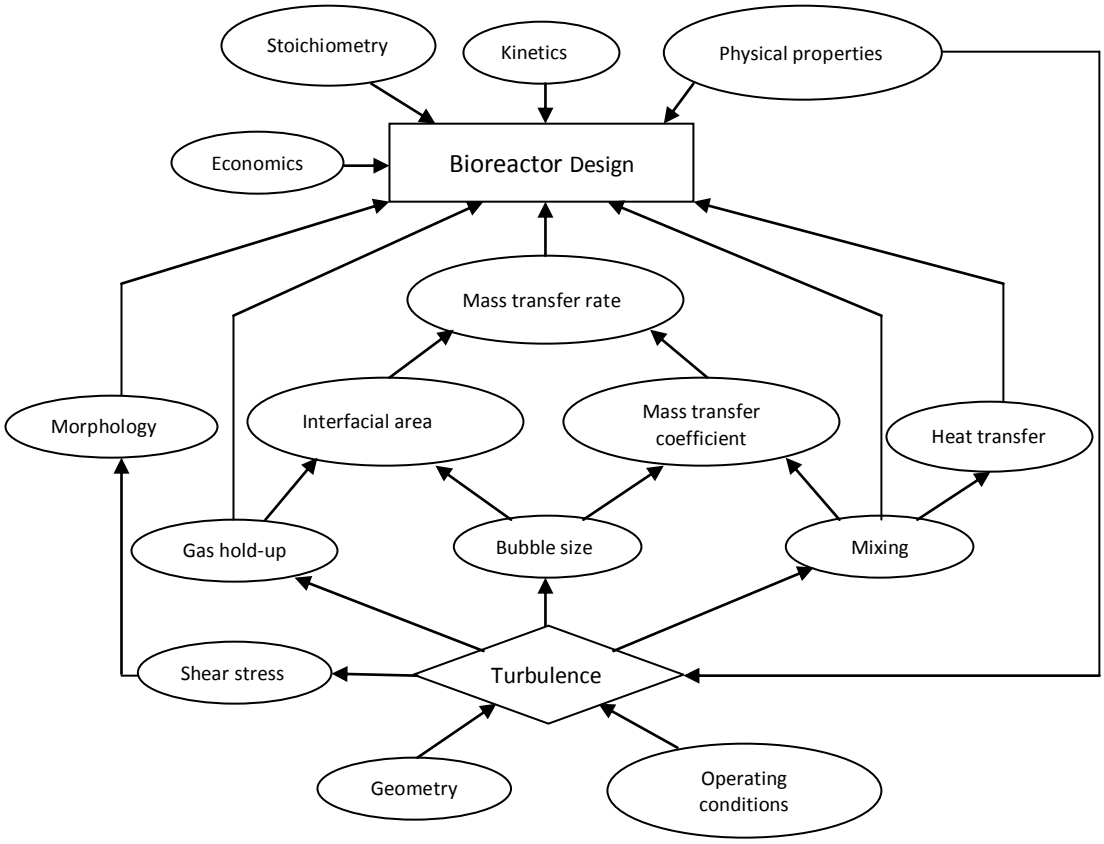

Figure 1.32 - Design interactions in bioreactors based on fluid dynamics (Kawase and Mooyoung, 1990)

Due to this complexity it would be impossible to cover all aspects of the vast array of current literature in this literature review. Given this situation, the main thrust of research has been directed towards the current applications of computation modelling using CFD software in photo-bioreactor designs, as this area is of direct relevance to the project. However, for reference a number of key review papers by authors using non computation methods are recommended; (Chisti, Halard and Mooyoung, 1988; Kawase and Mooyoung, 1990; Shah, et al., 1982; Vial, et al., 2000).

1.13.1 Computational Fluid Dynamics (CFD)

CFD is a powerful analytical tool that uses numerical techniques to simulate fluid flow interactions.The recent advent of increasingly powerful and inexpensive personal computers, along with CFD software packages such as ANSYS or COMSOL has facilitated the ability of cost effective computational models to be built commercially and academically, which can represent a complex system such as a photo-bioreactor(Bitog, et al., 2011).These simulations can provide significant insights into the behaviour of prototype systems virtually by applying fluid flow physics and chemistry, and save time and expense in producing physical models.The CFD numerical technique is based on the Navier-Stokes equations, with each cell of a mesh generated in the computational domain helping to provide an overall predictive solution (Andseron, 1995). CFD software can be used to study many factors in photo-bioreactor design that influence the fluid flow within the vessel, including;superficial gas velocity, gas hold-up, bubble diameter, column geometry, light propagation and pressure. However, to produce an accurate model of hydrodynamics in a photo-bioreactor vessel, numerous factors need to be considered, the chief being; mesh grid resolution and the selection of the most appropriate laminar/turbulence model(Gimbun, 2009). In multiphase flows, such as air and water, the most common model is based on the, the k-ε turbulence model published by Launder and Spalding in 1972, due to its relative simplicity and accuracy in predicting the behaviour of turbulent flows near wall boundaries (Singhal and Spalding, 1981). There have been variants of this model implemented in different CFD packages, with different specialisations for particular model conditions (Gimbun, 2009). Other turbulence models using different equations have also been employed, such as the large eddy simulation (LES) (Dhotre and Joshi, 2007). Although, when the gas hold-up in the reactor is less than 30%, a laminar flow model could also be applicable in the correct Reynolds regime, but care would be needed as boundary wall interactions can produce discrepancies in the final solution (Ekambara and Joshi, 2005; Gimbun, 2009; Pfleger, et al., 1999).

Multiphase simulation of the gas and liquid species is typically performed by the CFD software using one of the model approaches; Eulerian-Eulerian, Lagrangian-Eulerian and Volume of Fluid (VOF)(Bitog, et al., 2011).Within each of these transport models the conservation equations describing convection, diffusion, and reaction sources for each component species are solved.This can include multiple simultaneous chemical reactions (when rate constants are applied), modelling bulk phase (volumetric reactions) and/or on wall or particle surfaces, and in the porous region. Of these approaches only the Eulerian-Eulerian model will be discussed as it is the only method used in this study.

The Eulerian-Eulerian multiphase model averages the Navier-Stokes equations over a definedvolume, including any arbitraryparticles in a continuous phase.The continuity, mass and momentum equations for fluid and solid phases are solved, and the volume fraction (or gas hold-up) is tracked per element. A single pressure field is applied to all phases, regardless of whether the phase is continuous or dispersed.The interaction between the mean flows of phases is modelled through an interaction term, which includes drag force, and a virtual mass effect, when acceleration of secondary phase relative to the primary and additional lift forces exists.The Eulerian-Eulerian model accounts for both the continuous and dispersed phases in an Eulerian representation, creating the need for mass and momentum balances for each phase(Bitog, et al., 2011). An example of this would be the bubbles in the secondary phase (gas) are dispersed in the primary or continuous phase (liquid). As the phases mix (or separate)the secondary phase volume fraction (gas hold-up) can vary between zero and 100%.This modelling approach is highly versatile for various practical applications, but not suitable for simulations that need a precise description of the interface boundary layers, such as with large bubbles that are not rigid in shape. When used for modelling photo-bioreactors, the Eulerian-Eulerian method simulates a bubble cloud as a continuous medium with properties similar to those of a fluid.

1.13.2 Current CFD studies

A number of simulation studies have been produced in recent years using CFD techniques to model different aspects of photo-bioreactor design and operation, the majority thus far have focused on one or two of the design parameters such as light distribution, mixing inside the photo-bioreactor, or flow characteristics. Some notable highlights are included here; the work by Yu, et al. (2009) looked into the effects of changing draft tube geometry using CFD and physical growth experiments (*Isochrysis galbana*)in a flat plate photo-bioreactor, a secondary study was also performed using the same methods, but this time growing *Botryococcus braunii*(Xu, et al., 2012). Roncallo, et al. (2013) compared the effects of bubble column geometry versus airlift on the growth of *Nannochloropsis* along with CFD, a recent study by Wang and You (2013) looked at the effects that corrugation of the inner baffles in a flat plate photo-bioreactor has on light penetration and two studies have looked at the effects of cross-sections and bends in tubular photo-bioreactors to reduce frictional loss (Ramirez-Duque and Ramos-Lucumi, 2011; Wongluang, Chisti and Srinophakun, 2013). Open raceway ponds have also benefited from CFD based optimisation to reduce frictional losses (Hadiyanto, et al., 2013). Many more studies have been conducted in this subject area, the review paper by Bitog, et al. (2011) provides additional details.

1.13.3 Future CFD studies

Although the CFD approach has provided an excellent tool to help in the design of photo-bioreactors and analysis of their performance, many issues still need to be addressed in the application of its methodology, if further more detailed/integrated modelling is to be achieved (Bitog, et al., 2011). One of the biggest bottlenecks is the fact that no reliable systematic method for bioreactor scale-up presently exists. Many of the associated mathematical issues with CFD modelling, such as the limitations and applicability of certain flow models, are also rarely discussed. In addition, for simplicity many models are also just based on the interaction of air and water, rather than factoring in the effects that algal cells have on the properties of the fluids involved, which can lead to erroneous conclusions.To enable true optimisation and successful design of a photo-bioreactor system,all these factors and the direct ones influencing the growth of microalgae, such as; the propagation of light, algal growth responses to the various nutrient concentrations and temperature need to be dealt with. However, this will inevitably lead to increases in complexity and the requirement for more computing power, but given current technological developments rates, the real stumbling block will be with our understanding of fluid dynamics and the programming required to make the CFD software more inclusive to the elements previously mentioned. Given the current climate, incentives and rate of progress however, the future applications of CFD still look to be most promising.

1.14 Aims of the Project

The main aim of this study was to examine the current limitations within existing photo-bioreactor designs for the culture of marine based microalgae. A particular emphasis was placed on lipid production, mass transfer and fluid flow optimisation under the effects of fluidic oscillation. Photo-bioreactor light penetration was also a key area in the investigation. Based on these overall aims, a series of objectives were identified:

- To design, build and test multiple photo-bioreactor growth systems on varying scales, to quantify growth limitations and assess the impact of fluidic oscillation on algal growth.
- Construct computer models to assess the effectiveness of fluid flow and mass transfer within the various photo-bioreactor designs and use these data for iterative development work.
- Determine the optimalgrowth/lipid yielding conditions forselected algal strains within the developed growth system designs and their potential for biodiesel production.
- Find out whether it is feasible to increase algal growth productivity by enhancing PAR light using a new type of photo-bioreactor coating or 'smart skin'.

2 Materials and Methods

2.1 Media

2.1.1 Dunaliella Medium

Dunaliella growth medium (Hard and Gilmour, 1996) was prepared using the following stock solutions:

Stock Solution	Solid (g) to Distilled water (ml) ratio
2.4 M $MgSO_4.7H_20$	133.1g : 225 ml
2.0 M $MgCl_2.6H_20$	91.5g : 225 ml
1.0 M $CaCl_2.2H_20$	33.1g : 225 ml
4.0 M $NaNO_3$	34.0g : 100 ml
0.5 M Na_2SO_4	63.9g : 900 ml
0.1 M NaH_2PO_4	3g : 250 ml
2.0 M KCl	74.6g : 500 ml
1.0 M HEPES pH 7.6	59.6g : 250 ml
1.5 mMFeEDTA pH 7.6	0.0551g : 100 ml

Trace elements stock solution	
Element concentration	**Amount needed in 400 ml volume**
185 mM H_3BO_3	4.576 g
7 mM $MnCl_2.4H_20$	0.5541 g
0.8 mM $ZnCl_2$	0.0436 g
0.02 mM $CoCl_2$	4 ml of 2 mM
0.0002 mM $CuCl_2$	0.4ml of 0.2 mM

Per litre of medium, 0.8 L of distilled water was combined with the required amount of NaCl (1-3 M).The stock solutions were then added in the following quantities, excluding $NaHCO_3$:

Solution component	Concentration wanted (mM)	Volume added per 1litre (ml)
2 M KCl	10	5
2 M $MgCl_2$	20	10
1 M $CaCl_2$	10	10
2.4 M $MgSO_4$	24	10
4 M $NaNO_3$	5	1.25
0.5 M Na_2SO_4	24	48
100 mM NaH_2PO_4	0.1	1
1.5 mMFeEDTA	0.0015	1
Trace elements	1 ml $litre^{-1}$	1
1 M HEPES pH 7.6	20	20

The mixture was then made up to to 1 litre with distilled water and 1 g of $NaHCO_3$ was added. The medium was then autoclaved and left to cool to room temperature beforepH adjustment. 2 ml samples were taken aseptically and the pH was checkedand adjusted to 7.5 (if necessary) using HCl or NaOH solutions.

2.1.2 F/2 Medium

Standard F/2 growth medium(CCAP, 2000; Guillard and Ryther, 1962) was prepared using a series of stock solution combinations. Firstly, the following sub stocks were made with distilled water:

Trace metals- sub-stock solutions	
Element	**g / 100 ml dH_2O**
$MnCl_2.4H_2O$	18
$ZnSO_4.7H_2O$	2.2
$CoCl_2.6H_2O$	1
$CuSO_4.5H_2O$	0.98
$Na_2Mo_4.2H_2O$	0.63

Vitamin mix - sub-stock solution	
Element	**g / 100 ml dH_2O**
Biotin (d-Biotin)	0.1
Cyanocobalamin (Vitamin B_{12})	0.1

Sub stocks were then combined with other elements to make the following final stock solutions:

Final trace metals stock solution (made to 100 ml with dH_2O)	
Element	**g**
$FeCl_3.6H_2O$	0.315
Na_2 EDTA	0.436
Sub-stock	**ml**
$MnCl_2$	0.1
$ZnSO_4$	0.1
$CoCl_2$	0.1
$CuSO_4$	0.1
Na_2Mo_4	0.1

Final Vitamin - stock solution (made to 100 ml with dH_2O)	
Element	**g**
Thiamine HCl (Vitamin B_1)	0.002
Sub-stock	**ml**
Biotin (d-Biotin)	0.1
Cyanocobalamin (Vatamin B_{12})	0.1

Other Final Stock Solutions (g/100 ml dH_2O)	
$NaNO_3$	7.5
$NaH_2PO_4.2H_2O$	0.5

The final vitamin stock solution was filter sterilised. The artificial sea salt mixture was then made (table right). Per litre of medium, 33.6 g of sea salt mixture was dissolved in 950ml of distilled water. 1 ml of the $NaNO_3$, $NaH_2PO_4.2H_2O$ and final trace metals stock solutions were then added. 0.5 ml of the final vitamin mix was then added and the medium was made up to 1 litre.The medium was autoclaved and left to cool to room temperature beforepH adjustment. 2 ml samples were taken aseptically and the pH was checkedand adjusted to 7.5 (if necessary) using HCl or NaOH solutions.

Sea Salt Mixture (33.6g total/L media)		
Element	**g**	**Conc (mM)**
Na_2Cl_2	24	410
$MgSO_4.7H_2O$	2.9	24
$MgCl_2.6H_2O$	4.66	49
$CaCl_2.2H_2O$	1.17	16
$KCl.2H_2O$	0.62	8
$NaHCO_3$	0.178	2
$Na_2B_4O_7$	0.047	0.2
KBr	0.029	0.2
$SrCl_2.6H_2O$	0.029	0.2
H_3BO_3	0.029	0.2
$Na_2S_2O_3$	0.0039	0.002

2.2 Lipid Extraction and Determination

2.2.1 Gravimetric Extraction

Algal lipid extractionwas performed based on the methods byBligh and Dyer (1959) & Folch, Lees and Stanley (1957) . Algal culture was aseptically removed from a relevant growth device and transferred to a 50 ml Falcon tube. The container was centrifuged at 3000 *g*for 10 min. The supernatant fluid was discarded and the pellet re-suspended in 5 ml of distilled water. The sample was centrifuged again at 3000 *g* for 5 min and the supernatant fluid discarded. The pellet was re-suspended in 1ml of distilled water and the sample transferred to a pre-weighed 1.5 ml Eppendorf tube (fitted with a separate, pierced lid). The sample was frozen at -80°C overnight (12h minimum) and then lyophilised (freeze dried to remove the water) for 24 h. The sample was then weighed to estimate the weight of biomass. 500 µl of 2:1 v/v MeOH:$CHCl_3$ was added to each tube. The sample was then sonicated on ice for 1 min in 15 second bursts. The sample was centrifuged at 3000 *g* for 5 min and the volume of supernatant fluid estimated using a Gilson pipette and the pellet was discarded. MeOH, $CHCl_3$ and 1% NaCl(aq) were added to achieve a volume of 1.0 ml in the ratio 2:2:1. The sample was mixed, centrifuged at 3000 *g* for 2 min and the green, lower phase transferred to a pre-weighed Eppendorf tube. The solvent was allowed to evaporate in a fume cupboard for 24 h, or until dry, and the sample weighed to calculate the weight of total lipid recovered. This procedure was carried out in triplicate, the amount of culture used depended on the growth rate and total volume, no more than 50 ml was typically harvested per sample.

2.2.2 Nile Red Fluorescence

2.2.2.1 Fluorescence Spectrometry

Nile Red (9-diethylamino-5H-benzo[α]phenoxazine-5-one)fluorescence emission scans were performed on selected algal cultures using a Horiba Scientific FluoroMax 4 Spectrofluorometer (Model:81110 v1.1) linked to PC running Horiba's proprietary FluorEssence V software.Based on the methods developed by Cooksey, et al. (1987), Pick and Rachutin-Zalogin (2012) and Bertozzini, et al. (2011); scans were performed between 400-700 nm using an excitation slot aperture of 5 nm, emission slot aperture 5 nm with an excitation wavelength of 490 nm. The dark offset function was used and

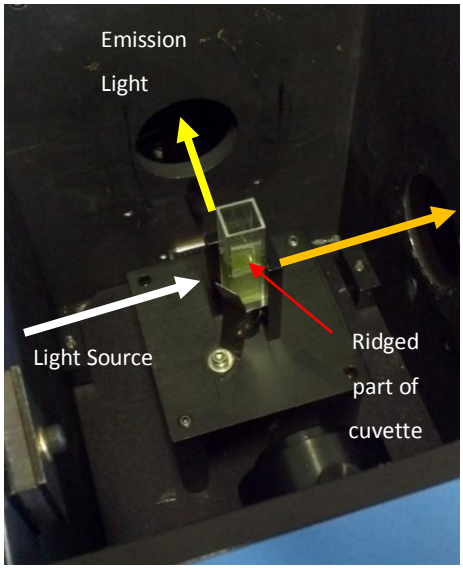

Figure 2.1. Fluorescence spectrometer cuvette light path

background readings were subtracted to give net fluorescence intensity in counts per second (CPS). For readings to be taken, algal cultures and media were added to a standard 1 ml polystyrene cuvette. The samples were mounted in a bracket with the ridged sections facing toward the detector (see Figure 2.1). Algal cultures in stationary growth phase (14-21 days old) were re-suspended in fresh media and adjusted to an optical density of 0.2 at 595 nm (1 sec integration), approximately $1x10^6$ cells/ml for *D. salina* cultures to avoid self shading (section 2.2.2.3).

Triolein spiked test samples were made in labelled 1.5 ml Eppendorf tubes by adding different ratios of triolein (1,2,3-Tri-[(cis)-9-octadecenoyl]glycerol, C57 H104 O6 ~99% -44895-U Supelco) to isopropanol (propan-2-ol) in a 10 µl volume. The samples were sealed, kept on ice or refrigerated and kept in the dark in between test runs to avoid degradation. 990µl of adjusted algal culture was added to the sample just prior to staining and the sample was mixed by pipetting (see Table 2.1).

Table 2.1. Triolein mixture concentrations for Nile Red lipid standard curve.

Triolein Conc (mg/ml):	0.05	0.04	0.03	0.02	0.01	0.005	0.0025	0
Culture (µl):	990	990	990	990	990	990	990	990
Triolein (µl):	10	8	6	4	2	1	0.5	0
Isopropanol (µl):	0	2	4	6	8	9	9.5	10

The sample was then transferred to the 1 ml cuvette and read on the spectrofluorometer to give a background reading. 20µl of 15.91 µg/ml Nile Red (NR) in acetone stock was then added to the 1 ml spiked sample, making a final NR concentration of 1µmole/ml in the sample. The sample was then mixed by pipette again and kept in the dark for 5 min, mixed again then read immediately.

2.2.2.2 Fluorescence Microscopy

D. salina cultures were grown until in stationary phase (14-21 days old) then diluted using fresh media to an optical density of 0.2 at 595 nm (1 sec integration), approximately $1x10^6$ cells/ml to avoid self shading (section 2.2.2.3). 1 ml of culture was added to a 1.5 ml Eppendorf tube along with 5 µl of Grams Iodine and shaken to kill the cells and stop motility. 20 µl of NR in acetone (31.83µg/ml) were then added to the sample, making the concentration in the sample 2 µM/ml. The tube was then mixed by inversion and the dye penetration time was monitored. 10 µl of the sample was then added to a clean microscope slide and a cover slip was added gently. The edges of the cover slip were then sealed with nail varnish to stop evaporation. Once the varnish had dried and after 4-5 mins of dye penetration, the slide was

ready to be viewed. Sample imaging was performed using a Nikon Eclipse E400 Microscope equipped with a Nikon DXM1200 Digital Camera. Excitation light was provided by a Nikon Super High Pressure Mercury Lamp via 450-490 nm monochromatic optical filter. General illumination was achieved using the microscopes built-in lighting system. All images were taken using a Nikon 100x oil immersion lens (Phase 3). A single drop of mineral oil was added to the cover slip and the image was brought in to focus using excitation light only. Two sets of photos were taken for each cell of interest, one using white light, one using excitation light only. White light intensity was controlled using the microscope iris and the fluorescence using the inbuilt shutter. To avoid light bleaching and quenching effects, samples were only illuminated when the photos were being captured. Image acquisition was performed using LUCIA G Software with the following capture settings; Red: 48, Green: 31, Blue: 68, Gain: 25, Gamma: 0.40, Offset: 23, Fine Preview: on, Exposure: 72ms.

2.2.2.3 Peak Fluorescence 96 Well

Isolation of the peak NR emission time was performed in a 96 well plate format based on the work byAlonzo and Mayzaud (1999), Bertozzini, et al. (2011), Chen, et al. (2009), Cooksey, et al. (1987), Elsey, et al. (2007), Gardner, et al. (2011), Gardner, et al. (2012), Pick and Rachutin-Zalogin (2012).*D. salina* cultures were grown until in stationary phase (14-21 days old) and a samplewas removed from the growth vessel (at least 10ml) and the OD was adjusted to 1.0 (A) at 595nm.The adjusted culture was then centrifuged for 5 min at *3000*g and the supernatant was discarded immediately when finished. An equivalent volumeof fresh mediumwas then used to replace the discarded supernatant and the algal pellet was re-suspended. The cultures were then diluted with fresh media and added to sections of an eight well multi-channel pipette reservoir (Thermo Scientific) in the amounts shown in Table 2.2 below.

Table 2.2. Algal culture concentrations for self shading testing.

Percentage:	100	87.5	75	62.5	50	37.5	25	12.5	Total (ml)
Culture (µl):	2000	1750	1500	1250	1000	750	500	250	9
Medium (µl):	0	250	500	750	1000	1250	1500	1750	7

Once diluted, the cultures were mixed with a multi-channel pipette and transferred to a 96-well flat bottomed clear plate (Greiner Bio-One Cellstar 655 185) in the following format (see Figure 2.2).

Dilution from 1(A) @ OD 595 (%):			100	87.5	75	62.5	50	37.5	25	12.5	Empty Wells			
			1	2	3	4	5	6	7	8	9	10	11	12
Nile Red Stained Cells	R1	A	200	200	200	200	200	200	200	200	0	0	0	0
	R2	B	200	200	200	200	200	200	200	200	0	0	0	0
	R3	C	200	200	200	200	200	200	200	200	0	0	0	0
	R4	D	200	200	200	200	200	200	200	200	0	0	0	0
Unstained Cells	R1	E	200	200	200	200	200	200	200	200	0	0	0	0
	R2	F	200	200	200	200	200	200	200	200	0	0	0	0
	R3	G	200	200	200	200	200	200	200	200	0	0	0	0
	R4	H	200	200	200	200	200	200	200	200	0	0	0	0

Figure 2.2. 96 Well plate layout for peak fluorescence test. **Note: Rows R1 to R4 are replicates from the same concentration**

Four x 200 µl were removed from the reservoir and added to the plate as the 'unstained cells' at the relevant concentration (i.e. wells E1, F1, G1, & H1 are 100% conc). 200 µl were then discarded from each reservoir to make the remaining volume 1 ml. The optical density was measured at 595 nm, using a Wallac Victor 2 Multi-label Plate Reader (see 'Shaken OD @ 595 (1.0s)' protocol below) set at a fixed temperature of 25^{o}C. 20 µl of the 15.9 µg/ml NR /acetone were added to each reservoir (making 2 µmoles/ml) using a multi-channel pipette and the cultures were quickly mixed. The stained samples were then transferred to the corresponding cell concentration 'Nile Red Stained Cells' using the multichannel pipette (4 x 200 µl, per concentration). A timer was started and the plate was then placed in the plate reader again and the stained wells were read using an excitation wavelength of 490 nm and emission of 580 nm with a 0.5 second integration (see 'NR KB – Peak Finder (1)' protocol). When the protocol was completed, the unstained wells were scanned using the same wavelengths (see 'NR KB – Peak Finder (2)' protocol) to get the background fluorescence values. When completed, the emission change over time is calculated (when the time for each reading is correlated with the timer reading) by subtracting the fluorescence readings for the stained cells away from the unstained. The OD 595 nm readings are used to correlate the relationship between fluorescence intensity and cell number to check for self shading issues.

Plate Reader Settings:

Fluorometry Label Properties -NR Stain (0.5s) Ex490 Em580; CW-Lamp Energy:9032, CW-Lamp Control:Stabilised Energy, CW-Lamp Filter:P490, Emission Filter:F580, Emission Aperture:Normal, Counter Position:Top, Counting Time:0.5 s. Photometry Label Properties - Absorbance @ 595 (1.0 s); CW-Lamp Filter:P595, Reading Time:1 s.

Protocol Settings:

NR KB – Peak Finder (1); First Step: Shaking – Settings; Duration: 5 s, Speed: Fast, Diameter: 1mm, Type: Double Orbit. Second Step: Reading using label settings (NR Stain (0.5s) Ex490 Em580) and plate layout (Fig 2.2), Readings taken from A1-D8. Repeats: 60, approx. time per repeat 50 s.

NR KB – Peak Finder (2); First Step: Shaking – Settings; Duration: 5 s, Speed: Fast, Diameter: 1mm, Type: Double Orbit. Second Step: Reading using label settings (NR Stain (0.5 s) Ex490 Em580) and plate layout (Fig 2.2), Readings taken from E1-H8. Repeats: 1.

Shaken OD @ 595 (1.0s); First Step: Shaking – Settings; Duration: 5 s, Speed: Fast, Diameter: 1mm, Type: Double Orbit. Second Step: Reading using label settings (Absorbance @ 595 (1.0 s)) and plate layout (Fig 2.2), Readings taken from A1-H12. Repeats: 1.

2.2.2.4 Nile Red Concentration 96 Well

NR concentration optimisation was performed in a 96 well plate format based on the work byAlonzo and Mayzaud (1999), Bertozzini, et al. (2011), Chen, et al. (2009), Cooksey, et al. (1987), Elsey, et al. (2007), Gardner, et al. (2011), Gardner, et al. (2012) and Pick and Rachutin-Zalogin (2012). Six stock NR solutions were prepared, one primary stock and five secondary stocks to produce final concentrations in algal culture of 0.25-3 μmoles/ml when added from a 20 μl aliquot. The primary stock was made using NR and acetone in a concentration of 0.25 mg/ml (or 250 μg/ml).Secondary stocks were made to give final in culture concentrations of 0.25, 0.5, 1, 2 and 3 μmoles/ml. Stocks were sealed, wrapped in aluminium foil to stop photo-degradation and stored at -80°C to reduced evaporation. Based on the data from procedure 2.2.2.3, a cell concentration large enough to produce a good fluorescent signal, whilst avoiding self shading was selected for this method; *D. salina* 19/30 optimum was found to be approx. $1x10^6$ cells /ml or OD 0.2 (595 nm). *D. salina* cultures were grown until in stationary phase (14-21 days old) and a samplewas removed from the growth vessel (at least 10ml) and adjustedto the optimal cell concentration.The adjusted culture was then centrifuged for 5 min at *3000*g and the supernatant was discarded immediately when finished. An equivalent volumeof fresh mediumwas then used to replace the discarded supernatant and the algal pellet was re-suspended. The cultures were then added to 5 sections (corresponding with NR concentration) of an eight well multi-channel pipette reservoir (Thermo Scientific), 2 ml in each. Using a multi-channel pipette 4 x 200 μl were transferred from each reservoir and added to the plate as the

'unstained cells' at the relevant concentration (i.e. wells E1, F1, G1, & H1 at are 3 μmoles/ml NR), see layout below (Figure 2.3).

NR Conc (μmoles/ml):			3	2	1	0.5	0.25	Empty Wells						
			1	2	3	4	5	6	7	8	9	10	11	12
Nile Red Stained Cells	R1	A	200	200	200	200	200	0	0	0	0	0	0	0
	R2	B	200	200	200	200	200	0	0	0	0	0	0	0
	R3	C	200	200	200	200	200	0	0	0	0	0	0	0
	R4	D	200	200	200	200	200	0	0	0	0	0	0	0
Unstained Cells	R1	E	200	200	200	200	200	0	0	0	0	0	0	0
	R2	F	200	200	200	200	200	0	0	0	0	0	0	0
	R3	G	200	200	200	200	200	0	0	0	0	0	0	0
	R4	H	200	200	200	200	200	0	0	0	0	0	0	0

Figure 2.3.96 Well plate layout for Nile Red concentration test. **Note: Rows R1 to R4 are replicates from the same concentration**

200 μl were then discarded from the each reservoir to make the remaining volume 1 ml. The optical density was measured at 595 nm, using a Wallac Victor 2 Multi-label Plate Reader (see 'Shaken OD @ 595 (1.0s)' section 2.2.2.3) set at a fixed temperature of 25°C. 20 μL of the NR/acetone secondary stocks were then added to the appropriate reservoir (0.25-3 μmoles/ml) using a multi-channel pipette and the cultures were quickly mixed. The stained samples were then transferred to the corresponding 'Nile Red Stained Cells' using the multichannel pipette (4 x 200 μL, per concentration). A timer was started and the plate was then placed in the plate reader again. At the appropriate time interval for peak fluorescence (found using procedure 2.2.2.3, 5 min) the all wells were read using an excitation wavelength of 490 nm and emission of 580 nm with a 0.1 s integration (see 'NR KB – Conc test 0.25-3 umoles/ml ' protocol). When completed, the emission change over concentration is given by subtracting the fluorescence readings for the stained cells away from the unstained. The OD 595 nm readings are used normalise the fluorescence intensity by cell concentration.

Plate Reader Settings:

Fluorometry Label Properties -NR Stain (0.1 s) Ex490 Em580; CW-Lamp Energy:9032, CW-Lamp Control:Stabilised Energy, CW-Lamp Filter:P490, Emission Filter:F580, Emission Aperture:Normal, Counter Position:Top, Counting Time:0.1 s. Photometry Label Properties - Absorbance @ 595 (1.0 s); CW-Lamp Filter:P595, Reading Time:1 s.

Protocol Settings:

NR KB – Conc test 0.25-3 µmoles/ml;First Step: Shaking – Settings; Duration: 5 s, Speed: Fast, Diameter: 1mm, Type: Double Orbit. Second Step: Reading (using label settings (NR Stain (0.1 s) Ex490 Em580) and plate layout (below)), Readings taken from A1-H5.

2.2.2.5 Triolein Calibration Curve 96 Well

A NR lipid concentration curve was created in a 96 well plate format based on the work byAlonzo and Mayzaud (1999), Bertozzini, et al. (2011), Chen, et al. (2009), Cooksey, et al. (1987), Elsey, et al. (2007), Gardner, et al. (2011), Gardner, et al. (2012), Pick and Rachutin-Zalogin (2012). A series of eight lipid standards was made using a ratio of 1:20 polar (PC - Phosphatidylcholine (L-lecithin Type XVI-E, from fresh egg yolk ~99%)) to neutral (TO - Triolein) lipids, isopropanol and re-suspended algal culture. A primary standard was made by adding 500 µl (2500 µg) of TO to 12.5 µl (125 µg) of PC (with chloroform) in an O-ring sealed 1.5 ml Eppendorf to create 512.5 µl of 'Stabilised' Triolein. Eight different secondary lipid standards were then made by combining isopropanol with varying amounts of the primary standard and algal culture in 2 ml Eppendorf tubes (Table 2.3).

Table 2.3. Triolein mixture concentrations for Nile Red lipid standard curve.

Conc Triolein (mg/ml):	0.05	0.04	0.03	0.02	0.01	0.005	0.0025	0	Total (ml)
Culture (µl):	1979.5	1979.5	1979.5	1979.5	1979.5	1979.5	1979.5	1979.5	15.836
1:20 Triolein (µl):	20.5	16.4	12.3	8.2	4.1	2.05	1.03	0	0.06458
Isopropanol (µl):	0	4.1	8.2	12.3	16.4	18.45	19.48	20.5	0.09943

The standards were sealed, kept on ice or refrigerated and kept in the dark in between test runs to avoid degradation. *D. salina* cultures were grown until in stationary phase (14-21 days old) and a samplewas removed from the growth vessel (at least 10ml) and adjustedto the optimal cell concentration.Based on the data from procedure 2.2.2.3, a cell concentration was selected that was large enough to produce a good fluorescence signal, whilst avoiding self shading. The adjusted culture was then centrifuged for 5 min at *3000*g and the supernatant was discarded immediately when finished. An equivalent volumeof fresh mediumwas then used to replace the discarded supernatant and the algal pellet was re-suspended. Just prior to the reading, algal culture was then added to each 2 ml Eppendorf tube (corresponding with the final lipid concentration in suspension, 0-0.05 mg/ml) and mixed well. The tube contents were then transferred to an eight well multi-channel pipette reservoir. Using a multi-channel pipette 4 x 200 µL were transferred from each reservoir and added to the plate as the 'unstained cells' at the relevant concentration (i.e. wells E1, F1, G1, & H1 for the 0.05 mg concentrations), see layout in Figure 2.4.

Triolein Conc (mg/ml):			0.05	0.04	0.03	0.02	0.01	0.005	0.0025	0	Empty Wells			
			1	2	3	4	5	6	7	8	9	10	11	12
Nile Red Stained Cells	S1	A	200	200	200	200	200	200	200	200	0	0	0	0
	S2	B	200	200	200	200	200	200	200	200	0	0	0	0
	S3	C	200	200	200	200	200	200	200	200	0	0	0	0
	S4	D	200	200	200	200	200	200	200	200	0	0	0	0
Unstained Cells	S1	E	200	200	200	200	200	200	200	200	0	0	0	0
	S2	F	200	200	200	200	200	200	200	200	0	0	0	0
	S3	G	200	200	200	200	200	200	200	200	0	0	0	0
	S4	H	200	200	200	200	200	200	200	200	0	0	0	0

Figure 2.4. 96 Well plate layout for triolein concentration curve.

200 µl were then discarded from the each reservoir to make the remaining volume 1 ml. The optical density was measured at 595 nm, using a Wallac Victor 2 Multi-label Plate reader (see 'Shaken OD @ 595 (1.0s)' section 2.2.2.3) set at a fixed temperature of 25^{o}C. 20 µl of the optimal NR/acetone concentration dye (as defined in section 2.2.2.4) were added to each reservoir using a multi-channel pipette and the cultures were quickly mixed. The stained samples were then transferred to the corresponding 'Nile Red Stained Cells' using the multichannel pipette (4 x 200 µl, per concentration). A timer was started and the plate was then placed in the plate reader again. At the appropriate time interval for peak fluorescence (found using procedure 2.2.2.3, 5 min) all wells were read using an excitation wavelength of 490 nm and emission of 580 nm with a 0.1 s integration (see 'NR KB Lipid curve' protocol). When completed, the emission change over triolein equivalent lipid concentration is given by subtracting the fluorescence readings for the stained cells away from the unstained. The OD 595 nm readings are used normalise the fluorescence intensity by cell concentration. Variations of this method used larger concentrations ranges and plain non-'stabilised' triolein. The plate reader settings are exactly the same as in section 2.2.2.4.

Protocol Settings:

NR KB – Conc test 0.25-3 umoles/ml;First Step: Shaking – Settings; Duration: 5 s, Speed: Fast, Diameter: 1mm, Type: Double Orbit. Second Step: Reading using label settings (NR Stain (0.1 s) Ex490 Em580) and plate layout (Fig 2.4), Readings taken from A1-H8.

Data processing:

Each four same concentration replicates were averaged and the stained cell values were subtracted from the non-stained values. The net fluorescence value was multiplied by 5 to make it per ml. The net fluorescence was then divided by the number of cells calculated by the

OD 595nm reading (see section 2.6.3), then normalised to 1x10^6 cells/ml. The net fluorescence per condition replicate per cell was multiplied by 5, a standard error performed on all four net/cell values, then the value was normalised to 1x10^6 cells/ml. When triolein concentration is plotted on the x-axis and the net fluorescence on the y-axis the following graph is given (Figure 2.5).

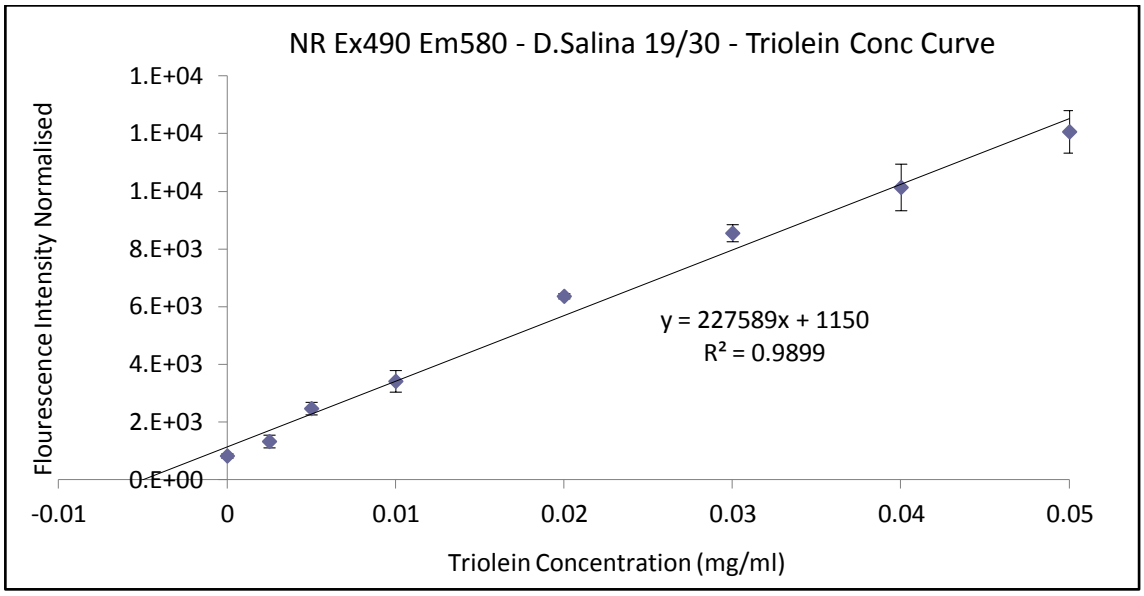

Figure 2.5. Triolein concentration versus Nile Red fluorescence intensity calibration curve.

As per the method by Bader (1980) and Bertozzini, et al. (2011) a compensated lipid curve can be made, by adding the negative x-axis intercept value (the number of mg of lipid present in the cells) to each point of the original calibration curve data.

Thus if; $y = mx + c \rightarrow (0 - c)/m = x_{intercept} = 0.005\ mg/ml$ then the following correction can be made (see Table 2.4).

Table 2.4. Correction of y axis triolein concentration values to compensate for the standard addition method.

Triolein Equiv (mg/ml):	**0.05**	**0.04**	**0.03**	**0.02**	**0.01**	**0.005**	**0.0025**	**0**
Triolein Equiv (compensated) (mg/ml):	**0.055**	**0.045**	**0.035**	**0.025**	**0.015**	**0.01**	**0.0075**	**0.005**

Based on the values in Table 2.4, the graph can be adapted to give direct values for triolein content, see Figure 2.6.

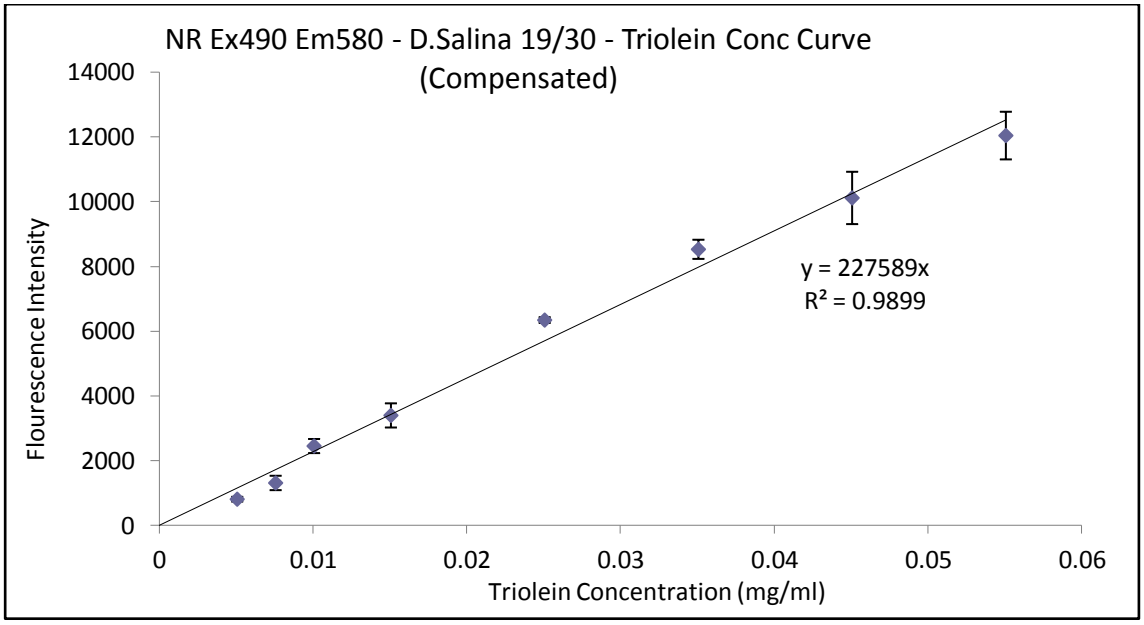

Figure 2.6.Standard addition compensated Triolein concentration versus Nile Red fluorescence intensity calibration curve.

2.2.2.6 Sample Reading 96 Well

Monitoring of neutral lipid production in growing cultures using NR was performed in a 96 well plate format based on the work byAlonzo and Mayzaud(1999), Bertozzini, et al. (2011), Chen, et al. (2009), Cooksey, et al. (1987), Elsey, et al. (2007), Gardner, et al. (2011), Gardner, et al. (2012), Pick and Rachutin-Zalogin (2012). NR measurements were begun when *D. salina* cultures had reached a sufficient level of growth, as defined by the data from procedure 2.2.2.3, to produce a clear fluorescence signal ($1x10^6$ cells /ml). For subsequent readings cultures were diluted to the same concentration to avoid self shading. 2 ml sampleswere removed from each growth vessel and added to a 2 ml Eppendorf tube. The culture was then centrifuged for 5 min at *3000*g and the supernatant was discarded immediately when finished. An equivalent volumeof fresh mediumwas then used to replace the discarded supernatant and the algal pellet was re-suspended. The tube contents were then transferred to an eight well multi-channel pipette reservoir. Using a multi-channel pipette 3 x 200µL were transferred from each reservoir and added to the plate as the 'unstained cells', labelled as the appropriate growth vessel/condition. In the layout below, S1-1, S1-2 and S1-3 are separate growth vessels under the same conditions, each sample with the same condition is equally spaced to ensure any transient effects due to sequential reading delays on the plate are averaged, see Figure 2.7.

Repeat Readings (R)		Nile Red Stained Samples (S)											
		S1-1	S2-1	S3-1	S4-1	S1-2	S2-2	S3-2	S4-2	S1-3	S2-3	S3-3	S4-3
		1	2	3	4	5	6	7	8	9	10	11	12
R1	A	200	200	200	200	200	200	200	200	200	200	200	200
R2	B	200	200	200	200	200	200	200	200	200	200	200	200
R3	C	200	200	200	200	200	200	200	200	200	200	200	200
	D	0	0	0	0	0	0	0	0	0	0	0	0
	E	0	0	0	0	0	0	0	0	0	0	0	0
R1	F	200	200	200	200	200	200	200	200	200	200	200	200
R2	G	200	200	200	200	200	200	200	200	200	200	200	200
R3	H	200	200	200	200	200	200	200	200	200	200	200	200
		S1-1	S2-1	S3-1	S4-1	S1-2	S2-2	S3-2	S4-2	S1-3	S2-3	S3-3	S4-3
		Un-Stained Samples (S)											

Figure 2.7. 96 Well plate layout for algal sample fluorescence readings.

400 µl were then discarded from the each reservoir to make the remaining volume 1 ml. The optical density was measured at 595 nm, using a Wallac Victor 2 Multi-label Plate reader (see 'Shaken OD @ 595 (1.0s)' section 2.2.2.3) set at a fixed temperature of 25^{o}C. 20 µL of the optimal NR/acetone concentration dye (as defined in section 2.2.2.4) were added to each reservoir using a multi-channel pipette and the cultures were quickly mixed. The stained samples were then transferred to the corresponding 'Nile Red Stained Cells' using the multichannel pipette (3 x 200 µL, per concentration). A timer was started and the plate was then placed in the plate reader again. At the appropriate time interval for peak fluorescence (found using procedure 2.2.2.3, 5 min) all wells were read using an excitation wavelength of 490 nm and emission of 580 nm with a 0.1 s integration (see 'NR KB – Sample Reading (1)' protocol). When completed, the emission change per culture condition can be plotted by subtracting the background unstained cell readings and the fluorescence values can be converted to a triolein equivalent using the graph produced by the procedure in section 2.2.2.5. The OD 595 nm readings are used to normalise the fluorescence intensity by cell concentration. The plate reader settings are exactly the same as in section 2.2.2.4.

Protocol Settings:

NR KB – Sample Reading (1);First Step: Shaking – Settings; Duration: 5 sec, Speed: Fast, Diameter: 1mm, Type: Double Orbit. Second Step: Reading using label settings (Nile Red Stain (0.1s) Ex490 Em580) and plate layout (Fig 2.7), Readings taken from A1-C12 and F1-H12.

2.2.3 Direct Transesterification

2.2.3.1 Sample Measurement

Algal direct transesterification was performed based on the methods by Griffiths, van Hille and Harrison (2010), Ichihara and Fukubayashi (2010), Laurens, et al. (2012), Lepage and Roy (1986). This method was developed with the help of MBiolSci student Stephen Marshall (Marshall, 2013). Algal culture was aseptically removed from a relevant growth device and transferred to a 50 ml Falcon tube. The container was centrifuged at 3000 *g*for 10 min. The supernatant fluid was discarded and the pellet re-suspended in 5 ml of distilled water. The sample was centrifuged again at 3000 *g* for 5 min and the supernatant fluid discarded. The pellet was re-suspended in 1ml of distilled water and the sample transferred to a pre-weighed 1.5 ml Eppendorf tube (fitted with a separate, pierced lid). The samples were frozen at -80 °C overnight (12h minimum) and then lyophilised (freeze dried to remove the water) for 24 h. The sample was then weighed to estimate the weight of biomass and 7-10 mg transferred to a clean glass crimp vial (11 mm, 2 ml, 12x30 mm Kinesis CRV12-02). 190 µl chloroform/methanol (2:1, v/v) were then added to each vial for lipid solubilisation. 10 µl (0.1 mg) of tridecanoic acid (C13 lipid) in chloroform/methanol (2:1, v/v) were then added as internal standard for reaction efficiency. 0.3 ml HCl/ MeOH (5%, v/v) catalyst were then added to each vial and crimp-sealed quickly with a PTFE lined cap (Kinesis CRC11-02 B2). The vials were mixed gently by hand and placed in a hot plate set at 85°C for 1 h to start transesterifying the lipids. When completed, the vials were removed and allowed to cool to room temperature for 5 min. The caps were then removed and 975 µl of Hexane added for FAME extraction. The tubes were then resealed, mixed well and left at room temperature for 1 h. After extraction, the caps were removed again and 487.5 µl of the top hexane phase were transferred into a fresh vial. 12.5 µl (0.125 mg) of the 10 mg/ml methyl nonadecanoate (C19 FAME) in hexane internal standard were then added and vials were sealed. The extracted FAMEs were then identified and quantified by gas chromatography mass spectroscopy (GC-MS) using a Perkin Elmer - AutoSystem XL Gas Chromatograph (CHM-100-790) and Perkin Elmer - TurboMass Mass Spectrometer (13657). The machine was fitted with a Zebron - ZB-5MS - 30 m 0.25 mm ID and 0.25 µm FT (7HG-G010-11) GC Capillary column and ran using the following settings;Autosampler Method:Injection volume: 5 µl, Preinjection solvent washes: 2, Post injection solvent washes: 6. Temperature Program (FAME03_100mins): 100–300°C, Ramp 1: 2^{o}C/min to 300, 20 ml/ min He constant carrier gas flow. MS Scan: El+, Start mass: 50, End mass: 600, Scan time: 0.5 s, Interscan time: 0.1 s, Start time: 0, End time: 100 min. The resultant peaks were identified and integrated using a Perkin Elmer's Turbomass software linked to a NIST database.

2.2.3.2 FAME Quantification

To calculate the concentration of algal FAMEs per biomass a 5 point calibration curve (0-8 mg/ml) was created using a pre-mixed set of FAME standards (Supelco 37 Component FAME mix 47885-U) combined with a 0.25 mg methyl nona-decanoate (C19 FAME) internal standard. The Supelco mix contained 10 mg of FAMEs/ml, individual FAMEs within are at 2, 4 & 6% of the total amount. To make a combined standard mix, 200 µl volume standards were diluted with hexane in the following amounts (Table 2.5).

Table 2.5. Standard concentrations and volumes used for GC-MS FAME calibration.

Supelco Mix total conc (mg/ml)	Supelco Mix individual FAME conc 2% (mg/ml)	Supelco Mix individual FAME conc 4% (mg/ml)	Supelco Mix individual FAME conc 6% (mg/ml)	Supelco amount (µl)	C19 FAME (0.25mg/ml) amount (µl)	Hexane (µl)
8	0.16	0.32	0.48	80	10	10
6	0.12	0.24	0.36	60	10	30
4	0.08	0.16	0.24	40	10	50
2	0.04	0.08	0.12	20	10	70
0	0	0	0	0	10	90

The FAME standards were run using the same parameters as section 2.2.2.1 and the resultant peaks were identified using Perkin Elmer Turbomass software linked to a NIST database when compared to a manufacturer's specification sheet. Peak integration was performed automatically using Turbomass, manual baseline separation was also required in some instances. External and internal 5 point standard calibration curves were produced from the integrated areas and Response Factors (RF)/ Internal Response Factors (IRF) of each FAME were calculated using the following formulas:

Multipoint External:

$$RF = \frac{FAME\ area_{supelco}}{FAME\ conc_{supelco}} = \frac{y\ axis}{x\ axis}$$

Multipoint Internal:

$$IRF = \frac{RF_{supelco}}{RF_{C19\ int\ std}} = \frac{(FAME\ area_{supelco}/FAME\ area_{C19\ int\ std})}{(FAME\ conc_{supelco}/FAME\ conc_{C19\ int\ std})} = \frac{y\ axis}{x\ axis}$$

Linear regression was performed on each FAME standard in Microsoft Excel.

Transesterification efficiency

The transesterification efficiency (%) was calculated based on the C13 lipid standard using the following equations:

Molecular weight (M_w) C13 fatty acid = 214.4 g/M, Molecular weight C13 FAME = 228.4 g/M

- Moles in 0.1 mg of C13 FA = $\frac{(0.1mg/1000)}{214.4g/M}$ = 4.66x10^{-7} M, so converted weight is;
- $(Mol_{C13FA} \times M_w C13\ FAME) \times 1000$ = (4.66x10^{-7} M x 228.4 g/M) x 1000 = 0.107 mg

External std transesterification efficiency:

$$\frac{(a_{C13\ std} - c_{C13\ yint})}{m_{C13\ RF}} = c_{c13\ std/mg} \rightarrow \left(\left(c_{c13\ std/mg}/0.107mg\right) \times 100\right) = e_{trans-ext}$$

Internal std transesterification efficiency:

$$\left(\frac{\left((a_{C13\ std}/a_{C19\ std}) - C_{C13\ yint}\right)}{m_{C13\ IRF}}\right) \times c_{C19\ std} = c_{c13\ std/mg} \rightarrow \left(\left(c_{c13\ std/mg}/0.107mg\right) \times 100\right) = e_{trans-int}$$

Where:

$e_{trans-ext}$ = External std transesterification efficiency, $a_{C13\ std}$ = The integrated area of the C13 FAME standard in the algal sample. $c_{C13\ yint}$ = The y-axis intercept of the line from the appropriate C13 calibration curve. $a_{C19\ std}$ = The integrated area of the C19 FAME standard in the algal sample. $m_{C13\ RF}$ = Gradient of the C13 calibration curve or RF. $c_{c13\ std}$ = The concentration of C13 FAME in the sample. 0.107 mg = The theoretical maximum concentration of C13 FAME transesterified in the sample. $m_{C13\ IRF}$ = Gradient of the C13 calibration curve (or IRF).

External Standard FAME Quantification

1. $\frac{(a_{AlgFAME} - c_{AlgFAME\ yint})}{m_{AlgFAME\ RF}} = c_{AlgFAME} \rightarrow$
2. $\rightarrow \left(\left(c_{AlgFAME}/e_{trans-ext}\right) \times 100\right) = c_{AlgFAME} \rightarrow$

   Compensates for the transesterification efficiency using C13 std.
3. $\rightarrow \left(\left(c_{AlgFAME}/w_{BM}\right) \times 10\right) = c_{AlgFAME} \rightarrow$

   Normalises the end result to 10 mg of algal biomass per sample based on actual (w_{BM}).
4. $\rightarrow \left(c_{AlgFAME} \times 0.1\right) \times 100 =$ FAME as % Biomass

Internal Standard FAME Quantification

$$\left(\frac{\left(\left(a_{AlgFAME}/a_{C19\,std}\right)-C_{AlgFAME\ yint}\right)}{m_{AlgFAME\ IRF}}\right)\times c_{C19\,std}=c_{AlgFAME}$$

Where; $c_{C19\,std}$ = The concentration of C19 FAME in the sample (0.25mg/ml).

With the transesterification efficiency term is provided by the internal standard equation; $e_{trans-int}$.

2.2.4 NMR

Proton Nuclear Magnetic Resonance (H-NMR) Spectroscopic Lipid Analysis was performed on algal samples with help from Prof Mike Williamson, MBB Sheffield University based on the methods from Derome (1987) .Algal culture was aseptically removed from a relevant growth device and transferred to a 50 ml Falcon tube. The container was centrifuged at 3000 *g*for 10 min. The supernatant fluid was discarded and the pellet re-suspended in 5 ml of distilled water. The sample was centrifuged again at 3000 *g* for 5 min and the supernatant fluid discarded. The pellet was re-suspended in 1ml of distilled water and the sample transferred to a pre-weighed 1.5 ml Eppendorf tube (fitted with a separate, pierced lid). The samples were frozen at -80°C overnight (12h minimum) and then lyophilised (freeze dried to remove the water) for 24 h. The sample was then weighed to estimate the weight of biomass.400 µl ofdeuterated chloroform ($CDCl_3$) and 100 µL of deuterated methanol (CD_3OD) were added to each sample for solubilisation of the biomass.The samples were then mixed and transferred to a 5 mm NMR tube, and 5 µl of Chloroform ($CHCl_3$) was added as an internal standard. NMR spectra were obtained on a BrukerAvance 600 equipped with a cryoprobe. Data was recorded into 16k complex data points with simple pulse-acquire pulse program and a 3 s recycle time. Fourier transformation was applied using a 1 Hz line broadening followed by manual baseline correction. All spectra were acquired using 8 scans (with 4 dummy background scans). Processing and integration was performed using Bruker Topspin v1.3 software. The position of the NMR spectrum was determined in relation to a tetramethylsilane (TMS) standard via the following equation:

$$ppm=\frac{distance\ from\ TMS\ \times 10^6}{operation\ frequency\ of\ spectrometer\ (MHz)}$$

Based on the *D. salina* lipid profile available in the literature (Guzman, et al., 2011), 94% of the biomass weight lipids are all C16-C18 chain length with a single double bond, therefore a

model fatty acid length of C17:1, with 9 CH_2 groups is used to quantify the total lipid content based on the total CH_2 group signal. As 5 µl of$CHCl_3$ was added per sample (500 µl), then 7.3 mg was the weight of internal standard. If this is converted to moles; Molecular weight of $CHCl_3$ (M_{w-chl}) = 119.4 g/M, so for 7.3 mg there is 61.1 µmoles/500 µl (or 122.2 µmoles/ml). The concentration of C17:1 can be calculated by the following equation:

$$\frac{122.2\ \mu\text{moles/ml} \times Area_{CH2}}{\left(\frac{Area_{CHCl3}}{1}\right) \times 18} = \mu moles_{C17:1}/ml$$

Where; $Area_{CH2}$ = Integrated area of the CH_2 signal, $Area_{CHCl3}$= Integrated area of the $CHCl_3$ signal, $122.2\ \mu\text{moles/ml}$ = concentration of $CHCl_3$, 1 = The protons signal in $CHCl_3$, 18 = The protons in one chain of C17:1 lipid and $\mu moles_{C17:1}$ =μ moles of C17:1 Lipid chains.

This value can then be converted to a weight value by multiplying by the molecular weight of the C17:1 fatty acid ($M_{w-C17:1}$), which is 270.45 µg/µmole.

$$M_{C17:1}/ml \times M_{w-C17:1} = L_{tot} = total\ lipids\ (\mu g)$$

The weight is then normalised by the original amount of dry biomass in the sample by:

$$\left(\frac{(L_{tot}/1000)}{BM_{samp}}\right) \times BM_{standard\ value} = L_{tot-strd}$$

Where; BM_{samp} = Biomass in sample being tested in mg,$BM_{standard\ value}$ = Biomass value to be used as standard comparator in mg and $L_{tot-strd}$ = Biomass normalised total lipid weight in mg.

Other molecules are quantified for concentration using the first two equations. An example of a *D. salina* NMR spectrum (baseline corrected) is shown in Figure 2.8 and Table 2.6.

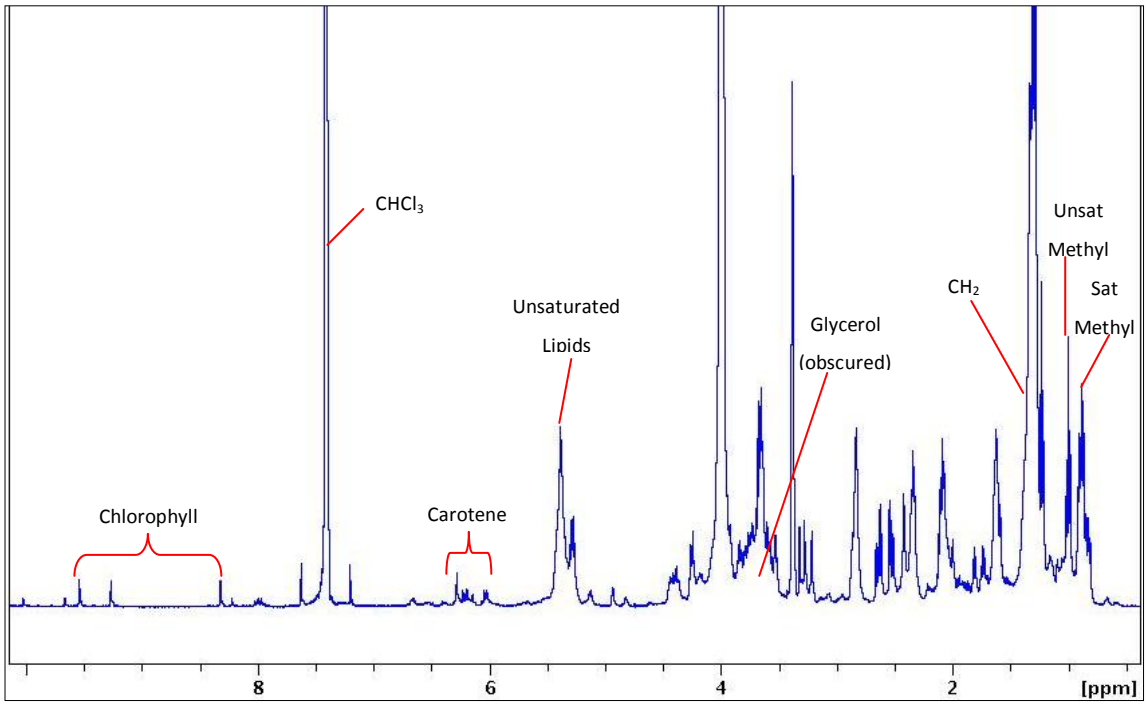

Figure 2.8. An example of *D. salina* spectrum, baseline corrected. Signature peaks for molecules of interest are indicated, areas underneath each peak are integrated for measurement.

Molecule of interest	Spectral location (ppm)
$CHCl_3$ (internal standard)	N/A
Chlorophyll (central peak only)	9.38
β-Carotene	6-6.5
Non-conjugated Unsaturated	5.4
Glycerol	4.3
CH_2	1.3
Unsaturated Methyl	1.01
Saturated Methyl	0.91

Table 2.6.The spectral location (ppm) of different molecules in an NMR spectra, see Figure 2.8 for corresponding data.

2.3 Algal Strains

The algal species used in this work were originally obtained from the Culture Collection of Algae and Protozoa (CCAP), Oban, UK:

Species	Strain Number	Culture collection	Algal Class	Growth Medium
Dunaliella salina	19/18	CCAP	Chlorophyceae	Dunaliella
Dunaliella salina	19/30	CCAP	Chlorophyceae	Dunaliella
Nannochloropsis oculata	849/1	CCAP	*Eustigmatophyceae*	F/2
Tetraselmis suecica	66/4	CCAP	Chlorophyceae	Dunaliella

2.4 Isolation of Unknown Microalga

For isolation of the unknown algal strain, a series of agar plates (5 conditions per strain) were made using the 'sloppy' agar method developed by Brown, et al. (1987) 40 ml of 1 M NaCl Dunaliella medium were combined with 1.5% (w/v) agar, microwave heated and poured into a series of Petri dishes and allowed to set. Another batch using the same medium and 0.5% (w/v) agar was made, whilst in liquid form, 9 ml aliquots were transferred to a series of 15 ml Falcon tubes and kept at 43^{o}C to maintain liquid phase. Samples were then taken from 14 day old cultures containing the unknown strain and were serially diluted. 1 ml of diluted cultures was then added to the appropriate tube containing the liquid agar. The tubes were then quickly mixed by inversion and spread on to the surface of the set 1.5% (w/v) agar. The combination process took less than 1 min to avoid cell damage.The plates were then sealed with Parafilm M (Bemis Flexible Packaging) around the join, placed upside-down in a sealed transparent bag and incubated in the MBB 25°C growth room under high light for two weeks until colonies were visible. Sections of agar with clear single colonies were then removed using disposable inoculation loops and added to sterile 15 ml centrifuge tubes containing 3 ml of fresh 1 M NaCl Dunaliella medium. The loop tips were left within the tubes and the lids were left loose to enable gas exchange. After another two weeks of growth, samples were taken and checked using optical microscopy to ensure the presence of a mono-culture. All remaining culture was then aseptically inoculated into a standard 250 ml flask with 100 ml of fresh medium for growth and characterisation tests (section 2.5, 2.7).

2.5 Scanning Electron Microscopy (SEM)

SEM determination of algal morphology was performed using a method developed in conjunction with MBioSci students Tom Champion and Stephen Marshall (Marshall, 2013)

.Sample slides were prepared by soaking standard glass microscope cover-slips (Scientific Labratory Supplies Ltd) in 0.1% polylysine solution in a 50 ml Falcon tube for 24 h. 1 ml was then taken aseptically from a clean 14 day old algal culture and adjusted to an OD of 0.8 (595 nm) using fresh medium. The adjusted culture was then transferred to a 1.5 ml Eppendorf tube and centrifuged at *3000*g for 3 min and the supernatant was discarded. 200 µl of fresh medium were then added and the pellet was re-suspended gently by agitation. The culture was then left for 4 h to recover from any damage. Following this period, 40 µl of 2% osmium tetroxide was added to the pellet (for microscope contrast) and the tube was sealed at ambient temperature for 30 min. Whilst the cells were being stained, the polylysine coated cover-slips were washed with filter sterilised dH_2O, and dried at 40˚C in an oven. Once staining was finished, the Eppendorf tube was gently agitated again to re-suspend the cultures into suspension. The coated cover-slips were then attached to a self adhesive SEM sample plate and 40 µl of the stained cells was added to the centre. The cover-slips were then left to air dry for 10 min then blotted using lab tissue. The samples were then washed using an ethanol gradient to remove the salt crystals, starting with 60 µl of a 50% ethanol solution, then 75% and waiting 10 min between each treatment (60 µl), before blotting dry with lab paper tissue. The final 95% and 100% washing gradients were not blotted; just air dried each time in the fume cupboard. When the last gradient was completely dry the samples were coated with gold (2 nm thick) using a Edwards S150B sputter coater and analysed with a scanning electron microscope (Philips XL-20 SEM) with an accelerating voltage of 20.0 kV. Images were taken at 1000-10000x magnification using Philips's own proprietary software running on Windows 2000 PC.

2.6 Cell Density Measurements

2.6.1 Direct Count

Direct measurement of cell culture density was performed using optical microscopy. 900 µl of algal culture was removed from the relevant growth system and combinedwith 100 µl of Gram's Iodine in a pre-sterilised 1.5ml Eppendorf tube to kill all motile cells. The solution was then mixed and aliquots of 20 µl were taken and transferred into the counting chamber of a Neubauer improved haemocytometer (Hawksley Z30000, 15002). The cells were viewed on a standard optical microscope with a x40 objective magnification. The algal cells were counted in the appropriate number of squares (depending on visual cell density) using a manual clicker. The count was repeated in triplicate (at least) for each sample. Using the mean number of cells

per small square, the number of cells in the original culture was calculated using the following equation:

1. Volume of one grid element:

   I. $Depth\ of counting\ chamber = 0.02\ mm$;

   II. $Area of small\ square = {}^{1}/_{400}\ mm^2 = 2.5 \times 10^{-3}\ mm^2$

   III. $\therefore Volume\ of small square = 2.5 \times 10^{-3} mm^2 \times 0.02\ mm$

   IV. $\therefore Volume\ of culture\ per\ small\ square = 5.0 \times 10^{-5} mm^3 = 5.0 \times 10^{-8} cm^3 (\equiv ml)$

2. Cells in 900 µl sample (if counted using all 400 squares):

   I. $Cell\ no. per\ small\ square = cellcount/400$

   II. $Cell\ no. per\ small\ square \times \frac{Vol of\ 1ml}{Vol of culture per S.square} = \frac{1mL^{-1}}{5\times10^{-8}mL^{-1}} = cells\ ml^{-1} sample$

   III. $Cells\ ml^{-1} original culture = \frac{cells mL^{-1} sample \times 1\ mL^{-1}}{0.9 mL^{-1}}$

2.6.2 Spectrophotometry

Optical density measurements were made at multiple wavelengths (chiefly 595 nm to measure turbidity and avoid absorption peaks of chlorophyll pigments) using a UNICAM Helios Alpha spectrophotometer set to 1 s integration time.1ml culture sampleswere taken from the relevant growth system and transferred aseptically to a 1ml plastic cuvette (Sarstedt 67.742 Polystyrene 10x4x45 mm). 1ml of appropriate sterile growth medium was used as the blank before reading the algal sample. OD was also measured in a 96 well microplate format with a Wallac Victor 2 Multilabel Plate Reader equipped with custom filters from Perkin Elmer (DC-03, 1420-533). 200-300µl of sample was used per well with a 1 s integration time, again an appropriate sterile growth medium was used as the blank.

2.6.3 OD - Cell Count Calibration

An optical density versus direct cell count calibration curve was performed based on the work by Madigan, et al. (2003), Reed (1998), Skoog, Holler and Crouch (2007). 30 ml of a 14 day old algal culture were taken aseptically and adjusted with fresh medium to an OD of 1 at 595 nm using a 1 ml plastic cuvette and spectrophotometer. The following dilutions were then made by combing the adjusted culture with fresh medium in 15 ml Falcon tubes (Table 2.7).

Table 2.7. Algal culture concentrations for cell calibration

Tube No	Conc (%)	Culture (ml)	Media (ml)
11	5.00	0.25	4.75
10	10.00	0.50	4.50
9	20.00	1.00	4.00
8	30.00	1.50	3.50
7	40.00	2.00	3.00
6	50.00	2.50	2.50
5	60.00	3.00	2.00
4	70.00	3.50	1.50
3	80.00	4.00	1.00
2	90.00	4.50	0.50
1	100.00	5.00	0.00

For every culture dilution, 1 ml was transferred to a plastic cuvette, 8 x 200 µl to the 96 well microplate (see Figure 2.9 below) and 0.9 ml to an autoclaved 1.5 ml Eppendorf tube.

Repeat Readings ®		Different Concentrations Samples (100-5%)												
		100	90	80	70	60	50	40	30	20	10	5	MED	
		1	2	3	4	5	6	7	8	9	10	11	12	
1	A	200	200	200	200	200	200	200	200	200	200	200	200	Blank Media
2	B	200	200	200	200	200	200	200	200	200	200	200	200	
3	C	200	200	200	200	200	200	200	200	200	200	200	200	
4	D	200	200	200	200	200	200	200	200	200	200	200	200	
5	E	200	200	200	200	200	200	200	200	200	200	200	0	Empty Wells
6	F	200	200	200	200	200	200	200	200	200	200	200	0	
7	G	200	200	200	200	200	200	200	200	200	200	200	0	
8	H	200	200	200	200	200	200	200	200	200	200	200	0	

Figure 2.9. 96 Well plate layout for OD versus cell count calibration.

96 well microplate OD readings were then taken on the plate reader using the 'Shaken OD @ 595 (1.0s)' protocol and settings (see section 2.2.2.3). Cuvette OD readings were performed at 595 nm (section 2.6.2), mixing before each reading and an OD scan from 350-700 nm was also performed for each concentration (Figure 2.11). Following the OD readings, cell counts were performed on the 0.9 ml Eppendorf cultures using the protocol specified in section 2.6.1 when 100 µl of Gram's Iodine was added to kill the motile cells. Ten replicates counts were performed for each culture dilution. The data were compiled to give OD 595 nm vs Cell count graph for the 1 ml cuvette and 96 well plate readings. Using linear regression a relation between OD and number of cells was calculated. Standard error measurements were performed on cell count and micro plate data, see Figure 2.10.

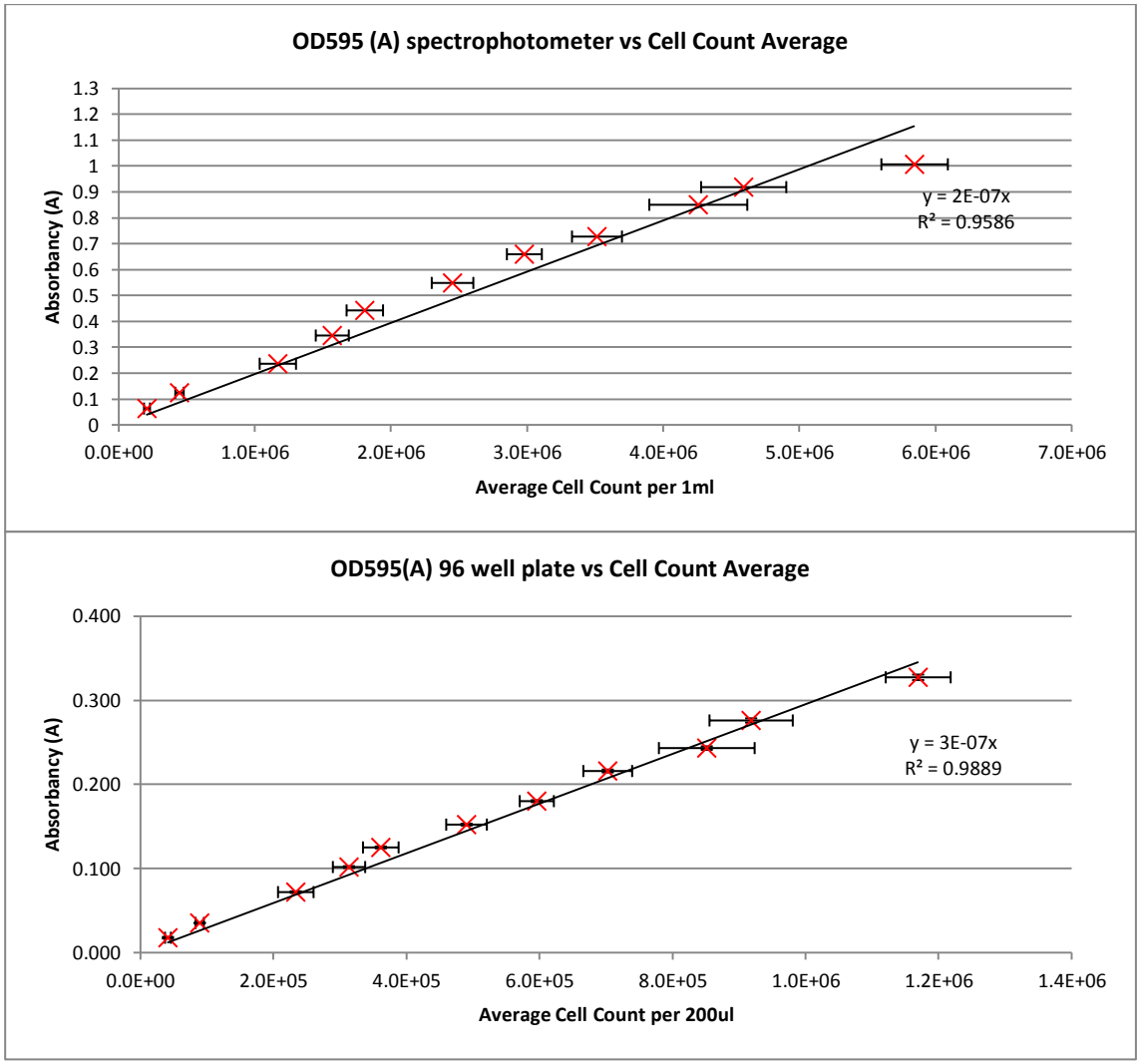

Figure 2.10. Cell count versus OD calibration curves; Top: 1ml sample spectrophotometer data, Bottom: 200µl 96 well plate data.

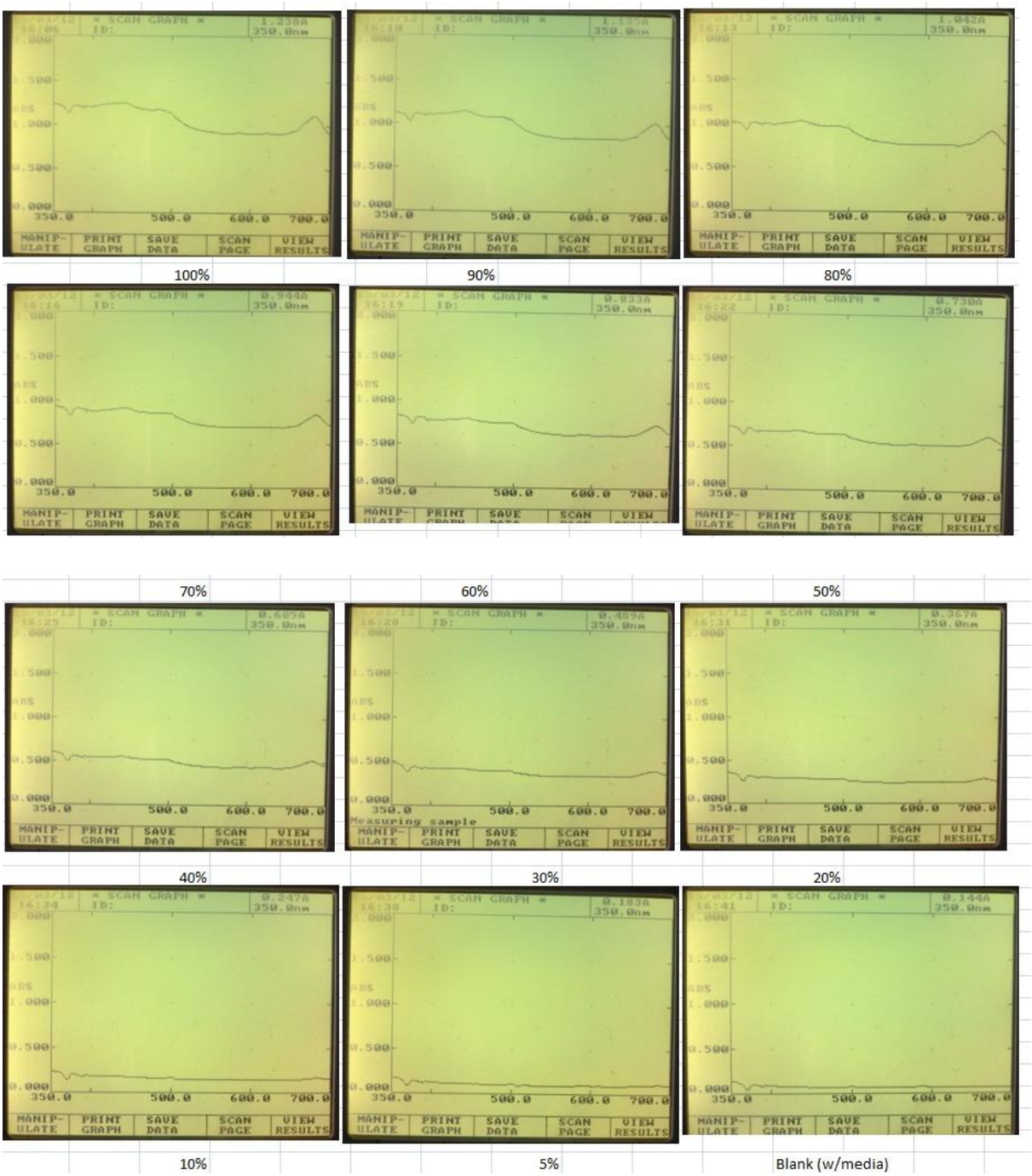

Figure 2.11. Spectrophotometer OD sweeps (350-700nm) performed at each culture dilution using 1ml cuvette samples.

2.6.4 Chlorophyll Extraction

Determination of chlorophyll content was carried out based on the methods developed by MacKinney (1941) and Arnon (1949). A 5ml sample of culture was taken from a relevant growth system and transferred aseptically to a 10ml Falcon tube. The sample was then centrifuged at 3000 *g* for 10 min, at ambient temperature in a bench centrifuge. The supernatant was then discarded immediately and the pellet was re-suspended in 1ml of

distilled water and whirlimixed thoroughly. 4ml of pure acetone was then added to the tube and the sample was whirlimixed again (note: some stickier pellets were also mixed with a pipette to aid cell dispersion). The 80% acetone (v/v) solution was then placed in a dark cupboard for 10-15 min to facilitate chlorophyll extraction, and then centrifuged under the same conditions as before for 5 min. If any colour was left in the pellet after this step, the sample was whirlimixed and centrifuged again until all pigment was extracted.1ml of the supernant was then transferred to a 1ml plastic cuvette and the optical density was measured at 645 and 663 nm using a UNICAM Helios Alpha spectrophotometer, 80% (v/v) acetone was used as reference. The chlorophyll concentration was that calculated using the following equations:

$$\text{Chlorophyll b: } OD_{645} \times 202 = X$$

$$\text{Chlorophyll a: } OD_{663} \times 80.2 = Y$$

$$(X + Y) / 2 = \mu g \text{ Chl. } 5\ ml^{-1} = Z$$

$$Z / 5 = \mu g \text{ Chl. } ml^{-1}$$

2.6.5 Dry weight

Algal dry weight measurement was performed using the following method. 5 ml of culture was removed aseptically from culture vessel and transferred to a 15 ml Falcon tube and centrifuged at 3000*g* for 10 min. The supernatant was then discarded and the pellet re-suspended in 5 ml of distilled water, gently pipetting to break up the pellet. The centrifugation step was then repeated and 1 ml of distilled water added to the pellet for re-suspension. The sample was then transferred to a pre-weighed oven drying crucible (a metal test tube cap), which was placed in a drying oven set at 50°C and left overnight. The weight of the crucible was then measured the next day to give the net biomass yield by subtraction of the initial empty crucible weight.

2.6.6 Specific Growth Rate and Generation Time

Specific algal growth rates (μ) and generation times (g) were calculated based on the work by Fogg (1965), Levasseur, Thompson and Harrison (1993), Madigan, et al. (2003). See Figure 2.12 (ANACC, 2010).

The following equations were used to calculate the growth rate in the exponential growth phase (2), based on lines of best fit: $Specificgrowthrate(\mu) = \frac{\mathrm{In}(N_2 / N_1)}{(t_2 - t_1)}$

Where$N_1$and N_2 are biomass concentrations at time intervalst_1 and t_2.

$$Cell\ divisions\ per\ day = Div.day^{-1} = \frac{\mu}{\ln 2}$$

$$Generation\ time\ = Gen't = \frac{1}{Div.day^{-1}}$$

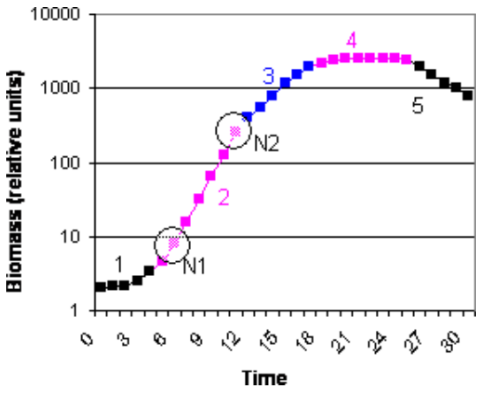

No	Phase
1	Lag
2	Exponential growth
3	Declining growth phase
4	Stationary
5	Death
N1	Upper and lower extremes of linear phase
N2	

Figure 2.12. Algal growth phase designation (ANACC, 2010)

2.7 Phylogenetic Identification

2.7.1 DNA Extraction and Purification

Genomic DNA (gDNA) was extracted from 10 ml samples of each algal strain using an Anachem KeyPrep Bacterial DNA extraction kit (AM-111113). The gDNA obtained was then resuspended in 50 µl Tris-EDTA buffer (100 mM Tris-HCl pH 7.5 and 10 mM EDTA pH 8.0), a gel was run to ensure the presence of gDNA (section 2.7.6) and the remainder was stored at -20°C.

2.7.2 Polymer Chain Reaction (PCR) Amplification of 18s rRNA

Following the extraction of gDNA in procedure 2.7.1 a PCR reaction was conducted to amplify the gDNA region containing a partial match of the conserved 18S ribosomal RNA (rRNA). The forward and reverse primers used to replicate the 18S rRNA were; 18S Forward, 5' GCGGTAATTCCAGCTCCAATAGC 3', 18S Reverse 5' GACCATACTCCCCCCGCAACC 3' (Lim, et al., 2012a). The primers were made by Biomers.net GmbH (01133816, 01133817). After gently thawing the gDNA samples, 5 µl of each gDNA sample were taken and combined in a 50 µl reaction within a microtube containing;17 µl of milliQ water, 20 µl of F-548 2X Phusion Flash PCR Mastermix (Thermo Scientific), and of 4 µl each of forward and reverse 18S primers. A negative control was also made using 32 µl of milliQ water and no gDNA, the other parts remained the same in volume. The tubes were transferred to a MyCycler Thermal Cycler (Bio-Rad Laboratories Inc) to undergo the PCR reaction using the following programme; 3 min at

94°C for DNA denaturing, 30 cycles of denaturing at 94°C for 1 min, annealing at 50°C for 1 min, and extension at 72°C for 2 min, prior to a final extension step at 72°C for 5 min. Once completed, a small amount (20 µl) was separated for purification (section 2.7.3) and the rest stored at -20°C.

2.7.3 Purification of PCR Products

PCR products (20 µl per sample) were cleaned up using a Qiagen QIAquick PCR purification kit (28104). The samples were then visualised by running out 15 µl of each on a 1% TAE agarose gel (see section 2.7.6) and the gDNA was quantified (section 2.7.4). If gDNA was present in large enough quantities, the cleaned PCR product was stored at 4°C until being sent for sequencing.

2.7.4 DNA Quantification

Samples of the PCR product were quantified using the QIAGEN recommended method (Qiagen Bench Guide). 15 µl of the cleaned PCR product were combined with 995 µl MilliQ water in a quartz cuvette (Z276677-1EA Sigma-Aldrich) and mixed well. The optical density was then measured using a deuterium bulb equipped spectrophotometer at 260 nm. To calculate the quantity in ng/µl, the following equation was used: $c_{DNA} = 50_{dsDNA} \times A_{260nm} \times 200_{Dil}$

Where; c_{DNA} = concentration of DNA (ng/µl), 50_{dsDNA} = conversion ratio of double sided DNA, A_{260nm} = Absorbance values at 260 nm and 200_{Dil} = the dilution factor of PCR product to water.

2.7.5 Sequencing of PCR Products

Based on the DNA quantification procedure and sequencing company requirements, the PCR products and primers were diluted to the required concentrations. Then 15 µl of each cleaned PCR product, along with 30 µl each of 18S forward and reverse primers were sent to Eurofins MWG for sequencing.

2.7.6 Phylogenetic Analysis

18S rDNA gene sequences were checked using the Basic Local Alignment Search Tool (BLAST) online at the National Centre for Biotechnology Information (NCBI) (www.ncbi.nlm.nih.gov) website. Sequences were viewed using the software FinchTV v.1.4.0 (Geospiza).

2.7.7 Agarose Gel Electrophoresis

Agarose gels were made in the following steps; 1.2 ml of 50x TAE buffer (242 g Tris Methylamine, 18.61g EDTA and 57.1ml Acetic Acid at pH 8.5, per litre) were added to a standard 250 ml conical flask and topped up to 60 ml with distilled water. 0.6g of agarose were then added to make a 1% gel as the DNA fragments were expected in the range of < 1000 base pairs (bp). The mixture was then microwaved (Matsui M185T 850W) on full power for 90 seconds, stirred, then microwaved for a further 30 seconds. 5 µl of ethidium bromide (Biorad #161-0433) were then added and the mixture stirred again. Whilst the mixture was cooling, the gel tank (Bio-Rad Laboratories Inc) was setup with a 20 lane comb. The molten gel was then poured into the tank and allowed to cool, once set the mould parts were removed. A 1x TAE solution (1.5 litres) was then prepared and added to the tank. The samples were then stained on Parafilm M (Bemis Flexible Packaging) by combining 2µl of 6x DNA loading dye (Fermentas life sciences, #R0611) with 5 µl of PCR product. 7µl of HyperLadder I (Bioline H1K5-1006) was placed on the gel at the outer most lanes to give relative scale and the stained samples were loaded in between. The tank was then connected to the power supply (Bio-Rad Laboratories Inc, Power PAC 300) and run at 80 volts for 45 min. The resulting gel was then transferred to a Uvitec UV light box and visualised.

2.8 Culture Conditions and Maintenance

2.8.1 Culture Maintenance

Pre-autoclaved 250ml conical flasks were inoculated by adding 5 ml of an actively growing culture, which had been established for at least 7-10 days, to 100 ml of appropriate growth medium. Both processes were conducted using aseptic techniques (i.e. the containers were flamed with a Bunsen burner before and after transfer, and all transfer pipette tips used were pre-sterililised). The flasks were shaken manually before taking samples and typically every couple of days regardless. Sub-culturing was performed at regular intervals, typically every 28 days using the aforementioned procedure.

2.8.2 MBB H-Floor Growth Room

Stock algal cultures were stored and incubated in 250 ml conical flasks (with foam bungs), under controlled environmental conditions (Figure 2.13). The MBB H-Floor growth room was maintained at a constant 25°C and had three different lighting intensities available depending on the tier of shelf used (see Appendix A for wavelengths). The top and middle have light sources above them and the bottom has only the light reflected from the shelves above. Each set of lights has a mixture of fluorescent tubes and tungsten filament bulbs, the highest light intensity is on the top tier, the middle shelf is lower, followed by the bottom shelf (see Table 2.8). Light intensity data was gathered from three equidistant locations along each shelf parallel to the relevant culture surface (see section 2.9.1). An average of the three readings was taken (with the exception of the bottom shelf where there was only the space for one reading), the light sources were tested independently and together.

Figure 2.13. Flasks growing in the MBB H-Floor Growth Room, Right hand side shelves.

Location	PAR (µmol/m^2/sec)		
	Fluorescent	Tungsten	Both
T1	178.4	12.1	202
T2	170.4	15.2	188.4
T3	157.9	10.28	162.7
M1	50.3	2.58	55.8
M2	70.4	3.8	72.6
M3	44.1	2.35	44.5
B1	13	0.58	12.64

Table 2.8. MBB H-Floor Growth Room, Right hand side shelf PAR values.

2.8.3 MBB E-Floor Lab

Experiments in the MBB E-Floor lab were conducted at ambient air temperature with air conditioning to approximately 25°C. Ambient light was always present, but experiments in the room always had dedicated light sources (see appendix A).

2.8.4 Animal and Plant Sciences Upper Growth Annex (APS-UGA)

Experiments conducted in the APS-UGA were conducted in a Sanyo-Gallenkamp / SGC2352/FM growth unit (number 503). Chamber size: Internal 1.6m^2, dimensions 2.0m x 0.8m x 1.4m (w x d x h). Growth area: 1.6 m^2, 2 half shelves, adjustable (Figure 2.14). Growth height: 1.4m. Lighting was provided by a mixture of tungsten filament and fluorescent tubes (see appendix A for wavelengths), with a light/dark cycle of 16/8 hours a day (lights on from midnight to 4 pm).The top has light sources above it and the bottom has the light reflected from the shelf above. Light intensity readings were taken at five equidistant locations along each tier parallel to the relevant culture surface (see Table 2.9). Temperature was maintained at a constant 25°C and humidity control was turned off. Temperature and atmospheric CO_2 was continually monitored and logged by the technicians in APS. Air, pure CO_2 and electrical supplies were all available externally to the growth unit and fed inside through a 66 mm port on the side.

Figure 2.14. Growth unit 503 in the APS-UGA. Top - Outside appearance, Bottom - inside view.

PAR (µmol/m^2/sec)				
Top shelf - Left to right				
1	**2**	**3**	**4**	**5**
100.5	145.4	156.9	164.1	114.4
Bottom Shelf - Left to right				
1	**2**	**3**	**4**	**5**
46.3	58.7	58.5	59.7	49.6

Table 2.9 - Growth unit 503PAR values.

2.8.5 Photo-bioreactor Cleaning

3L Photo-bioreactors: Prior to all experimental runs, the reactor was taken apart and rinsed with distilled water 3 times. The separate small parts were then sterilised in a bath of Virkon (Dupont) or Microsol 3+ (Anachem) solution for at least 10 minutes and the reactor body was filled with the same solution for the same period. All items were then rinsed with autoclaved distilled water 3 times, with the exception of the spargers and control valves. These items were then submerged in a bath of sterile distilled water and pumped with filtered sterile air for

10 minutes to clear the pores of disinfectant. The reactor was then reassembled using sterile gloves and was ready to be used.

100ml mini photo-bioreactors: In between runs, these reactors were stripped down rinsed 3 times with distilled water and scrubbed clean. The spargers were pumped with distilled water to clean the pores. The reactors were then re-assembled and autoclaved.

2.9 Spectral Measurement

2.9.1 Light Intensity

Measurement ofinsolation intensity in the photosynthetically active region (PAR) (McCree, 1973) was performed manually using a SKYE Instruments Ltd - SKP200/SKP 216 hand held photometer with a Hansatech - Quantum Sensor (QSRED). The sensor was held in three equidistant locations parallel to the relevant culture surface and an average of the three readings was taken in µmol/m^2/sec, Wm^{-2} or Lux.

2.9.2 Light Wavelength

Measurement of spectral light distribution was performed with an Ocean Optics USB2000+UV-VIS-ES sensor using an Ocean Optics P600-1-SR Optical fibre and a cosine corrector attachment on the input (to capture light from an increased angle of incidence). Ocean Optics's SpectraSuite software (v1.6) was used to collect the data from the sensor. The software settings used for capture were a scan average of 4 and box car width of 4, to smooth out any signal interference. Electronic dark and stray light correction options were also enabled and the integration time was varied to minimise the input overloading the sensor whilst maintaining the best data resolution.

2.9.3 Light Sources

With the exceptions of the light sources in the MBB growth room and APS-UGA, the only other external light sources used in course of this study (Figure 2.15) were the following:

1. Thin fluorescent tubes (Wotan L13W/23 White - Italy) - 34.7 µmol/m^2/sec.
2. Generic fluorescent tubes in the trans-illuminator - 11.6 µmol/m^2/sec (central).
3. Ring fluorescent tubes (Philips TLE 22W/29) (3) - 34.9 µmol/m^2/sec.

4. Thick fluorescent tubes (White: Wickes 18W 50 D6, UV: General Electric F18T8 BLB) -These light sources were attached to a metal frame, white fluorescent tubes and UV fluorescent tubes were fitted depending on the experiment (see Table 2.10 for light intensity readings).

All light source wavelengths are given in appendix A.

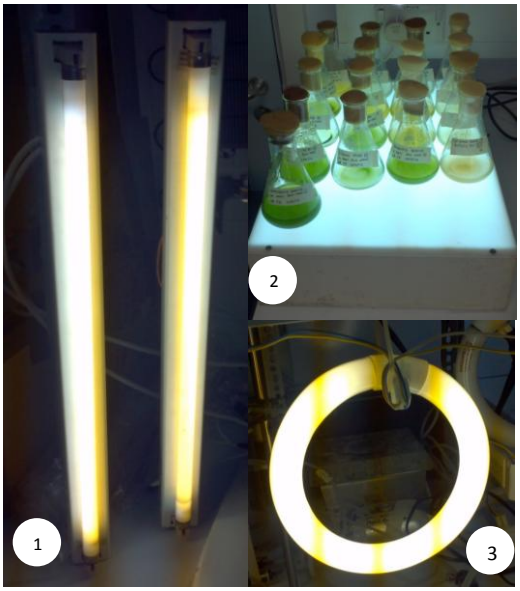

Condition	PAR (µmol/m^2/sec)	
	Top	Side
All Lights	1.43	9.51
UV Only	1.48	0.6
White Only	1.45	8.96
Background	0.92	0.54

Table 2.10Light sourcePAR values.

Figure 2.15. Laboratory fluorescent light sources (left) - 1) Thin Fluorescent Tube x2 (MBB Lab F3), 2) Trans-illuminator , 3) Ring fluorescent tubes.

2.10 Dye Coating

2.10.1 Dye Selection

The following dyes were used to create the 'smart skin' coatings:

- Coumarin 1 ($C_{14}H_{17}NO_2$) – (SigmaAldrich: D87759)
- Rhodamine B ($C_{28}H_{31}ClN_2O_3$)- (SigmaAldrich: 83689)

2.10.2 Dye Composition and Sub-straight

The 'smart skin' coatings used in this project were made in conjunction with fellow PhD student Kezhen Ying and MSc student David Hosking. The mixture ratios of dye to substrate were developed by these students in relation to the facilities available at the time, both sets of coatings used PMMA (polymethylmethacrylate – Polymer Laboratories,Mp: 685000, Mw/Mn: 1:1) as the matrix to suspend the dye.

The initial batch of coatings developed by Kezhen Ying had the followingcompositions with different solvents (Table 2.11). The ratio of solution weight to powder (dye + PMMA) weight was used to work out the final concentration of the coating.

Table 2.11. Dye coating compositions developed by Kezhen Ying

Comp ID	Dye type	Dye (g)	PMMA (g)	Dye/ PMMA	Solvent	Solution Weight (g)	Solid/ solution
1	Coumarin	0.02436	0.9293	0.026	Dichlorobenzene/ chloroform (1:1)	20.33	5%
2	Rhodamine	0.01927	0.705	0.027	Dichlorobenzene/ chloroform (1:1)	20	5%
3	Coumarin	0.02487	0.9266	0.0268	Toluene	20.33	5%
4	Rhodamine	0.01924	0.704	0.0273	Tetrahydrofuran (THF)	19.55	5%
5	Coumarin	0.009859	0.365	0.027	Dichlorobenzene/ chloroform (1:1)	7.5	5%
6	Coumarin	0.01972	0.73	0.027	Dichlorobenzene/ chloroform (1:1)	7.5	10%
7	Rhodamine	0.01734	0.642	0.027	Dichlorobenzene/ chloroform (1:1)	13.19	5%
8	Rhodamine	0.0394	1.459	0.027	Dichlorobenzene/ chloroform (1:1)	15	10%

Dye was assembled in 15 ml glass vial by manual mixing with metal spatulas. The solvents used were; toluene - anhydrous, 99.8% (Sigma-Aldrich 244511), tetrahydrofuran (THF)– 99.8+% (GLC) unstabilised. (Fisher Scientific: T/0706/PB17), dichlorobenzene (Alfa Aesar) and chloroform (Fisher Scientific).

The second batch of coatings, developed by David Hosking as a part of his Masters thesis are detailed in Table 2.12 (Hosking, 2013) :

Table 2.12. Dye coating compositions developed by David Hosking.

Test ID	Dye type	Dye (g)	PMMA (g)	Dye/ PMMA	Solvent	Solvent Weight (g)	Solid/ solution
9	Coumarin	2.0141	8.0134	0.25	Toluene	N/A	20%
10	Rhodamine	1.0064	9.0081	0.112	Toluene: Methanol (5.33:1)	N/A	10%

The solvents selected were not the best for dissolving the dyes, but were the only types suitable for use in the spin coating device (see section 2.10.3).

2.10.3 Dye Coating Methods

The first generation mini-photobioreactor bodies (Schott Duran square bottle 100 ml, 21 0820 245) were coated by Kezhen Ying using a manual application of the dye solution (Comp ID: 1-4) using a fine paint brush.

The first batch of glass microscope slides (J. Melvin Freed Brand Premium Plain Glass Microscope Slides 2950WX- 003, Category Number 7525M. Dimensions: 75 mm x 25 mm) were coated in conjunction with Kezhen Ying using a bar spreading method. A dropper pipette

was used to place three drops of dye coating at one end of the slide, this was then spread along the length of the slide using the bar spreader. Due to the high viscosity of the coatings Gilson pipettes proved to be ineffective at precise measurement of the coating volume.

The second batch of microscope slides were coated by David Hosking using a Laurell Technologies Corporation Model WS-400BZ-6NPP/LITE (REV. MS) Spin Coater using a spin program of: 1000 RPM for 60 s with an acceleration index of 15. Slide residence time of 2 min. Prior to coating, the slides were cleaned using toluene and dried with compressed air then placed in a plasma cleaner (Diener Electronics Model Zepto Low Pressure Plasma System; Including O_2 gas supply, 40 kHz Plasma Generator, and Preiffer Vacuum Pump) for 2 min. 2 ml of each coating solution was added to the spin coater during the programmed run.

2.10.4 Experiments and Coatings Used

The experiments in this part of the work used the following combinations of coating mixtures and methods specified in Table 2.13 below and in section 2.10.5.

Table 2.13 Dye coatings, application methods and experimental usage

Experiment	Date	Surface	Coating	Coating Method	Comp ID
Fish tank rig White + UV	2012/01/09-2012/01/20	Mini-reactors	Coumarin & Rhodamine 5%	Painted	3,4
Fish tank rig UV	2012/01/27-2012/02/06	Mini-reactors	Coumarin 5%	Painted	3
Fish tank rig UV	2012/02/13-2012/02/24	Mini-reactors	Coumarin 5%	Painted	1,2
Trans-illuminator initial test	2012/02/09-2012/02/20	Microscope slides	Coumarin & Rhodamine 5%	Bar spread	1,2
UV-Box test, evaporation issues 6 days	2012/07/09-2012/07/14	Microscope slides	Coumarin 5% & 10%	Bar spread	5,6
UV-Box test proof of concept, wavelength shift	2012/07/06	Microscope slides	Coumarin 5+10% & 5+10% Rhodamine	Bar spread	5,6,7,8
UV-Box test	2012/09/25-2012/10/08	Microscope slides	Coumarin 5% & 10%	Bar spread	5,6
UV-Box test (evaporation after 6 days)	2012/10/10-2012/10/08	Microscope slides	Coumarin 5% & 10%	Bar spread	5,6
UV-Box test	2013/03/04	Microscope slides	Coumarin 20% & Rhodamine 10%	Spin-coating	9,10

2.10.5 96 Well Plate / Mini-reactor Coating Configuration

Cultures grown in the 96 well micro-plate configuration (Greiner bio-one sensoplate black, glass bottom, sterile 655892) used a 20:1 ratio of medium to inoculum (190.5:9.5 µl). For growth, microplates were placed on top of the relevant light source (see section 2.10.6), with the appropriate coated slide underneath the target well (see Figure 2.16 below) and in between the plate and the light source. Due to the black walls, only the wavelengths filtered through the coatings were allowed to enter the cultures. To ensure evaporative losses were not significant a layer of Parafilm M (Bemis Flexible Packaging) sterilised with 100% ethanol was used to seal the top of the plate after inoculation. Culture growth was monitored using a Wallac Victor 2 Multi-label Plate reader using the 595 nm wavelength (see 'Shaken OD @ 595 (1.0s)' section 2.2.2.3) and compared to cell calibration curve (see section 2.6.3). The Parafilm was replaced in between readings and excess water was dabbed using a lab paper towel. Half way through a 14 day growth cycle the wells were topped up with 100 µl of sterile distilled water.

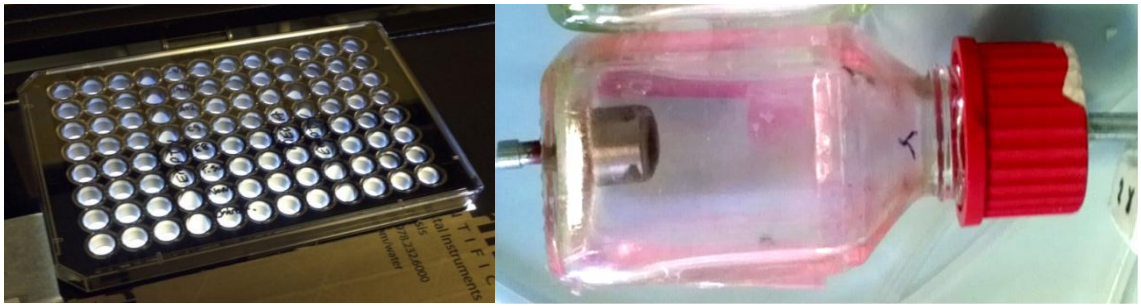

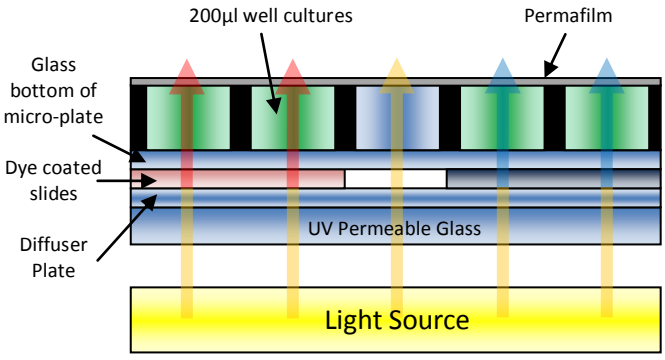

Figure 2.16Top left: 96 well plate slide test on transilluminator, Top right: Mk I Mini-bioreactor coated with the relevant dyes evenly up to the threaded section of the bottle(section 2.10.3-4), Bottom middle: Diagram of light propagation into 96 well algal cultures.

2.10.6 Modified Transilluminator

The modified algal transilluminator setup consists of a heavily modified RS-555-279 UV Exposure Unit fitted with;1x Philips F8T5/BL Fluorescent Bulb, 1x General Electric F8W/35

Fluorescent Bulb, a 250 x 150 mm custom ground UV permeable glass diffuser (White crown glass B270, instrument glasses) and a 120 mm 240 V Electric Fan (RS Electronics). Ventilation holes were added into the side, where compressed air could be blown through to maintain ambient temperature. Zones were masked using black card and attached with masking tape (Figure 2.17).

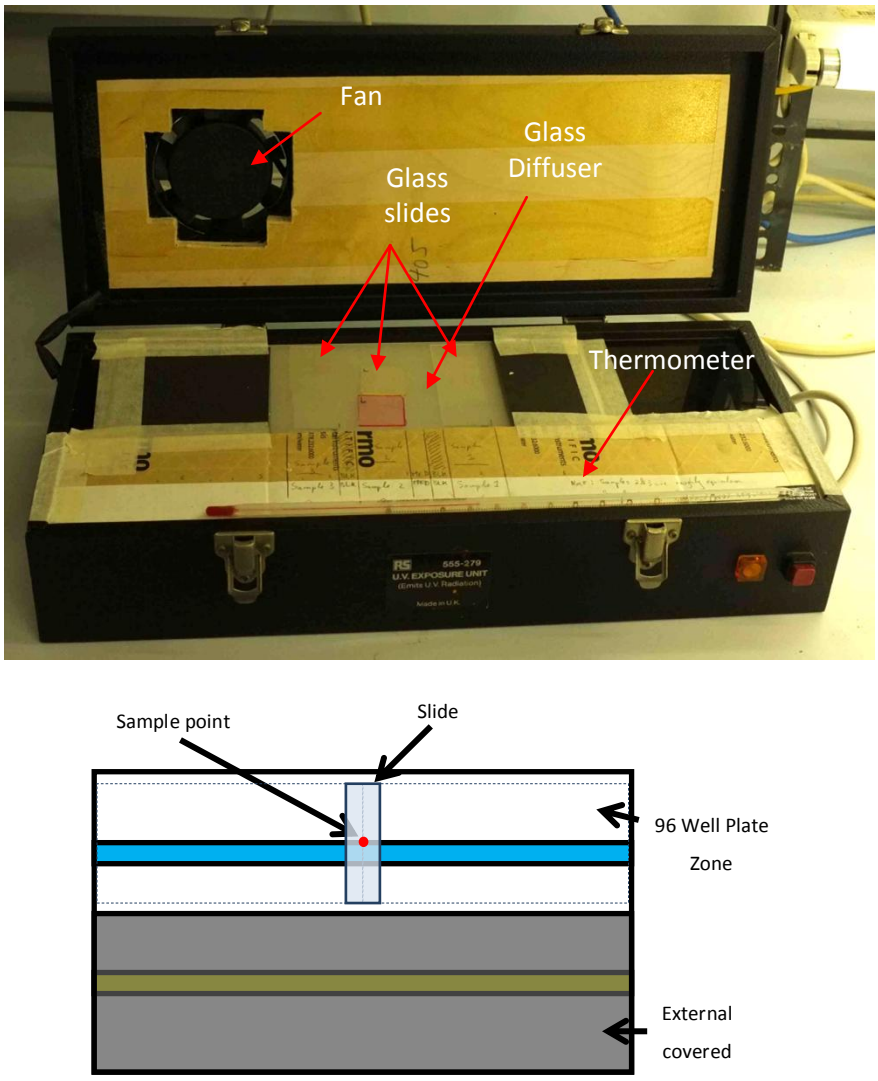

Figure 2.17.Top: Modified transilluminator setup, Bottom: Diagram of slide position relative to light sources, where; Blue = UV Tube, Yellow = Standard Fluorescent Tube.

2.11 Data logger setup and calibration

2.11.1 DrDAQ logger

A Pico Technology USB DrDAQ Data logger equiped with DrDAQ Temperature sensor and/or DrDAQ pH Probe was used for experimental logging. The DrDAQ was connected to a Windows based PC running Pico Technology's PicoLog Software. External and onboard temperature probes were pre-calibrated. Connected pH probes were calibrated using three NIST buffer solutions (4, 7 and 10), with a manually programmed reference lookup table. A Mettler Toledo pH Electrode (LE409) also used with logger for k_La experiments using the same software setup.

2.11.2 Orion logger

A Thermo Scientific Orion 5-Star pH /DO/Conductivity Waterproof portable meter (1218000) was equiped with a epoxy low maintenance gel pH/ATC Triode with 3 meter cable (9107WMMD) and a DO probe with 3 meter cable (083010MD) for logging purposes. Star Navigator 21 software with RS232 computer Cable (1010007) was used for logging whilst connected to a Windows based PC. The pH probe was calibrated using three NIST buffer solutions (4, 7 and 10), using an auto-detect/manual override value. The DO probe calibrated with a two point reference, a 0 value derived by submersing the probe in a 2 M sodium sulphite solution and a water saturated air value found by using the supplied calibration tube with a water dampened sponge.

2.11.2 LabNavigator logger

A Forston Labs LabNavigator 1 Handheld Multi-Parameter Meter/Analyzer was also used for logging. The device was equiped with a LabNavigator General purpose pH sensor, LabNavigator Dissolved oxygen probe and a pre-calibrated NavTMP temperature probe.The pH probe was calibrated using two NIST buffer solutions (4 and 7 or 7 and 10 depending on the experiment range), using a manual lookup table. The DO probe calibrated with a two point reference as in section 2.11.2. During testing data was logged directly on to a 1Gb USB stick plugged directly into the unit.

2.12 Algal Growth System Setup

2.12.1 Fluidic Oscillator Control

In every experiment involving the usage of the (Zimmerman and Tesar, 2006) fluidic oscillator, the equipment setup was maintained in the same way. The oscillator input was fed with 45 litres/per min air at 1 bar pressure. The air supply was controlled using a 0-100 L/min 1 bar calibrated Platon NGX rotormeter (Roxspur Measurement & Control Ltd), filtered using a Whatman HEPA-VENT 0.3 µm filter (6723-5000 – General Electric) and regulated using a

Norgren R72G-2GK-RMNpressure regulator (RS 239-0670) fitted with a WIKA pressure gauge (RS 777-081). All fitments used 1/4" BSP thread and 8 mm ID hose connectors (RS 795-146). 8 mm ID Reinforced hose (RS 440-054) was used on all tubing until connection to the target reactors. Jubilee clips (RS 525-177) and PTFE sealing tape (RS 512-238) were used on all joints to ensure no leakage. The oscillator outputs were split into two using 8 mm ID 'Y-piece' connectors (RS 795-534), and the venting rate was controlled using two Panam PNV-18-S-4-FF-Rneedle valves (Ogleys, Sheffield). To get an effective airflow oscillation effect the feedback loop on the fluidic oscillator was fixed at 1 m in length, 6 mm ID, 9.5 mm OD silicone tube. To get a sensible equal output on both oscillator outputs, the bleed valves were manually balanced until the fluidic oscillator could be heard to be functioning correctly and the bubble flow in the reactor(s) was equal by visual assessment. Kinks and sharp turns in the pipe airflow were avoided to minimise turbulence impeding the fluid oscillation process(Zimmerman, et al., 2010a; Zimmerman, et al., 2010b).'Y-piece' connectors were using in preference to the 'T-piece' type to also aid in this process (Figure 2.18).

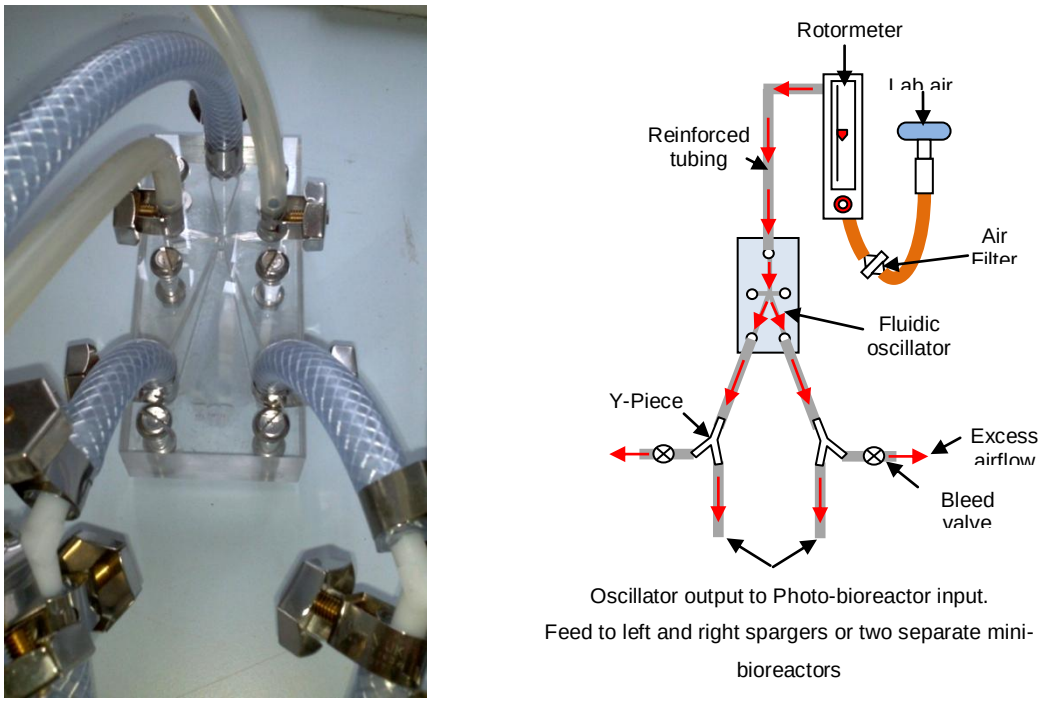

Figure 2.18. Left: Fluidic oscillator with hose connections attached. Right: A diagrammatic representation of the typical connection and control setup used with the fluidic oscillator.

The oscillator air pulse frequency was monitored using a Pico Technology DrDAQ data logger (section 2.11.1) equiped with a Bimorph vibration element (4 V 5 mm, RS 285-784) attached to the scope input. The sensor was manually pressed on one of the oscillator output pipes until a stable waveform was produced and the trace was recorded using Pico Technology's PicoScope 6.5.78.5 software (see Figure 2.19).

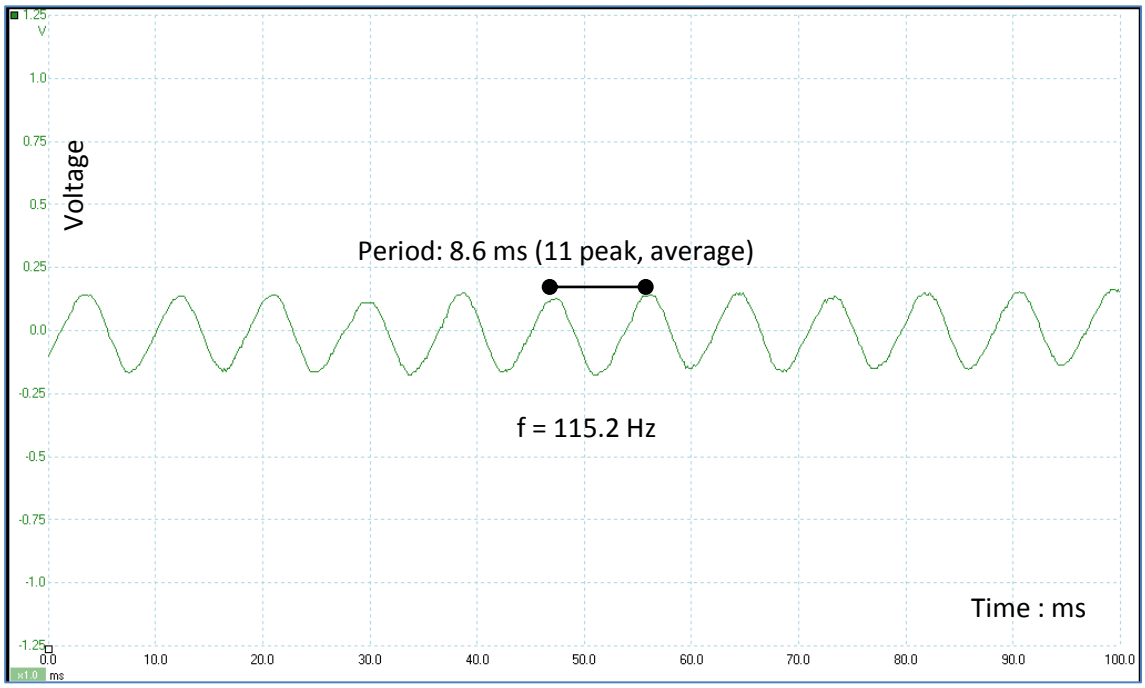

Figure 2.19. Oscillation vibration frequency measured by a bimorph vibration element, frequency calculated from peak to peak measurement.

Measurement of the resultant waveforms was performed using ImageJ v1.47 (National Institutes of Health USA, http://rsbweb.nih.gov/ij/) software. It was found that this frequency was approximately the same regardless of variations in amount of air flow bleed. In this work as the main oscillator flow is constant, the frequency is assumed to be fixed.

2.12.2 Three Litre Flat Plate Photo-bioreactor

The two, 3 litre flat plate photo-bioreactors used in this study were designed and constructed by technician Mike Omeara and subsequently modified by technicians Andy Patrick and Cliff Burton (to accommodate test probes) of Sheffield University's Chemical Biological Engineering workshop. Dimensions included in Figure 2.20.

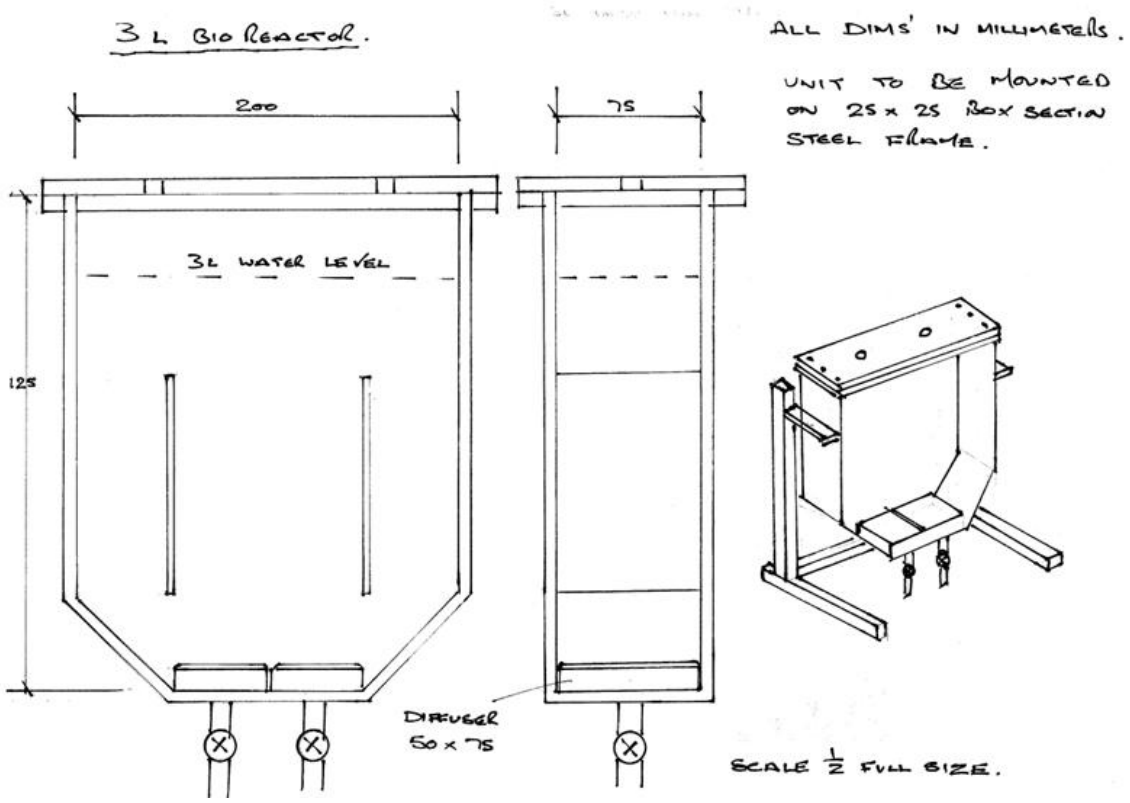

Figure 2.20.Technical drawing of 3L flat plate photo-bioreactor design.

The reactor body was made from Perspex Altuglas (cast acrylic sheets) bonded with extruded acrylic bonder - AB3 (RS 144-383). The spargers were made in house by setting micro-porous ceramic with a 50 µm pore size (developed in Sheffield University's Department of Engineering Materials) into a stainless steel (316 type) welded chassis with a threaded bar inlet using Plexus epoxy resin. Air inflow was controlled using two ETG ball valves, probes were mounted in modified stainless steel ports by FTI (768 LOK SS 12mm x ¾"). The reactor lid was sealed with a sheet of 1 mm thick reinforced nitrile rubber and all other compression fittings were sealed with Viton o-rings. A single 1/4" BSP outlet was left for monitoring outgas flows.

2.12.3 APS Annex Photo-bioreactor Setup

For the experiments conducted in the APS-UGA (section 2.8.4) an external supply of gas was needed to supply the two 3 litre photo-bioreactors (section 2.12.2) inside the growth unit. Using a series of push fit adaptors (RS 287-4061, 287-3327) the annex mains air supply was split into two separated feeds which were regulated and filtered at 1 bar using a Whatman HEPA-VENT 0.3 µm filter (6723-5000 – General Electric) and regulated using a Norgren R72G-2GK-RMNpressure regulator (RS 239-0670) fitted with a WIKA pressure gauge (RS 777-081). One air feed was setup with the fluidic oscillators as in section 2.12.1, the second was connected to a 0-100 cc/min air calibrated 1 bar rotormeter (FTI). For the 100% CO_2 feed, the supply to the 100cc/min rotormeter was simply swapped.

2.12.3 Mk I Mini-Photobioreactor

The Mk I mini photo-bioreactor bodies consisted of a Schott Duran square bottle 100 ml (21 0820 245) with a 5.5 mm hole drilled centrally in the glass bottom. The spargers were made in house by setting micro-porous ceramic with a 50 µm pore size (developed in Sheffield University's Department of Engineering Materials) into a one piece turned chassis made from a single section of stainless steel (316 type) bar (see technical drawing below). The ceramic was sealed into place using Hysol 9497 high temperature epoxy resin (Henkel). The ceramics were hand and machine sanded after curing to give a smooth finish with a 1.5mm bevel. The completed spargers were sealed into the bottle bodies using Geocel Plumba Flue high temperature silicone sealant. The reactor lids were Duran GL32 201-1924 with silicone/PTFE septum seals. A hollow stainless steel 5mm ID x 50mm length tube was used for ventilation. See Figure 2.21 below.

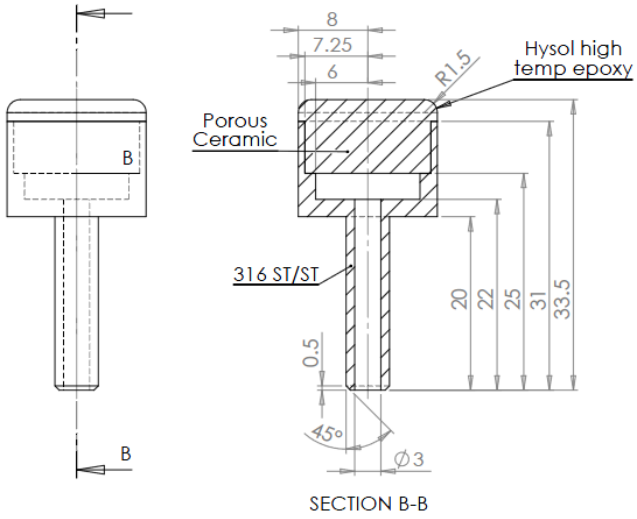

Figure 2.21.Top right: Annotated Mk I mini photo-bioreactor design, Bottom left: Technical drawing of Mk Imini photo-bioreactor sparger design, Bottom right: Actual Mk Imini photo-bioreactor sparger prototype.

2.12.3 Bench top MK1 mini-reactor setup

The MK I mini-reactor setup was housed on a bench in the MBB E-Floor lab (section 2.8.3). The equipment setup consisted of a glass walled, plastic framed fish tank (John Allan 0284-755051 70 x 40 x 45 cm), one quarter filled with sterilised distilled water which was circulated and heated by a Thermomix 1441 temperature controlled/ pump set at 25°C. The mini-reactors were mounted on a series of standard wire coated tube racks, with the bottles submerged up to the 'shoulder' section below the lids. Aeration was provided by the lab air supply, which was filtered (Hepa-Vent, 6-10mm OD, 515-0113) and pressure regulated to 1 bar pressure with a Norgren R72G-2GK-RMNpressure regulator (RS 239-0670) fitted with a WIKA pressure gauge

(RS 777-081). Air flow control was achieved via a series of air calibrated flowmeters (Roxspur & FTI) with needle valves connected via 8 mm ID Reinforced hose (RS 440-054). Air was fed to each reactor sparger using 1 meter of 3mm Silicone tubing (platinum cured FB68856) linked to 5mm Silicone tubing (platinum cured FB68860) using a series of autoclavable adapters (Fisher ADF-602-031T, ADF-745-050H, CNK-481-T). Lighting was provided by four thick fluorescent tubes (section 2.9.3), two above and to the side which were mounted in a modular adjustable steel frame. The type used in the experiment varied depending on the experiment. A light absorbent barrier was created using matt black paint on a cardboard box that fitted over the apparatus. The light absorbent partition in the tank was a black plastic lid from an old Gel tank. The barrier was also used for selected experiments. All silicone tubing and mini-reactors were autoclaved prior to use and non-autoclavable items were sterilised with Microsol or Virkon. See Figures 2.22 and 2.23.

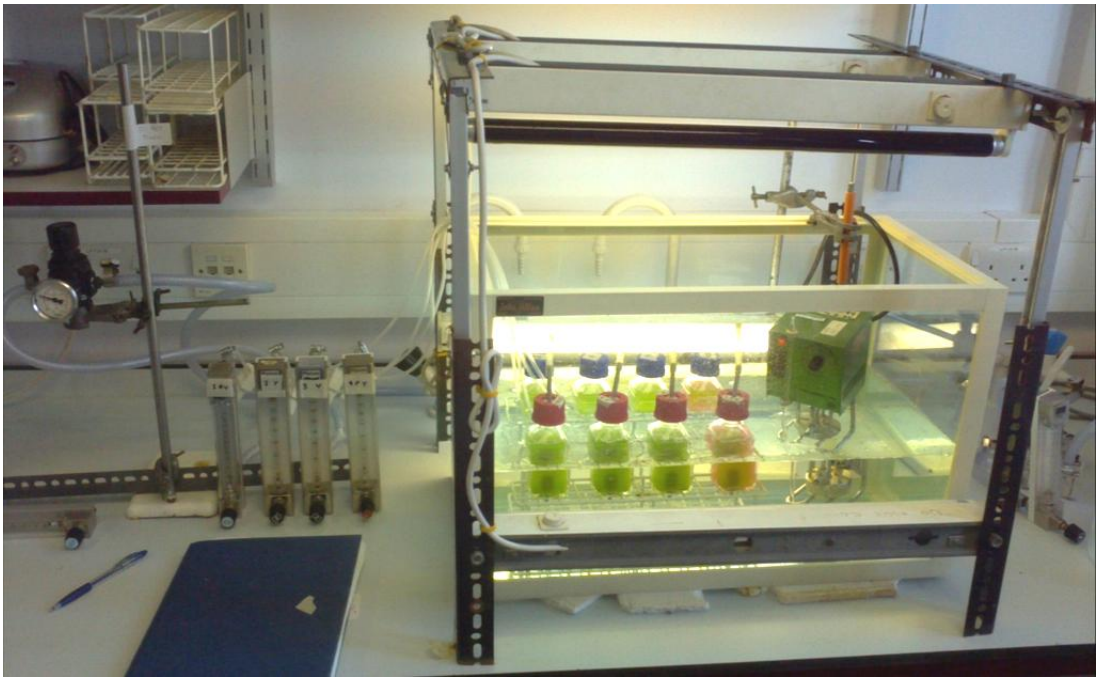

Figure 2.22. Laboratory bench top Mk I mini photo-bioreactor setup

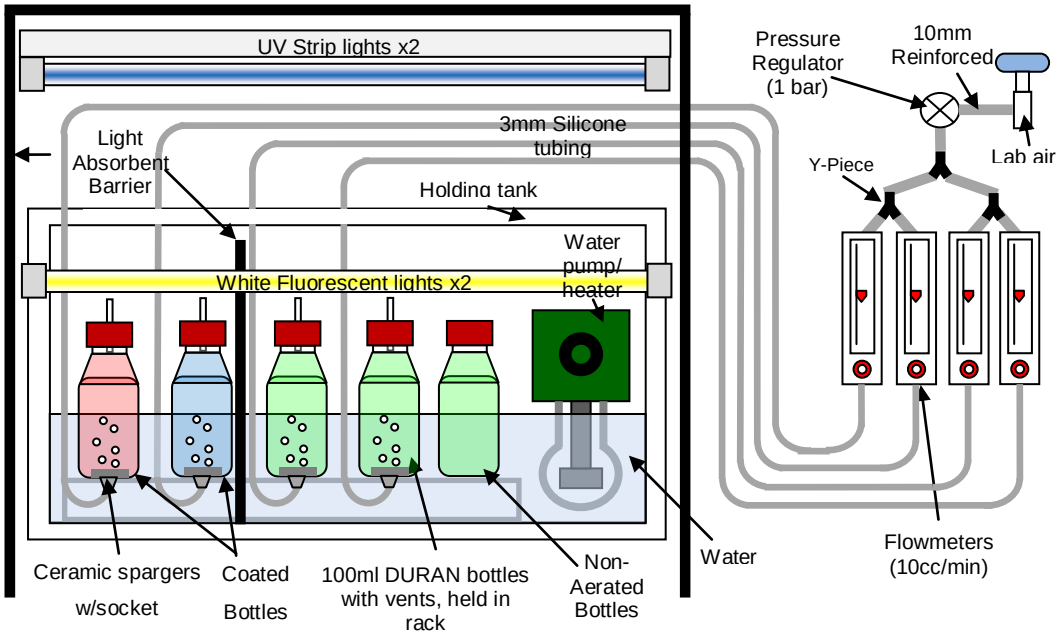

Figure 2.23. Laboratory bench top Mk I mini photo-bioreactor setup diagram

2.12.4 Mk II Mini-Photobioreactor

The Mk II mini photobioreactor bodies were made by glass blower Daniel Jackson in Sheffield University's Department of Chemistry. Schott tube parts with GL 45 screw threads (width: 40 mm, length: 170 mm, wall thickness: 2.3 mm, part: 007005745 VWR) were fused to a small length of 20 mm OD glass tubing (Borosilicate 3.3, 1.8 mm thick, Kavalier T/20/1.8) using the following method; the Screw threads were heated, closed flattened using a carbon paddle. The 20 mm tubing was then cut to size and a hole was blown in the bottom of sealed screw threat section (the same size as the 20 mm tube). The sections were then fused and the bottom of the 20 mm section was then sealed using the carbon paddle. A hole was then added to this section, large enough to accommodate the sparger assembly thread. The central draft tube was made using a section of the same 20 mm tubing. First the tube was cut to size, then fire polished to remove any sharp edges. Nine 4 mm OD prongs made from glass rod (Borosilicate 3.3, Simax R/4) were then attached to the tube sides and bottom edge to maintain the draft tube orientation when in the reactor vessel. Both parts were then annealed in a glass oven at 565°C to remove any micro-stresses fractures and cooled over 24 h. A Schott GL45 membrane screw cap (10 88655) was then used with a high temperature silicone o-ring (BS 220 SIL70, RS 528-0009) to seal the top of the reactor. The spargers for the MK-II were minor adaptations on the previous design (section 2.12.3, developed with technician Andy Patrick). The same ceramic, epoxy and steel were used, but the main body was machined to include a British standard 0.5 mm thread. This modification enabled the spargers to be physically sealed to the reactors using two 2 mm OD Viton O-rings (RS) coupled with an 8 mm stainless steel nut and washer (Figure 2.24).

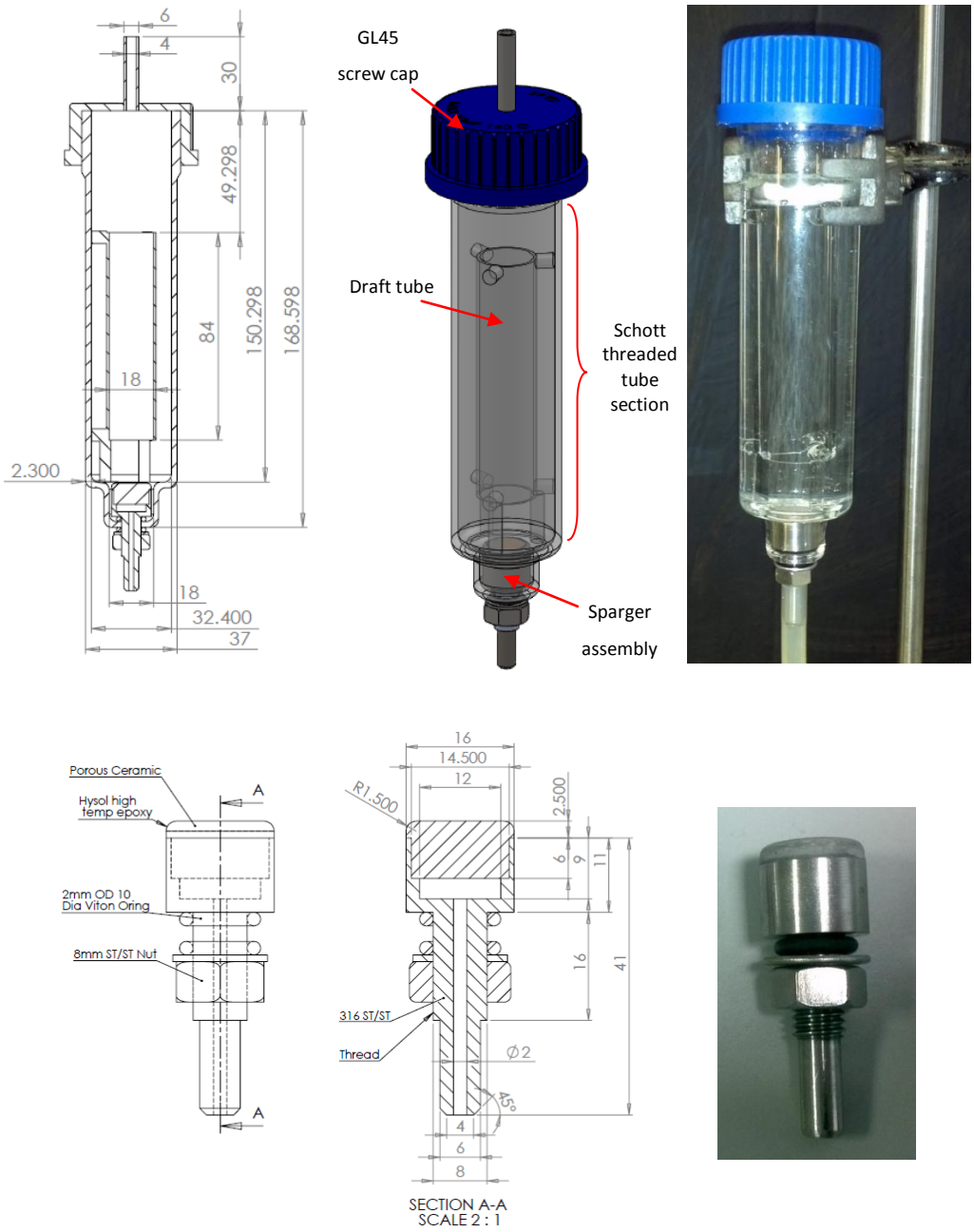

Figure 2.24.Top (left to right) Mk II mini photo-bioreactor: Technical drawing, annotated Solidworks model assembly and physical prototype. Bottom (left to right) Mk II mini photo-bioreactor sparger: Technical drawing and physical prototype.

2.12.5 Bench top Mk II mini-reactor setup

The MK II mini-reactor setup was housed on a bench in the MBB E-Floor lab (section 2.8.3), all experiments were conducted at ambient lab temperature which was logged in three locations using a Picotech DrDAQ device linked to a PC (section 2.11.1). The 10 mini-reactors were mounted using a series of standard laboratory clamps and bosses at two different heights. Lighting was provided by three ring fluorescent tubes (section 2.9.3) held equidistantly between each reactor using a modular adjustable steel frame. A light reflective surround was created using attaching aluminium foil to a cardboard box that fitted over the apparatus. All silicone tubing and mini-reactors were autoclaved prior to use and non-autoclavable items were sterilised with Microsol or Virkon. The air and CO_2 supplies were setup differently depending on the experiments.

Variable flow rate experiments

In these experiments, standard air was provided by the lab air supply, which was filtered (Hepa-Vent, 6-10mm OD, 515-0113) and pressure regulated to 1 bar pressure with a Norgren R72G-2GK-RMNpressure regulator (RS 239-0670) fitted with a WIKA pressure gauge (RS 777-081). Air/CO_2 (depending on experiment) was fed to 8 flowmeters (Roxspur & FTI) with needle valves using 8 mm ID Reinforced hose (RS 440-054) and silicone tubing with y-piece adaptors. Air was fed to each reactor sparger using 1 meter of 5 mm Silicone tubing (platinum cured FB68860) using a series of auto-clavable adapters (Fisher ADF-602-031T, ADF-745-050H, CNK-481-T). Reactors 1 & 2 were set at 5cc/min flow rate, 3 & 4 - 10cc/min, 5 & 6 - 15cc/min, 7 & 8 - 20cc/min and reactors 9 & 10 were used as non-aerated standards. Due to the very low flow rates, the flowmeters were just used for their needle valves. The aeration rate was measured on each reactor exhaust using a 0-100cc/min digital mass flow meter (Cole-Palmer 32908-59) using a modified Schott GL45 lid with a 1/8" BSP adapter attached to a 3mm silicone tube. Cultures were inoculated using the standard 1:20 inoculum to medium ratio in 100 ml volume using well grown cultures. To ensure all readings were performed with purely planktonic cultures, the reactor dead zones were agitated using a 5000 µl Gilson pipette before samples were taken (Figure 2.25).

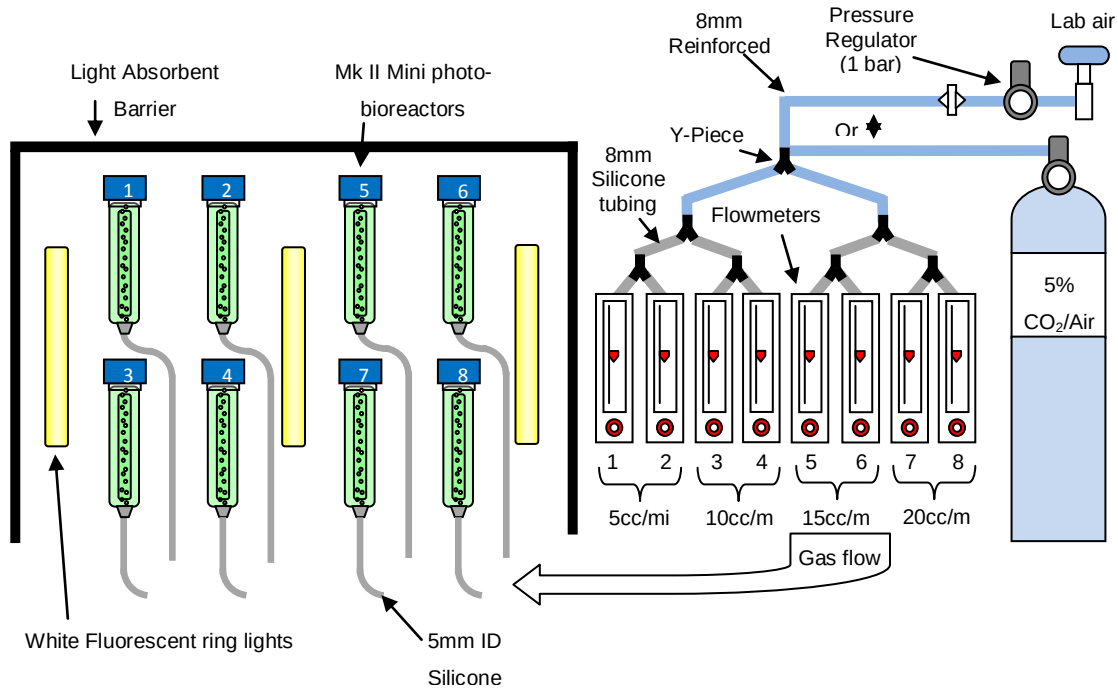

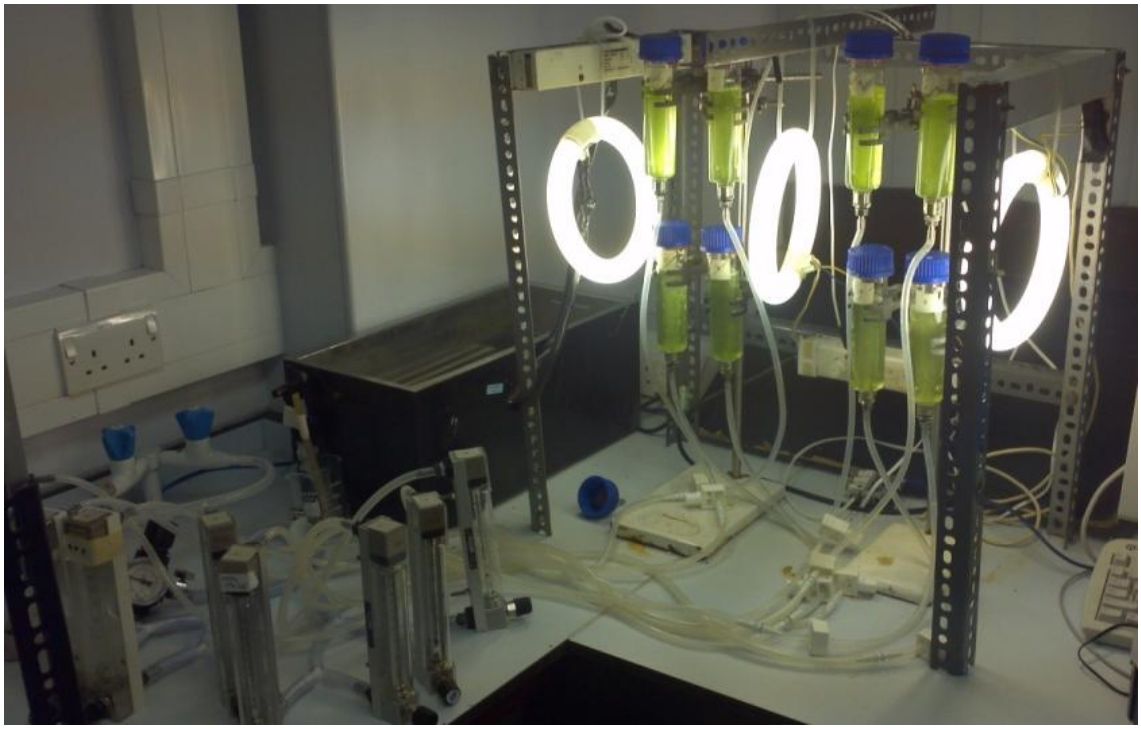

Figure 2.25. Variable flow experiment Mk II mini photo-bioreactor bench top setup. Top: Diagrammatic representation, Bottom: Physical setup.

Oscillator comparison experiments

In these experiments, all standard air was again provided from the same source and the oscillator was also configured as in section 2.12.1. Reactors 1-4 were controlled using four flowmeters (Roxspur & FTI) with needle valves, the feed to each of these came from lab air or 5% CO_2 depending on the activation of an electronic control valve (Burket 2/2 way solenoid valve direct acting - 213552 via Thorite). Due to the air feed being for 23.5 hours compared to the CO_2, the air valve was a normally open (NO) type and the CO_2 a normally closed (NC). Reactors 5-8 fed air from the fluidic oscillator left and right outputs, or connected to four flowmeters (Roxspur & FTI) with needle valves attached to the 5% CO_2 supply. The oscillator left and right outputs were split into two after the initial bleed, this was in-turn divided again into another bleed section for fine control using the other set of needle valves (RS 262-0640). The oscillator air supply was controlled by a NO electronic control valve and the CO_2 supply by a NC valve using the same dosing regime (Figure 2.26). The reactors were monitored and maintained in the same way as the previous experiment.

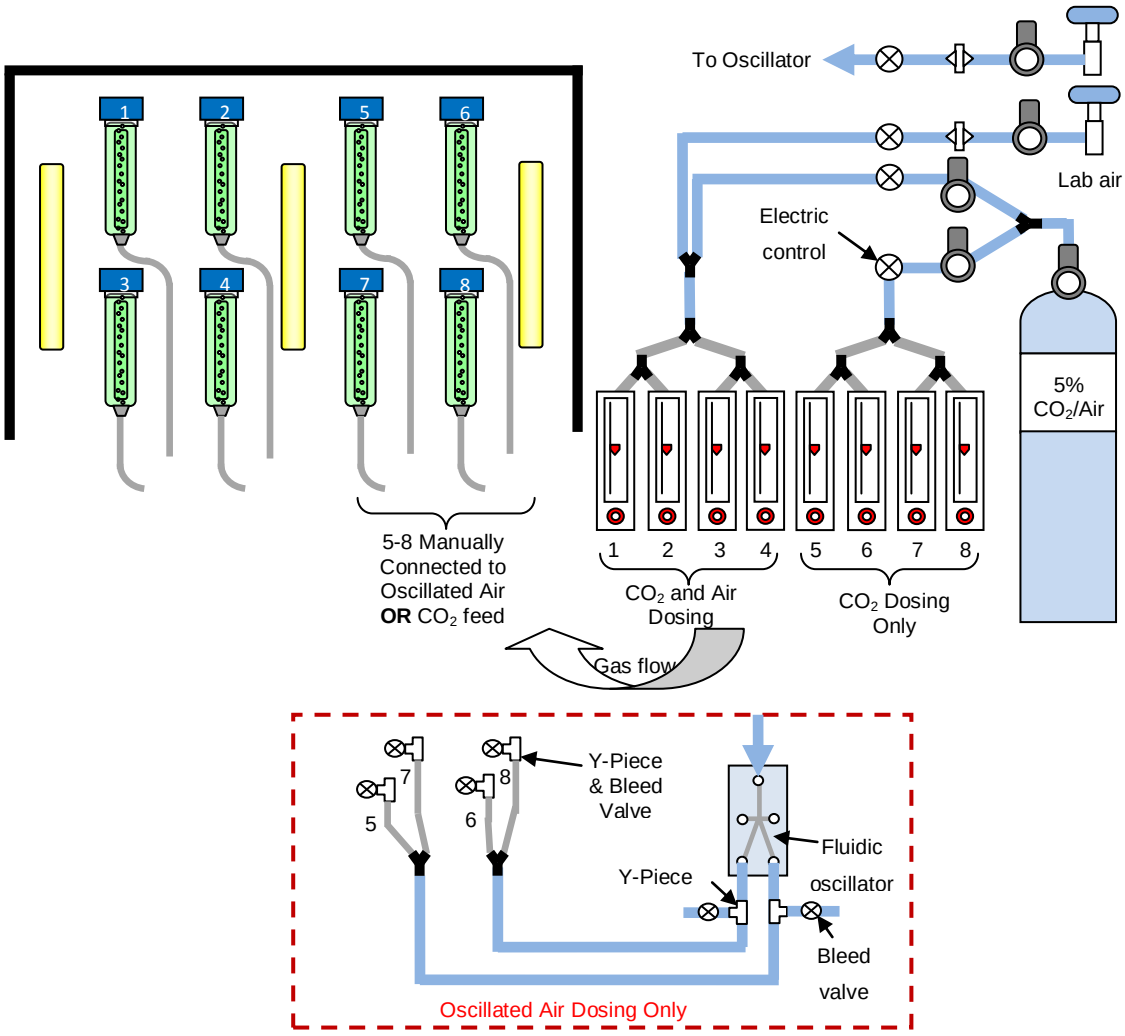

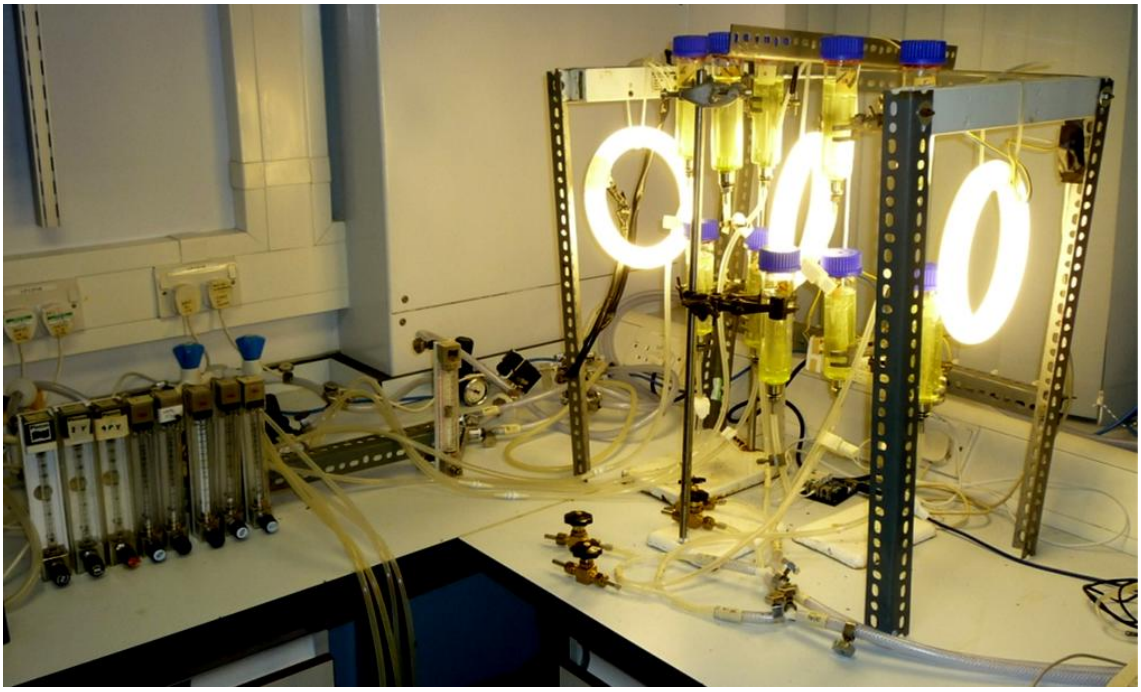

Figure 2.26. Oscillator comparisonexperiment Mk II mini photo-bioreactor bench top setup. Top: Diagrammatic representation, Bottom: Physical setup.

2.13 k_La Determination

The dynamic absorption method of determining k_La(Doran, 1995) was chosen to determine the rate of oxygen and carbon dioxide dissolution. Dissolved oxygen (DO) was measured using the Thermo-Scientific Orion data logger (section 2.11.2) and Clarke electrode (083010MD). Dissolved carbon dioxide (dCO_2, via pH inference) was measured using the DrDAQ data logger equipped with a regular glass pH electrode (section 2.11.1). Both loggers were attached to a windows XP based PC with the relevant logging software enabled. The probes were mounted at 90^o to draft tube, mid plane (horizontally and vertically) in the down-comer region of one of the 3 litre flat plate bioreactors (section 2.12.2). The reactors were filled with 3 litres of liquid (deionised water with and without 1 M NaCl added) before each set of triplicate readings. The air was provided by the lab air supply, which was pressure regulated to 1 bar pressure with a Norgren R72G-2GK-RMNpressure regulator (RS 239-0670) fitted with a WIKA pressure gauge (RS 777-081).The fluidic oscillator was configured as in section 2.12.1 and nitrogen was provided from a pressure regulated cylinder. See Figure 2.27.

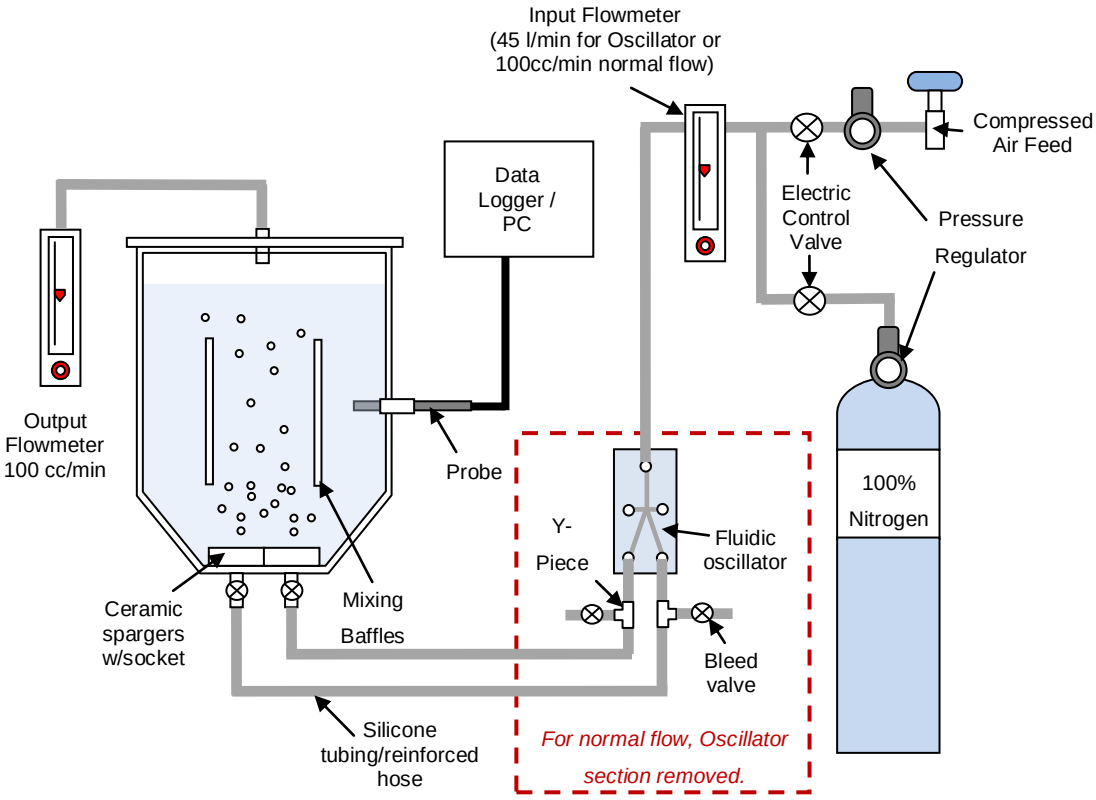

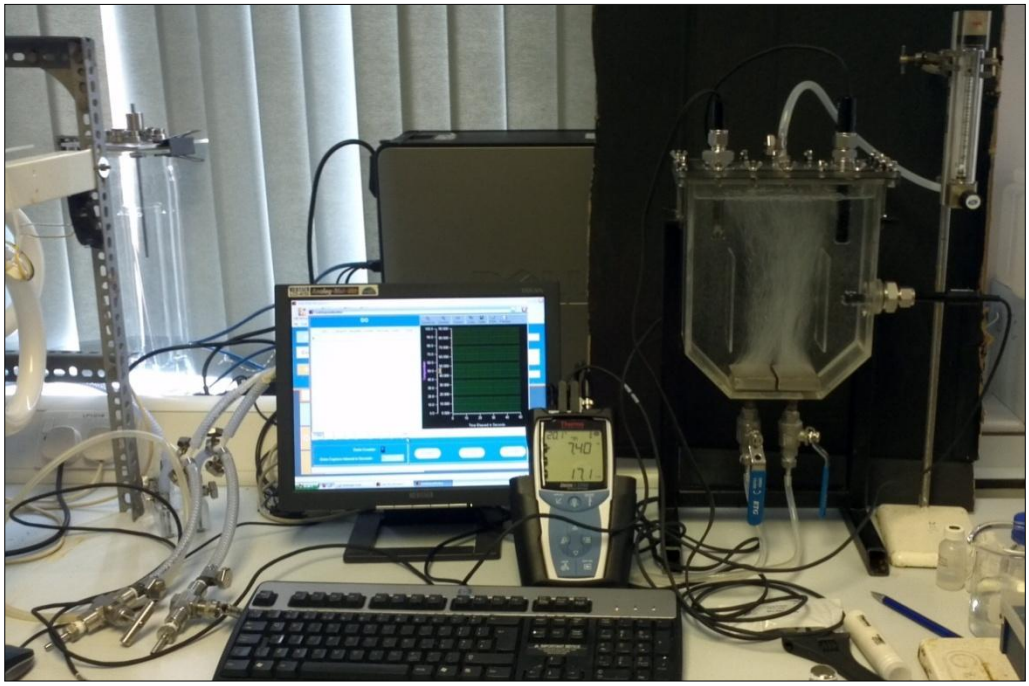

Figure 2.27. 3L Photo-bioreactor k_La measurement setup. Top: Diagrammatic representation, Bottom: Physical setup.

2.14 Fluorescent Dye Tracing

Visual characterisation of fluid flow around each of the reactor designs was performed using fluorescein sodium salt (Sigma-Aldrich F6377-100G) mixed with distilled water (100 mg/ml).10 µl of the dye solution was added to the top liquid surface of a bioreactor before commencing bubbling, illumination of the dye was performed using UV light from two fluorescent tubes (section 2.9.3). Distilled water was mixed with glycerol (50/50) to increase viscosity and slow the mixing speed, so photos could be taken.

2.15 Acoustic Bubble Spectroscopy (ABS)

Bubble size measurement was performed using a two portable Dynaflow Inc. Acoustic Bubble Spectrometer (ABS) systems. Eight transducer/hydrophones were connected to a signal generator/amplifier, which was in turn connected to a computer system, Dynaflow proprietary software was used for data logging. Bubble size population and gas hold-up data were gathered by taking acoustical measurements at multiple frequencies. Hydrophones were connected in matching pairs, each with a particular frequency band assigned. A large glass fish tank (59.3 x 29.5 x 21 cm) was filled with either distilled water only or distilled water plus 1 M NaCl. A single sparger from one of the 3 litre bioreactors (section 2.12.2) was then placed in centre of the tank and each hydrophone pair was then mounted in parallel across the sparger area, held by a series of clamps and stands. Before the aeration, a background reading was taken to determine and remove background noise from the readings. Default settings were used in the software for readings, with the exception of the frequency ranges, which were tailored for the sub 1 mm range using the software recommendations. For the 1 M NaCl salt readings, the water properties in the software were adjusted to match the physical properties of sea water. Air supply came from a regulated 1 bar lab air source. Laminar air was supplied at 50cc/min using a 0-100 cc/min calibrated flowmeter (FTI). Oscillated air supply setup was as in section 2.12.1, but with one output connected to a sparger in the fish tank and the second connected to a sparger in a separate 3 litre reactor. The flow rates were calibrated to 50cc/min, using the sparger in the 3 litre bioreactor with a flowmeter on the exhaust. The water depth of the tank was matched to that of the reactor to ensure the pressure head was the same in both cases. Bubble size measurements were taken for laminar and oscillated supplies in both water and saltwater. See Figure 2.28.

A - Fish tank setup side

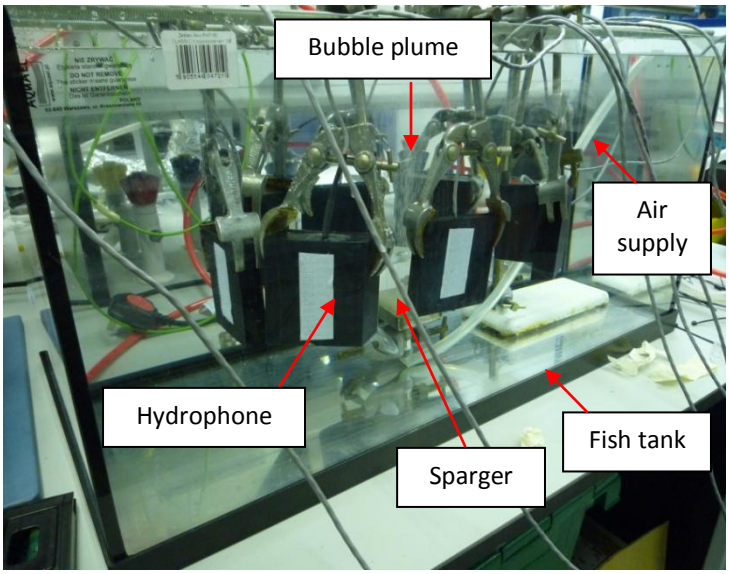

Figure 2.28. (A-B): ABS physical test setup using a single 3L Photo-bioreactor sparger.

(C): Manufacturer setup diagram.

B - Fish tank setup above

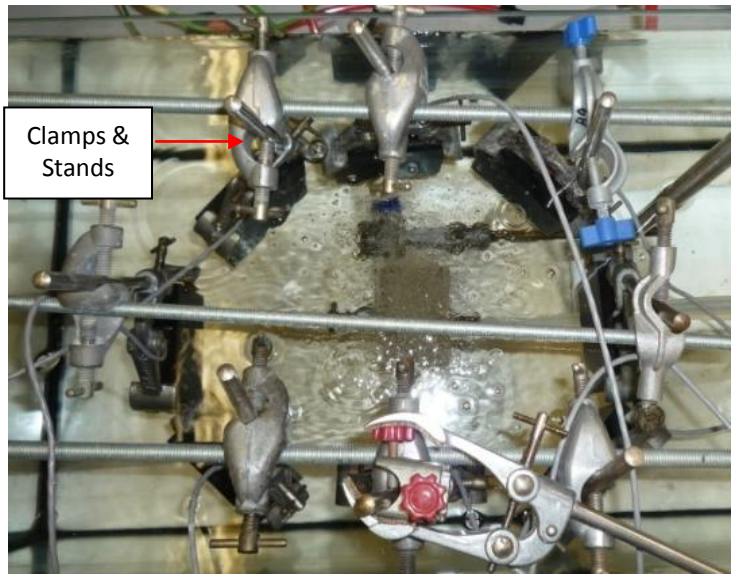

C - Manufacturer diagram

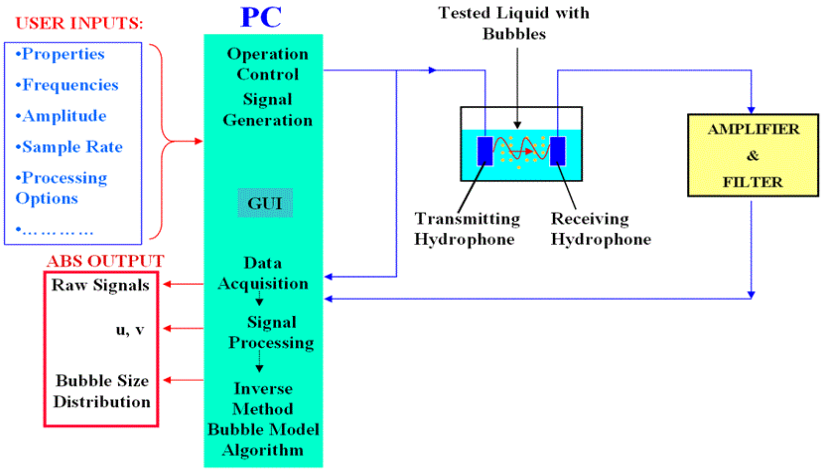

2.16 High Speed Camera Imaging

Bubble size imaging was performed using a Photron high speed camera set to a 500 frames/s capture rate using the manufacturer's native software. A 3 litre flat plate bioreactor (section 2.12.2)was filled with 3 litres of distilled water with and without 1 M NaCl. Air was provided by the lab air supply, which was pressure regulated to 1 bar pressure with a Norgren R72G-2GK-RMNpressure regulator (RS 239-0670) fitted with a WIKA pressure gauge (RS 777-081). Air flow rates were measured on the reactor exhaust using a 0-100 cc/min flowmeter (FTI), laminar flow was controlled at the reactor input using another 0-100 cc/min flowmeter (FTI) and oscillated air was provided using the same configuration as in section 2.12.1. After the air flow was calibrated and established at 100cc/min, the reactor lid was removed and a tape measure was held in the reactor using a clamp and boss, to provide scale for the measurements. Videos and still images were taken under illumination with a black card backdrop for oscillated and laminar flow with and without the addition of salt (see Figure 2.29, below).

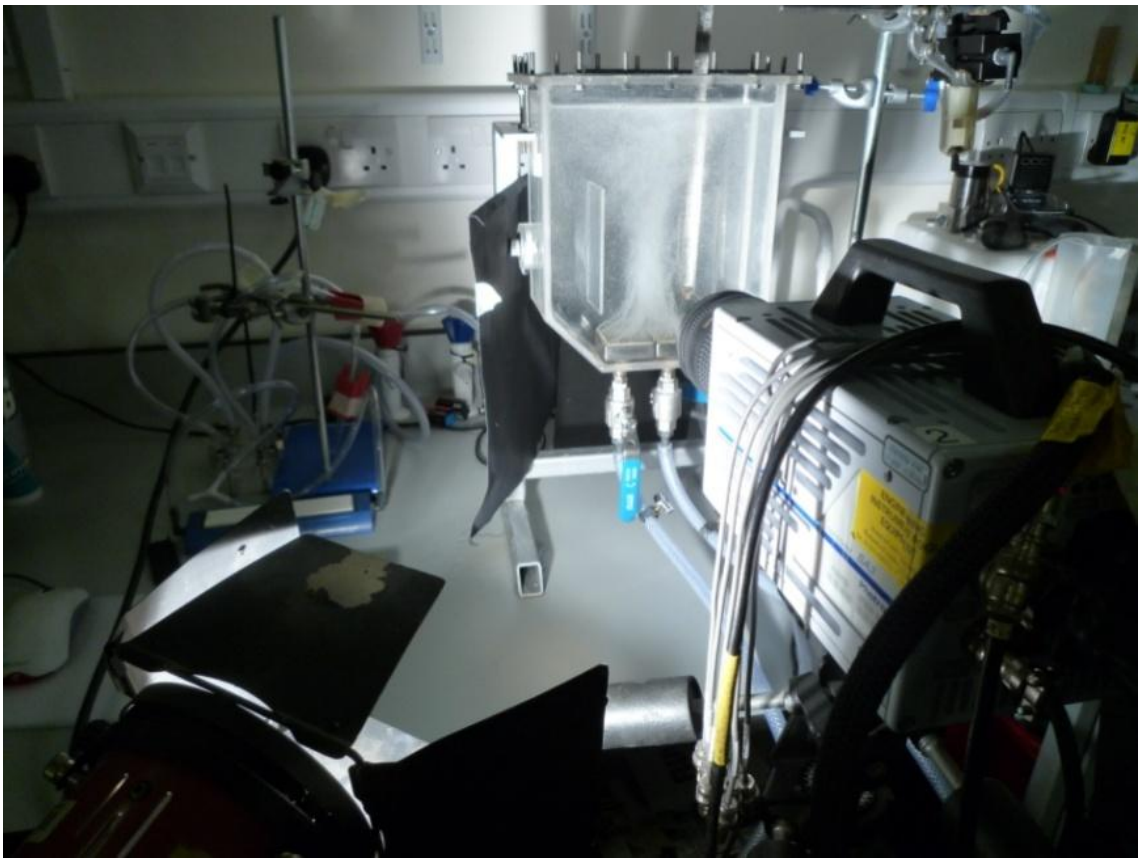

Figure 2.29. Slow motion camera 3L Photo-bioreactor setup.

2.17 COMSOL Multiphysics

All Computational fluid dynamics (CFD) models were performed using COMSOL Multiphysics 4.2 + CFD Module with the laminar bubble flow (bf) physics model. More information is included in section 3.6.

2.18 Statistics

All statistical work was carried out using Microsoft Excel, with standard deviation and standard error functions.

3 Photo-Bioreactor Development and Modelling - Part 1

3.1 Introduction

Photo-autotrophic organisms such as microalgae have two key requirements for growth: CO_2 as a carbon source and light for energy to conduct photosynthesis. In the design of a photo-bioreactor system both need to be taken into consideration, along with many other climatic variables such as temperature, pH, DO etc which in accumulation can have an equally important impact on the health of a culture. For the optimal production of any strain within a photo-bioreactor system the secret, as with all things in life, is balance. If any one factor becomes limiting or in excess, the target yield for the algal crop i.e. oil, starch, hydrogen, poly-saccharides, will be reduced and the entire production process can become uneconomical or more importantly, not carbon neutral. In this section, the effects of photo-bioreactor fluid dynamics and mass transfer will be studied with a particular emphasis on the impact of micro-bubble generation using fluidic oscillation.

3.2 Modelling the Effects of Media Salinity on CO_2 and O_2 Solubility.

To be able to accurately study the effects of mass transfer in a photo-bioreactor system, the solubility of the gases needed for culture growth in the growth media is of great importance. This factor is especially important when high levels of salinity are present, such as with the artificial sea water media needed to grow halophilic algae like *Dunaliella salina*. The high ionic content of sea water produces a 'salting out' effect, where the capacity of water to contain dissolved gases is significantly reduced, and the time it takes to dissolve is much longer. The severity of the effect increases with the concentration of the ions dissolved in the medium. So, to accurately measure the mass transfer in a reactor system, modelling the effect is crucial.

3.2.1 Gas pressure, partial pressure and Henry's law

To model the amount of gas diffusion in a bioreactor system, firstly the pressures involved on the gases used need to be considered. The partial pressure of the gas used in aeration affects the magnitude of the gas solubility in the medium (C_{AL}^*). The partial pressure of a gas can be calculated by multiplying the mole fraction of the gas in the mixture by the overall pressure; i.e. for N_2 in Air, this would be 0.78 x 1 atm = 0.78 atm.

The relationship between these pressure parameters and how much gas diffuses into a liquid is governed by Henry's law: $p_{AG} = p_T y_{AG} = HC_{AL}^*$

Where; p_{AG} = the partial pressure of component A in the gas, p_T = the total gas pressure, y_{AG} = is the mole fraction of A in the gas, H = Henry's constant (a function of temperature) and C_{AL}^* = is the solubility of component A (or its concentration) in the liquid.

From the Henry's law equation it can be deduced that if p_T or y_{AG} are increased at a constant temperature, then the solubility C_{AL}^* will also increase. This in turn will increase the driving force for mass transfer which is the difference between the actual concentration in the liquid C_{AL} and the solubility (i.e.$(C_{AL}^* - C_{AL})$). Based on this, culture growth can potentially be enhanced by sparging at higher pressure or using a more enriched gas source, but this has to be done carefully due to potential inhibition effects and issues with reactor vessel integrity. In this work, as the main area of study is the effect of interfacial area, so all gassing is performed at standard atmospheric pressure.

3.2.2 Calculating gas solubility

The solubility of the gases relevant to algal growth, $CO_2$and O_2, change with ambient temperature and pressure. There are many data tables available giving these data in relation in distilled water (Perry, Green and Maloney, 1997), but in highly saline media further calculations are required to compensate for the ionic effects of the salts present (Quicker, et al., 1981). Since there are no non-ionic solutes such as sugars present in any of the media used in this study, only the ionic constituents will be considered. To make use of the saline calculations over a range of temperatures at atmospheric pressure, an equation for the solubility of each gas in distilled water is first needed.

Oxygen

The level of oxygen solubility in distilled water can calculated by numerous empirical based equations (Montgomery, Thom and Cockburn, 1964; Truesdale and Downing, 1954; Whipple and Whipple, 1911). For the purposes of this work, the equation derived by Karlsson and Torstens. (1974) has been used due to its high accuracy:

$$C_{AL}^* = 14.1271 - 0.33935T + 5.1333 \times 10^{-3}T^2 - 3.5556 \times 10^{-5}T^3$$

Where; C_{AL}^* = oxygen solubility (mg l^{-1}) and T = Temperature (°C). The equation is valid in the temperature region of 10 to 40°C, based on atmospheric pressure of (760 mmHg). To compensate for other pressures the following equation is used:

$$C_{AL@760} = C_{AL}\frac{760\ mmHg - p}{P - p}$$

Where, $C_{AL@760}$ = the pressure compensated DO concentration, p = The saturated water vapour pressure in mmHg and P = The barometric pressure required.p can be calculated using the Antoine equation(Antoine, 1888) , which for pure water (between 1-100°C) is the following:

$$p = 10^{\left(8.07131 - \frac{1730.63}{T + 233.426}\right)}$$

For an example, the oxygen solubility at 25°C (298.15K) at 1 atm:

$$C_{AL}^{*} = 14.1271 - 0.33935T + 5.1333 \times 10^{-3}T^{2} - 3.5556 \times 10^{-5}T^{3}$$

$$= 14.1271 - 0.33935 \times (298.15K - 273.15K) + 5.1333 \times 10^{-3} \times (298.15K - 273.15K)^{2} - 3.5556 \times 10^{-5} \times (298.15K - 273.15K)^{3} =$$

$$14.161 - 8.484 + 3.2 - 0.5555 = 8.2961 \text{mg l}^{-1} \text{ or } 0.0082961 \text{ g l}^{-1}$$

To make future Henry's law values more consistent, as most are in the form M/L format, this value is converted by dividing by the molecular weight of O_2(=32) to give 2.59x10^{-4} M/L.

So, if the mole fraction of oxygen in air (y_{AG}) is 0.2099 and the total air pressure (p_T) is 1 atmosphere (atm), the Henry's Coefficient can be related to the solubility and the partial pressure of oxygen in air (p_{AG}) and calculated as follows:

$p_{AG} = p_T y_{AG} = HC_{AL}^{*}$, therefore: $H = \frac{p_T y_{AG}}{C_{AL}^{*}} = \frac{1 \times 0.2099}{2.59 \times 10^{-4}} = 809.63 \ \frac{atm \cdot L}{mol}$

To make the data applicable to the salinity calculations, the Henry's Coefficient needs to be converted to a dimensionless SI value. To do this, the concentration of O_2in air (M/l) needs to be calculated using the ideal gas law (below) to cancel out the existing units.

$$PV = nRT$$

Where P = Atmospheric pressure (atm), V = Volume of gas (L), n = the moles of gas, R = Ideal gas constant 0.08205746 (L atm K^{-1} mol^{-1}) and T = temperature in K.

If the ideal gas equation above is re-arranged to have the molar concentration on the left: $\frac{n}{V} = \frac{P}{RT}$ And: P = 1 atm, the following can be derived:

$$\frac{n}{V} = \frac{1 \text{ (atm)}}{0.08205746 \ (LatmK^{-1}mol^{-1}) \times 298.15 \ (K)} = 0.04087 \text{ M/L}$$

So if 809.63$\frac{atm \cdot L}{mol}$is multipliedby 0.04087 M/L; 809.63 x 0.04087 = 33.09, and the units cancel out like thus:

$\frac{atm}{(M/L)} \times \frac{(M/L)}{1} = \frac{atm \times \cancel{(M/L)}}{\cancel{(M/L)}}$ to remove the atm unit, H = $\frac{1atm}{33.09}$ = 3.02x10^{-2} dimensionless.

Because of the way the units were removed, although the Henry's constant is dimensionless, it is so in a particular ratio as explained below. The first set of equations is worked out in $\frac{atm \cdot L}{mol}$ or the 'partial pressure of the gas above the liquid in atm' / 'concentration of gas in the liquid in mol/L'. The dimensions were removed using the ideal gas equation, which produced a value

for the gas concentration in $\frac{mol}{atm \cdot L}$, which is the 'solubility' form $\frac{C_l}{C_g}$, where (C_g) is the concentration of gas and (C_l) is the concentration of liquid. Note that other definitions of the Henry's law constant define it as the inverse of the above ratio which leads to confusion and is the reason for the careful explanation given here.

To allow the equation to work with the salinity model the$H$ value has to be converted to a Bunsen coefficient (α), this is done with the following equation from Schumpe, Quicker and Deckwer (1982):

$$\alpha = \left(\frac{273.15}{T}\right) H$$

Where; T temperature is in Kelvin.

Carbon dioxide

The solubility of CO_2 is calculated using the following equations. The reference value of 100% CO_2 solubility in pure water can be calculated using the following expression defined by (Versteeg and Vanswaaij, 1988)as:$H = 3.54 \times 10^{-7} exp\left(\frac{2044}{T}\right)$ in mol m^{-3} Pa^{-1} and made dimensionless in the $\frac{C_l}{C_g}$ form byDarmana, et al. (2007):

$$H = 3.59 \times 10^{-7} RT exp\left(\frac{2044}{T}\right)$$

Where R = the ideal gas constant 8.314 ($J \cdot K^{-1} mol^{-1}$), T = Temperature in K. The equation is valid in the temperature region of 293 to 303 K (20-30°C).

Thus, at 25°C:

$$H_w = 3.59 \times 10^{-7} RT exp\left(\frac{2044}{T}\right) = 3.59 \times 10^{-7} \times 8.314 \times 298.15 \times exp\left(\frac{2044}{298.15}\right)$$
$$= 0.8447$$

Again this value can be converted into the appropriate α value using the previously mentioned equation.

3.2.3 Solubility of media

Once the Henry's coefficients for the gases in distilled water have been calculated (and converted into the correct format), the solubility effects of the ions in the media can be calculated using the following equations from Schumpe (1993), Schumpe, Quicker and Deckwer (1982), Weisenberger and Schumpe (1996). In their work they conducted a series of

experiments (and collected data from others) for a number of gases and ions, where they plotted the effect their interrelation had on solubility at different temperatures. The central core of this work is based around the Sechenov relation(Schumpe, Quicker and Deckwer, 1982), which was expanded to cover a greater temperature range and include more gases and salts:

$$K = \sum (h_i + h_G) n_i$$

Where; h_G = the gas specific constant, K = Sechenov constant ($m^3 \cdot kmol^{-1}$), n_i = the index of ion i in the formula of the salt and h_i = ion specific parameter ($m^3 \cdot kmol^{-1}$).

To calculate h_G the following equation was used: $h_G = h_{G,0} + h_T(T - 298.15)$

Where; $h_{G,0}$ = gas specific parameter ($m^3 \cdot kmol^{-1}$), h_T = gas specific parameter for the temperature effect ($m^3 \cdot kmol^{-1}K^{-1}$), T = temperature (K).

These values can then be embedded in the following equation relation:

$$\log(c_{G,0}/c_G) = \sum_i (h_i + h_G) c_i$$

Where; c_i = ionic concentration for component i;c_G = solubility of a gas (Bunsen coefficient α); $c_{G,0}$ = solubility of gas in pure water (Bunsen coefficient α); and h_i is a parameter for each component i as given in the table below.

Model details and example for Dunaliella Medium

Dunaliella medium contains many constituent elements, predominantly salts (see section 2.1.1). To calculate the solubility of O_2 and CO_2, the main ions in the media were taken into consideration. The model parameters derived by Weisenberger and Schumpe (1996) relevant to this medium are included in Table 3.1.

Table 3.1. Cation, anion and gas model parameter values applicable to Dunaliella medium.

Cation	h_i (m^3 $kmol^{-1}$)	Anion	h_i (m^3 $kmol^{-1}$)	Gas	$h_{G.o}$ (m^3 $kmol^{-1}$)	h_T (m^3 $kmol^{-1}$ K^1)	Temp range (K)
H^+	0	NO_3^-	0.0128	CO_2	-0.0172	-0.338×10^{-3}	273-313
Na^+	0.1143	CO_3^{2-}	0.1423	O_2	0	-0.334×10^{-3}	273-353
K^+	0.0922	SO_4^{2-}	0.1117				
Mg^{2+}	0.1694	PO_4^{3-}	0.2119				
Ca^{2+}	0.1762	Cl^-	0.0318				

The total molarity of each of the different ions in the media was then calculated (Tables 3.2 and 3.3 below).

Table 3.2(left) - Concentration of chemical elements in Dunaliella medium. Table 3.3 (right) - Total molar concentration of each ion inDunaliella medium.

Chemicals	M/l
$MgSO_4.7H_20$	0.024
$MgCl_2.6H_20$	0.02
$CaCl_2.2H_20$	0.01
$NaNO_3$	0.005
Na_2SO_4	0.024
NaH_2PO_4	0.0001
KCl	0.01
NaCl	1
$NaHCO_3$	0.012

Ion	Molarity (M/litre) or (kmol/m^3)
Mg^{2+}	(1x0.024)+(1x0.02)=0.044
SO_4^{2-}	(1x0.024)+(1x0.024)=0.048
Cl^-	(2x0.02)+(2x0.01)+(1x0.01)+1=1.07
Na^+	(1x0.005)+(2x0.024)+(1x0.0001)+1+(1x0.012)=1.0651
NO_3^-	0.005
H^+	(2x0.0001)+(1x0.012)=0.0122
PO_4^{3-}	0.0001
K^+	0.01
CO_3^{2-}	0.012
Ca^{2+}	0.01

Note: The 0.0015 mM FeEDTA, Trace elements and 0.02M HEPES have not been included in the above calculations, due to their very small amounts in solution.

Once the ionic properties and quantities were established, a temperature could be then specified so the reference data for gas solubility can be inputted into the equations. For example, if the temperature is 25°C or 298.15 Kelvin, the solubility can be calculated using the following:

CO_2Gas Constant:

$$h_G = h_{G,0} + h_T(T - 298.15) = -0.0172 + -0.338 \cdot 10^{-3}(298.15 - 298.15) = -0.0172$$

O_2 Gas Constant:

$$h_G = h_{G,0} + h_T(T - 298.15) = 0 + -0.334 \cdot 10^{-3}(298.15 - 298.15) = 0$$

With the gas specific constants calculated for the relevant temperatures, the solubility can be derived for the electrolyte solution composition. The contribution of each of the ions is calculated using the expression $(h_i + h_G)c_i$. These contributions are then summated and translated to a Henry's constant using: $\log(c_{G,0}/c_G) = \sum(h_i + h_G)c_i$.

CO_2- Ion calculations:

$(h_i + h_G)c_i$ *Values:*

$\boldsymbol{Mg^{2+}} = 0.044(0.1694 \pm 0.0172) = 0.0067,$ $\boldsymbol{SO_4^{2-}} = 0.048(0.1117 + -0.0172) = 0.0045,\boldsymbol{Cl^-} = 1.07(0.0318 + -0.0172) = 0.0156,\boldsymbol{Na^+} = 1.065(0.1143 + -0.0172) = 0.1034,\boldsymbol{NO_3^-} = 0.005(0.0128 + -0.0172) = -0.000022,\boldsymbol{H^+} = 0.012(0 + -0.0172) = -0.000208,\boldsymbol{PO_4^{3-}} = 0.0001(0.2119 \pm 0.0172) = 0.0000195,\boldsymbol{K^+} = 0.01(0.0922 + -0.0172) = 0.00075,\boldsymbol{CO_3^{2-}} = 0.012(0.1423 + -0.0172) = 0.00149$

Thus: $\log(c_{G,0}/c_G) = [\boldsymbol{Mg^{2+}}] + [\boldsymbol{SO_4^{2-}}] + [\boldsymbol{Cl^-}] + [\boldsymbol{Na^+}] + [\boldsymbol{NO_3^-}] + [\boldsymbol{H^+}] + [\boldsymbol{PO_4^{3-}}] + [\boldsymbol{K^+}] + [\boldsymbol{CO_3^{2-}}]$

So: $\log(c_{G,0}/c_G) = 0.1338$ so, $c_{G,0}/c_G = 1.361.$

If the Bunsen coefficient is known for CO_2 in distilled water (from the previous section), $0.774/1.361 = c_G = 0.5686$

Maximum atmospheric CO_2concentration:

To convert the c_G (or α) values into a more useful solubility measure (mg/L), the following equation is used Schumpe, Quicker and Deckwer (1982):

$$c = \frac{10^6 M_G p}{V_0 101.3}\alpha \rightarrow \frac{10^6 \times 44 \times (0.04 \times 101.3)}{22.258 \times 101.3 \times 1000}\alpha = 0.0078 \times 101.3 \times 0.5686 = 0.45\ mg/L$$

Where; p = partial pressure of gas (kPa), the mole fraction of carbon dioxide in air (y_{AG}) is 0.000397, so for an air pressure (p_T) of 1 atm (101.3 kPa) hence 0.04 x 101.3,M_G = the gas molecular weight (g/M), V_0 = Gas molar volume at 0°C, 101.3 - Pressure (kPa).

Maximum atmospheric O_2 concentration:

Using the previous set of equations, the oxygen concentration in the aqueous Dunaliella media that is in equilibrium with atmospheric air can also be calculated:

$$c = \frac{10^6 \times 32 \times (0.2094 \times 101.3)}{22.395 \times 101.3 \times 1000}\alpha = 2.954 \times 0.0185 \times 101.3 = 7.693\ mg/L$$

Model details for F/2 Medium

Using the same method as for Dunaliella medium, the solubility of O_2 and CO_2 in F/2 medium (see section 2.1.1) was also calculated, see Tables 3.4 to 3.6.

Table 3.4.Cation and anion model parameter values applicable to F/2 medium

Cation	h_i(m^3 $kmol^{-1}$)	Anion	h_i(m^3 $kmol^{-1}$)
H^+	0	NO_3^-	0.0128
Na^+	0.1143	CO_3^{2-}	0.1423
K^+	0.0922	SO_4^{2-}	0.1117
Mg^{2+}	0.1694	PO_4^{3-}	0.2119
Ca^{2+}	0.1762	Cl^-	0.0318
Sr^{2+}	0.1881	$S_2O_3^{-2}$	0.1149
		Br^-	0.0269

The total molarity of each of the different ions in the media was then calculated (Tables 3.5 and 3.6 below).

Chemicals	M/l
$MgSO_4.7H_20$	0.024
$MgCl_2.6H_20$	0.049
$CaCl_2.2H_20$	0.016
$Na_2B_4O_7$	0.0002
KBr	0.0002
$SrCl_2$	0.0002
H_3BO_3	0.0002
$Na_2S_2O_3$	0.000002
KCl	0.0008
NaCl	0.41
$NaHCO_3$	0.002

Ion	Molarity (M/litre) or ($kmol/m^3$)
Mg^{2+}	(1x0.024)+(1x0.049)=0.073
SO_4^{2-}	0.024
Cl^-	(2x0.049)+(2x0.016)+(1x0.41)+(1*0.0008)=0.54
Na^+	(1x0.002)+(1x0.41)+(2x0.000002)+(2x0.0002)=0.412
H^+	(1x0.002)+(3x0.0002)=0.0026
K^+	(1x0.0008)+(1x0.0002)
CO_3^{2-}	0.002
Ca^{2+}	0.016
Sr^{2+}	0.0002
$S_2O_3^{-2}$	0.000002
Br^-	0.0002

Table 3.5(left) - Concentration of chemical elements in F/2 medium. Table 3.6 (right) - Total molar concentration of each ion in F/2 medium.

3.2.4 Solubility model data

Using the ionic data and the equations stated previously, a model was made to simulate the effects of changes in temperature and gas partial pressure on the solubility of gases in the media used in this study and plain distilled water with 1 M NaCl. Pure distilled water was also

modelled as a point of reference, along with a set of empirical data on distilled water compiled by Schumpe, Quicker and Deckwer (1982) for validaton purposes, see Figure 3.1.

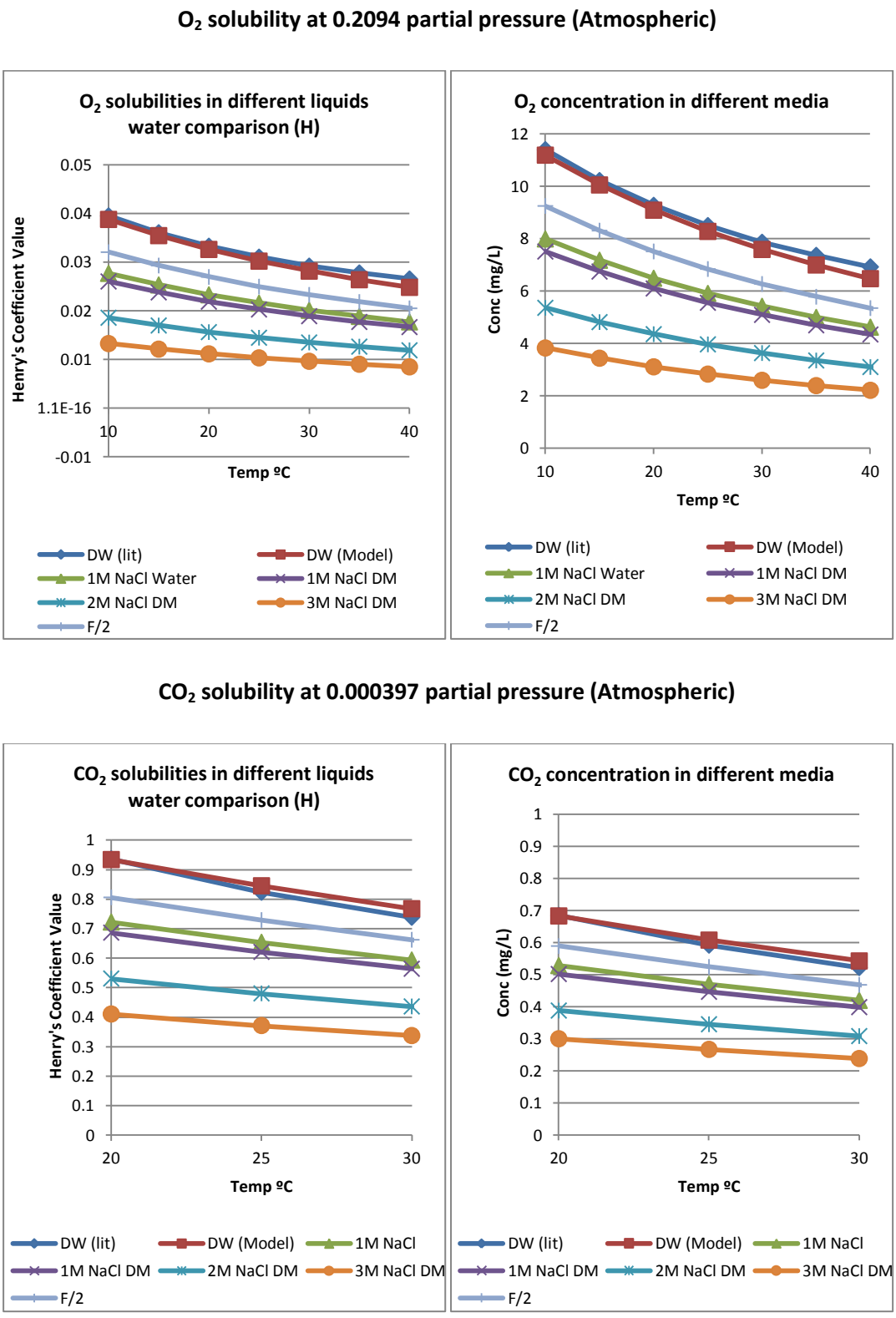

Figure 3.1 Solubility model data, Henry's coefficient left and gas solubility right. Top: Solubility of oxygen in different media. Bottom: Solubility of carbon dioxide in different media. DW = Distilled water (from literature and modelled), 1 M NaCl = DW plus 1 M NaCl, DM - Dunaliella medium (1-3M NaCl variants) and F/2 = F/2 medium.

It can be seen that for each of the models, the increase in overall salinity dramatically reduces the gas solubility within all the media (Figure 3.1). The main driver in each of the media examined is NaCl. As this provides the highest concenration of ions in every type, this makes sense. Interestingly, there is very little difference in effect between the 1 M NaCl Dunaliella medium and just 1 M NaCl salt with water, which suggests that further simulation work could be simplified by ignoring the effects of the other constiuent ions. Within the working range of the equations, the published experimental data for distilled water versus the modelled distilled water data also shows a good agreement. A further model was devloped to investigate the effects if the temperature and pressure were maintained at 25°C and 1 bar, whilst the partial pressure of the gas was varied,resulting in the following graphs (Figure 3.2):

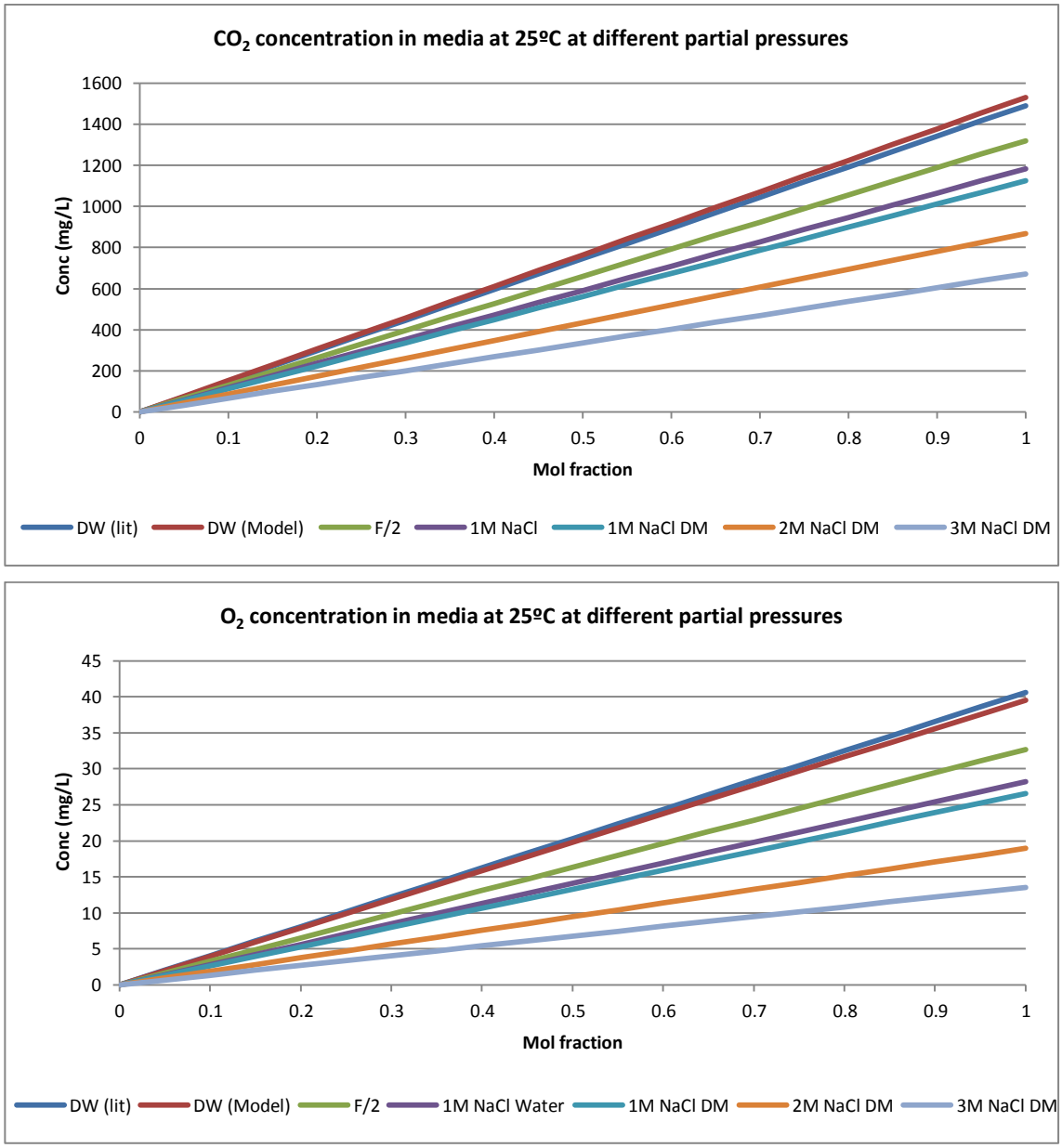

Figure 3.2. Solubility model data with varying partial pressures. Top: Solubility of carbon dioxide in different media. Bottom: Solubility of oxygen in different media. DW = Distilled

water (from literature and modelled), 1 M NaCl = DW plus 1 M NaCl, DM - Dunaliella medium (1-3 M NaCl variants) and F/2 = F/2 medium.

For reference purposes, in this study 5% and 100% CO_2 concentrations have been used (0.05 and 1 partial pressures) whereas a flue gas concentration of 23% (0.23 partial pressure) was used in the work by Zimmerman, et al. (2011). In this study, oxygen was only present at atmospheric concentration of 21%. The data shows just how soluble CO_2 is compared to O_2, and because of this the effects at high salt concentrations are much greater with higher concentrations of CO_2 used.

3.3 Fluidic Oscillation Effects on Reactor Mass Transfer (k_La) with Different Media.

In previous work by the Zimmerman research group (Zimmerman, Tesar and Bandulasena, 2011), it has been demonstrated that the use of fluidic oscillation can greatly increase the productivity of algal cultures (and many other processes) by producing smaller bubble sizes for increased mass transfer and better mixing, whilst still providing net energy savings compared with traditional laminar sparging methods (see section 1.12.3).In the majority of the experiments they performed, however, the focus of the work was concentrated on the stripping of gases, oxygen inhibition and comparisons between different sparger types (Mahmood, et al., 2011; Zimmerman, et al., 2011) rather than looking at the effects of fluidic oscillation on saline or plain media using the same apparatus. In this work, the salinity effect is looked at in more detail. As discussed previously, the addition of ionic compounds greatly affects the maximum gas solubility of a medium. This has a direct knock-on effect on the overall value of K_La because the overall mass transfer rate is defined with reference to this maximal solubility value C_{AL}^*(Mahmood, et al., 2011): $k_La = \frac{1}{\mathrm{T}}\ln\left(\frac{C_{AL}^* - C_{AL1}}{C_{AL}^* - C_{AL2}}\right)$

A series of mass transfer experiments were performed to ascertain how the interfacial area mass transfer coefficient (k_La) varies with and without oscillation in the presence of three different types of media; deionised water, deionised water + 1 M NaCl and 1 M NaCl Dunaliella medium. To keep the conditions as similar as possible to the ones used in rest of this study (for algal culture), atmospheric air was used for dosing, rather than 5% CO_2. Also, only 1 M NaCl based media was included due to the faster growth rate of *Dunaliella* at this molarity (see Chapter 4). Each type of media was degassed with nitrogen and then aerated with 100 cc/min air at 1 bar pressure, with laminar and oscillated flows with at least 3 replicates. Samples were taken every three seconds for the duration of the data gathering period. The dissolved oxygen concentration (DO Conc) (mg/L) along with temperature and pressure (mm Hg) were recorded in the first batch of experiments, pH was recorded in the second. pH readings were not

recorded for the 1 M NaCl Dunaliella medium experiments as a pH buffer was included in the medium. It is acknowledged that this semi-log plot approach could be slightly flawed in terms of getting a truly accurate value of $k_L a$, due to the smaller gas capacity of the microbubbles which can lead to a significant decrease in their internal gas concentration over the time they spend in the reactor (Bredwell and Worden, 1998; Worden and Bredwell, 1998). However, as comparator, it has been proven to be a useful technique for the assessment of oscillatory performance (Mahmood, et al., 2011) and will be used as such in this work. Section 2.13 describes the method and setup used.

3.3.1 Dissolved oxygen $k_L a$

For the DO measurement the 3 L reactor (as described in section 2.12.2) was sparged with pure nitrogen gas to strip the dissolved oxygen out of the liquid and chamber above causing the DO concentration (C_{AL}) to reduce to close to zero. When the DO value reached 0.1 mg/ml, the nitrogen feed was disconnected and the air supply was attached. The aeration rate was 100 cc/min air measured on the reactor exhaust using a 0-100cc/min 1 bar air calibrated flow meter (FTI). C_{AL} was recorded over time until a steady state concentration was achieved. The rate of oxygen re-gasification was then calculated using the values between selected points on the curve denoted by concentrations C_{AL1} and C_{AL2} at times t_1 and t_2 respectively. This was calculated using a rearrangement and expansion of the following equation (Doran, 1995):

$$\frac{dC_{AL}}{dt} = k_L a(C_{AL}^* - C_{AL}) \rightarrow k_L a = \frac{\ln\left(\frac{C_{AL}^* - C_{AL1}}{C_{AL}^* - C_{AL2}}\right)}{t_2 - t_1}$$

The maximum solubility of oxygen (C_{AL}^*) in distilled water based solutions (mg l^{-1}) was calculated using the empirical equation by (Karlsson and Torstens.Lg, 1974) , the maximum solubility for the salt media was calculated in the manner described in the section 3.2 (Schumpe, Quicker and Deckwer, 1982). The DO $k_L a$ was then calculated by linear regression by plotting $\ln\left(\frac{C_{AL}^* - C_{AL1}}{C_{AL}^* - C_{AL2}}\right)$ on the y-axis and $t_2 - t_1$ on the x-axis in Microsoft Excel. Note that t_1 is the constant reference time relative to which the concentrations C_{AL2} at a series of subsequent times t_2 were measured. To make the $k_L a$ results comparable, the data was truncated to the first 255 seconds of each run, which is within the 30% threshold specified by (Merchuk, et al., 1990) , so the data should be valid with a probe response of 3 seconds (Garcia-Ochoa and Gomez, 2009) . The concentration readings were taken without using any automatic adjustment for salinity which was available on the probe used. As such, the readings with NaCl present were only useful for comparison with and without oscillation (see Figure 3.3). The original data sets for this experiment can be found in appendix H1 - H3.

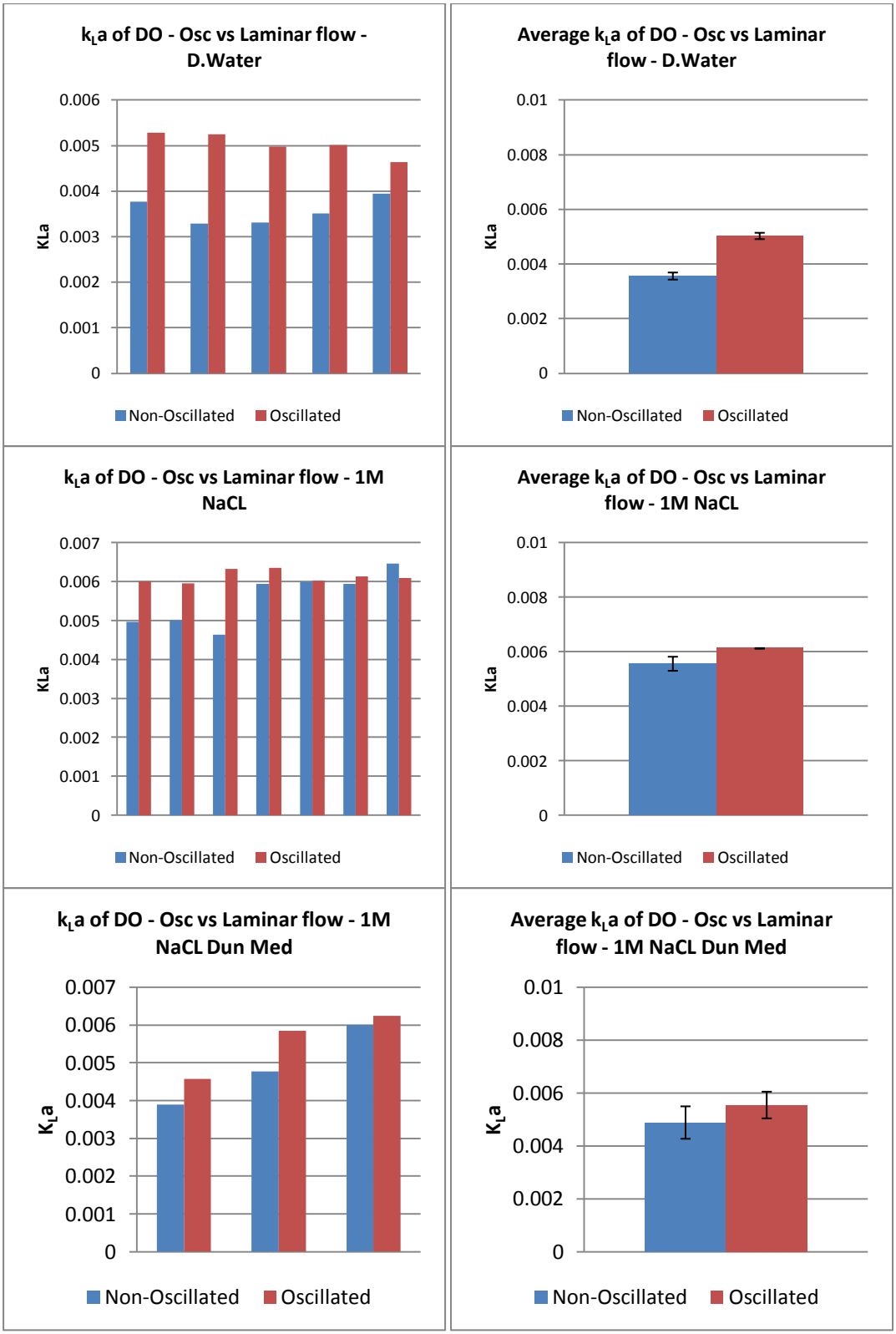

Figure 3.3. Comparison of DO k_La between standard and oscillated aeration at 100 cc/min in various media.Top: Distilled water, Middle: Distilled water plus 1M NaCl, Bottom: 1M NaCl Dunaliella medium.

The results indicate the oscillator does cause an increase in oxygen mass transfer, although the difference is relatively small, especially in the salt media. The increase in k_La is indicative of a

change in the bubble size and hence interfacial area as the rest of the parameters are constant in both cases.

3.3.2 pH/dCO$_2$ inference

To calculate the amount of dissolved CO_2 present in the reactor vessel, the relationship between pH and CO_2 needed to be evaluated. When CO_2 is sparged into pure water a series of reactions take place, the first of which being the production of carbonic acid:

$$CO_{2(aq)} + H_2O_{(aq)} \leftrightarrow H_2CO_{3(aq)}$$

The proportion of CO_2 that is kinetically converted in this reaction is very small (the reaction is also very slow), at 25°C the ratio of $CO_{2(aq)}$ to $H_2CO_{3(aq)}$ is just 99.76 to 0.24, the reaction is also independent of pH and the ionic strength of the media (Musvoto, et al., 2000). Because carbonic acid is a weak diprotic acid (i.e. it has two hydrogen atoms that are weakly bound), water molecules are capable of pulling the molecule apart (dissociating it) to form bicarbonate (HCO_3^-) and carbonate ions (CO_3^-), which happens successively in two steps:

$$1)\quad H_2CO_3 \underset{K_{a1}}{\longleftrightarrow} HCO_3^- + H^+$$

$$2)\quad HCO_3^- \underset{K_{a2}}{\longleftrightarrow} CO_3^- + H^+$$

Due to the relative stability of the initial carbonic acid reaction, the two reaction steps can be combined to make; $CO_{2(aq)} \underset{K_{a1}}{\longleftrightarrow} HCO_3^- + H^+$, as this results in little cumulative error (Contreras, 2007). This reaction and the second can then be put in the form of a general equilibrium-constant expression, based on the law of mass action because the reactions are reversible.The equilibrium constraint for each of the dissociation steps can be written as:

$$K_{a1} = \frac{[HCO_3^{-1}][H^+]}{[CO_{2(aq)}]} \& \; K_{a2} = \frac{[CO_3^{-2}][H^+]}{[HCO_3^-]}$$

There are empirically derived equations available in the literature that give the two equilibrium constants in a range of temperatures:

1) $[CO_2] \underset{K_{a1}}{\longleftrightarrow} or \underset{k_{1,2}}{\overset{k_{1,1}}{\rightleftharpoons}} HCO_3^- + H^+$

K_{a1} is given by; $\frac{K_3}{K_w}$(Darmana, et al., 2007), where:

- K_3 (kmol m^{-3}) $= \frac{[HCO_3^{-1}][H^+]}{[CO_2]} = exp\left(\frac{-12092.1}{T} - 36.786\ln(T) + 235.482\right)$ from Edwards, et al. (1978) and
- K_w (kmol^2 m^{-6}) $= [H^+][OH^-] = 10^{-(5839.5/T + 22.4773\log(T) - 61.2062)}$from Tsonopoulos, Coulson and Inman (1976)

As the ionic charges balance, they do not need to be factored into this equilibrium constant.

2) $HCO_3^- \underset{K_{a2}}{\longleftrightarrow} or \underset{k_{2,2}}{\overset{k_{2,1}}{\rightleftharpoons}} CO_3^- + H^+$

K_{a2}(m^3 kmol^{-1}) calculated by Hikita, Asai and Takatsuka (1976), who gave the following:

- $\log K_{a2} = \log K_2^{\infty} + \frac{1.01\sqrt{[Na^+]}}{1+1.27\sqrt{[Na^+]}} + 0.125\,[Na^+]$
- And; $\log K_2^{\infty} = \frac{1568.94}{T} + 0.4134 - 0.00673T$

For the distilled water calculations the Na^+ term is reduced to 0. This second reaction is very rapid, in the order of 10^{10}-10^{11} m^3 kmol^{-1}s^{-1} (Eigen, 1954).

With these constants, the amount of dissolved CO_2 can be calculated by considering the total concentration of inorganic carbon in the system (Rubio, et al., 1999):

$$[C_T] = [CO_2] + [HCO_3{}^-] + \left[CO_3{}^{2-}\right]$$

And, the electro-neutrality which enforces that small changes in positive and negative ion concentrations must satisfy the following (Rubio, et al., 1999):

$$d[H^+] + d[Cat^+] = d[OH^-] + d[HCO_3^-] + 2d[CO_3^{-2}] + d[An^-]$$

The concentration of aqueous H^+ ions present in solution can be calculated using the pH scale relation; $\mathrm{pH} = -\log[\mathrm{H}^+]$. Thus, if a reactor system is well mixed and the pH equilibrium is in place, the dissolved concentration of CO_2can be calculated from a pH in the solution. As the charges exactly balance for the salt cation $[Cat^+]$ and anions $[An^-]$ due to only the presence of 1 M NaCl in the salt tests, these terms cancel from the equation above to yield the following (Rubio, et al., 1999):

$$d[H^+] = \frac{\frac{K_{a1}}{[H^+]} + 2\frac{K_{a1}K_{a2}}{[H^+]^2}}{1 + \frac{K_w}{[H^+]^2} + \frac{K_{a1}[CO_2]}{[H^+]^2} + 4\frac{2K_{a1}K_{a2}[CO_2]}{[H^+]^3}} d[CO_2]$$

Another equation can be constructed using the same method to make $[CO_2]$ the subject of the formula in the following steps:

1. $[H^+] = [OH^-] + [HCO_3^-] + 2[CO_3^{-2}] \rightarrow [HCO_3^-] = [H^+] - [OH^-] - 2[CO_3^{-2}]$
2. As; $[CO_3^{-2}] = \frac{K_{a2}[HCO_3^-]}{[H^+]}$
3. Substituted into 1; $[HCO_3^-] = [H^+] - [OH^-] - 2\left(\frac{K_{a2}[HCO_3^-]}{[H^+]}\right)$
4. So; $[HCO_3^-] + 2\left(\frac{K_{a2}[HCO_3^-]}{[H^+]}\right) = [H^+] - [OH^-]$

5. Factorising; $[HCO_3^-]\left(1+2\left(\frac{K_{a2}}{[H^+]}\right)\right)=[H^+]-[OH^-] \rightarrow [HCO_3^-]=\frac{[H^+]-[OH^-]}{\left(1+2\left(\frac{K_{a2}}{[H^+]}\right)\right)}$
6. If; $\left[CO_{2(aq)}\right]=\frac{[HCO_3^{-1}][H^+]}{K_{a1}}$, then; $\frac{\left(\frac{[H^+]-[OH^-]}{\left(1+2\left(\frac{K_{a2}}{[H^+]}\right)\right)}\right)[H^+]}{K_{a1}}$
7. Thus; $\frac{[H^+]([H^+]-[OH^-])}{K_{a1}\left(1+2\left(\frac{K_{a2}}{[H^+]}\right)\right)} \rightarrow \frac{[H^+]^2-[H^+][OH^-]}{K_{a1}+2K_{a1}\left(\frac{K_{a2}}{[H^+]}\right)}$
8. As; $[H^+][OH^-]=10^{-(5839.5/T+22.4773\log(T)-61.2062)}$ from (Tsonopoulos, Coulson and Inman, 1976).
9. And; $\mathrm{pH}=-\log[\mathrm{H}^+]$, so $[\mathrm{H}^+]=10^{-\mathrm{pH}}$
10. Also; $10^{-14+\mathrm{pH}}=10^{-14}/10^{-\mathrm{pH}}=10^{-14}/[\mathrm{H}^+]=[OH^-]$
11. So if; $[\mathrm{H}^+]=10^{-\mathrm{pH}}$ and $[OH^-]=10^{-14+\mathrm{pH}}$
12. Then; $\left[CO_{2(aq)}\right]=\frac{\left[10^{-\mathrm{pH}}\right]^2-K_w}{K_{a1}+2K_{a1}\left(\frac{K_{a2}}{[10^{-\mathrm{pH}}]}\right)}$

The constants and pH values can then be substituted into the equation to calculate the concentration of dissolved CO_2. The concentration can then be converted from M to mg/L by multiplying by the molecular weight of CO_2, 44 and 1000 to change the units from g to mg. Thus we have an explicit relationship to calculate the CO_2concentration from the pH measurements as required.

3.3.3 Dissolved carbon dioxide k_La

The dCO_2 measurement was performed in the same manner as the DO but with some timing differences due to the slow reaction rates of gassing with air. The reactor was sparged with pure nitrogen for 40 minutes, before re-gassing with air at 100 cc/min, 1 bar for one hour. Unfortunately, despite the use of 3 different pH probes and extensive recalibration, we got very unreliable and inconsistent pH readings as given in the graphs below. According to the equation above, the pH of neutral distilled water (the starting point of our CO_2sparging experiment) should be 7. It can be seen from the data below that this was far from the case with disagreement between the probes and pH values starting at above 7. Despite considerable investigation, we were unable to find any obvious reason for the way in which pH varied during sparging with N_2followed by CO_2. Since it is not meaningful to convert our pH values into gas concentrations, therefore, we can instead just compare the relative decrease of pH for the oscillated (microbubbles) and non-oscillated case (see Figure 3.4). The rate of pH decrease can be seen clearly to be greater for the microbubble sparging which indicates a higher k_La which is in qualitative agreement with the results for oxygen. The erroneous semi-log plots using the conversion formulas mentioned previously are included in appendix H4.

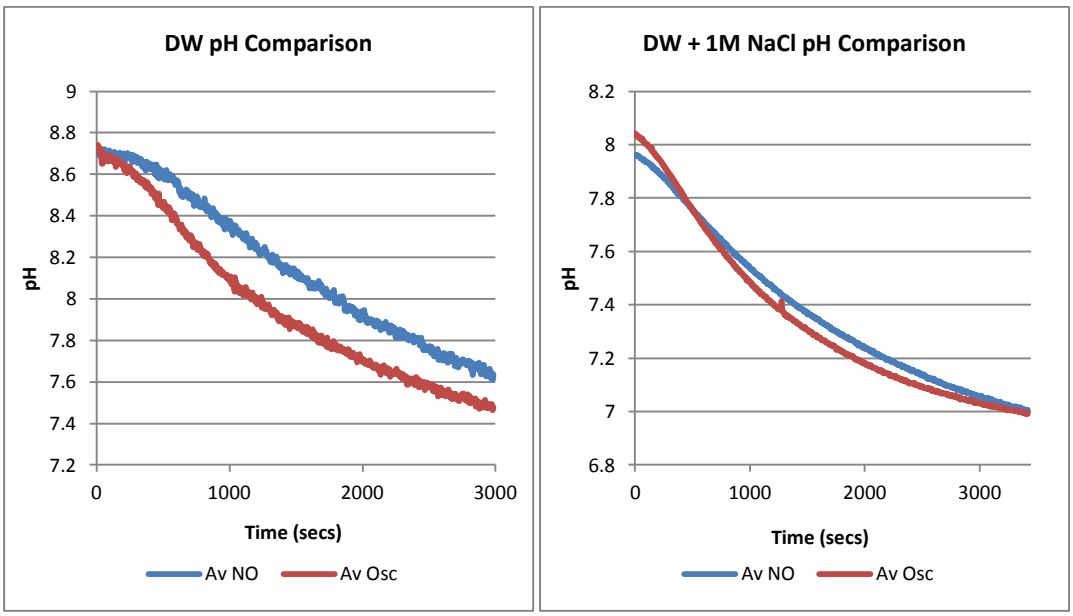

Figure 3.4. A comparison of pH rates of change under re-aeration between oscillated and standard flows with and without the addition of 1M NaCl. Each reading data set was a triplicate average.

3.4 Influence of Fluidic Oscillation on Bubble Size in Different Media

In the previous sections, the effects of adding NaCl and other ions to algal growth media were modelled and $k_L a$ measurements were taken to see the impact of fluidic oscillation on the mass transfer of oxygen and carbon dioxide in plain water and saline solutions. The results of this work seems to indicate that the beneficial mass transfer effects of fluidic oscillation are much less pronounced in solutions containing high levels of dissolved NaCl. This factor could have implications for the commercial use of fluidic oscillation for culture of marine species of algae. One possible explanation for this phenomenon is a change in bubble size and hence the amount of interfacial area. Even small changes in bubble diameter could significantly affect the interfacial area both directly via altered surface area to volume ratio of the bubbles and indirectly via changes in total gas hold-up in the reactor. In the experiments described below we explore the hypothesis that changes to interfacial area $a$are likely to be the main cause for variations in $k_L a$rather than changes in k_L. The latter would imply changes in diffusivity or boundary layer thickness which is possible (e.g. due to altered viscosity/density of the saline solution) but likely to be less important than changes in the average size of bubbles formed at the sparger.

3.4.1 Slow motion camera imaging

Rough visual observations during the previous experiment indicated a difference in bubble size with the addition of 1 M NaCl to the media. To confirm this trend a series of still images and videos were taken using a high speed camera using the same conditions and setup as the previous $k_L a$ experiment (see section 2.16). Due to the high flow rate (100 cc/min) and resultant large bubble plume, using image analysis software (such as image J) to calculate bubble size would be very problematic and provide low quality data, so the images were provided for qualitative purposes only. The inclusion of a tape measure was used to provide a rough sense of scale for the images, see Figures 3.5 and 3.6.

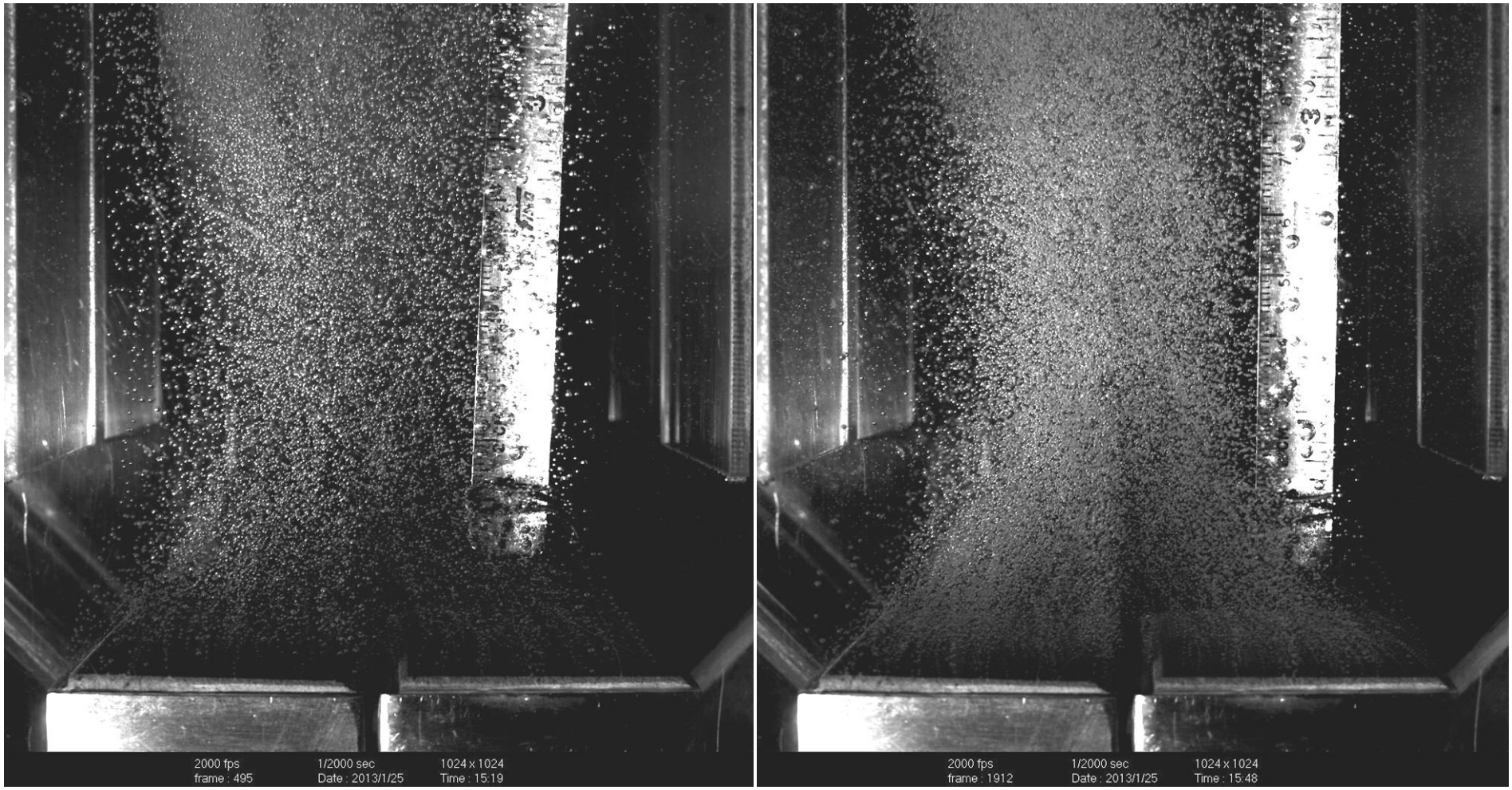

Figure 3.5. Slow motion camera image comparison; Non-Oscillated Distilled water 100cc/min (left), Oscillated Distilled water 100cc/min (right)

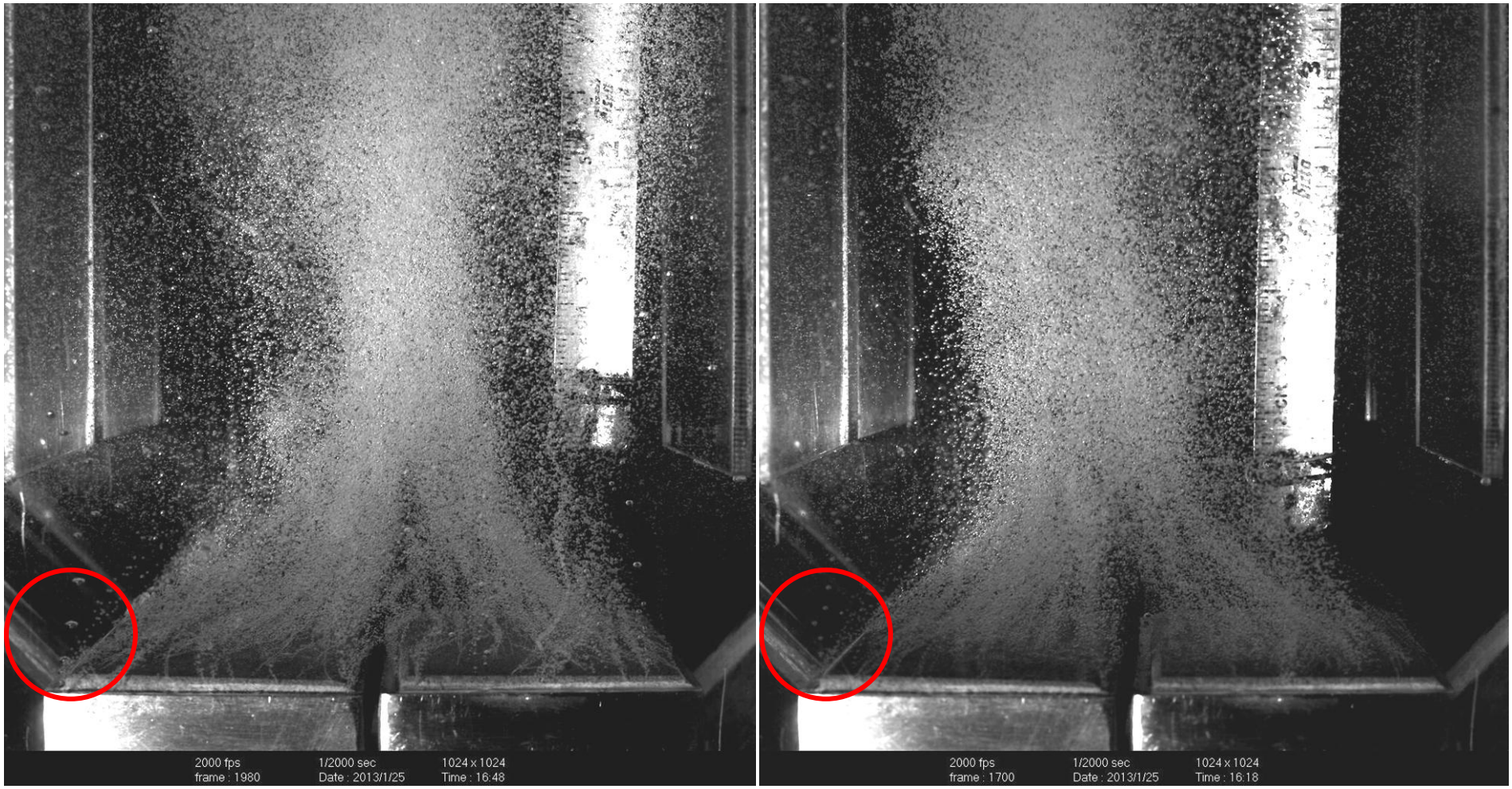

Figure 3.6. Slow motion camera image comparison; Non-Oscillated Distilled water + 1M NaCl 100cc/min (left), Oscillated Distilled water + 1M NaCl 100cc/min (right). Area in red circle shows evidence of differences in bubble formation.

The slow motion images clearly demonstrate a reduction of bubble size within the salt water medium in general. The oscillated air flow is also shown to be having a visible effect in the distilled water tests, but far less pronounced in the saline equivalent. This evidence helps to explain the data gathered from the $k_L a$ tests very well, because the bubble size difference is much smaller in the 1 M NaCl media, however an effect is still visible. Bubbles in certain locations (see the red ringed area at the edge of the sparger - Figure 3.6) under oscillation are not continuing to grow to larger sizes, which fits with the explanation by (Zimmerman, et al., 2007) which suggests the wetting force that allows the bubble size to increase is being overcome by the pulsing effect of the oscillation.

3.4.2 Acoustic bubble spectroscopy

As the calculation of bubble size using optical methods would be problematic as discussed previously, another approach was tried using acoustic bubble spectroscopy (ABS). To quantify the bubble size difference, a single sparger from the 3 L photo-bioreactor was removed and placed in a fish tank equipped with an ABS system (see section 2.15). However, the data produced was highly dubious (see Figure 3.7 below), as the bubble sizing did not change between conditions. It could be seen by eye that there was a huge difference between the pure water and saline media in the setup, the same as validated previously. One factor that could explain this error was the setup itself, as the hydrophones were not in perfect alignment due to clamping limitations. Note: a purpose built measurement rig is currently under construction, but unfortunately will not be completed in time for this study.

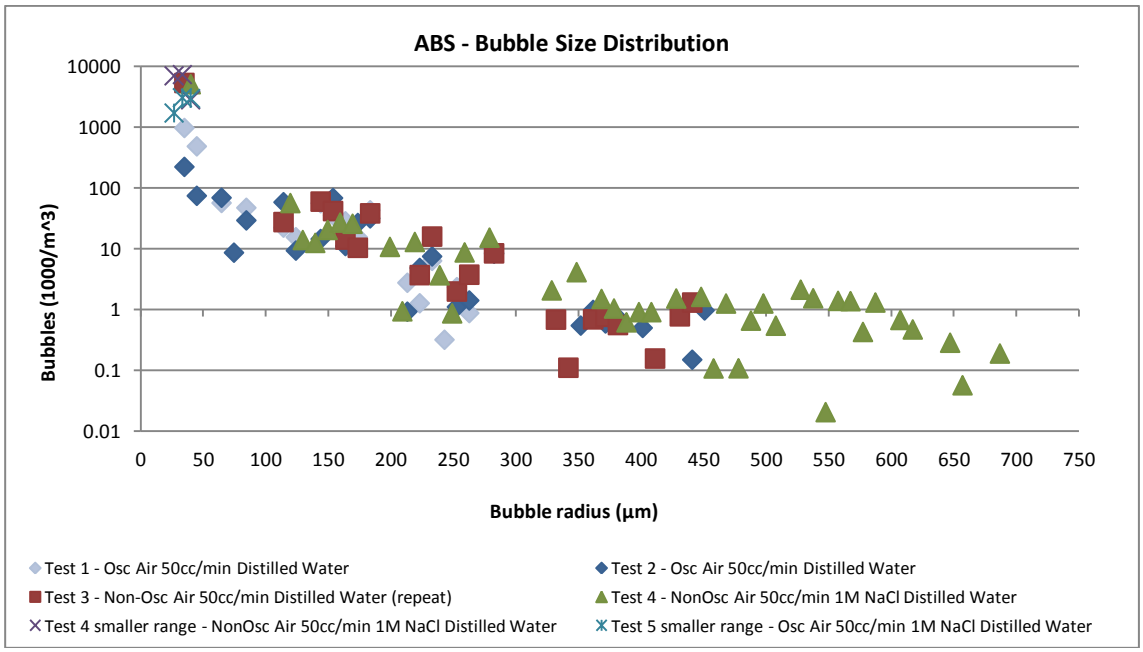

Figure 3.7. ABS bubble size data for distilled water with and without 1 M NaCl.

3.4.3 Bubble formation

As the data indicates the oscillator is still having an effect in the presence of salt, albeit a much less significant one comparatively, this indicates that other factors must be coming into play, such as ionically influenced bubble formation and coalescence. To understand this, the overall mechanisms involved in bubble propagation need to be looked at in detail.

In its most simple form, bubble formation is typically affected by two main forces and a number of variables (Wang, et al., 2010) (see Figure 3.8):

- $F_{int} = internal\ force = Pressure(P) \times Area(A)$. So; $F_{int} = P(\pi D^2)/4$
- $F_{sur} = surface\ force = Surface\ tension \times perimeter$. So; $F_{sur} = r\pi D$

Where; A = area of cross-section, both $F_{internal}$ & $F_{surface}$ are in dyne, r = surface tension (dyne/cm^2 or psi), D = bubble diameter (cm or inch) and P = the internal bubble pressure (dyne/cm^2 or psi).

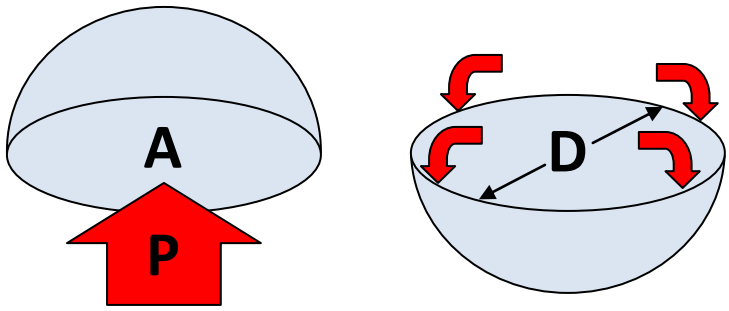

Figure 3.8. Main forces involved in bubble growth and attachment.

F_{int} of the air in the bubble is opposed by F_{sur} holding the bubble onto the sparger surface by surface tension. During bubble formation, the forces are in equilibrium so:

$$F_{int} = F_{sur} \text{ or } P(\pi D^2)/4 = r\pi D \rightarrow P = 4r/D$$

In non-oscillated gas flow, bubble separation only occurs when the buoyancy force (which increases proportionately with the size of the bubble), or currents in the medium, cause the equilibrium to shift by exceeding the attachment forces. In the buoyancy case, this typically only occurs when the bubble is much larger than the diameter of the original gas inlet hole of the pore (Zimmerman, et al., 2010a).

The separation process is also highly dependent on the attachment forces caused by the wetting properties of the sparger surface. In surface-chemistry, solid surfaces are defined as hydrophilic (wettable by water) or hydrophobic (non-wettable, repels water).

Hydrophobic surfaces typically behave in an aerophilic manner, that is, they readily attach to an air interface which displaces water on the surface (Wang, et al., 2010), see Figure 3.9. If the surface is hydrophobic this creates an additional force that needs to be overcome by increased buoyancy force, which makes the bubble size even bigger. The sparger designs used in this work (initially developed by the Zimmerman group), use a highly hydrophilic ceramic, so this effect can effectively be disregarded.

As the effects of fluidic oscillation counter the buoyancy effect to reduce the bubble size (see Chapter 2), the presence of NaCl therefore must be producing a comparable effect with a non-oscillating gas stream by modifying the bubble surface tension.

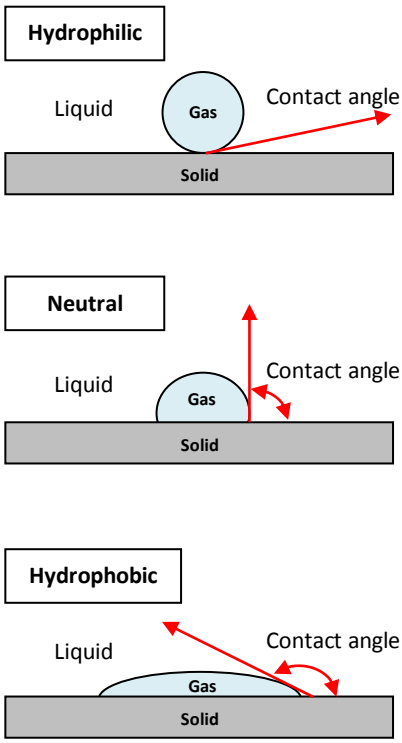

Figure 3.9. Gas bubble attachment dependant on material properties.

3.4.4 Ionic effects on surface tension and coalescence

The stability of a bubble is heavily influenced by the surface tension of the medium, so when substances that can reduce the surface tension (such as surfactants) are added this leads to smaller bubble sizes (Wang, et al., 2010). However, paradoxically, saline solutions which have a stronger surface tension and higher viscosity still seem to achieve the same effect (Ruen-ngam, et al., 2008). The explanation for this behaviour is currently still unknown, but there are many hypotheses. The reviews by Nguyen, et al. (2012) and Horn, Del Castillo and Ohnishi (2011) cover the current ideas and data in great detail, but to summarise; the average bubble size seems to be strongly related to the amount of bubble coalescence, which is influenced by the addition of salts.

The rate of coalescence is impacted by three sequential factors:

1. The speed of bubble collision, which results in the creation of a thin liquid film between the liquid and gas interfaces.
2. The removal of the liquid film by external forces such as gravity, inertia and flow, proportional to the bubble volume and the surface molecular forces which are proportional to the film area (the common rate limiting step).
3. The rupture of the film layer when both forces are exceeded by surface attractive forces and mechanical disturbances, causing the film to reach a critical thinness of a few tens of nm then break.

The rate of bubble coalescence has been found to be highly dependent on the type of ion and its concentration, the data by Craig (2004) shows which combinations of ions increase or decrease a bubbles propensity to coalesce (see Table 3.7).

Table 3.7. Depicting the effect of a range of electrolytes on bubble coalescence. A tick indicates that the salt inhibits bubble coalescence. A cross indicates that no bubble coalescence inhibition has been observed(Craig, 2004).

	Cations	H^+	Li^+	Na^+	K^+	Cs^+	Mg^{2+}	Ca^{2+}	NH_4^+	$(CH_3)_4N^+$	$(CH_3)_3NH^+$	$(CH_3)_2NH_2^+$	$(CH_3)NH_3^+$
Anions	Type	β	α	α	α	α	α	α	α	β	β	β	β
OH^-	α	×		✓	✓								
Cl^-	α	×	✓	✓	✓		✓	✓		×	×	×	×
Br^-	α	×		✓	✓	✓							
NO_3^-	α	×	✓	✓	✓			✓					
ClO_3^-	β			×									
ClO_4^-	β	✓		×			×		×				
CH_3COO^-	β	✓		×	×	×	×		×	✓			
SO_4^{2-}	α	×	✓	✓			✓						
$(COO)_2^{2-}$	α	×			✓								

The molecular dynamic (MD) simulation work by Jungwirth and Tobias (2006) has also demonstrated that there could be an unequal distribution of ions at the gas-liquid interface (see Figure 3.10 below). It has been hypothesised that this is one of the key factors in explaining the specific coalescence behaviour of different ion combinations in water, as the attractive and repulsive forces vary significantly (Henry and Craig, 2010).

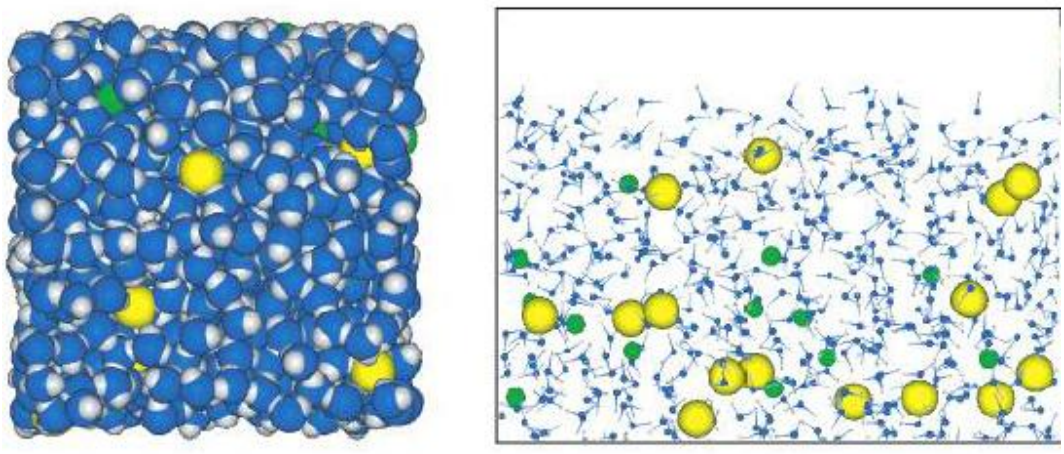

Figure 3.10. MD Snapshot (top and side view) of the solution/air interfaces of a 1.2 M aqueous NaCl solution (Jungwirth and Tobias, 2006)

Many studies have subsequently compared ion concentration to the rate of coalescence with pure water as the 100% coalescing reference. This helped to produce a series of ion specific

concentration transition thresholds that can be used for predictive purposes when coupled with physical interaction data, such as the NaCl concentration vs bubble approach speed map compiled by Horn, Del Castillo and Ohnishi (2011), Figure 3.11 for ~4mm bubbles. This work demonstrated how the speed of bubble collision and NaCl concentration could make bubble coalescence more (or less) prevalent within a reactor system, due to their effects on the bubble surface. The collision velocity can lead to the bubbles bouncing off each other elastically, rupturing and coalescing (due to the surface draining on impact) or remaining rigid, but the prevalence of these scenarios is dictated by the effect of NaCl (or other salts) on the bubble surface stability.

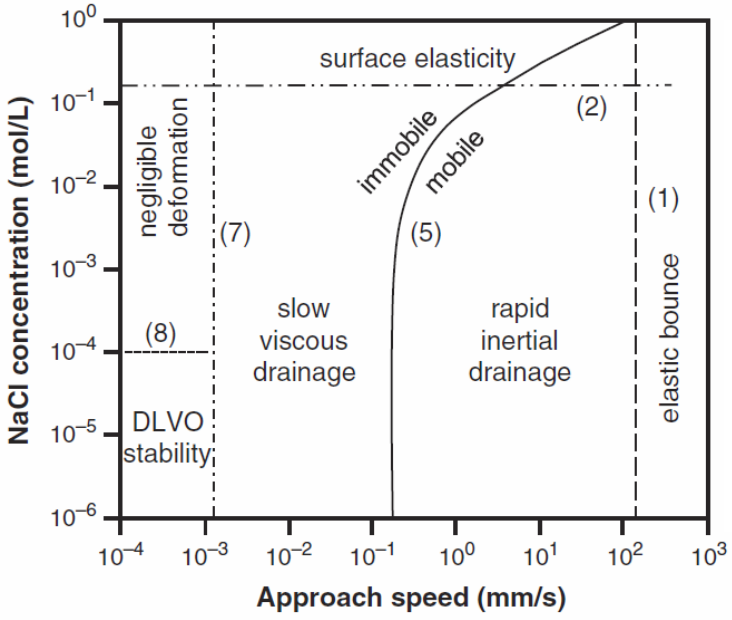

Figure 3.11. Graphical representation showing transitions between different types of behaviour during bubble collisions affected by surface forces, thin film drainage and boundary conditions at the air/water interface. All calculations were made for ~4 mm diameter bubbles.

(Horn, Del Castillo and Ohnishi, 2011)

Recent work by Botello-Alvarez, et al. (2011) looked at how coalescence and bubble size were affected by different concentrations of NaCl (0-0.37 M) at different superficial velocities (0.0005-0.0196 m/s) using a 160-250 µm pore glass diffuser. It was found that the bubble diameter increased as the superficial gas velocity increased but decreased with increasing ion concentration. At the lowest gas velocity, bubble size was independent of the salt concentration which was due to a lower gas fraction and hence a decreased rate of bubble collision. Significantly, it was found that beyond 0.175 M NaCl coalescence practically no longer occurred, which led to a fixed bubble size. Based on these relations these researchers published a model for predicting the effects of salinity on bubble size. However the scope of the model is limited to a quadratic regression equation for lower salt concentrations which renders it totally inapplicable for the 1 M NaCl used in this study.

A previous study by Henry, et al. (2008) looked at the effects of salts on the bubble rise velocity to determine if the mobility of the gas-liquid interface would affect bubble rise velocity and coalescence inhibition. It was found that for small bubbles (<110 µm, chosen to

avoid larger bubble measurement issues) the presence of salts has no effect. Both with and without coalescence inhibiting salts present, the rise velocity closely followed the Hadamard-Rybczynski equation which was derived assuming that the interface between gas and liquid cannot support shear stress surface tension and is fully mobile, compared with the Stokes law alternative which has an immobile interface. This work is significant because it shows that salts do not influence the rise velocity of small bubbles (compared with water), and thus do not affect bubble coalescence through bubble rise velocity (see the compiled graph, by Nguyen, et al. (2012) Figure 3.12).

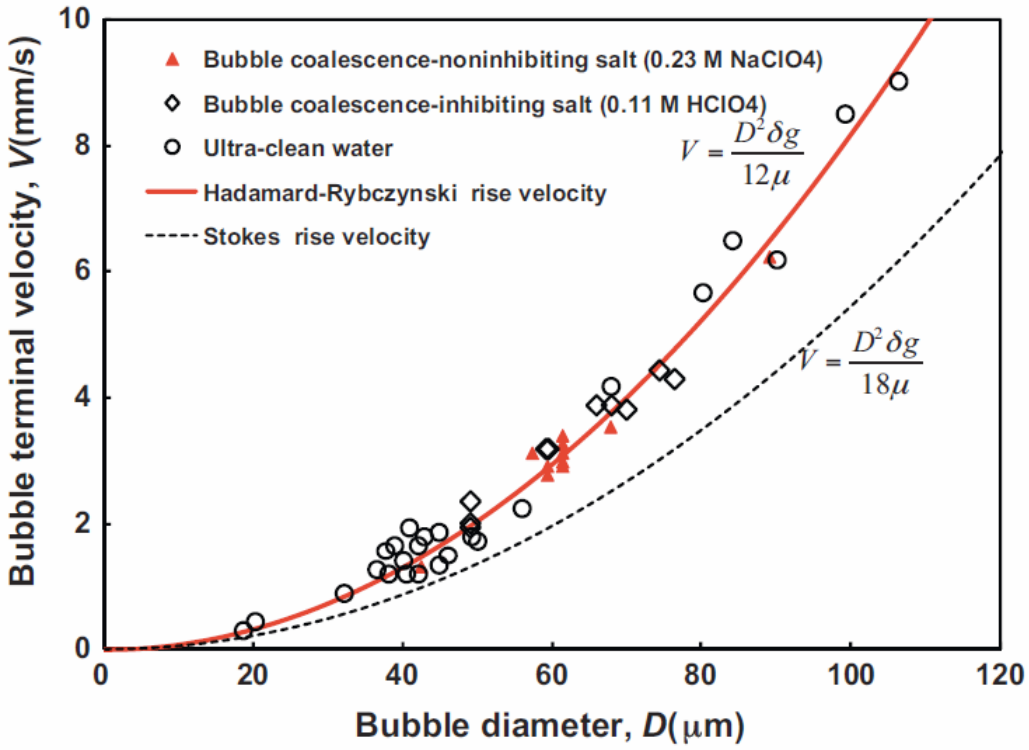

Figure 3.12. Experimental (symbols) and model (lines) results for terminal rise velocity of N_2bubbles as a function of bubble size in ultra-clean water, bubble coalescence-inhibiting and non-inhibiting salt aqueous solutions. δ, μ and g describe the liquid density and viscosity, and gravity acceleration.

Thus by the process of elimination, it makes sense that the majority of the bubble size/coalescence effects due to NaCl occur in the sparger surface region, where the bubbles are in close contact. Indeed, Nguyen, et al. (2012) observed that bubble coalescence occurred at this interface with high speed video. They suggested that the high momentum of the gas stream in this region overcomes the resistance of the liquid films resulting in rupture and coalescence. This led to them concluding that the gas velocity is the "primary factor in causing bubble coalescence in the different salt solutions". As these experiments were conducted with a pore range of 11-16 μm, compared to 20 μm in this study, it indicates that this would be the

same in the current work. It is also worthy of note, that they demonstrated with a NaCl concentration of above 1M the amount of coalescence was effectively zero. Although their observations of 0% coalescence were not taken at the sparger interface, their 'primary factor' hypothesis is probably still valid.

3.4.5 Conclusions

As the effects of the salt transition concentration will change from one experimental system to the next, due to changes in gas velocity, pore size and reactor geometry etc, only broad assumptions can be made based on the current scientific literature. In doing so, the following explanations are proposed for the observed experimental mass transfer/bubbling behaviour:

1. The 1M NaCl ionic content has effectively stopped bubble coalescence in all regions of the reactor other than at the sparger liquid interface, as its concentration is much higher than the coalescence impeding threshold. This has radically reduced the overall average bubble size in the standard flow case, bringing it much closer to the oscillated equivalent.
2. As the oscillated bubble growth mechanism produces consistently small sizes of bubbles, which are reasonably uniformly spaced with bubble rise rate approximately the same, the plume is non-coalescent in theory (Crabtree and Bridgwat.J, 1969; Zimmerman, et al., 2007). This means that the addition of NaCl would have no impact on the overall bubble size, whereas under standard flow and bubble growth mechanisms the difference is very important.
3. The small mass transfer differences between the regular and oscillated flows with NaCl present could also be explained by the differences in bubble growth mechanisms. In the regular flow case, when a bubble grows beyond the hemispherical shape, according to the Young-Laplace law of surface tension (see eq below), the pressure force needed to create the bubble decreases rapidly. When this happens within the sparger, the gas follows the path of least resistance and preferentially forms bubbles from that pore, at the expense of other pores in the vicinity (Zimmerman, et al., 2007). This leads to an uneven bubble formation at the sparger surface, which can lead to larger bubbles, a distribution of rise rates in the bubble plume and an increased chance of coalescence. In the oscillated case, there is a more even distribution as the bubble growth is halted at the end of each oscillation period, hence no bubble can keep growing in one pore at the expense of another (Zimmerman, et al., 2007). One caveat to this explanation is that the magnitude of this effect is dependent on the frequency of the oscillation period. However, the photographic evidence in the previous section (the red rings in Figure 3.6), does tentatively validate this hypothesis as there are comparatively less areas producing noticeably larger

bubble sizes under oscillation. The data from section 3.8 also shows the usage of more pores under oscillated flow conditions.

$$\Delta p = 2\sigma/R$$

Where; Δp = the pressure difference across the gas/liquid interface, σ = surface tension and R = bubble curvature radius.

Based on these findings, it is hypothesised that if the frequency of the oscillation rate was increased, the difference in mass transfer rate could be much larger. Unfortunately, due to time considerations and equipment availability, there was not enough time to pursue this avenue of research in this study. The previous findings by Zimmerman, et al. (2010b), which used the same type of sparger and media, did demonstrate a favourable algal growth response, but a comparison with a non-oscillated standard was not carried out. Also differences in setup i.e. oscillator length of control loop, gases used, reactor geometry etc, would be significant factors hindering comparison. Based on this set of circumstances, further work was carried out using the same oscillator setup and sparger material as the tests in this section.

3 Photo-Bioreactor Development and Modelling - Part 2

3.5 Introduction

In Part 1 of this chapter we looked at one of the key factors affecting algal growth, namely gas transfer into the liquid phase. In this second part of the chapter, the other key aspect of fluid dynamics crucial to algal growth and photo-bioreactor design will be considered; mixing. Many of the factors covered in the previous chapter rely of the premise of a 'well mixed system' to be valid and applicable in the context of this study. Without sufficient distribution of nutrients and dissolved gases, cultures will cease to grow and eventually die. To ensure effective mixing, the geometry of a reactor vessel has to be sympathetic to the needs of a target species. The flow rates within system have to be fast enough to ensure enough bulk mass transfer occurs (not just localised diffusion), whilst ensuring each cell is exposed to enough light to photosynthesise. This needs to be carried out while making sure the cells are not damaged by excessive shear forces and maintaining sufficient fluid movement in every part of the reactor. If mixing is incomplete, stratification can occur, which subsequently leads to stagnation zones and eventually cell death. With this many variables to consider, modelling approaches in the design of a reactor system are crucial. Fortunately, with the increase of computational power readily available, this process has never been easier to achieve. Multi-parameter CFD packages, such as COMSOL Multi-physics now enable complex fluid flow simulations to be run on even relatively modestly powered modern computers. In this section, multiphase CFD simulations were run based on different reactor geometries to calculate the internal flow rates and highlight zones of stagnation. This work was then verified by the use of a fluorescent tracers and visual observation. Based on this data, a series of prototype mini photo-bioreactors was developed for further testing of the micro-bubble effects mentioned in Part 1 of this chapter. The reactor designs were then tested using CFD and dye tracing to characterise their flow behaviour. The effects of flow induced cell breakage were also discussed and modelled, with an emphasis on the effects of bubble size.

3.6 CFD Overview and Modelling 3 L Photo-bioreactor

All of the CFD modelling work carried out in this study was created and performed using the COMSOL Multiphysics v.4.2 software with the CFD Module (section 2.17). This software was chosen because of its ability to easily combine multiphase flow (fluid and gas) with small bubble sizes (using the Hadamard-Rybczynski equation) using a robust inbuilt Laminar bubble flow (bf) physics model.The bf module is based on a two-fluid Euler-Euler macroscopic model for two-phase fluid flow (AB, 2011). In this approach the separate phases (air and water/media) are treated as interpenetrating fluids, so in any particular position all phases are present as an averaged volume fraction (the gas hold up). As such no interface between the liquid and gas phases can be given. Each phase has an associated velocity field, momentum

balance equation and continuity equation to describe the fluid dynamics. The bubbly flow model works with three main assumptions; the gas density is very small compared with that of the liquid, the balance between viscous drag and pressure forces determines the movement of the gas bubbles and both phases are exposed to one master pressure field. From this, the summation of the momentum equations for each of the phases gives a net momentum equation for liquid velocity and equations for continuity and transport for the volume fraction of the gas phase.

Resulting in the following (1):

$$\phi_l \rho_l \frac{\partial \boldsymbol{u}_l}{\partial t} + \phi_l \rho_l \boldsymbol{u}_l \cdot \nabla \boldsymbol{u}_l = -\nabla \mathrm{p} + \nabla \cdot \left[\phi_l (\mu_l + \mu_T) \left(\nabla \boldsymbol{u}_l + \nabla \boldsymbol{u}_l{}^{\mathrm{T}} - \frac{2}{3} (\nabla \cdot \boldsymbol{u}_l) \mathbf{I} \right) \right] + \phi_l \rho_l \boldsymbol{g} + \boldsymbol{F}$$

Where; $\boldsymbol{u}_l$= velocity (SI unit: m/s), p = pressure (SI unit: Pa), ϕ_l= phase volume fraction (SI unit: m^3/m^3),ρ_l = density (SI unit: kg/m^3), $\boldsymbol{g}$ **=** the gravity vector (SI unit: m/s^2), $\boldsymbol{F}$ = any additional volume force (SI unit: N/m^3), μ_l = dynamic viscosity of the liquid (SI unit: Pa·s), and μ_T = turbulent viscosity (SI unit: Pa·s). Subscripts " $_l$" and " $_g$" denote liquid phase and gas phase variables respectively.

Due to the complex nature of the partial differential equations used in this software (above), in this study it was treated as a tool, with the relevant functions selected that are appropriate to model needs. As such, the majority of software settings were left as the default values and an in depth discussion of the derivation of the previous equation (1) is beyond the scope of this work, although the rationale for some of the model inputs is given below:

- The **continuity** equation is given by (2 & 3):
  $\frac{\partial}{\partial t}(\rho_l \phi_l + \rho_g \phi_g) + \nabla \cdot (\rho_l \phi_l \boldsymbol{u}_l + \rho_g \phi_g \boldsymbol{u}_g) = 0$ (2) **or** (eq8-4) $\rho_l \nabla \cdot \boldsymbol{u}_l = 0$. (3)
  When $\phi_g < 0.1$ the gas volume fraction can be considered low and continuity equation (2) can be replaced by (3) which neglects the compressibility of the mixture. Since the reactor to gas volume ratios is this study are <0.1, (3) is used, which is the default 'Low gas concentration' setting.
- The **transport** of the volume fraction of gas is given by: $\frac{\partial \rho_g \phi_g}{\partial t} + \nabla \cdot (\phi_g \rho_g \boldsymbol{u}_g) = -m_{gl}$
  Where; m_{gl} = the mass transfer rate from gas to liquid ($kg/(m^3 \cdot s)$). The physical flow rates used experimentally (cc/min) are converted to this value by first converting them to m^3/sec, then multiplying by air density (kg/m^3). That value was then divided by the surface area of the sparger zone, to make it into a 2D value. If the study has a plane of symmetry, this value was halved.
- The program solves p, $\boldsymbol{u}_l$and $\tilde{\rho}_g = \rho_g \phi_g$, or the **effective gas density**.

- The **gas velocity** $\boldsymbol{u}_g$ is given by: $\boldsymbol{u}_g = \boldsymbol{u}_l + \boldsymbol{u}_{slip} + \boldsymbol{u}_{drift}$

  where; $\boldsymbol{u}_{slip}$ = the relative velocity between phases and $\boldsymbol{u}_{drift}$ = contribution from the turbulence model (disregarded in this work as the flow was laminar).

- $\boldsymbol{u}_{slip}$ is modelled using the **'Pressure-drag balance'** equations, which make the assumption that the viscous drag forces balance with the pressure forces on the bubble: $\frac{3}{4}\frac{C_d}{d_b}\rho_l|\boldsymbol{u}_{slip}|\boldsymbol{u}_{slip} = -\nabla p$

  Where, d_b = bubble diameter (SI unit: m), C_d = viscous drag coefficient (dimensionless).

- However, as the bubbles in this study are all typically smaller than 2 mm this is replaced by the 'Small spherical bubbles' or **Hadamard-Rybczynski** model (Crowe, Sommerfeld and Tsuji, 1998): $C_d = \frac{16}{Re_b}$, where $Re_b = \frac{d_b \rho_l |\boldsymbol{u}_{slip}|}{\mu_l}$.

- **Gas density** is calculated from the ideal gas law: $\rho_g = \frac{(p+p_{ref})M}{RT}$

  Where, M = Molecular weight of the gas (SI unit: kg/mol), R = Ideal gas constant (8.314472 J/(mol·K)), p_{ref} a reference pressure (SI unit: Pa) and T is temperature (SI unit: K). p_{ref} is a scalar variable, with a default value of 101325 Pa (1 atmosphere). The liquid volume fraction ϕ_l is calculated from the gas volume fraction ϕ_g by: $\phi_l = 1 - \phi_g$

Materials:

The inbuilt material properties in COMSOL were used for air and liquid water, but to simulate 1 M NaCl salt water, another material profile was created based on the existing one for water. As this modification was based on empirical data rather than an equation, this material was only suitable to simulate at a temperature of 25°C and 1 bar pressure:

- **Air:** Density (ρ_g) in kg/m^3
  Ref equation: ρ_g (pA,T), Where; pA = pressure area (1/Pa), T = Temperature (1/K)

- **Water:**
  - Density (ρ_l) in kg/m^3 , Ref equation: ρ_l(T)
  - Dynamic viscosity (μ_l) in Pa·s, where: η (T)

- **Water + 1M NaCl**:
  - Density (ρ_l) - kg/m^3 – 1041.279. Source: (Millero, et al., 1980)
  - Dynamic viscosity (μ_l) in Pa·s – 0.000975809. Source: (Ozbek, 1977)

Other program specific settings

Laminar Bubbly Flow (bf): Reference pressure (p_{ref}): 1 [atm]

Fluid properties:

- Temperature (T) - User defined - 298.15 K or 25°C)
- Absolute pressure - p_A:
    - Pressure p =(bf/fp1)
    - p_{ref} = 1[atm] - Reference pressure = ticked
    - $p_A = p + p_{ref}$

Materials (Specified referenced to materials properties section):

- Liquid: Water
- Gas: Air

Liquid Properties:

- Density, liquid phase - p_l: From material
- Dynamic viscosity, liquid phase - μ_l: From material

Gas Properties:

- Density, gas phase - ρ_g: From material
- Bubble diameter - d_b: User specified, i.e. 0.5e-3[m] = 0.5mm diameter (various sizes from 0.1-1mm modelled).

Slip Model:

- Slip model - Pressure-drag balance
- Drag coefficient model - Small spherical bubbles (Hadamard-Rybczynski)

Wall assignments (see Figure 3.13):

- Majority of walls with liquid boundary conditions set to: no slip. That is $\boldsymbol{u}_l = 0$.
- Majority of walls is gas boundary conditions set to: No gas flux. That is $n \cdot (\phi_d \boldsymbol{u}_d) = 0$.
- Sparger zone wall, also has No slip for liquid but the Gas boundary condition is: **Gas flux**. That is $-n \cdot (\tilde{\rho}_g \boldsymbol{u}_g) = \mathbf{N}_{\phi_g \rho_g}$, in (SI unit: kg/(m^2·s).
- The top wall of the model is slip for liquid and the Gas boundary condition is set to: **Gas outlet**.This allows the gas phase flow outward with the gas velocity, $\boldsymbol{u}_g$ at the boundary.
- A pressure point of $p_0 = 0$ was added as a reference for computation.
- A gravity vector of -9.81 m/s^2 was added along the z axis, which corresponds with $-\phi_l \rho_l \boldsymbol{g}$.

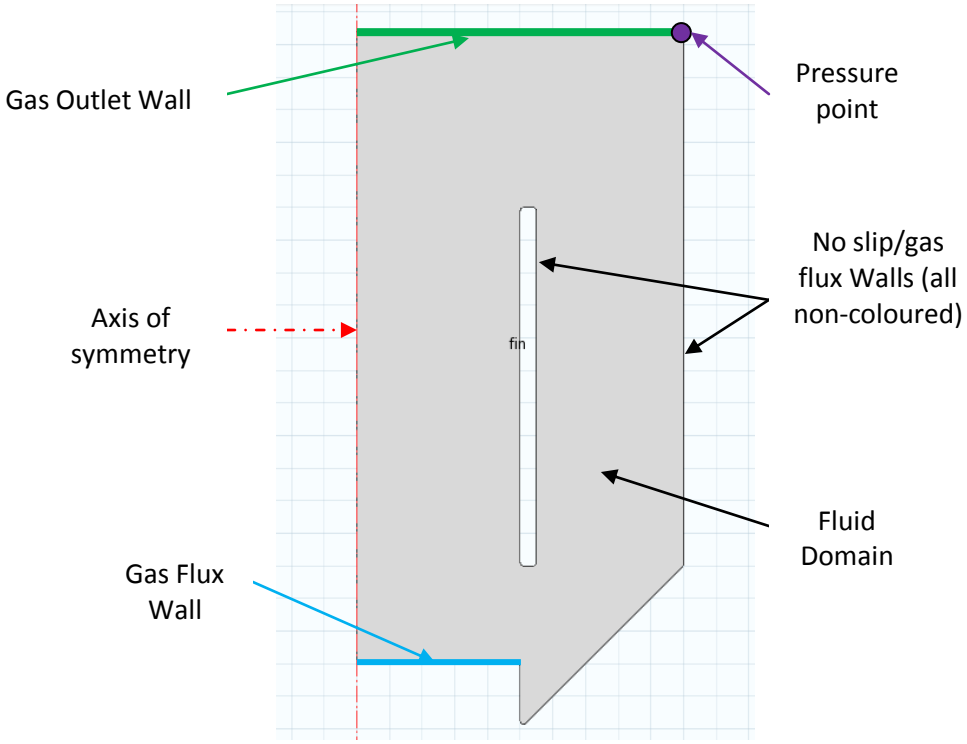

Figure 3.13. Wall and boundary assignments in 2D axis-symmetric 3 L flat plate photo-bioreactor model.

All reactor geometries were modelled in 2D with a plane of symmetry down the centre to reduce computing expense. The decision to use the laminar flow model rather than k-epsilon turbulent flow was based on visual observation of a highly ordered flow patterns in the physical reactor prototypes and the preliminary work by Mahmood, et al. (2011), which indicated using a similar setup that this model should be applicable. It is also worth noting, that one of the main recommendations from that study was to use flow validation using particle image velocimetry (PIV) in future to test for turbulence. As this procedure is currently unavailable at this time, the fluorescein dye tracer was used as a rough indicator. Each model was run for varying lengths of time, specific on the objective needs. In each case, the criteria for the successful convergence of the models were controlled by the default settings in the program's CFD module.

3.6.1 3L flat plate reactor CFD flow modelling

A model of the 3 L photo-bioreactor (section 2.12.2) was created to find out how the airlift effect performed in the current design and what range of velocities were produced. The CFD flow simulations were performed using COMSOL based on the geometry of the reactor. The geometry was simplified to a 2D vertical axis symmetric approximation to ensure computation tractability (Figure 3.14). The mesh was auto-calibrated for fluid dynamics with a 'normal' mesh size with a max element size of 0.0045 m and min element size of 0.002 m. Due to limitations with the flow averaging method in the way the multi-phase flow is solved, it is not

possible to simulate a distribution of different bubble sizes in one study. So, based on previous data using the same sparger type, a bubble size of 0.5 mm was selected as this had the highest frequency of occurrence (Zimmerman, et al., 2011). Given the previous mass transfer similarities, this bubble size was also seen as an adequate compromise between the oscillated and regular flows. An air flow rate of 0.00013 kg/m^{2}sec (~100 cc/min) was used at 1 bar pressure. The global temperature was set to 25°C and the domain material to plain water. The simulation was run over 5 minutes to ensure the flow rates were well established.

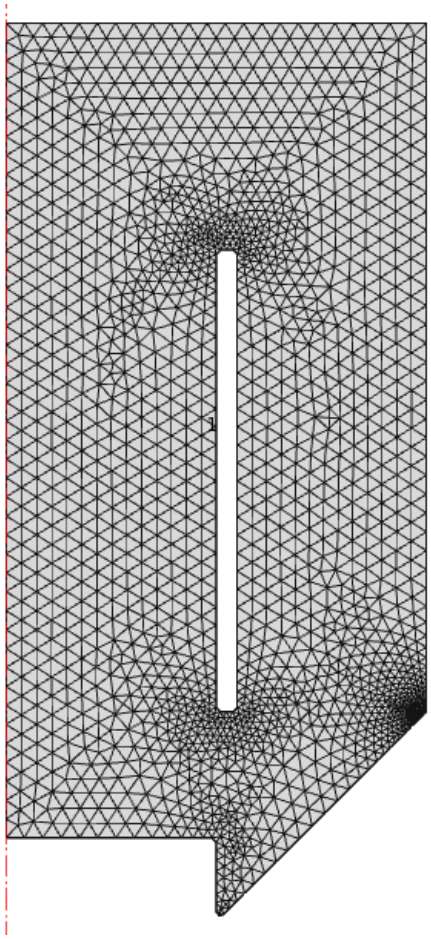

Figure 3.14.Element mesh used for 2D axis-symmetric 3L flat plate photo-bioreactor model

Figure 3.15. 2D Fluid velocity simulation results. A) Liquid velocity surface colour profile (m/s) with vector arrows. Labels 1 and 2, show regions of major vortices. B) Mass-less particle tracing of airlift loop in the fluid domain, colour denotes velocity magnitude (m/s).

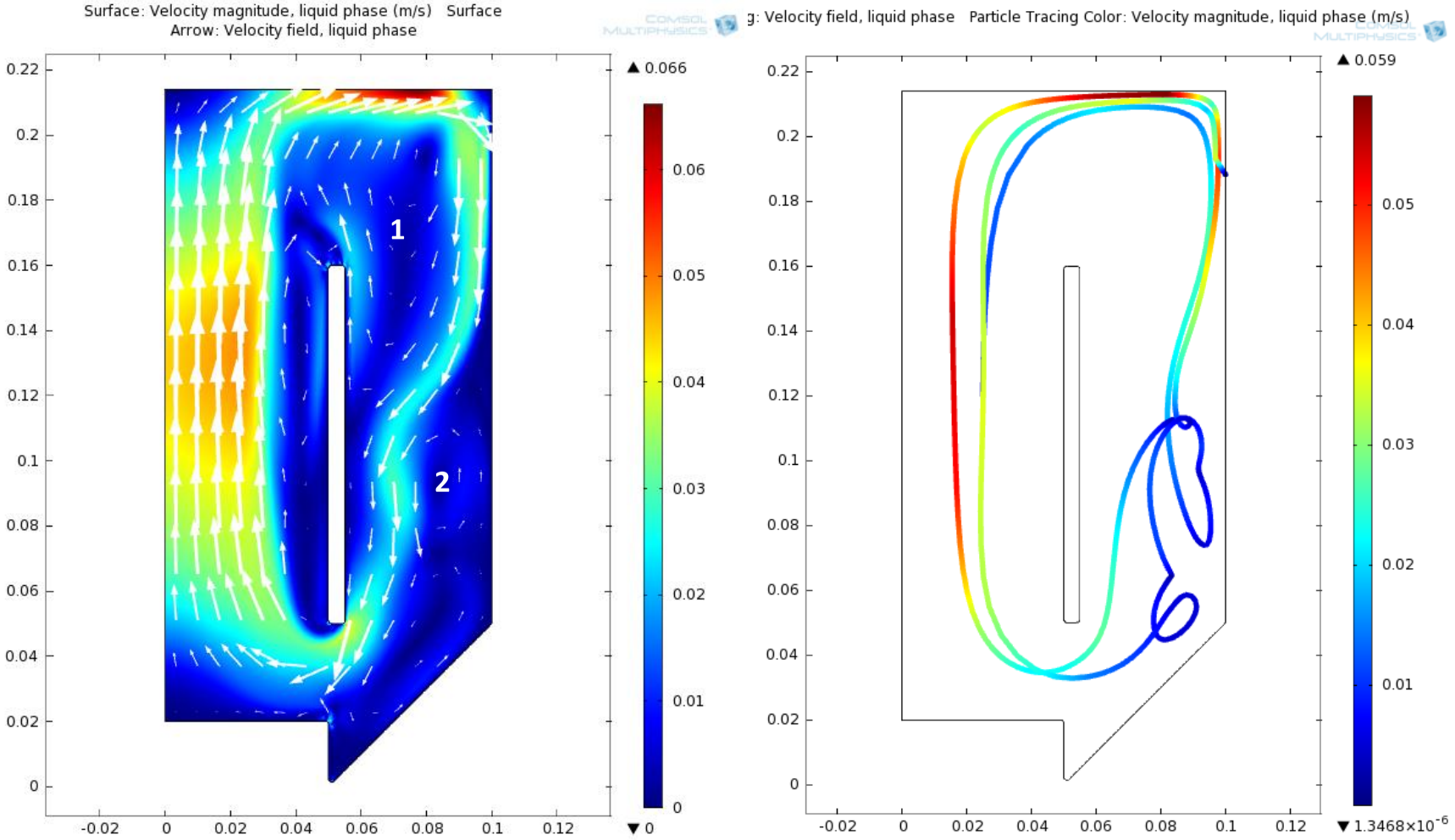

The results indicate clear buoyancy driven liquid flow and the establishment of an airlift loop. Although there is a consistent general flow pattern, there is evidence of two internal vortices (labelled 1 and 2 in Figure 3.15) that do tend to move slightly in an oscillating pattern, which causes periods of increased and decreased flow accordingly. The images below (Figure 3.16) show this effect. The data seems to indicate the transitory flow pattern is approximately 30 seconds in length before repeating.

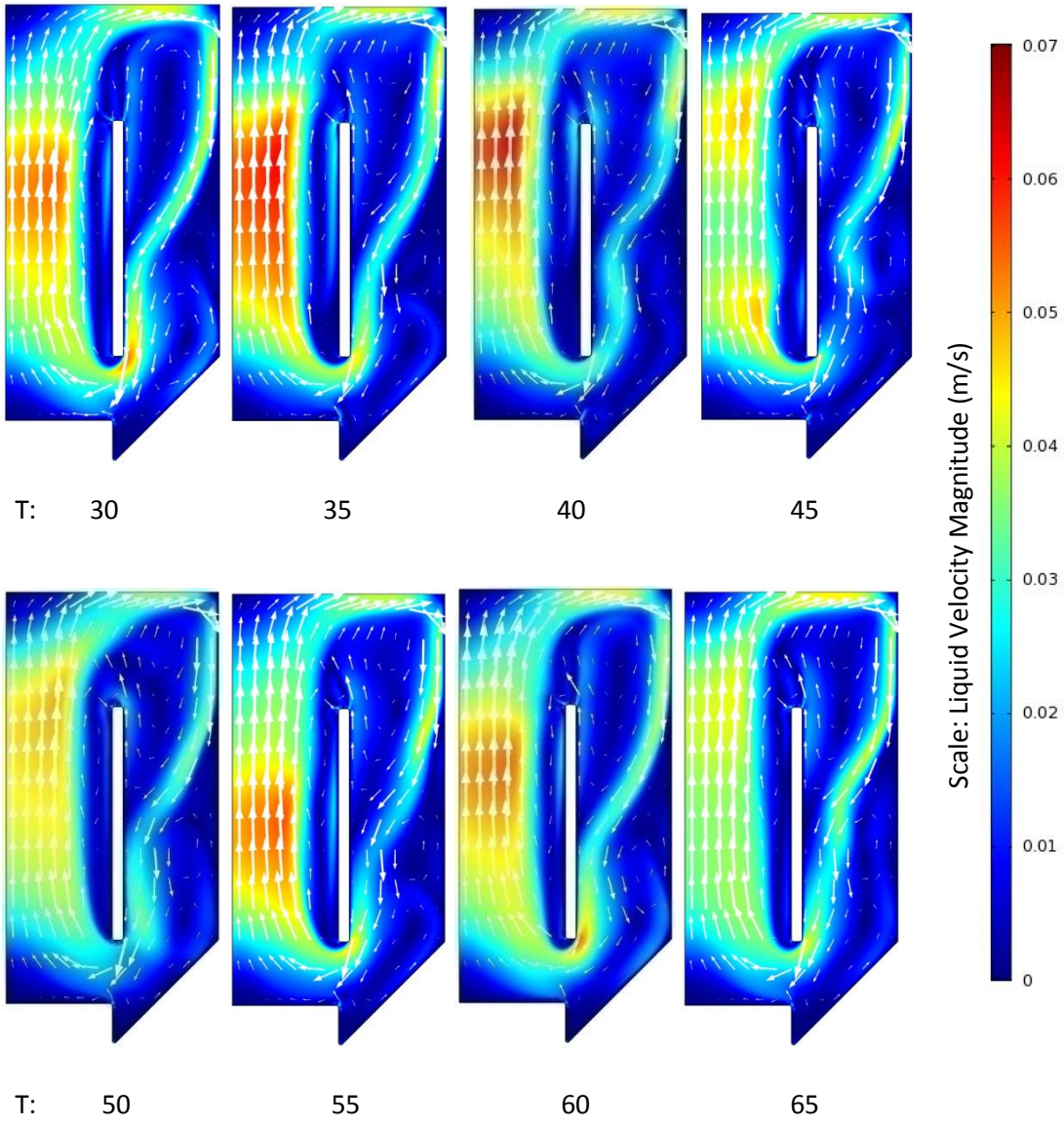

Figure 3.16. 2D liquid velocity surface colour profiles(m/s) with vector arrows, demonstrating variance in simulation results at 5 second increments from 30 seconds.

The particle tracing plot shows the effect these vortices would have on the algal mixing, creating a slight more convoluted transport path. However, seeing as the flow rates are not particular high in these zones, this could actually be a boon as more algae would be exposed to the external light source. Based on the particle trace, the approximate re-circulation time is

around 20-30 seconds (interestingly the same length as the flow altering period), however without considering mass, this measurement is very subjective.

3.6.2 3 L flat plate reactor dye validation.

To demonstrate the photo-bioreactor was producing the desired air lift loop effect in reality with complete mixing, a fluorescein dye tracer was employed using the method specified in section 2.14. Due to the incredibly rapid mixing of the dye with distilled water and the lack of a slow motion camera, a 50/50 glycerol water media was employed to increase liquid viscosity and slow the rate of dispersion. Aeration was provided by lab air regulated at 1 bar pressure, flow rates of 20 cc/min were used to induce a slow fluid circulation.

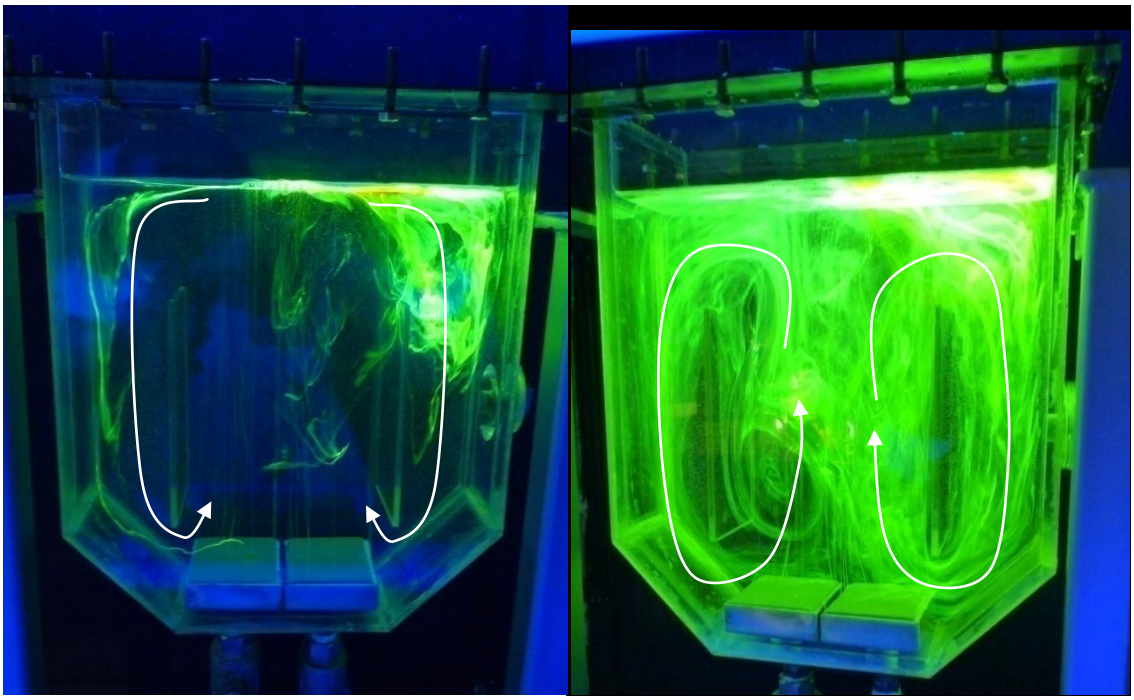

Figure 3.17. Fluorescein dye tracing of the 3L photo-bioreactor design demonstrating the airlift loop effect (left) and complete mixing within the fluid domain (right).

Figure 3.17 (left), shows the establishment of the airlift loop as the bubble rise generating fluid flow (Wang, Lan and Horsman, 2012). In Figure 3.17 (right), the mixing is complete and the dye is well distributed with clear circulatory mixing patterns emerging. These qualitative results demonstrate good mixing in this geometry and the clear presence of the airlift effect in the design. Videos of experiments run using just plain water and 100 cc/min air are included in the digital appendix.

3.7 Development of a Mini Photo-bioreactor System for the Testing of Micro-bubbles.

In microalgal bioprospecting or bioprocess development it is common for many different strains to be tested in multiple conditions simultaneously to save time and expense (Mutanda, et al., 2011). The initial tests are typically performed using shake flasks for cheap high throughput screening of desirable characteristics, before the selected strains are grown in pilot scale reactor systems. However, this method is not suitable for the testing of the effects of microbubbles. As there were only two 3 Litre photo-bioreactors available in this study capable of creating micro-bubbles (mainly due to the sparger design), it would have taken much longer than the time available to complete the project to get any meaningful biological replication of growth data. Also, the requirement for large quantities of media, 6 litres at a time of pH buffered medium would be prohibitively expensive. To address these issues, a series of cheap mini photo-bioreactor systems needed to be developed as a matter of necessity.

In recent years, small scale reactor systems have been of increasing interest commercially and academically due to the screening benefits described previously and other advantages such as reduced labour intensity, materials costs and rapid data replication (Garcia-Ochoa and Gomez, 2009). Culturing using traditional conical flasks, although cheap, is totally dependent on mass transfer at the gas-liquid surface layer which severely restricts the k_La value due to a fixed and limited interfacial area. Because of this, the k_La also decreases in proportion to the volume of liquid in the flask, making them less efficient (Liu, Wu and Ho, 2006). Even though shaking does slightly help to compensate for this effect, compared to the effects of stirring and bubbling in reactor systems, the overall mass transfer is much lower. Another benefit of minireactor systems compared to flasks is scaling. If they are designed correctly the data gathered can be used to make good predictions as to the performance in large scale equivalent experiments and pilot programmes (Doig, et al., 2005; Garcia-Ochoa and Gomez, 2009). Many different systems have been developed in the literature for various purposes and scales; the reviews by Kim, Diao and Shuler (2012) and Betts and Baganz (2006) give an excellent overview. However, until relatively recently, the majority of the systems have been designed for the culture of mammalian cells and not photosynthetic organisms like algae. Commercial systems from companies such as Infors (Switzerland), Diachrom Biotechnology (Switzerland), HiTecZang (Germany), Applikon Biotechnology (Netherlands) and Medorex (Germany), offer mini-reactor options with gas sparging and illumination systems for the growth of algae. But the costs of these systems are incredibly high and very few of the systems use bubble mixing exclusively; most are equipped with mechanical stirring mechanisms like impellers or magnetic stir bars. This latter trend is also prevalent in the academic field, with the majority of mini reactor

systems being based around such stirring mechanisms (Bulnes-Abundis, et al., 2013; Gill, et al., 2008; Lamping, et al., 2003; Nunes, Fernandes and Ribeiro, 2013; Soley, et al., 2012). However, there are one or two designs that have been developed just using bubble driven flow at different small scales. The first type is based on the microplate scale with 48 wells with a 2 ml capacity, the aeration provided by polyethylene frits with a 20 µm pore size (Doig, Diep and Baganz, 2005). The second type is based around small scale bubble columns with slightly larger volume (100-200 ml), closer to that of a flask, again with frits encompassing the whole bottom of the column (Altenbach-Rehm, et al., 1999; Betts and Baganz, 2006; Doig, et al., 2005; Weuster-Botz, Altenbach-Rehm and Hawrylenko, 2001). It has been shown in tests comparing this type of design to shake flasks and traditional stirred tank reactors, that there are benefits in terms of decreased power input and increased k_La (Table 3.8).

Table 3.8. Reaction-engineering comparison of the shaking flask, the small-scale column, and the stirred-tank reactor for cultivation of micro organisms (data collected for use with low-viscosity Newtonian fermentation medium) (Weuster-Botz, Altenbach-Rehm and Hawrylenko, 2001)

Parameter	Shaking flask	Small-scale column	Stirred-tank reactor
Volume (L)	0.01-0.2	0.1-0.3	0.5-50,000
Power input (W/L)	<4.5	<0.2	<8
Aeration	Surface	Volume	Volume
Gas exchange	Diffusion	Convection	Convection
k_La / sec	<0.07	<0.16	<0.35
OTR_{max} gO_2 /L hour	~2	~4.5	~10
Mixing time θ_{90} sec	-	~4	2-200
Sampling	Off-line (no power input)	Off-line	Off-line, on-line

However, the conditions under which these data were gleaned are very dissimilar to the ones needed for the cultures of marine micro-algae. Also, more importantly, these parameters are heavily based on bubble size. As all of the designs currently in the literature and commercially do not include fluidic oscillation, which could increase performance (by reducing bubble size), this difference in performance could be even greater still. Other details, such as sparger design and draft tube placement also have seemingly been overlooked, the latter fact is probably a result of the development bias toward non-photosynthetic organisms which have historically been more financially lucrative. Based on this information, the development of an algal mini photo-bioreactor system will not only be fulfilling a necessity to progress this study, but also potentially opening the fluidic oscillator applicability to an entirely new niche in biotechnology for rapid throughput algal screening.

3.7.1 Mk I prototype development

To ensure that fluidic oscillation would have the desired effect, the reactor design needed to be based around a sparger with similar properties to the ones used in the 3 L reactor system i.e. a hydrophilic surfaced, high porosity material with small pore size. To simplify the growth data comparisons with the 3 L reactor system, the same 20 µm pore ceramic was used. As the design would need to be used in a laboratory within the bench spaces available, a 105 ml capacity was decided upon. This volume is the same as used in typical 250 ml conical flask algal experiments, so it would provide a useful bench mark and also transferable scales for biological procedures. Because the sizes were reduced, this brought in the possibility of allowing the entire reactor to be autoclaved, rather than sterilised with Virkon/Microsol. This meant the materials used needed to be able to withstand temperatures of up to 125^{o}C for prolonged periods. To enable cheap manufacture, replication and temperature stability, a series of Schott Duran 100ml bottles were selected for the reactor bodies. The bottles were drilled to allow the fitting of a sparger and a silicone membrane screw lid with a stainless steel tube was used for gas exhaust.

A number of iterations of the sparger design were tried (Figure 3.18), with different materials and geometries. The final design selected used a high temperature epoxy that was tolerant to autoclave conditions and high salinities, rather than standard epoxy (which released harmful chemicals when heated) and a single one piece stainless steel housing (see section 2.12.3). The sparger was fitted into the reactor bottle using a high temperature silicone sealant.

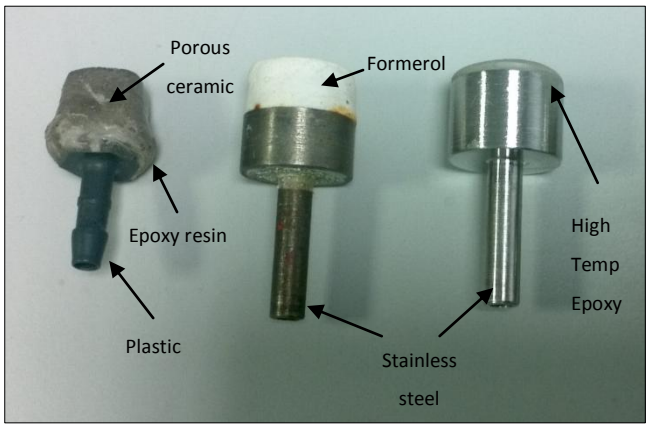

Figure3.18.Sparger prototype development from left to right.

3.7.2 Flow effects and dye tracing simulation of Mk I prototype.

Although fulfilling the design brief of producing micro-bubbles (visual comparison only) with the use of the fluidic oscillator, the performance of the Mk I design was very poor (see section 5.4). In all of the tests carried out, the *D. salina* 19/30 repeatedly settled at the bottom of the reactor and came out of suspension (see Figure 3.19). It was hypothesised that this could be due to the natural photo-taxis of the algae (not enough light present to encourage movement) or a lack of motility due to algal flagella damage, but inefficient mixing was assumed to be primary cause.

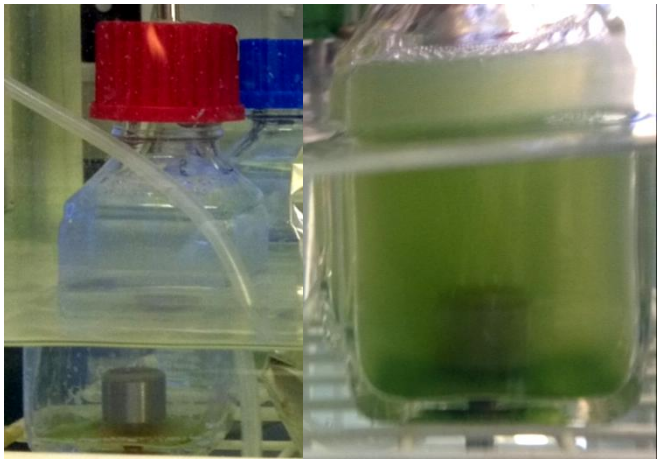

Figure3.19.Algal flock formation due to incomplete mixing in Mk I mini photo-bioreactor.

To test this theory, fluorescein dye was employed once again as a flow tracer using the same method as in section 2.14. It can be seen from the images produced (Figure 3.20) that the mixing is incomplete,creating a fractionation effect with the reactor.

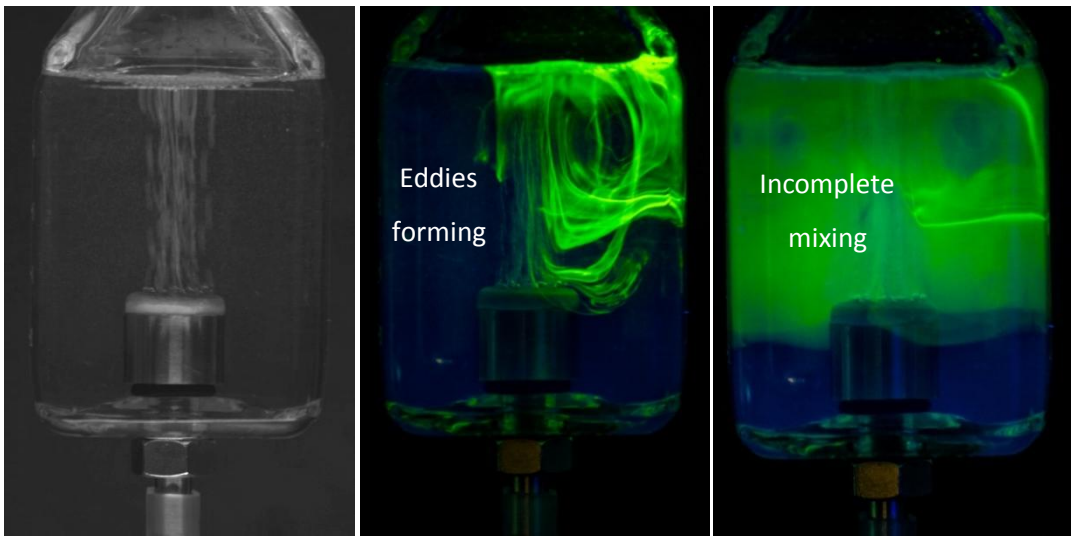

Figure 3.20. Fluorescein dye tracing of the 100ml Mk 1 photo-bioreactor design demonstrating incomplete mixing and stratification.

Based on this evidence it is probable that the algae, when leaving the well mixed region, are settling to form flocks at the bottom of the vessel. This phenomenon coupled with low lighting conditions, provides a good explanation to the observed experimental behaviour.

3.7.3 CFD dye tracing verification of Mk I prototype.

It was suspected that the poor mixing performance of the Mk I photo-bioreactor was due to the sparger height relative to reactor base and the lack of a draft tube in the design. To try and ascertain whether this hypothesis was true, a 2D CFD model of the reactor geometry was run. The model used the same conditions as in section 3.6.1, but with a 8 minute run time and a flow rate of 0.00087kg/m^2sec (or 10 cc/min, with a 5.65x10^{-5} m^2sparger area). When the results were compared with still images of the actual experiment (Figure 3.21), there appears to be an excellent correlation with the streamlines in both cases. Two main vortices are in place in the fluid domain, a small circular one at the top (1) and much larger one the length of the reactor (2). A clear dead zone (3) is also present in both the simulation and photos, which agrees well with the area of flocculation.

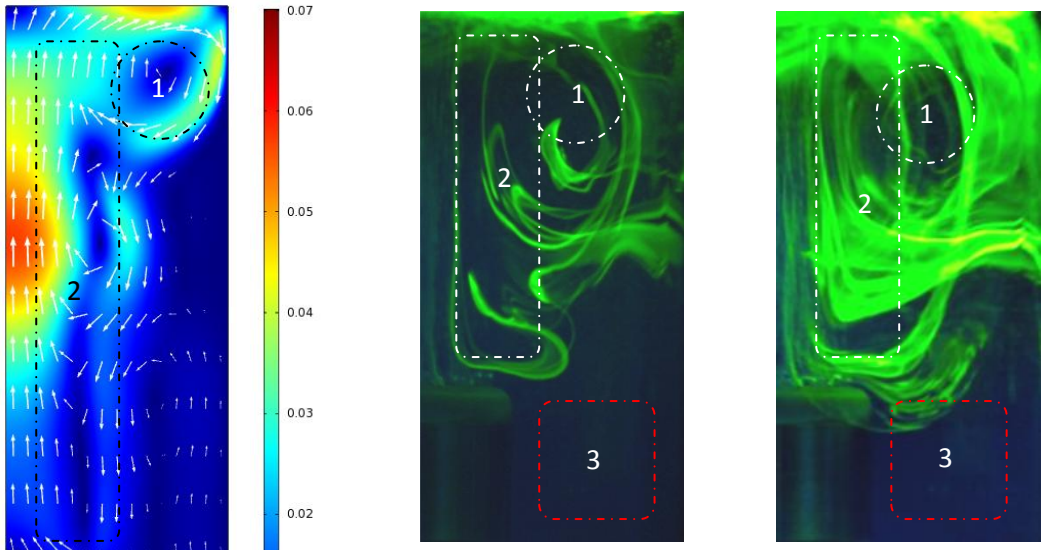

Figure3.21. Comparison of 2D COMSOL CFD simulation (liquid velocity surface colour profiles(m/s) with vector arrows- left) to Fluorescein dye tracing of the 100ml Mk 1 photo-bioreactor design (right). Zones 1 and 2 denote major vortices, 3 dead flow zones.

As the correlation between the simulation and real flow patterns seemed to be very good a series of further models were run to see the effects of adding a draft tube and lowering the sparger. The same flow rates and overall volume were kept, but the run time was reduced to 60 seconds to save on computation expense (Figure 3.22).

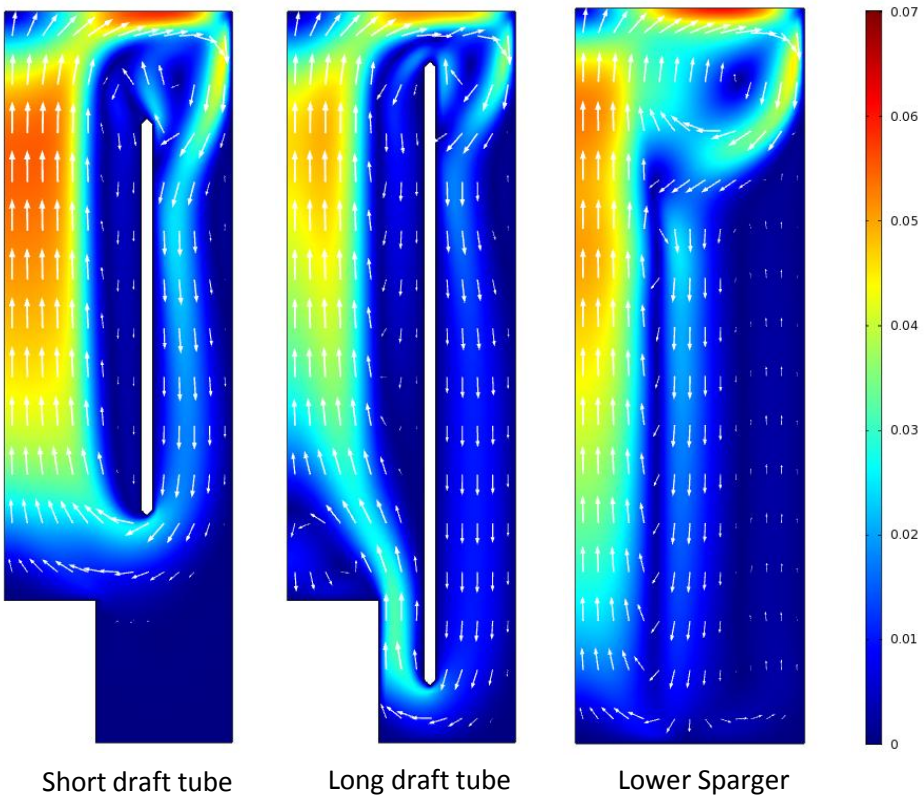

Figure 3.22. 2D liquid velocity surface colour profiles(m/s) with vector arrows of Mk I mini photo-bioreactor designs with geometry variation.

The results from the simulation demonstrate there is a considerable benefit to the mixing by adding a draft tube, but this is only effective if it is long enough to promote mixing in all areas. Interestingly lowering the sparger actually creates a reasonably large recirculation loop, however this still results in a moderately large dead zone and little movement around the crucial outer surface of the reactor.

3.7.4 Design and manufacture of Mk II prototype.

Based on the lessons learnt operating and testing the Mk I prototype, a second iteration Mk II design was produced (section 2.12.4). Again, to keep costs down and maintain uniformity, the design was based around off the shelf parts that are autoclavable. The reactor body was made from a Schott tube with a GL 45 thread that was modified to encase the sparger design. This part was also chosen because of its surface area to volume ratio was very good; 3.54 cm ID and 10.67 cm length for a 105 cc capacity, so a **146.44** m^{-1} ratio. This is much better than other photo-bioreactor designs (see Table 3.9) which gave us confidence to assume that illumination would not be a limiting factor.

Table 3.9. Typical surface to volume ratios in reactor systems (Tredici and Zittelli, 1998)

Photo-bioreactor type	Outdoor/Indoor	Culture volume (L)	Surface to volume ratio (m^{-1}), under direct illumination
Coiled tubular	Outdoor	111	53
Near-horizontal tubular	Outdoor	32.3	70
Near-horizontal flat panel	Outdoor	32.3	40
Flat chamber	Indoor	4.8	40
Curved chamber	Indoor	6.4	46

Also, in terms of light penetration the size is ideal with an internal radius of 1.77 cm, well within the 3 cm extinction range specified by Kumar, Sirasale and Das (2013) in recent work. The inclusion of the air lift loop effect also improves the effects of light propagation and mass transfer (Miron, et al., 1999). Based on the previous CFD simulations it was decided that the sparger should be flush with the reactor bottom and the draft tube should be most of the length of the reactor body to promote good circulation. This design is an improvement on previous linear mini bubble columns developed in the literature, which do not make use of the air lift loop effect (Weuster-Botz, Altenbach-Rehm and Hawrylenko, 2001). The sparger was also re-designed to incorporate an o-ring screw thread attachment mechanism, to avoid the need for silicone sealant.

3.7.5 CFD dye tracing verification of Mk II prototype.

A series of CFD model simulations were performed to calculate the mixing performance of the new design. The impact of bubble size variation on the mixing speed relating to superficial gas velocity was also examined. These experimental conditions were also replicated in some physical experiments for comparison (see Chapter 4). The modelling was again performed in COMSOL Multiphysics, using the same program modules as before. The reactor was modelled in 2D with a plane of symmetry down the centre to reduce computing expense. Gas inflow was modelled at 5, 10, 15 and 20 cc/min at a range of 0.2-1 mm bubbles. The density/viscosity effects of 1 M NaCl water were also looked at for comparison. Each model was run for 120 seconds, so representative mixing could be achieved before readings were taken. Along with fluid flow for the entire domain, data was extracted at the mid-plane of the model in the riser section of the draft tube (riser 'rake') and the fluid return section down the outside (downcomer 'rake'), see Figure 3.23.

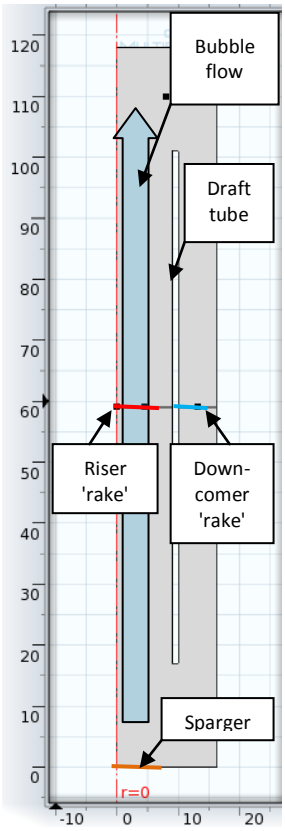

Figure 3.23. Wall, boundary and measurement assignments in 2D axis-symmetric Mk II photo-bioreactor model.

The magnitude of the fluid velocity across these measurement boundaries was taken as an indicator of the efficiency of mixing within the reactor, as the cultures would need to pass through both these boundaries.

3.7.6 Meshing & mesh variance tests

As this set of simulations would be used for detailed comparison, the selection of mesh was looked at in greater detail. Comsol has a number of meshing options and for this study a triangular based mesh for fluid dynamics was selected as node matching is easier to achieve. The default element size steps as specified by the software were used, from 'extremely coarse' to 'extra fine'. As the size selected for the mesh elements has a major impact on the overall accuracy of the model solution and the processing time, a mesh needs to be selected that was both accurate and relatively computationally inexpensive. To find this optimal mesh, a series of mesh variance tests were run using a fixed bubble size of 0.5 mm and a gas flow rate of 0.00087238 kg/(m^2sec) (see Table 3.10 and Figure 3.24). These tests compared liquid velocity at from 5 data probe points (see Figure 3.24, represented by white dots) at defined locations within the 2D flow domain. The sampling at these points was carried out using a mesh independent probe function, so the data values extracted from the solution at these points gave the closest average from the elements nearest to the geometry location specified. Sampling was performed at the same probe point locations for each mesh simulation, starting with the largest elements ('extremely coarse') and finishing with the smallest ('extra fine'). The degree of mesh dependency, i.e. the amount the mesh size influences the final flow solution, was calculated by comparing the standard deviation of flow data from the probe points in each simulation, to the most accurate solution (the one with the smallest mesh size, 'extra fine'). Another factor examined was the 'computational expense', which was a comparison between the number of elements used and the overall solution time (see Figure 3.24). The results from these tests led to the conclusion that the 'normal' mesh size has the best compromise between accuracy and solution time. Based on the data the rest of the modelling work was performed in batches using this size and type of mesh.

Table 3.10. Mesh variance test data

Mesh	Number of elements	Degrees of freedom (BDF)	Solution time (sec)	File size (KB)	Free triangular mesh: Max element size (mm)	Free triangular mesh: Minimum element size (mm)	Liquid velocity magnitude (m/s) values at 120 seconds: P1	P2	P3	P4	P5	StdDev from Largest Mesh: P1	P2	P3	P4	P5
Extremely coarse	484	3601	21	62968	3.56	1.13	0.0598	0.0152	0.0052	0.0116	0.0383	0.002687	0.005091	0.000636	0.011526	0.00601
Extra coarse	1206	8588	48	151748	2.11	0.81	0.0594	0.0127	0.005	0.0204	0.0366	0.002404	0.003323	0.000495	0.005303	0.004808
Coarser	2635	18237	71	325150	1.41	0.648	0.0574	0.0102	0.0046	0.0251	0.033	0.00099	0.001556	0.000212	0.00198	0.002263
Coarse	4089	28003	100	499976	1.09	0.486	0.0565	0.009	0.0045	0.0263	0.031	0.000354	0.000707	0.000141	0.001131	0.000849
Normal	9090	61213	421	1100320	0.729	0.324	0.056	0.0081	0.0043	0.0272	0.0299	0	7.07E-05	0	0.000495	7.07E-05
Fine	14652	97947	475	1760993	0.567	0.162	0.0559	0.0078	0.0043	0.0273	0.0296	7.07E-05	0.000141	0	0.000424	0.000141
Finer	22829	151787	724	2740212	0.454	0.0648	0.0559	0.0078	0.0043	0.0273	0.0296	7.07E-05	0.000141	0	0.000424	0.000141
Extra fine	105567	693469	16383	12567234	0.211	0.0243	0.056	0.008	0.0043	0.0279	0.0298	0	0	0	0	0

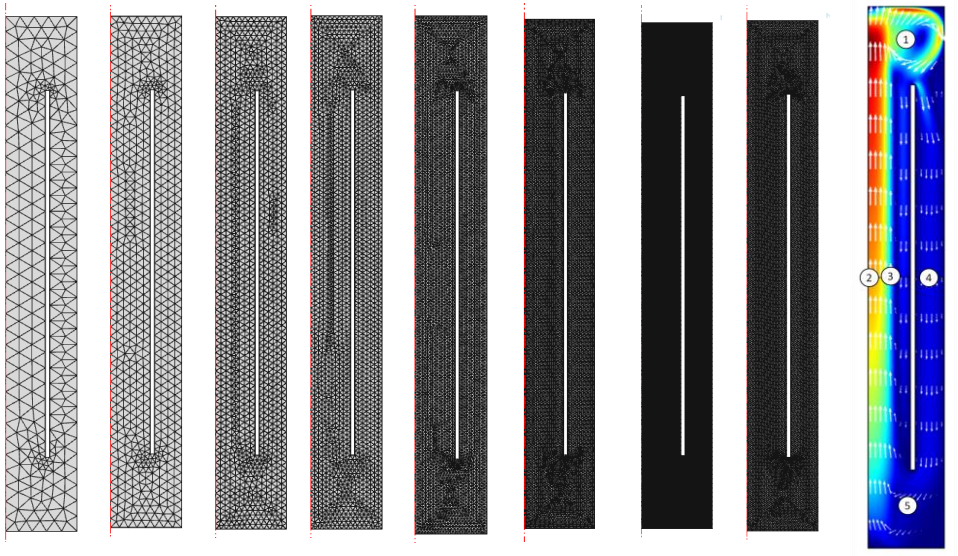

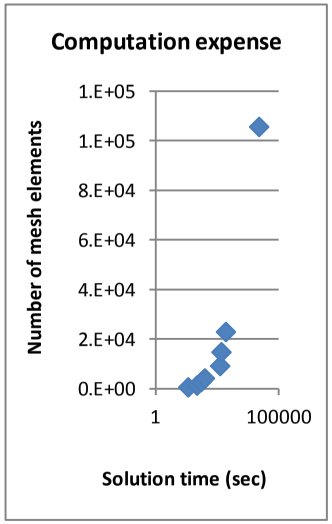

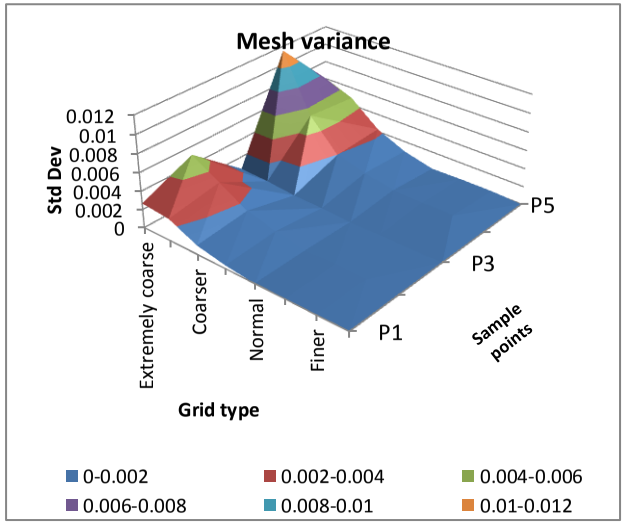

Figure 3.24 - Far left : Increase in mesh density from 'Extremely coarse' to 'Extra fine', Middle left: Date probe locations in 2D model plane,Middle right: Graph showing computational expense, Far right: Graph showing effect of mesh size on solution accuracy.

3.7.7 Fluid flow at 5, 10, 15, 20 cc/min air with bubble sizes 0.2-1 mm in water at 25°C

Using the 'normal' mesh size the simulations using plain water were run first. The velocity rake profiles are compiled below (see Figure 3.25):

5 cc/min

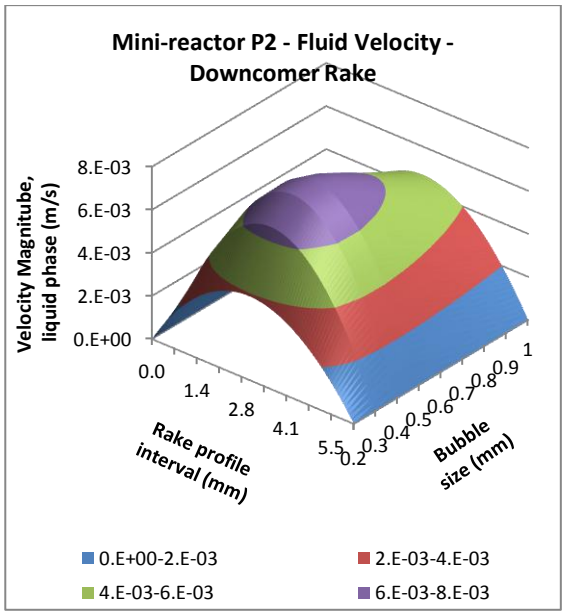

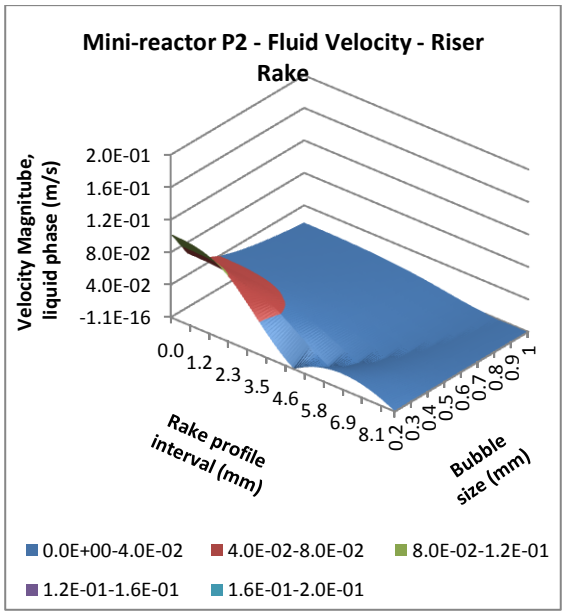

10 cc/min

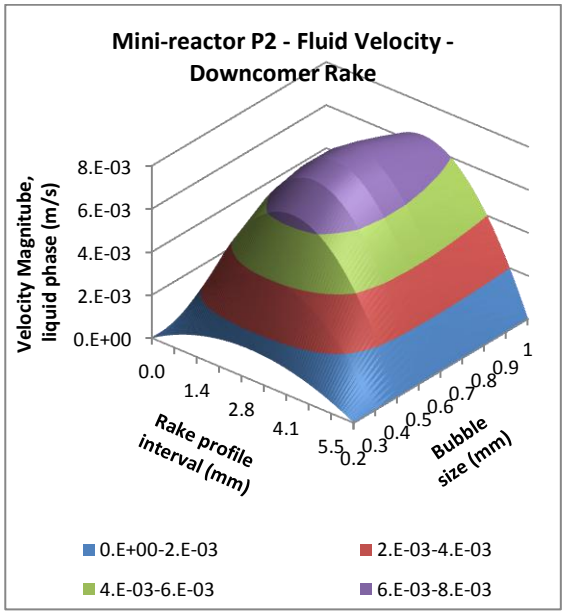

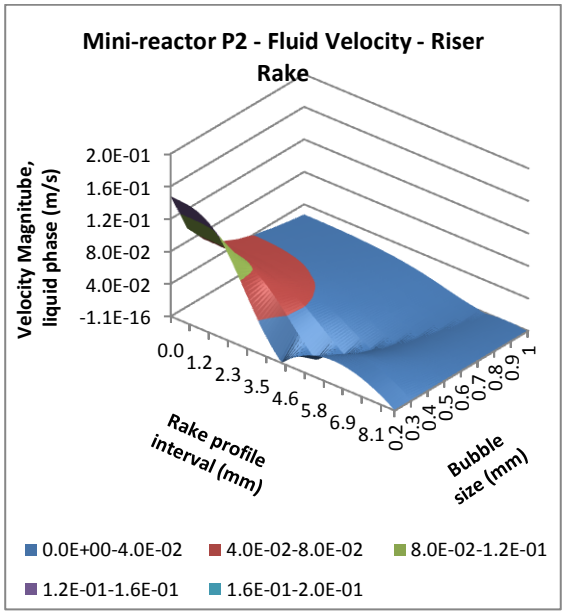

15 cc/min

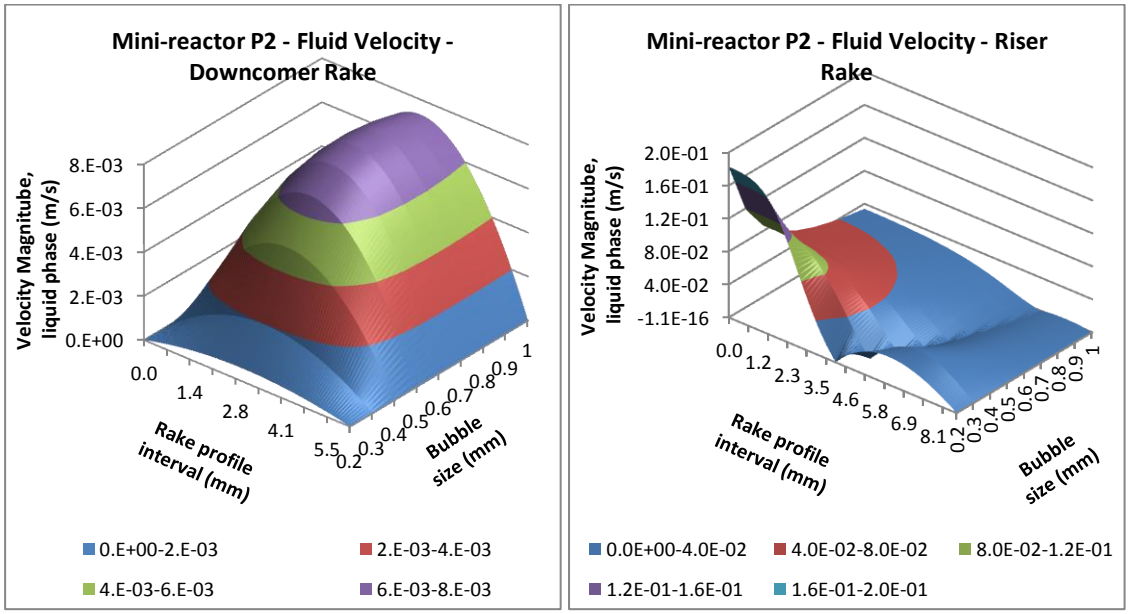

20 cc/min

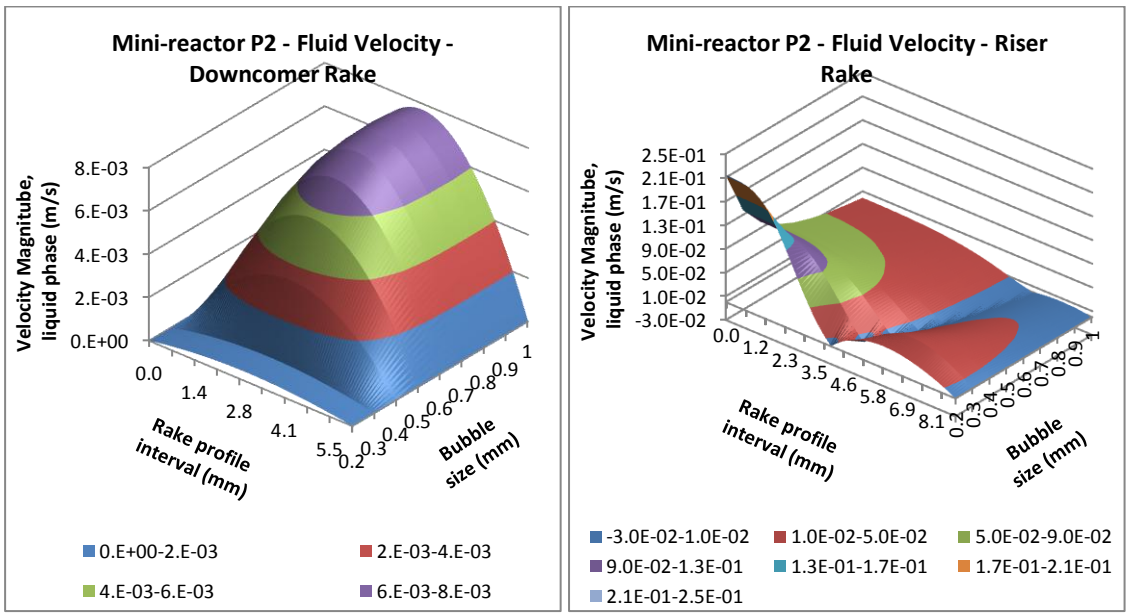

Figure 3.25. Graphs showing the velocity rake profiles of the riser and downcomer regions in relation to bubble size (0.2-1 mm) and flow rate (5-20 cc/min) from compiled 2D COMSOL CFD fluid velocity simulations with water.

The data seem to indicate that the bubble size has quite a large impact on the performance of the airlift loop. Depending on the superficial gas velocity, there appears to be a different optimal bubble size to produce the best overall mixing as determined by the highest flow in the down comer region. Interestingly, at the lowest gas flow rate simulated (5 cc/min), the bubble size that maximizes liquid circulation rate is around 0.5 mm, whereas at the highest gas

flow rate (20 cc/min), this optimal bubble size is increased to around 1 mm. It can be seen that the velocity profile in the riser is more complex than in the downcomer. In the riser, an internal circulation loop is established with negative or downward flow furthest from the centreline which increases with decreasing bubble size.

3.7.8 Fluid flow at 5, 10, 15, 20 cc/min air with bubble sizes 0.2-1 mm in water + 1 M NaCl at 25°C

The simulations using 1 M NaCl water were run second, the rake profiles are compiled below (see Figure 3.26):

5 cc/min

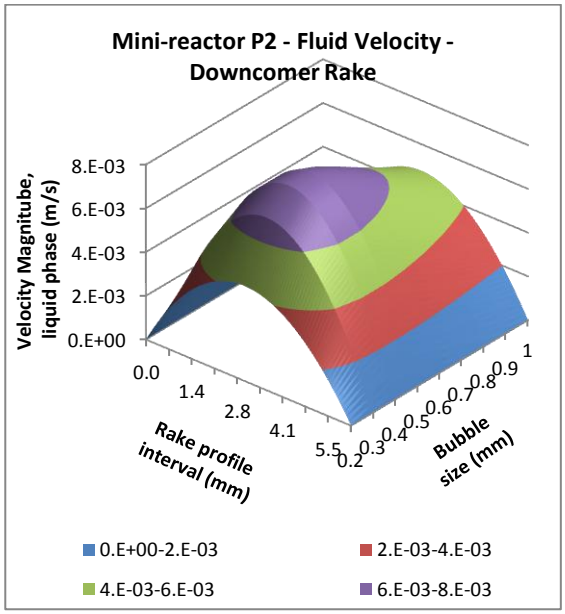

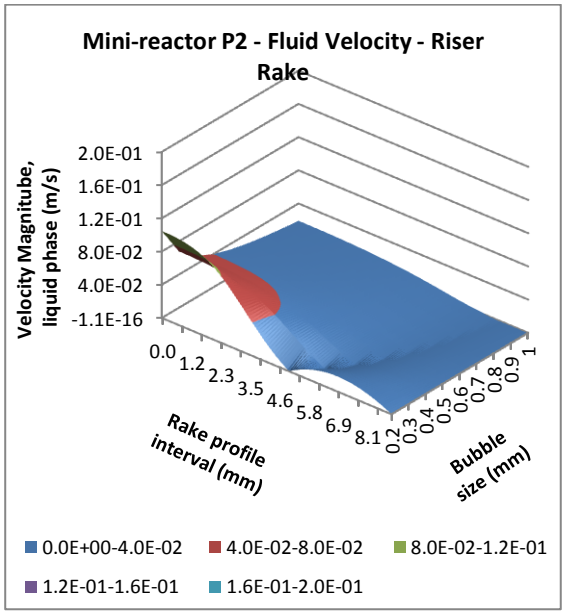

10 cc/min

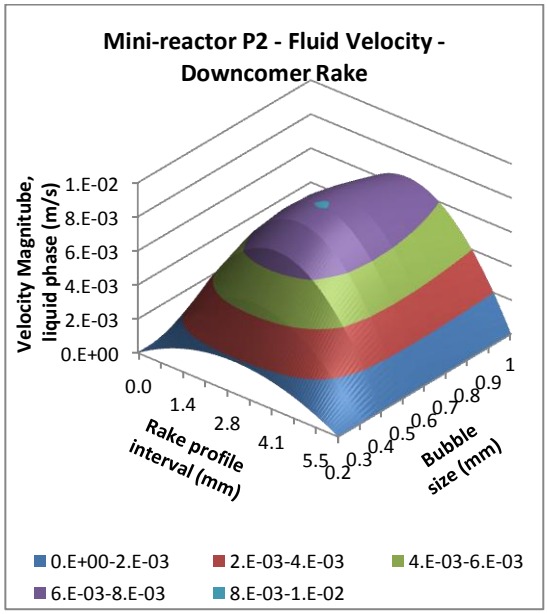

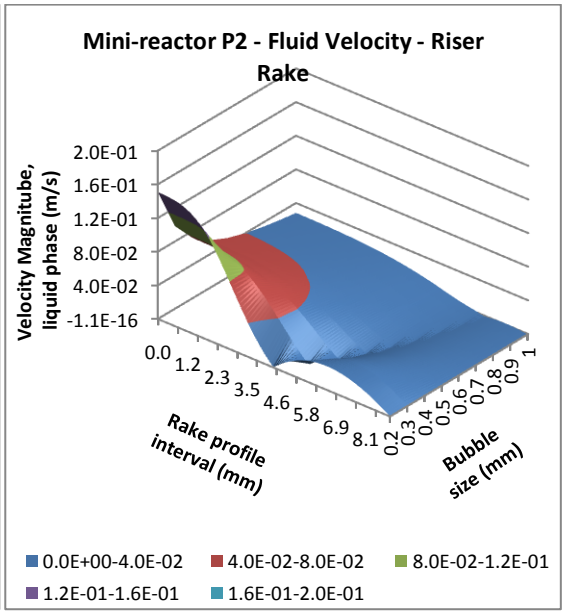

15 cc/min

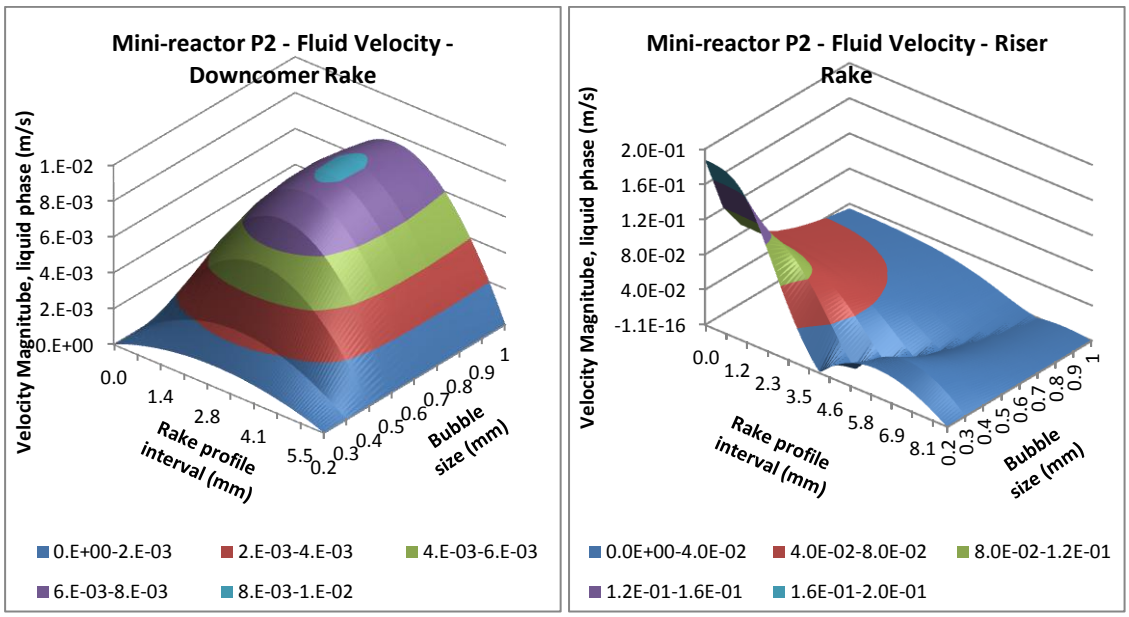

20 cc/min

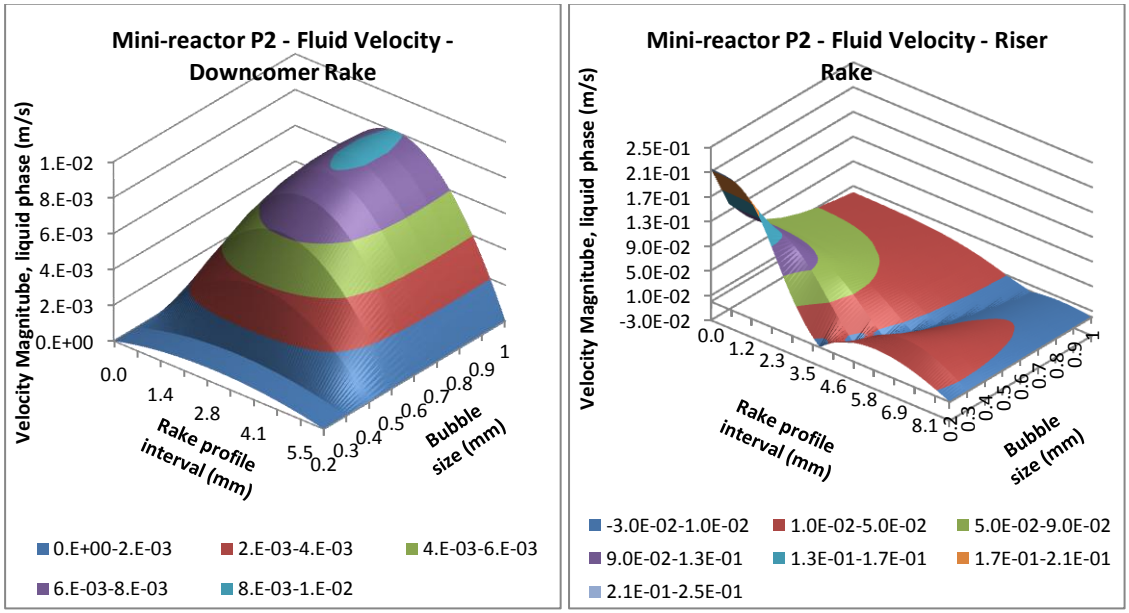

Figure 3.26. Graphs showing the velocity rake profiles of the riser and downcomer regions in relation to bubble size (0.2-1 mm) and flow rate (5-20 cc/min) from compiled 2D COMSOL CFD fluid velocity simulations with 1 M NaCl plus water.

The data again shows the relationship between the bubble size and the airlift performance. The added salt seems to increase the speed of mixing slightly compared to the plain distilled water. This would seem reasonable since the liquid circulation is driven by the density difference between the downcomer and the riser which, for the same voidage profile, will be higher for the higher density salt solution than for the distilled water. A more detailed comparison was performed on the downcomer region between the two conditions. An

average was take across the entire downcomer rake and the percentage difference relative to the water simulations was calculated (see Table 3.11 and Figure 3.27).

Table 3.11. The average % difference between average maximal flow rates with and without the inclusion of 1M NaCl into the CFD simulation.

Flow rate (cc/min)	Bubble size (mm) - Av % difference between water and 1M NaCl water								
	0.2	**0.3**	**0.4**	**0.5**	**0.6**	**0.7**	**0.8**	**0.9**	**1**
5	10.48	5.34	4.25	3.58	3.08	2.76	2.42	2.17	1.96
10	25.56	9.86	6.00	4.85	4.22	3.39	3.35	3.07	2.80
15	49.71	17.02	8.12	5.83	4.78	4.52	4.44	3.63	3.41
20	40.23	36.91	9.76	6.64	5.76	4.57	4.51	4.14	3.83

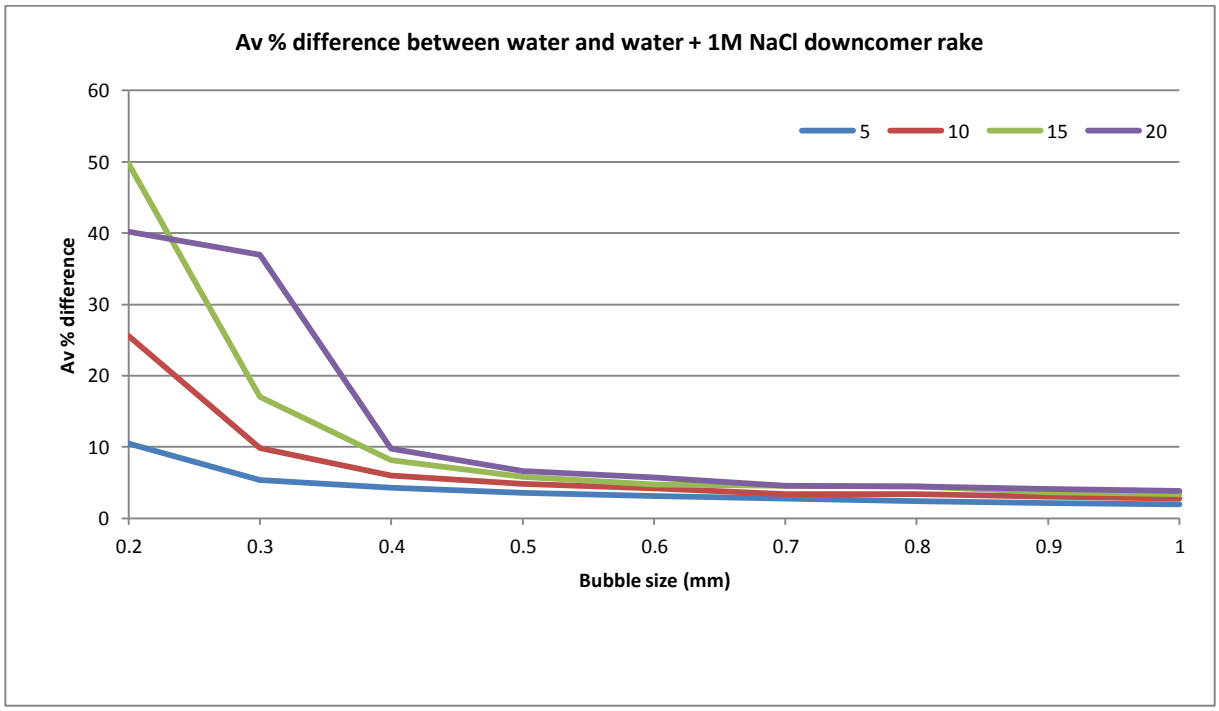

Figure 3.27. Graph demonstrating the average % difference between average maximal flow rates with and without the inclusion of 1M NaCl into the CFD simulation.

The results show that the salt solution with an increased density of 4.12% compared to distilled water has a velocity increase of between 0-7% for bubble sizes in the range 0.5-1 mm across the different airflow rates. Below sizes lower than 0.5 mm, the difference in velocity is more dramatic. Although this effect could be merely an artefact of the simulation, it could well be a physically correct result. If so, it could illustrate the positive feedback loop in which smaller bubbles cause higher liquid circulation which, in turn, results in the recirculation of more bubbles and a higher voidage difference between the downcomer and the riser, and, consequently, even higher liquid circulation velocities.This shows the power of the CFD

modelling used in this study to reveal subtle but important effects, for small bubble sizes, that are worthy of further investigation.

As the simulation with increased salinity is of main interest for the growth studies, further analysis of the flow patterns was performed, to see if the mixing loop within the entire reactor exhibited the same optimal 'window' relating to bubble size that was found in the downcomer rake comparison. See sections 3.7.9 to 3.7.12 and Appendix K for the data.

3.7.9 Fluid flow at 5 cc/min air with bubble sizes 0.2-1 mm in water + 1 M NaCl at 25°C

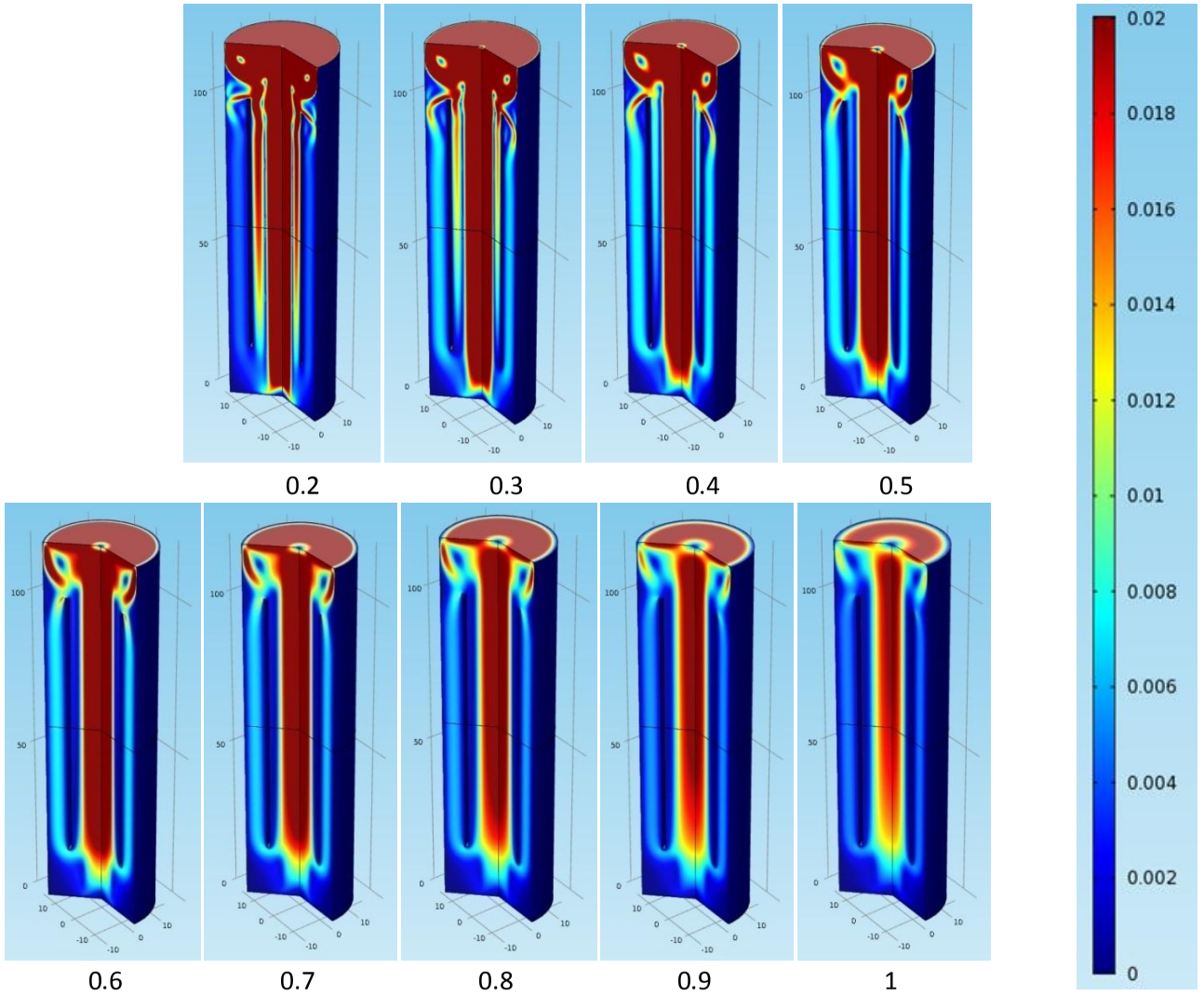

Bubble size (mm)	Maximum Velocity (m/s)
0.2	0.1356
0.3	0.0912
0.4	0.0682
0.5	0.0531
0.6	0.0433
0.7	0.0361
0.8	0.0306
0.9	0.0262
1	0.0227

3.7.10 Fluid flow at 10 cc/min air with bubble sizes 0.2-1 mm in water + 1 M NaCl at 25°C

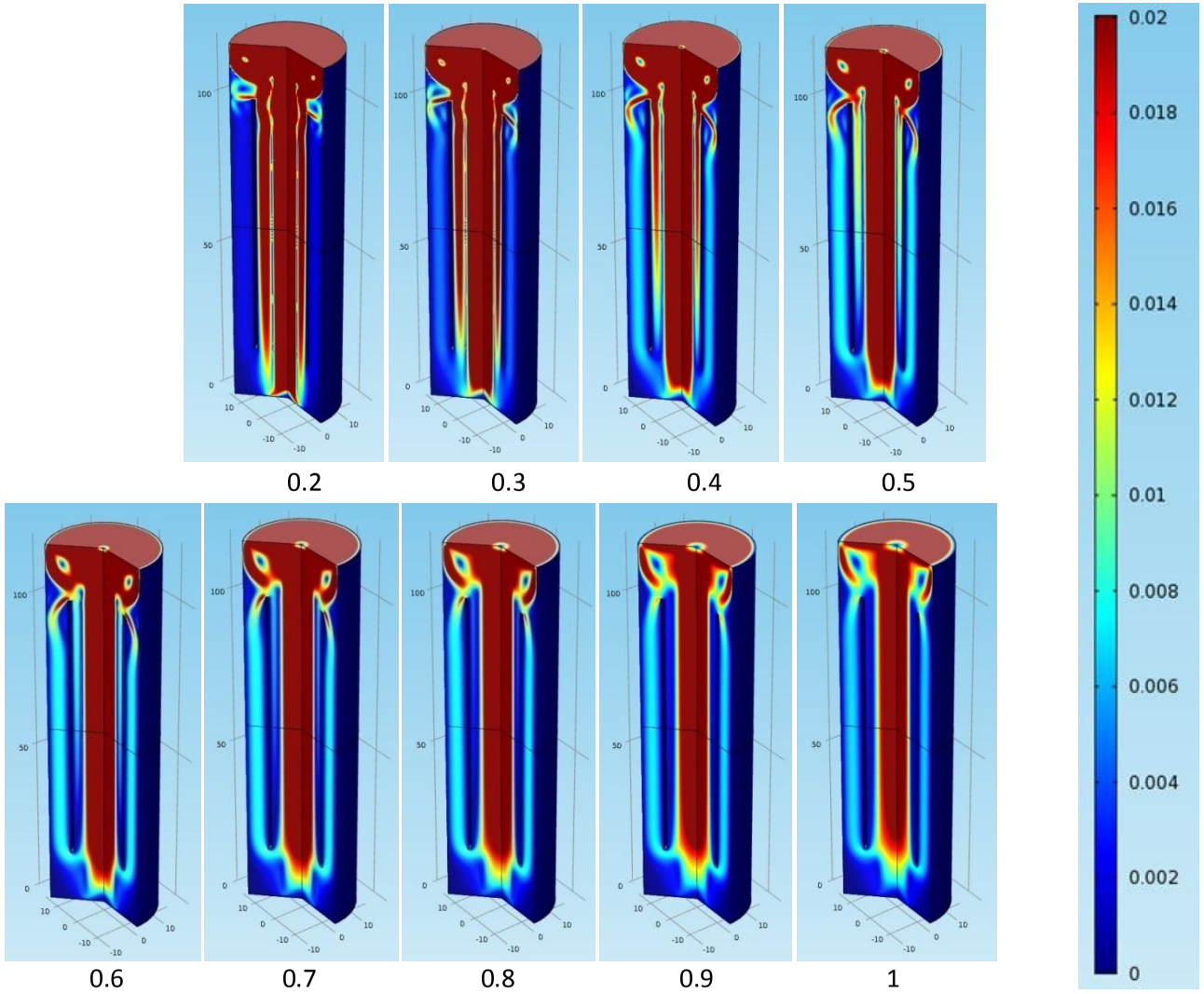

Bubble size (mm)	Maximum Velocity (m/s)
0.2	0.195
0.3	0.133
0.4	0.1013
0.5	0.08
0.6	0.0652
0.7	0.0545
0.8	0.0463
0.9	0.0405
1	0.0357

3.7.11 Fluid flow at 15 cc/min air with bubble sizes 0.2-1 mm in water + 1 M NaCl at 25°C

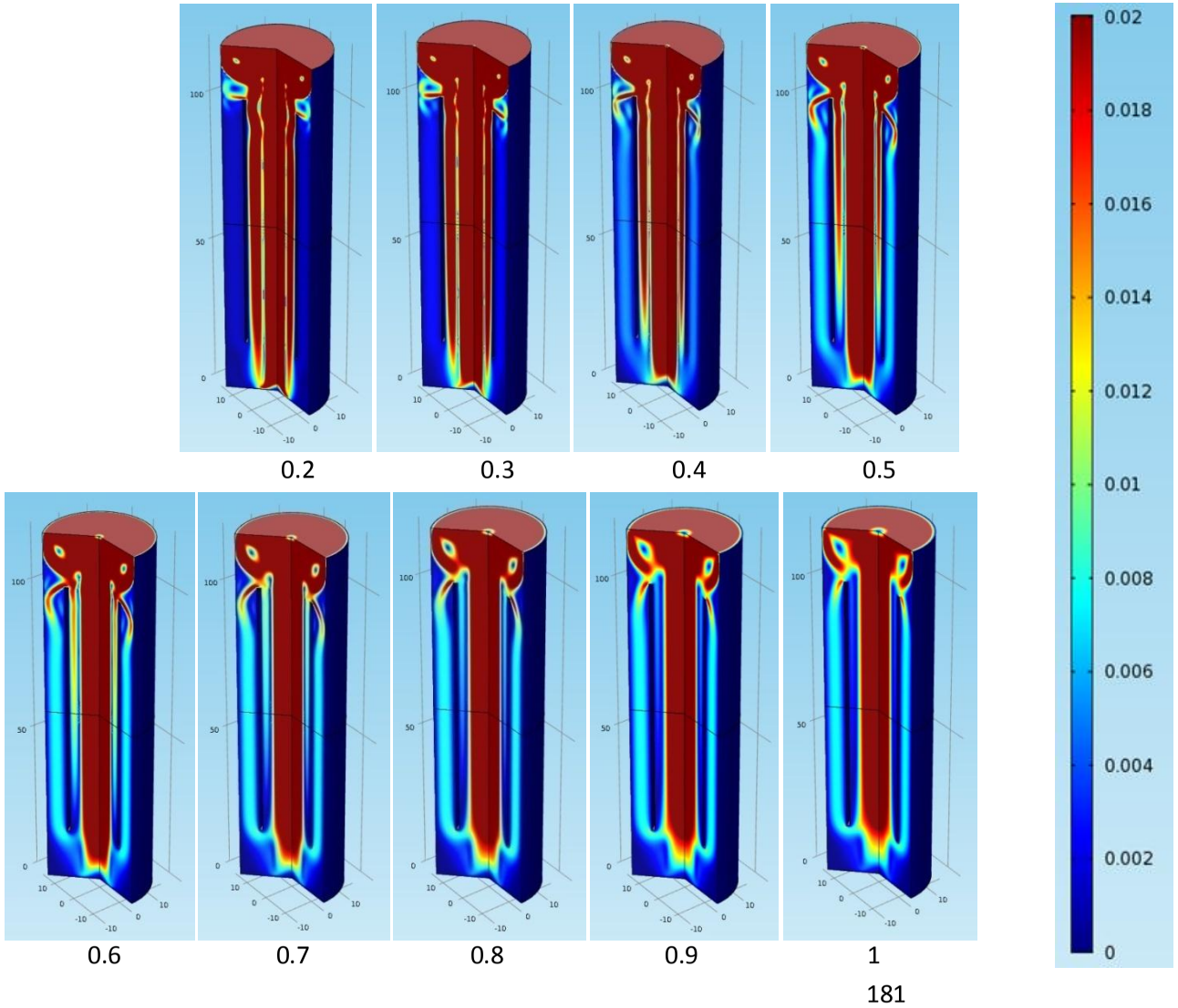

Bubble size (mm)	Maximum Velocity (m/s)
0.2	0.2385
0.3	0.1648
0.4	0.1267
0.5	0.1008
0.6	0.0826
0.7	0.0694
0.8	0.0594
0.9	0.0515
1	0.0453

3.7.12 Fluid flow at 20 cc/min air with bubble sizes 0.2-1 mm in water + 1 M NaCl at 25°C

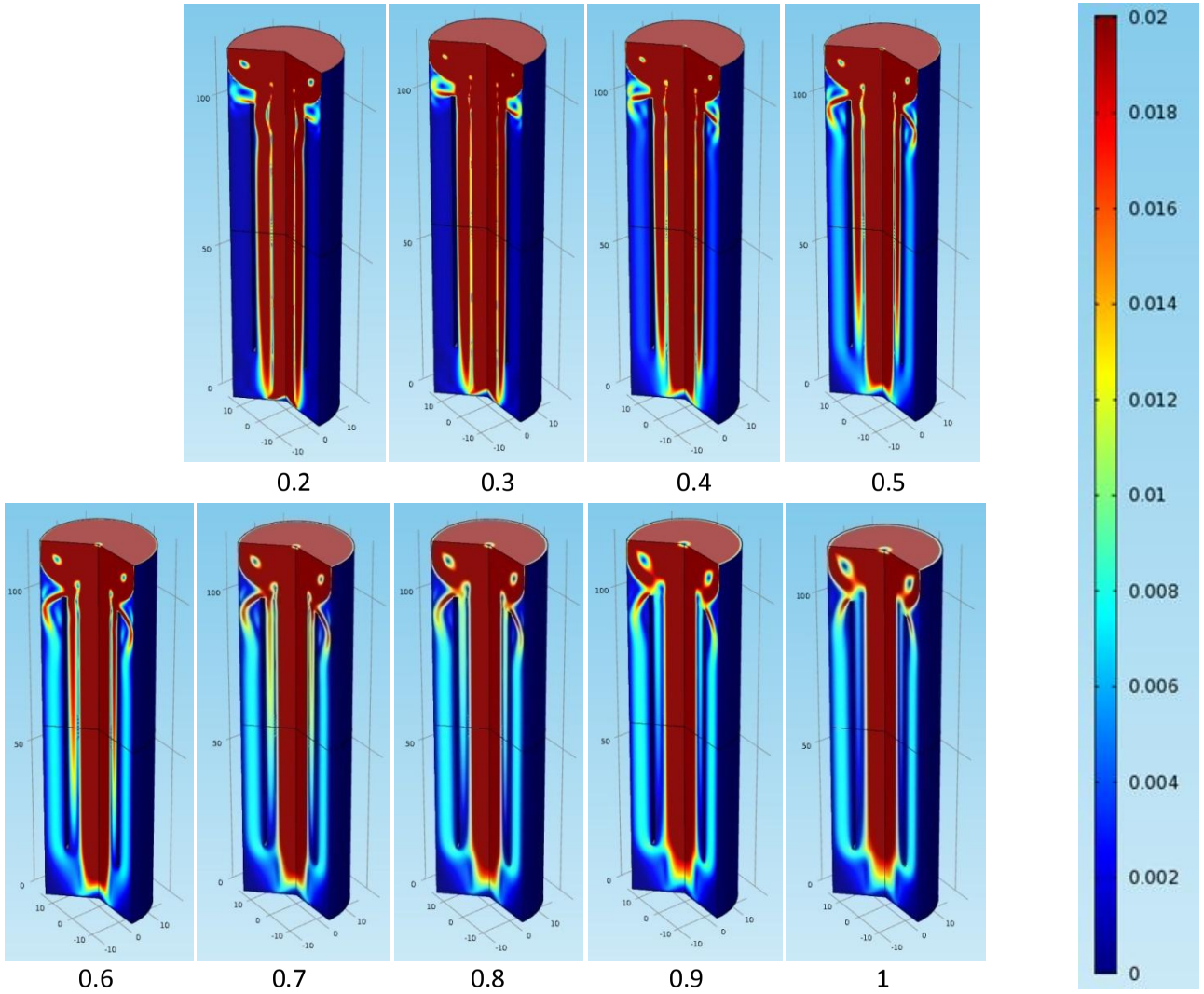

Bubble size (mm)	Maximum Velocity (m/s)
0.2	0.284
0.3	0.1915
0.4	0.148
0.5	0.1183
0.6	0.0973
0.7	0.082
0.8	0.0705
0.9	0.0614
1	0.0541

3.7.13 CFD results discussion

It can be seen from all the sets of CFD simulation data that the size of bubble has a significant effect on the overall mixing within the reactor. As the bubble size decreases beyond 0.5 mm under both media conditions, the airlift loop intensity is affected negatively. The significance of the effect is directly proportional to the overall rate of gas influx, which leads to the different flow rates producing optimal mixing at different bubble sizes. To clarify, if the downcomer values are used as the main indicator of mixing, in the 5cc/min case the optimal bubble size for mixing is 0.5-0.6 mm and in the 20 cc/min case 0.9-1 mm. This shift seems to be linked to the amount of backflow of fluid down the draft tube at the higher aeration rates. The maximum velocity in each simulation increased with decreasing bubble size (see Figure 3.28), which correlates well with the increased momentum transfer that smaller bubbles can achieve (Zimmerman, et al., 2010a). As the speed increases in the riser section, more liquid was pulled back down the draft tube, add to this the tendency for smaller bubbles to rise in narrower air columns which seemed to amplify the recirculation dampening effect.

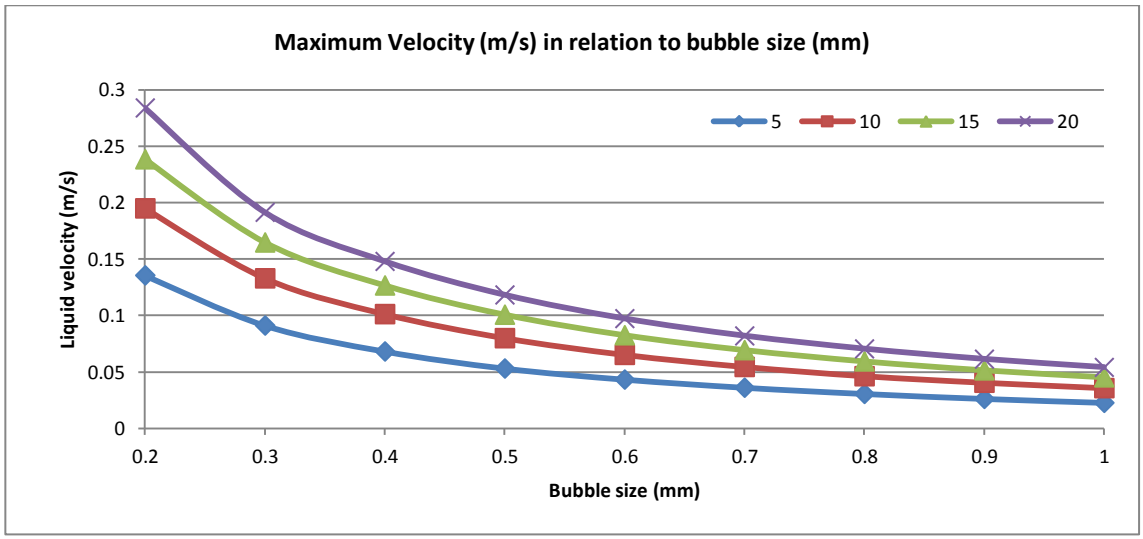

Figure 3.28. Compiled maximum velocity values (m/s) from the Mk II mini photo-bioreactor 1M NaCl water CFD simulations in relation to bubble size (0.2-1 mm) and gas flow rate (5-20 cc/min).

Given these findings, it could be possible to 'tune' the reactor mixing based on the draft tube height for a particular flow rate and bubble size, which has interesting implications. Also, interestingly, the addition of 1 M NaCl salt to the system seems to marginally enhance the mixing effects. Seen as the salting out effect reduces the bubble size down into the 0.5 mm range, and the 5 cc/min is optimal for mixing at that size, there seems to be an interesting correlation between this fact and the growth data collected in Chapter 4. Also, if the oscillator decreases the size of the bubble further still at this flow rate, it can be seen that slightly more

mixing will take place in the top section of the reactor, which could have knock-on consequences for cell breakage, as the bubbles will burst in this region and potentially cause more damage.

3.7.14 CFD and dye tracing simulation of Mk II prototype.

To ensure the mixing was following the predictions of the CFD models and would rapidly result in a homogenous mixture within the reactor, fluorescein dye was again added under UV lighting as a tracer. The results showed a great improvement over the previous Mk I design (Figure 3.29).

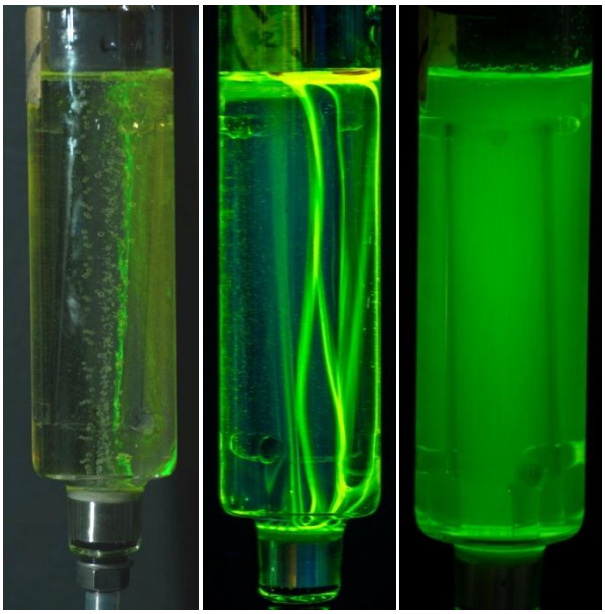

Figure 3.29. Fluorescein dye tracing of the 100ml Mk II photo-bioreactor design demonstrating the airlift loop effect (left, middle) and complete mixing (right).

3.8 The effects of flow induced cell breakage

Thorough mixing has a host of benefits in the production of microalgae (increased exposure to light, better mass transfer etc), however if the rates are too high, it can also lead to detrimental effects such as the breakage of flagella, membrane damage and eventually cell lysis. The effects of damaging shear stress on mammalian cells have been extensively studied in the field of medical related biotechnology for many years now (Hu, Berdugo and Chalmers, 2011). Although these cells are often radically different to microalgae, many of the lessons learnt from these studies are very much applicable to this field of research due to the fluidic scales involved. Mixing energy in photo-bioreactors is typically supplied by pneumatic or mechanical means (sometimes both). This energy is dissipated into the culture via bubbles or

propellers which form small eddies that distribute the energy to the liquid via shear forces. The sensitivity of a microalga to this shear force is a function of its strain type, cell wall (or lack of it in *D. salina*), size, morphology, the type of shear stress and culture conditions (e.g. osmotic stress) (Fernandez, Sevilla and Grima, 2013). If the amount of turbulence in a reactor is of sufficient intensity to produce fluid micro-eddies on the same scale as the cells themselves, then damage will occur (Kawase and Mooyoung, 1990).

The following equation by Chisti (1999) was used to calculate the Kolmogoroff microeddy length scale (l, meters) using the specific energy dissipation rate, to see if the geometry of the MkII reactor produced eddies of a similar size to *D. salina* cells in the riser section:

$$l = \left(\frac{\mu_L}{\rho_L}\right)^{3/4} E^{-1/4}$$

Where:μ_L = Viscosity of liquid (Pa Sec) - 0.000976 for 1 M NaCl water at 25°C, ρ_L = Density of liquid (kg/m^3) - 1041.279 for 1 M NaCl water at 25°C.

E is the specific energy dissipation rate (W/Kg) which is calculated using the frictional force that is overcome by the fluid flow as follows:

$$C_f = 0.0792\left(\frac{\rho_L U_L d}{\mu_L}\right)^{-0.25} \rightarrow \Delta P = 2C_f \frac{L}{d}\rho_L {U_L}^2 \rightarrow E = \frac{U_L \Delta P}{\rho_L L}$$

Where: U_L = average liquid circulation velocity in the riser tube (m/s), ΔP = Pressure drop (Pa) and L = length of the riser tube = 0.084 (m), C_f = Fanning friction factor (i.e boundary wall friction), d = riser tube diameter = 0.018 (m).

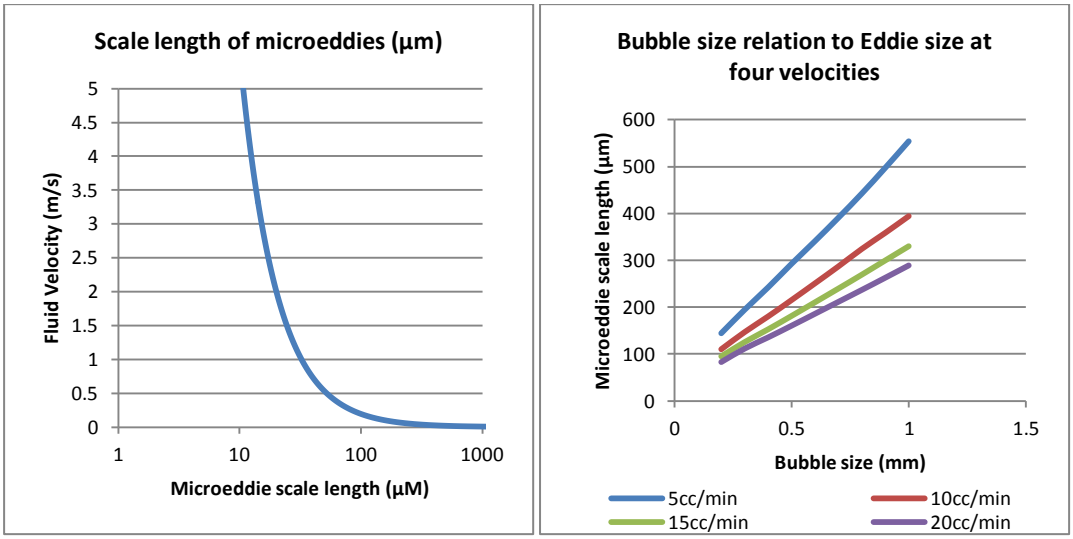

Figure 3.30. Left : A graph of microeddy scale length (µM) in relation to fluid velocity (m/s) in the Mk II mini photo-bioreactor riser section. Right : A graph of bubble size (0.2-1 mm) in relation to microeddy scale length (µM) at different aeration rates (5-20 cc/min) based on the Mk II mini photo-bioreactor riser geometry.

It can be seen that with an increase in velocity, the scale length decreases very rapidly (Figure 3.30). As the average size of a *D. salina* cell varies between in 5-30 µm long and 2.5-21 µm wide (Ben-Amotz, E.W. Polle and Subba Rao, 2009), there is potential for cell damage at high flow rates (i.e. > ~ 1 m/s). As the fastest flow rates occurred in the draft tube riser section of the CFD simulations, the maximum values obtained were put into these equations to see if any bubble size/flow rate combination could potentially create damaging scale lengths. Note that this might seem a slightly pessimistic approach since we are using local liquid velocity whereas the Fanning friction formula is based on the average velocity for turbulent flow down a pipe. However, unlike flow down a pipe, there are areas of high local shear in the reactor (i.e. the reversal of flow in the riser and at the top of the downcomer) and this justifies the use of the maximum local velocity to quantify the level of turbulence in the zones most likely to cause cell damage.

It can be seen that none of the conditions produce a length equal to that of the cellular sizes, but interestingly the smaller bubble results were the closest, if the trends were extended, it does indicate that micro-bubbles could potentially cause problems. However, it should be noted that the data is based on the maximum velocities produced from simulations that assume the flow is laminar. Hence, it could be argued that this analysis, which is based on turbulent eddies is flawed. In practice, this form of shear damage is unlikely to be a factor for normal bubble sizes, a conclusion that is backed up in the literature, where it is observed that damage seldom occurs in the airlift or bubble columns by this mechanism (Chisti, 1999;Miron,

et al., 1999). For smaller bubbles or micro-bubbles, however, these preliminary results suggest that shear damage is an effect that is worthy of further investigation.

Typically, most damage to algal cultures occurs due to interactions with the bubbles used for aeration and mixing. The work by Silva, Cortinas and Ertola (1987) demonstrated the fragility of a species of *Dunaliella* to mixing with bubbles. In their study, it was suggested that an upper limit of mixing occurred, beyond which cell death increased significantly. The cause of this was suspected to be in the three regions of gas liquid interaction; bubble formation, coalescence and rupture at the surface, based on the data gathered in previous mammalian cell studies. Interestingly, they also found that by increasing the viscosity of the medium with carboxymethyl cellulose and agar, the rates of cell death were significantly reduced. It is possible this effect was caused by the additives stabilising the bubbles by reducing the thin film drainage (Handacorrigan, Emery and Spier, 1989).

In 1995 another study was performed on *Dunaliella*. This time the species was *D. tertiolecta*(Suzuki, et al., 1995). In this research it was discovered that the alga grew optimally in a bubble column reactor, but when a baffle was added to convert it into an airlift type the rates of cell death increased. This effect was found to be caused by hydrodynamic stress, as the flow accelerated in into the downcomer region. However, in the bubble column setup, a threshold superficial gas velocity was also found which reduced growth rates. This result indicated that the addition of the loop effect, was potentially just amplifying the underlying effects due to faster mixing and thus greater hydrodynamic stresses.

In the paper by Barbosa, Hadiyanto and Wijffels (2004) it was found that the specific death rate of *D. salina* was directly affected by the gas entrance velocity (v) in the reactor setup if the values are above 30 ms^{-1}. As explained in the previous chapter, when a bubble forms at the sparger site it undergoes two main processes: firstly the bubble grows while attached to the surface, and secondly the buoyancy force causes the bubble to rise. When the bubble rises the neck connecting it to the surface narrows and eventually closes when the bubble breaks free. When this happens fluid rushes into this zone to fill the void, it is hypothesised that this is the region where cell damage occurs. This could possibly by due to the localised production of Kolmgorov eddies at the same scale as the cells (or even at smaller scales). If more pores or large pores are used for the same overall flow rates, the entrance velocity will decrease and hence so will the energy for cellular damage. If, however, the same volumetric flow of gas issues from a small number of very fine pores, this can be very damaging to cells, due to the scales being similar to the cell sizes. A key aspect of flow through fine pore spargers is that the flow can be highly asymmetric with most flow going through a small fraction of the available pores. This is examined in more detail below.

Using the simple gas entrance velocity equation from Barbosa, Hadiyanto and Wijffels (2004) a basic model was produced to predict the potential damage that could occur in the 100ml mini-reactor systems based on the velocity threshold:

$$v = \frac{F_g}{n \cdot \frac{1}{4} \cdot \pi d_i^2}$$

Where; F_g = the volumetric gas flow rate ($m^3\ s^{-1}$), n = the number of nozzles, d_i= the diameter of the nozzle (or pore in this case).

Based on the following parameters for the sparger material (Table 3.12) (Mahmood, et al., 2011), the surface area of the mini sparger, the velocity for each flow rate in the previous experiment can be calculated using the equation above:

Gas entrance velocity (v)		
Flow rate (cc/min)	**Flow rate (m^3/sec)**	**v (m/s)**
5	8.33333E-08	0.046907955
10	1.66667E-07	0.093815911
15	0.00000025	0.140723866
20	3.33333E-07	0.187631822

Mini Sparger properties (from (Mahmood, et al., 2011))*	
Pore number density (per cm^2)*:	10000
Pore number density (per m^2):	100000000
Pore diameter (µm)*:	20
Pore diameter (m):	0.00002
Area mini sparger (m^2):	5.65487E-05
Pore number mini sparger:	5654.866776

Table 3.12. Conversion of gas flow rates (cc/min) to gas entrance velocity (v) (left) based on sparger material data and geometry (right).

Note that the velocities above are the minimum values based on the unrealistic assumption that the gas flow is equally distributed among all the available holes. Experimental experience indicates that, in practice, gas issues from a very small fraction of the pores. Based on this observation, the gas entrance velocity can be plotted in relation to the number of 20 µm pores used (see Figure 3.31).

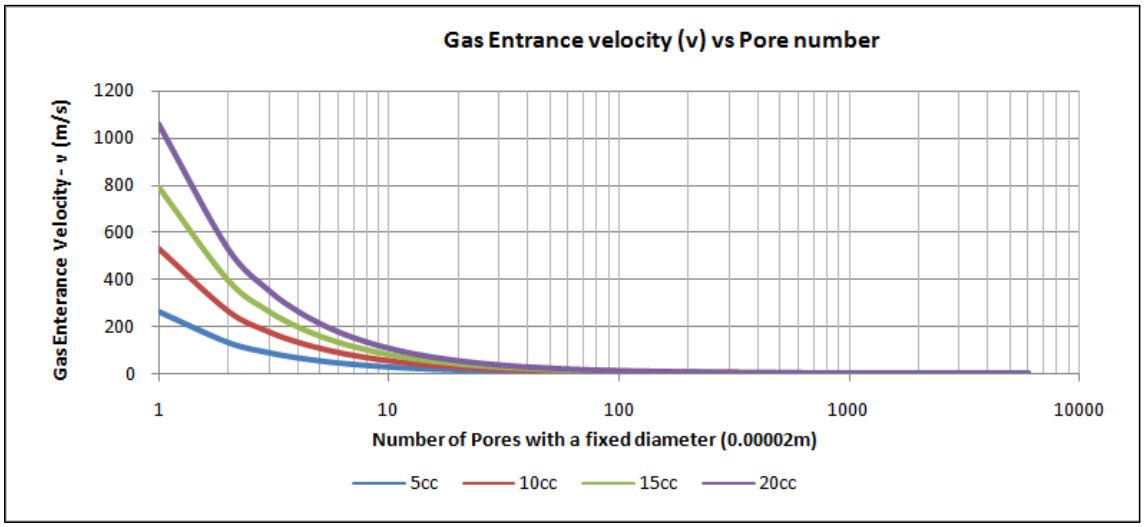

Figure 3.31.Graph of gas entrance velocity (m/s) in relation to the number of pores used with a fixed diameter (20µM) under four different gas flow rates (5-20 cc/min).

When the strain specific damage threshold of 30 ms^{-1} from Barbosa, Hadiyanto and Wijffels (2004) is applied to the graph (see Figure 3.32), it can be seen that, for the highest flow rate (20 cc/min) the largest number of pores (around 36) would need to be in use to avoid damaging the cells.

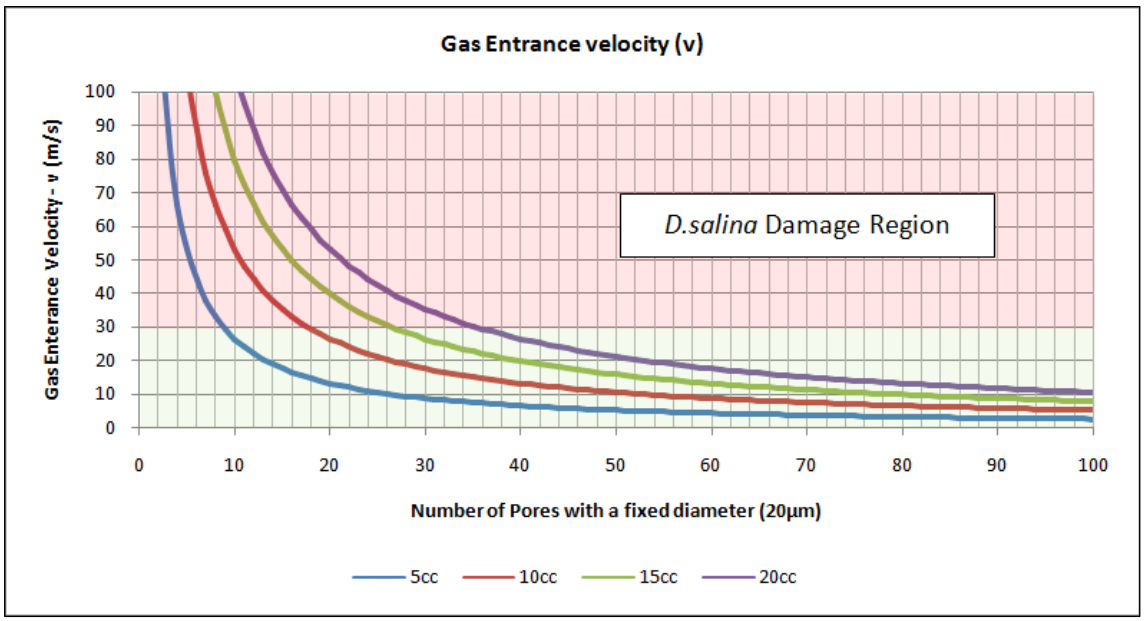

Figure 3.32.Graph of gas entrance velocity (m/s) in relation to the number of pores used with a fixed diameter (20µM) under four different gas flow rates (5-20 cc/min). Red region denotes gas entrance velocity capable of damaging *Dunaliella salina* cells (>30 m/s), green region shows safegas entrance velocities for culture of the alga.

A series of tests was performed to find out how many pores were in use at each different flow rate, with and without fluidic oscillation in distilled water and distilled water with 1M NaCl. The pore usage was counted by eye. Because of this five replicates were done to reduce error. The maximum value was 35, because counting beyond this was almost impossible due to the size of the bubble plume.

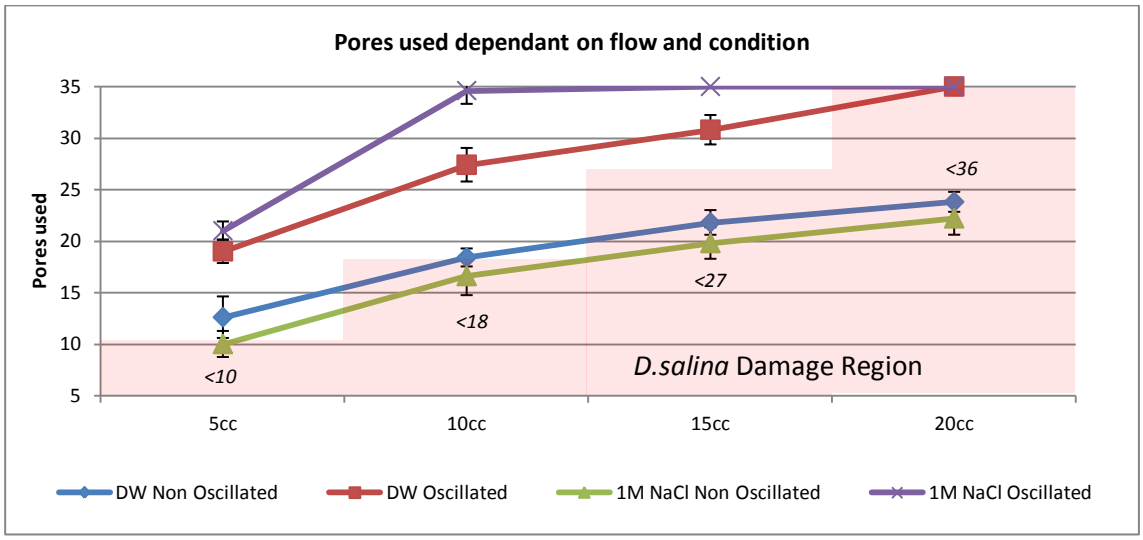

Figure 3.33.A graph of the number of pores used at four different gas flow rates (5-20 cc/min), under two different media conditions; distilled water with and without 1M NaCl, each with two types of aeration; oscillated and standard. Red region denotes the number of pores below which damaging effects to *Dunaliella salina* cells will occur at the four different flow rates.

It can be seen from the data (Figure 3.33) that the oscillated flows increase the number of pores in use in all conditions compared with regular flow. This result was expected, as the oscillation effect stops the development of bubble growth beyond the hemispherical growth stage and ensures there is no pore 'favouritism' due to decreased resistance (Zimmerman, et al., 2010a) , see section 3.4.5. Because of this, it is possible that oscillation could potentially make the hydrodynamic conditions safer for the cells by ensuring that the gas entrance velocity is lower than the damage threshold. This may be one factor that explains the difference between oscillated versus normal flow under CO_2 limiting conditions (see Chapter 4). However, further more targeted experimental work would be required to test this hypothesis.

Although the work by Barbosa, Hadiyanto and Wijffels (2004) indicates that cell death is caused almost exclusively in the gas entrance region, there is still a large body of evidence that implicates bubble rupture and coalescence as the main sources of damage (Cherry and Hulle, 1992). Physical observations of bubbles in cell cultures confirm that damage can occur around

rupturing bubbles at the liquid surface (Chalmers and Bavarian, 1991) and the effects of bubble cavitation have been modelled, demonstrating a 'blast radius' of cellular damage (Guzman, et al., 2003). It has also been found that the energy dissipation rate (EDR) significantly increases with the reduction of bubble size (Hu, Berdugo and Chalmers, 2011). This is significant because the EDRs generated (10^7-10^9 W/m^3 for 1-2 mm bubbles) are orders of magnitude bigger than those used for mixing in typical bioreactors (Hu, Berdugo and Chalmers, 2011). When this energy is translated to localised turbulence at the Kolmogorov scale, cells will be damaged. As bubbles are produced with smaller sizes due to fluidic oscillation, this factor could potentially cause increased instances of cell death, compared with regular flow. Further work is needed in this area.

3.9 Suggested Mk III design.

Based on the lessons learnt from the CFD simulation and the experimental work in Chapter 4, a further update to the micro-bubble mini-reactor is proposed (see Figures 3.34 and 3.35):

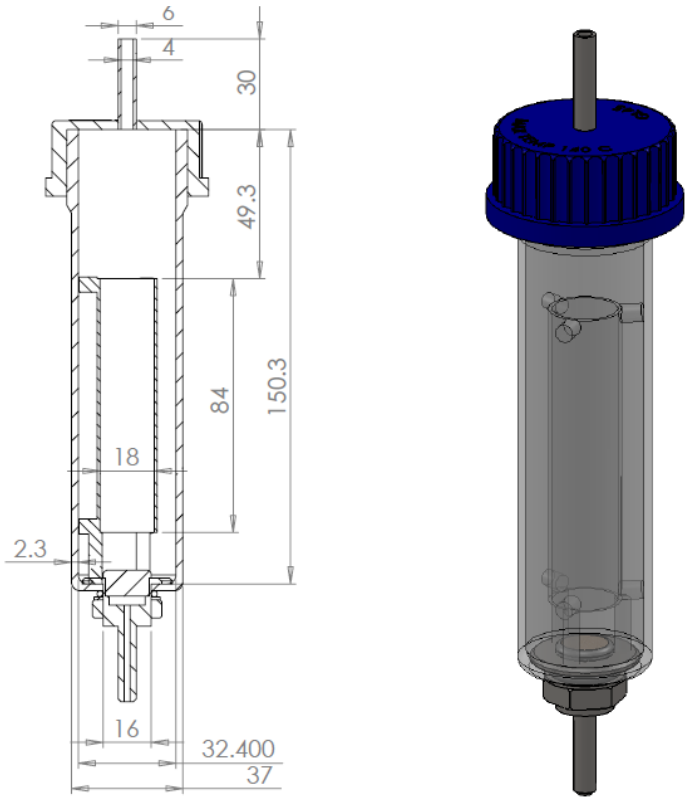

Figure 3.34. A suggested Mk III mini photo-bioreactor design featuring a enhanced seal around the sparger region.

The new sparger/body design would significantly reduce the problems faced in this study with algal flocks forming around the sparger seating within glass reactor tube. Another suggestion would be a push fit connection for the air feed to each reactor.

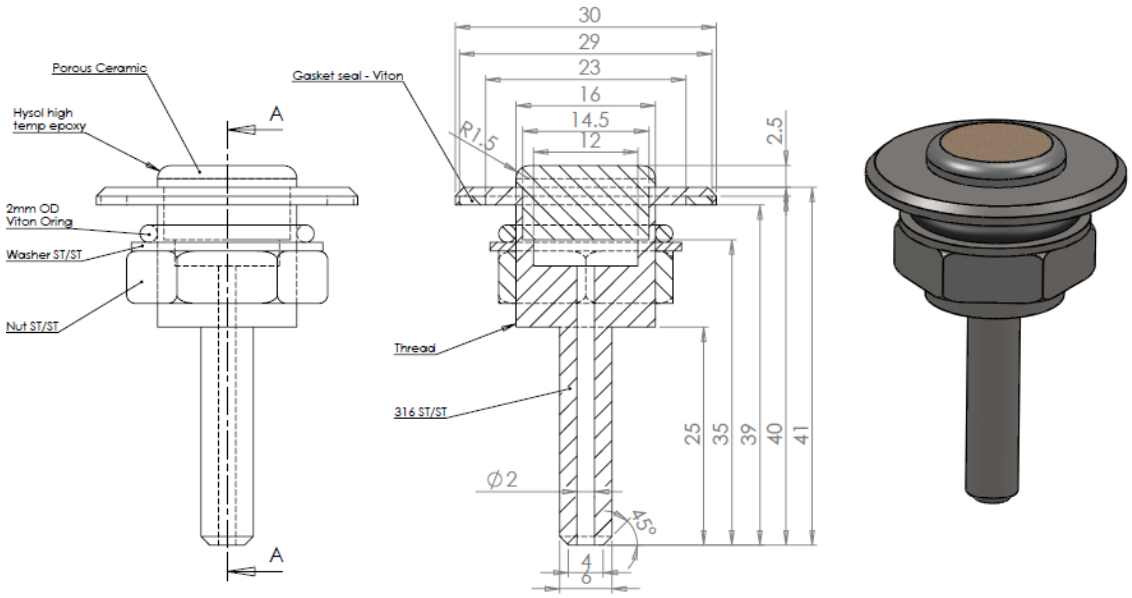

Figure 3.35. A suggested Mk III mini photo-bioreactor sparger design with a greater sealing area to avoid flock formation.

3.10 Conclusions

The modelling and experimental work in this section has been very informative in predicting the mixing behaviour of all photo-bioreactors used in this study. The CFD models have been used to demonstrate why the Mk I mini photo-bioreactors were producing ineffective mixing and growth, which was validated by dye tracing observation. The models also indicated what the effect of changing the geometry would have, which led to the development of the Mk II prototype design. This second design has been successfully used for testing the effects of micro-bubbles (Chapter 4). CFD testing of this Mk II design has revealed that the size of the bubbles and the gas influx rate have a large impact on the effectiveness of the overall design, opening the possibility for future work that could tailor the design of a reactor based on the average bubble size. Inversely, given that power reduction rates of up to 18% have been demonstrated using the oscillator and the fact that smaller bubbles produce faster mixing (Mahmood, et al., 2011), existing designs could also be analysed and 'tuned' to maintain the same levels of mass transfer and mixing at a lower operating cost.

The CFD flow results were also used to predict the impact of shear stress in relation to bubble size using the concept of the Kolmogorov eddie scale. Experimentally, the impact of shear damage was also looked into at the sparger surface based on the superficial gas velocity. The data from this indicated that fluidic oscillation could have an unexpected benefit, by increasing the number of pores used in a sparger. However, this effect could possibly be offset by the

potential destructive effects of a smaller bubble size at the fluid surface. Based on these findings there is further interesting research work that should be performed. The impact of fluidic oscillation on sparger shear damage is completely virgin academic territory. Further work to understand the effect that this new technology has on fragile cells and the way in which shear damage can be minimised looks to be an exciting avenue for further investigation in the same spirit as the work of Silva, Cortinas and Ertola (1987), which demonstrated that *Dunaliella*cell death could be reduced by extracellular glycerol.

4 Microalgal Growth and Lipid Analysis

4.1 Introduction

To test the impact of micro-bubbles on algal growth rates and lipid productivity, a stable model organism was needed. The alga *Dunaliella salina* 19/30 was selected for this purpose, based on the previous successful pilot scale studies conducted by Zimmerman, et al. (2011) using the same strain for testing micro-bubbles. The alga's inherent ease of harvest and resilience to contamination due respectively to its lack of cell wall and halophilic adaptations were also key factors in its inclusion in this study (Hosseini Tafreshi and Shariati, 2009). A series of initial experiments were performed using un-aerated flasks to establish effective lipid testing techniques and the best salinity media for growth. This was then followed by a series of photo-bioreactor experiments which looked at the impact of micro-bubbles and different flow rates on the productivity of the strains.

4.2 Lipid analysis and method development

Many methods of stress induced lipid production have previously been studied in strains of *Dunaliella,* including; nitrate depletion (Jiang, Yoshida and Quigg, 2012), nutrient deprivation (Roleda, et al., 2013), temperature variation (Thompson, 1996), light exposure (Park, Lee and Jin, 2013) and various combinations of these stresses (Mixson and Burkholder, 2012), but given the nature of the current work with micro-bubbles, the effects of NaCl stress have the greatest synergy in this study. Salt stress induced lipid synthesis in *Dunaliella* has been studied a few times in the past three decades, but the comparability of lipid response and composition between the different publications is made very difficult due to the different sub strains used, which often have poor/contradictory identification (Olmos, et al., 2009; Oren, 2005). A selection of the most applicable literature and lipid findings are summarised in Table 4.1.

Table 4.1. Key studies examining the effect of salt stress on lipid production and composition in various strains of the green alga *Dunaliella.*

Dunaliella Strain	Conditions (media, temp, light)	Lipid method used	Increase lipid w/NaCl	Decrease lipid w/NaCl	Ref:
Isolate from Antarctic hypersaline lake (no genetic ID)	0.4,1.0,1.6,2.2,2.8,3.4, 4.0 M NaCl, PHK medium. 10^{O}C. 45µE m^{-2} s^{-2}.	Gravimetric, Trans-esterification, GC-FID	Sat-FA and mono-unsat-FA	PUFA	(Xu and Beardall, 1997)
D. tertiolecta ATCC 30929	0, 0.5, 1, 1.5, 2 M NaCl NORO medium. 28-30^{O}C. 65-150 µmol $s^{-1}m^{-2}$.	Gravimetric, Triacylglyceride G-test.	Addition of 0.5 & 1.0M NaCl +ve 1.4-4.1% TAG	N/A	(Takagi, Karseno and Yoshida, 2006)
Isolate from salt marsh in Kuwait (no genetic ID)	Custom media w/2.5 & 20% NaCl. 22^{O}C 61µE m^{-2} s^{-2}.	Gravimetric, TLC, IR-spectroscopy, GLC-GC.	PUFA	Sat-FA and mono-unsat-FA	(Alhasan, et al., 1987)
Dunaliella sp Aquiculture Technology Center (Fortaleza-CE) bank	25 & 35 g/L F/2 medium. 28^{O}C. 600 µerg/cm^{2}s	Gravimetric.	Oil yield (w/w %) NaCl 25g/L: 12, NaCl 35g/L: 30.12	N/A	(Araujo, et al., 2011)
D. Salina Culture collection of Dr W H Thomas, La Jolla, CA.	0.5 & 3.5 M NaCl adjusted custom media by (Benamotz and Avron, 1983) . 25^{O}C. 10 kergs cm^{-2} s^{-1}.	Gravimetric, Trans-esterification, GC	C18:1-4 FA types in plasma membrane*	C16 FA in plasma membrane*	(Azachi, et al., 2002) . **Note, see paper amendment in lit*
D.Salina (UTEX 1644)	0.85, 1.7 & 3.4M adjusted custom media by (Lynch and Thompson, 1982) NaCl. 30^{O}C. 100 µmol $s^{-1}m^{-2}$.	Gravimetric, TLC, Trans-esterification, GC	C18:1-2 FA in plasma membrane	C18:3 FA in plasma membrane	(Peeler, et al., 1989)

It can be seen from Table 4.1. that the lipid data is fragmented and in some cases the findings are contradictory. This is probably due to the different strains used and the lipid extraction methods employed. Based on this research, it appears there have been no studies to date looking at the effects of salt stress on *D. salina* 19/30 and 19/18 with a particular emphasis on neutral and total lipid quantification for biofuel production. This gives an opportunity for novel research to be performed in this area alongside the unique aspects of the micro-bubble and photo-bioreactor development work, but first, an appropriate method of lipid analysis needed to be selected.

There are many different methods of measuring lipid productivity within the scientific literature (see section 1,10 Table 1.9 above), but thus far in general, there is a lack of consensus within the algal community on a particular standard on which should be adhered to. One of the biggest reasons for this difference is the fact that lipid methods tend to be fundamentally strain specific in terms of the pickup of a particular region of a strain's lipid profile. This makes any form of accurate data comparison between studies very difficult and quite often the results themselves can have very large error margins. Due to this situation, of the range of techniques represented in the literature, the ones that could be performed using the facilities available at Sheffield University were considered based on a series of selection criteria (Table 4.2). Ratings were given from 0-10 in each category based on an estimation of how they would suit the species of *D.salina* used in this study.

Table 4.2 - Comparison of lipid methods available in this study, green highlights indicate methods used in this study.

Analysis method:	Lipid Specificity:	Rating:	Time total (h):	Rating:	Outlay:	Rating:	Quantification:	Rating:	Sample size needed:	Rating:	Total (average):	Reference:
Micro Gravimetric	Total Lipids	3	72	3	Basic solvents	9	Difficult, highly variable. Large biomass needed.	4	Large >10mg biomass	2	21 (4.2)	(Bligh and Dyer, 1959)
Colorimetric	Total Lipids	4	48	5	Basic solvents + cheap reagent	8	Difficult and variable.	5	Large >10mg biomass	2	24 (4.8)	(Vanhandel, 1985)
Rapid Colorimetric - 96 well plate format	Total Lipids	5	48	5	Basic solvents + cheap reagent, std micro-plates	7	Difficult and variable.	5	Large >10mg biomass	3	25 (5)	(Cheng, Zheng and VanderGheynst, 2011)
Nile Red Staining (Fluorometric)	Polar & Neutral (depending on signal overlap)	7	3-4	8	Expensive dye, standards and filters. Std micro-plates.	6	Standard comparison very difficult. Relative values good.	6	Very low $1x10^6$ cells	9	36 (7.2)	(Alonzo and Mayzaud, 1999;Cooksey, et al., 1987,Chen, et al., 2009)
FTIR	Entire Composition (limited groups due to signal overlap)	8	1-2	9	Standards only.	8	Very difficult and variable due to machine.	4	Medium 5-10mg biomass	6	35 (7)	(Dean, et al., 2010;Laurens and Wolfrum, 2011)
Direct Trans-esterification + MS-GC	Entire Composition	9	24-48	6	Basic solvents and vials. Standards and machine time expensive.	4	Very precise and consistant (depending on column).	9	Med-Large ~10mg biomass	5	33 (6.6)	(Griffiths, van Hille and Harrison, 2010; Laurens, et al., 2012)
NMR	Entire Composition (limited groups due to signal overlap)	7	48	5	Basic solvents, reasonable machine time costs.	6	Generalised assumptions made, but very consistent.	8	Medium 2-10mg biomass	7	33 (6.6)	N/A - In house

Based on this comparison the Nile Red, Direct transesterification and NMR techniques were selected for use in this study. The Nile Red method was used to monitor cultures for general lipid trends due to the low amounts of biomass needed. The NMR and direct transesterification methods were used to provide more detailed lipid analysis. It is worth noting that although the FTIR method is very good overall, difficulties in machine setup for quantification and the lack of a dedicated technician made NMR a more preferable technique for use in this study (for interest preliminary data using this method is included in appendix I). Wherever possible, to aid in reliable quantification and comparison with other studies, lipid amounts have been expressed in quantities related to the physical amount of biomass present in this study.

4.2.1 Cell Fragility

In Chapter 3 the fragility of *D. salina* cells was discussed, due to the lack of a rigid cell wall they are highly susceptible to physical damage and osmotic shock. In a bid to ensure that losses of cell contents were minimised during harvesting by centrifugation, a series of tests were performed using chlorophyll (section 2.6.4) as an indicator, as the cell membrane has to be damaged to release chlorophyll from the cells. *D. salina* 19/30 was grown in the MBB growth room (section 2.8.2, middle shelf) in three molarities of Dunaliella medium (1-3 M NaCl). When stationary phase was reached (23 days), 20 ml of culture was taken in triplicate from each flask. The chlorophyll procedure was followed four times per condition, the first with no washing, then subsequent additional washing steps were added to the procedure. Each of the additional washing steps was centrifuged for 5 minutes rather than 10 minutes and 5 ml of distilled water was used for re-suspension. The results are shown in Figure 4.1.

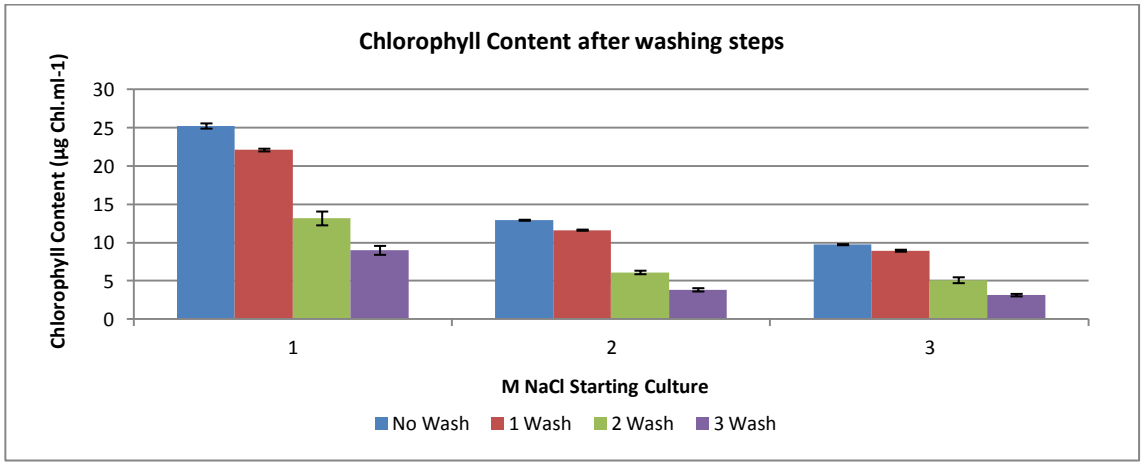

Figure 4.1. Chlorophyll content of *D. salina* 19/30 cells measured after varying amounts of washes in distilled water. Cultures grown in three different molarities (1, 2 and 3 M NaCl) of Dunaliella medium were tested.

Based on the data shown in Figure 4.1, it was found that beyond one washing step cell breakage or leakage dramatically increased. As some washing was required to remove the salt, one washing step was used for all future extraction procedures.

4.2.2 Nile Red Method Development

Nile red (9-diethylamino-5H-benzo[a]phenoxazine-5-one or $C_{20}H_{18}N_2O_2$) is a highly effective fluorescent dye typically used for the detection of lipid droplets by fluorescence microscopy and flow cytometry using a fluorescence-activated cell sorter [FACS] (Guzman, et al., 2012). The lipid staining properties of Nile Red were first discovered by Smith and Thorpe in the early part of the 20th century (Greenspan, Mayer and Fowler, 1985; Smith, 1908; Smith, 1911; Thorpe, 1907). Smith found that the phenoxazone Nile Red was entering the neutral lipid droplets and producing an intense fluorescence (Smith, 1908). This attribute was not fully exploited until Greenspan, Mayer and Fowler (1985) used the stain as a lipid soluble fluorescence probe in 1985.

4.2.2.1 Dye behaviour

In their work Greenspan & Fowler performed a detailed chemical and physical characterisation of the stain and its effects on living cells in a series of seminal papers in the late 1980s (Fowler, et al., 1987; Fowler and Greenspan, 1985; Greenspan and Fowler, 1985; Greenspan, Mayer and Fowler, 1985). They found that the dye was reasonably photostable, highly fluorescent in many organic solvents and hydrophobic environments (with the exception of heptane and higher alkanes), but poorly so in water, with a low emission efficiency (or quantum yield) (Elsey, et al., 2007; Fowler, et al., 1987; Greenspan and Fowler, 1985). In comparison with other solvents water quenched the dye fluorescence by up to 40 times, enabling it to be used as an efficient hydrophobic lipid fluorescence probe in most biological applications due to the high contrast between the background and stained cells (Greenspan and Fowler, 1985).

Depending on the hydrophobicity of the solvent used, the maximal excitation and emission wavelength for the Nile Red stain was found to vary considerably (over a range of 100 nm). Because of this behaviour, the dye can be classified as solvatochromistic and red-shifts in relation to the dielectric constant of the solvent (or blue-shifts as the solvents polarity decreases)(Cooksey, et al., 1987; Greenspan and Fowler, 1985). This fact allows the dye to be used to differentiate between the two main lipid types (polar and neutral) depending on the peak excitation and emission wavelengths used (Elsey, et al., 2007). The wavelengths that

Greenspan determined were 549/628 nm for polar lipids and 480/575 nm for neutral lipids (excitation and emission respectively).

4.2.2.2 Algal applications and issues

Although Greenspan pioneered the use of Nile Red assays in living biological cells in 1985, it wasn't until the work of Cooksey, et al. (1987) that fluorescent quantification of lipids was performed in microalgae. Cooksey combined Nile Red with acetone to stain various strains of diatoms and green algae in situ. His work included fluorescence microscopy, flow cytometry, spectrofluorometry and lipid quantification experiments to prove the method viable for strain selection and monitoring of neutral lipid synthesis as a basis for biofuel production. Cooksey et al also noted that the time it took for the stain to reach peak fluorescence varied and suggested that individual species may have different stain absorption rates possibly related to cellular permeability and lipid globule sizes. This hypothesis was subsequently proven correct in follow up studies, which showed the cell walls of different species have a large effect on the level of dye penetration (Chen, Sommerfeld and Hu, 2011; Chen, et al., 2009) and there is also a time delay in the dye getting through the lipid membrane and into the lipid globules (Pick and Rachutin-Zalogin, 2012). However, one crucial area that was mostly overlooked in Cooksey's work (and that of others that subsequently followed) was the fluorescence interference effects caused by both types of lipid being present at the same time and read at a fixed wavelength. This factor was looked at in great detail by Alonzo and Mayzaud (1999), and they demonstrated that the wavelength spectra for isolated algal lipids overlapped. Hence at any particular wavelength the fluorescence intensity for total lipid was a sum of fluorescent responses in different ratios (Figure 4.2). Whereas in previous work by Cooksey and Greenspan the selection of excitation and emission wavelengths had been chosen to minimise interference between polar and neutral lipids with the use of the 549/628 nm (polar) and 480/575 nm (neutral) wavelengths, Alonzo and Mayzaud suggested that selection should instead be based on maximising fluorescence sensitivity to increase accuracy and

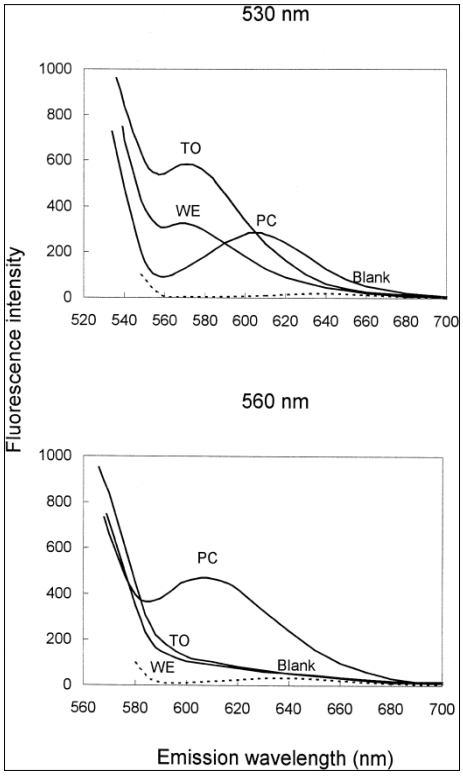

Figure 4.2 Demonstration of overlapping emission spectra for isolated algal lipids.- PC = Polar lipids, TO=Neutral lipids, WE=Waxy esthers (Alonzo and Mayzaud, 1999)

demonstrated that 560/610 (polar) and 530/580 (neutral) would be better optimised. Their work also had two other key findings and suggestions. Firstly the use of lipid standards such as triolein induced large errors in quantification and could only be used with relative units, they suggested that if they were to be used a ratio of 1:20 (polar lipid to neutral) would be needed to produce a stable micro-emulsion. Secondly, only lipid standards derived from the organism under study could be used to provide accurate quantification (errors lower than 5%) when calibrated with the interference between the polar and neutral lipids in the fluorescence signal.

Recently the Nile Red method has been adapted to a 96 well microplate format for high throughput screening of strains, using some of the recommendations mentioned previously (Chen, Sommerfeld and Hu, 2011; Chen, et al., 2009; Held and Raymond, 2011). The method of Chen et al brought many advancements (aside from the rapid format); the use of 25% dimethyl sulfoxide (DMSO) as the Nile Red solvent to get the stain through tough cell walls, microwaving to also help in this process and the use of higher optimal temperatures (35-40^{o}C) to increase the reaction time (Chen, Sommerfeld and Hu, 2011). The experiments of Chen et al also proved that in practical applications the use of the 560/610 nm wavelengths to detect the polar lipids was not feasible due to interference from algal chlorophyll auto-fluorescence in that part of the spectrum (Chen, et al., 2009). Other microplate variations using different combinations of the former methods have also been tried recently in academia (Gardner, et al., 2011; Gardner, et al., 2012) and by biotech firms (Held and Raymond, 2011). However, many issues still remain regarding accurate quantification of the types of lipid using the Nile Red process. One potential solution was suggested by Bertozzini, et al. (2011) using the standard addition method (Bader, 1980) for quantification of neutral lipids with a triolein standard. Previous methods determined unknown quantities of lipid by comparing them with a single standard or calibration curve made from multiple standards. These methods are only truly effective if all samples are the same, but algal samples can vary radically in composition depending on the environment they are exposed to, making the calibration error prone. The standard addition method reduces the number of parasitic errors by incorporating the algal variations into the direct proportionality of the flourescence signal, this is done by 'spiking' algal cultures of a fixed cell concentration with varying amounts of triolein to produce a lipid calibration curve.

In this work, a series of Nile Red staining protocols have been developed which are drawn from the literature discussed above. The protocols were developed using different salinities of medium (1-3 M NaCl) to look at the effects of different salinity media on Nile Red staining, nitrogen deprivation was also studied in 1 M NaCl medium for comparison purposes.

4.2.2.3 Nile Red Fluorescence Microscopy

To visually confirm if the Nile Red stain could penetrate into the *D. salina* lipid vesicles and label them in the correct manner, a series of images were taken using a Nikon Eclipse E400 fluorescence microscope equipped with a Nikon DXM1200 Digital Camera using a method based on the work by Cooksey, et al. (1987) and Pick and Rachutin-Zalogin (2012) (see section 2.2.2.2). The samples were excited with a monochromatic optical filter with band pass of 450-490 nm, which corresponded with the 480 nm wavelength specified by Greenspan, Mayer and Fowler (1985) and Cooksey, et al. (1987) for neutral lipids. For qualitative sample contrast, nitrate depleted cultures were used alongside regular cultures as they have been proven in the literature and previous tests to have the largest amounts of lipid production.

All cultures were grown in variations of Dunaliella medium (see below) from a 14 day old progenitor culture which was acclimatised to the standard 1 M NaCl growth media variant. The following cultures and media were used; Dunaliella medium 1 M NaCl – as a control, under the same conditions as the progenitor culture (Figure 4.3B). Dunaliella medium 1 M NaCl with $1/10^{th}$ of the normal nitrate (Figure 4.3A) – leading to nitrate deprivation in the second week of growth. Dunaliella medium 2 M NaCl (Figure 4.3C) – giving the culture an osmotic shock of double molarity NaCl and Dunaliella medium 3 M NaCl (Figure 4.3D)– resulting in an even greater osmotic shock.

A

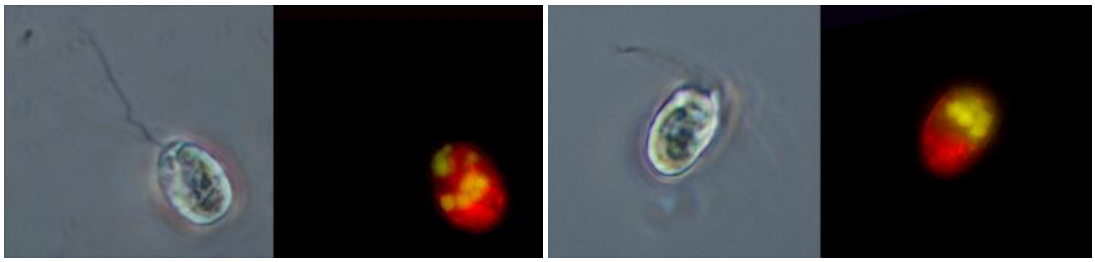

B

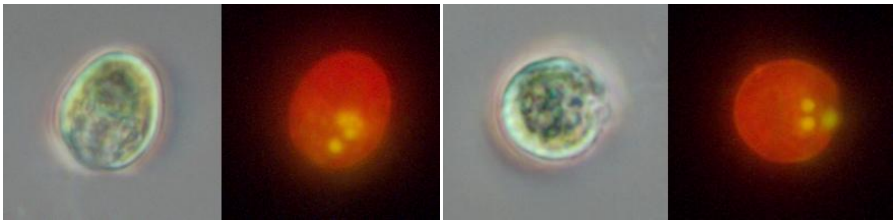

C

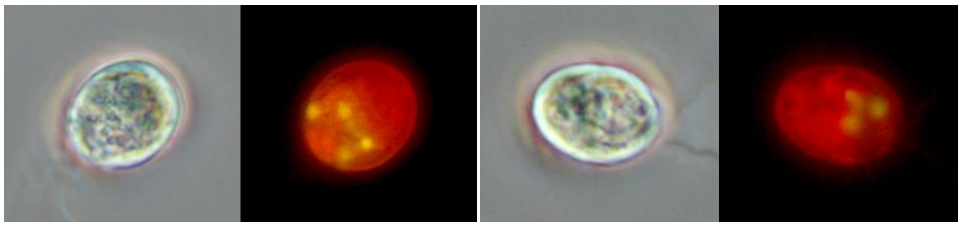

D

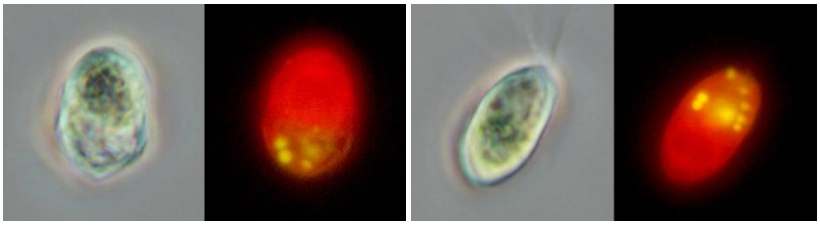

Figure 4.3. Fluorescence microscopy images of *D. salina* 19/30 cells stained with Nile Red after exposure to different growth conditions. A) Cells grown for 16 days in 1 M NaCl Dunaliella medium with 1/10th nitrate; B) Cells grown for 17 days in 1 M NaCl Dunaliella medium (control); C) Cells grown in 2 M NaCl Dunaliella medium for 17 days and D) Cells grown for 17 days in 3 M NaCl Dunaliella medium. Images show the same cell under non-fluorescing and fluorescing conditions. Red = chlorophyll autofluorescence and yellow = neutral lipid droplets.

The results showed a marked increase in yellow fluorescence associated with neutral lipid droplets in the nitrate depleted strains (Figure 4.3A), as expected (Jiang, Yoshida and Quigg, 2012), but the 1 – 3 M NaCl cultures were slightly more ambiguous, it was difficult to tell if increasing salinity stress induced more neutral lipid synthesis (Figure 4.3B, C and D). However under all grown conditions, neutral lipid droplets were clearly visualised under the fluorescence microscope, thus further method development was justified.

Background artefacts:

It was also worth noting that during image processing, many background artefacts were observed, which corresponded with information given in the literature (Figure 4.4).

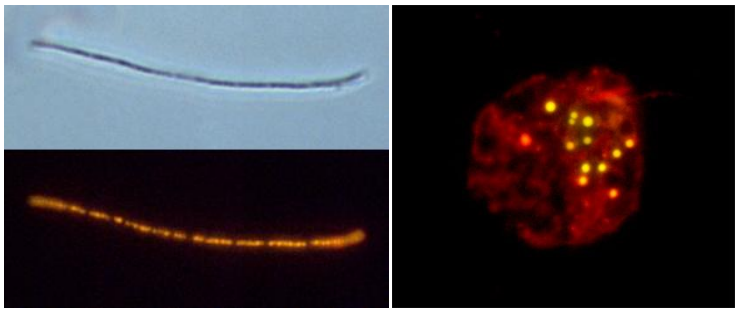

Figure 4.4. Right – A lysed cell releasing its lipid vesicles, this was especially prominent in the nitrate deplete cultures which could indicate greater fragility. Left – shows contamination from bacteria (suspected to be halotolerant *Halomonas elongata*).

As shown in Figure 4.4, there were a number of dead (lysed) cells in the nitrate deplete cultures. Lysed cells have been suggested as a source of increased background interference by Cooksey, et al. (1987). Evidence of bacterial contamination was also notedthis could also cause significant background interference due to their turbidity effects and inherent lipid stores within the bacterial cells (Figure 4.4).

Following this initial microscopy work, further tests were performed based on the methods described by Cooksey, et al. (1987), Gardner, et al. (2012), Chen, et al. (2009) and Bertozzini, et al. (2011), using Nile Red with both acetone and DMSO as solvents (data not shown). It was eventually decided that the acetone solvent method, would be better to proceed with because the disposal of used DMSO solvent is more troublesome and the chemical is skin permeable. As *Dunaliella* lacks a cell wall, DMSO is also considered to be unnecessary as an aid to dye

penetration. In addition, the decision was also made to stick with the wavelengths of 490 and 580 nm for excitation and emission respectively, due the appropriate mono-chromatic filter being readily availability. It is acknowledged that using these wavelengths will reduce the overall sensitivity of assays (Alonzo and Mayzaud, 1999), but given the data gathered will be chiefly used in comparison tests, the signal should be valid. Recent studies by Davidi, Katz and Pick (2012), Gardner, et al. (2011), Gardner, et al. (2012) have successfully demonstrated these wavelengths are suitably accurate for this purpose.

4.2.2.4 - Nile Red Spectrofluorometery

To ensure that the fluorophore was producing the correct Stokes shift and amplitude of signal within the band-pass of the lab plate reader's fixed monochromators a series of tests were performed based on the work by Bertozzini, et al. (2011) using a Horiba JobinYvon Fluromax 4 Spectrofluorometer (see section 2.2.2.1). The effects of triolein spiking (Figure 4.5) and salinity (Figure 4.6) were looked at in detail using this method.

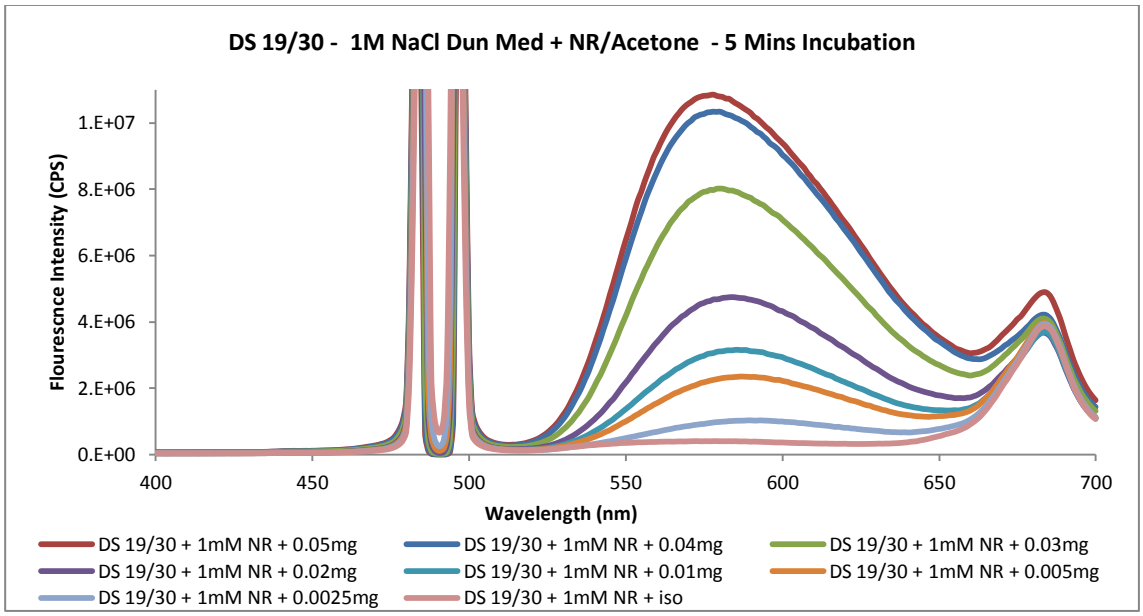

Figure 4.5. Triolein spiking using the standard addition method with *D. salina* 19/30 cells grown in 1 M NaCl Dunaliella medium. Nile Red was dissolved in acetone, incubation time was 5 minutes. Triolein was dissolved in isopropanol and added in amounts between 0.0025 mg to 0.05 mg.

The data from this test shown in Figure 4.5 demonstrated that the excitation and emission are in the correct range for the plate reader and there is an excellent correlation over the range of Triolein concentrations (0.0025 - 0.05 mg).

The effects of changing media salinity were looked at next to see if fluorescence was quenched as reported by Pick and Rachutin-Zalogin (2012).A culture of *D. salina* 19/30 in 1 M NaCl Dunaliella medium (25 days) was grown to an OD (595 nm) of 0.541. Three 0.99 ml samples were spun down and re-suspended in fresh Dunaliella medium of different NaCl molarities (1 to 3 M) with 0.03 mg of triolein added (6µl + 4 µl isopropanol) and stained with Nile Red in acetone. Readings were taken from each after 10 minutes (stored in the dark) to allow full stain propagation. Measurements were taken before staining and the procedure was also run on plain media (i.e. without algae present) of the same molarity for comparison.

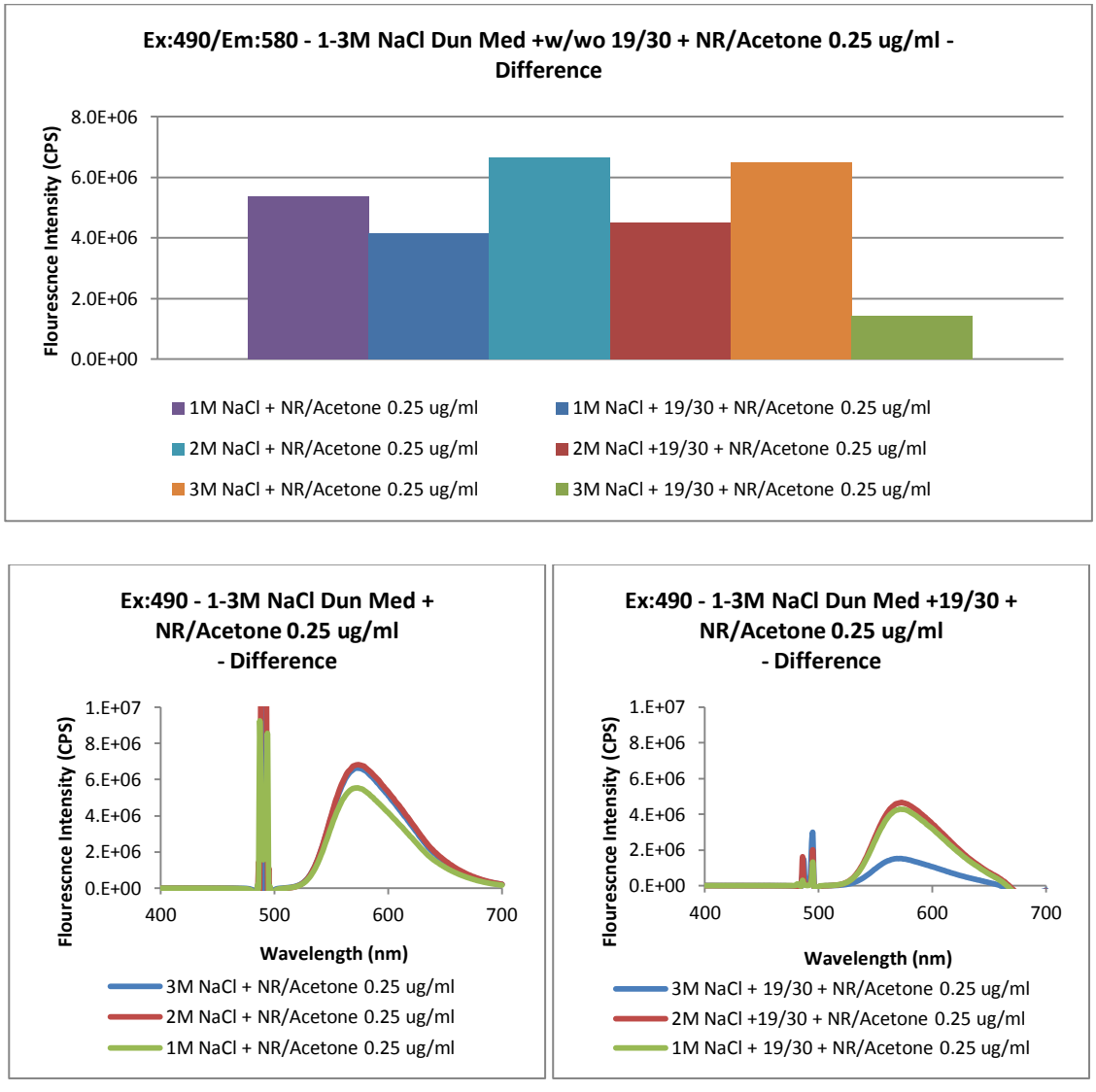

Figure 4.6.Effect of changing the medium salinity (1 to 3 M NaCl) on fluorescence intensity of Nile Red staining (0.25 µg/ml in acetone). Triolein (0.3 mg/ml) was added and the samples were kept in the dark for 10 mins before the flurescence intensity was measured.

The data demonstrate that as expected, higher salinity does have an effect on the overall fluorescence, but surprisingly at 2 M NaCl it produces a boost. Interestingly in the plain media tests 2 and 3 M NaCl produce similar outputs, but when cells are present this alters to 1 and 2 M NaCl. This confirms the results from previous experiments (not included) that indicate there is a considerable difference between plain media doping and that with live cells, hence quantification needs to be based around samples with cells present to be accurate. Although the salinity fluorescence boost is anomalous, the test does prove that the presence of salt does cause a variation in intensity, whilst not altering the peak wavelength, which was the objective of this experiment. The results also suggest that when comparisons are performed between strains grown in different types of media, standard curves need to be made for each type of media or the cultures need to be re-suspended in the same medium prior to lipid analysis taking place. Based on this finding it was decided to re-suspend any future cultures in one salinity of medium for testing.

Impact of re-suspension and washing on fluorescence

From the data in the last experiment and the previous data on chlorophyll loss due to cell breakage during cell harvesting tests, it was decided that the effects of re-suspending cells in fresh medium and performing a number of washing steps had also to be quantified. *D. salina* 19/30 was cultured in 1 M NaCl Dunaliella medium for 14 days before harvesting and adjusting to an OD of 0.2 (595 nm). The samples were combined with 1 µM NR/Acetone then tested with various washing steps (Figure 4.7).

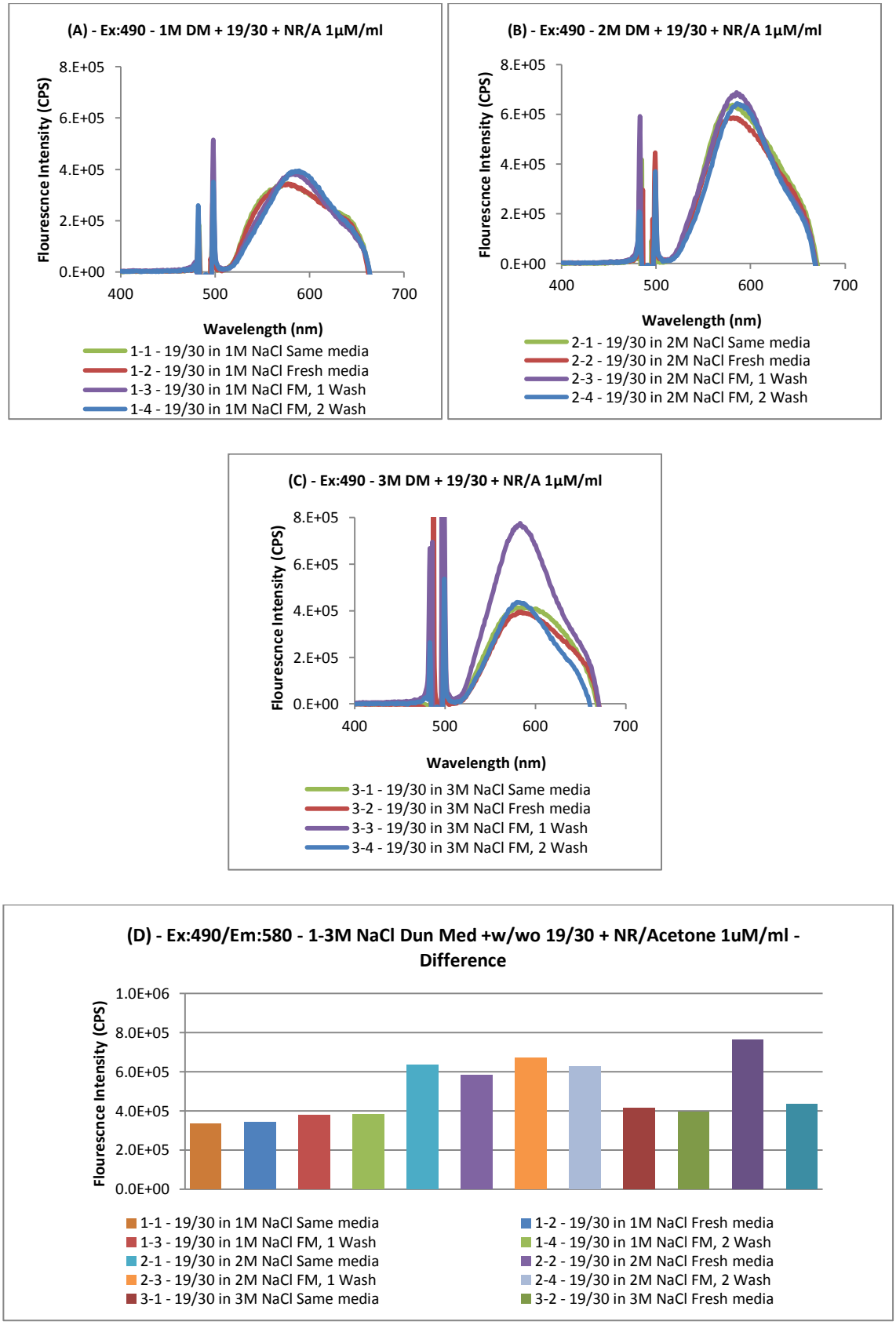

Figure 4.7. The effects of suspending *D. salina* 19/30 cells in fresh medium with or without subsequent washing steps on the Nile Red fluorescence intensity. A) Fluorescence spectra for cells in 1 M NaCl, B) Fluorescence spectra for cells in 2 M NaCl, C) Fluorescence spectra for cells in 3 M NaCl, D) Summary of data from the previous three graphs.

It can be seen from the data that re-suspension in fresh media seems to make only a slight difference in signal intensity, whereas washing the cultures increases the intensity marginally in all cases (excluding the 3 M wash steps which appear to be erroneous). Interestingly, the washing steps seem to 'sharpen' the fluorescence peak profiles. This could be because some chlorophyll is escaping into the media due to cell breakage and interacting with fluorescence spectra in some way. In further tests, re-suspension in fresh medium was carried out, rather than washing, based on these findings as the emission profile was the most similar.

NR Concentration

The effect of different NR concentrations (0.25-3 µM with Acetone) was then looked at in samples of *D. salina* 19/30 in 1 M NaCl Dunaliella medium (14 days old). The samples were re-suspended in fresh medium and adjusted to an OD of 0.2 (595nm), staining time was kept at 5 minutes. The results are shown in Figure 4.8.

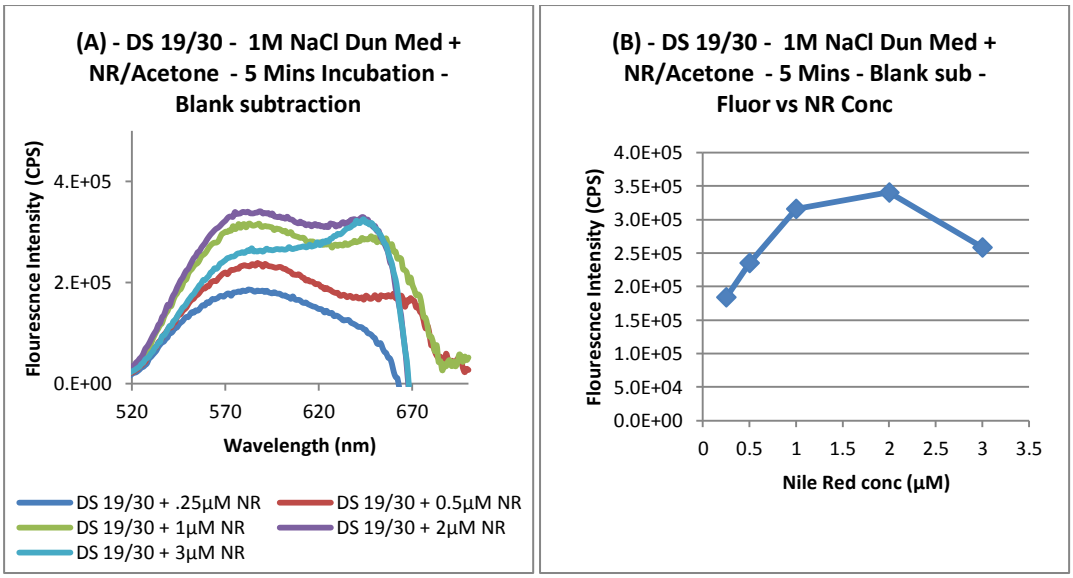

Figure 4.8. The effect of varying the concentration of Nile Red on the fluorescence intensity. A) Spectra at different concentrations of Nile Red and B) Maximum intensity of fluorescence at 580 nm plotted against Nile Red concentration.

The results indicated 1 µM to be the highest concentration before self shading (due to dye stacking) began to quench the fluorescence, which is in agreement with the findings of Pick and Rachutin-Zalogin (2012).

4.2.2.5 - Nile Red 96 well plate calibration

Based on the data from the data gathered from the spectrofluorometer (section 4.2.2.4), the literature and some personal communication with Prof Cooksey and Dr Gardner, a series of 96 well plate protocols were developed (see sections 2.2.2.3 to 2.2.2.6); one to look at the time of the peak fluorescence and cell shading, one to look at dye concentration and one to perform a lipid concentration curve based on triolein spiking.

Peak fluorescence time

Samples of *D.salina* 19/30 in 1 M NaCl Dunaliella medium (14 days old) were re-suspended in fresh medium and adjusted to 8 different % dilutions of the original OD of 0.37 (595 nm). In this initial experiment, due to the availability of only one multi-pipette the stain (1 µM NR/Acetone) was added sequentially, limiting the time to start the initial reading to 4.7 minutes. The fluorescence was read at 1.4 minute intervals (the fastest the reader would do), with automated shaking steps in between, for 39 minutes to try and capture the time of peak fluorescence and the rate of fluorescence decay for different cell concentrations (Figure 4.9).

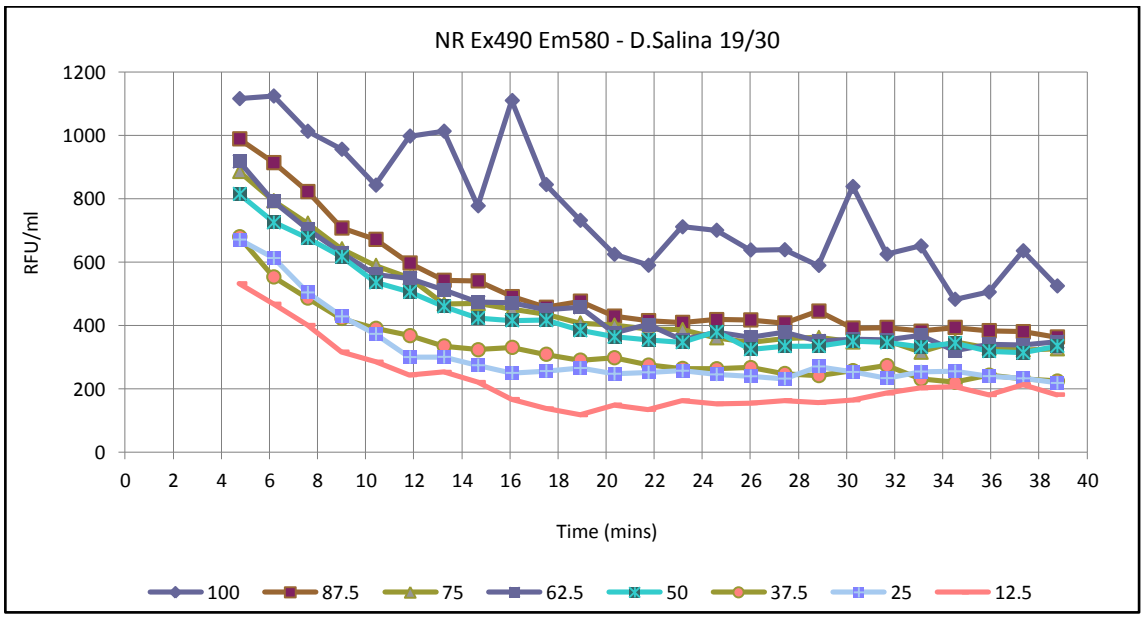

Figure 4.9. Time course of fluorescence emission from Nile Red stained *D. salina* 19/30 cells (1 µM in acetone). Eight different cell concentrations were used, 100% = OD_{595} of 0.37.

The data produced showed that the peak was almost instantaneous under all concentrations at 5 minutes, this fitted well with the literature, so 5 minutes was adopted at the standard for this strain. The cell concentration in some prior tests (not included in report) was shown to have some fluorescence quenching effects above $1.5x10^6$ cells/ml, so based on this and the data in the literature (Pick and Rachutin-Zalogin, 2012) a standard concentration of $1x10^6$ cells/ml was adopted to ensure no self shading took place.

Triolein Concentration curve

Using the results of the previous experiments (5 mins before reading, 1 µM NR concentration, $1x10^6$ cells/ml) a concentration curve was made (Figure 4.10) using 14 day old *D. salina* 19/30 cells with the standard addition method described by Bertozzini, et al. (2011).

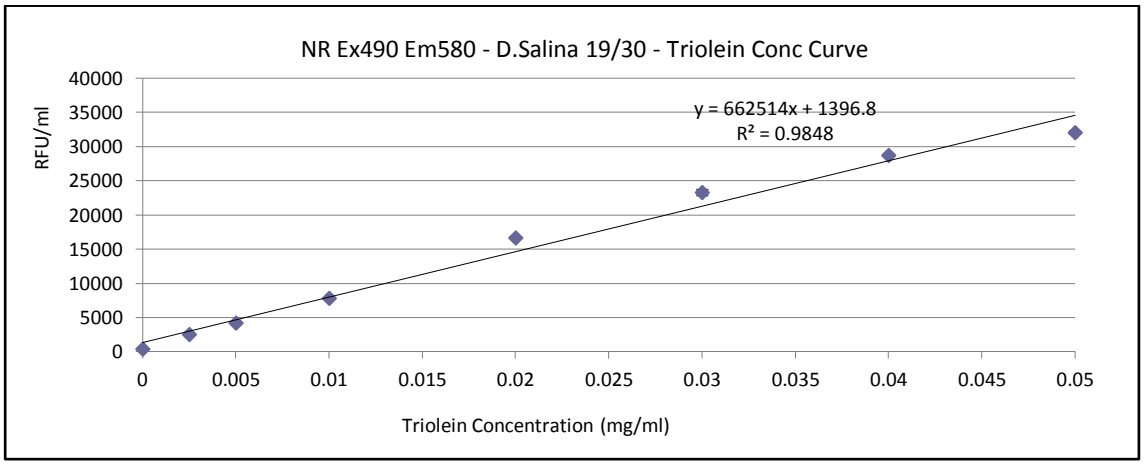

Figure 4.10. Triolein concentration curve based on the standard addition method.

The plot showed a very good correlation, so was adopted as a reference point for future readings.

Nile Red issues and procedure updates

Upon application of these methods, it soon became clear that the data produced results that were not replicable (see section 4.4.2, other data not included). The difference between runs, and during runs was subsequently found to be due to a creeping change in concentration in the Nile Red/Acetone stocks due to evaporation. Because a series of dilutions were made to make the final concentrations of the stain, changes in the master stock produced increasingly large experimental errors. Also, the results from other lipid tests also showed that the cells used in the calibration procedures had a very low lipid content, which could give an

unrepresentative reading. To address these issues, a series of repeat calibration experiments were performed using both regular and nitrate depleted *D. salina* 19/30 1 M NaCl grown cells at 14 days old to ensure high lipid contents. The experimental procedures were also modified to incorporate two sets of multi-channel pipettes, speeding up the procedure and making stain time exactly the same for all cells (these are shown in sections 2.2.2.3 to 2.2.2.6). Also, the NR/Acetone stocks were stored in the -80°C freezer in tightly sealed tubes to reduce evaporation effects.

NR Concentration - repeat with updated method

The concentration test was repeated first at 5 minutes again, but the range of concentrations was extended to see the effects of variance. The old slower method (OM) was also compared to the new one (NM) using nitrate replete and deplete cells.

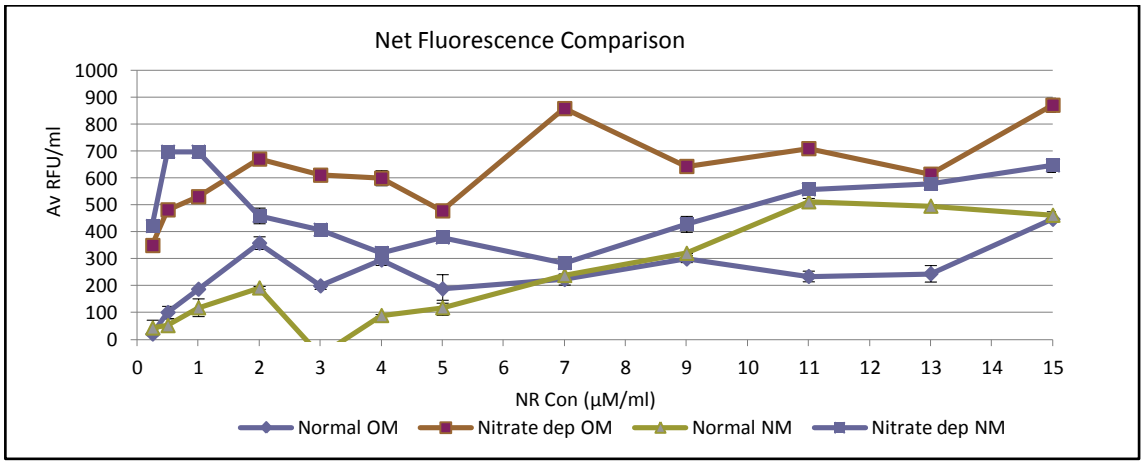

Figure 4.11. Comparison of original slower method (OM) with new method (NM) for *D. salina* 19/30 cells stained with Nile Red (concentrations up to 15 µM) in acetone. Measurements made 5 minutes after addition of Nile Red

The data produced from this test was very different to the initial experiments (Figure 4.8B), beyond an NR concentration of 2 µM there seems to be very little correlation at all. This could be due to the time discrepancy between the wells been read (35 seconds for the entire plate), glycerol quenching/excitation, dye stacking, salinity and many of other potential factors, too many to assessed in detail (Pick and Rachutin-Zalogin, 2012). Because of this, it was decided to stick with the new method, as it reduced time skew and use the maximum concentration in standard cells before anomalous effects became apparent i.e. 2 µM (Figure 4.11).

Concentration values lower than this had been shown also not to produce enough signal during some prior testing on the new methods (not included in report).

Peak fluorescence time - repeat with updated method

Having decided on the 2 µM NR concentration, a repeat of the peak finding experiment was run using the updated more rapid method (section 2.2.2.3) and 14 day old nitrate deplete cells to ensure a good signal.

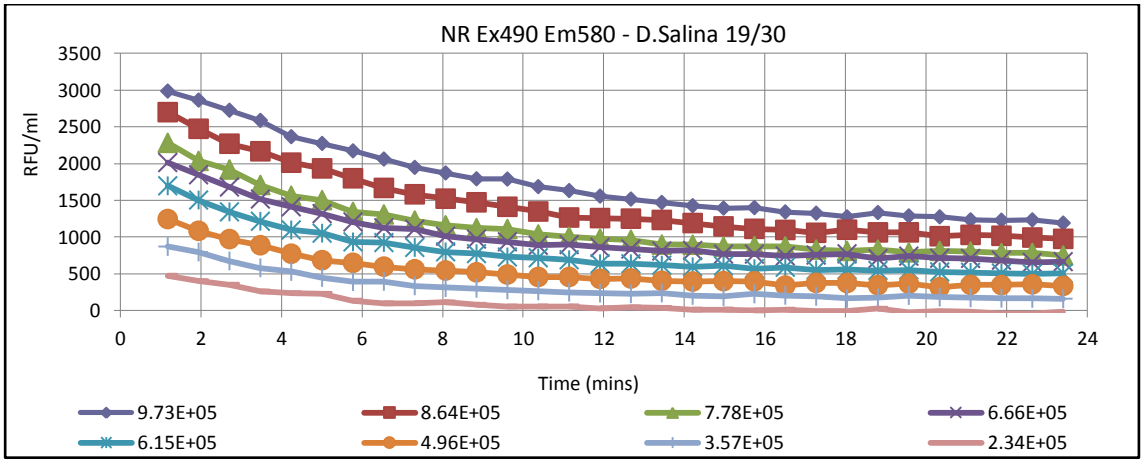

Figure 4.12. Time course of fluorescence emission from Nile Red stained *D. salina* 19/30 cells (2 µM in acetone). Eight different cell concentrations were used (cells ml^{-1}) as shown in the figure.

The data from the test demonstrates that the peak is not actually at 5 minutes, as suggested by Pick and Rachutin-Zalogin (2012), but even sooner than 1 minute. Unfortunately, it is not possible to prepare the samples any quicker by hand to find if there is an increase at any earlier stage. The difference between this result and the literature could be due to the different solvent used (acetone rather than dimethylformamide) or one of many other setup differences. Based on this data and for the sake of constancy, 5 minutes was still adopted for the rest of the experiments as any point in time looks to be highly transient.

Triolein concentration curve updated

A repeat of the concentrations test was performed using the new quicker method with a higher concentration of NR (Figure 4.13). Also, to make the readings more representative, the

triolein was 'stabilised' based on the methods by Alonzo and Mayzaud (1999) with a 1:20 ratio between triolein and phosphatidylcholine. This was run in the Betozzini standard addition format with 14 day old Nitrate deplete cells for an increased signal. The graph produced, is greater in accuracy and had a more representative lipid value offset on the y-axis.

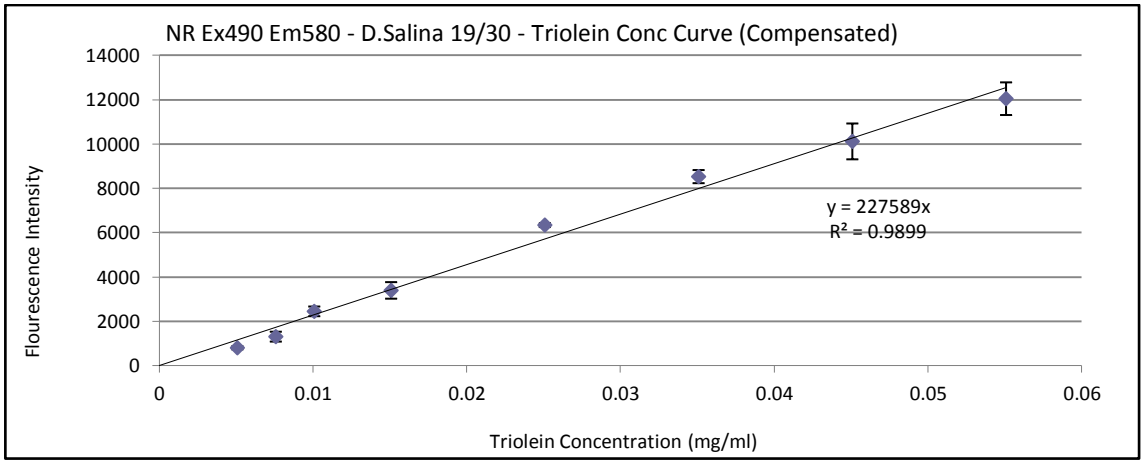

Figure 4.13. Triolein concentration curve using quicker new method plus stabilised triolein (see text). The standard addition format was again used with 14 day old nitrate deplete *D. salina* 19/30 cells. Measurement time was 5 minutes and Nile Red concentration was 2 µM in acetone.

4.3 Effects of Salt Stress on D. salina 19/18

A series of initial tests were performed looking at the affect NaCl stress has on the β carotene over producing strain *Dunaliella salina* 19/18. The main aim of the study was to establish if there was a correlation between increased molarity of NaCl in the medium, and production of lipids (TAG) within this strain of *Dunaliella*. A secondary objective of the study was to also establish the number of samples that could be taken from a growth culture with no replacement of medium and how this impacts on the data, along with learning how to culture the strain effectively. These experiments were conducted in collaboration with Post Doctoral researcher Joey Shepherd, who was working for the Carbon Trust at the time.

D. salina 19/18 was cultured in six 250 ml conical flasks each with 100 ml of Dunaliella medium to which 5 ml of well grown inoculum was added (aseptic procedures followed throughout). The medium salinity was varied (1, 2 and 3 M NaCl), two flasks were inoculated per salinity.The inoculated cultures were incubated in MBB H-Floor Growth Room (see section 2.8.2). Samples were taken from the day after inoculation, to try and pinpoint the start of the exponential growth phase. Chlorophyll and OD (630 nm) readings were taken using a UNICAM Helios Alpha spectrophotometer, cell counts were also performed using a haemocytometer (see sections 2.6.1-2.6.2). The amount of culture taken for each measurement was also reduced in an effort to avoid data skew due to low culture volumes. 1 ml each for OD and chlorophyll reading, the method in section 2.6.4 was followed with the ratios of solvents scaled from 5 to 1. The gravimetric lipid method (section 2.2.1) was also carried out three times over the experimental period, on the 1st, 7th and 14th days, with a single sample of 3 x 15ml taken from a flask of each salinity on each occasion. The experiment was concluded on the day 21 due to lack of remaining culture and inconsistent lipid results (Figures 4.14, 4.15 and Tables 4.3, 4.4).

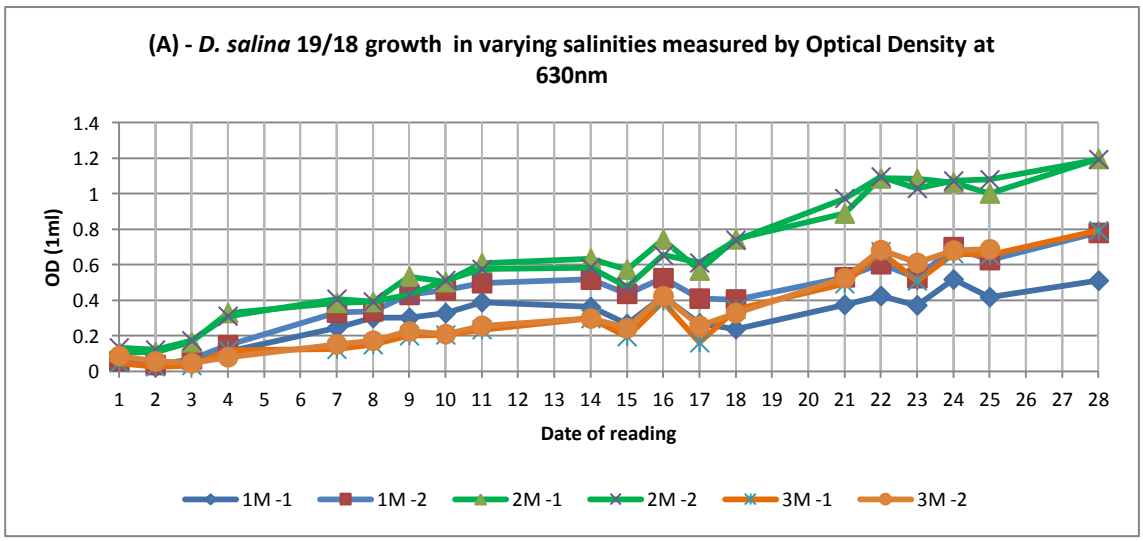

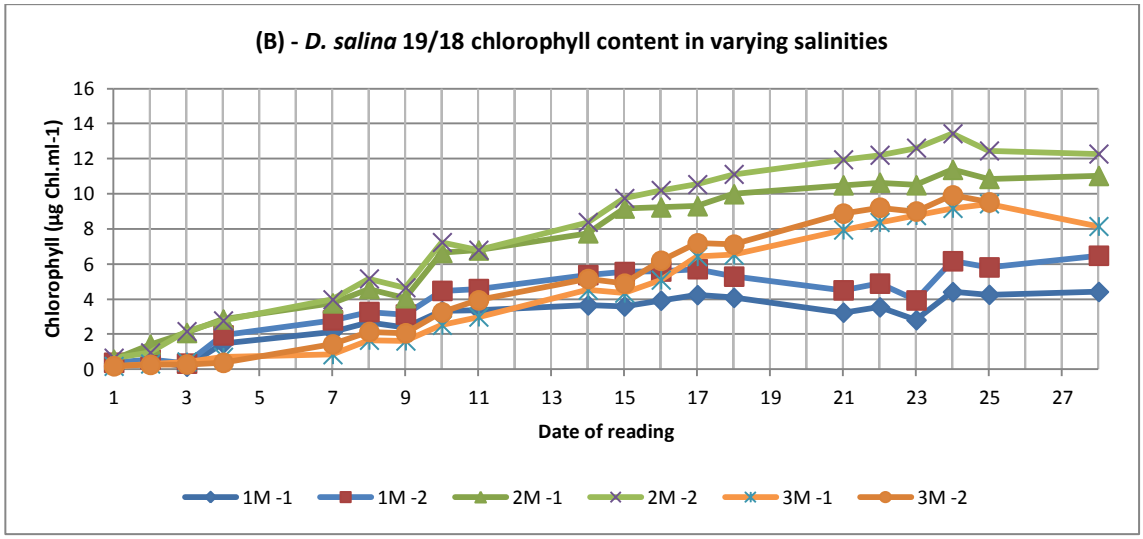

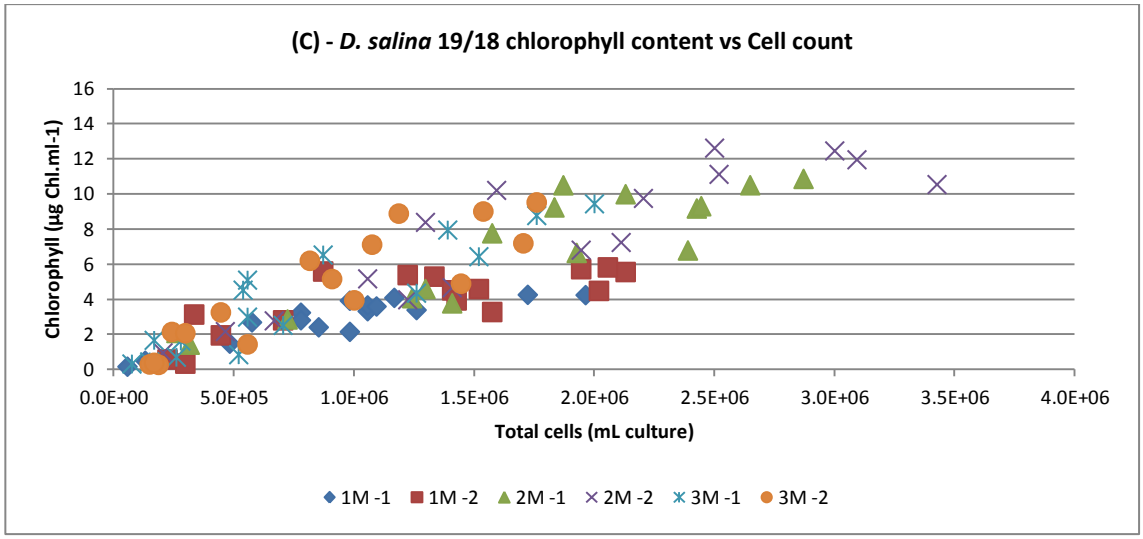

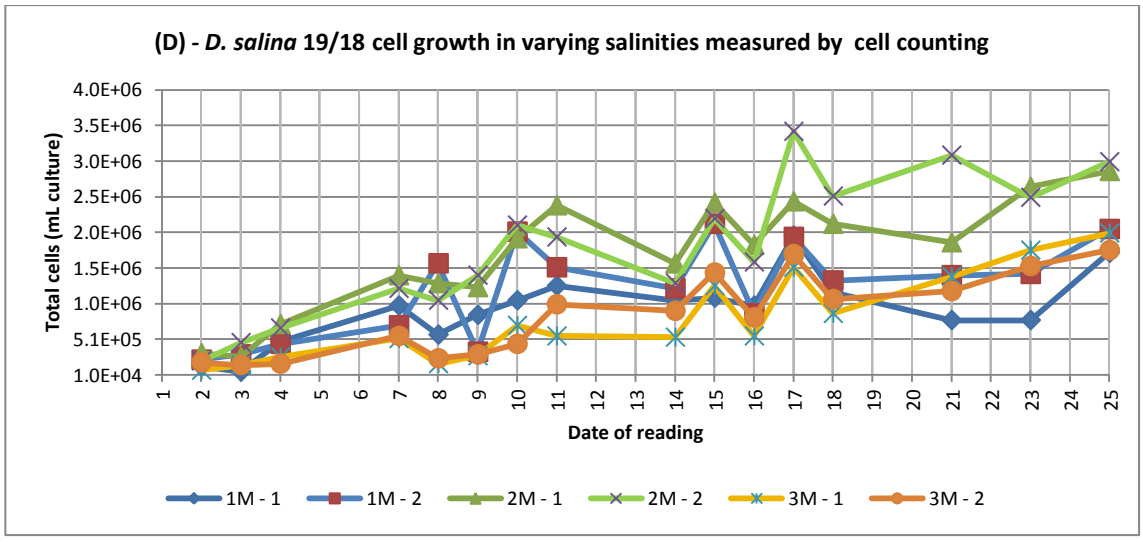

Figure 4.14. Growth measurements of *D.salina* 19/18 in a range of salinities (1 – 3 M). A) OD 630 nm, B) Chlorophyll content (µg Chl.ml^{-1}), C) Correlation of OD versus Chlorophyll and D) Cell counts.

Table 4.3 - Calculated *D. salina* 19/18 Growth rates (see section 2.6.6)

Culture & media	Equation	Phase Limits		Time of phase		Specific growth rate (K')	Divisions per day (Div.day^{-1})	Generation time = doubling time	
		N1:	N2:	t1:	t2:			Days	Hours
1M-1 NaCl DM	y = 216524x - 504274	145298	1011394	3	7	0.485074513	0.6998	1.43	34.29
1M-2 NaCl DM	y = 210784x - 404684	227668	1281588	3	8	0.345593357	0.4985	2.01	48.14
2M-1 NaCl DM	y = 273504x - 480057	340455	1434471	3	7	0.359567115	0.5187	1.93	46.27
2M-2 NaCl DM	y = 199735x - 160053	239417	1238092	2	7	0.328623992	0.4741	2.11	50.62
3M-1 NaCl DM	y = 89947x - 109788	70106	519841	2	7	0.400702923	0.5780	1.73	41.52
3M-2 NaCl DM	y = 81481x - 214815	111109	681476	4	11	0.259107048	0.3738	2.68	64.20

Table 4.4 - Total lipid production (% Dry weight) from gravimetric extraction (see section 2.2.1)

Day	1M - 1	1M - 2	2M - 1	2M - 2	3M - 1	3M - 2
1	22.22	15.00	22.76	16.22	32.00	23.91
7	15.38	12.64	11.52	23.91	21.92	13.64
14	24.74	21.09	24.07	19.47	25.32	2.54

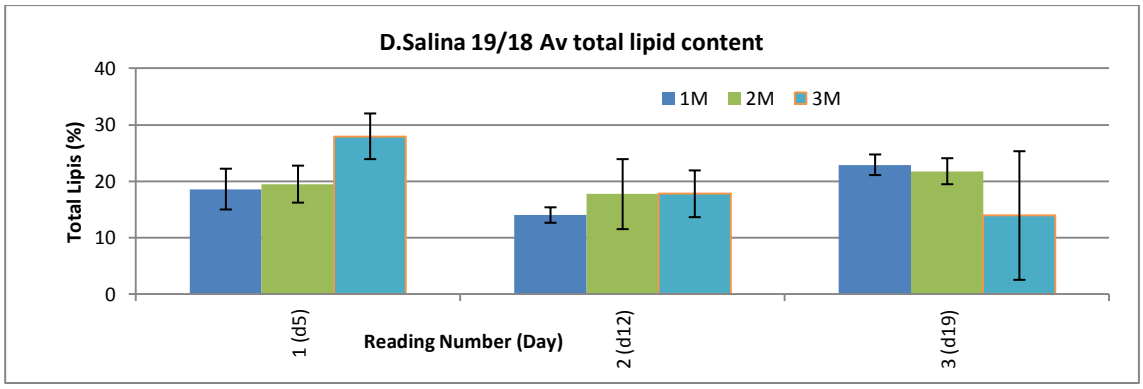

Figure 4.15. Comparison of average total lipid accrual at three different time intervals (5, 12 and 19 days)

Conclusions

Upon comparison of the growth data (Figure 4.14), it is clear that the cultures in 2 M medium were the fastest growing overall, followed by the 3 M cultures and then the 1 M cultures. However, when all three growth trends are compiled in relation to the linear growth phase, the 1 M cultures have the shortest average generation time of 1.72 days (Table 4.3 above). Unfortunately, the lipid data was too inconsistent to draw any real conclusions in comparison to the growth data (Figure 4.15). It is hypothesised that this variance originates from the losses of culture in the centrifugation steps and low cell concentrations in the initial starting cultures. This idea is discussed in the lipid measurement work by Honeycutt, McFarland and McCant

(1995), who suggest the micro-gravimetric method (Gardner, et al., 1985) might be a better approach for samples under 5 g equivalent starting weight. However, the recent lipid review paper by Griffiths, van Hille and Harrison (2010) highlights that levels of lipid underestimation of up to 81% are still possible with this method and the work by Smedes and Askland (1999) shows that different solvent ratios can also preferentially select different lipid groups, which would be a concern if the work was a basis for biofuel production. This preliminary data and experience subsequently prompted research into other lipid measurement approaches (section 4.2) and led to further collaborative work with Dr Shepherd on the *D. salina* 19/18 to isolate lipid over producing mutants using Nile Red staining and flow cytometry. Due to the loss of the Carbon Trust's funding and Dr Shepherd from the lab, this work is still ongoing (see the draft paper manuscript in Appendix L).

4.4 Effects of Salt and Nitrate Stress on D.Salina 19/30

Further tests to find the effects of salt stress on neutral lipid production and growth rate were performed on a different strain of *D. salina;* 19/30. It was decided to proceed using the non β carotene over producing 19/30 strain because the work was eventually to be compared with the previous studies conducted by the Zimmerman research group on the effects of fluidic oscillation and micro-bubbles, which also used the 19/30 strain. In addition, this research was also coupled with the concurrent selection, development and testing of three types of lipid techniques based on existing literature; Nile Red staining, direct trans-esterification with GC-MS and NMR (see sections 2.2.3, 2.2.4 and 4.2).

In all four tests, the following conditions remained constant; cultures were grown in 250 ml flasks (using the same inoculum to medium ratio specified in the previous test) under constant lighting on the middle shelf of the MBB H-Floor Growth Room (section 2.8.2) for a minimum of 14 days before harvesting for final lipid analysis (monitoring continued after in some cases). Each salinity condition was grown in triplicate, with one flask used for dry weight measurements only (see section 2.6.5) to avoid the variation found the previous 19/18 test (note: the first test didn't measure dry weight). Growth was monitored using measurement of OD (595 nm) and converted to cells/ml via a previously made calibration curve (see section 2.6.3). All data calculations were performed using Microsoft Excel and standard error margins were given wherever possible.

4.4.1 – 1-3M NaCl Dunaliella Medium Test 1

The initial test inoculum was sourced from a 12 day old culture of *D. salina* 19/30 in 1 M NaCl Dunaliella medium with an OD (595 nm) of 1.370. Nile red tests were performed using the old single multi-pipette method (see Appendix I) with 1 µM/ml NR of culture (20 µl of stain 0.318 µg/ml added). Harvested cultures were washed once and freeze dried for subsequent NMR analysis (using a 500 µl $CDCl_3$/CD_3OD in a ratio 1:8. .

The results in Figure 4.16A show that *D. salina* 19/30 grows best at the lowest salinity (1 M NaCl) and the growth rate declines with increasing salinity. The opposite trend is seen with Nile Red net fluorescence i.e. the higher lipid production is seen at 3 M NaCl (Figure 4.16B). NMR analysis shows that the highest total lipid is in the low salinity (1 M NaCl) grown cells (Table 4.5), which is not in agreement with the trend in Figure 4.12B.

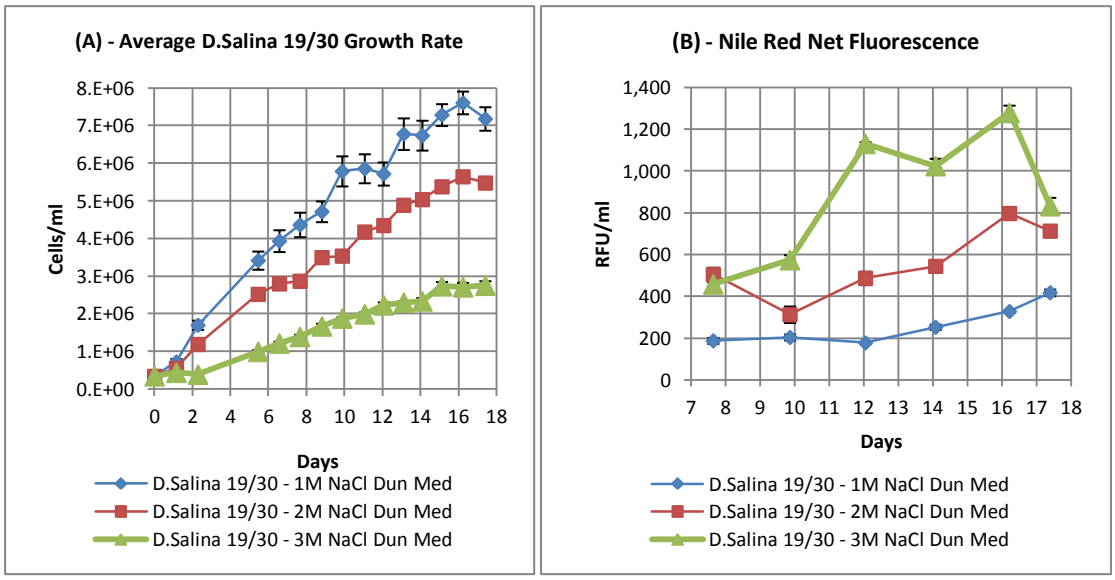

Figure 4.16. A) Growth rate of *D. salina* 19/30 in three different salinities (1 – 3 M) measured from OD 595 nm inferred cells per ml. B) Nile Red fluorescence (RFU/ml) Ex: 490 nm Em: 580 nm.

Table 4.5 - NMR and Nile Red, pigment and lipid data.

Sample	NMR β-Carotene (mg/10mg BM)	NMR total lipid – C17:1 equivalent (mg/10mg BM)	Nile Red Triolein equivalent (g/105ml)	Std Err
DS 19/30 1M NaCl Dun Med	0.13	2.36	0.0046	0.0004
DS 19/30 2M NaCl Dun Med	0.15	1.74	0.0053	0.0003
DS 19/30 3M NaCl Dun Med	0	0.67	0.0032	0.0001

4.4.2 – 1–3M NaCl Dunaliella Medium Test 2

The second test inoculum was sourced from a 14 day old culture of *D.salina* 19/30 in 1 M NaCl Dunaliella medium with an OD (595 nm) of 1.344. Nile red tests were performed using the old single multi-pipette method again (see Appendix I) with 1µM NR/ml of culture (20 µl of stain added). Dry weight was recorded throughout the test. Harvested cultures were washed once and freeze dried for subsequent GC-MS processing on day 15. The growth rate and Nile Red fluorescence results are shown in Figure 4.17 and follow the same trends as the previous experiment i.e. best growth at low salinity, high net Nile Red fluorescence at high salinity, but highest total lipid at low salinity (Table 4.6). FAME analysis is shown in Table 4.7 and Figure 4.18 and is discussed in section 4.4.5.

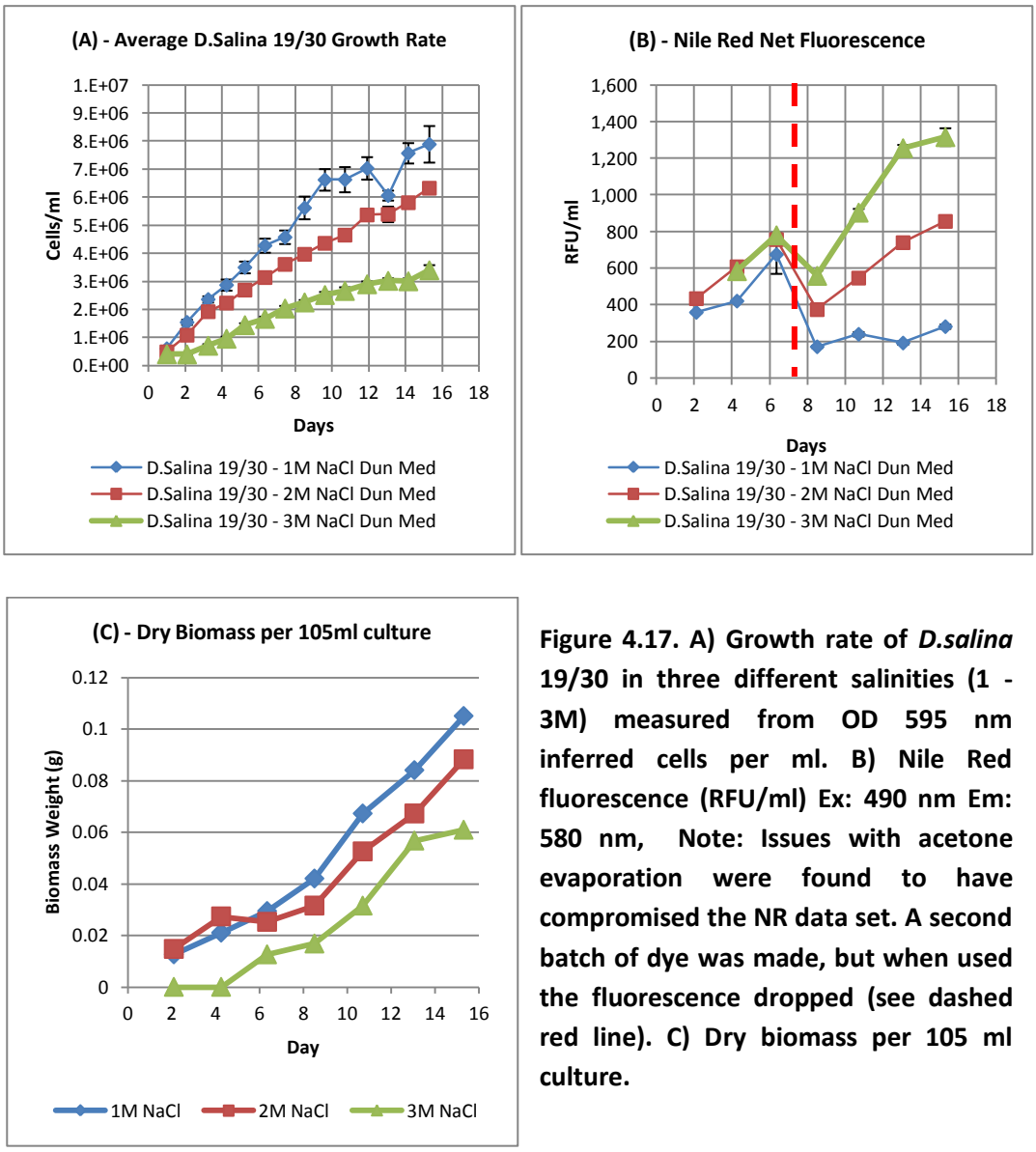

Figure 4.17. A) Growth rate of *D.salina* 19/30 in three different salinities (1 - 3M) measured from OD 595 nm inferred cells per ml. B) Nile Red fluorescence (RFU/ml) Ex: 490 nm Em: 580 nm, Note: Issues with acetone evaporation were found to have compromised the NR data set. A second batch of dye was made, but when used the fluorescence dropped (see dashed red line). C) Dry biomass per 105 ml culture.

Table 4.6 - *D.salina* 19/30 in 1 - 3 M NaCl - NMR and Nile Red lipid data.

Sample	Direct Trans total lipid (mg/10mg BM)	Std Err	Nile Red Triolein equivalent(g/105ml)	Std Err
DS 19/30 1M NaCl Dun Med	1.058	0.108	0.0033	0.0007
DS 19/30 2M NaCl Dun Med	0.82	0.077	0.00705	0.0002
DS 19/30 3M NaCl Dun Med	0.651	0.037	0.0144	0.0002

Table 4.7 - *D.salina* 19/30 in 1 - M NaCl - Direct transesterification FAME profile (% of total FAME):

FAME	Structure	Lipid Profile (% of total FAME)					
		1M NaCl	Std Err	2M NaCl	Std Err	3M NaCl	Std Err
Methyl 4,7,10,13-hexadecatetraeoate	16,4 (cis n3)	10.51	0.22	9.69	0.87	9.79	0.10
9,12,15-Octadecatrienoic acid ME	18,3 (trans)	1.52	0.12	1.49	0.08	1.85	0.19
Hexadecanoic Acid ME	16,0	24.09	1.70	25.65	2.50	23.36	0.72
7-Hexadecenoic acid ME	16,1 (cis)	0.98	0.09	0.96	0.04	0.00	0.00
γ linolenic ME	18,3 (n6)	2.07	0.24	1.57	0.25	2.16	0.23
Methyl Stearidonate	18,4	1.19	0.21	0.00	0.00	0.00	0.00
9,12-Octadecadienoic Acid ME	18,2 (6 cis)	3.70	0.66	5.95	0.10	7.78	0.68
9,12,15-Octadecadienoic Acid ME	18,3 (n3)	48.47	5.48	45.06	5.06	45.36	2.98
9-Octadecadienoic Acid ME	18,1 (9 Cis)	3.37	0.90	4.84	0.26	6.59	0.51
9-Octadecadienoic Acid ME	18,1 (9 trans)	2.28	0.25	3.05	0.20	1.71	0.13
Octadecanoic Acid ME	18,0	0.78	0.17	0.98	0.02	1.41	0.07
Methyl 9,10-methylene-octadecanoate	19,0D (cis 9,10)	1.06	0.12	0.77	0.00	0.00	0.00
	Total:	100.00	10.17	100.00	9.38	100.00	5.62

Note: Blue FAMEs are assumed, green are direct matches to standards on column

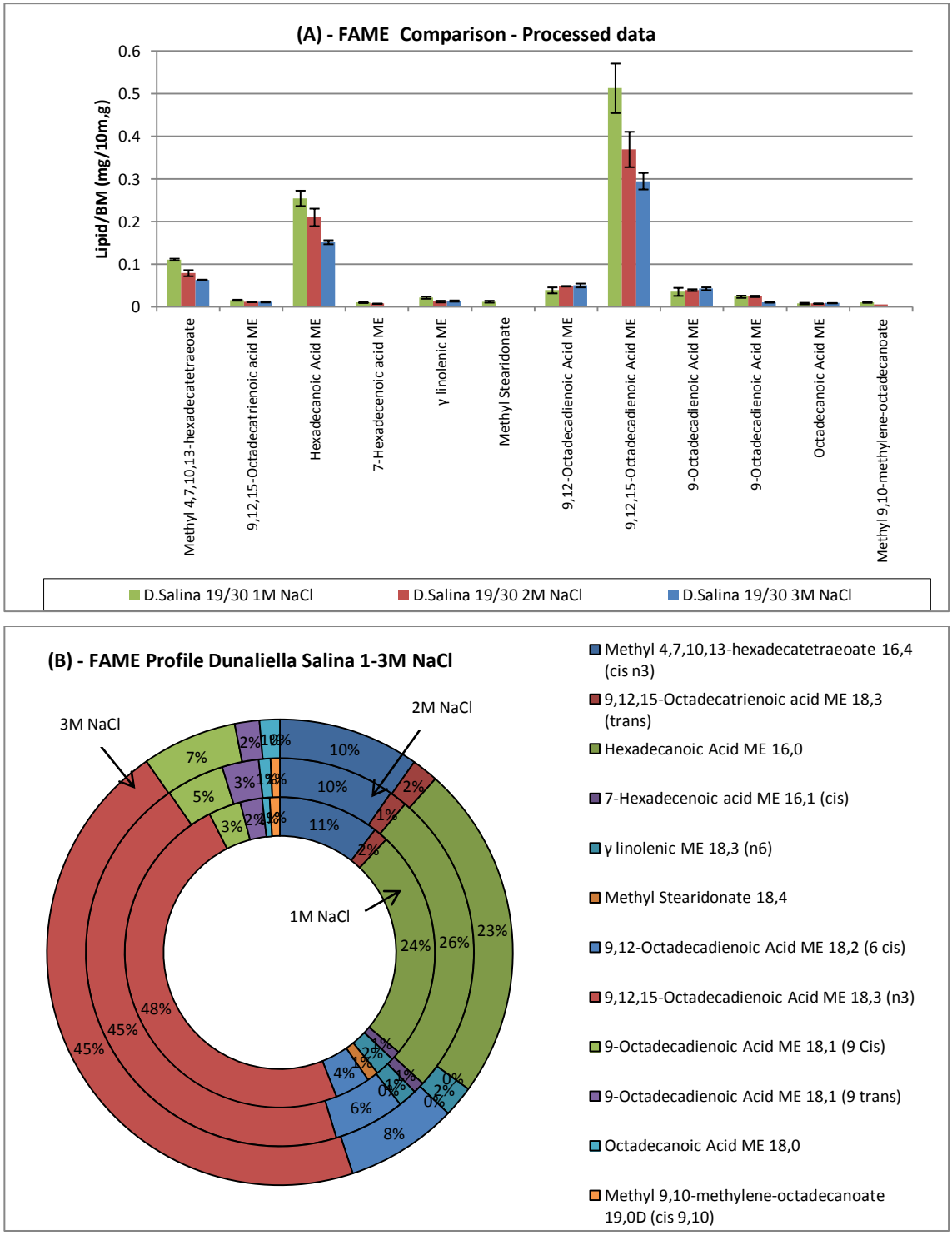

Figure 4.18. *D.salina* 19/30 in 1 - 3 M NaCl - A) FAME quantity comparison, Lipid/Biomass (mg/10mg) and B) FAME lipid profile (%).

4.4.3 - 1-3M NaCl Dunaliella Medium Test 3

The third test inoculum was sourced from a 14 day old culture of *D. salina* 19/30 in 1 M NaCl Dunaliella medium with an OD (595nm) of 1.607. Nile red tests were performed using a single multi-pipette method using 25% DMSO rather than acetone (see appendix I) with 1 µM NR/ml

of culture. This method was trailed to counter acetone evaporation issues (DMSO has a much higher evaporation point). Dry weight was recorded throughout the test. Harvested cultures were washed once and freeze dried for subsequent NMR (using a NMR 560 µl $CDCl_3/CD_3OD$ in a ratio 1:4) on day 15. The results shown in Figure 4.19 are again similar to the previous two tests, but in this case more extensive NMR analysis was carried out as described in Tables 4.8 to 4.10, which will be discussed in section 4.4.5.

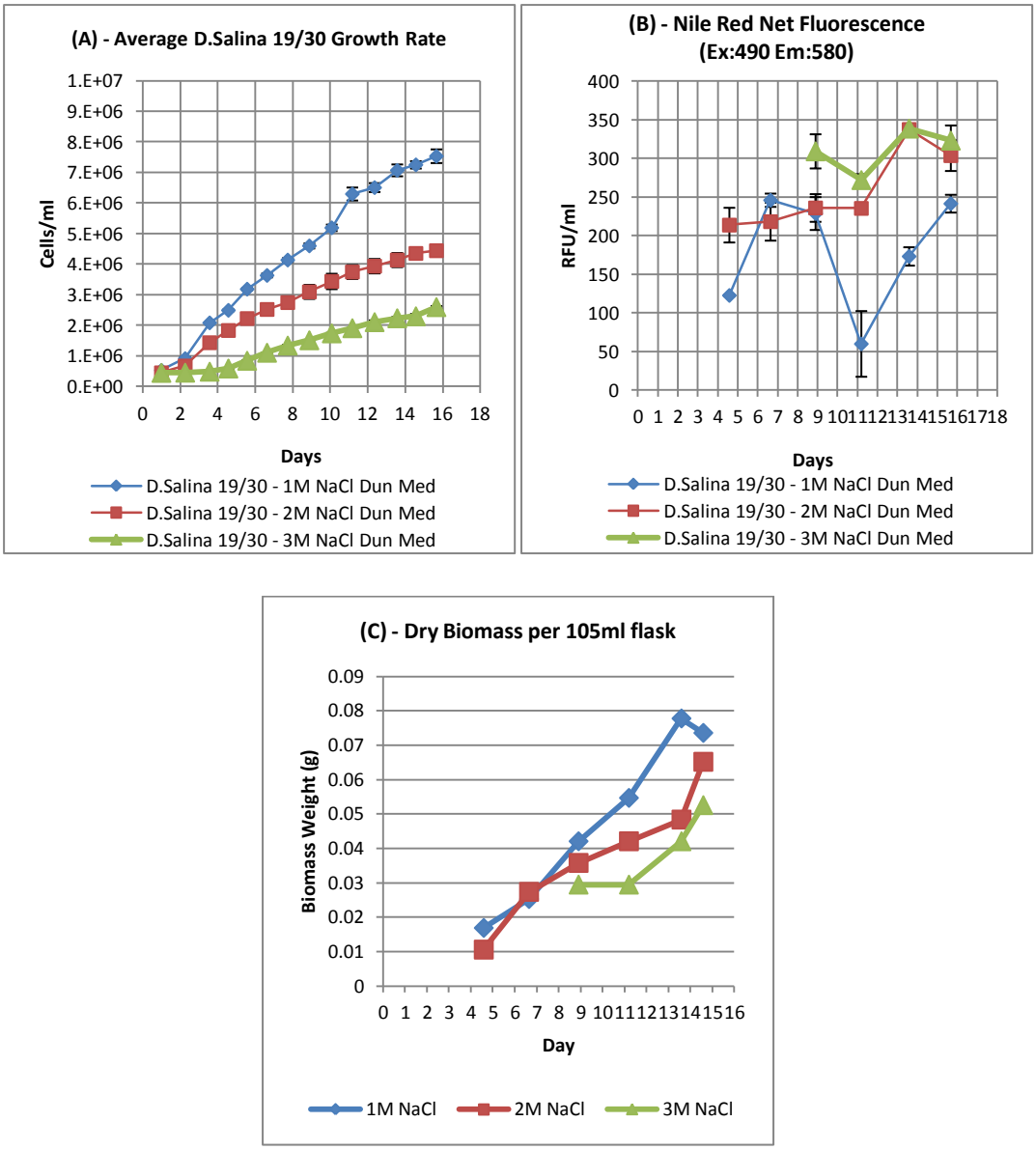

Figure 4.19. A) Growth rate of *D.salina* 19/30 in three different salinities (1 – 3 M) measured from OD 595 nm inferred cells per ml. B) Nile Red fluorescence (RFU/ml) Ex: 490 nm Em: 580 nm. C) Dry biomass per 105 ml culture.

Table 4.8 – *D.salina* 19/30 in 1 - 3 M NaCl - NMR pigment data.

Sample	NMR Chlorophyll (mM/10mg BM)	NMR β-Carotene (mg/10mg BM)
DS 19/30 1M NaCl Dun Med	0.21	0.20
DS 19/30 2M NaCl Dun Med	0.14	0.19
DS 19/30 3M NaCl Dun Med	0.17	0.24

Note: Only enough sample for single readings was harvested.

Table 4.9 - *D.salina* 19/30 in 1 - 3 M NaCl - NMR lipid data.

Sample	NMR total lipid – C17:1 equivalent (mg/10mg BM)
DS 19/30 1M NaCl Dun Med	1.65
DS 19/30 2M NaCl Dun Med	1.27
DS 19/30 3M NaCl Dun Med	1.44

Table 4.10 - *D.salina* 19/30 in 1 - 3 M NaCl - NMR lipid group data.

Sample	NMR Unsat lipid signal (mM/10mg BM)	NMR Unsat Me lipid signal (mM/10mg BM)	NMR Sat Me lipid signal (mM/10mg BM)
DS 19/30 1M NaCl Dun Med	10.88	3.20	5.42
DS 19/30 2M NaCl Dun Med	9.38	2.55	4.51
DS 19/30 3M NaCl Dun Med	11.36	2.90	5.35

4.4.4 - 1-3M NaCl Dunaliella Medium Test 4

The fourth test inoculum was sourced from an 18 day old culture of *D. salina* 19/30 in 1 M NaCl Dunaliella medium with an OD (595 nm) of 1.445. Nile red tests were performed using the dual updated multi-pipette method with acetone (see section 2.2.2.6) with 2 µM NR/ml of culture. Dry weight was recorded throughout the test. Harvested cultures were washed once and freeze dried for subsequent NMR (using a NMR 560 µl $CDCl_3/CD_3OD$ in a ratio 1:4 1 M & 2 M samples. 500 µl $CDCl_3/CD_3OD$ in a ratio 1:4 3 M) on day 14. Growth data (Figure 4.20) was in line with the previous three tests, but in this case the growth at 2 M NaCl was only very slightly less than at 1 M NaCl. The NMR analysis is shown in Tables 4.11 to 4.13 and will be fully discussed in the next section.

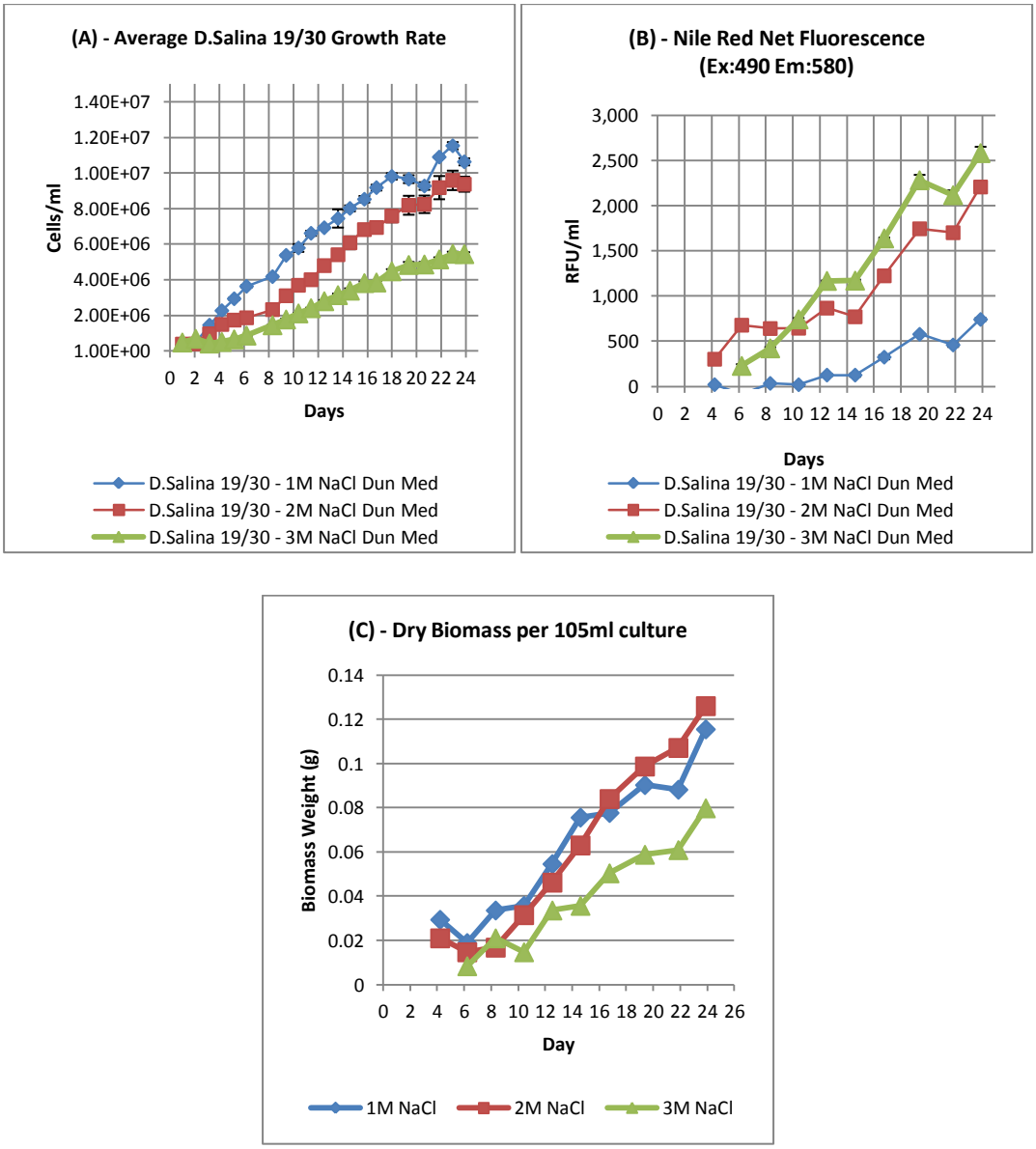

Figure 4.20. A) Growth rate of *D.salina* 19/30 in three different salinities (1-3M) measured from OD 595 nm inferred cells per ml. B) Nile Red fluorescence (RFU/ml) Ex: 490 nm Em: 580 nm, note: NR method improved and stable, however issues with concentration remain. Bacteria contamination visibly high in 2 M cultures. C) Dry biomass per 105ml culture.

Table 4.11 - *D.salina* 19/30 in 1-3 M NaCl - NMR pigment data.

Sample	NMR Chlorophyll (mM/10mg BM)	Std Err	NMR β-Carotene (mg/10mg BM)	Std Err
DS 19/30 1M NaCl Dun Med	0.22	0.02	0.2	0.01
DS 19/30 2M NaCl Dun Med	0.08	0.01	0.11	0.01
DS 19/30 3M NaCl Dun Med	0.28	0.01	0.26	0.02

Table 4.12 - *D.salina* 19/30 in 1-3 M NaCl - NMR lipid data.

Sample	NMR total lipid – C17:1 equivelent (mg/10mg BM)	Std Err
DS 19/30 1M NaCl Dun Med	1.87	0.13
DS 19/30 2M NaCl Dun Med	1.69	0.02
DS 19/30 3M NaCl Dun Med	1.70	0.17

Table 4.13 - *D.salina* 19/30 in 1-3 M NaCl - NMR/Nile Red lipid group data.

Sample	NMR Unsat lipid signal (mM/10mg BM)	Std Err	NMR Unsat Me lipid signal (mM/10mg BM)	Std Err	NMR Sat Me lipid signal (mM/10mg BM)	Std Err	Nile Red Triolein equivalent (g/105ml)	Std Err
DS 19/30 1M NaCl Dun Med	12.47	0.32	3.40	0.15	5.93	0.45	0.0013	0.0006
DS 19/30 2M NaCl Dun Med	8.16	0.53	1.95	0.15	4.44	0.10	0.0144	0.0009
DS 19/30 3M NaCl Dun Med	14.74	1.74	3.79	0.29	6.32	0.52	0.0285	0.0011

4.4.5 Conclusions

When the data from the four experiments is compiled into equivalent formats (values per 105 ml of culture) a few trends become apparent (see Figure 4.21, below).

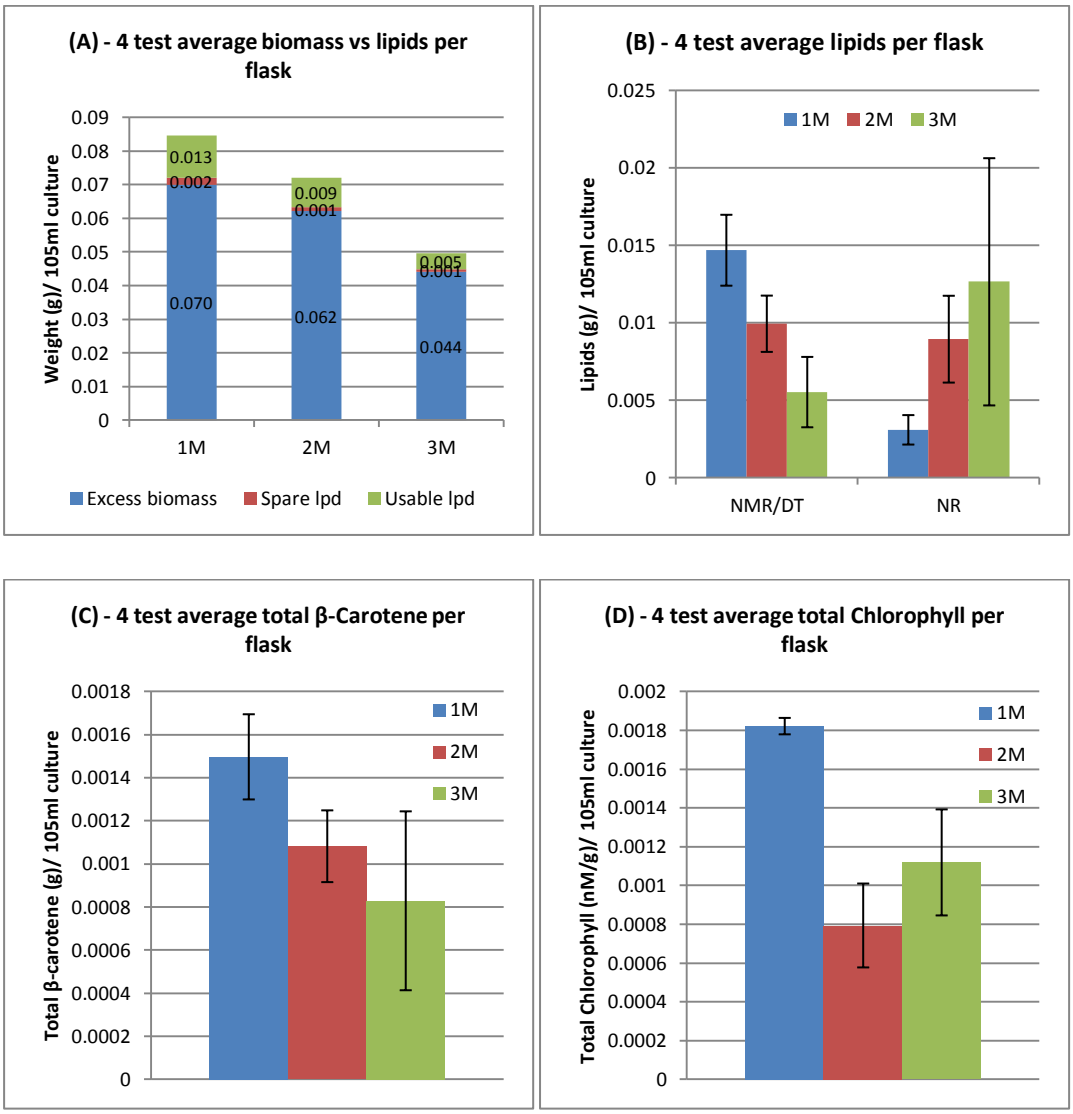

Figure 4.21. Compiled data for *D.salina* 19/30 in three different salinities (1 – 3 M) - A) Proportion of lipid to biomass per flask, useable lipid referring to biodiesel suited FAMEs. B) NMR/DT lipids per flask (g) compared with NR lipid data. C) NMR β-carotene per flask (g). D) NMR total chlorophyll per flask (nM/g).

The NMR and GC-MS data show good agreement that the 1 M cultures have the largest amount of lipid present, with a decrease in the 2 to 3 M conditions. The difference between the 2 – 3 M cultures seems to vary, but overall the 2 M seems to be higher on average. Based on the FAME profile from the test described in section 4.4.2 (Table 4.7 and Figure 4.18), if the assumption was made that only lipids with structures ranging from 16:0 to 18:3 were to be used for biodiesel, avoiding highly poly-unsaturated types (typically associated with the polar groups), of the total lipid amounts the following would be useable in each case (%); 1 M - 85.73

±9.49, 2 M - 88.05 ±8.43 and 3 M - 88.36 ±5.32. When these data are coupled with the average dry weight data to show the proportion of lipid to biomass, it can seen that there is again a decrease of net lipid production with increased salinity. However, with the higher salinity, the lipid profile seems to become more suitable for biodiesel production with a shift from unsaturated C16:0 and polyunsaturated C18:3 to C18:1 and C18:2. If this trend is compared with the data in the previous studies looking at salt stress for *Dunaliella,* there is a partial match in trends withXu and Beardall (1997) with an increase in C18:1 and C18:2 and decrease in PUFA, but the C16:0 there is the opposite correlation, which is more akin to the work by Alhasan, et al. (1987). The closest match seems to be with the papers by Azachi, et al. (2002) and Peeler, et al. (1989), which suggests that the shift in profile is associated with the cells lipid membranes. This shift in membrane composition is hypothesised to be due to the intracellular membrane compartments changing to function with increased internal glycerol, which is needed to balance the increased osmotic pressure (Guschina and Harwood, 2006). However, even with the observed shift in FA profile, there is still a high amount of PUFA mainly in the form of 18:3 (45.06-48.47%). It is generally considered that feedstocks with over 12% of this type are ill suited for biodiesel production (Guzman, et al., 2012; Mutanda, et al., 2011).This fact coupled with low overall lipid yield (6.51-10.59% total lipids) do not bode well for this strain as a biofuel crop, a conclusion shared by other authors recently (Araujo, et al., 2011).

The real mystery with this data set is the inverse correlation between the NMR/GC-MS with the NR; although each experiment has different NR techniques applied the fluorescence (and resultant triolein equivalent data) the trends seem to have a reasonable correlation. As the interaction of the NR dye with lipids in algal cells in highly complex, there could be many causes for this discrepancy. The work by Pick and Rachutin-Zalogin (2012) highlighted that salinity can have a blue-shifting (20 nm for 3 M NaCl) and quenching effect, but as the cells were re-suspended in the same salinity media for testing to avoid this issue, it is thought to be less probable. Pick also showed that glycerol can also have an effect on dye fluorescence, although this is the compatible solute for *Dunaliella*which increases with salinity (Mishra, Mandoli and Jha, 2008), their work suggested that it was a lesser factor compared with saline quenching. It is more probable that the differences are caused by pigment interference and increases in bacterial contamination. The correlation of the β-carotene and chlorophylls a & b concentrations shown by the NMR data (Figure 4.21 B-C) seem to almost mirror the NR fluorescence trends. In work performed in collaboration with former MBioSci student Steven Marshall (not included) it was found that β-carotene in particular seemed to have a large inhibition effect on the fluorescence using the β-carotene overproducing mutants of D. *salina* 19/18 (Marshall, 2013). This effect was hypothesised to be caused by the interception of the excitation wavelength by the pigment. There has also been evidence of the pigment interfering

with NR fluorescence emission in the tests by Wu, et al. (2011). As the NR settings were calibrated using 1 M NaCl adapted cells, if the pigments (both β-carotene and chlorophylls a & b) were to change relative to this standard due to exposure to different in salinities (possibly due to osmotic shock and resultant cell lysis), this could create significant error.

The second major factor could be bacterial absorbance/quenching of the dye, although this is suspected to be less of an effect, as the contamination which was in higher levels in the last experiment still showed the same net NR fluorescence correlations between the 1-3 M NaCl cultures compared with the previous experiments (see Figure 4.20 B).

The final test run showed that the more contaminated 2 M cultures had a closer fluorescence to the 3 M, but the overall fluorescence trend was still the same. If the bacterium was *Halomonas elongata* as suspected due to its visual morphology (long rods), salt tolerance (0.05-3.4 M NaCl) and ability to use glycerol as a carbon source (Ventosa, Nieto and Oren, 1998; Vreeland, et al., 1980) there is some scope for influence on the overall lipid profiles.*H.* elongata has a phospholipid fatty acid composition with 61.5% C18:1, 23.3% C16:0, 10.2% C16:1, along with 5% total other factional contributors (Skerratt, et al., 1991). As these lipids are in the highly polar region, it is more probable that they would have more influence on the direct trans-esterification data than the NR. Fortunately, a sample of the bacterium from a sister 1 M NaCl Dunaliella medium algal culture was available to test this hypothesis and it was possible to perform a direct trans-esterification reaction analysis on a pure culture *ofH. elongata* (Table 4.14).

Table 4.14 - Bacterial FAME profile data for *Halomonas elongata* from (Skerratt, et al., 1991) pure bacterial sample FAME profile data from direct transesterification (see digital appendix 4-4-5). (% of total FAME)

FAME	Structure	Lipid Profile (% of total FAME)		
		Bac Sample	Std Err	Literature
Hexadecanoic Acid ME	16,0	14.91	1.63	23.3
7-Hexadecenoic acid ME	16,1 (cis)	3.82	0.53	10.3
9-Octadecadienoic Acid ME	18,1 (9 Cis)	14.87	2.13	61.7
Octadecanoic Acid ME	18,0	0	0	0.5
Methyl 9,10-methylene-octadecanoate	19,0D (cis 9,10)	60.92	11.86	2.4
Cis-13-eicosenoic acid ME	C20:1	5.49	0.99	0

Note: Blue FAMEs are assumed, green are direct matches to standards on column

Comparing the direct-transesterification data with that of the literature FAME analysis, the same groups are there in high quantities (C16:0 and C18:1), but the amounts are considerably different. This could be due to a number of reasons related to the growth conditions/stress, or simply it could be another strain of bacteria. The important data related to this work is the evidence of considerable overlap of certain lipid groups with that of the algal types, which has the potential to cause errors in quantification. However, due to amount of lipid to biomass, the likely skew is minimal, as this data was gleaned from pure cultures with favourable conditions for the bacteria. Even so, in the interests of future work a series of bacterial indicators were looked for in the NMR and GC-MS traces which could be used to highlight high levels of bacterial contamination (Figures 4.22 and 4.23).

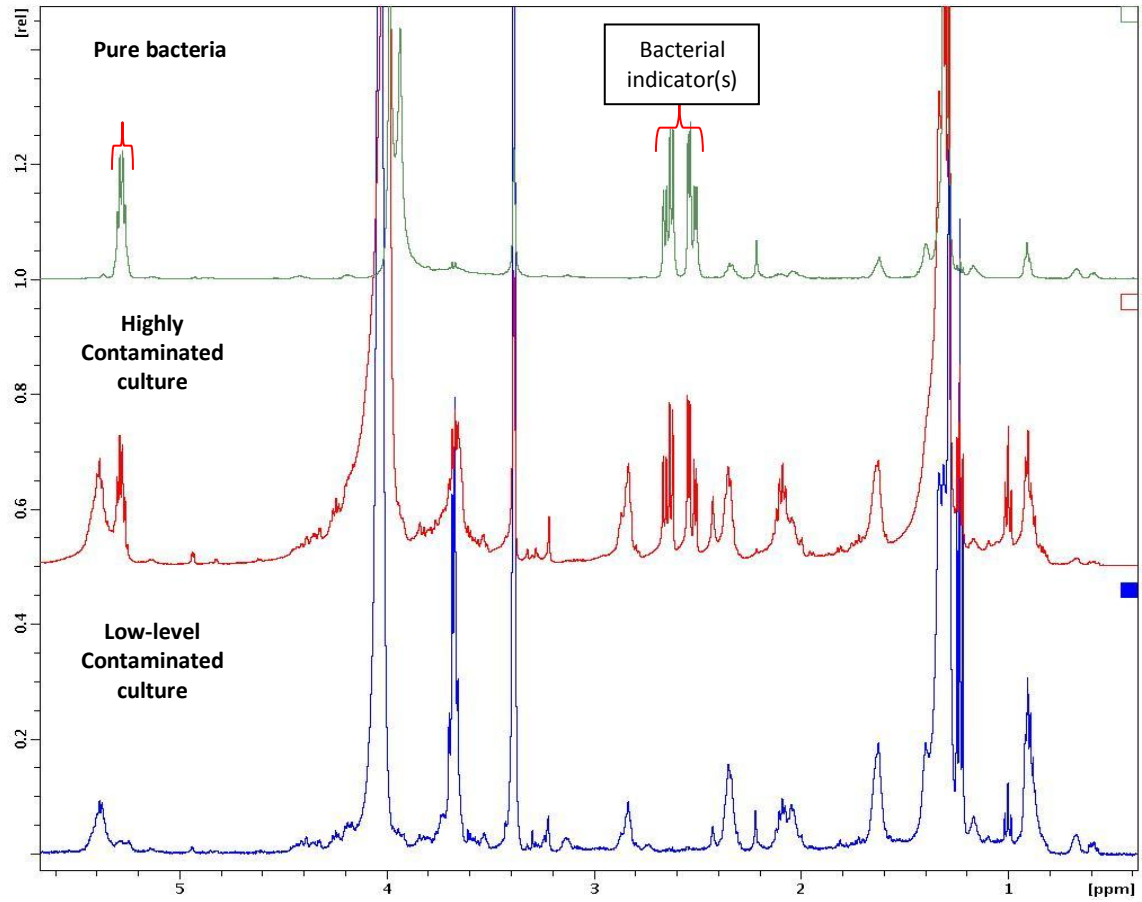

Figure 4.22. Comparison of NMR signals from three bacteria containing samples - Pure Bacteria isolate - Green, highly contaminated*D. salina* 19/30 culture - Red (from NO 10cc/min Osc vs Lam sample 3-2b), less contaminated*D. salina* 19/30 culture - Blue from 5-2b. Both from section 4.8.5.

The bacterial indicator signal is thought to be aspartic acid based on the response, but further work is needed to produce a true identification, which is outside the scope of this study.

A

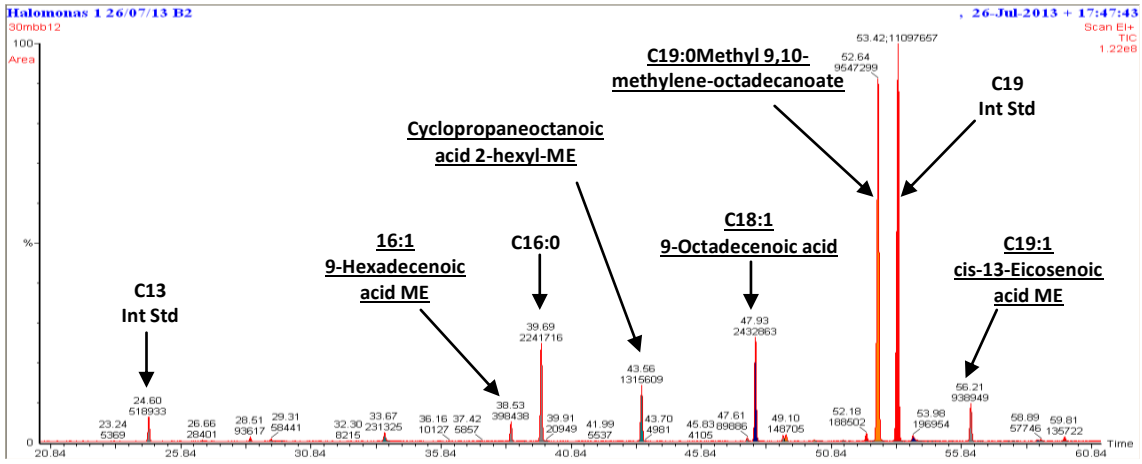

B

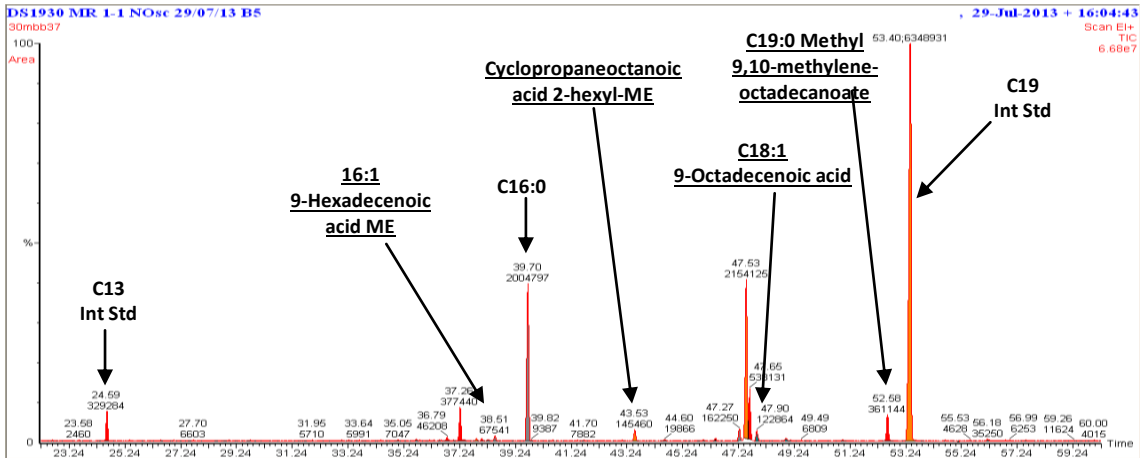

C

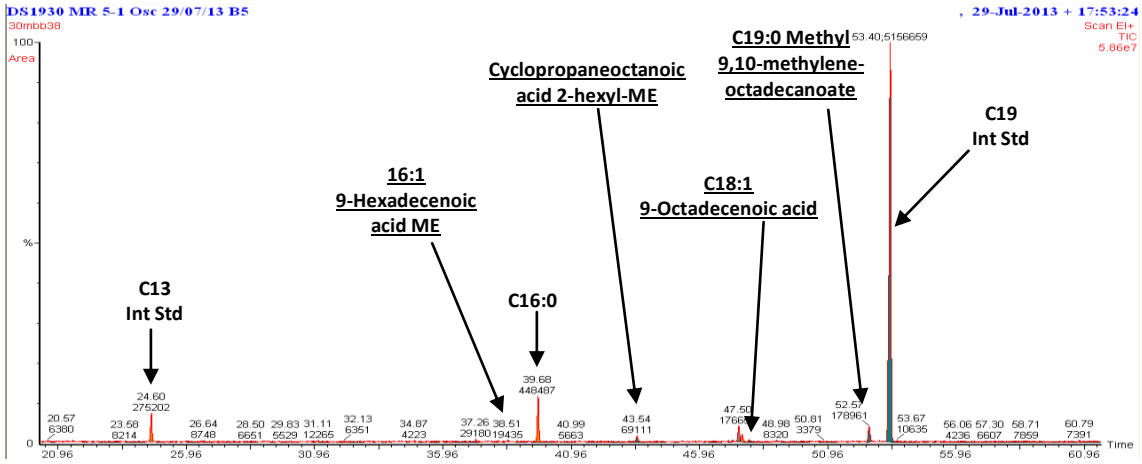

Figure 4.23. Comparison of GC-MSchromatographs from three bacteria containing samples - A) Pure *Halomonas*bacterial culture, B) Heavily contaminated *D.salina* 19/30 algal culture and C)Low contamination*D.salina* 19/30 algal culture

The pronounced bacterial FAMEs are underlined. With C19:0 Methyl 9,10-methylene-octadecanoate seeming to be the strongest indicator. Interestingly, in the previous 1 - 3 M NaCl experiment this FAME seemed to increase with decreasing salinity, which correlated well with visual observation of bacterial growth. Also, in the last batch of 1 – 3 M NaCl NMR data, the bacterial signature is present in the 1 – 2 M NaCl cultures. Based on these findings, the NMR and C19:0 Methyl 9,10-methylene-octadecanoate indicators will be assessed in all following experiments to flag up large amounts of bacterial contamination, along with visual observation of the pellets.

Another effect indirectly related that could have an impact to the cultures and their productivity is the mass transfer rate. The model in section 3.2 showed that increases in salinity of the media, reduced the solubility of the media to carbon dioxide. This could give the 1 M NaCl cultures an advantage over the others in terms of respiration rate, which could also have implications for lipid synthesis.

In conclusion, the salinity experiments show that the 1 M NaCl cultures are the most productive in terms of net biomass and lipid yield, while the lipid profiles of the increased salinity cultures are more amenable to biofuel production. It is possible that the overall yield could be affected by CO_2 solubility limitation and bacterial contamination. The tests have also shown that there are possible limitations to the application of NR techniques with *Dunaliella*, which is thought to be related to pigmentation interference. In recent studies, the NR/Acetone approach has been applied to *D. salina* successfully, but without direct NR lipid quantification and spectro-flourometery (Guzman, et al., 2012). Their method was to use cell sorting and lipid quantification via a predefined ratio. They also demonstrated that the cell sorting method is less sensitive to pigmentation overlap issues compared with other approaches, such as the one used in this study.

Based on the conclusions of this current study, future work will be conducted using cultures grown at one salinity, 1 M NaCl. This will avoid interference from solubility dependency and changes in salinity affecting future NR analysis.

4.5 Growth of *D. salina* 19/30 and 19/18 in 3L Photobioreactors with Microbubbles

Following the lipid method calibration and salinity comparisons in section 4.4, a series of experiments were performed in the Annex growth facility (section 2.8.4) and the MBB growth

room (section 2.8.2) using two custom built 3 L flat plate photo-bioreactors (section 2.12.2) to look at the impact of fluidic oscillation on the generation of air bubbles (section 2.12.1 & 2.12.3) and the growth of *D. salina*. In all growth experiments at least one reactor was monitored for pH, DO and temperature using data loggers and inbuilt sensors (section 2.11) and OD was used to monitor growth (sections 2.6.2). Biomass was harvested at the end of each run after 14 days for lipid analysis using NMR and direct trans-esterification (section 2.2.3-2.2.4).

4.5.1 *D.Salina* 19/18 - With and without Microbubbles, Air 100 cc/min

The first experiment used the β-carotene overproducing strain *D. salina* 19/18 following on from the study in section 4.3. The initial test inoculum was sourced from an 11 day old culture of *D. salina* 19/18 in 1 M NaCl Dunaliella medium with an OD (450 nm) of 0.311. 50 ml of the inoculum was added to 3 L of fresh 1 M NaCl Dunaliella medium in each reactor vessel. Air was provided at 1 bar pressure and set to 100cc/min using control valves, flow rate measurements were made using calibrated flowmeters on the reactor exhausts. Reactor 1 had a regular air feed and reactor 2 was oscillated. Data logger readings were taken at 30 minute intervals in reactor 2 and OD samples were taken every 24 hours, replacing volume for volume with fresh medium.

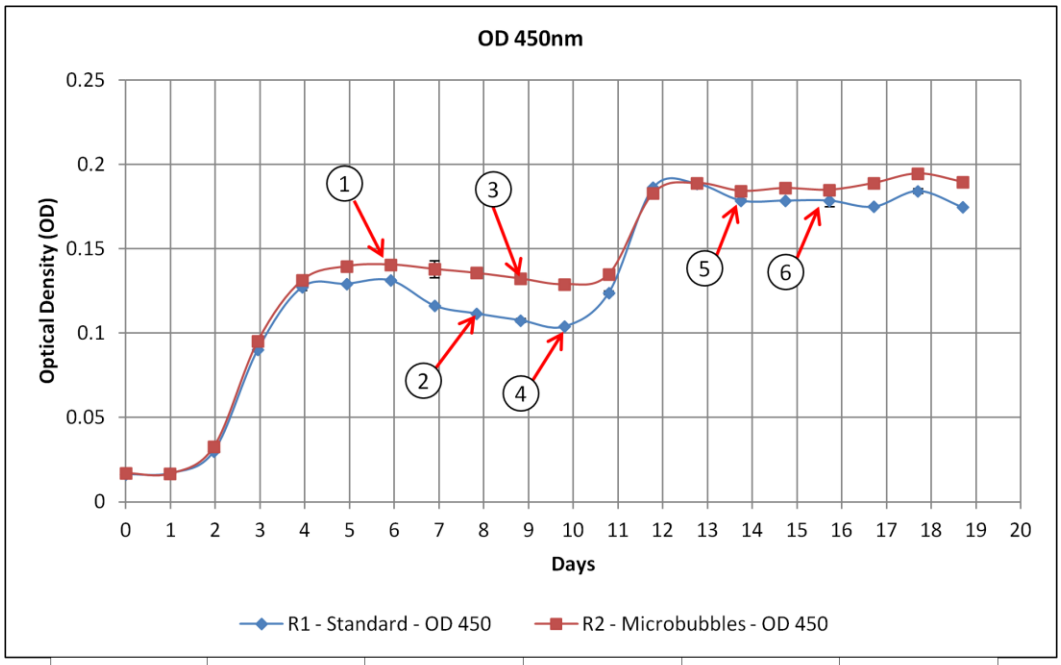

(**1**) -Flow dropped to 40-50cc.min	(**2**) - pH Adjusted to 8.03	(**3**) - Flow back to 90-100cc/min	(**4**) - 1L Cult taken, 1L media added	(**5**) - $NaNO_3$& NaH_2PO_4 Added	(**6**) - More $NaNO_3$& NaH_2PO_4

Figure 4.24.Growth rate of *D.salina* 19/18 under 100 cc/min continuous air, with and without fluidic oscillation. Culture growth measured using OD at 450 nm, Parameters 1 - 6 were altered to try and encourage further growth.

As shown in Figure 4.24, the experimental run did not progress as expected, with the growth of the culture in both reactors plateauing unexpectedly at day 5. Various parameters were changed (see details under graph) in a bid to make the culture grow normally (as per the flask work in section 4.3), but only the addition of fresh medium seemed to have a large effect. Interestingly, the oscillation did seem to still have a small impact versus standard laminar flow, even under these growth limited conditions with a more consistent 'stationary' phase. During testing, an unknown alga was also found alongside the regular 19/18 strain (see section 4.6 on the subsequent work to identify this contaminant), it was believed at the time that this other strain could have stopped the culture growing properly due to competition for resources. Also, due to the differences in morphology and shape, it was highly probably that the OD readings taken were erroneous in comparison to a calibration curve because the experiment was no-longer effectively a mono-culture (excluding bacteria). It was decided following this to revert to the *D.Salina* 19/30 strain following this, as it was definitely an algal mono-culture. The change was also prompted for the reasons mentioned in section 4.3, for future comparable data.

4.5.2 *D.Salina* 19/30 - With and without Microbubbles, Air 100 cc/min

The second experiment was a repeat of the previous one but with the strain *D. salina* 19/30. The initial test inoculum was sourced from a 20 day old culture of *D. salina* 19/30 in 1 M NaCl Dunaliella medium with an OD (595 nm) of 1.093. 50 ml of the inoculum was again added to 3 L of fresh 1 M NaCl Dunaliella medium in each reactor vessel and the air and monitoring procedures were kept then same. Nile red tests were performed using the old single multi-pipette method (see appendix I) with 1 µM NR/ml of culture (20 µl of stain added). 10 ml was taken each time to enable enough cells to be used for the NR process, fresh medium was used to replace this volume for volume again. Harvested cultures were washed once and freeze dried for subsequent NMR (500µl $CDCl_3$/CD_3OD in a ratio 1:4, quadruplicate replicates) processing on day 14. In addition, chlorophyll was extracted using the method in section 2.6.4for comparison with the NMR data on the same day.

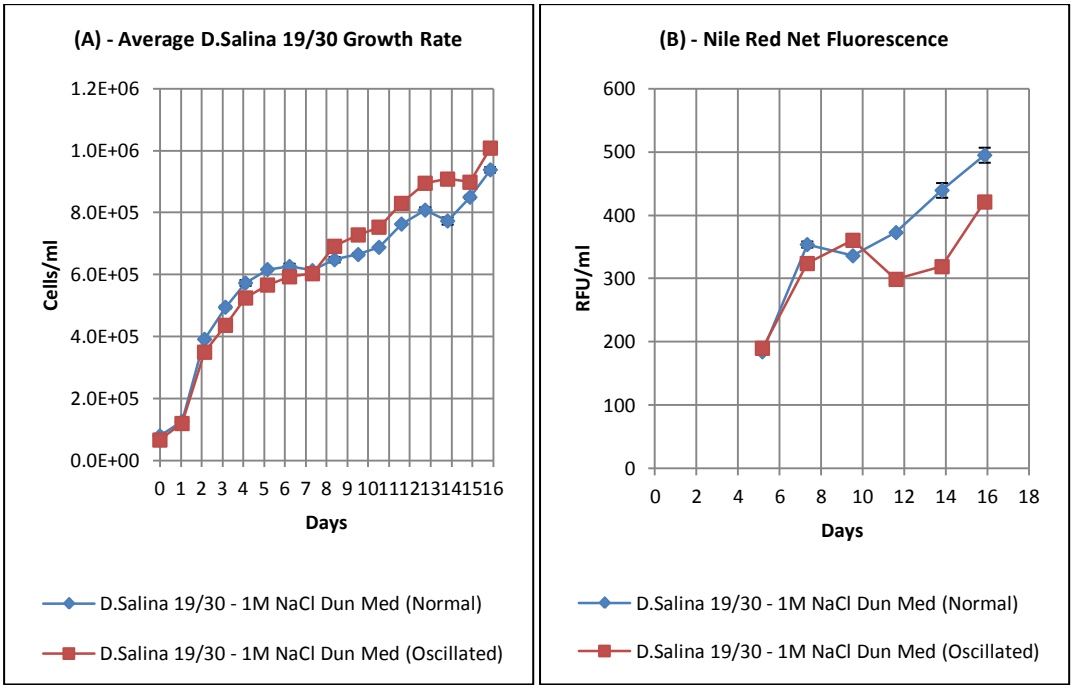

Figure 4.25.A) Growth rate of *D.salina* 19/30 under 100 cc/min continuous air, with and without fluidic oscillation. Culture growth measured using OD at 595 nm to produce an inferred cells per ml. B) Nile Red fluorescence (RFU/ml) Ex: 490 nm Em: 580 nm.

Table 4.15 - *D.salina* 19/30 - NMR pigment data.

Sample	Extracted Chlorophyll content (µg Chl ml^{-1})	Std Err	NMR Chlorophyll (mM/10mg BM)	Std Err	NMR β-Carotene (mg/10mg BM)	Std Err
Normal	1.882	0.1	0.17	0.0259	0.15	0.04877473
Oscillated	1.898	0.037	0.27	0.0212	0.22	0.00887153

Table 4.16 - *D.salina* 19/30 - NMR total lipid data.

Sample	NMR total lipid – C17:1 equivelent (mg/10mg BM)	Std Err
Normal	1.43	0.0506
Oscillated	1.46	0.0581

Table 4.17 - *D.salina* 19/30 - NMR/Nile Red total lipid data per 3L reactor.

Sample	Freeze dry BM (g/3L)	Std Err	NMR total lipid – C17:1 equivalent (g/3L)	Std Err	Nile Red Triolein equivalent (g/3L)	Std Err
Normal	0.1275	0.006	0.01823	$3.011x10^{-5}$	0.0205	0.0013
Oscillated	0.125	0.0035	0.01825	$2.054x10^{-5}$	0.018	0.0031

Table 4.18 - *D.salina* 19/30 - NMR/Nile Red lipid group data.

Sample	NMR Unsat lipid signal (mM/10mg BM)	Std Err	NMR Unsat Me lipid signal (mM/10mg BM)	Std Err	NMR Sat Me lipid signal (mM/10mg BM)	Std Err
Normal	8.82	0.2809	2.54	0.0968	6.49	0.11983
Oscillated	9.83	0.2146	2.83	0.151	7.03	0.469087

From the data in Figure 4.25 and Tables 4.15 to 4.18, it was clear that the same limiting effect was still present despite the swapping of strains. The oscillation effect also seemed to generate the same slight increase in productivity toward the end of the experiment (day 8 onward). The NR data showed at net increase in lipid accrual throughout the experiment, with the oscillated culture showing a lower response after day 10. This also culminated with a slightly lower NR triolein equivalent than the standard conditions. Both the NR and NMR lipid data were in the same region of 0.018-0.02 g/reactor, but the NMR data showed a slight opposite correlation. Based on the work in section 4.4.5, this could be explained by the differences in pigmentation as the amount of chlorophyll and β-carotene were both higher in the oscillated culture. Based on the data set as a whole it looks like the lipid levels were very similar, but the oscillated reactor may have a slightly higher productivity. This trend looks to be also the same for general growth rates.

4.5.3 *D. salina* 19/30 - No Air, reactor lid off ambient air test.

Given the results in the previous two tests, it was suspected that the cultures may have been limited by the level of aeration in some way. To rule out the possibility of pressure build-up within the reactors due to a restriction on the gas outlet and turbulence related cell damage, the experiment was repeated without any aeration and the reactor lids left ajar. The initial test inoculum sourced from a 23 day old culture of *D. salina* 19/30 in 1 M NaCl Dunaliella medium with an OD (595nm) of 1.103. 50 ml of the inoculum was again added to 3 L of fresh 1 M NaCl Dunaliella medium in each reactor vessel. All monitoring procedures were kept the same, but no harvesting was performed.

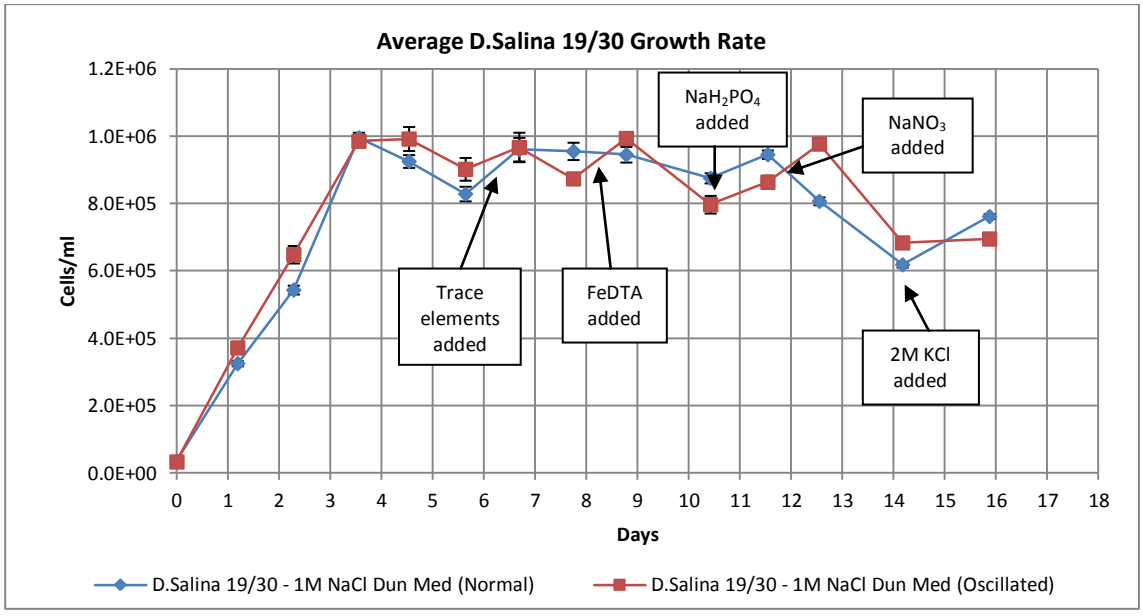

Figure 4.26.Growth rate of *D.salina* 19/30 with no aeration and reactor lid off. Culture growth measured using OD at 595 nm to produce an inferred cells per ml, Parameters were altered to try and encourage further growth.

A very similar trend was found to the previous two experimental runs, but the growth rate was actually higher without aeration or mixing (Figure 4.26). Again, a number of elements of the original media were added, but there was no growth response. Although, it was interesting to note that both reactors behaved in the same way, there was no difference as observed before, so this proved the oscillation is having an effect.

4.5.4 *D. salina* 19/30 - Conditions & Media testing

To avoid further costly repeats of the 3 L experiments to isolate the source of growth limitation, an experiment was performed using 250 ml flasks and 50 ml tubes to test every available parameter with the exclusion of bubbling. Because the growth in flasks in the MBB growth room had such higher growth rates compared with that of the Annex growth chamber, location was included as a part of the test. Cultures and media were taken from the previous experiment to isolate if the problems were apparatus specific and fresh media and inoculum were also used for comparison. The new inoculum was from a 28 day old culture of *D. salina* 19/30 in 1 M NaCl Dunaliella medium with an OD (595 nm) of 1.78. The following conditions/cultures were set up and ran for 16 days, monitoring growth by OD at 595 nm (see Table 4.19 below):

Table 4.19 - *D.salina* 19/30 - Conditions and media variant tests.

ID	Location	Growth vessel	Parameter tested	
F1	APS Annex (section 2.8.4)	250ml Flask	100ml taken from previous experiment.	
F2			100ml taken from previous experiment, re-suspended in fresh medium.	
F3			New inoculum added to fresh media.	
F4			100ml taken from previous experiment, algae discarded, fresh inoculum added to used media.	
N1		50ml Falcon Tube	30ml taken from previous experiment. Lid sealed for 7 days, then $NaHCO_3$ added and lids resealed. The following stocks were spiked initially depending on which ID:	KCl added
N2				$MgCl_2$ added
N3				$CaCl_2$ added
N4				$MgSO_4$ added
N5				$NaNO_3$ added
N6				$NaSO_4$ added
N7				NaH_2PO_4 added
N8				FeEDTA added
N9				Trace Elements added
N10				HEPES Buffer added
N11				$NaHCO_3$ added
M1			30 ml taken from previous experiment, algae discarded, fresh inoculum added to used media. Lid sealed for 7 days, then replaced with foam bung for last 7.	
M2				
M3				
M4			30 ml taken from previous experiment, re-suspended in fresh medium. Lid sealed for 7 days, then replaced with foam bung for last 7.	
M5				
M6				
A1	MBB Growth room (section 2.8.2)		30 ml taken from previous experiment, re-suspended in fresh medium. Lid sealed for 7 days, then replaced with foam bung for last 7.	
A2				
A3				
A4			30 ml taken from previous experiment. Lid sealed for 7 days, then replaced with foam bung for last 7.	
A5				
A6				

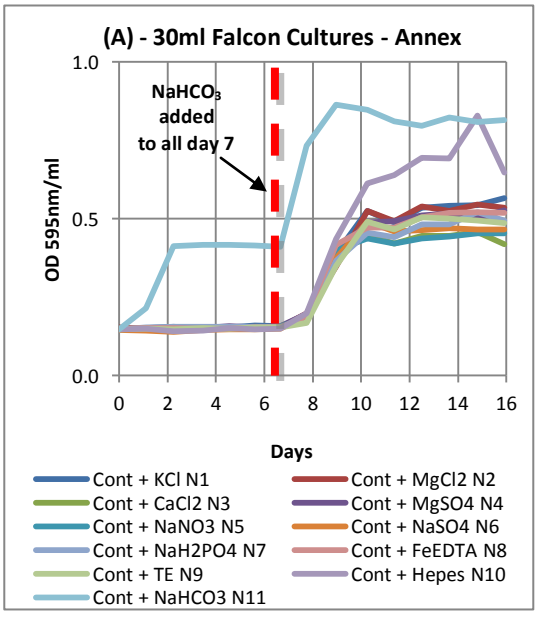

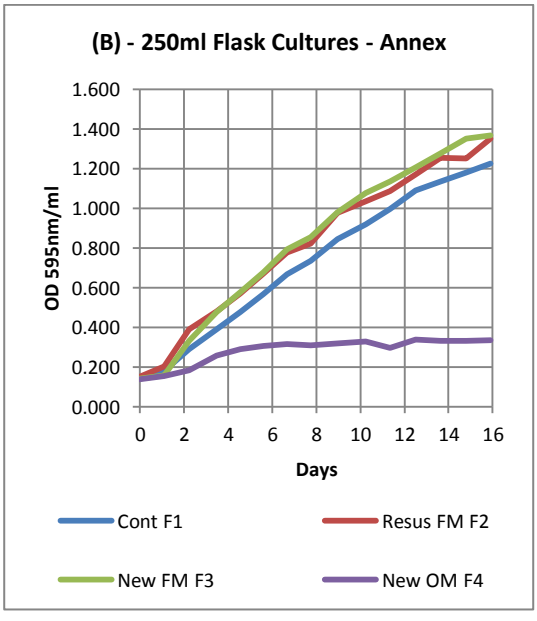

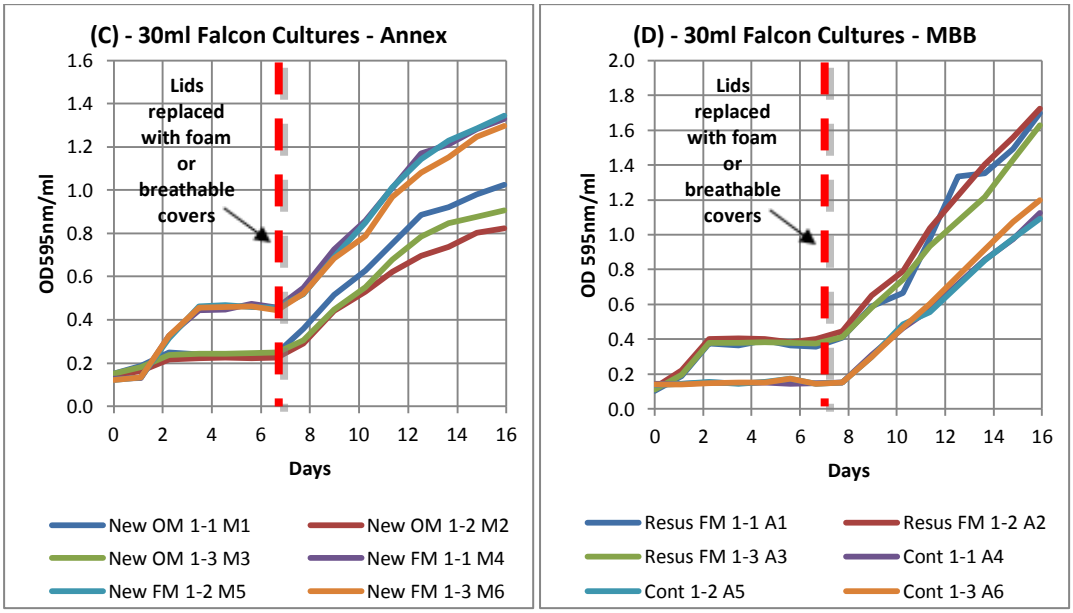

Figure 4.27.Growth rate of *D.salina* 19/30 under different conditions and media variants. Culture growth measured using OD at 595 nm to produce an inferred cells per ml, A) 30 ml cultures grown in Falcon tubes in APS annex (conditions N1-N10), B) 250 ml flask cultures grown in the APS annex (conditions F1-F4), C) 30 ml cultures grown in Falcon tubes in APS annex (conditions M1-M6), D) 30 ml cultures grown in Falcon tubes in MBB growth room (conditions A1-A6).

It can be seen from the data, that when any of the cultures are sealed that despite of the nutrients spiked, the only samples that demonstrate growth are the ones with $NaHCO_3$ which indicates the cultures are clearly limited due the lack of a carbon source, i.e. CO_2. The cultures re-suspended in fresh media show a growth boost, it is highly probably this is caused by $NaHCO_3$ present in the fresh media. The data also indicates that the cultures are not carbon limited when not sealed, clearly a different results to that of the 3 L reactor, even with lid off. This effect is possibly due to the interfacial area volume ratio been different in scale. Interestingly, in culture N10 when the HEPES buffer is exposed to increased bicarbonate, the growth increase is more significant than the other spiked conditions. This is possibly due to its influence on the pH and therefore the equilibrium relationship between the three forms of dissolved CO_2 available for uptake by the *D. salina* cells (Ben-Amotz, E.W. Polle and Subba Rao, 2009) . The data also shows that the conditions are slightly more favourable in the MBB growth room compared to that of the Annex growth chamber. To test if this was a factor, air samples were taken in each location and from the air feeds in those areas (including the F3 lab, section 2.8.3) using a Vaisala M170 Carbon dioxide probe (Serial: Y2140022) equipped with a GMP343 Carbo-cap (0-2000 ppm sensitivity), see graphs in Figure 4.28 below.

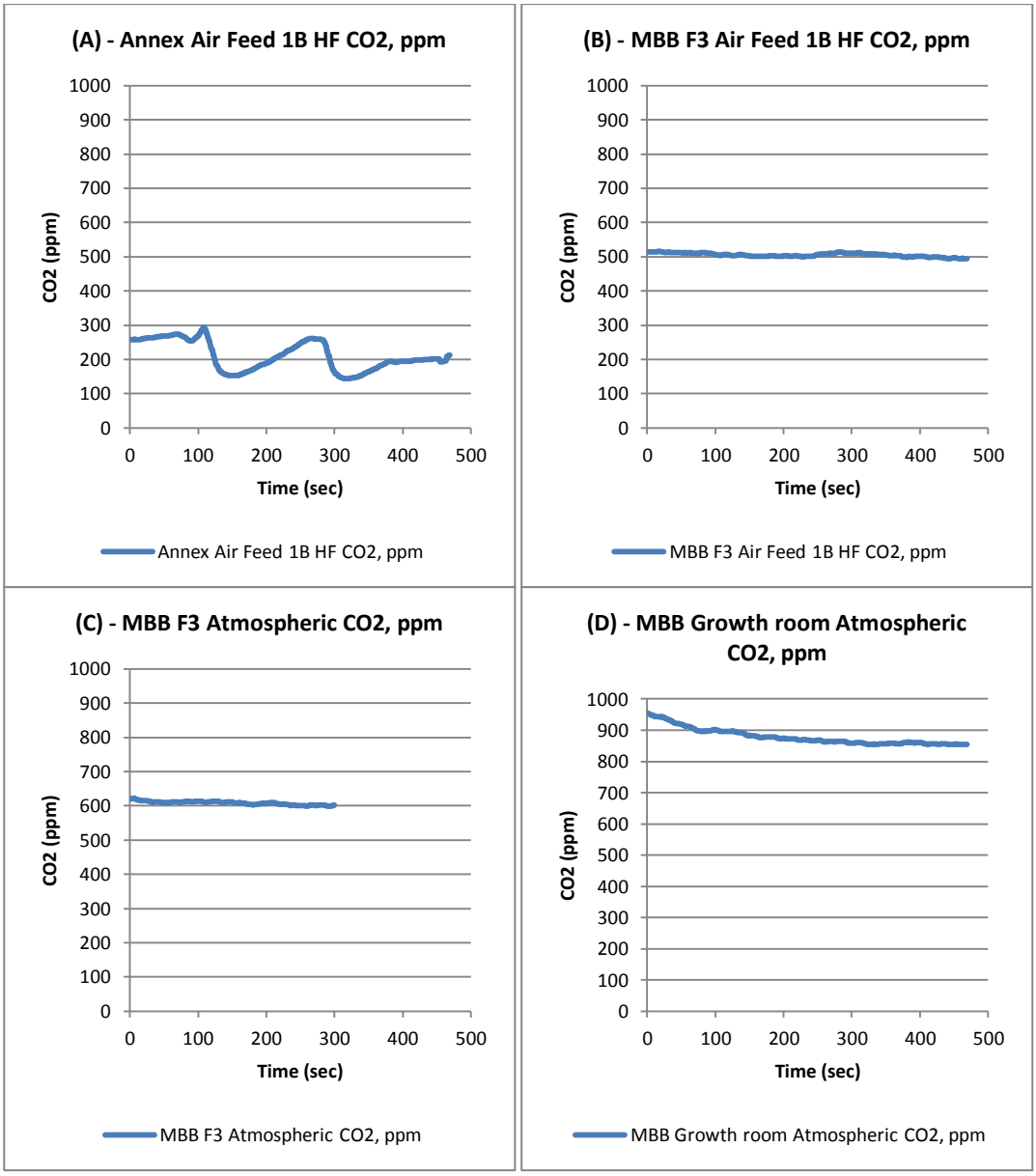

Figure 4.28.Carbon dioxide concentration (ppm) from air from four different sources. A) APS Annex air supply at high flow rate, B) MBB F3 lab air supplyat high flow rate, C) MBB F3 ambient lab air, D) MBB growth room ambient air.

It can be seen from the data that the different locations have radically different levels of available CO_2. 500 ppm corresponds with 0.05% CO_2 in air, which is the atmospheric 'normal' (see section 3.2), so the only supply with that correct range is in MBB from the air supply line. The Annex feed is approximately 40% lower and the growth room atmospheric value in MBB is 70% higher, which is possibly why the cultures grown in the MBB growth room are not CO_2 limited and inversely so in the annex.

To ensure no other factors were coming into play, a mini-reactor sparger (section 2.12.3) made with the same material as the ones in the bigger 3 L reactor types (section 2.12.2) was also tested to see if there was any effect on growth. The sterilisation procedure using Microsol was

also tested to see if there were any detrimental effects. 40 ml of fresh 1 M NaCl Dunaliella medium was added to 9 x 50ml centrifuge tubes, 3x of which contained a sparger, 3x were standards and 3x had been pre-washed with Microsol detergent. To each of these tubes, 2 ml of a 28 day old *D. salina* 19/30 culture was added (in 1 M NaCl Dunaliella medium with an OD (595 nm) of 1.352). The tubes were held in a wire rack and incubated in the MBB growth room (section 2.8.2) for 9 days to see if there were any negative growth effects. Monitoring was performed using OD at 595nm.

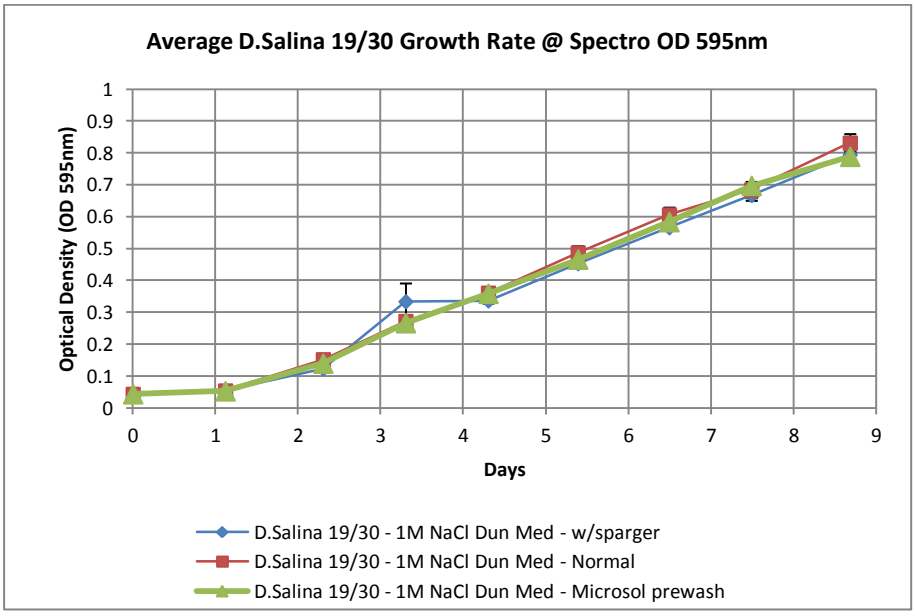

Figure 4.29. Growth rate of *D.salina* 19/30 with and without Microsol pre-wash and in the presence of a sterilised micro-sparger. Culture growth measured using OD at 595 nm to produce an inferred cells per ml.

The results from the test showed no major differences between each of the conditions, thus it was concluded these factors were not involved in the growth inhibition.

4.5.5 *D. salina* 19/30 - With and w/out Microbubbles.

To test out the carbon source limitation hypothesis, another repeat experiment of the second 3 Litre run was performed, but this time with the lid left ajar and on day 9 the non-oscillated reactor was sparged with 100% CO_2 at 100 cc/min for 5 minutes a day (the rest of the time using air as standard). Data logging was carried out on both reactors during this experiment as new equipment had arrived. The initial test inoculum was sourced from a 14 day old culture of *D. salina* 19/30 in 1 M NaCl Dunaliella medium with an OD (595 nm) of 1.108, to rule out any culture age issues. 50 ml of the inoculum was again added to 3 L of fresh 1 M NaCl Dunaliella medium in each reactor vessel and the air and monitoring procedures were kept then same. Nile red tests were performed using the old single multi-pipette method (Appendix I) with 1 µM NR/ml of culture (20 µl of stain added) when the cultures were harvested on day 15. 10 x 50 ml samples were harvested, washed once and freeze dried for subsequent NMR (Normal + CO2: 660 µl $CDCl_3/CD_3OD$ in a ratio 1:4, Oscillated: 500µl $CDCl_3/CD_3OD$ in a ratio 1:4. triplicate replicates) and direct trans-esterification (triplicate again). In addition, chlorophyll was extracted using the method in section 2.6.4for comparison with the NMR data on the same day.

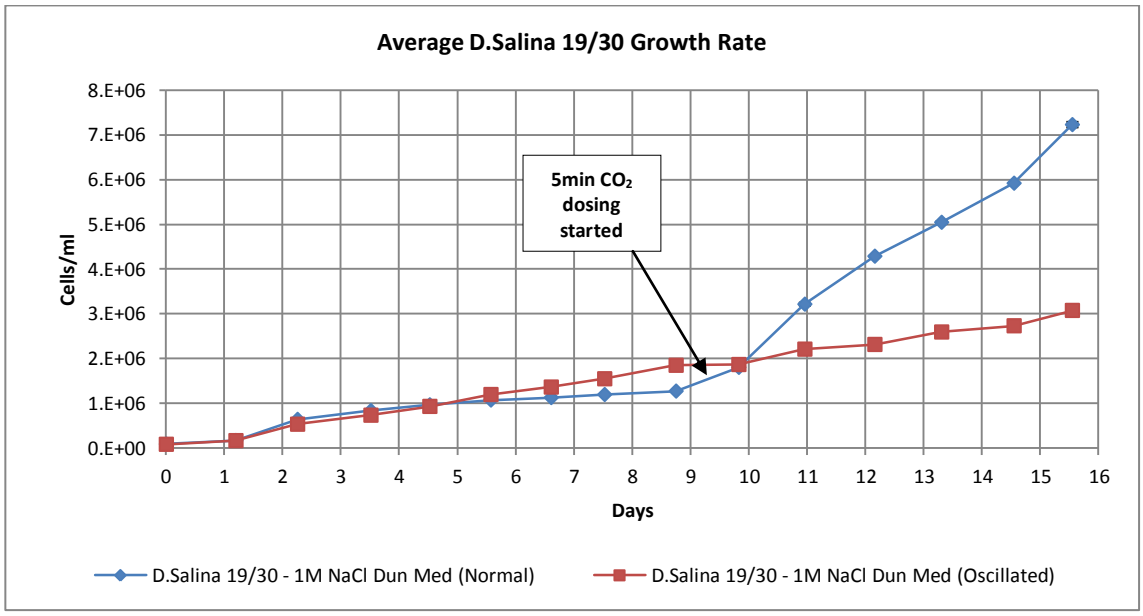

Figure 4.30.Growth rate of *D.salina* 19/30 under 100 cc/min continuous air, with and without fluidic oscillation. Dosing with 100 cc/min of 100% CO_2 for 5 min per day started on day 9, to the normal aerated reactor only. Culture growth measured using OD at 595 nm to produce an inferred cells per ml.

Table 4.20 - *D.salina* 19/30 - NMR / extracted pigment data.

Sample	Extracted Chlorophyll content (µg Chl ml^{-1})	Std Err	NMR Chlorophyll (mM/10mg BM)	Std Err	NMR β-Carotene (mg/10mg BM)	Std Err
Normal + CO2	16.98	0.15	0.31	0.04	0.20	0.04
Oscillated	6.66	0.14	0.41	0.03	0.33	0.02

Table 4.21 - *D.salina* 19/30 - NMR/Nile Red total lipid data per 3 L reactor.

Sample	NMR total lipid – C17:1 equivalent (g/3L)	Std Err	Direct Trans total lipid (g/3L)	Std Err	Nile Red Triolein equivalent (g/3L)	Std Err
Normal + CO2	0.1673	0.000252	0.2663	0.000271	0.0904	0.0122
Oscillated	0.1128	0.000167	0.1004	0.000335	0.0344	0.0063

Table 4.22 - *D.salina* 19/30 - NMR lipid group data.

Sample	NMR Unsat lipid signal (mM/10mg BM)	Std Err	NMR Unsat Me lipid signal (mM/10mg BM)	Std Err	NMR Sat Me lipid signal (mM/10mg BM)	Std Err
Normal + CO2	9.24	1.79	2.78	0.52	4.43	0.82
Oscillated	15.22	0.96	4.23	0.27	7.58	0.46

Table 4.23 - *D.salina* 19/30 - Direct transesterification FAME profile (% of total FAME):

FAME	Structure	Lipid Profile (% of total FAME)			
		Non-Osc + CO2	Std Err	Oscillated	Std Err
Methyl 4,7,10,13-hexadecatetraeoate	16,4 (cis n3)	11.43	1.29	9.53	1.00
9,12,15-Octadecatrienoic acid ME	18,3 (trans)	2.16	0.25	2.10	0.21
Hexadecanoic Acid ME	16,0	22.58	2.58	23.95	2.54
γ linolenic ME	18,3 (n6)	3.10	0.43	3.20	0.34
9,12-Octadecadienoic Acid ME	18,2 (6 cis)	5.02	0.69	5.37	0.66
9,12,15-Octadecadienoic Acid ME	18,3 (n3)	44.84	7.90	44.11	6.90
9-Octadecadienoic Acid ME	18,1 (9 Cis)	4.30	0.54	3.69	0.48
9-Octadecadienoic Acid ME	18,1 (9 trans)	3.01	0.37	4.28	0.52
Octadecanoic Acid ME	18,0	0.84	0.14	0.91	0.09
Methyl 9,10-methylene-octadecanoate	19,0D (cis 9,10)	2.71	0.05	2.86	0.00
	Total:	**100.00**	**14.25**	**100.00**	**12.72**

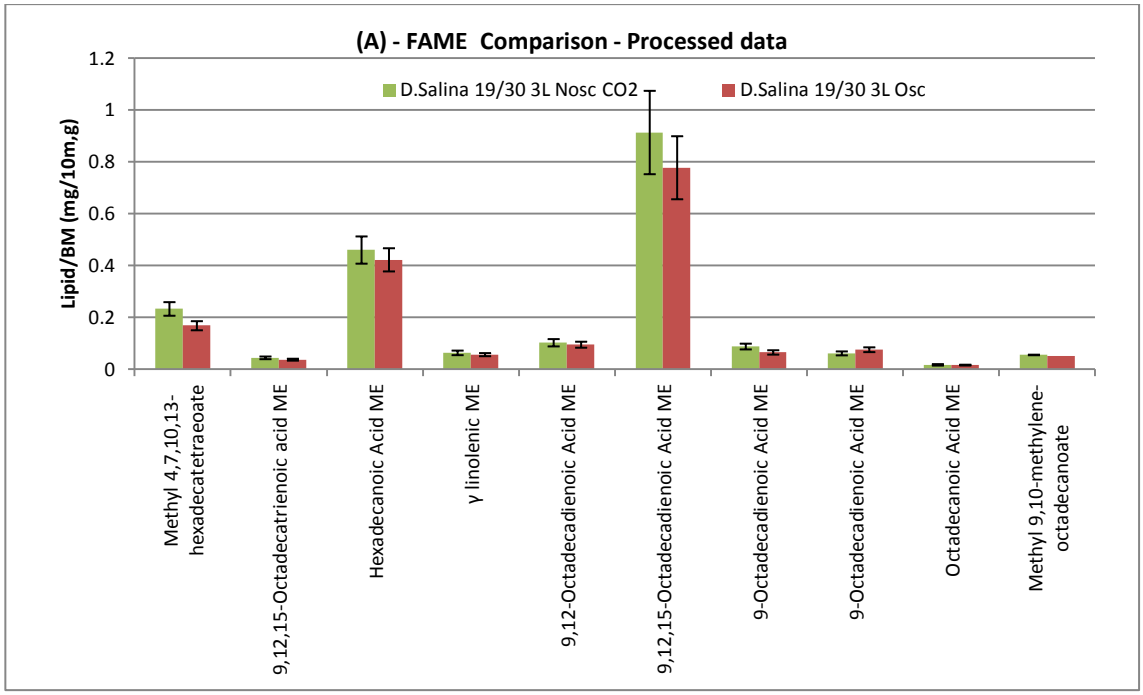

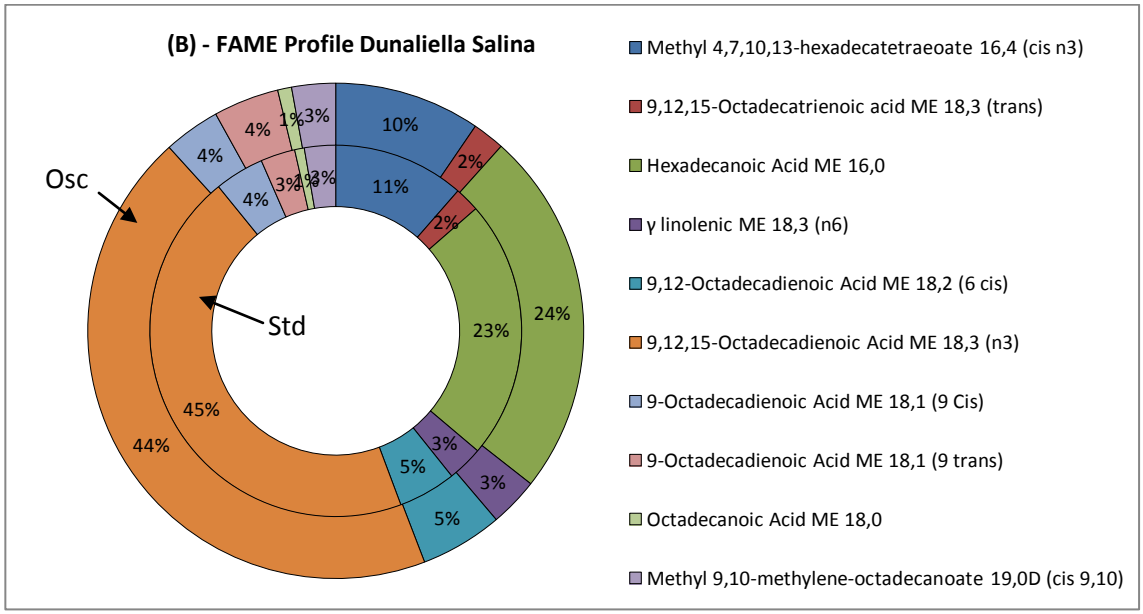

Figure 4.31. *D.salina* 19/30 with and without fluidic oscillation - A) FAME quantity comparison, Lipid/Biomass (mg/10mg) and B) FAME lipid profile (%).

It can be seen from the data that growth before CO_2 addition is slightly increased in both cases with the lid open and aeration, with the oscillated cultures showing marginally better results again. When the CO_2 is added to the standard reactor the growth rate is almost exponential immediately, which confirms the test hypothesis. The increased growth also seems to be coupled with an increased lipid yield, which is confirmed using all three lipid methods. But unfortunately there is a large discrepancy in terms of overall yield. Based on the large difference in pigmentation between the conditions (and also a lack of correlation in this

regard), the NR quantification would be also potentially suspect. The FAME profiles between the two conditions are almost the same, but a slight reduction in the PUFAs in the oscillated cultures make that strain slightly better for fuel production. Interestingly, the C19:0 (cis 9,10) amounts were also the same, so no major difference in bacterial contamination was evident. If scope was limited from 16:0 to 18:3 again, the total lipid amounts the following would be useable in each case (%); R1 - 85.86 ±12.91, R2 - 87.61 ±11.73 (note this was applied to the net NMR and GC-MS total lipid calculated yields).

Unfortunately, following this experiment there was no further time left in the Annex lease to do further experiments as originally planned with different amounts of dosing with micro bubbles, so work was focussed on the use of the mini reactor systems.

4.6 Isolation and Identification of Unknown Alga

Following the first attempt to grow *D. salina* 19/18 in the 3 Litre reactors and the appearance of the unknown algae (see Figure 4.32 below), it was decided to isolate it and perform an 18S rDNA identification (see section 2.7) to see if it may be a contaminating strain or possibly a gamete form of DS 19/18 (Borowitzka and Siva, 2007). This work was performed at the same time as genetic tests of the *D. salina* 19/30 strain to ensure it was also the correctly specified organism.

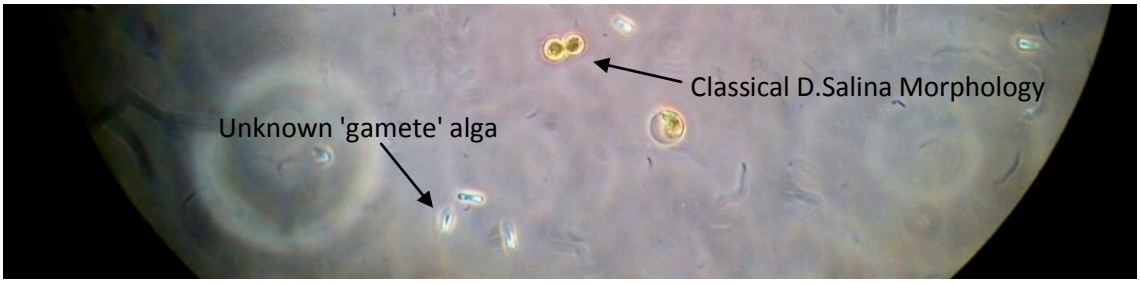

Figure 4.32 - Photo by x40 optical microscopy of mixed culture with unknown 'gamete' strain and regular DS 19/18

4.6.1 Overview and isolation

Three samples were selected that have been shown to contain the 'gamete' variant of *D. salina* 19/18; A sister culture of the flask used to inoculate the reactors in the section4.5.1 experiments, another older culture displaying similar characteristics and a sample harvested from the second 3 Litre photo-bioreactor in the section4.5.1 experiment. A series of agar plates were made using the 'sloppy' agar method developed by Brown, et al. (1987), see section 2.4, with 5 different concentrations of the cultures from each of the three sources. The

plateswere sealed with permafilm and placed upside-down in a sealed transparent bag and incubated in the MBB growth room under high light for two weeks (see section 2.8.2). When colonies had formed, sections of agar were removed and the cultures were successively scaled up using fresh media until a viable mono-culture was produced at flask scale (100 ml). The cultures were then checked using optical microscopy to ensure the target algal types were present and bacterial contamination was minimal.

4.6.2 Visual characterisation

The morphology of each strain was visually characterised using two methods, standard optical microscopy and scanning electron microscopy (SEM), see section 2.5. Standard microscope images were taken using a Nikon Eclipse E400 Microscope equipped with a Nikon DXM1200 Digital Camera. General illumination was achieved using the microscopes built-in lighting system. All images were taken using a Nikon 100x Oil immersion lens (Phase 3). Image acquisition was performed using LUCIA G Software.

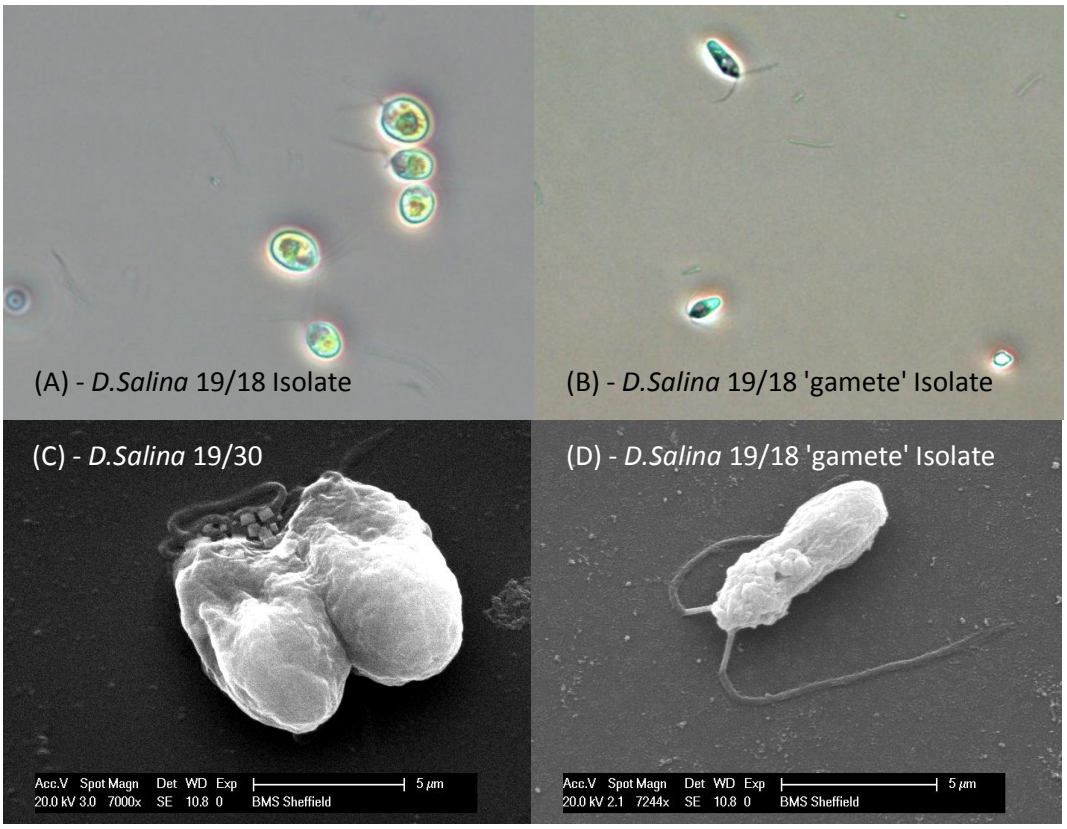

Figure 4.33 - Optical (x40, top) and Scanning electron (bottom) microscopy images of algal strains used in this study. A) *D.salina* 19/18 plated isolate, B) *D.salina* 19/18 plated 'gamete' isolate, C) *D.salina* 19/30 CCAP strain, D) *D.salina* 19/18 plated 'gamete'

It can be seen that the 19/18 'gamete' isolate (Figure 4.33 B & D) is very different in shape to the standard 19/18 and the 19/30 strains of *D. salina* (Figure 4.33 A & C). There is much more of a rod shape to the cell body and darker pigmentation toward the flagella end of the cell. Although, due to *D. salina*'s lack of a cell wall its shape can be highly variable, which can make visual identification problematic (Oren, 2005). A search through the literature yielded a couple of *Dunaliella* strains with a striking similarity to that of the 'gamete'; The first is 'MUR202' in the paper by Borowitzka and Siva (2007), Figure 4.34c. They state that this strain may be an entirely new species, according to the authors, this strain shows a "typically elongated cell form and the absence of a stigma" with a length of around 12 µm, slightly longer than that of the 'gamete' isolate. This strain is interesting because with no stigma or eye spot, potentially leading to limited phototaxis, which the isolated 'gamete' strain does exhibit when grown in flasks. The second strain which also bares a distinct similarity is *D. primolecta* 'MUR55'=CCAP 11/43, Figure 4.34e. This strain has one eye spot and is around 6 µm in length, which correlates with the SEM scale images in Figure 4.33D. The possibility of this strain being present is high, as it was used by the post doc Dr Shepherd in experiments at the same time as the cultures of *D. salina* 19/18 (Figure 4.34a), which were subsequently used as inoculates in my experiments. Based on this observation, three separate strain variants were present in the original *D. salina* 19/18 culture, which after plating has reduced to two.

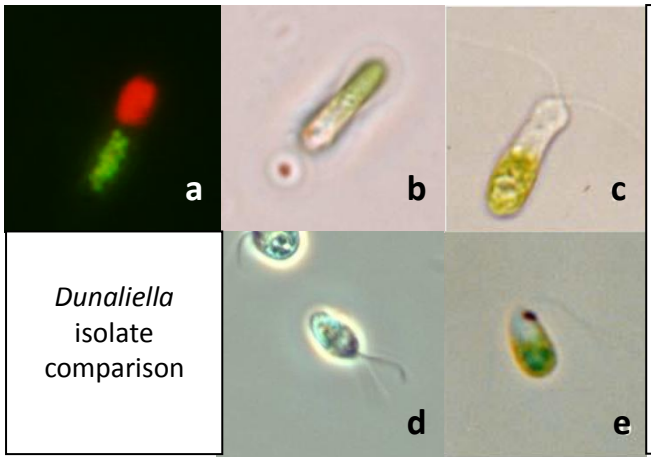

Figure 4.34 -Microscope photos:

a - 'unknown' algae found by Dr Shepherd in D.S 19/18 cultures.
b - 'gamete' appearance in 19/18 cultures
c - 'MUR202' strain
d - 'gamete' isolate from reactor experiment
e - 'MUR55' *D.primolecta* CCAP 11/43 strain

4.6.3 18s rDNA Identification

Molecular identification of species-specific oligonucleotidesis currently one of the most powerful tools available in biology that is capable of performing the tricky task of differentiating between morphologically similar species with mixed populations (Olmos, et al., 2009; Olmos, Paniagua and Contreras, 2000).The molecular characterisation of micro-algal groups is typically performed based on the genetic information encoded within the 16S and 18S ribosomal RNA (rRNA) genes (Alonso, et al., 2012). The 16S gene (and its homologue the 18S) encode for the rRNA molecules present in the subunit of the ribosome, a region which has high genetic conservation between different micro-algal strain types. This property makes these genes very useful to perform identification work as they are relatively genetically stable and can provide a consistent molecular 'fingerprint'.

In this work, genomic DNA (gDNA) was extracted from *D. salina* 19/30 and the two plated isolates originally from *D. salina* 19/18. A PCR reaction was then performed to amplify a specified region in the gDNA corresponding with the 18S rRNA. The PCR products were then purified and the amount of DNA was quantified, before sending the samples for sequencing. Details of the procedures used and the forward and reverse primers applied are detailed in section 2.7. For ease of comparison during this work the two isolates for referred to as 'isolate' for the typical *D. salina* 19/18 shaped cells and 'gamete' for the rod shaped 19/18 cells. Extracts and PCR products were visualised by agarose gel electrophoresis (section 2.7.6), typically the bands ranged from ~700bp to ~1500bp in size, see Figure 4.35 below.

A

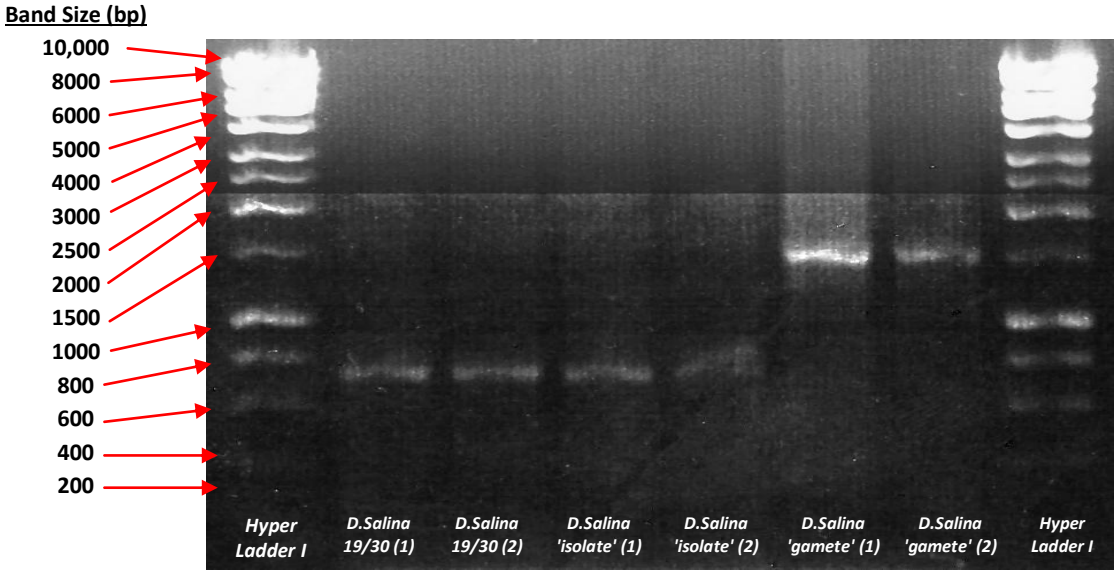

B

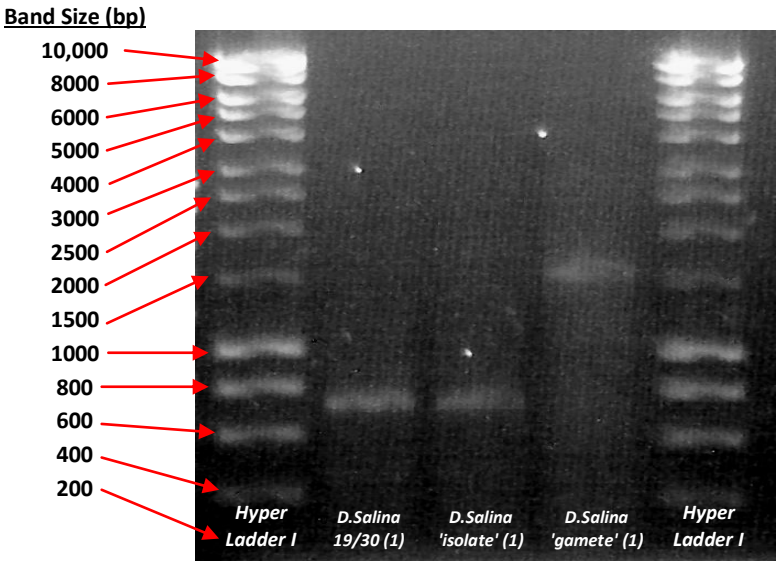

Figure 4.35 - DNA gel electrophoresis images.

A) After PCR Extraction, B)Gel after PCR Clean-up

Sequence of 18s rDNA Gene of Algal Isolates

One purified PCR product of each strain was sent to Eurofins MWG in London for sequencing, the results are as follows:

18S rRNA gene sequence of 'DS 19/30' (1)

Forward sequence (499 letters):

"AGTTAAAGCTCGTAGTTGGATTTCGGGTGGGTTGTAGCGGTCAGCCTTTGGTTAGTACTGCTACGGCC
TACCTTTCTGCCGGGGACGAGCTCCTGGGCTTAACTGTCCGGGACTCGGAATCGGCGAGGTTACTTTGA
GTAAATTAGAGTGTTCAAAGCAAGCCTACGCTCTGAATACATT
AGCATGGAATAACACGATAGGACTCTGGCTTATCTTGTTGGTCTGTAAGACCGGAGTAAT
GATTAAGAGGGACAGTCGGGGGCATTCGTATTTCATTGTCAGAGGTGAAATTCTTGGATT
TATGAAAGACGAACTTCTGCGAAAGCATTTGCCAAGGATGTTTTCATTAATCAAGAACGA
AAGTTGGGGGCTCGAAGACGATTAGATACCGTCGTAGTCTCAACCATAAACGATGCCGAC
TAGGGATTGGCAGGTGTTTCGTTGATGACCCTGCCAGCACCTTATGAGAAATCAAAGTTT
TTGGGTTGCGGGGGGAATAT"

Reverse sequence (503 letters):

"TATAGGTGCTGGCAGGGTCATCAACGAAACACCTGCCAATCCCTAGTCGGCATCGTTTAT
GGTTGAGACTACGACGGTATCTAATCGTCTTCGAGCCCCCAACTTTCGTTCTTGATTAAT
GAAAACATCCTTGGCAAATGCTTTCGCAGAAGTTCGTCTTTCATAAATCCAAGAATTTCA
CCTCTGACAATGAAATACGAATGCCCCCGACTGTCCCTCTTAATCATTACTCCGGTCTTA
CAGACCAACAAGATAAGCCAGAGTCCTATCGTGTTATTCCATGCTAATGTATTCAGAGCG
TAGGCTTGCTTTGAACACTCTAATTTACTCAAAGTAACCTCGCCGATTCCGAGTCCCGGA
CAGTTAAGCCCAGGAGCTCGTCCCCGGCAGAAAGGTAGGCCGTAGCAGTACTAACCAAAG
GCTGACCGCTACAACCCACCCGAAATCCAACTACGAGCTTTTTAACTGCAACAACTTAAA
TATACGCTATTGGAGCTGAAATTA"

18S rRNA gene sequence of 'isolate' (1)

Forward sequence (499 letters):

"GTTAAAAGCTCGTAGTTGGATTTCGGGTGGGTTGTAGCGGTCAGCCTTTGGTTAGTACTG
CTACGGCCTACCTTTCTGCCGGGGACGAGCTCCTGGGCTTAACTGTCCGGGACTCGGAAT
CGGCGAGGTTACTTTGAGTAAATTAGAGTGTTCAAAGCAAGCCTACGCTCTGAATACATT
AGCATGGAATAACACGATAGGACTCTGGCTTATCTTGTTGGTCTGTAAGACCGGAGTAAT
GATTAAGAGGGACAGTCGGGGGCATTCGTATTTCATTGTCAGAGGTGAAATTCTTGGATT
TATGAAAGACGAACTTCTGCGAAAGCATTTGCCAAGGATGTTTTCATTAATCAAGAACGA
AAGTTGGGGGCTCGAAGACGATTAGATACCGTCGTAGTCTCAACCATAAACGATGCCGAC
TAGGGATTGGCAGGTGTTTCGTTGATGACCCTGCCAGCACCTTATGAGAAATCAAAGTTT
TTGGGTTGCGGGGGGGGTTA"

Reverse sequence (512 letters):

"ATAATGTGCTGGCAGGGTCATCAACGAAACACCTGCCAATCCCTAGTCGGCATCGTTTAT
GGTTGAGACTACGACGGTATCTAATCGTCTTCGAGCCCCCAACTTTCGTTCTTGATTAAT
GAAAACATCCTTGGCAAATGCTTTCGCAGAAGTTCGTCTTTCATAAATCCAAGAATTTCA
CCTCTGACAATGAAATACGAATGCCCCCGACTGTCCCTCTTAATCATTACTCCGGTCTTA
CAGACCAACAAGATAAGCCAGAGTCCTATCGTGTTATTCCATGCTAATGTATTCAGAGCG
TAGGCTTGCTTTGAACACTCTAATTTACTCAAAGTAACCTCGCCGATTCCGAGTCCCGGA
CAGTTAAGCCCAGGAGCTCGTCCCCGGCAGAAAGGTAGGCCGTAGCAGTACTAACCAAAG
GCTGACCGCTACAACCCACCCGAAATCCAACTACGAGCTTTTTAACTGCAACAACTTAAA
TATACGCTATTGGAGCTGAAATTTTACCGCAAA"

18S rRNA gene sequence of 'gamete' (1)

Forward sequence (510 letters):

"GTTAAAGCTCGTAGTTGGATTTCGGGTGGGTTGTAGCGGTCAGCCTTTGGTGAGTACTGC
TACGGCCCACCTTTCTGCCGGGGACGTGCTCCTGGGCTTAACTGTCCGGGACACGGAATC
GGCGAGGTTACTTTGAGTAAATTAGAGTGTTCAAAGCAAGCCTACGCTCTGAATACATTA
GCATGGAATAACACGATAGGACTCTGGCTTATCTTGTTGGTCTGTAAGACCGGAGTAATG
ATTAAGAGGGACAGTCGGGGGCATTCGTATTTCATTGTCAGAGGTGAAATTCTTGGATTT
ATGAAAGACGAACTTCTGCGAAAGCATTTGCCAAGGATGTTTTCATTAATCAAGAACGAA
AGTTGGGGGCTCGAAGACGATTAGATACCGTCGTAGTCTCAACCATAAACGATGCCGACT
AGGGATTGGCAGGTGTTTCGTTGATGACCCTGCCAGCACCTTATGAGAAATCAAAGTTTT
TGGGTTGCGGGGGGGGTATGGTCAAAATTGC"

Reverse sequence (516 letters):

"TATAGGTGCTGGCAGGGTCATCAACGAAACACCTGCCAATCCCTAGTCGGCATCGTTTAT
GGTTGAGACTACGACGGTATCTAATCGTCTTCGAGCCCCCAACTTTCGTTCTTGATTAAT
GAAAACATCCTTGGCAAATGCTTTCGCAGAAGTTCGTCTTTCATAAATCCAAGAATTTCA
CCTCTGACAATGAAATACGAATGCCCCCGACTGTCCCTCTTAATCATTACTCCGGTCTTA
CAGACCAACAAGATAAGCCAGAGTCCTATCGTGTTATTCCATGCTAATGTATTCAGAGCG
TAGGCTTGCTTTGAACACTCTAATTTACTCAAAGTAACCTCGCCGATTCCGTGTCCCGGA
CAGTTAAGCCCAGGAGCACGTCCCCGGCAGAAAGGTGGGCCGTAGCAGTACTCACCAAAG
GCTGACCGCTACAACCCACCCGAAATCCAACTACGAGCTTTTTAACTGCAACAACTTAAA
TATACGCTATTGGAGCTGAAATTACCGCAACAGATGT"

Phylogenetic Analysis

The 18S rDNA gene sequences were then checked and compared with other sequences on record using the Basic Local Alignment Search Tool (BLAST) online at the National Centre for Biotechnology Information (NCBI) (www.ncbi.nlm.nih.gov) website. The results showed that the D.S 19/30 and 19/18 'isolate' algae was similar to species Dunaliella salina and the 19/18 'gamete' also showed a distinct similarity. However, the 'gamete' strain did also show a match for *Dunaliella viridis* and *parva* strains (Tables 4.24 and 4.25).

Table 4.24- Similarity between forward 18S rRNA gene sequences of the three strains and other related species/strains from the NCBI database.

D.S 19/30 (1)		D.S 19/18 - 'isolate' (1)		D.S 19/18 - 'gamete' (1)	
Sequence Name	**% Match (Total Score)**	**Sequence Name**	**% Match (Total Score)**	**Sequence Name**	**% Match (Total Score)**
Uncultured Dunaliella isolate LTAH2162010_M1	99 (905)	Uncultured Dunaliella isolate LTAH2162010_M1	99 (904)	**Dunaliella sp. GSL019**	**99 (913)**
Dunaliella salina strain KMMCC 1428	99 (905)	Dunaliella salina strain KMMCC 1428	99 (904)	Dunaliella salina strain KMMCC 1428	99 (891)
Dunaliella bardawil strain KMMCC 1346	99 (905)	Dunaliella bardawil strain KMMCC 1346	99 (904)	Dunaliella bardawil strain KMMCC 1346	99 (891)
Dunaliella sp. ABRIINW-G22	99 (905)	Dunaliella sp. ABRIINW-G22	99 (904)	Dunaliella sp. ABRIINW-G22	99 (891)
Dunaliella salina strain JR101	99 (905)	Dunaliella salina strain JR101	99 (904)	Dunaliella salina strain JR101	99 (891)
Dunaliella salina strain CCAP 19/18	99 (905)	Dunaliella salina strain CCAP 19/18	99 (904)	Dunaliella salina strain CCAP 19/18	99 (891)
Dunaliella salina strain CCAP 19/3	99 (905)	Dunaliella salina strain CCAP 19/3	99 (904)	Dunaliella salina strain CCAP 19/3	99 (891)
Dunaliella salina strain CCAP 19/30	99 (905)	Dunaliella salina strain CCAP 19/30	99 (904)	Dunaliella salina strain CCAP 19/30	99 (891)
Dunaliella primolecta strain UTEX LB 1000	99 (905)	Dunaliella primolecta strain UTEX LB 1000	99 (904)	**Dunaliella viridis strain CONC002 (Gonzalez)**	**99 (913)**
Dunaliella parva strain SAG 19-1	99 (905)	Dunaliella parva strain SAG 19-1	99 (904)	**Dunaliella parva**	**99 (913)**

Table 4.25 : Similarity between reverse 18S rRNA gene sequences of the three strains and other related species/strains from the NCBI database.

D.S 19/30 (1)		D.S 19/18 - 'isolate' (1)		D.S 19/18 - 'gamete' (1)	
Sequence Name	**% Match (Total Score)**	**Sequence Name**	**% Match (Total Score)**	**Sequence Name**	**% Match (Total Score)**
Uncultured Dunaliella isolate LTAH2162010_M1	99 (920)	Uncultured Dunaliella isolate LTAH2162010_M1	99 (918)	**Dunaliella sp. GSL019**	**99 (928)**
Dunaliella salina strain KMMCC 1428	99 (920)	Dunaliella salina strain KMMCC 1428	99 (918)	Dunaliella salina strain KMMCC 1428	99 (905)
Dunaliella bardawil strain KMMCC 1346	99 (920)	Dunaliella bardawil strain KMMCC 1346	99 (918)	Dunaliella bardawil strain KMMCC 1346	99 (905)
Dunaliella sp. ABRIINW-G22	99 (920)	Dunaliella sp. ABRIINW-G22	99 (918)	Dunaliella sp. ABRIINW-G22	99 (905)
Dunaliella salina strain JR101	99 (920)	Dunaliella salina strain JR101	99 (918)	Dunaliella salina strain JR101	99 (905)
Dunaliella salina strain CCAP 19/18	99 (920)	Dunaliella salina strain CCAP 19/18	99 (918)	Dunaliella salina strain CCAP 19/18	99 (905)
Dunaliella salina strain CCAP 19/3	99 (920)	Dunaliella salina strain CCAP 19/3	99 (918)	Dunaliella salina strain CCAP 19/3	99 (905)
Dunaliella salina strain CCAP 19/30	99 (920)	Dunaliella salina strain CCAP 19/30	99 (918)	Dunaliella salina strain CCAP 19/30	99 (905)
Dunaliella primolecta strain UTEX LB 1000	99 (920)	Dunaliella primolecta strain UTEX LB 1000	99 (918)	**Dunaliella viridis strain CONC002 (Gonzalez)**	**99 (928)**
Dunaliella parva strain SAG 19-1	99 (920)	Dunaliella parva strain SAG 19-1	99 (918)	**Dunaliella parva**	**99 (928)**

Conclusion

The genetic tests have shown conclusively that all three of the sequenced strains are species of *Dunaliella*. However, due to the small encoding region of the primers used the subtle phylogenetic and taxonomic differences between the different strains, a complete match could not be made. The data has shown a strong indication that the 'gamete' 19/18 isolate is genetically different to the D.S 19/30 and 19/18 'isolate', due to the larger number of base pairs in the gel screening and slight variation in sequence matches (see differences in bold in Tables 4.24 and 4.25). This difference adds credence to the morphological differences previously observed, so it is quite possible that the 'gamete' could be another strain or some form of gamete. To be certain of this though, further 18S tests will need to be performed with full primers, but this is outside the scope of this current work. Having subsequently observed

the 19/18 'isolate' and 19/30 strain growth under high light conditions and their subsequent lack of β-carotene accrual, it is hypothesised that they could both be the same strain; D. salina 19/30. As the differences between the 'standard' and β-carotene overproducing variants are so genetically small it is not surprising there is no clear difference in identification based on the current procedure (Gomez and Gonzalez, 2004).

4.7 Mk II Mini photo-bioreactor growth experiments

Due to limitations in space, funding and lease, it was no longer possible to perform further experiments at the 3 L photo-bioreactor scale to look at the effect of micro-bubbles. This set of conditions and the need to provide biological replication in those experiments led to the development of a series of novel mini photo-bioreactor designs (see section 3.7). The first batch of experiments used the Mk I design mini-reactor design to look at the effects of 'smart skin' on algal growth (see Chapter 5), but ultimately the design was shown to have poor mixing (section 3.7.2). Based on this data and subsequent mixing analysis and CFD simulation an improvement to the design was made, culminating with the Mk II variant (section 3.7.4). In this section, the Mk II design (section 2.12.4) was used to perform a series of tests looking at algal strain growth behaviour, the reaction of D. salina 19/30 to differing gas flow rates (linking with the CFD simulation in section 3.7.5) and the effects of fluidic oscillation (section 2.12.1 & 2.12.3). All experiments were performed in the MBB F-Floor lab (section 2.8.3) at ambient temperature (approx 25^{o}C) with light provided by three ring fluorescent tubes (section 2.9.3 and appendix A9). Inoculum to medium ratio was maintained at 5 ml:100 ml in each test, as per the flask experiments run previously (section 4.4). Aeration was supplied from lab air at 1 bar pressure and controlled using needle valve equipped flowmeters. Growth rates were monitored using OD (sections 2.6.2) and lipid analysis/chlorophyll extraction was performed when appropriate.

4.7.1 Strain Growth Comparison

The first experiment was performed using a variety of strains (in stationary phase) maintained by the lab, to look at their growth response in the new Mk II mini photo-bioreactor design. The strains selected were as follows; *Tetraselmis suecica* (CCAP 66/4), *Nannochlropsis occulata* (CCAP 849/1), *D.Salina* 19/30 and the *D.Salina* 19/18 'isolate' from the previous section. All cultures used 1 M NaCl Dunaliella medium apart from *Nannochloropsis* which was grown in F/2 (section 2.1.2). The aeration rate was set to approximately 10cc/min air and balanced using visual approximation and a set of clamps (section 2.12.5). As a control, one of the *D. salina* 19/30 cultures was left un-aerated. 3 x 200 µl of sample was taken from each reactor daily for

reading on a 96 well microplate (OD 595 nm), the volume was replaced with fresh medium each time.

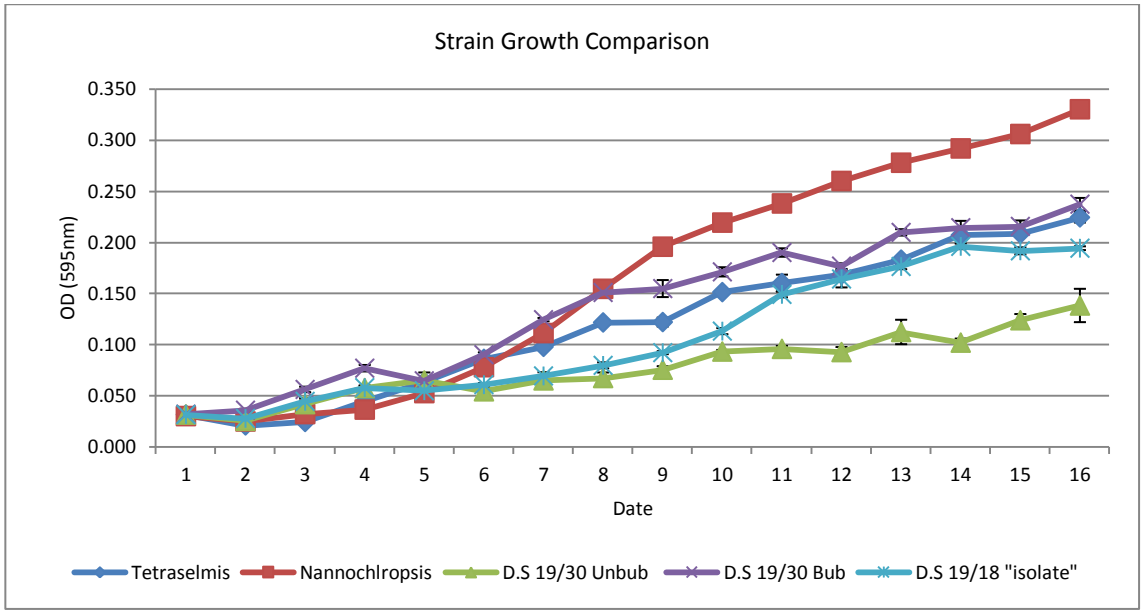

Figure 4.36. Growth rate of various strains in Mk II mini photo-bioreactors under 10 cc/min continuous air. Culture growth measured using OD at 595 nm only.

All strains grew successfully in the new mini-bioreactor design, with *Nannochlorpsis* performing the best and the un-aerated standard performing the least well, as expected due to CO_2 limitation or lack of mixing (Figure 4.36). Interestingly the aerated *D. salina* strains showed almost the same plateau of growth observed in the 3 L photo-bioreactor experiments, so they were also quite probably CO_2 limited. There are a couple of reasons the *Nannochlorpsis*culture could have performed better than the others, the first is its morphology i.e. smaller size, lack of motility and its cell wall, which could have made it less susceptible to mixing damage. The second is its growth medium, F/2 as shown by the model in section 3.2.4 has a greater solubility to CO_2, so the culture could have been slightly less carbon limited than the others.

Fig 4.37 - Algal flocks forming due to mixing/ sealing limitations.

During the test some other issues with the Mk II design mini-photobioreactor came to light, chiefly wall growth around the sparger (see Figure 4.37, right). Due to the slight variations in the glass blown sparger fitting section at the bottom of the reactor, culture had started to get trapped in this area and form flocks. The number of cells in these flocks, could have skewed the OD data. There were

also issues withcontrol of the air flow using the flowmeters, as the reading fluctuated highly. This is quite possibly due to the aeration rates approaching the edge of the readable scale and the porous sparger creating back pressure.

4.7.2 Growth of D. salina 19/30 with and without aeration

The second test using the Mk II mini-photobioreactor design was performed to compare the the effect of different aeration rates on the growth rate of *D. salina* 19/30 and its lipid accrual, whilst trying to counter the problems found in the previous experiment. 8 mini photo-bioreactors were used this time to ensure good biological replication, 4 as non-aerated standards and 4 with air. To provide more consistent aeration the four bubbled reactors were fed from a single specially calibrated 0-10 cc/min (at 1 bar air) flowmeter (supplied by FTI), the output of which was split 4 ways with exactly the same length of silicone tubing to provide 2.5 cc/min to each reactor. The test inoculum was sourced from a culture of *D. salina* 19/30 in 1 M NaCl Dunaliella medium in stationary phase with an OD (595nm) of 0.683. 3 x 200 µl of sample was taken from each reactor daily for reading on a 96 well microplate (OD 595 nm), the volume was replaced with fresh media each time. Nile red tests were performed from day 5 using the old single multi-pipette method (Appendix I) with 1 µM NR/ml of culture (20 µl of stain added). To counter the flocculation issues experienced in the previous run, each reactor was swirled gently for 20 seconds before any readings were taken.

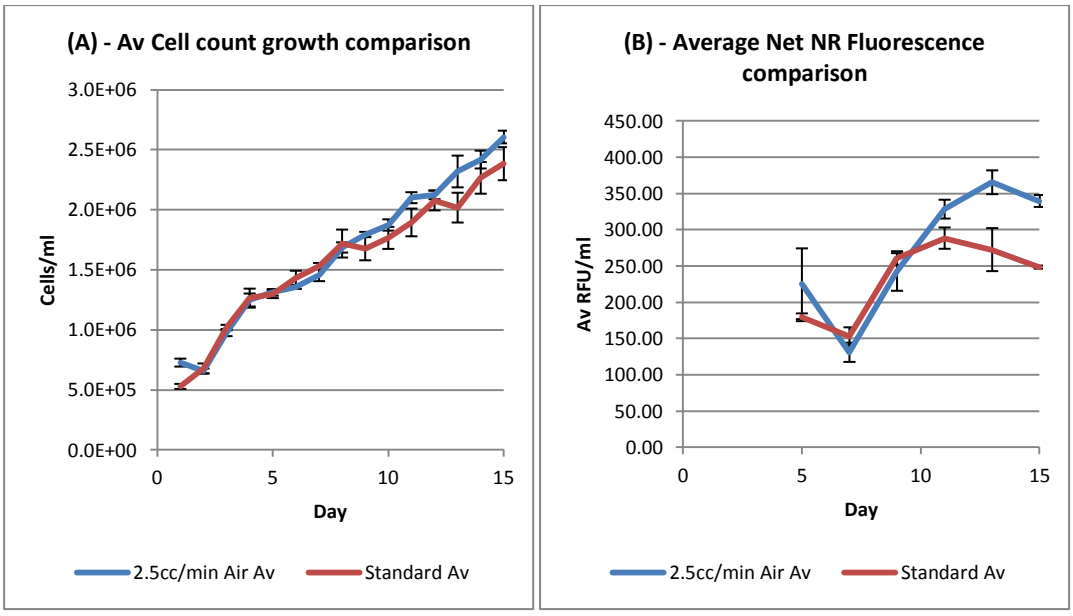

Figure 4.38.A) Growth rate of *D.salina* 19/30 with and without continuous airat 2.5 cc/min. Culture growth measured using OD at 595 nm to produce an inferred cells per ml. B) Nile Red fluorescence (RFU/ml) Ex: 490 nm Em: 580 nm.

The results showed only a marginal difference between each of the conditions in terms of OD, but a more significant one in lipid fluorescence (Figure 4.38). However, the experiment on the whole was severely compromised again by poor air flow regulation, wall growth around the sparger area even with the updated methods. The biggest issue was subsequently found to be the exhaust air flow from the reactors was restricted by the 'breathable' Schott Duran lids, which led to a mass transfer limitation again. It is also suspected that the difference in NR performance between the two conditions could be due to more chlorophyll being present in the standard cultures based on visual observations of the colour of the supernatant when both cultures were centrifuged during harvesting. Based on these observations a re-think of the set-up and procedures was performed.

4.7.3 Air flow rate effects on the growth of *D. salina* 19/30

The next experiment was performed to look at the effects varying the level of aeration within the Mk II photo-bioreactor had on the growth of *D. salina* 19/30, this work was to tie in with the CFD experiments performed in section 3.7.7 and find the best flowrate for the oscillation comparison. To help with the air flow monitoring issues, a Cole Palmer digital mass flow meter was purchased with a range of 0-100 cc/min (see section 2.12.5). This allowed measurements to be made accurately based on the gas vented at reactor exhausts, bypassing the back pressure issues previously experienced. 10 reactors were used in the experimentwith an initial test inoculum sourced from a culture of *D. salina 19*/30 in 1 M NaCl Dunaliella medium in stationary phase with an OD (595 nm) of 1.324. Reactors 1 & 2 were set at 5cc/min flow rate, 3 & 4 - 10cc/min, 5 & 6 - 15cc/min, 7 & 8 - 20cc/min and reactors 9 & 10 were used as non-aerated standards. Due to the very low flow rates, the flowmeters were just used for their needle valves.Again, 3 x 200 µl of sample was taken from each reactor daily for reading on a 96 well microplate (OD 595nm), the volume was replaced with fresh medium each time. Before each reading the area around the sparger was mixed using a 5 ml pipette. Cultures were harvested on day 17, washed once and freeze dried for subsequent NMR (500µl $CDCl_3$/CD_3OD in a ratio 1:4, quadruplicate replicates) and direct trans-esterification processing. In addition, chlorophyll was extracted using the method in section 2.6.4for comparison with the NMR data on the same day.

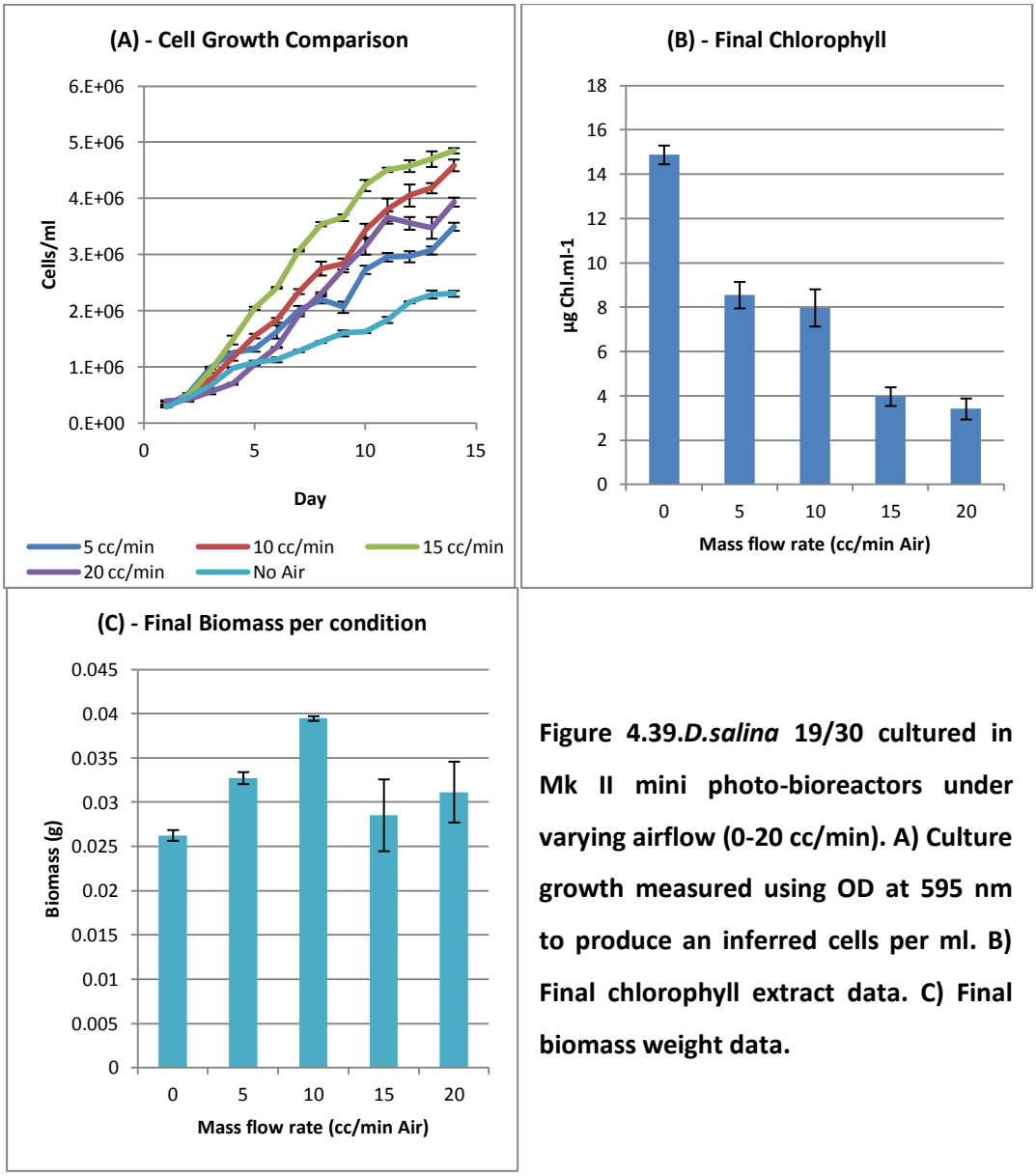

Figure 4.39.*D.salina* 19/30 cultured in Mk II mini photo-bioreactors under varying airflow (0-20 cc/min). A) Culture growth measured using OD at 595 nm to produce an inferred cells per ml. B) Final chlorophyll extract data. C) Final biomass weight data.

Table 4.26 - *D.salina* 19/30 - NMR / extracted pigment data.

Sample	Extracted Chlorophyll content (µg Chl ml^{-1})	Std Err	NMR Chlorophyll (mM/10mg BM)	Std Err	NMR β-Carotene (mg/10mg BM)	Std Err
0 cc/min	14.87541	0.42285	0.59	0.0255	0.43	0.02050669
5 cc/min	8.54771	0.59781	0.20	0.0361	0.19	0.00603477
10 cc/min	7.97173	0.83931	0.18	0.0246	0.19	0.02857244
15 cc/min	3.96813	0.42137	0.05	0.0065	0.17	0.05802956
20 cc/min	3.40967	0.47513	0.13	0.0052	0.17	0.00332838

Table 4.27 - *D.salina* 19/30 - NMR/Direct transesterification total lipid data per 3 L reactor.

Sample	NMR total lipid – C17:1 equivalent (mg/10mg BM)	Std Err	Direct Trans total lipid (mg/10mg BM)	Std Err
0 cc/min	2.01	0.1221	1.32	0.252
5 cc/min	1.86	0.0929	1.76	0.175
10 cc/min	1.70	0.142	1.64	0.413
15 cc/min	1.85	0.3862	1.04	0.049
20 cc/min	1.89	0.2208	0.94	0.280

Table 4.28 - *D.salina* 19/30 - NMR lipid group data.

Sample	NMR Unsat lipid signal (mM/10mg BM)	Std Err	NMR Unsat Me lipid signal (mM/10mg BM)	Std Err	NMR Sat Me lipid signal (mM/10mg BM)	Std Err
0 cc/min	21.54	1.2063	6.05	0.2543	9.27	0.388664
5 cc/min	13.95	0.2263	4.08	0.0151	7.07	0.181119
10 cc/min	13.79	0.9116	3.69	0.1403	6.43	0.282429
15 cc/min	10.85	2.5675	3.14	0.7583	5.48	1.445167
20 cc/min	12.04	1.7256	3.03	0.332	7.26	0.029368

Table 4.29 - *D.salina* 19/30 - Direct transesterification FAME profile (% of total FAME):

FAME	Structure	Lipid Profile (% of total FAME)									
		0cc	Std Err	5cc	Std Err	10cc	Std Err	15cc	Std Err	20cc	Std Err
Methyl 4,7,10,13-hexadecatetraeoate	16,4 (cis n3)	14.48	3.08	9.54	0.78	9.65	1.29	8.04	0.03	9.99	1.06
Hexadecanoic Acid ME	16,0	14.81	3.99	20.64	2.89	21.13	4.97	29.30	0.29	20.46	5.15
γ linolenic ME	18,3 (n6)	4.67	0.00	3.63	0.25	3.15	0.72	4.25	0.00	0.00	0.00
9,12-Octadecadienoic Acid ME	18,2 (6 cis)	4.73	0.05	4.31	0.64	4.34	1.21	4.18	0.27	7.20	1.78
9,12,15-Octadecadienoic Acid ME	18,3 (n3)	52.73	10.77	48.38	3.56	47.76	12.39	34.37	3.50	35.17	14.02
9-Octadecadienoic Acid ME	18,1 (9 Cis)	4.23	0.55	5.77	1.12	7.94	2.83	7.99	0.00	13.25	5.31
9-Octadecadienoic Acid ME	18,1 (9 trans)	4.34	0.68	4.16	0.08	3.46	0.93	4.35	0.22	7.51	1.99
Methyl 9,10-methylene-octadecanoate	19,0D (cis 9,10)	0.00	0.00	3.57	0.66	2.57	0.83	7.51	0.41	6.42	0.42
	Total:	100	19.1	100	9.98	100	25.1	100	4.73	100	29.7

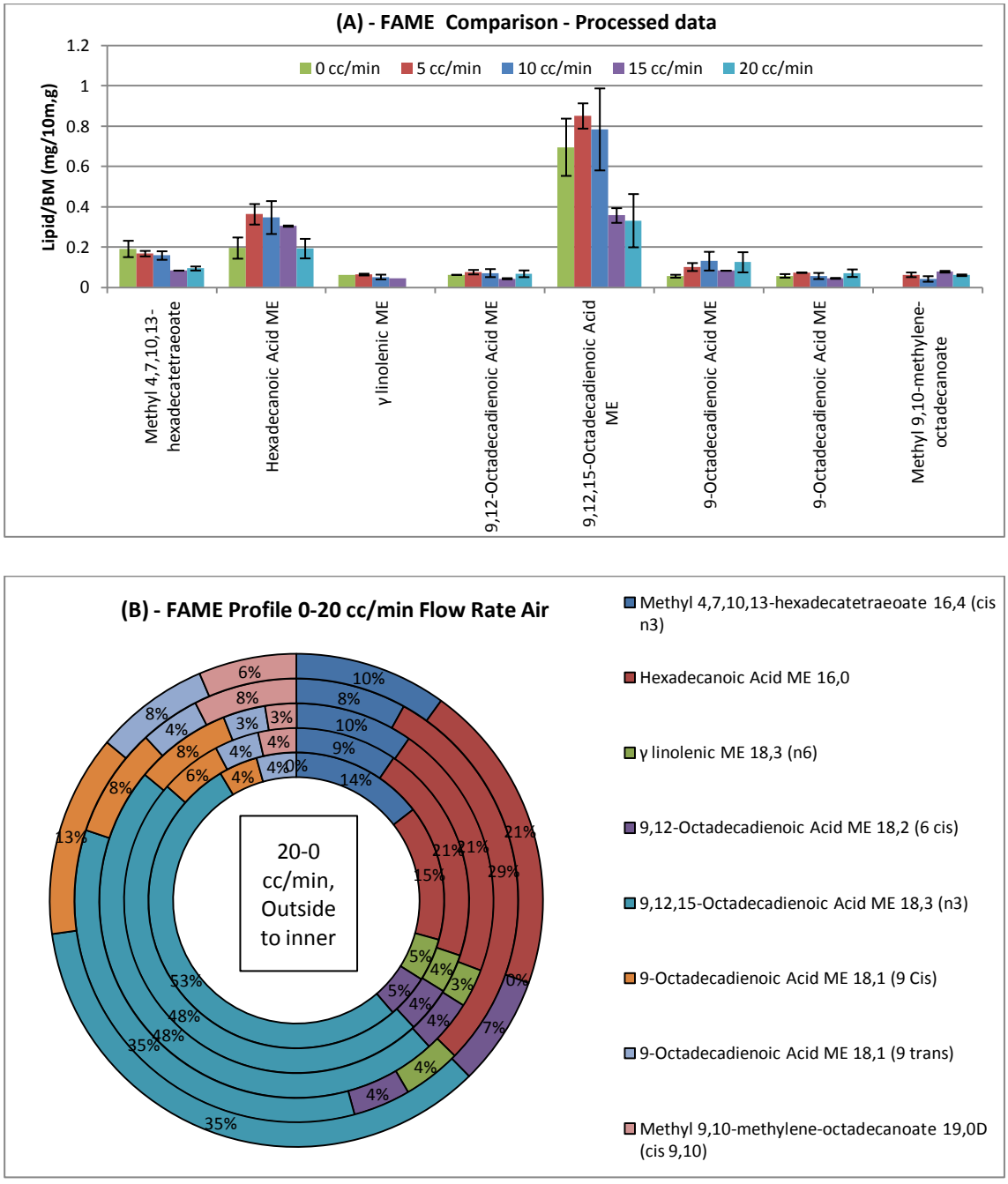

Figure 4.40. *D.salina* 19/30 grown at different flow rates of air (0-20 cc/min) - A) FAME quantity comparison, Lipid/Biomass (mg/10mg) and B) FAME lipid profile (%).

The data from the experiment showed improved algal productivity (based on OD) with increased air flow up to 15cc/min (Figures 4.39 & 4.40 and Tables 4.26 – 4.29), . However, the pigment readings performed on harvest show a dramatic reduction with increased flow rate. These effects are hypothesised to be due to increase in cell breakage and subsequent co-growth of *Halomonas* bacteria being picked up at OD 595. This hypothesis is backed up by the amounts of C19:0 (cis 9,10) present in the FAME profile, which significantly increases at the 15-20cc/min flow rates. The lipid extracts show differing conclusions depending on which method

is used, the NMR C17:1 equivalent indicates a very similar lipid amount under all conditions, with a marginal reduction for each of the aerated cultures. The trans-esterified samples indicate a peak at 5 cc/min followed by 10, 0, 15 and 20. In either case, the total lipids range between 9-20% of the total biomass. Interestingly the increased flow rate also seems to make the lipid profile more favourable to biodiesel production, with a decrease in C18:3 and a increase in C18:1.

4.7.4 5% CO_2 Air flow rate effects on the growth of *D. salina* 19/30

A second flow rate comparison was performed to see if carbon limitation was a significant factor. To perform this experiment the same setup was used from the previous, but the air replaced with 5% CO_2 in nitrogen. An initial test inoculum was sourced from a culture of 14 day old *D. salina* 19/30 in 1 M NaCl Dunaliella medium with an OD (595 nm) of 1.340. 1 ml of sample was taken from each reactor daily for OD reading (595 nm), the volume was replaced with fresh medium each time. Before each reading the area around the sparger was again mixed using a 5 ml pipette. pH measurements were taken every day and Nile red tests were performed when the OD was sufficient using the old single multi-pipette method again (Appendix I) with 1 µM NR/ml of culture (20 µl of stain added). Cultures were harvested on day 15, washed once and freeze dried for subsequent NMR (560 µl $CDCl_3/CD_3OD$ in a ratio 1:4, quadruplicate replicates) and direct trans-esterification processing. In addition, chlorophyll was extracted using the method in section 2.6.4for comparison with the NMR data on the same day and final biomass was compared using the freeze died samples (30 ml taken from each reactor).

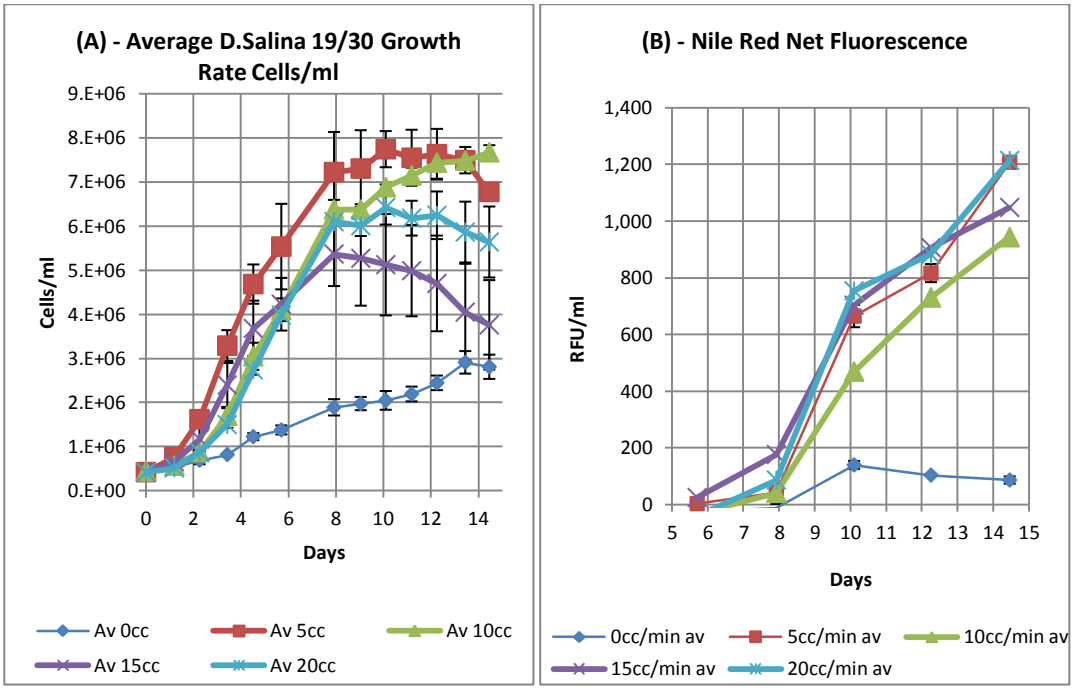

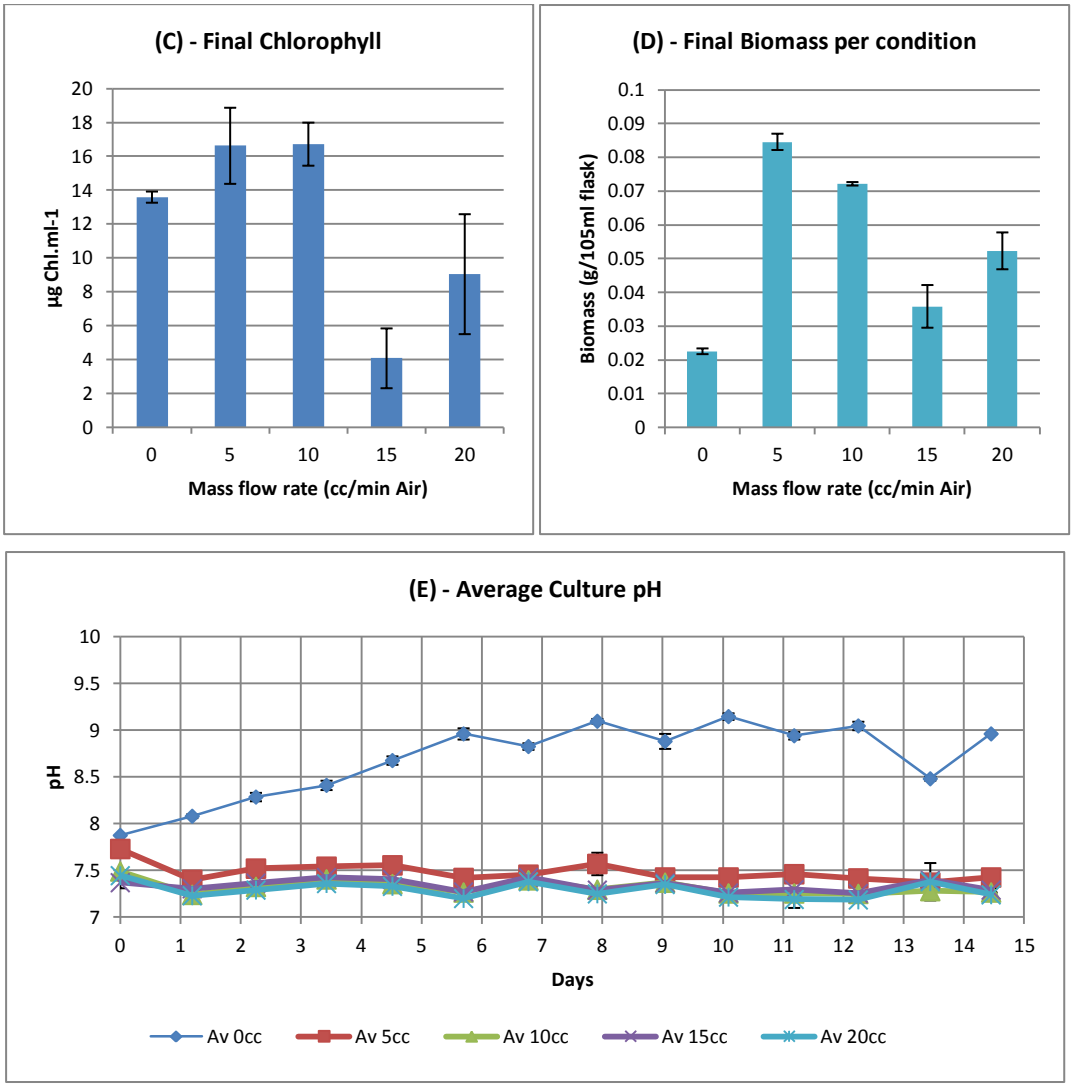

Figure 4.41.*D.salina* 19/30 cultured in Mk II mini photo-bioreactors under varying flows of 5% CO_2 gas (0-20 cc/min). A) Culture growth measured using OD at 595 nm to produce an inferred cells per ml. B) Nile Red fluorescence (RFU/ml) Ex: 490 nm Em: 580 nm. C) Final chlorophyll extract data. D) Final biomass weight data. E) pH measurments.

Table 4.30 - *D.salina* 19/30 - NMR / extracted pigment data.

Sample	Extracted Chlorophyll content (µg Chl ml^{-1})	Std Err	NMR Chlorophyll (mM/10mg BM)	Std Err	NMR β-Carotene (mg/10mg BM)	Std Err
0 cc/min	13.59528	0.33002	0.78	0.0287	0.51	0.00421373
5 cc/min	16.62818	2.24836	0.22	0.0483	0.16	0.03393481
10 cc/min	16.7247	1.27226	0.25	0.0152	0.21	0.00311402
15 cc/min	4.06986	1.76714	0.08	0.0174	0.10	0.01321932
20 cc/min	9.04259	3.54423	0.06	0.0049	0.10	0.0119755

Table 4.31 – *D.salina* 19/30 - NMR/Direct transesterification total lipid data per 3L reactor.

Sample	NMR total lipid – C17:1 equivalent (mg/10mg BM)	Std Err	Direct Trans total lipid (mg/10mg BM)	Std Err
0 cc/min	1.67	0.0134	2.254	0.647
5 cc/min	1.51	0.1567	1.446	0.184
10 cc/min	1.77	0.1914	1.592	0.085
15 cc/min	1.46	0.0129	0.966	0.222
20 cc/min	1.85	0.1227	1.097	0.116

Table 4.32 - *D.salina* 19/30 - NMR/Nile Red lipid group data.

Sample	NMR Unsat lipid signal (mM/10mg BM)	Std Err	NMR Unsat Me lipid signal (mM/10mg BM)	Std Err	NMR Sat Me lipid signal (mM/10mg BM)	Std Err	Nile Red Triolein equiv (g/105ml)	Std Err
0 cc/min	19.86	1.3003	5.27	0.0883	8.17	0.149974	0.00037	0.00032
5 cc/min	9.10	0.4255	2.50	0.1296	4.80	0.431532	0.01063	0.00053
10 cc/min	11.89	0.7625	3.34	0.1551	5.65	0.504516	0.00901	0.00059
15 cc/min	5.63	0.8692	1.63	0.2222	5.87	0.90798	0.00448	0.00022
20 cc/min	9.51	0.7863	2.98	0.4931	5.94	0.284126	0.00824	0.00076

Table 4.33 - *D.salina* 19/30 - Direct transesterification FAME profile (% of total FAME):

FAME	Structure	Lipid Profile (% of total FAME)									
		0cc	Std Err	5cc	Std Err	10cc	Std Err	15cc	Std Err	20cc	Std Err
Methyl 4,7,10,13-hexadecatetraeoate	16,4 (cis n3)	14.31	3.76	9.53	1.27	12.03	0.26	8.68	0.96	10.19	2.00
9,12,15-Octadecatrienoic acid ME	18,3 (trans)	2.96	0.54	2.80	0.00	2.70	0.05	4.82	1.36	3.72	0.35
Hexadecanoic Acid ME	16,0	15.84	3.41	23.54	2.16	20.21	0.24	24.75	6.25	21.03	0.32
γ linolenic ME	18,3 (n6)	3.30	0.78	3.43	0.28	2.70	0.13	3.68	0.00	2.92	0.55
9,12-Octadecadienoic Acid ME	18,2 (6 cis)	3.91	0.56	4.48	0.39	3.90	0.16	4.52	0.16	3.98	0.60
9,12,15-Octadecadienoic Acid ME	18,3 (n3)	52.61	18.74	43.32	6.94	47.32	3.58	29.43	10.15	41.36	5.77
9-Octadecadienoic Acid ME	18,1 (9 Cis)	2.78	0.62	7.04	0.36	6.68	0.80	8.15	0.98	8.66	0.57
9-Octadecadienoic Acid ME	18,1 (9 trans)	3.17	0.29	2.74	0.44	2.24	0.12	4.73	0.64	3.64	0.16
Methyl 9,10-methylene-octadecanoate	19,0D (cis 9,10)	1.13	0.00	3.12	0.86	2.22	0.03	11.24	2.52	4.51	0.24
	Total:	100.00	28.70	100.00	12.72	100.00	5.37	100.00	23.02	100.00	10.56

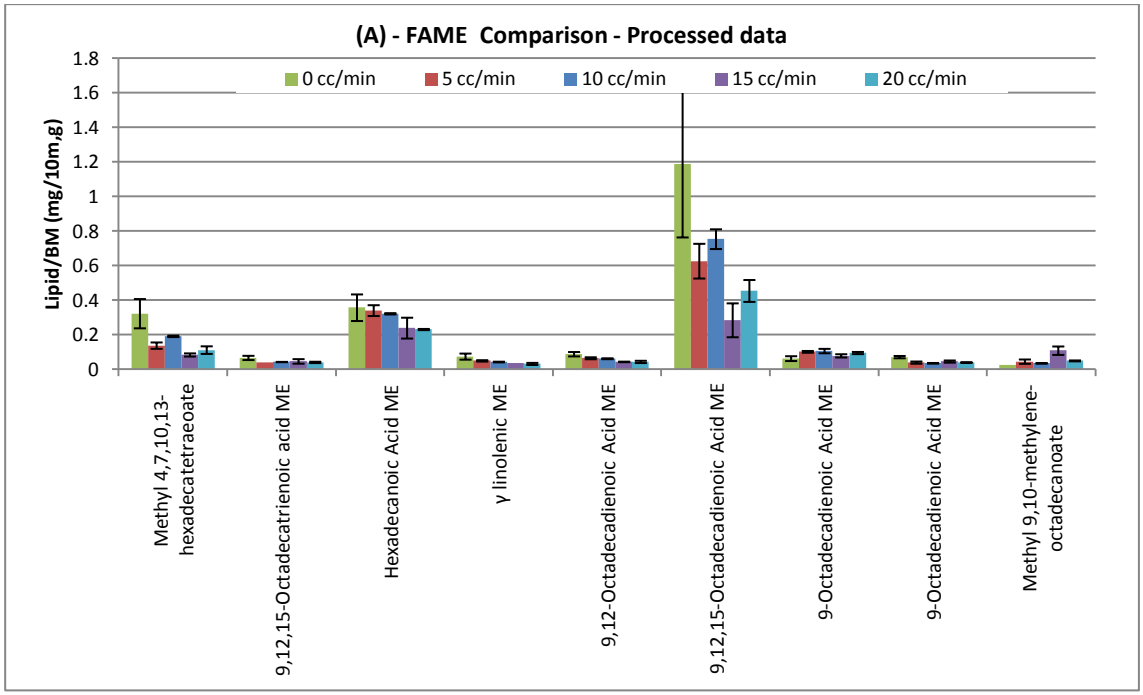

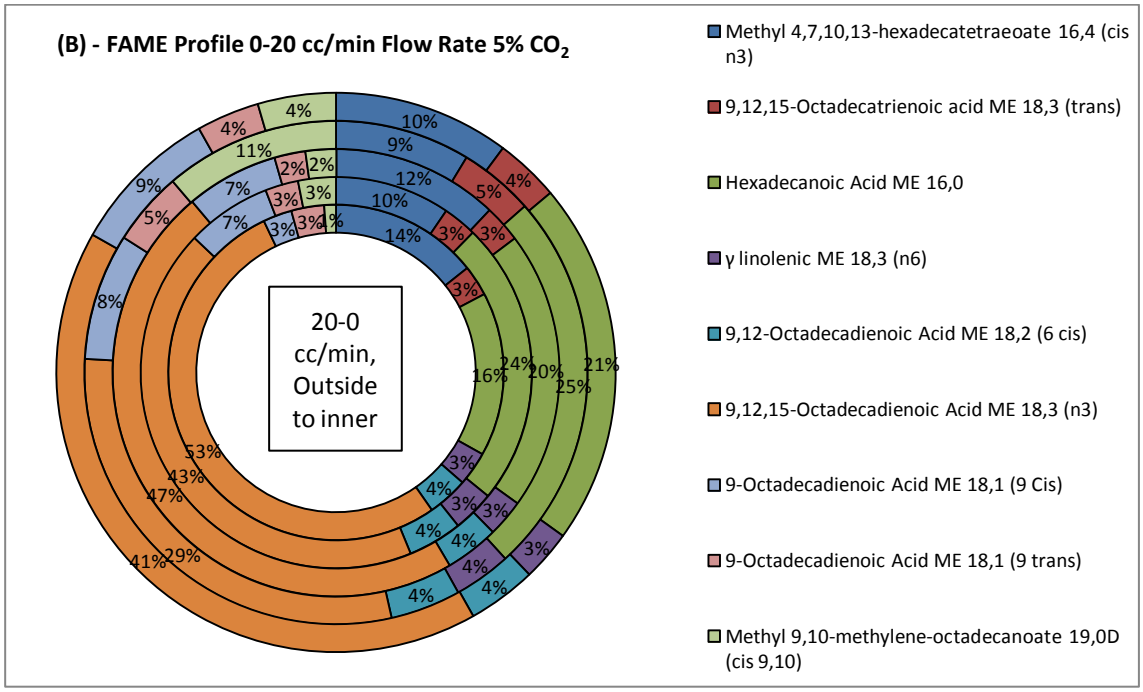

Figure 4.42. *D.salina* 19/30 grown at different flow rates of 5% CO_2 gas (0-20 cc/min) - A) FAME quantity comparison, Lipid/Biomass (mg/10mg) and B) FAME lipid profile (%).

The data for this flow experiment showed that the optimal flow rate was either 5 or 10cc/min with the 10cc cultures being the only ones still growing based on OD (Figures 4.41 & 4.42 and Tables 4.30 to 4.33). This result is slightly different to the air test, but it terms of overall levels of biomass there is a similar trend with the 5 or 10cc/min cultures again being the most productive. The Nile red data indicates that with no aeration the neutral lipid production was

greatly reduced compared with the maximal 5 or 10cc/min cultures, however, the 0cc/min cultures also have the highest amounts of β- carotene present, which could potentially be blocking the fluorescence signal. The total lipid measurements are again contradictory between methods, with no clear trend emerging. However, the amounts of C19:0 (cis 9,10) present in the FAME profile, does again indicate an increase in bacteria at the higher velocity flows, particular at 15cc/min flow rate, which based on the OD data could be entering death phase based on the contamination. This finding is also backed up with a significant bacterial signal present in the NMR data for all of the aerated cultures. The lipid/biomass yields are also comparable with the air tests, so the major difference is due to the overall increase in the number of cells and no particular stress effect. The chlorophyll pigment show a very large difference between the two tests, with the 5 or 10cc/min cultures having larger amounts of pigment than the standards with a surplus of CO_2. This could indicate that the cells are slightly more structurally stable with more of carbon source available (up to 10 cc/min) or they are able to manufacture more pigment. Interestingly the β-carotene correlation between the two experiments is the same, with more in the non-mixed cultures. These pigment results could also be linked to the amount of light exposure, as the faster flow rates would need less due to increased exposure.

4.7.5 Air regular vs Oscillated flow 10 cc/min with 30 mins 5% CO_2/day

Based on the results of the two previous flow rate experiments, it was decided to use a flow rate of 10cc/min, as this had been consistently productive in both experiments. To perform this test the setup from the previous experiments was modified to incorporate the usage of the Fluidic oscillator (see section 2.12.5). Reactors 1-4 were controlled using four flowmeters with needle valves, the feed to each of these came from lab air **or** 5% CO_2. Reactors 5-8 fed air from the fluidic oscillator left and right outputs, **or** connected to four flowmeters with needle valves attached to the 5% CO_2 supply. The oscillator left and right outputs were split into two after the initial bleed, this was in-turn divided again into another bleed section for fine control using another set of needle valves.So 8 reactor cultures were sparged with air, 4 laminar, 4 oscillated and 2 were non-aerated standards. The aerated cultures were also sparged with 5% CO_2 in N_2 (laminar in all cases) for 30 minutes a day to provide sufficient carbon for growth. An initial test inoculum was sourced from a culture of 18 day old *D. salina* 19/30 in 1 M NaCl Dunaliella medium with an OD (595 nm) of 1.725. 3 x 200 µl of sample was taken from each reactor daily for reading on a 96 well microplate (OD 595 nm), the volume was replaced with autoclaved distilled water with 1 M NaCl each time to avoid carbonate skewing the growth data. Before each reading the area around the sparger was again mixed using a 5 ml pipette. pH measurements were taken every day and Nile red tests were performed when the OD was sufficient.The Nile red tests were performed using the dual updated multi-pipette method

with acetone (see section 2.2.2.6) with 3 µM NR/ml of culture to ensure a good signal. The cultures were harvested on day 14, washed once and freeze dried for subsequent NMR (560 µl $CDCl_3/CD_3OD$ in a ratio 1:4, quadruplicate replicates) and direct trans-esterification processing. In addition, Chlorophyll was extracted using the method in section 2.6.4for comparison with the NMR data on the same day and final biomass was compared using the freeze died samples (20 ml taken from each reactor).

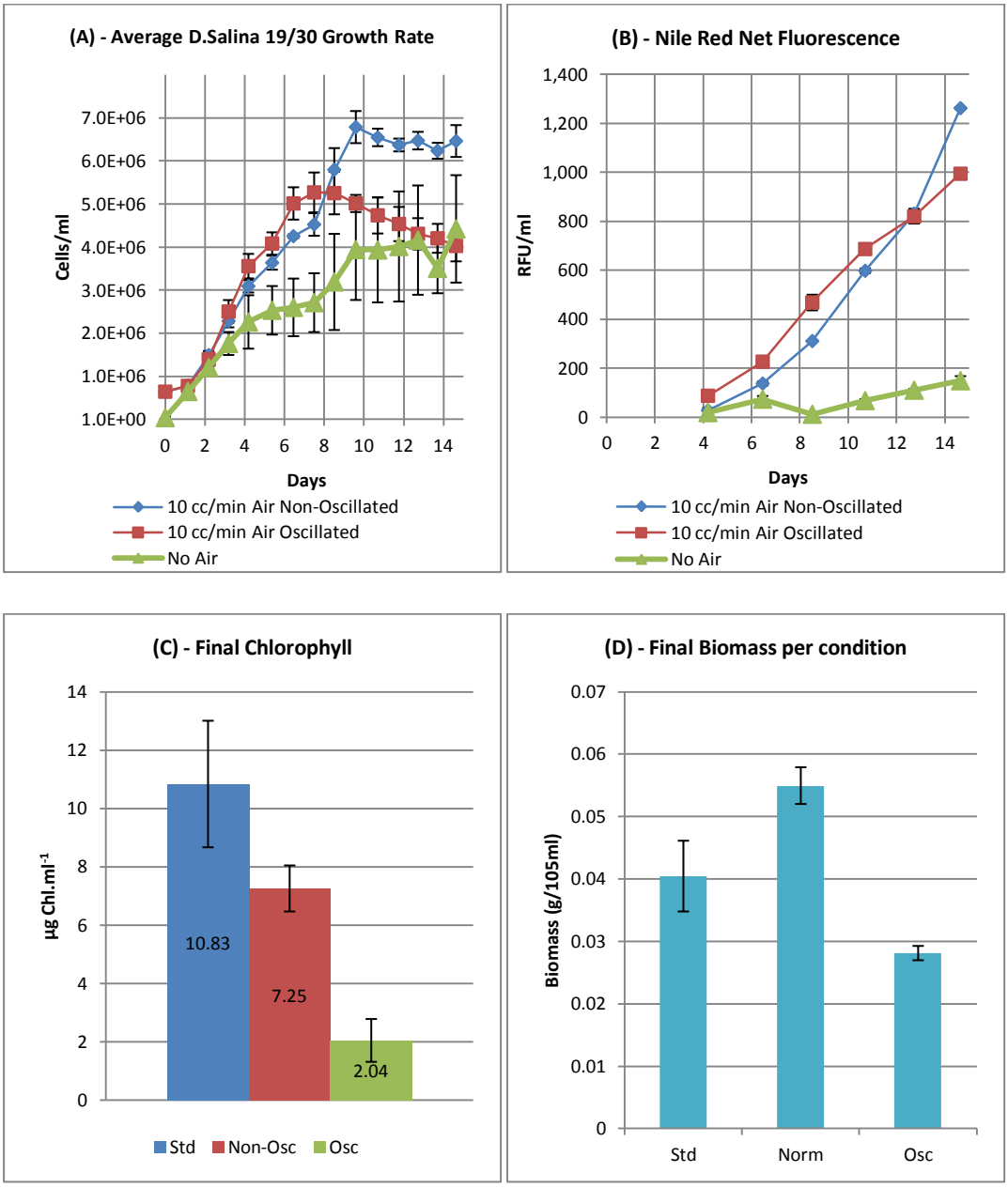

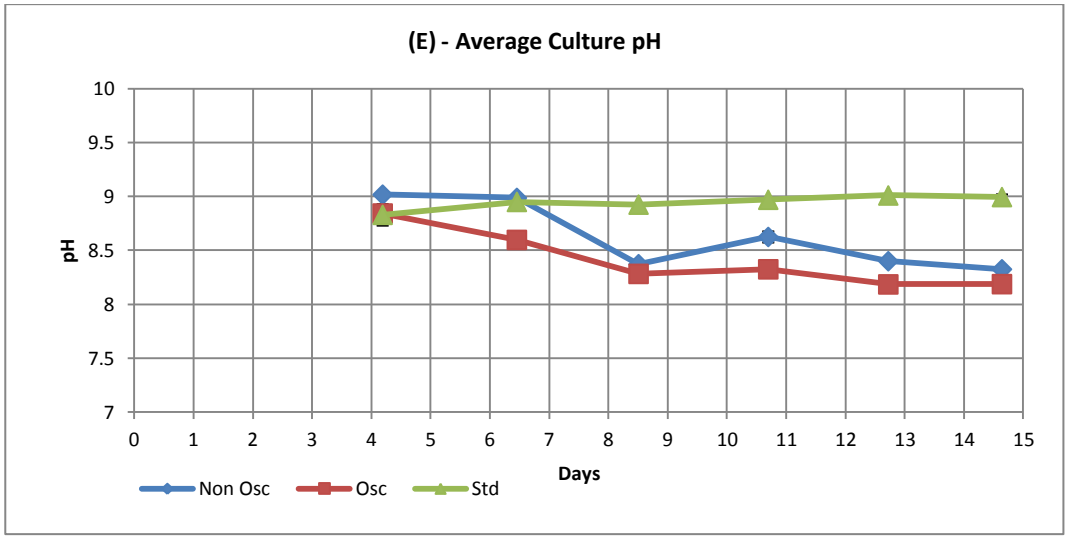

Figure 4.43.*D.salina* 19/30 cultured in Mk II mini photo-bioreactors under three conditions; non-aerated and aerated 10 cc/min air flow with and without fluidic oscillation. Aerated cultures were also sparged with regular flows of 10 cc/min 5% CO2 gas for 30 mins a day. A) Culture growth measured using OD at 595 nm to produce an inferred cells per ml. B) Nile Red fluorescence (RFU/ml) Ex: 490 nm Em: 580 nm. C) Final chlorophyll extract data. D) Final biomass weight data. E) pH measurements.

Table 4.34 - *D.salina* 19/30 - NMR / extracted pigment data.

Sample	Extracted Chlorophyll content (µg Chl ml^{-1})	Std Err	NMR Chlorophyll (mM/10mg BM)	Std Err	NMR β-Carotene (mg/10mg BM)	Std Err
Non-Osc	7.250175	0.789293	0.11	0.0036	0.15	0.01191325
Oscillated	2.042465	0.734346	0.07	0.0314	0.08	0.03770885
Standard	10.8296	2.16854	0.57	0.1213	0.40	0.04538219

Table 4.35 - *D.salina* 19/30 - NMR/Direct transesterification total lipid data per 100ml reactor.

Sample	NMR total lipid – C17:1 equivelent (mg/10mg BM)	Std Err	Direct Trans total lipid (mg/10mg BM)	Std Err
Non-Osc	1.93	0.1009	1.087	0.078
Oscillated	1.87	0.0965	0.941	0.1
Standard	2.02	0.3372	1.056	0.136

Table 4.36 - *D.salina* 19/30 - NMR/Nile Red lipid group data.

Sample	NMR Unsat lipid signal (mM/10mg BM)	Std Err	NMR Unsat Me lipid signal (mM/10mg BM)	Std Err	NMR Sat Me lipid signal (mM/10mg BM)	Std Err	Nile Red Triolein equivalent (g/105ml)	Std Err
Non-Osc	9.90	0.4827	2.53	0.0904	5.47	0.196557	0.021	0.0008
Oscillated	7.31	1.0569	1.93	0.2876	5.98	0.609819	0.010	0.0005
Standard	13.59	2.5985	4.41	1.0191	7.74	1.008298	0.002	0.0006

Table 4.37 - *D.salina* 19/30 - Direct transesterification FAME profile (% of total FAME):

FAME	Structure	Lipid Profile (% of total FAME)					
		Non-Osc	Std Err	Osc	Std Err	Std	Std Err
Methyl 4,7,10,13-hexadecatetraeoate	16,4 (cis n3)	8.99	0.31	8.15	0.89	12.12	2.91
9,12,15-Octadecatrienoic acid ME	18,3 (trans)	0.00	0.00	0.00	0.00	3.09	0.00
Hexadecanoic Acid ME	16,0	28.01	2.64	27.07	2.38	22.96	2.44
γ linolenic ME	18,3 (n6)	0.00	0.00	6.36	0.00	2.97	0.00
9,12-Octadecadienoic Acid ME	18,2 (6 cis)	5.04	0.20	6.14	0.59	4.00	0.13
9,12,15-Octadecadienoic Acid ME	18,3 (n3)	37.90	2.55	23.30	4.23	43.34	6.87
9-Octadecadienoic Acid ME	18,1 (9 Cis)	10.75	0.57	10.83	0.76	4.20	0.13
9-Octadecadienoic Acid ME	18,1 (9 trans)	3.87	0.22	6.90	0.62	4.42	0.14
Methyl 9,10-methylene-octadecanoate	19,0D (cis 9,10)	5.44	0.72	11.25	1.26	2.89	0.24
	Total:	100.00	7.21	100.00	10.73	100.00	12.86

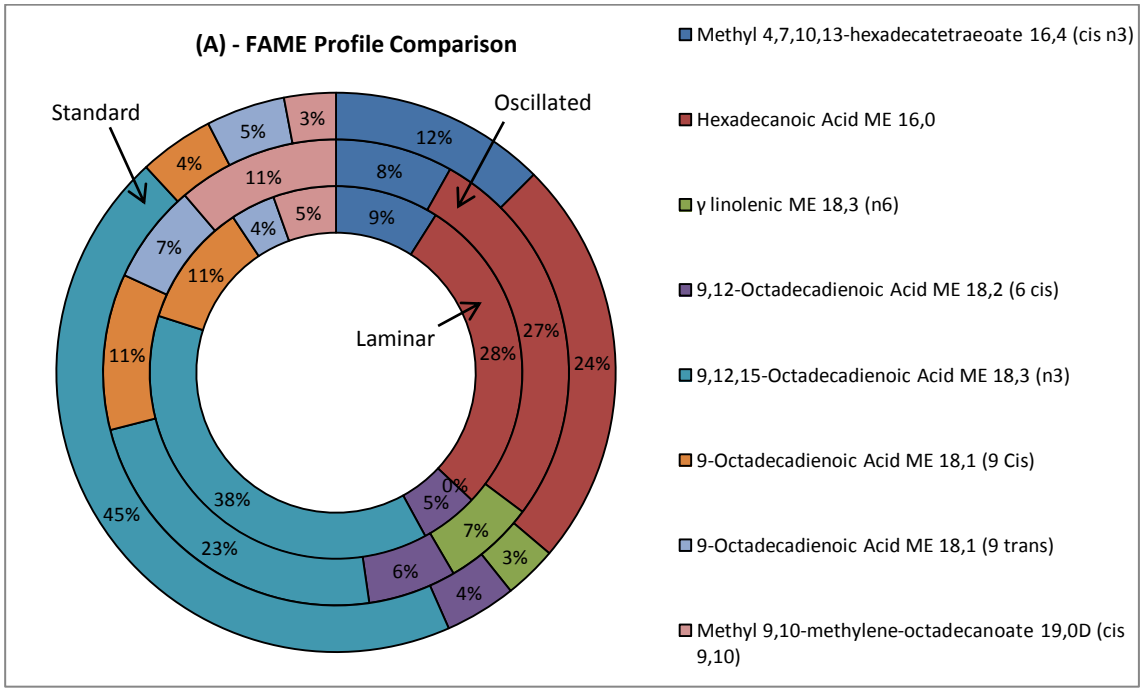

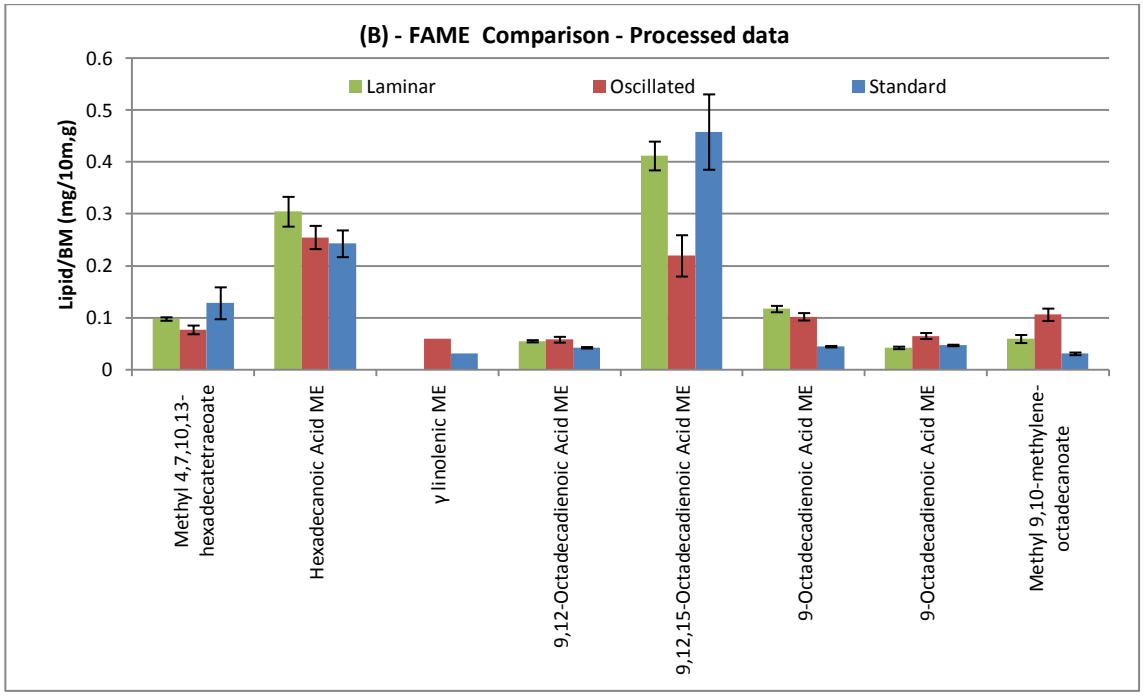

Figure 4.44. *D.salina* 19/30 grown with and without fluidic oscillation at 10 cc/min - A) FAME quantity comparison, Lipid/Biomass (mg/10mg) and B) FAME lipid profile (%).

The OD results from this experiment showed that until day 7 the oscillated culture was out growing the laminar flow equivalent and the standard, in a very similar way to the 3L photo bioreactor experiments in section 4.5. However, beyond this point a very large increase in *Halomonas* bacteria became prevalent in the oscillated culture which seemed to induce death phase (Figure 4.43 & 4.44 and Tables 4.34 to 4.37). Data from the FAME profile for the presence of C19:0 (cis 9,10) also validates this observation, with contamination again linked to type of aeration. Interestingly the other two conditions continued to grow until day 10 and reached stationary phase. The final pigment data also seems to correlate with this data, with the standard having the highest and the oscillated the lowest, which again could correlate with cell damage/death. The final NR data, also makes sense if the pigment data is factored in, as the β-carotene is much higher in the standard and marginally higher in the non-oscillated, the signals could potentially be very similar if the pigment's NR excitation light interception was removed. This would make the results fit with both the NMR and GC-MS data which show a similar amount of lipid/biomass under each condition. The overall biomass yield also reflects the apparent crash in the oscillated cultures with the standard aerated cultures having the largest yield and the oscillated the least. The lipid profile shows interesting data, with the Oscillated culture having the most suitable type i.e. less PUFA, but due to the contamination this could be heavily influenced by the significant bacterial presence which can also produce C18:1 FAME.

4.7.6 Air regular vs Oscillated flow 5 cc/min with 30 mins 5% CO_2/day

For the second oscillation comparison test the aeration rate was reduced to 5cc/min, with the hope of reducing bacterial contamination due to less shear related cell breakage/oxygen availability. The experimental conditions and setup were kept the same as the previous run. To reduce the likelihood of significant contamination further all silicone tubing was autoclaved and other surfaces (including the inside of the reinforced plastic tubes) were disinfected with 70% ethanol prior to the start of the test. The test inoculum was sourced from a culture of 16 day old *D. salina* 19/30 in 1 M NaCl Dunaliella medium with an OD (595 nm) of 0.8, this culture had also previously been centrifuged with a Percoll gradient to remove the majority of the bacteria. All monitoring procedures and protocols were conducted in the same way as the previous run. The cultures were harvested on day 14, washed once and freeze dried for subsequent NMR (500 µl $CDCl_3$/CD_3OD in a ratio 1:4, quadruplicate replicates) and direct trans-esterification processing. In addition, chlorophyll was extracted using the method in section 2.6.4for comparison with the NMR data on the same day and final biomass was compared using the freeze died samples (20ml taken from each reactor).

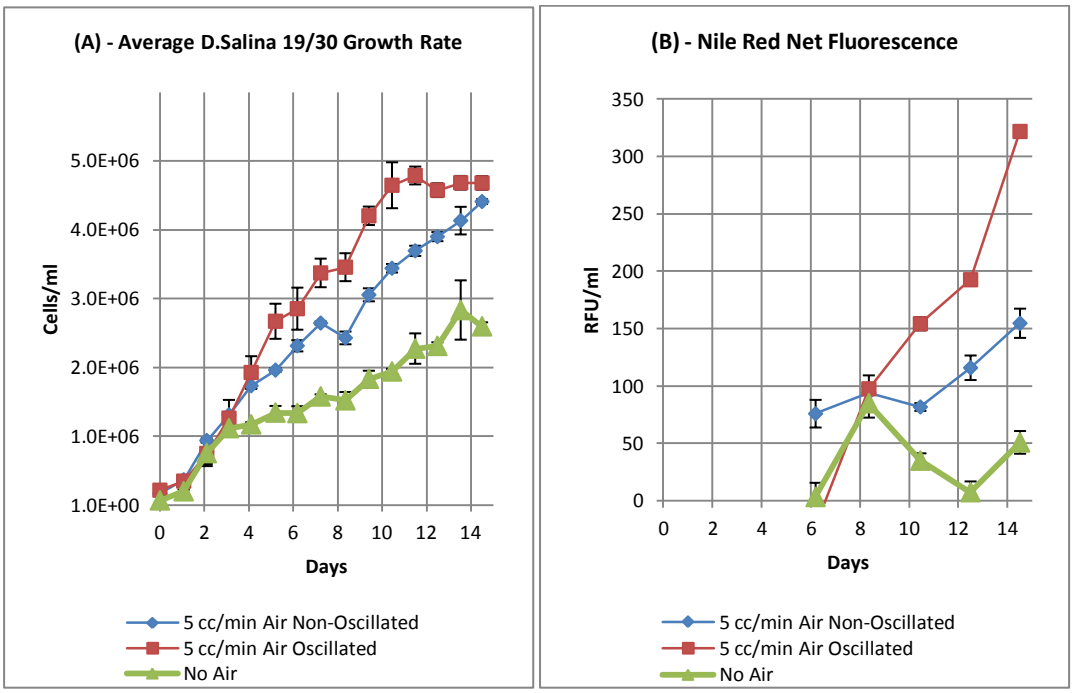

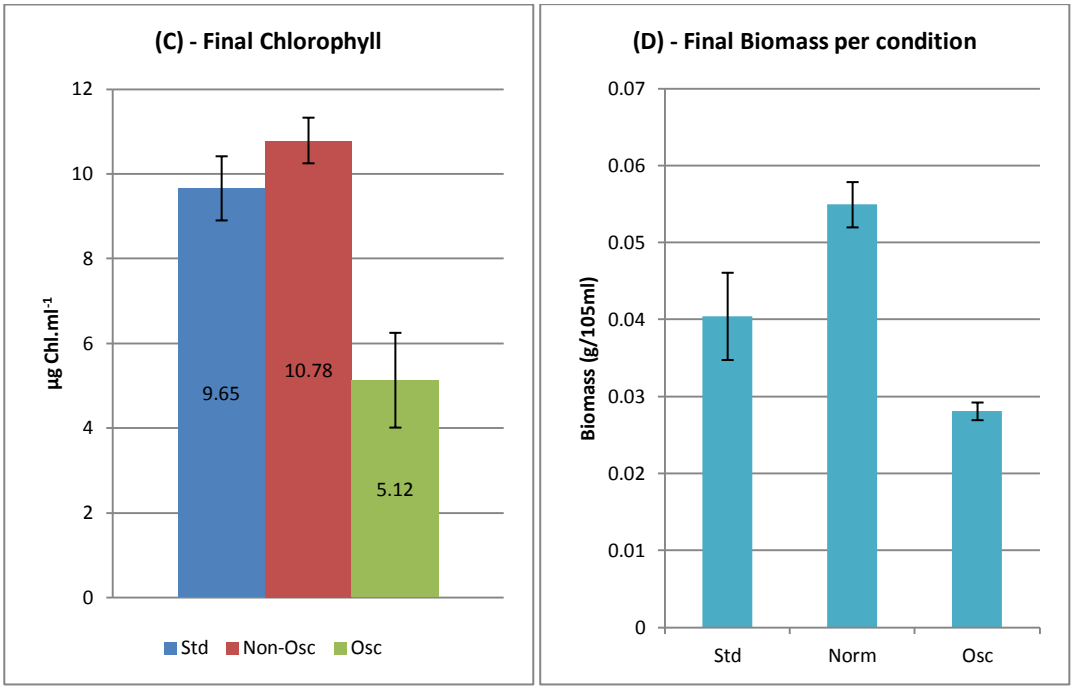

Figure 4.45.*D.salina* 19/30 cultured in Mk II mini photo-bioreactors under three conditions; non-aerated and aerated 5 cc/min air flow with and without fluidic oscillation. Aerated cultures were also sparged with regular flows of 5 cc/min 5% CO_2 gas for 30 mins a day. A) Culture growth measured using OD at 595 nm to produce an inferred cells per ml. B) Nile Red fluorescence (RFU/ml) Ex: 490 nm Em: 580 nm. C) Final chlorophyll extract data. D) Final biomass weight data.

Table 4.38 - *D.salina* 19/30 - NMR / extracted pigment data.

Sample	Extracted Chlorophyll content (µg Chl ml^{-1})	Std Err	NMR Chlorophyll (mM/10mg BM)	Std Err	NMR β-Carotene (mg/10mg BM)	Std Err
Non-Osc	10.78585	0.538691	0.31	0.0431	0.28	0.03285877
Oscillated	5.12593	1.118547	0.17	0.0344	0.20	0.02514307
Standard	9.65571	0.75735	0.63	0.0467	0.44	0.06332389

Table 4.39 - *D.salina* 19/30 - NMR/Direct transesterification total lipid data per 100ml reactor.

Sample	NMR total lipid – C17:1 equivelent (mg/10mg BM)	Std Err	Direct Trans total lipid (mg/10mg BM)	Std Err
Non-Osc	2.07	0.0819	1.515	0.203
Oscillated	2.00	0.1638	1.265	0.092
Standard	2.00	0.0046	1.619	0.323

Table 4.40 - *D.salina* 19/30 - NMR/Nile Red lipid group data.

Sample	NMR Unsat lipid signal (mM/10mg BM)	Std Err	NMR Unsat Me lipid signal (mM/10mg BM)	Std Err	NMR Sat Me lipid signal (mM/10mg BM)	Std Err	Nile Red Triolein equivalent (g/105ml)	Std Err
Non-Osc	17.26	1.1887	4.25	0.2937	7.56	0.515362	0.002	0.0004
Oscillated	14.26	1.0429	3.09	0.2924	7.06	0.475504	0.004	0.0006
Standard	19.78	1.4122	5.02	0.4993	8.37	0.465793	0.0004	0.0002

Table 4.41 - *D.salina* 19/30 - Direct transesterification FAME profile (% of total FAME):

FAME	Structure	Lipid Profile (% of total FAME)					
		Non-Osc	Std Err	Osc	Std Err	Std	Std Err
Methyl 4,7,10,13-hexadecatetraeoate	16,4 (cis n3)	10.72	1.80	8.92	0.13	11.28	1.46
9,12,15-Octadecatrienoic acid ME	18,3 (trans)	5.71	2.09	3.54	0.17	3.24	0.00
Hexadecanoic Acid ME	16,0	21.15	1.60	24.98	0.39	16.96	0.29
γ linolenic ME	18,3 (n6)	4.24	0.30	4.44	0.36	3.64	0.00
9,12-Octadecadienoic Acid ME	18,2 (6 cis)	4.46	0.25	5.22	0.75	4.33	0.57
9,12,15-Octadecadienoic Acid ME	18,3 (n3)	40.06	5.76	34.03	2.93	36.98	4.57
9-Octadecadienoic Acid ME	18,1 (9 Cis)	6.03	0.44	8.84	1.47	4.10	0.97
9-Octadecadienoic Acid ME	18,1 (9 trans)	3.89	0.41	4.64	0.52	16.48	10.90
Methyl 9,10-methylene-octadecanoate	19,0D (cis 9,10)	3.75	0.72	5.38	0.55	2.99	1.20
	Total:	100.00	13.38	100.00	7.26	100.00	19.97

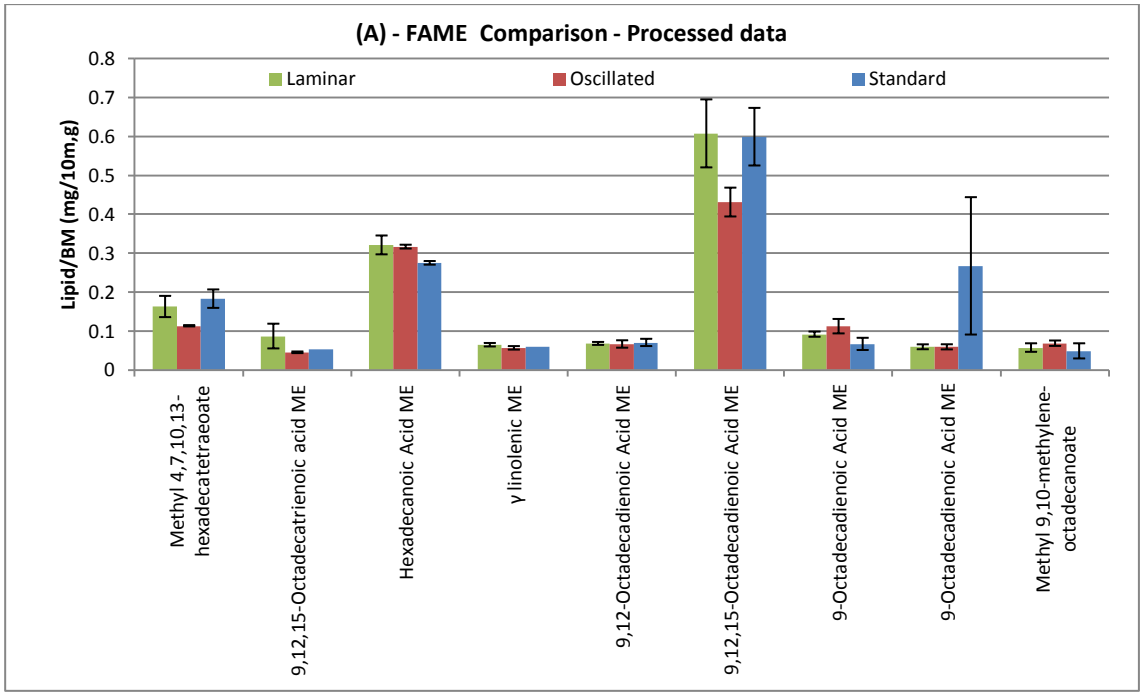

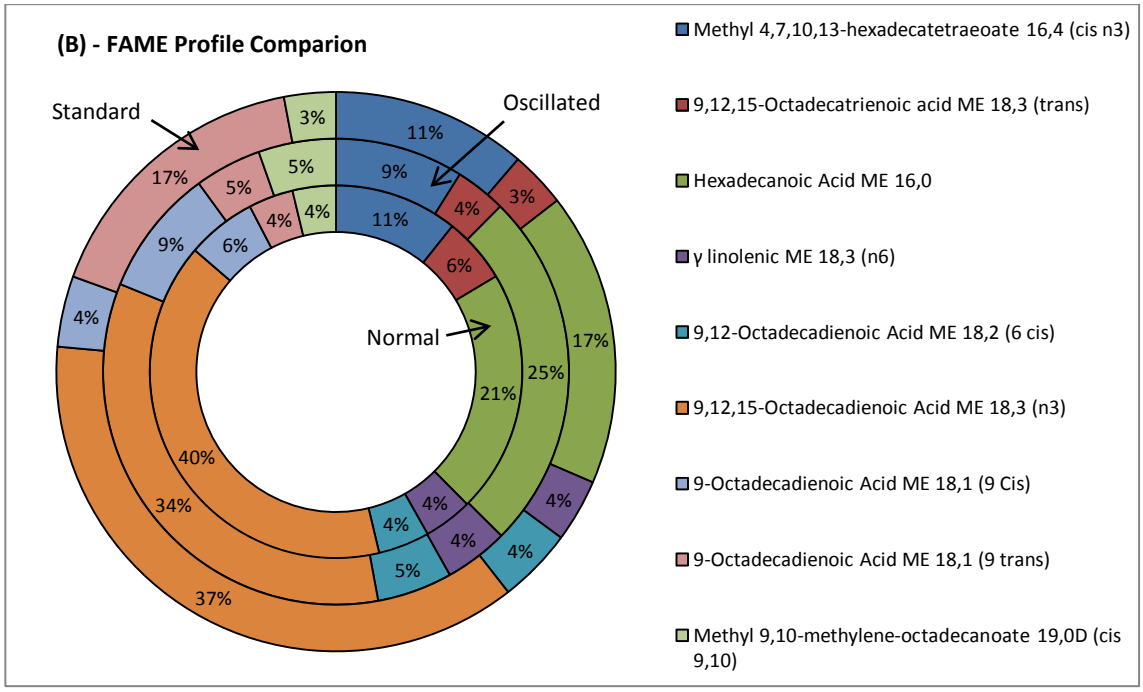

Figure 4.46. *D.salina* 19/30 grown with and without fluidic oscillation at 5 cc/min - A) FAME quantity comparison, Lipid/Biomass (mg/10mg) and B) FAME lipid profile (%).

The OD results from this second comparison experiment showed that the oscillated culture seemed to outperform the regular air and standard cultures throughout the duration of test (Figures 4.45 & 4.46 and Tables 4.38 to 4.41) . However, if the number of days had of been increased though, this trend could have potentially changed due to the oscillated cultures apparent entry into stationary growth phase where the other conditions had not. Either way, when the final biomass is considered the yields show an inverse correlation, this could be due to variation of pigment/contamination/broken cells giving an artificially high OD reading. Both the chlorophyll and β-carotene amounts are also higher in the two reference conditions. Interestingly the regular flow cultures seem to have the largest amount of extracted chlorophyll, which contradicts the NMR. However, based on visual observation this extraction result is thought to be anomalous and the NMR data more accurate. The difference in pigment does again seem to suggest slightly more damage is been dealt to the oscillated and regular flow cultures. The data from the FAME profile for the presence of C19:0 (cis 9,10) again adds credence to this observation. The NR data seems to again have a correlative discrepancy between the trend and the other lipid methods, which could be possibly explained by the amounts of the β-carotene/chlorophyll pigments under the different conditions. The NMR and GC-MS total lipid data shows very similar lipid/biomass yields under each condition, but with a marginal advantage for the non-oscillated conditions. If the biomass yield is factored in to this the normal air flow yield seems to be the most productive overall. But considering the FAME

profile, the standard culture has the best composition for biodiesel with a much larger amount of C18:1 and reduced PUFAs.

4.8 Conclusions

Based on the series of experiments performed in this chapter, a set of conclusions were drawn looking at the effectiveness of the methodologies employed and how they can be improved in future work.

Although there have been multiple calibration and characterisation tests performed to create a reliable NR method for use with *D. salina* 19/30 in this chapter, with good results, the premise for usage in any form of quantification or comparison between stains may well be flawed. Data comparing the NR results to direct trans-esterification/GC-MS and NMR in nearly every experiment (the exception been 4.5.2, where the pigments were very similar) has shown an inverse correlation. Given that the other two methods are more established and do not suffer from the various photonic interference issues that NR does (Pick and Rachutin-Zalogin, 2012), they are most probably more correct. The reasons for the NR discrepancies are hypothesised to be related to the differences in the chlorophyll and β-carotene pigments between the culture conditions (see section 4.4.5). The work by Chen, et al. (2009), Pick and Rachutin-Zalogin (2012) and Wu, et al. (2011) have demonstrated that these pigments can interfere with the excitation or emission of the NR fluorophore. Typically this obstacle is removed when there is no observable change in the amount of pigment between experimental conditions, or calibrations are performed in each case which takes into account the pigment variation. However, in this work that was not possible due to the osmotic shock or shear stress applied to the fragile *Dunaliella* cells.

In the varying salinity experiments the cells had to be re-suspended into the same medium molarity to avoid NaCl NR quenching issues, but this in turn could have lead to osmotic shock and the cells to rupture leading to pigment increase in the background which could affect the readings. Given the lack of cell wall in this strain and its resultant fragility, there appears to be no escaping a compromise using NR whilst looking at the effects of salinity. Interestingly, the results from these studies seem to slightly contradict other research which suggests that increased salt actually promotes the production of carotenoids in *D. salina*(Farhat, et al., 2011). Another paper also suggests that beyond 3 M NaCl there is a sharp increase in chlorophyll production, although even with genetic identification the sub species of *Dunaliella* is not specified (Mishra, Mandoli and Jha, 2008). Based on this it is assumed that the

pigment/salinity response is highly strain specific, thus *D. salina* 19/30 does not react in the same way.

In the second batch of experiments with different types of aeration, the difference in pigment (and hence NR response) is hypothesised to be due to the shear flow effects in the reactor inducing cell lysis. In the literature, it has been observed that the breakage of cells is due to aeration and one of chief causes of pigment release into the growth medium. The *D. salina* pigment 'milking' experiments by Kleinegris, et al. (2010) demonstrated this effect. Interestingly, this paper also showed that some 'leaky' strains also release pigment with no rupture of the cell taking place. Based on the research performed in Chapter 3, it is highly possible that the cells were been disrupted by the higher flow rates and/or the effects of the smaller bubbles produced under 1 M NaCl, which have a higher inherent energy dissipation rate (EDR) and hence more destructive power.

In conclusion, Nile Red is most probably not a suitable method for lipid comparison/quantification for use with *Dunaliella*, due to its fragility and the effects this has on its pigment accrual due to breakage/leakage. If any further work was to be performed on this organism using the stain, the media would need to be of a fixed salinity and the aeration set at a specific constant to get any sort of useful data for comparison. Also, any sub-strain with a high production of β-carotene would possibly need to use a different excitation wavelength to avoid absorbency issues. To that end, the dye BODIPY 505/515, has similar lipid staining properties to NR could potentially be useful as its excitation and emission wavelengths would be further outside of pigment interference range (Govender, et al., 2012).

Regarding the experiment looking at the effects of saline stress on *D. salina,* the increase in molarity was found to reduce growth rates and lipid productivity, but induce a subtle shift in the FAME distribution profile (see section 4.4.5). Based on these findings, it is likely that *D. salina* is not the best candidate for biofuel production. However, these conclusions could be skewed due to the reduced solubility of the medium with greater salinity (see section 3.2) and due to bacterial contamination in the lower salinities. So based on this, the findings of the experiments in terms of overall lipid yield are most likely inaccurate and unrepresentative of optimal growth conditions. If the experiment was to be performed again, it is suggested that the carbon source be supplied directly from bicarbonate within the medium and the flasks sealed to minimise the solubility effects and the lipids be monitored using NMR/DT methods. To reduce the impact of the sample collection needed for these methods bigger volumes would also be beneficial.

The three litre reactor experiments were very useful in indicating that the air supply did not provide enough carbon dioxide for culture growth and in doing so, highlighting the fact that oscillation was potentially also having impacts other than mass transfer. It is therefore unfortunate that there was not sufficient time or resources to continue the comparison between the two conditions, as this was the only setup capable of providing a high enough flow rate of 5% CO_2 (45 l/min) to look at the effects of continual dosing such as in the Zimmerman group steel work sequestration trial (Zimmerman, et al., 2010b). If further experiments were to be performed using this setup, continuous oscillation with a higher CO_2 content would be very beneficial.

The mini photo-bioreactor experiments provided an excellent proof of concept of the design, the tests showed excellent mixing and a variety of different cultures were grown successfully in the vessel. The flow rate experiments showed that increased aeration seemed to correlate with increased damage and bacterial contamination in all cases. However, it was also shown that certain flow rates also seemed to be optimal, which if the average bubble size was taken to be 0.5 mm based on previous tests using the same sparger (Mahmood, et al., 2011) correlated well with the CFD data gleaned in Chapter 3, showing the 5-10 cc/min flow rates to provide the best general mixing at that bubble size. The subsequent data comparing oscillated versus normal flows at these gas influx rates, also showed a subtle difference in growth behaviour. This difference based on pigment and bacterial contamination, indicated that the oscillated flow could potentially be more damaging. However, this issue is complicated by the bacterial presence which could be forming a negative feedback scenario; i.e. where some cells break and release glycerol which is metabolised by the bacteria which have a slightly more abundant supply of O_2 due to the increased rate of mass transfer caused by fractionally smaller bubbles (in the sparger region, see Chapter 3). So in a way fluidic oscillation could potentially be a victim of its own success. Another factor may also be coming into play, in that if the algal cells were carbon limited they may have also become more fragile, which could explain the differences between the two flow comparison experiments. Further comparison work is needed in this research area to look at these oscillated differences. A first recommendation for future work would be the use of an axienic *D. salina* culture (with bacterial vitamin supplements to compensate), which could be used to fully characterised cell damage. The second would be if oscillation could be induced at a lower flow rate, or using a mechanical valve setup so 5% CO_2 could also be used in the comparison experiments. There were also issues with uniformity of lighting, temperature and pH readings, so some redesign of the apparatus would be very beneficial. Recommendations of changes to the mini-reactor design to avoid flocks forming and provide better mixing are included in Chapter 3.

5 Photo-Bioreactor Coatings

5.1 Introduction

One of the major limiting factors to algal growth aside from the mass transfer and nutrient factors discussed in the previous chapters, is light uptake for photosynthesis (Blankenship and Chen, 2013). To enable the mass production of algal biomass, light must be in plentiful supply for adequate amounts of carbon fixation and therefore lipid accrual to take place. However, due to climatic factors such as cloud formation and season light variation, quite often natural insolation can be sub-optimal for algal growth needs, leading to growth limitation (Xu, et al., 2009). Artificial light can be used to replace or augment natural light inputs, but it comes at great cost, financially and in terms of indirect carbon emissions (Chisti, 2013). A few potential solutions to this problem have been suggested in the literature thus far, including; exposing the algae to rapid light/dark cycles (Yago, et al., 2012), genetic modification of the algal light harvesting antennae (Williams and Laurens, 2010), extending the absorption range of algal pigments (Blankenship and Chen, 2013) and other metabolic/regulatory approaches (Stephenson, et al., 2011). Although, many of these approaches require further extensive research to be realised or they may have parasitic energy costs.

Recently, other concepts using passive means, such as the integration of fluorescent compounds, 'light funnelling' and reflective particles into photobioreactor designs, have shown great promise for increased algal growth productivity without inherent energy costs (Carvalho, et al., 2011; Giannelli and Torzillo, 2012; Mohsenpour, Richards and Willoughby, 2012; Mohsenpour and Willoughby, 2013; Wondraczek, et al., 2013). However, these approaches have expensive setup costs and chemicals, or inflexibility for scale-up.

In this chapter a potential solution to these problems is described using a variation of the passive fluorescence approach (Wondraczek, et al., 2013). An optically permeable ‘smart’ photo-bioreactor coating has been developed, that can theoretically make the light supply from natural sources more consistent and reduce or eliminate the input cost of artificial illumination. The ‘smart’ coating makes use of the natural wavelength shifting properties of two fluorescent dyes; Rhodamine B and Coumarin 1 (section 2.10.1). The dyes were selected for two reasons; firstly, their absorbance bands are in the regions of light poorly utilized by algal cells and secondly, their re-emission wavelengths overlap with the absorption peaks of the light harvesting pigments in most algal strains (Figure 5.1). This set of properties allow the coatings to act as a light filter, shifting un-utilised light at the reactor surface making light ingress more energetically efficient, so less light is wasted as a heat and more is available for algal photosynthesis.

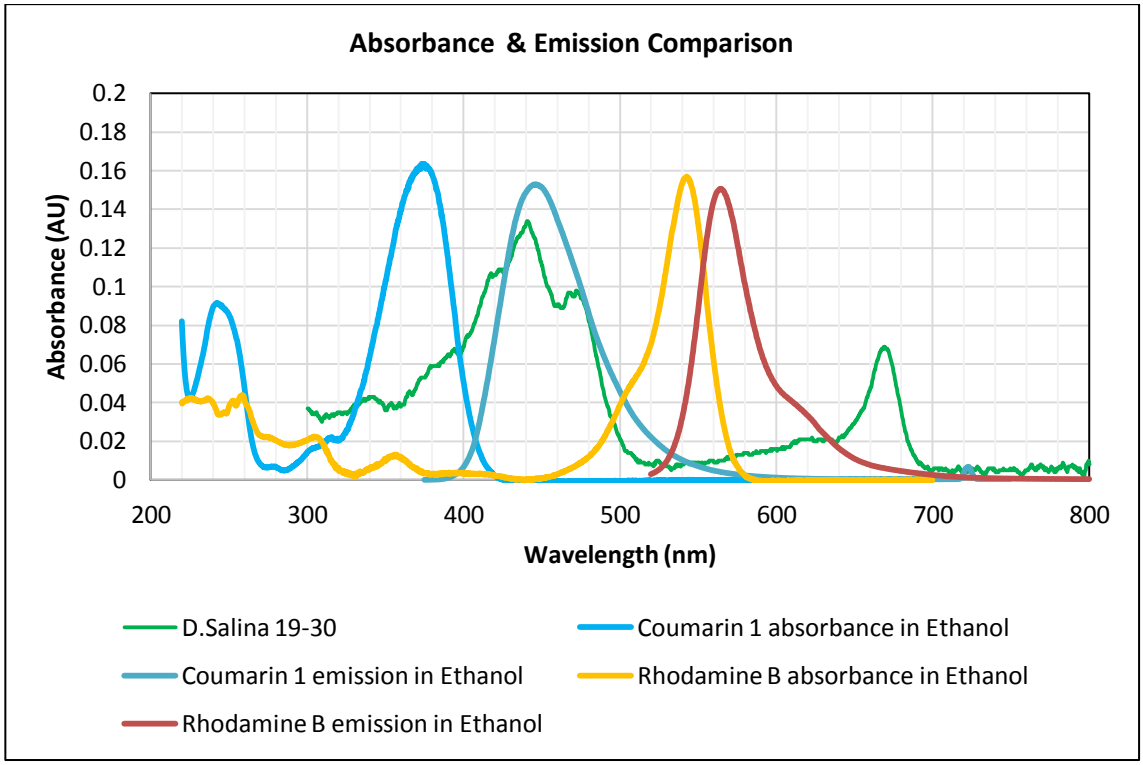

Figure 5.1.The absorbance and emission wavelengths of both dyes (source; PhotochemCAD 2.1 software package (Dixon, Taniguchi and Lindsey, 2005)) alongside the pigment absorption spectrum for *Dunaliella salina* 19/30 (extracted from a month old culture using iso-propanol alcohol, data kindly donated by Dr Alan Dunbar from the University of Sheffield's CBE department). The graphs show the Stokes shift from un-utilised areas of the spectra, i.e. green light (495-570 nm) used by Rhodamine B and violet light (380-450 nm) used by Coumarin 1, towards the light quality absorbed by light harvesting pigments of *D. salina*.

To make the coatings suitable for testing, the two dyes were suspended in a matrix using a solvent (or a mixture of such). Many different combinations of matrix and solvent were tried by Ying and (Hosking, 2013), before they eventually settled upon PMMA and the solvents specified in section 2.10.2. PMMA was found to be a suitable matrix because of its low cost, availability, biocompatibility, ease of process and its optical properties (optically transparent down to 300 nm (Zidan and Abu-Elnader, 2005)).

In this work a series of coatings were trialled in two types of experiment; the first used the first generation of mini-bioreactors (section 2.12.3) and the second used a series of dye coated slides and 96 well plates (section 2.10.3, 2.10.5).

5.2 Initial Test Slide Results

A series of initial tests were performed using a selection of coated slides and a 'modified transilluminator' equipped with both normal white and UV fluorescent tubes (section 2.10.6). Each slide was placed in the area on the transilluminator with the most balanced intensity and wavelength distribution using the equipment specified in section 2.9.2 (see Figure 5.2 on the right). Bar spread 5 and 10% coated Rhodamine and Coumarin slides (comp ID 5-8, section 2.10.2, 2.10.4) were compared against plain untreated slides to see if there was any evidence of a Stokes shift of light into the PAR region (Carvalho, Meireles and Malcata, 2006). The absorbance spectrum of *D. salina* was included as a reference to show the wavelengths of light that drive most photosynthesis.

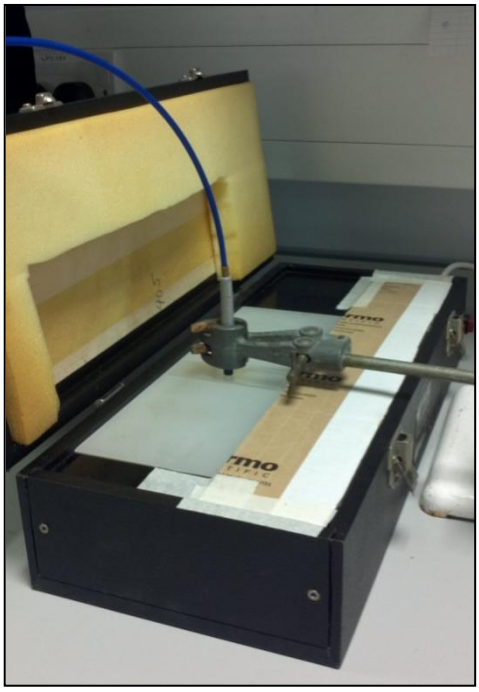

Figure 5.2. Custom trans-illuminator set-up.

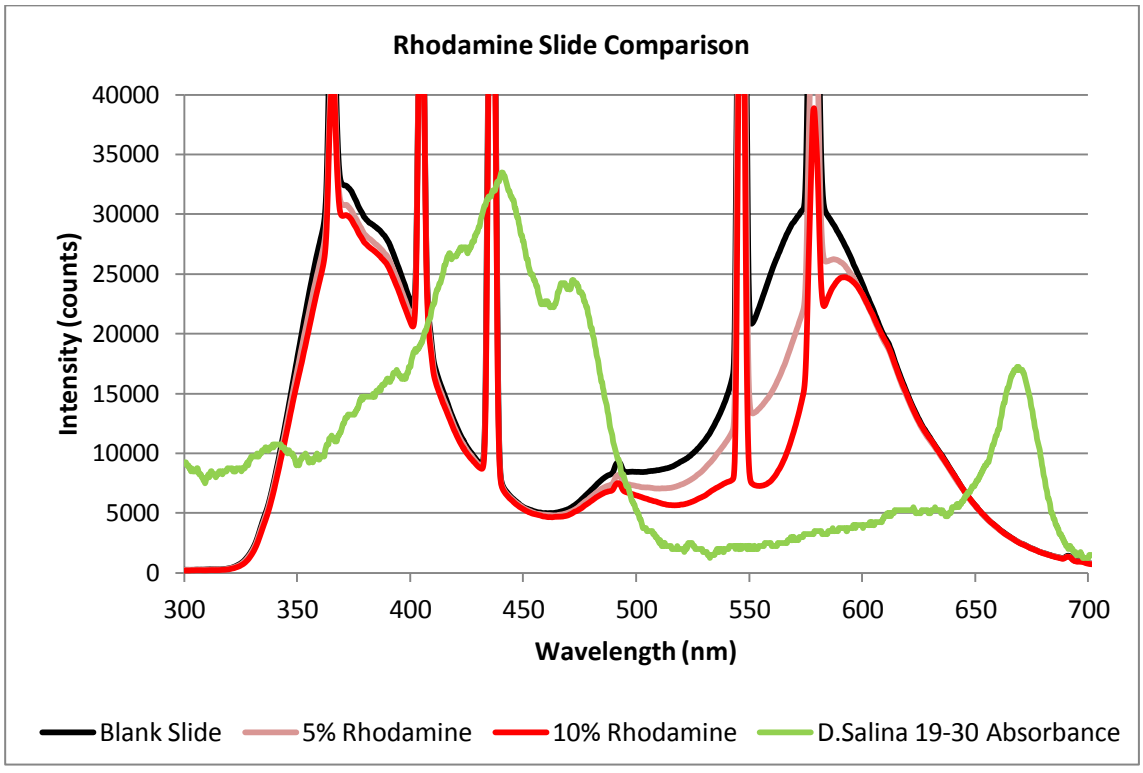

Figure5.3. Uncoated slide compared with 5 and 10% Rhodamine B

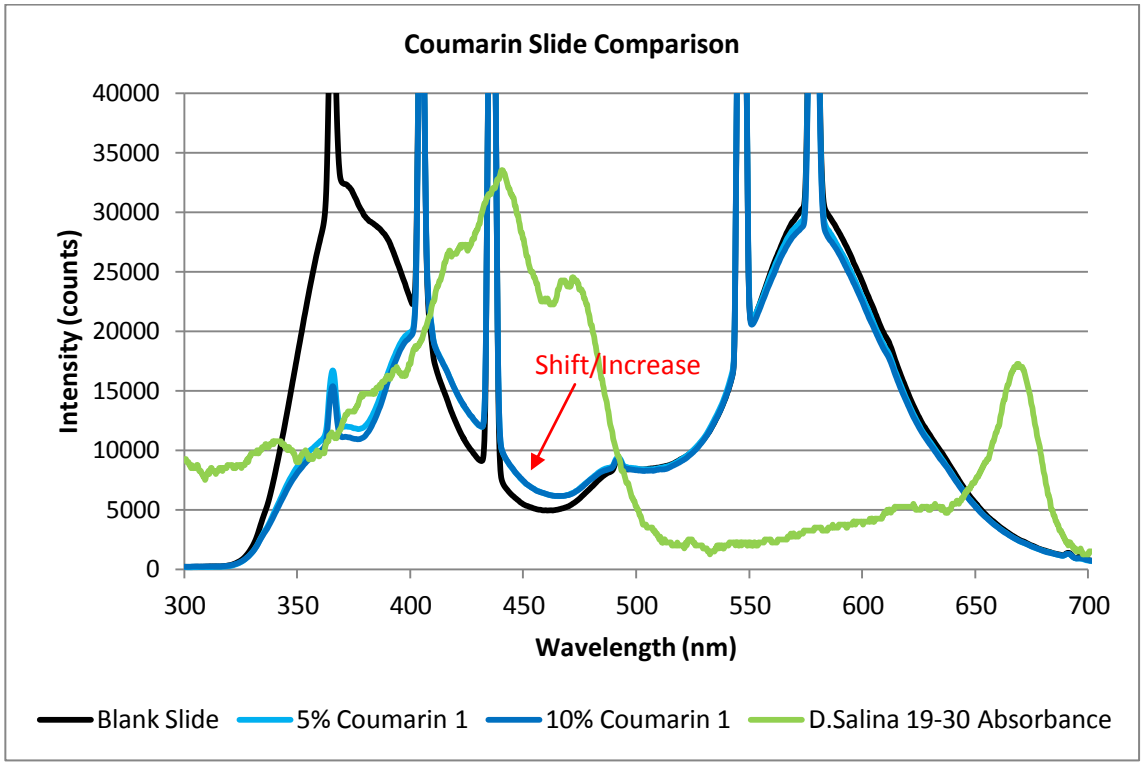

Figure 5.4. Uncoated slide compared with 5 and 10% Coumarin 1

The results in Figure 5.3 show no discernible shift or increase in the light intensities in the Rhodamine slides, but a cut to the light intensities in the 460-580 nm range was evident. As the main dye absorbance is in this area, this is to be expected. Theoretically, the emission should compensate by producing a shift in the 520-700 nm range, but there is no evidence of this in either of the two coating concentrations. As re-emmission is omnidirectional, this effect could possibly be due to some of the light not reaching the cosine corrector and light sensor (Mohsenpour, Richards and Willoughby, 2012).

The results shown in Figure 5.4 were slightly more promising. Coumarin is expected to absorb at 300-420 nm and re-emit in the 400-600 nm region and there is clear evidence of both phenomena. Due to the opacity of of the slide material, diffuser and source no light is produced below 325 nm, so no absorpbtion can take place at that point, but from 325 to 400 nm a clear decrease in light intensity can be observed. A Stokes shift is evident in both concentration of dyes from 410-480 nm (indicated on Figure 5.4 by a red arrow). As this shift is toward the chlorophyll peaks, it could be of benefit to the algal strains. However, this benefit will only be applicable if the cut due to the dye absorbance in the shorter wavelengths (where some chlorophyll pigment is present), is more than compensated by the smaller shift to the longer wavelengths where the majority of pigment is present, thus producing a net energetic gain.

5.3 Further Slide Tests

Based on this preliminary data, further slide tests were performed by Hosking (2013) under guidance, to confirm the coating effects. Coated slides were mounted in an Ocean Optics 4-way cuvette holder and light was guided to the sample from a Ocean Optics UV-VIS-NIR Deuterium Tungsten Halogen light source (Model DT-MINI-2-GS) for absorbance readings or from a StellarNet Ltd SL1-LED light source for emission testing using a series of fibre optic cables (see appendix B for details). The light readings were detected using the Ocean Optics portable spectrometer as in the previous tests.

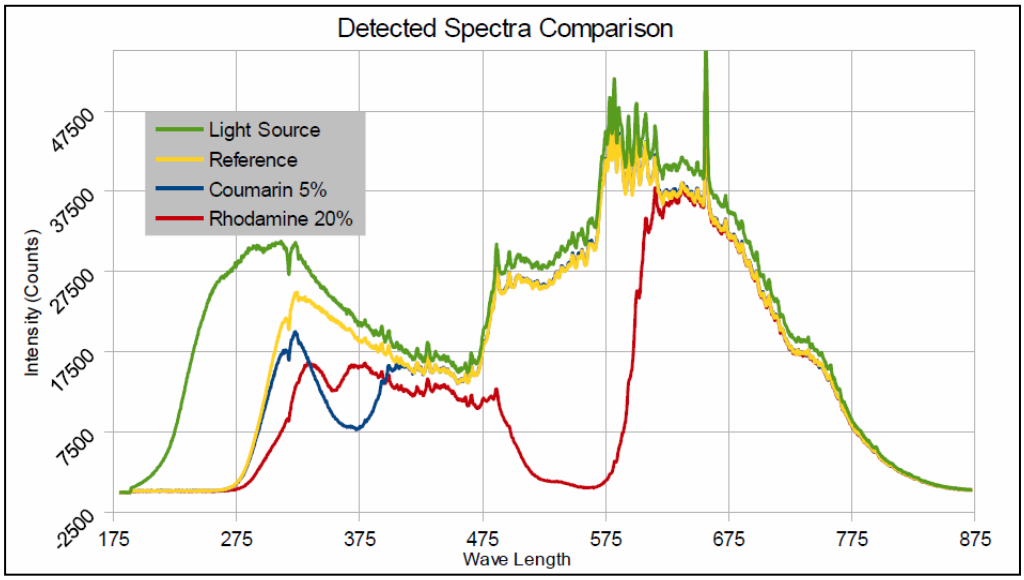

Figure 5.5.Intensity comparison using Ocean Optics UV-VIS-NIR full spectral light source with 5% Coumarin and 20% Rhodamine spin coated slides compared to a plain glass reference sample (Hosking, 2013).

The data from this test (Figure 5.5) demonstrate and confirm a number of observations from the previous transilluminator test. The slides are restricting the lower wavelengths (<275 nm), but after that have a very good match to the source illumination. The Coumarin absorption is modest and matches the literature (Dixon, Taniguchi and Lindsey, 2005) and previous test. The Rhodamine absorbance is much higher, but also matches the literature very well (Dixon, Taniguchi and Lindsey, 2005). Neither sample show any major evidence of a shift towards emission, but this could be hidden by the experimental inconsistencies mentioned previously. To test if any emission was achieved, the test setup was changed to use the StellarNet Ltd SL1-LED light source, fitted with the appropriate wavelength producing LED (appendix B). As this would remove any extraneous excitation wavelengths and highlight any emission response.

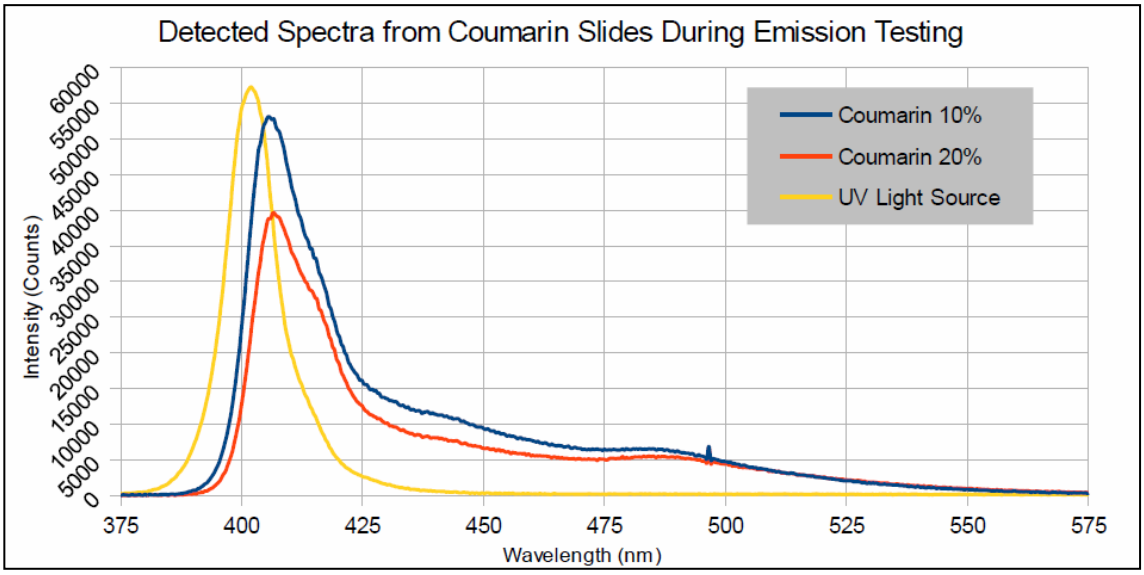

Figure 5.6. Emission comparison using StellarNet Ltd SL1-LED light source with 10% and 20% Coumarin spin coated slides (Hosking, 2013).

The data from the emissions comparison for Coumarin (Figure 5.6) clearly indicates a stokes shift and increase in intensity compared to the original light source. Interestingly the higher concentration of dye, in the previous transilluminator test, also resulted in a lower output intensity. This effect could be an example of self quenching, or a slight discrepancy in the reading.

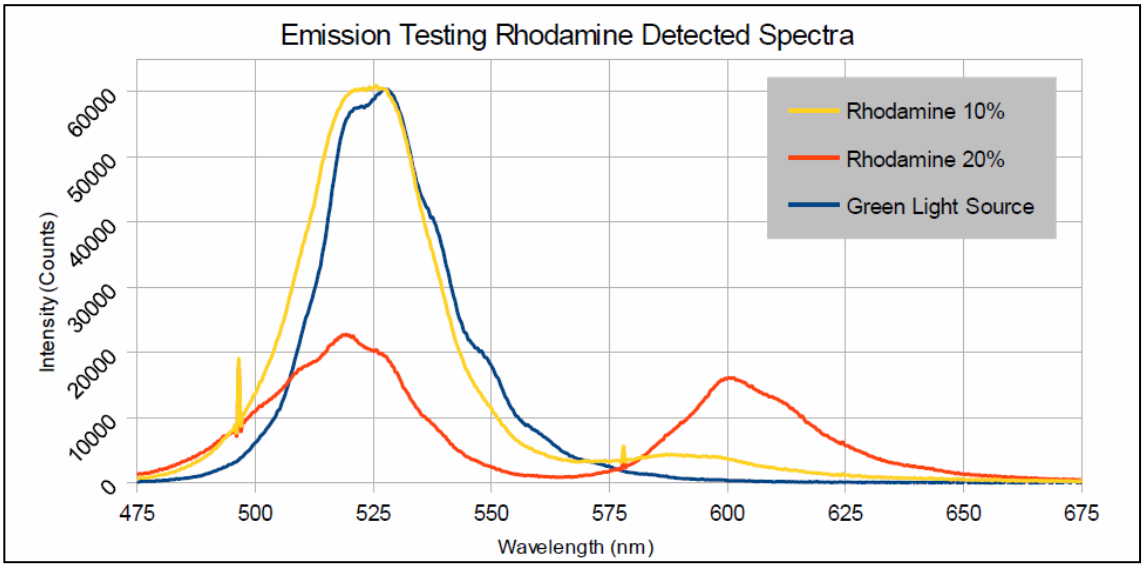

Figure 5.7. Emission comparison using StellarNet Ltd SL1-LED light source with 10% and 20% Rhodamine spin coated slides.

The results from the Rhodamine emission test (Figure 5.7) also demonstrate a shift and increase compared to the original light source, albeit a very different one between the two dye concentrations. The 10% dye shows only a marginal increase from 575 -625 nm, while the 20% shows a much stronger peak in the same area. The differences in reading are slightly

anomalous in relation to the previous data, however both sets of data (Figures 5.6 and 5.7) do show the improvement sought after in the aims of this part of the research.

Based on this positive data, a series of experiments were devised to test out how various strains of algae (mainly *Dunaliella* species) would respond to the change in lighting distribution.

5.4 Mk I Photobioreactor Tests

The first batch of experiments were performed using the mk1 photobioreactors (section 2.12.3, 2.10.5) and standard100 ml Schott Duran square bottles (21 0820 245). The reactors and bottles were setup on the lab bench and temperature controlled using a water bath arrangement (section 2.12.3,25^{o}C constant). Lighting was provided by a mixture of white light and UV thick fluorescent tubes (section 2.9.3, appendix A6). The lab air supply (1 bar regulated) was used for aeration (10cc/min) and controlled using a set of calibrated flowmeters and manual clamps. Three batches of experiments were performed using minor variations of this experimental set up, with the*D. salina* 19/30 (growing in 1 M NaCl Dunaliella medium) used in every test (section 2.1.1, 2.3).Selected photobioreactors and bottles were coated with the dye mixtures using a manual painting technique, due to the geometry being unsuitable for bar spreading and spin coating (section 2.10.4). Conditions with and without air/coatings were studied and samples were taken daily and cell counts were performed in triplicate. The standard inoculation ratio of 5:100 ml well grown culture to fresh medium was used in each test.

5.4.1 Mixed lighting for 10 days, then UV only for 6. Both dyes used.

Due to the positive response of both types of dyes in the previous concept tests, the first experiment used both coatings but at the lower 5% concentration. This figure was selected because in general there appeared to be less absorbance needed for the same intensity of emission. The experiment setup consisted of 4 photobioreactors and 4 bottles (see Table 5.1 and section 2.10.2-4). Illumination was provided by 3x white bulbs and 1 x UV bulb. The white lights were switched off from day 10 onward to see if the Coumarin 1 coatings could enable the algae to grow in the absence of visible light.

Reactor /Bottle No	Aeration	Dye Type	Comp ID
1	Yes	Coumarin 1 - 5%	3
2	Yes	None	N/A
3	Yes	None	N/A
4	Yes	Rhodamine B - 5%	4
5	No	Coumarin 1 - 5%	3
6	No	None	N/A
7	No	None	N/A
8	No	Rhodamine B - 5%	4

Table 5.1. MkI mini photobioreactor set-up

Growth results

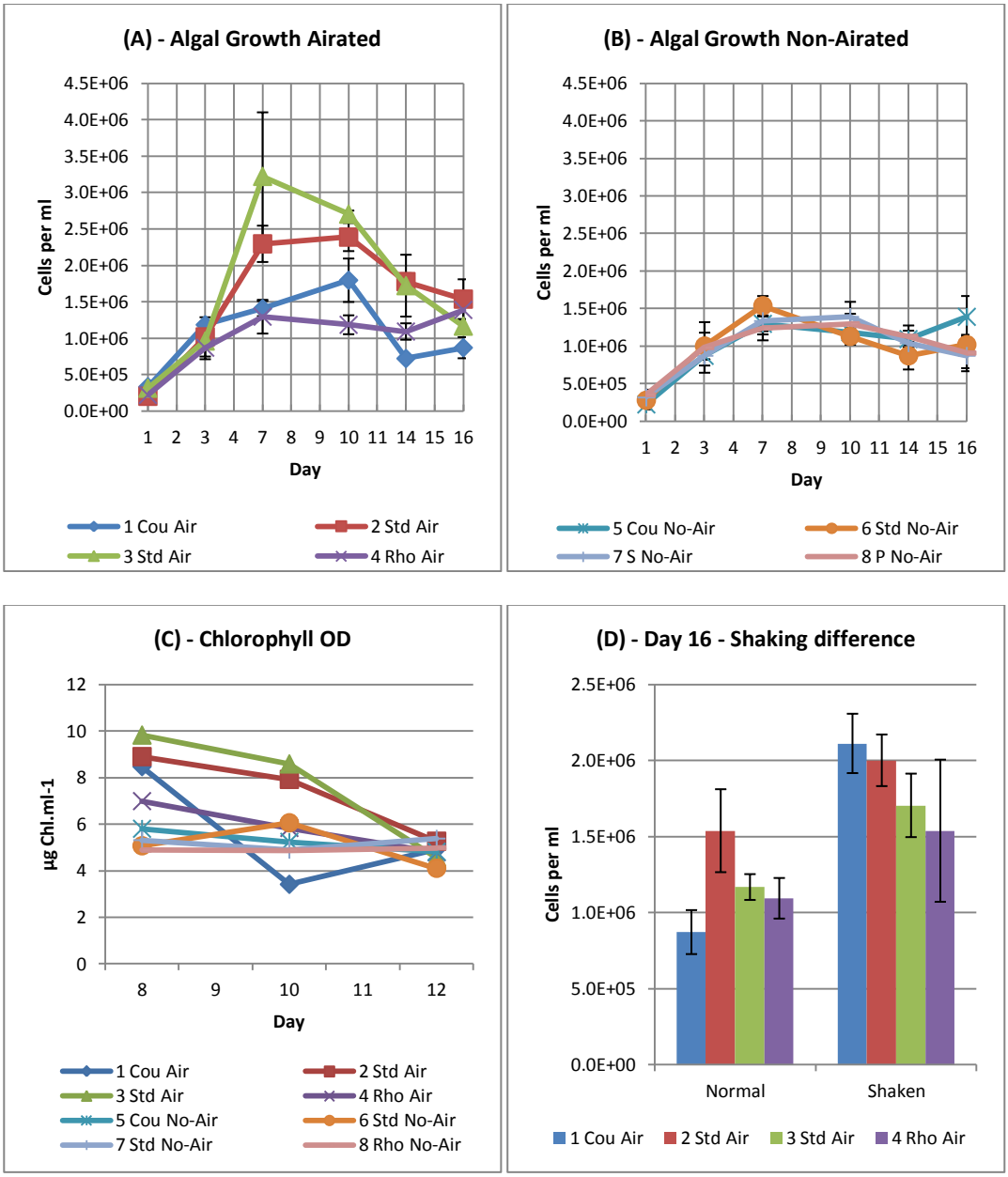

Figure 5.8. Algal growth (*D. salina* 19/30) in the presence and absence of Coumarin and Rhodamine dyes. A) Aerated (cells/ml), B) Non-aerated (cells/ml), C) Chlorophyll contents of aerated and non-aerated cultures, D) Difference in cell counts before and after shaking on day 16.

The results from the experiment show that in the aerated case the two standards seem to perform better the two types of coating in levels of growth and chlorophyll production (Figure 5.8 A and C). The non-aerated cultures show very little difference between any of the conditions (Figure 5.8 B and C). After day 10 when the white light was removed there was a general decline in most cases, however the Coumarin dye shows a slight indication of increased growth at the end under both aerated and non-aerated conditions (Figure 5.8 A, B and C). This conclusion is very tenuous, as the mixing in the reactor vessels was poor and wall

growth was prevalent. To try and ascertain the wall growth impact on the last day, two sets of readings were taken from the aerated cultures; one as normal and the second after shaking (Figure 5.8 D). The amount of cells in the reading doubled following the shaking step, so for future work shaking was adopted before every reading.

5.4.2 UV lighting and Coumarin dye only

A second test was performed with just the Coumarin coatings to determine if the UV light sources were having an effect. This time the two UV fluorescent tubes were used from the start with no white light. The aeration methods and rate were kept the same, a barrier of aluminium foil was placed between the coated vessels and the reference standards to minimise luminescence effects. Five reactors and bottles were used in the test (Table 5.2).

Reactor/ Bottle No	Aeration	Dye Type	Comp ID
1	Yes	Coumarin 1 - 5%	3
3	Yes	None	N/A
4	No	Coumarin 1 - 5%	3
5	No	None	N/A
6	No	None	N/A

Table 5.2.MkI mini photobioreactor set-up

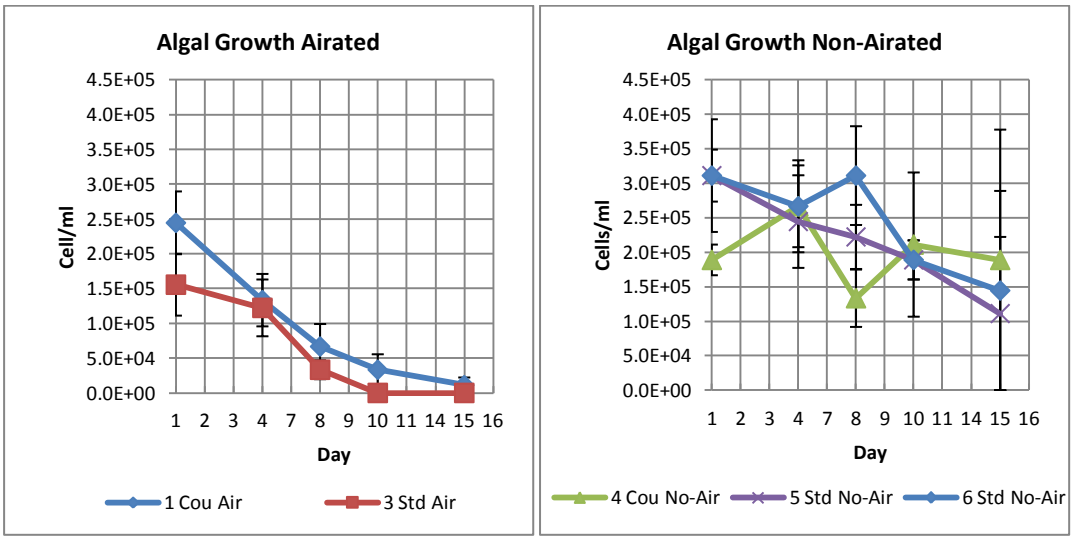

Figure 5.9. Comparison of algal growth rates in the presence or absence of Coumarin dye under aerated or non-aerated conditions.

The results show a net decline in all cultures (Figure 5.9), but again, the coated ones decreased at a slightly lower pace. However, considering the size of the error bars, the conclusion is far from clear. Another phenomenon was also noticed during the tests, the insides of the cardboard box surrounding the setup had patches of white paper coating. It was speculated that the re-emission lightfrom the dye and the light from the UV was also exciting these zones (optical brightner used in white paper production also has UV fluorescent properties) which

could be skewing the results data. Also, there were still issues with improper mixing within the glass bottles.

5.4.3 UV lighting and Coumarin dye only, matt black surround.

A repeat run of previous experiment was performed, but this time the inside of the cardboard box surround was painted matt black and a black matt plastic barrier was placed between the coated vessels and the standards to avoid any lighting issues.

Reactor/ Bottle No	Aeration	Dye Type	Comp ID
1	Yes	Coumarin 1 - 5%	1
2	Yes	None	N/A
3	Yes	None	N/A
4	No	Coumarin 1 - 5%	1
5	No	None	N/A
6	No	None	N/A

Table 5.3. MkI mini photobioreactor set-up

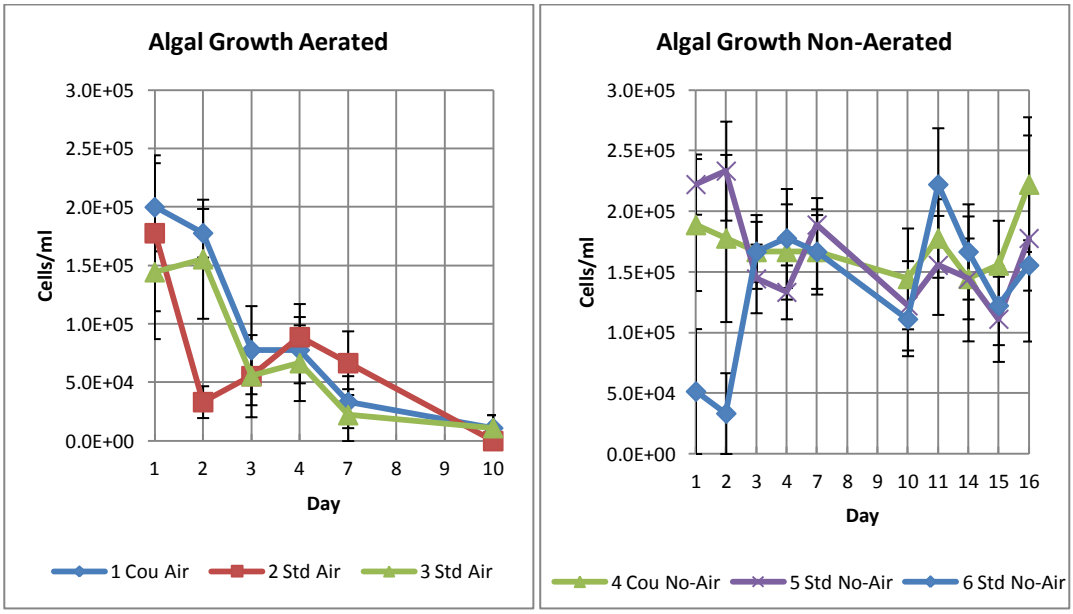

Figure 5.10. Growth of *D. salina* in UV light only with our without Coumarin coatings. A. Under aerated conditions and B. Under non-aerated conditions.

The results from the repeat (Figure 5.10) were almost the same as the previous run (Figure 5.9), with all cultures declining again and showing no conclusive difference between the coating and standard.

5.4.4 Discussion

All three Mk1 photobiorector experiments failed to show any significant growth differences between the dye coated vessels and the standards. Due to poor mixing in the aerated reactors the growth readings were severely compromised (a test before and after shaking proved the difference was considerable), also problems with flow regulation due to the flowmeter range being at the edge of tolerance led to inconsistencies in air supply in some cases. The non-aerated vessels showed much more consistent results, but little evidence of a trend. This was a

curious result, because on examination the dye-coated reactors were fluorescing considerably while the rest of the cultures were in darkness (Figure 5.11).

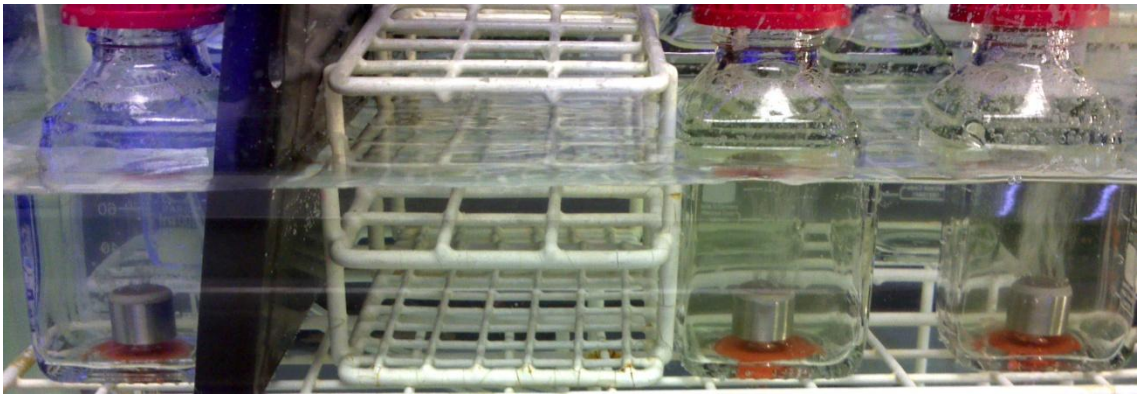

Figure 5.11. Evidence for fluorescence from dye-coated bottles under UV – light.

One possible explanation for this would be a 'light guiding' effect occurring due to total internal reflection (Mohsenpour, Richards and Willoughby, 2012). If this was occurring it is possible that the light was reflected around the edge of the bottle glass and emitted in the "wrong" direction, so possibly never actually reaching the algae. To test this hypothesis a wavelength reading was performed from inside one of the coated vessels (Figure 5.12).

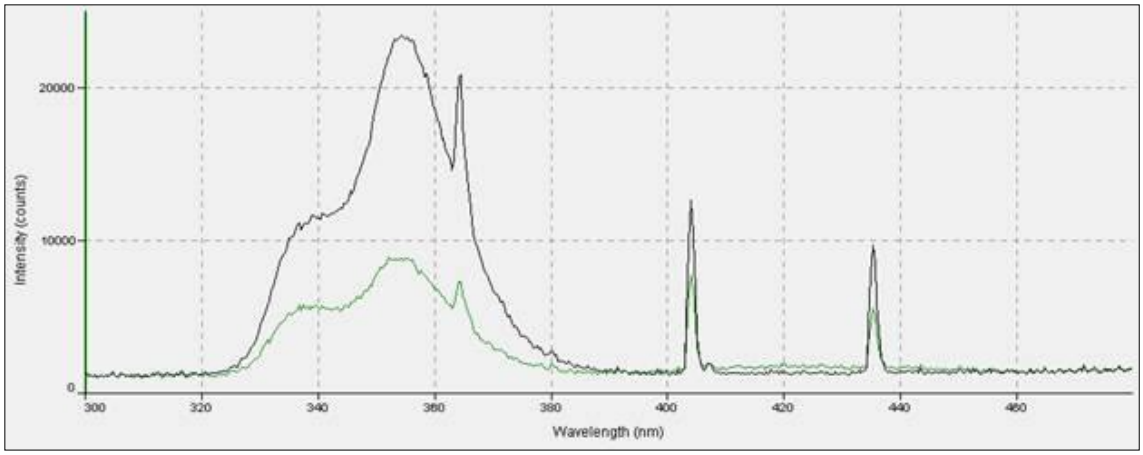

Figure 5.12. Comparison of spectra from inside a UV dyed vessel (green) and no dye (black).

The spectral output from the UV lamps is shown in black and the spectrum as recorded behind the Coumarin coated glass is shown in green. There is a clear absorbance in the UV-blue area of the spectrum and only a very slight shift increase in intensity around 420 nm, providing some credence to the theory and explaining the lack of difference in the growth results.

5.5 96 Well Plate Experiments

The second set of experiments were performed using a series of 96 well plates, dye coated slides and a trans-illuminator. The slides were placed in between the trans-illuminator light

source and the base of the micro-plate (section 2.10.5). Due to the much simpler geometry (compared with the photo-bioreactors) and no aeration, coupled with the previously demonstrated Stokes shift, it was thought there would be a better chance to show some evidence of difference in algal growth using this arrangement.

At the start of each test 286 µl of the appropriate fresh medium were added to each specified growth well, along with 14µl of a well grown algal inoculum. 300 µl of blank medium were included in selected wells for use as a blank in the OD measurements. All the OD measurements were performed using the Wallac Victor 2 Multi-label Plate reader.

5.5.1 Standard trans-illuminator, standard plate with both dyes

The first experiment was conducted at ambient lab temperature using the standard generic transilluminator (section 2.9.3, spectra appendix A8) along with a 96-well flat bottomed clear plate (Greiner Bio-one Cellstar 655 185) that had the cover and sides painted in matt black paint to prevent illumination from other sources skewing the results.Two coated slides were used (5% Coumarin and Rhodamine, Comp ID 1-2, section 2.10.4) along with an uncoated slide as the standard. Absorbance was measured at 450 nm with an integration of 1 second. Seven species of green algae were tested, *Dunaliella salina* (various strains), *Tetraselmis suecica* and *Nannochloropsis oculata*(see layout below). Between readings condensation on the lid was removed and sterile plastic spreaders were used to mix each well.

Plate Layout:

Species rows	1	2	3	4	5	6	7	8	9	10	11	12	
D.salina 19/30 1M NaCl Dun Med													A
D.salina 19/18 1M NaCl Dun Med													B
D.S 19/18 A12 1M NaCl Dun Med													C
D.S 19/18 C9 1M NaCl Dun Med													D
D.S 19/18 E8 1M NaCl Dun Med													E
Tetraselmis suecica 1M NaCl Dun Med													F
Nannochlropsis oculata F/2 Media													G
N/A - Empty													H

5% Coumarin Dye	Empty	Plain Slide	Media	Empty	5% Rhodamine Dye

Results:

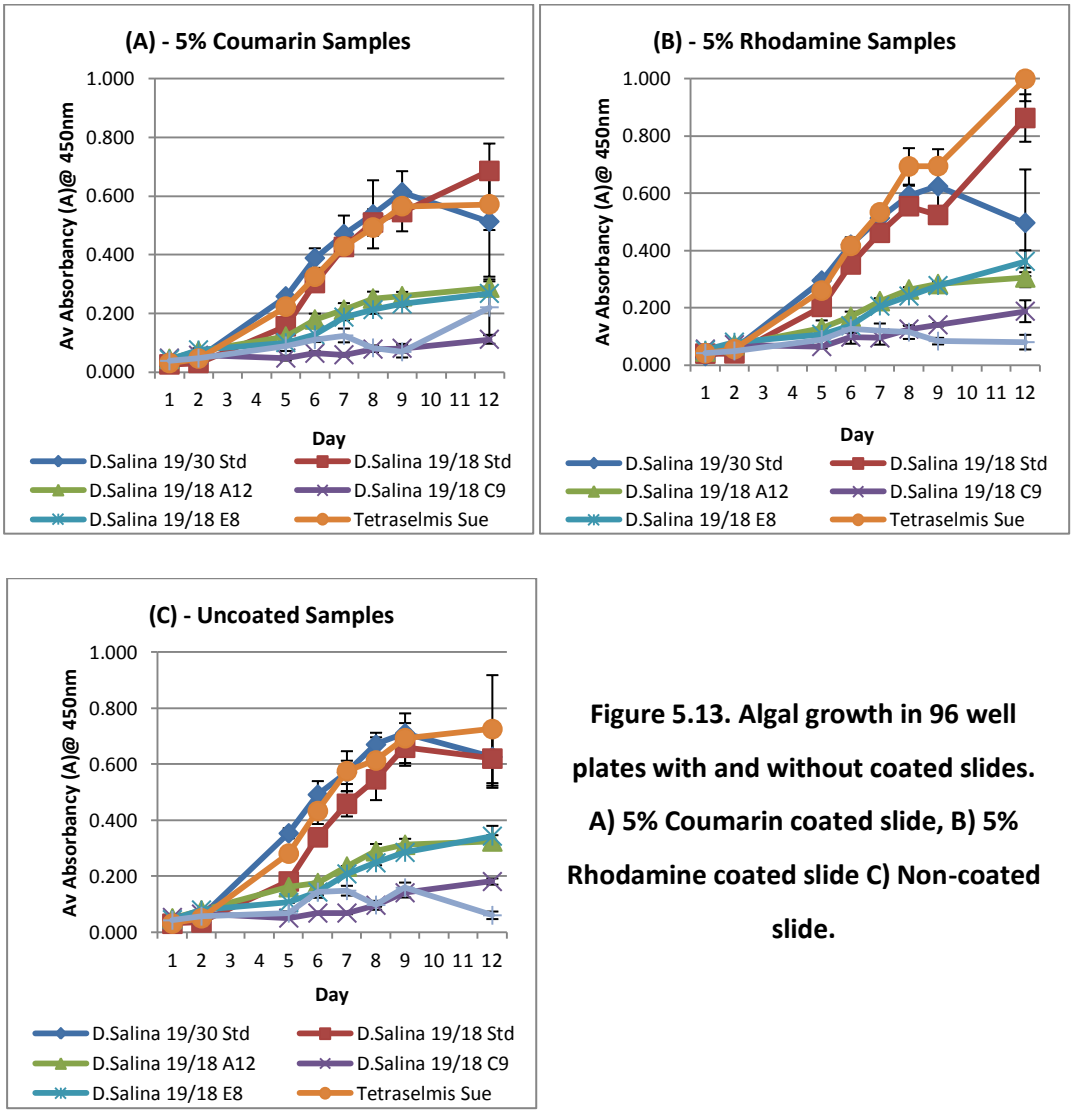

Figure 5.13. Algal growth in 96 well plates with and without coated slides. A) 5% Coumarin coated slide, B) 5% Rhodamine coated slide C) Non-coated slide.

The results from the first experiment (Figure 5.13) showed that *D. salina* 19/30, *Tetraselmis suecica* and *D. salina* 19/18 all grew more favourably in the microplate format than the other strains. The differences between conditions were marginal, the Rhodamine dye exposed cultures appeared to have a slight growth boost (Figure 5.13 B) and the Coumarin dye exposed cultures seemed to have a slight drop in growth compared to the untreated standards (Figure 5.13 A). This could possibly be explained because the standard transilluminator light source produces no light below 400 nm and a notable peak around 540 nm. This meant that the Coumarin had no light in its absorbance band and that the input light for the Rhodamine was optimal. There were also issues with evaporative losses, which could have skewed the data sets in the last two readings.

5.5.2 Modified trans-illuminator, black plate with Coumarin dye only

A second series of tests was performed in the micro-plate format with coated slides. The experiment was conducted using modified transilluminator (section 2.10.6) due to its better distribution of light frequencies and temperature regulation. The regular 96-well plates were also swapped for a Greiner Bio-one Sensoplate (655892), with black walls and a flat glass bottom, to mitigate the need for painting and better simulate a photo-bioreactor setup. The two coated slides were both Coumarin this time (5% and 10%, Comp ID 5-6, section 2.10.4), the same slides used previously in the successful spectral tests, along with an uncoated slide as the standard again. Absorbance was measured at 595 nm with an integration of 1 second, using the Shaken OD @ 595 protocol (section 2.2.2.3) which included a shaking step to negate the need for a stirring step using disposable stirring loops. Eight species of green algae were tested, the same as in the previous run with the addition of *Dunaliella primolecta* (see layout below). The cultures were grown along the same axis of the UV bulb in the transilluminator as in the previous slide wavelength tests, to ensure the wavelengths for dye excitation were available. The plates were also sealed using Parafilm employing the method described in section 2.10.5.

Plate Layout:

Species rows	1	2	3	4	5	6	7	8	9	10	11	12	
D.Salina 19/30 1M NaCl Dun Med													A
D.Salina 19/18 "isolate" 1M NaCl Dun Med													B
D.S 19/18 A12 1M NaCl Dun Med													C
D.S 19/18 C9 1M NaCl Dun Med													D
D.S 19/18 E8 1M NaCl Dun Med													E
Tetraselmis Suecica 1M NaCl Dun Med													F
Nannochlropsis Occulata F/2 Media													G
D.Primolecta 1M NaCl Dun Med													H

5% Coumarin Dye	Empty	Standard	Media	Empty	10% Coumarin Dye

Results:

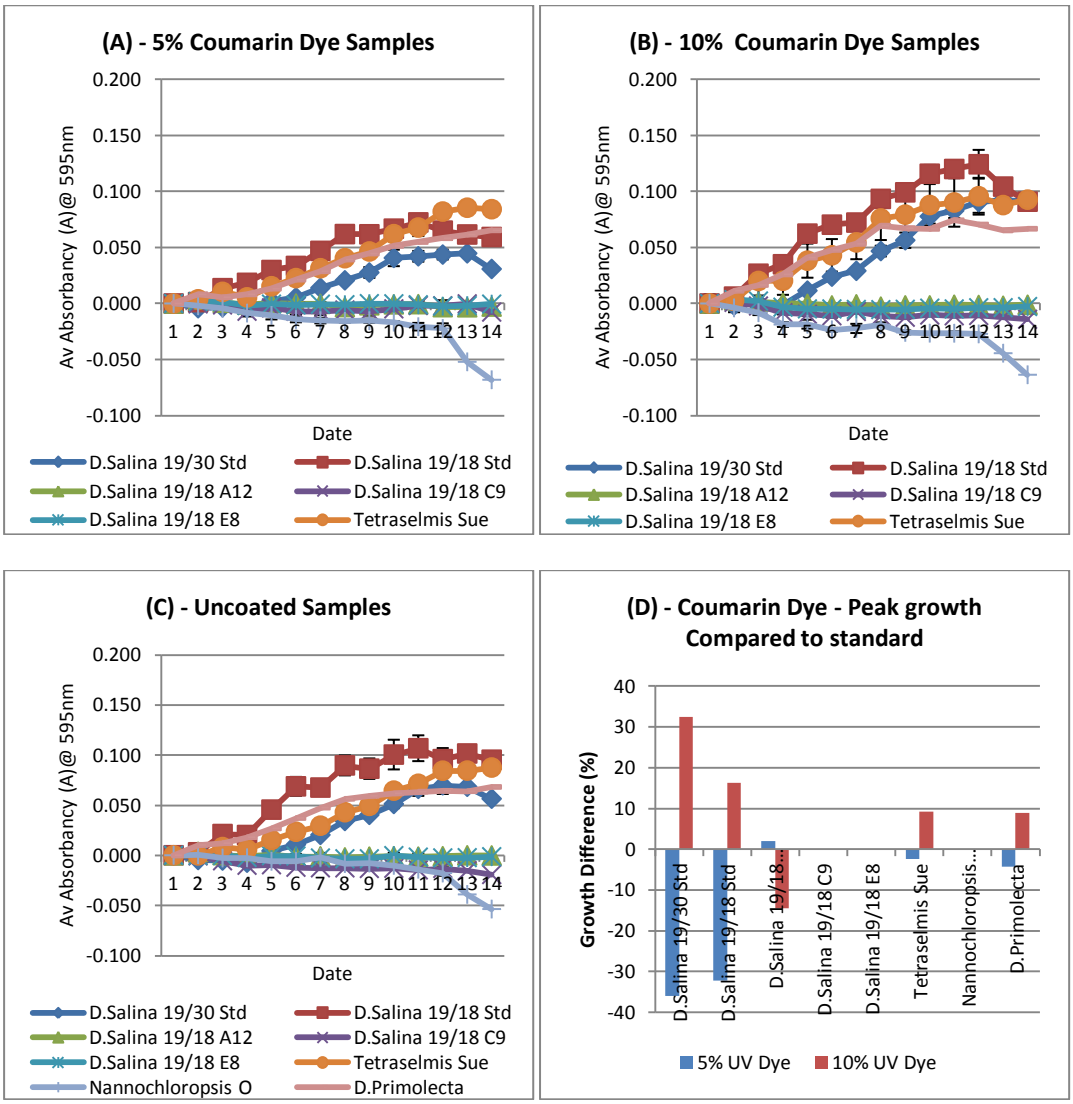

Figure 5.14. Growth of a range of green algae in the modified transilluminator in the presence of A) 5% Coumarin coating, B) 10% Coumarin coating or C) no coating. Growth difference comparisons are summarised in D).

The results from this test showed that not all of the strains were able to cope with the slightly broader spectrum and UV radiation produced by the transilluminator, fortunately the 'model' organism using in this study, *D. salina*, seemed to be the most resilient and produced good data. Interestingly, when compared to the standard condition, the 10% dye seemed to be producing the best growth rate, while the 5% showed the opposite effect. This trend was very

odd, as an increase or decline would be expected in the case of both dye concentrations compared to the standard, given the previous data and variables on offer.

5.5.3 Modified trans-illuminator, black plate with Coumarin dye only

To ensure that the previous experimental results were not a one off due to variations in atmospheric CO_2 availability (i.e. tightness of the Parafilm seal) and the strains used, a repeat was performed with breathable seals (Alpha laboratories) and the two best performing strains from the previous experiment.

Plate Layout:

Species rows	1	2	3	4	5	6	7	8	9	10	11	12	
D.Salina 19/30 1M NaCl Dun Med (1)													A
D.Salina 19/18 1M NaCl Dun Med "isolate" (1)													B
D.Salina 19/30 1M NaCl Dun Med (2)													C
D.Salina 19/18 1M NaCl Dun Med "isolate" (2)													D
D.Salina 19/30 1M NaCl Dun Med (3)													E
D.Salina 19/18 1M NaCl Dun Med "isolate" (3)													F
D.Salina 19/30 1M NaCl Dun Med (4)													G
D.Salina 19/18 1M NaCl Dun Med "isolate" (4)													H

5% Coumarin Dye	Empty	Standard	Media	Empty	10% Coumarin Dye

Results:

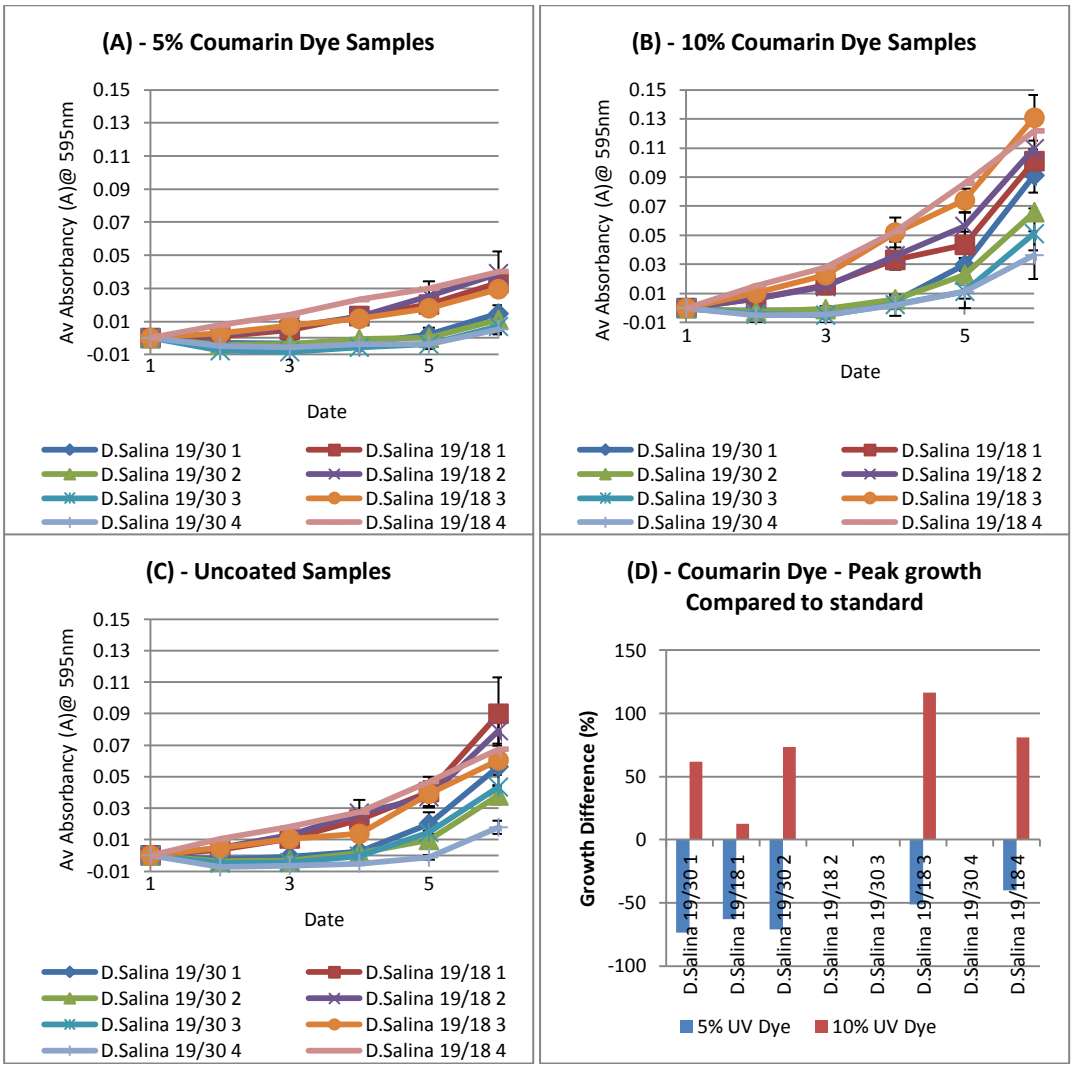

Figure 5.15.Growth of *D. salina* 19/30 and 19/18 in the modified transilluminator in the presence of A) 5% Coumarin coating, B) 10% Coumarin coating or C) no coating. Growth difference comparisons are summarised in D).

As with the previous run of the experiment (Figure 5.14), the results seemed to favour the higher concentration of Coumarin dye (Figure 5.15). However the experiment had to be finished prematurely due to large evaporation issues. A closer visual inspection of the sample wells showed that the algal cells were growing very differently depending on the wells location, with a net migration of cells due to phototaxis. The movement seemed to indicate that certain zones were more favourable (due to the flock orientation), so the differences in lighting could be skewing the growth data considerably (along with the evaporation).

5.5.4 Zone isolation

Further tests were performed to find out if the lighting hypothesis was correct with the assistance of Hosking (2013). This involved the segregation of each 96-well area on the transilluminator and performing wavelength sweeps in each zone. The trans-illuminator was then divided up into grouped zones which produced the best spectra to excite both the Rhodamine and Coumarin dyes, whilst giving the same lighting conditions to the standards. Also, during this process some more slides were produced using the spin coater rather than the bar spreader as before.

5.5.5 Modified trans-illuminator, black plate with both dyes

Following the zone isolation tests another repeat experiment was performed, but this time to avoid evaporation issues the Parafilm technique was reverted to. Also, to avoid any other issues, *D. salina* 19/30 was the sole strain used for the test. The two coatings selected for the test were 20% Coumarin and 10% Rhodamine (section 2.10.4, Comp ID 9-10), the slides were broken into 3 x 3 well segments, to ensure that they fitted into the compatible lighting zones on the transilluminator (see below).

Plate Layout:

<table>
<tr><th></th><th>1</th><th>2</th><th>3</th><th>4</th><th>5</th><th>6</th><th>7</th><th>8</th><th>9</th><th>10</th><th>11</th><th>12</th></tr>
<tr><td>A</td><td></td><td></td><td></td><td></td><td></td><td></td><td></td><td></td><td></td><td></td><td></td><td></td></tr>
<tr><td>B</td><td></td><td></td><td></td><td></td><td></td><td></td><td></td><td></td><td></td><td></td><td></td><td></td></tr>
<tr><td>C</td><td colspan="3" rowspan="3">Matched Standard Zonefor Coumarin Comparison</td><td></td><td colspan="3" rowspan="3">20% Coumarin Zone</td><td rowspan="3">Media</td><td>Empty</td><td></td><td></td><td></td></tr>
<tr><td>D</td><td></td><td></td><td></td><td></td><td></td><td></td></tr>
<tr><td>E</td><td></td><td></td><td></td><td></td><td></td><td></td></tr>
<tr><td>F</td><td></td><td></td><td></td><td></td><td colspan="3" rowspan="3">10% Rhodamine Zone</td><td></td><td colspan="3" rowspan="3">Matched Standard Zone for Rhodamine Comparison</td></tr>
<tr><td>G</td><td></td><td></td><td></td><td></td><td></td><td></td></tr>
<tr><td>H</td><td></td><td></td><td></td><td></td><td></td><td></td></tr>
</table>

Results:

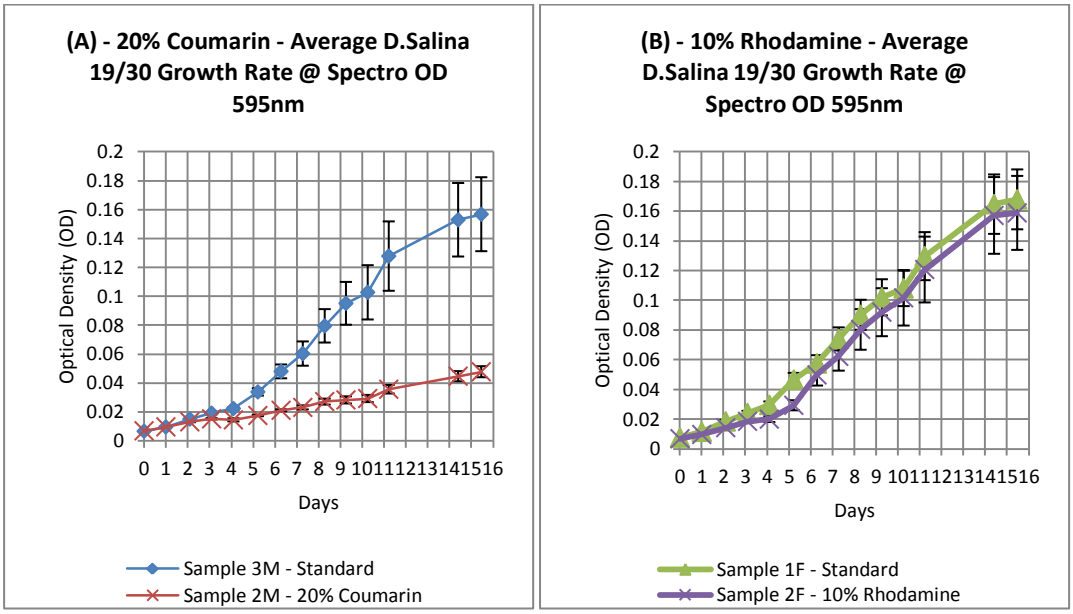

Figure 5.16. Effect of 20% Coumarin (A) and 10% Rhodamine (B) on growth of *D. salina* 19/30 using the matched lighting zones for each dye.

The results from the test are curious (Figure 5.16), the 10% Rhodamine cultures produced very little or no effect at all, which was to be expected based on previous measurements, but the 20% Coumarin showed a significant reduction compared with the standard. There are a few hypotheses that could possibly explain this result, with the obvious explanations being evaporation, temperature, contamination and lighting differences. However, based on the previous work they are very unlikely. It is more probable that the dye is absorbing some of the useful light and the wave guiding phenomenon is stopping the remitted light reaching the algal cultures, retarding the growth rate.

5.6 Conclusions

The experiments performed on the coatings developed during this work have provided some tantalising glimpses of the objective shift in spectrasought at the beginning of the project, but thus far any clear algal growth data to back up the hypothesis has proven elusive. Issues with flow control and reactor geometry severely hampered the first batch of experiments, as did evaporation and lighting non-uniformity in the second. However, the data gathered has shown the dyes to be having an effect, particularly with the Coumarin coatings which theoretically have the largest overall potential. Based on the data and experience gathered, the following recommendations are made for future work:

- Further tests to try and quantify the amount of light loss that is occurring due to effects like internal reflection (Mohsenpour, Richards and Willoughby, 2012).
- Using the spin coating system to apply a coating to the Mk II/III photo-bioreactors to eliminate the mixing issues experienced by the previous designs.
- Develop an LED based lighting system for further tests, which can provide illumination with much greater uniformity and control, such as the systems by Lee, et al. (2013) and Mertiri, et al. (2011).
- Increasing the thickness of the dye layer, by spraying several layers with the spin coater.
- Add glass micro-beads or nano-particles to help reduce issues with internal reflection. The system by Giannelli and Torzillo (2012) has shown benefits to this approach, with better light penetration into algal cultures.
- Perform further proof of concept experiments using the 96-well microplate setup only when a significant shift is observed with light intensity within each well, rather than per slide on the light source.

6 Discussion and Further Work

6.1 Discussion

In this research project, the effects of fluidic oscillation on the growth and lipid productivity of the alga *Dunaliella salina* were studied. This work was coupled with CFD and salinity based modelling to look at the impact of shear damage and mass transfer on growth behaviour. In addition, development studies were also performed looking into an innovative new 'smart skin' photo-bioreactor coating technique on the growth of various algal strains.

The work encompassed many novel aspects of photo-bioreactor design and algal culture, including; a comparison of algal growth responses to laminar and oscillated air using an identical set-up, the development of a algal media model suitable for use in computational modelling over a range of temperatures, the design, manufacture and testing of a new fully autoclavable miniature airlift photo-bioreactor system, a CFD model looking into the optimisation of photo-bioreactor flows based on bubble size, new insight into the cell damage limitation effects of fluidic oscillation, further development of the Nile Red lipid testing method, data on salt stress induced lipid accumulation in two species of *D. salina*(CCAP 19/18 and CCAP 19/30) and a proof of concept using a new photo-bioreactor coating system.

Experiments performed using a custom built 3 L flat plate photo-bioreactor into the mass transfer effects of fluidic oscillation provided interesting data. Based on an extensive review of associated literature, slow motion camera observation and aeration experiments to measure k_La, it was shown that fluidic oscillation, when compared to regular flow, provided a net increase in the transfer of oxygen (41%) in distilled water using the same volumetric flow rates. However, with the addition of 1 M NaCl ionic content, the mass transfer rate was increased in both cases (56% regular and 72% oscillated) relative to the original plain distilled water benchmark, thus the difference between the two types of flow was radically reduced (16%). Visual observation indicated that the majority of bubble sizes were almost indistinguishable and the only differences were due to bubble formation in the sparger zone. This observation correlated well with data in the literature, which indicated that bubble coalescence (one of the main drivers in bubble size increase) in all regions of the reactor would be impeded beyond a certain salinity threshold. Thus the addition of salt reduced the average bubble size in both flow conditions. Based on this, the small net difference in mass transfer between the two cases was hypothesised to be due to the beneficial bubble formation effects due to oscillation. i.e. when the bubbles are produced they are not as heavily restricted by the Young-Laplace law of surface tension, which means that a more even distribution of pores are in use and the bubble sizes are more likely to be on the same scale as the pores.

The CFD studies into the Mk I & II mini photo-bioreactor designs coupled with dye tracing observations, were of great significance in the development of the prototypes and explaining overall growth behaviour in each device. The models provided an explanation for the poor mixing performance of the MK I design discovered in the photo-bioreactor coating work and allowed various changes to the geometry to be tested, which culminated with the development of the Mk II prototype design. The fluid flows of the second design provided an interesting insight in that the sizes of bubbles and gas influx rates have a large impact on the effectiveness of the airlift loop effect. This finding suggests the possibility that new and existing photo-bioreactor designs could be analysed and 'tuned' to maintain the same levels of mass transfer and mixing at a lower operating cost, based around the average bubble size produced by the sparger system and the draft tube geometry. Also, inversely it highlights the possibility that if the frequency of oscillation can be used to dictate the bubble size by controlling of the growth period, the bubble size can also be optimised to induce the most efficient flows for the photo-bioreactor applications. The data from the CFD also provided corroborating evidence for the growth experiments carried out using the same range of flow rates. The average bubble size in the experiments (~0.5 mm based on previous experiments) had the best productivities at 5 and 10 cc/min flow rates, which correlated with optimal ranges of airlift circulation in the CFD simulations. The CFD flow results were also used to predict the impact of shear stress in relation to bubble size using the Kolmogorov eddy scale calculation, but this was shown to not be a factor. Another experiment was also performed to look at the effects of shear damage at the sparger surface based on the superficial gas velocity. The data from this indicated that fluidic oscillation could have an unexpected benefit, due to the increased usage of pores (due to the different bubble growth mechanism) the gas velocity was more evenly distributed across the sparger surface, which reduced the amount of localised damaging turbulence. However, in either case due to the potential destructive effects of a smaller bubble sizes at the fluid surface (i.e. a higher inherent energy dissipation rate (EDR)), the net benefits could not be inferred without an estimate of net cell death under each damage scenario.

Experimental work looking at the effects of salinity on the production of algal lipids was carried out to find the most productive medium for biofuel culture in the photo-bioreactors and to compare/develop different lipid assessment techniques to be used for subsequent fluidic oscillation studies. It was found that the 1 M NaCl based cultures were the most productive in terms of net biomass and lipid yield, while the lipid profile of the increased salinity cultures (2-3 M NaCl) were more amenable to biofuel production due to a reduction in PUFAs and an increase in mono-unsaturated FAMEs. It is thought this shift was caused due to changes in lipid

membrane metabolism, induced by the stress. However, based on the data generated by a model that was constructed to examine the gas solubility effects of various salts, it is thought to be highly possible that overall yield could be affected by CO_2 solubility limitation, which could have skewed the productivity data. Using microscopic observation and GC-MS indicators, it was also shown that bacterial contamination/co culture was higher in the decreased salinities studies, which may have also clouded the productivity data, as some lipids produced by this species were found to overlap with the algal variants.

Regarding the Nile Red (NR) lipid analysis work; despite extensive calibration and characterisation tests, it was found that the measurement method had many issues which severely restricted its application as an indicator for lipid accrual in the *D.salina* algal strains. The direct trans-esterification/GC-MS and NMR data sets in the majority of experiments showed an inverse correlation to the NR data, the only exceptions to these trends seemed to be when the photosynthetic pigments were very similar between conditions. Based on these findings, the reliability/consistency of the other methods and the excitation/emission wavelengths of the NR fluorophore, it was thought that the differences in lipid measurement were most probably due to Chlorophyll and β-carotene pigment interference (Chen, et al., 2009; Pick and Rachutin-Zalogin, 2012; Wu, et al., 2011) (see section 4.4.5). As the experimentation undertaken in this work produced high levels of cell breakage due to osmotic shock and shear stress, it is thought that the use of NR in these conditions is too inaccurate due to aforementioned factors affecting the variability of pigments in and out of the cells.

The data produced from the three litre flat plate photo-bioreactor experiments indicated that the air supply did not provide enough carbon dioxide for culture growth in either oscillated or regular flow conditions. However, it did show the oscillated culture has slightly better growth in every repeat, which ties in with the previous experimental work comparing mass transfer rates, bubble size and shear stress. CFD simulations and dye tracing imagery of the 3 L design also demonstrated excellent mixing and a strong air lift loop effect present, which indicates carbon dioxide availability as the primary source of growth limitation.

The mini photo-bioreactor growth experiments were very successful and provided an excellent proof of concept with a variety of different cultures grown successfully in the vessel design. As mentioned previously in the *D. salina* growth experiments, optimal flows correlated well with comparative CFD simulations. In addition to this it was observed that increases in non-optimal aeration seemed to correlate with increases in bacterial contamination, based on visual observation and GC-MS/NMR data. In the subsequent experiments comparing oscillated versus normal flows at the two optimal gas influx rates (5-10 cc/min), the subtle differences in

growth behaviour observed in the 3 L experiments were observed again. Although the general OD was higher in the oscillated cases, the loss of pigment and increased bacterial contamination indicated that the oscillated flow could be potentially more damaging and the OD could have been skewed by the bacterial presence. It was hypothesised that there could be a possible negative feedback scenario, where algal cells were been broken more under oscillatory flow, which released their compatible solute glycerol, which was in turn metabolised by the bacteria which have a slightly more abundant supply of O_2 due to the increased rate of mass transfer caused by fractionally smaller bubbles. Another factor that was assumed to be significant was carbon limitation, which could have made the cells less structurally stable, although *D. salina* is a very fragile algal strain to begin with due to its lack of a cell wall.

The work conducted into the development of a 'smart coating' for photo-bioreactors that shifted un-utilised wavelengths into the PAR range, provided some limited proof of concept data. However, due to experimental limitations and suspected wave guiding effects, the growth experiments were inconclusive. The coating with the highest potential was based on the Coumarin dye.

6.2 Further Work

Based on the conclusions drawn in this study, these recommendations for future work have been made:

- Firstly, it is recommended that further systematic studies should be performed into the effects of oscillation frequency on bubble size generation. This could be achieved by varying the oscillator control loop whilst maintaining the same flow rate, or the inverse.
- The monitoring of bubble generation at the sparger interface using slow motion camera footage, with and without the addition of salt would also provide a great insight into the oscillator effect as no work has been done in this area currently. A comparison of sparger materials and bubble formation under oscillation would also be of benefit.
- Experimentation in this project was limited in its effectiveness due to the difficulty in measuring bubble size easily. Based on this experience the successful implementation of the ABS system is of great importance for future analysis as optical methods are insufficient for the complex bubble plumes that are produced in photo-bioreactor systems.
- Thus far only one study has been performed that indicates the power saving possibilities of using fluidic oscillation, an additional recommendation is that further studies are

performed to find its impacts and precisely identify the method of energy saving, whether that be reduced friction of the Coanda effect.

- Comparison experiments between oscillation and standard flows in this study were only performed continuously using air, as the 45 L/min flow rates needed to operate the fluidic oscillator were too expensive to perform using 5% CO_2 from gas canisters. Future studies could be performed using a blending system of air and 100% CO_2, as proposed in this study (unfortunately not conducted due to time limitations). Or, alternatively a gas valve based pulsing system could be used to simulate the effects of Coanda based fluidic oscillation, so much lower flow rates could be used making CO_2 cylinders a viable option. However, extensive characterisation of the frequencies produced by the fluidic oscillator would need to be performed to ensure scale up would produce the same effects.
- The CFD results in this work are only corroborated using very basic dye tracing. Implementation of particle image velocimetry for validation would be of great use in further studies. The technique would also be of benefit in the 'tuning' of bubble sizes or flow rates to optimise reactor flows, proposed in this work. Controlling oscillator frequencies would have great synergy in this process.
- The impacts of fluidic oscillation on cell shear damage are also thought to be completely unstudied, so there is great potential for further work. If an organism's death rate can be quantified, such as using a correlation of *Dunaliella* cell death to the release of extracellular glycerol as suggested by Silva, Cortinas and Ertola (1987), the impacts of shear damage can be inferred.
- The salinity gas solubility prediction model used in this study has great potential for implementation into COMSOL's Chemical species/CFD module. When combined with appropriate reaction rate constants it could be used to predict mass transfer behaviour using k_La values over a range of temperatures in the program, which would be a significant benefit in photo-bioreactor design. A series of experiments could then be performed to compare the simulation to actual mass transfer readings. The updated pH to dissolved CO_2 relation developed in this work could also be of benefit in this endeavour.
- Numerous experiments in this work were hypothesised to be carbon limited due to insufficient CO_2 content in the aeration or in higher salinities, which reduced gas solubility. Future experiments, especially the conical flask based types, would benefit from the carbon source being supplied directly from bicarbonate within the medium.
- In many of the aerated experiments bacterial contamination became prevalent at higher volumetric flow rates. To rule out data skew in terms of cell count and lipid accrual, the use of axenic cultures (with bacterial vitamin supplements to compensate) would be useful in future experiments.

- Given the numerous issues with the Nile Red staining technique during this study, an alternative dye such as BODIPY 505/515 could be used. This stain has similar lipid staining properties to NR, but has the benefit of a different excitation and emission wavelengths which are further outside of the algal pigment interference range (Govender, et al., 2012).
- Due to the tiny genetic differences between the *Dunaliella* strains used in this work and the confusion in the classification system for this strain, further 18S rDNA identification tests would be beneficial using primers to generate full length 18S rDNA sequences.
- During the course of the mini photo-bioreactor experiments there have been minor issues with uniformity of lighting and temperature. A recommendation would be to make some sort of reactor holding system that can both regulate temperature and provide uniform LED based lighting (Jacobi, et al., 2012). Also, measurement of pH and DO was difficult in this work, the inclusion of an automated fibre-optic system for measurement would also be highly beneficial, see (Betts and Baganz, 2006). The construction and testing of Mk III mini-reactor prototype specified in chapter 3 (designed to avoid flocks forming and provide better mixing), would also be of significant use in future experiments.
- Regarding the 'smart skin' work in Chapter 5, numerous improvements could be made to enable future work, including: Performing further tests to quantify the amount of light lost due to effects like internal reflection. Using the spin coating system to apply a coating to the Mk II-III photo-bioreactors to eliminate the mixing issues experienced by the previous design. Develop an LED based lighting system for further tests, which can provide illumination with much greater uniformity, specificity and control, see (Lee, et al., 2013; Mertiri, et al., 2011). Increasing the thickness of the dye layer, by spraying several layers with the spin coater to ensure a significant wavelength shift. The addition of other elements to the coating to help reduce issues with reflection and wave-guiding.

References

AB, C. (2011). **COMSOL Multi-physics 4.2 Manual**.

Adam, F., et al. (2012) "Solvent-free" ultrasound-assisted extraction of lipids from fresh microalgae cells: A green, clean and scalable process. **Bioresource Technology**, 114Jun, pp.457-465.

Ahmad, A. L., et al. (2012) Crossflow microfiltration of microalgae biomass for biofuel production. **Desalination**, 302Sep 17, pp.65-70.

Aleklett, K., et al. (2010) The Peak of the Oil Age - Analyzing the world oil production Reference Scenario in World Energy Outlook 2008. **Energy Policy**, 38(3) Mar, pp.1398-1414.

Alhasan, R. H., et al. (1987) CORRELATIVE CHANGES OF GROWTH, PIGMENTATION AND LIPID-COMPOSITION OF DUNALIELLA-SALINA IN RESPONSE TO HALOSTRESS. **Journal of General Microbiology**, 133Sep, pp.2607-2616.

Alonso, M., et al. (2012) Molecular characterization of microalgae used in aquaculture with biotechnology potential. **Aquaculture International**, 20(5) Oct, pp.847-857.

Alonzo, F. and Mayzaud, P. (1999) Spectrofluorometric quantification of neutral and polar lipids in zooplankton using Nile red. **Marine Chemistry**, 67(3-4) Nov, pp.289-301.

Altenbach-Rehm, J., et al. (1999) Parallel bubble columns with fed-batch technique for microbial process development on a small scale. **Chemical Engineering & Technology**, 22(12) Dec, pp.1051-1058.

ANACC. (2010) **Algal growth phases including determination of the growth rate and population doubling time** [Internet]. Available from: <http://www.marine.csiro.au/microalgae/methods/> [Accessed].

Andseron, J. (1995) **Computational fluid dynamics - The basics with applications**.

Antoine, C. (1888). **Tensions des vapeurs; nouvelle relation entre les tensions et les temperatures**.

Araujo, G. S., et al. (2011) Bioprospecting for oil producing microalgal strains: Evaluation of oil and biomass production for ten microalgal strains. **Bioresource Technology**, 102(8) Apr, pp.5248-5250.

Arnon, D. I. (1949) COPPER ENZYMES IN ISOLATED CHLOROPLASTS - POLYPHENOLOXIDASE IN BETA-VULGARIS. **Plant Physiology**, 24(1), pp.1-15.

Atabani, A. E., et al. (2012) A comprehensive review on biodiesel as an alternative energy resource and its characteristics. **Renewable & Sustainable Energy Reviews**, 16(4) May, pp.2070-2093.

Azachi, M., et al. (2002) Salt induction of fatty acid elongase and membrane lipid modifications in the extreme halotolerant alga Dunaliella salina. **Plant Physiology**, 129(3) Jul.

Bader, M. (1980) A SYSTEMATIC-APPROACH TO STANDARD ADDITION METHODS IN INSTRUMENTAL ANALYSIS. **Journal of Chemical Education**, 57(10), pp.703-706.

Balasubramanian, S., et al. (2011) Oil extraction from Scenedesmus obliquus using a continuous microwave system - design, optimization, and quality characterization. **Bioresource Technology**, 102(3) Feb, pp.3396-3403.

Balat, M. and Balat, H. (2010) Progress in biodiesel processing. **Applied Energy**, 87(6) Jun, pp.1815-1835.

Banerjee, C., et al. (2012) Study of polyacrylamide grafted starch based algal flocculation towards applications in algal biomass harvesting. **International Journal of Biological Macromolecules**, 51(4) Nov, pp.456-461.

Barbosa, M. J., Hadiyanto and Wijffels, R. H. (2004) Overcoming shear stress of microalgae cultures in sparged photobioreactors. **Biotechnology and Bioengineering**, 85(1) Jan 5, pp.78-85.

Bardavid, R. E., Khristo, P. and Oren, A. (2008) Interrelationships between Dunaliella and halophilic prokaryotes in saltern crystallizer ponds. **Extremophiles**, 12(1) Jan, pp.5-14.

Barreiro, D. L., et al. (2013) Hydrothermal liquefaction (HTL) of microalgae for biofuel production: State of the art review and future prospects. **Biomass & Bioenergy**, 53Jun, pp.113-127.

Basha, S. A., Gopal, K. R. and Jebaraj, S. (2009) A review on biodiesel production, combustion, emissions and performance. **Renewable & Sustainable Energy Reviews**, 13(6-7) Aug-Sep, pp.1628-1634.

Basova, M. M. (2005) Fatty acid composition of lipids in microalgae. **International Journal on Algae**, 7(1) 05, pp.33-57.

Baten, R. and Stummeyer, K. (2013) How sustainable can desalination be? **Desalination and Water Treatment**, 51(1-3) Jan, pp.44-52.

Batten, D., et al. (2013) Using wastewater and high-rate algal ponds for nutrient removal and the production of bioenergy and biofuels. **Water Science and Technology**, 67(4), pp.915-924.

Beach, E. S., et al. (2012) Preferential technological and life cycle environmental performance of chitosan flocculation for harvesting of the green algae Neochloris oleoabundans. **Bioresource Technology**, 121Oct, pp.445-449.

Becker, E. W. (1994) **Microalgae: Biotechnology and Microbiology**. **Cambridge Univ. Press, Cambridge, NY, 178.**

Ben-Amotz, A., E.W. Polle, J. and Subba Rao, D. V. (2009) **The Alga Dunaliella - Biodiversity, Physiology, Genomics and Biotechnology**. Science Publishers.

Benamotz, A. and Avron, M. (1983) ON THE FACTORS WHICH DETERMINE MASSIVE BETA-CAROTENE ACCUMULATION IN THE HALOTOLERANT ALGA DUNALIELLA-BARDAWIL. **Plant Physiology**, 72(3), pp.593-597.

Bergmann, P., et al. (2013) Disposable Flat Panel Airlift Photobioreactors. **Chemie Ingenieur Technik**, 85(1-2) Feb, pp.202-205.

Bertozzini, E., et al. (2011) Application of the standard addition method for the absolute quantification of neutral lipids in microalgae using Nile red. **Journal of Microbiological Methods**, 87(1) Oct, pp.17-23.

Betts, J. I. and Baganz, F. (2006) Miniature bioreactors: current practices and future opportunities. **Microbial Cell Factories**, 5May 25.

Bilad, M. R., et al. (2012) Harvesting microalgal biomass using submerged microfiltration membranes. **Bioresource Technology**, 111May, pp.343-352.

Bilanovic, D., et al. (2009) Freshwater and marine microalgae sequestering of CO2 at different C and N concentrations - Response surface methodology analysis. **Energy Conversion and Management**, 50(2) Feb, pp.262-267.

Biller, P., Friedman, C. and Ross, A. B. (2013) Hydrothermal microwave processing of microalgae as a pre-treatment and extraction technique for bio-fuels and bio-products. **Bioresource Technology**, 136May, pp.188-195.

Biller, P. and Ross, A. B. (2011) Potential yields and properties of oil from the hydrothermal liquefaction of microalgae with different biochemical content. **Bioresource Technology**, 102(1) Jan, pp.215-225.

Bioethics, N. C. o. (2011). **Biofuels: Ethical issues**.

Bitog, J. P., et al. (2011) Application of computational fluid dynamics for modeling and designing photobioreactors for microalgae production: A review. **Computers and Electronics in Agriculture**, 76(2) May, pp.131-147.

Blaha, K., et al. (1987) NOMENCLATURE RULES OF ORGANIC-CHEMISTRY AND BIOCHEMISTRY - IUPAC-IUB NOMENCLATURE OF LIPIDS. **Chemicke Listy**, 81(7) 1987, pp.715-748.

Blankenship, R. E. and Chen, M. (2013) Spectral expansion and antenna reduction can enhance photosynthesis for energy production. **Current Opinion in Chemical Biology**, 17(3) Jun, pp.457-461.

Blatti, J. L., Michaud, J. and Burkart, M. D. (2013) Engineering fatty acid biosynthesis in microalgae for sustainable biodiesel. **Current Opinion in Chemical Biology**, 17(3) Jun, pp.496-505.

Bligh, E. G. and Dyer, W. J. (1959) A RAPID METHOD OF TOTAL LIPID EXTRACTION AND PURIFICATION. **Canadian Journal of Biochemistry and Physiology**, 37(8), pp.911-917.

Borowitzka, L. J. (1981) THE MICROFLORA - ADAPTATIONS TO LIFE IN EXTREMELY SALINE LAKES. **Hydrobiologia**, 81-2(JUN) 1981, pp.33-46.

Borowitzka, M. A. (1988) Fats, oils and hydrocarbons. In: **Micro-algal biotechnology.** Cambridge University Press, Cambridge, New York.

Borowitzka, M. A. (1992) ALGAL BIOTECHNOLOGY PRODUCTS AND PROCESSES - MATCHING SCIENCE AND ECONOMICS. **Journal of Applied Phycology**, 4(3) Sep, pp.267-279.

Borowitzka, M. A. (1999) Commercial production of microalgae: ponds, tanks, tubes and fermenters. **Journal of Biotechnology**, 70(1-3), pp.313-321.

Borowitzka, M. A. and Borowitzka, L. J. (1988) **Micro-algal biotechnology**. Cambridge, Cambridge University Press.

Borowitzka, M. A. and Moheimani, N. R. (2013) Sustainable biofuels from algae. **Mitigation and Adaptation Strategies for Global Change**, 18(1) Jan, pp.13-25.

Borowitzka, M. A. and Siva, C. J. (2007) The taxonomy of the genus Dunaliella (Chlorophyta, Dunaliellales) with emphasis on the marine and halophilic species. **Journal of Applied Phycology**, 19(5) Oct, pp.567-590.

Bosma, R., et al. (2008) Growth Inhibition of Monodus subterraneus by Free Fatty Acids. **Biotechnology and Bioengineering**, 101(5) Dec 1, pp.1108-1114.

Bosma, R., et al. (2003) Ultrasound, a new separation technique to harvest microalgae. **Journal of Applied Phycology**, 15(2-3) Mar-Jun, pp.143-153.

Botello-Alvarez, J. E., et al. (2011) Effect of Electrolytes in Aqueous Solution on Bubble Size in Gas-Liquid Bubble Columns. **Industrial & Engineering Chemistry Research**, 50(21) Nov 2, pp.12203-12207.

Brandt, A. R., Englander, J. and Bharadwaj, S. (2013) The energy efficiency of oil sands extraction: Energy return ratios from 1970 to 2010. **Energy**, 55Jun 15, pp.693-702.

Bredwell, M. D. and Worden, R. M. (1998) Mass-transfer properties of microbubbles. 1. Experimental studies. **Biotechnology Progress**, 14(1) Jan-Feb, pp.31-38.

Brown, A. D., et al. (1987) A SALT-SENSITIVE MUTANT OF DUNALIELLA-TERTIOLECTA - A ROLE OF CARBONIC-ANHYDRASE. **Archives of Microbiology**, 147(4) May, pp.309-314.

BSI (2009). **BS EN 14214:2008+A1:2009 -** Automotive fuels. Fatty acid methyl esters (FAME), for diesel engines. Requirments and test methods. British Standards Institution.

Bulnes-Abundis, D., et al. (2013) A simple eccentric stirred tank mini-bioreactor: Mixing characterization and mammalian cell culture experiments. **Biotechnology and Bioengineering**, 110(4) Apr, pp.1106-1118.

Burlew, J. (1953a) Algal culture from laboratory to pilot plant. **Algal culture from laboratory to pilot plant**,1953, pp.3-357.

Burlew, J. S. (1953b). **Algae Culture - From Laboratory to Pilot Plant**, Carnegie Institution of Washington.

Butler, A. (1998) Acquisition and utilization of transition metal ions by marine organisms. **Science**, 281(5374) Jul, pp.207-210.

Camarasa, E., et al. (1999) Influence of coalescence behaviour of the liquid and of gas sparging on hydrodynamics and bubble characteristics in a bubble column. **Chemical Engineering and Processing**, 38(4-6) Sep, pp.329-344.

Carvalho, A. P., Meireles, L. A. and Malcata, F. X. (2006) Microalgal reactors: A review of enclosed system designs and performances. **Biotechnology Progress**, 22(6) Dec 1, pp.1490-1506.

Carvalho, A. P., et al. (2011) Light requirements in microalgal photobioreactors: an overview of biophotonic aspects. **Applied Microbiology and Biotechnology**, 89(5) Mar, pp.1275-1288.

CCAP (2000) f/2 Medium.

CCAP. (2013a) **Strain information: Dunaliella salina 19/18** [Internet]. Available from: <http://www.ccap.ac.uk/strain_info.php?Strain_No=19/18> [Accessed].

CCAP. (2013b) **Strain information: Dunaliella salina 19/30** [Internet]. Available from: <http://www.ccap.ac.uk/strain_info.php?Strain_No=19/30> [Accessed].

CCAP. (2013c) **Strain information: Nannochloropsis oculata 849/1** [Internet]. Available from: <http://www.ccap.ac.uk/strain_info.php?Strain_No=849/1> [Accessed].

CCAP. (2013d) **Strain information: Tetraselmis suecica 66/4** [Internet]. Available from: <http://www.ccap.ac.uk/strain_info.php?Strain_No=66/4> [Accessed].

CCC (2010). **The Fourth Carbon Budget**.

CCC (2013). **Meeting Carbon Budgets – 2013 Progress Report to Parliament**.

Chalmers, J. J. and Bavarian, F. (1991) MICROSCOPIC VISUALIZATION OF INSECT CELL BUBBLE INTERACTIONS .2. THE BUBBLE FILM AND BUBBLE RUPTURE. **Biotechnology Progress**, 7(2) Mar-Apr, pp.151-158.

Chen, M., et al. (2011) Effect of nutrients on growth and lipid accumulation in the green algae Dunaliella tertiolecta. **Bioresource Technology**, 102(2) Jan, pp.1649-1655.

Chen, W., Sommerfeld, M. and Hu, Q. A. (2011) Microwave-assisted Nile red method for in vivo quantification of neutral lipids in microalgae. **Bioresource Technology**, 102(1) Jan, pp.135-141.

Chen, W., et al. (2009) A high throughput Nile red method for quantitative measurement of neutral lipids in microalgae. **Journal of Microbiological Methods**, 77(1) Apr, pp.41-47.

Chen, Y. M. and Vaidyanathan, S. (2012) A simple, reproducible and sensitive spectrophotometric method to estimate microalgal lipids. **Analytica Chimica Acta**, 724Apr, pp.67-72.

Cheng, Y.-S., Zheng, Y. and VanderGheynst, J. S. (2011) Rapid Quantitative Analysis of Lipids Using a Colorimetric Method in a Microplate Format. **Lipids**, 46(1) Jan, pp.95-103.

Cherry, R. S. and Hulle, C. T. (1992) CELL-DEATH IN THE THIN-FILMS OF BURSTING BUBBLES. **Biotechnology Progress**, 8(1) Jan-Feb, pp.11-18.

Chi, Z. Y., O'Fallon, J. V. and Chen, S. L. (2011) Bicarbonate produced from carbon capture for algae culture. **Trends in Biotechnology**, 29(11) Nov, pp.537-541.

Chisti, M. Y., Halard, B. and Mooyoung, M. (1988) LIQUID CIRCULATION IN AIRLIFT REACTORS. **Chemical Engineering Science**, 43(3), pp.451-457.

Chisti, Y. (1999) Shear sensitivity. In: **Encyclopedia of Bioprocess Technology, Fermentation, Biocatalysis and Bioseparation, Volumes 1 - 5, 5 Volume Set**.

Chisti, Y. (2007) Biodiesel from microalgae. **Biotechnology Advances**, 25(3) May-Jun, pp.294-306.

Chisti, Y. (2008a) Biodiesel from microalgae beats bioethanol. **Trends in Biotechnology**, 26(3) Mar, pp.126-131.

Chisti, Y. (2008b) Response to Reijnders: Do biofuels from microalgae beat biofuels from terrestrial plants? **Trends in Biotechnology**, 26(7) Jul, pp.351-352.

Chisti, Y. (2013) Constraints to commercialization of algal fuels. **Journal of Biotechnology**, 167(3) Sep, pp.201-214.

Chiu, S.-Y., et al. (2009a) The air-lift photobioreactors with flow patterning for high-density cultures of microalgae and carbon dioxide removal. **Engineering in Life Sciences**, 9(3) Jun, pp.254-260.

Chiu, S. Y., et al. (2009b) Lipid accumulation and CO2 utilization of Nannochloropsis oculata in response to CO2 aeration. **Bioresource Technology**, 100(2) Jan, pp.833-838.

Cobelas, M. A. and Lechado, J. Z. (1989) LIPIDS IN MICROALGAE - A REVIEW .1. BIOCHEMISTRY. **Grasas Y Aceites**, 40(2) Mar-Apr, pp.118-145.

Contreras, E. M. (2007) Carbon dioxide stripping in bubbled columns. **Industrial & Engineering Chemistry Research**, 46(19) Sep, pp.6332-6337.

Cooksey, K. E., et al. (1987) FLUOROMETRIC-DETERMINATION OF THE NEUTRAL LIPID-CONTENT OF MICROALGAL CELLS USING NILE RED. **Journal of Microbiological Methods**, 6(6) Sep, pp.333-345.

Crabtree, G. W., Dresselhaus, M. S. and Buchanan, M. V. (2004) The hydrogen economy. **Physics Today**, 57(12) Dec, pp.39-44.

Crabtree, J. R. and Bridgwat.J (1969) CHAIN BUBBLING IN VISCOUS LIQUIDS. **Chemical Engineering Science**, 24(12), pp.1755-&.

Craggs, R., Sutherland, D. and Campbell, H. (2012) Hectare-scale demonstration of high rate algal ponds for enhanced wastewater treatment and biofuel production. **Journal of Applied Phycology**, 24(3) Jun, pp.329-337.

Craggs, R. J., et al. (2011) Algal biofuels from wastewater treatment high rate algal ponds. **Water Science and Technology**, 63(4), pp.660-665.

Craig, V. S. J. (2004) Bubble coalescence and specific-ion effects. **Current Opinion in Colloid & Interface Science**, 9(1-2) Aug, pp.178-184.

Croft, M. T., Warren, M. J. and Smith, A. G. (2006a) Algae need their vitamins. **Eukaryotic Cell**, 5(8) Aug, pp.1175-1183.

Croft, M. T., Warren, M. J. and Smith, A. G. (2006b) Algae need their vitamins - suplementary dataset.

Crowe, C. T., Sommerfeld, M. and Tsuji, Y. (1998) **Multiphase flows with droplets and particles**. Boca Raton, Fla. ; London, CRC Press.

Danquah, M. K., et al. (2010) Cultivation Medium Design Via Elemental Balancing for Tetraselmis suecica. **Chemical and Biochemical Engineering Quarterly**, 24(3) Sep, pp.361-369.

Darmana, D., et al. (2007) Detailed modelling of hydrodynamics, mass transfer and chemical reactions in a bubble column using a discrete bubble model: Chemisorption of CO2 into NaOH solution, numerical and experimental study. **Chemical Engineering Science**, 62(9) May, pp.2556-2575.

Davidi, L., Katz, A. and Pick, U. (2012) Characterization of major lipid droplet proteins from Dunaliella. **Planta**, 236(1) Jul, pp.19-33.

Day, J. G. and Fenwick, C. (1993) CRYOPRESERVATION OF MEMBERS OF THE GENUS TETRASELMIS USED IN AQUACULTURE. **Aquaculture**, 118(1-2) Dec, pp.151-160.

de Almeida, P. and Silva, P. D. (2009) The peak of oil production-Timings and market recognition. **Energy Policy**, 37(4) Apr, pp.1267-1276.

Dean, A. P., et al. (2010) Using FTIR spectroscopy for rapid determination of lipid accumulation in response to nitrogen limitation in freshwater microalgae. **Bioresource Technology**, 101(12), pp.4499-4507.

DECC (2009). **Climate change act 2008 - Impact assessment**. change, D. o. e. a. c.

DECC (2011a). **The Carbon Plan: Delivering our low carbon future**.

DECC (2011b). **UK Renewable Energy Roadmap**. Change, D. o. E. a. C.

DECC (2012). **International aviation and shipping emissions and the UK's carbon budgets and 2050 target**.

Degen, J., et al. (2001) A novel airlift photobioreactor with baffles for improved light utilization through the flashing light effect. **Journal of Biotechnology**, 92(2) Dec 28, pp.89-94.

Demirbas, A. (2008) Relationships derived from physical properties of vegetable oil and biodiesel fuels. **Fuel**, 87(8-9) Jul, pp.1743-1748.

Derome, A. (1987) **Modern NMR Techniques for Chemistry Research**.

Dhotre, M. T. and Joshi, J. B. (2007) Design of a gas distributor: Three-dimensional CFD simulation of a coupled system consisting of a gas chamber and a bubble column. **Chemical Engineering Journal**, 125(3) Jan 15, pp.149-163.

Dijkstra, A. J. (2006) Revisiting the formation of trans isomers during partial hydrogenation of triacylglycerol oils. **European Journal of Lipid Science and Technology**, 108(3) Mar, pp.249-264.

Dixon, J. M., Taniguchi, M. and Lindsey, J. S. (2005) PhotochemCAD 2: A refined program with accompanying spectral atabases for photochemical calculations. **Photochemistry and Photobiology**, 81(1) Jan-Feb, pp.212-213.

Doig, S. D., Diep, A. and Baganz, F. (2005) Characterisation of a novel miniaturised bubble column bioreactor for high throughput cell cultivation. **Biochemical Engineering Journal**, 23(2) Apr, pp.97-105.

Doig, S. D., et al. (2005) Characterization of oxygen transfer in miniature and lab-scale bubble column bioreactors and comparison of microbial growth performance based on constant k(L)alpha. **Biotechnology Progress**, 21(4) Jul-Aug, pp.1175-1182.

Doran, P. M. (1995) **Bioprocess engineering principles**. London, Academic Press.

DoT (2012). **Renewable Transport Fuel Obligation statistics:obligation period5,2012/13,report 2**. Transport, D. o.

Dunn, S. (2002) Hydrogen futures: toward a sustainable energy system. **International Journal of Hydrogen Energy**, 27(3) Mar, pp.235-264.

Durrett, T. P., Benning, C. and Ohlrogge, J. (2008) Plant triacylglycerols as feedstocks for the production of biofuels. **Plant Journal**, 54(4) May, pp.593-607.

Edwards, T. J., et al. (1978) VAPOR-LIQUID-EQUILIBRIA IN MULTICOMPONENT AQUEOUS-SOLUTIONS OF VOLATILE WEAK ELECTROLYTES. **Aiche Journal**, 24(6) 1978, pp.966-976.

EIA (2013). **Short-Term Energy Outlook - Sept 2013**. Administration, E. I.

Eigen, M. (1954) METHODS FOR INVESTIGATION OF IONIC REACTIONS IN AQUEOUS SOLUTIONS WITH HALF-TIMES AS SHORT AS 10-9 SEC - APPLICATION TO NEUTRALIZATION AND HYDROLYSIS REACTIONS. **Discussions of the Faraday Society**,(17) 1954, pp.194-205.

Ekambara, K. and Joshi, J. B. (2005) Computational fluid dynamics simulations in bubble-column reactors: Laminar and transition regimes. **Industrial & Engineering Chemistry Research**, 44(5) Mar, pp.1413-1423.

Elsey, D., et al. (2007) Fluorescent measurement of microalgal neutral lipids. **Journal of Microbiological Methods**, 68(3) Mar, pp.639-642.

Eroglu, E. and Melis, A. (2009) "Density Equilibrium" Method for the Quantitative and Rapid In Situ Determination of Lipid, Hydrocarbon, or Biopolymer Content in Microorganisms. **Biotechnology and Bioengineering**, 102(5) Apr, pp.1406-1415.

Fabregas, J., et al. (2001) Growth rate of the microalga Tetraselmis suecica changes the biochemical composition of Artemia species. **Marine Biotechnology**, 3(3) May-Jun, pp.256-263.

Farhat, N., et al. (2011) OPTIMIZATION OF SALT CONCENTRATIONS FOR A HIGHER CAROTENOID PRODUCTION IN DUNALIELLA SALINA (CHLOROPHYCEAE). **Journal of Phycology**, 47(5) Oct, pp.1072-1077.

Farooq, W., et al. (2013) Efficient microalgae harvesting by organo-building blocks of nanoclays. **Green Chemistry**, 15(3) 2013, pp.749-755.

Fernandez, F. G. A., Sevilla, J. M. F. and Grima, E. M. (2013) Photobioreactors for the production of microalgae. **Reviews in Environmental Science and Bio-Technology**, 12(2) Jun, pp.131-151.

Figueroa, J. D., et al. (2008) Advancesn in CO(2) capture technology - The US Department of Energy's Carbon Sequestration Program. **International Journal of Greenhouse Gas Control**, 2(1) Jan, pp.9-20.

Fogg, G. E. (1965) **Algal cultures and phytoplankton ecology**. London, Athlone Press.

Folch, J., Lees, M. and Stanley, G. H. S. (1957) A SIMPLE METHOD FOR THE ISOLATION AND PURIFICATION OF TOTAL LIPIDES FROM ANIMAL TISSUES. **Journal of Biological Chemistry**, 226(1), pp.497-509.

Fowler, S. D., et al. (1987) USE OF NILE RED FOR THE RAPID INSITU QUANTITATION OF LIPIDS ON THIN-LAYER CHROMATOGRAMS. **Journal of Lipid Research**, 28(10) Oct.

Fowler, S. D. and Greenspan, P. (1985) APPLICATION OF NILE RED, A FLUORESCENT HYDROPHOBIC PROBE, FOR THE DETECTION OF NEUTRAL LIPID DEPOSITS IN TISSUE-SECTIONS - COMPARISON WITH OIL RED O. **Journal of Histochemistry & Cytochemistry**, 33(8) 1985.

Fujii, S. and Hellebust, J. A. (1992) RELEASE OF INTRACELLULAR GLYCEROL AND PORE FORMATION IN DUNALIELLA-TERTIOLECTA EXPOSED TO HYPOTONIC STRESS. **Canadian Journal of Botany-Revue Canadienne De Botanique**, 70(7) Jul, pp.1313-1318.

Fujikawa, S., et al. (2003) The control of micro-air-bubble generation by a rotational porous plate. **International Journal of Multiphase Flow**, 29(8) Aug, pp.1221-1236.

Fukuda, H., Kondo, A. and Noda, H. (2001) Biodiesel fuel production by transesterification of oils. **Journal of Bioscience and Bioengineering**, 92(5) Nov, pp.405-416.

Galloway, J. N., et al. (2013) A chronology of human understanding of the nitrogen cycle. **Philosophical Transactions of the Royal Society B-Biological Sciences**, 368(1621) Jul 5.

Ganan-Calvo, A. M. and Gordillo, J. M. (2001) Perfectly monodisperse microbubbling by capillary flow focusing. **Physical Review Letters**, 87(27) Dec, p.4.

Gao, S., et al. (2010) Electro-coagulation-flotation process for algae removal. **Journal of Hazardous Materials**, 177(1-3) May 15, pp.336-343.

Garcia-Ochoa, F. and Gomez, E. (2009) Bioreactor scale-up and oxygen transfer rate in microbial processes: An overview. **Biotechnology Advances**, 27(2) Mar-Apr, pp.153-176.

Gardner, R., et al. (2011) Medium pH and nitrate concentration effects on accumulation of triacylglycerol in two members of the chlorophyta. **Journal of Applied Phycology**, 23(6) Dec, pp.1005-1016.

Gardner, R. D., et al. (2012) Use of sodium bicarbonate to stimulate triacylglycerol accumulation in the chlorophyte Scenedesmus sp. and the diatom Phaeodactylum tricornutum. **Journal of Applied Phycology**.

Gardner, W. S., et al. (1985) MICROMETHOD FOR LIPIDS IN AQUATIC INVERTEBRATES. **Limnology and Oceanography**, 30(5), pp.1099-1105.

Garg, S., et al. (2012) Flotation of marine microalgae: Effect of algal hydrophobicity. **Bioresource Technology**, 121Oct, pp.471-474.

Gebreslassie, B. H., Waymire, R. and You, F. Q. (2013) Sustainable Design and Synthesis of Algae-Based Biorefinery for Simultaneous Hydrocarbon Biofuel Production and Carbon Sequestration. **Aiche Journal**, 59(5) May, pp.1599-1621.

Giannelli, L. and Torzillo, G. (2012) Hydrogen production with the microalga Chlamydomonas reinhardtii grown in a compact tubular photobioreactor immersed in a scattering light nanoparticle suspension. **International Journal of Hydrogen Energy**, 37(22) Nov, pp.16951-16961.

Gill, N. K., et al. (2008) Design and characterisation of a miniature stirred bioreactor system for parallel microbial fermentations. **Biochemical Engineering Journal**, 39(1) Apr, pp.164-176.

Gimbun, J. (2009). **Assessment of the turbulence models for modelling of bubble column**. The Institution of Engineers, Malaysia.

Goh, C. S. and Lee, K. T. (2010) A visionary and conceptual macroalgae-based third-generation bioethanol (TGB) biorefinery in Sabah, Malaysia as an underlay for renewable and sustainable development. **Renewable & Sustainable Energy Reviews**, 14(2) Feb, pp.842-848.

Gomez, P. I. and Gonzalez, M. A. (2004) Genetic variation among seven strains of Dunaliella salina (Chlorophyta) with industrial potential, based on RAPD banding patterns and on nuclear ITS rDNA sequences. **Aquaculture**, 233(1-4) Apr, pp.149-162.

Gonzalez, L. E. and Bashan, Y. (2000) Increased growth of the microalga Chlorella vulgaris when coimmobilized and cocultured in alginate beads with the plant-growth-promoting bacterium Azospirillum brasilense. **Applied and Environmental Microbiology**, 66(4) Apr, pp.1527-1531.

Govender, T., et al. (2012) BODIPY staining, an alternative to the Nile Red fluorescence method for the evaluation of intracellular lipids in microalgae. **Bioresource Technology**, 114Jun, pp.507-511.

Greenspan, P. and Fowler, S. D. (1985) SPECTROFLUOROMETRIC STUDIES OF THE LIPID PROBE, NILE RED. **Journal of Lipid Research**, 26(7), pp.781-789.

Greenspan, P., Mayer, E. P. and Fowler, S. D. (1985) NILE RED - A SELECTIVE FLUORESCENT STAIN FOR INTRACELLULAR LIPID DROPLETS. **Journal of Cell Biology**, 100(3) 1985.

Greenwell, H. C., et al. (2010) Placing microalgae on the biofuels priority list: a review of the technological challenges. **Journal of the Royal Society Interface**, 7(46) May, pp.703-726.

Griffiths, M. J. and Harrison, S. T. L. (2009) Lipid productivity as a key characteristic for choosing algal species for biodiesel production. **Journal of Applied Phycology**, 21(5) Oct, pp.493-507.

Griffiths, M. J., van Hille, R. P. and Harrison, S. T. L. (2010) Selection of Direct Transesterification as the Preferred Method for Assay of Fatty Acid Content of Microalgae. **Lipids**, 45(11), pp.1053-1060.

Grobbelaar, J. U. (2000) Physiological and technological considerations for optimising mass algal cultures. **Journal of Applied Phycology**, 12(3-5) Oct, pp.201-206.

Grobbelaar, J. U., Nedbal, L. and Tichy, V. (1996) Influence of high frequency light/dark fluctuations on photosynthetic characteristics of microalgae photoacclimated to different light intensities and implications for mass algal cultivation. **Journal of Applied Phycology**, 8(4-5), pp.335-343.

Guillard, R. R. and Ryther, J. H. (1962) STUDIES OF MARINE PLANKTONIC DIATOMS .1. CYCLOTELLA NANA HUSTEDT, AND DETONULA CONFERVACEA (CLEVE) GRAN. **Canadian Journal of Microbiology**, 8(2), pp.229-&.

Guschina, I. A. and Harwood, J. L. (2006) Lipids and lipid metabolism in eukaryotic algae. **Progress in Lipid Research**, 45(2), pp.160-186.

Guzman, H. M., et al. (2011) Analysis of interspecific variation in relative fatty acid composition: use of flow cytometry to estimate unsaturation index and relative polyunsaturated fatty acid content in microalgae. **Journal of Applied Phycology**, 23(1) Feb, pp.7-15.

Guzman, H. M., et al. (2012) Quick estimation of intraspecific variation of fatty acid composition in Dunaliella salina using flow cytometry and Nile Red. **Journal of Applied Phycology**, 24(5) Oct, pp.1237-1243.

Guzman, H. R., et al. (2003) Bioeffects caused by changes in acoustic cavitation bubble density and cell concentration: A unified explanation based on cell-to-bubble ratio and blast radius. **Ultrasound in Medicine and Biology**, 29(8) Aug, pp.1211-1222.

Hadiyanto, H., et al. (2013) Hydrodynamic evaluations in high rate algae pond (HRAP) design. **Chemical Engineering Journal**, 217Feb, pp.231-239.

Halim, R., Danquah, M. K. and Webley, P. A. (2012) Extraction of oil from microalgae for biodiesel production: A review. **Biotechnology Advances**, 30(3) May-Jun, pp.709-732.

Halim, R., et al. (2012) Microalgal cell disruption for biofuel development. **Applied Energy**, 91(1) Mar, pp.116-121.

Handacorrigan, A., Emery, A. N. and Spier, R. E. (1989) EFFECT OF GAS-LIQUID INTERFACES ON THE GROWTH OF SUSPENDED MAMMALIAN-CELLS - MECHANISMS OF CELL-DAMAGE BY BUBBLES. **Enzyme and Microbial Technology**, 11(4) Apr, pp.230-235.

Hanotu, J., Bandulasena, H. C. H. and Zimmerman, W. B. (2012) Microflotation performance for algal separation. **Biotechnology and Bioengineering**, 109(7) Jul, pp.1663-1673.

Hard, B. C. and Gilmour, D. J. (1991) A MUTANT OF DUNALIELLA-PARVA CCAP 19/9 LEAKING LARGE AMOUNTS OF GLYCEROL INTO THE MEDIUM. **Journal of Applied Phycology**, 3(4), pp.367-372.

Hard, B. C. and Gilmour, D. J. (1996) The uptake of organic compounds by Dunaliella parva CCAP 19/9. **European Journal of Phycology**, 31(3) Aug, pp.217-224.

Hasegawa, H., Nagasaka, Y. and Kataoka, H. (2008) Electrical potential of microbubble generated by shear flow in pipe with slits. **Fluid Dynamics Research**, 40(7-8) Jul-Aug, pp.554-564.

Heaton, E. A., Dohleman, F. G. and Long, S. P. (2008) Meeting US biofuel goals with less land: the potential of Miscanthus. **Global Change Biology**, 14(9) Sep, pp.2000-2014.

Held, P. and Raymond, K. (2011). **Determination of Algal Cell Lipids Using Nile Red Using Microplates to Monitor Neutral Lipids in Chlorella Vulgaris**. **Application note - Biofuel Research**. BioTek Website, BioTek.

Henderson, R. K., Parsons, S. A. and Jefferson, B. (2010) The impact of differing cell and algogenic organic matter (AOM) characteristics on the coagulation and flotation of algae. **Water Research**, 44(12) Jun, pp.3617-3624.

Henry, C. L. and Craig, V. S. J. (2010) The Link between Ion Specific Bubble Coalescence and Hofmeister Effects Is the Partitioning of Ions within the Interface. **Langmuir**, 26(9) May 4, pp.6478-6483.

Henry, C. L., et al. (2008) A mobile gas-water interface in electrolyte solutions. **Journal of Physical Chemistry C**, 112(39) Oct 2, pp.15094-15097.

Hikita, H., Asai, S. and Takatsuka, T. (1976) Absorption of carbon dioxide into aqueous sodium hydroxide and sodium carbonate-bicarbonate solutions. **The Chemical Engineering Journal**, 11(2), pp.131 - 141.

Ho, S. H., et al. (2013) Engineering strategies for improving the CO2 fixation and carbohydrate productivity of Scenedesmus obliquus CNW-N used for bioethanol fermentation. **Bioresource Technology**, 143Sep, pp.163-171.

Hoek, C. v. d., Jahns, H. M. and Mann, D. G. (1995) **Algae : an introduction to phycology**. Cambridge, Cambridge University Press.

Honeycutt, M. E., McFarland, V. A. and McCant, D. D. (1995) COMPARISON OF 3 LIPID EXTRACTION METHODS FOR FISH. **Bulletin of Environmental Contamination and Toxicology**, 55(3) Sep, pp.469-472.

Horn, R. G., Del Castillo, L. A. and Ohnishi, S. (2011) Coalescence map for bubbles in surfactant-free aqueous electrolyte solutions. **Advances in Colloid and Interface Science**, 168(1-2) Oct 14, pp.85-92.

Hosking, D. B. (2013) **Converting Unused Solar Radiation to Radiation Usable in Photosynthesis in Algal Bio-Reactors**. University of Sheffield, Chemical and Biological Engineering.

Hosseini Tafreshi, A. and Shariati, M. (2009) Dunaliella biotechnology: methods and applications. **Journal of applied microbiology**, 107(1) 2009 Jul (Epub 2009 Feb, pp.14-35.

Hu, Q., Guterman, H. and Richmond, A. (1996) A flat inclined modular photobioreactor for outdoor mass cultivation of photoautotrophs. **Biotechnology and Bioengineering**, 51(1) Jul 5, pp.51-60.

Hu, Q., et al. (2008) Microalgal triacylglycerols as feedstocks for biofuel production: perspectives and advances. **Plant Journal**, 54(4), pp.621-639.

Hu, W. W., Berdugo, C. and Chalmers, J. J. (2011) The potential of hydrodynamic damage to animal cells of industrial relevance: current understanding. **Cytotechnology**, 63(5) Oct, pp.445-460.

Huang, G., et al. (2010) Biodiesel production by microalgal biotechnology. **Applied Energy**, 87(1) Jan, pp.38-46.

Huntley, M. and Redalje, D. (2007). **CO2 Mitigation and Renewable Oil from Photosynthetic Microbes: A New Appraisal**. Mitigation and Adaptation Strategies for Global Change. **12**: p.pp 573-608.

Ichihara, K. i. and Fukubayashi, Y. (2010) Preparation of fatty acid methyl esters for gas-liquid chromatography. **Journal of Lipid Research**, 51(3) Mar.

IEA (2013). **Key World Energy Statistics 2013**.

Inc, S. (2013). **Recombinant Microalgae Cells Producing Novel Oils**. office, U. P.

IPCC (2007). **Climate Change 2007: Synthesis Report**. **Contribution of Working Groups I, II and III to the Fourth Assessment Report of the Intergovernmental Panel on Climate Change**. Core Writing Team, P., R.K and Reisinger, A. (eds.). Geneva, Switzerland, IPCC.

IPCC (2011). **Renewable Energy Sources and Climate Change Mitigation**. **Special Report of the Intergovernmental Panel on Climate Change**.

IPCC (2013). **Working group I contribution to the IPCC fifth assessment report (AR5), climate change 2013: The physical science basis**. **Final Draft Underlying Scientific-Technical Assessment**.

Jacobi, A., et al. (2012) Advanced photobioreactor LED illumination system: Scale-down approach to study microalgal growth kinetics. **Engineering in Life Sciences**, 12(6) Nov, pp.621-630.

Jang, E. S., Jung, M. Y. and Min, D. B. (2005) Hydrogenation for low trans and high conjugated fatty acids. **Comprehensive Reviews in Food Science and Food Safety**, 4(1), pp.22-30.

Jha, A., et al. (2008) Studies on gas holdup in a bubble column using porous spargers with additives. **Asia-Pacific Journal of Chemical Engineering**, 3(4) Jul-Aug, pp.417-424.

Jiang, Y. L., Yoshida, T. and Quigg, A. (2012) Photosynthetic performance, lipid production and biomass composition in response to nitrogen limitation in marine microalgae. **Plant Physiology and Biochemistry**, 54May, pp.70-77.

Jin, G., et al. (2012) Enzyme-assisted extraction of lipids directly from the culture of the oleaginous yeast Rhodosporidium toruloides. **Bioresource Technology**, 111May, pp.378-382.

Jones, J., et al. (2012) Extraction of Algal Lipids and Their Analysis by HPLC and Mass Spectrometry. **Journal of the American Oil Chemists Society**, 89(8) Aug, pp.1371-1381.

Jung, K. A., et al. (2013) Potentials of macroalgae as feedstocks for biorefinery. **Bioresource Technology**, 135May, pp.182-190.

Jungwirth, P. and Tobias, D. J. (2006) Specific ion effects at the air/water interface. **Chemical Reviews**, 106(4) Apr, pp.1259-1281.

Kanda, H. and Li, P. (2011) Simple extraction method of green crude from natural blue-green microalgae by dimethyl ether. **Fuel**, 90(3) Mar, pp.1264-1266.

Karlsson, R. and Torstens.Lg (1974) COULOMETRIC DETERMINATION OF DISSOLVED-OXYGEN IN WATER. **Talanta**, 21(9), pp.957-959.

Kawase, Y. and Mooyoung, M. (1990) MATHEMATICAL-MODELS FOR DESIGN OF BIOREACTORS - APPLICATIONS OF KOLMOGOROV THEORY OF ISOTROPIC TURBULENCE. **Chemical Engineering Journal and the Biochemical Engineering Journal**, 43(1) Feb, pp.B19-B41.

Kazakis, N. A., Mouza, A. A. and Paras, S. V. (2008) Experimental study of bubble formation at metal porous spargers: Effect of liquid properties and sparger characteristics on the initial bubble size distribution. **Chemical Engineering Journal**, 137(2) Apr, pp.265-281.

Kazakis, N. A., Papadopoulos, I. D. and Mouza, A. A. (2007) Bubble columns with fine pore sparger operating in the pseudo-homogeneous regime: Gas hold up prediction and a criterion for the transition to the heterogeneous regime. **Chemical Engineering Science**, 62(12) Jun, pp.3092-3103.

Kazamia, E., Aldridge, D. C. and Smith, A. G. (2012) Synthetic ecology - A way forward for sustainable algal biofuel production? **Journal of Biotechnology**, 162(1) Nov, pp.163-169.

Keshtacherliebson, E., Hadar, Y. and Chen, Y. (1995) OLIGOTROPHIC BACTERIA ENHANCE ALGAL GROWTH UNDER IRON-DEFICIENT CONDITIONS. **Applied and Environmental Microbiology**, 61(6) Jun, pp.2439-2441.

Ketheesan, B. and Nirmalakhandan, N. (2011) Development of a new airlift-driven raceway reactor for algal cultivation. **Applied Energy**, 88(10) Oct, pp.3370-3376.

Khoo, H. H., et al. (2013) Bioenergy co-products derived from microalgae biomass via thermochemical conversion - Life cycle energy balances and CO2 emissions. **Bioresource Technology**, 143Sep, pp.298-307.

Khozin-Goldberg, I. and Cohen, Z. (2006) The effect of phosphate starvation on the lipid and fatty acid composition of the fresh water eustigmatophyte Monodus subterraneus. **Phytochemistry**, 67(7) Apr, pp.696-701.

Khozin-Goldberg, I. and Cohen, Z. (2011) Unraveling algal lipid metabolism: Recent advances in gene identification. **Biochimie**, 93(1) Jan, pp.91-100.

Kim, B. J., Diao, J. P. and Shuler, M. L. (2012) Mini-scale bioprocessing systems for highly parallel animal cell cultures. **Biotechnology Progress**, 28(3) May-Jun, pp.595-607.

Kim, D.-G., et al. (2011) Harvest of Scenedesmus sp with bioflocculant and reuse of culture medium for subsequent high-density cultures. **Bioresource Technology**, 102(3) Feb, pp.3163-3168.

Kim, J., et al. (2012) Continuous microalgae recovery using electrolysis with polarity exchange. **Bioresource Technology**, 111May, pp.268-275.

Kim, J., et al. (2013) Methods of downstream processing for the production of biodiesel from microalgae. **Biotechnology Advances**, 31(6) Nov 1, pp.862-876.

Kjarstad, J. and Johnsson, F. (2009) Resources and future supply of oil. **Energy Policy**, 37(2) Feb, pp.441-464.

Kleinegris, D. M. M., et al. (2010) The Selectivity of Milking of Dunaliella salina. **Marine Biotechnology**, 12(1) Feb, pp.14-23.

Knothe, G. (2005) Dependence of biodiesel fuel properties on the structure of fatty acid alkyl esters. **Fuel Processing Technology**, 86(10) Jun, pp.1059-1070.

Kosourov, S., et al. (2005) The effect of sulfur re-addition on H-2 photoproduction by sulfur-deprived green algae. **Photosynthesis Research**, 85(3) Sep, pp.295-305.

Krichnavaruk, S., Powtongsook, S. and Pavasant, P. (2007) Enhanced productivity of Chaetoceros calcitrans in airlift photobioreactors. **Bioresource Technology**, 98(11) Aug, pp.2123-2130.

Kumar, A., et al. (2010) Enhanced CO2 fixation and biofuel production via microalgae: recent developments and future directions. **Trends in Biotechnology**, 28(7) Jul, pp.371-380.

Kumar, K., Sirasale, A. and Das, D. (2013) Use of image analysis tool for the development of light distribution pattern inside the photobioreactor for the algal cultivation. **Bioresource technology**, 1432013 Sep (Epub 2013 Jun, pp.88-95.

Lam, M. K. and Lee, K. T. (2012) Immobilization as a feasible method to simplify the separation of microalgae from water for biodiesel production. **Chemical Engineering Journal**, 191May 15, pp.263-268.

Lam, S. M. and Shui, G. H. (2013) Lipidomics as a Principal Tool for Advancing Biomedical Research. **Journal of Genetics and Genomics**, 40(8) Aug, pp.375-390.

Lamb, H. H. (1966) **The changing climate : selected papers**. London, Methuen.

Lamping, S. R., et al. (2003) Design of a prototype miniature bioreactor for high throughput automated bioprocessing. **Chemical Engineering Science**, 58(3-6) Feb-Mar, pp.747-758.

Lang, X., et al. (2001) Preparation and characterization of bio-diesels from various bio-oils. **Bioresource Technology**, 80(1) Oct, pp.53-62.

Lapuerta, M., Armas, O. and Rodriguez-Fernandez, J. (2009) Effect of biodiesel fuels on diesel engine emissions (vol 34, pg 198, 2008). **Progress in Energy and Combustion Science**, 35(4) Aug, pp.383-383.

Laurens, L. M. L., et al. (2012) Accurate and reliable quantification of total microalgal fuel potential as fatty acid methyl esters by in situ transesterification. **Analytical and Bioanalytical Chemistry**, 403(1) Apr.

Laurens, L. M. L. and Wolfrum, E. J. (2011) Feasibility of Spectroscopic Characterization of Algal Lipids: Chemometric Correlation of NIR and FTIR Spectra with Exogenous Lipids in Algal Biomass. **Bioenergy Research**, 4(1) Mar, pp.22-35.

Lee, D.-J., et al. (2012) Coagulation-membrane filtration of Chlorella vulgaris. **Bioresource Technology**, 108Mar, pp.184-189.

Lee, J. M., et al. (2013) Switchable Gene Expression in Escherichia coli Using a Miniaturized Photobioreactor. **Plos One**, 8(1) Jan 17.

Leman, J. (1997) Oleaginous microorganisms: An assessment of the potential. **Advances in Applied Microbiology, Vol 43**, 43, pp.195-243.

Lemoine, Y. and Schoefs, B. (2010) Secondary ketocarotenoid astaxanthin biosynthesis in algae: a multifunctional response to stress. **Photosynthesis Research**, 106(1-2) Nov, pp.155-177.

Lepage, G. and Roy, C. C. (1986) DIRECT TRANSESTERIFICATION OF ALL CLASSES OF LIPIDS IN A ONE-STEP REACTION. **Journal of Lipid Research**, 27(1) Jan.

Lestari, S., et al. (2009) Transforming Triglycerides and Fatty Acids into Biofuels. **Chemsuschem**, 2(12), pp.1109-1119.

Levasseur, M., Thompson, P. A. and Harrison, P. J. (1993) PHYSIOLOGICAL ACCLIMATION OF MARINE-PHYTOPLANKTON TO DIFFERENT NITROGEN-SOURCES. **Journal of Phycology**, 29(5), pp.587-595.

Liang, Y. N. (2013) Producing liquid transportation fuels from heterotrophic microalgae. **Applied Energy**, 104Apr, pp.860-868.

Lim, D. K. Y., et al. (2012a) Isolation and Evaluation of Oil-Producing Microalgae from Subtropical Coastal and Brackish Waters. **Plos One**, 7(7) Jul 11.

Lim, J. K., et al. (2012b) Rapid Magnetophoretic Separation of Microalgae. **Small**, 8(11) Jun 11, pp.1683-1692.

Lin, L., et al. (2011) Opportunities and challenges for biodiesel fuel. **Applied Energy**, 88(4) Apr, pp.1020-1031.

Liu, B. S. and Benning, C. (2013) Lipid metabolism in microalgae distinguishes itself. **Current Opinion in Biotechnology**, 24(2) Apr, pp.300-309.

Liu, X. Y., Sheng, J. and Curtiss, R. (2011) Fatty acid production in genetically modified cyanobacteria. **Proceedings of the National Academy of Sciences of the United States of America**, 108(17) Apr, pp.6899-6904.

Liu, Y. S., Wu, H. Y. and Ho, K. P. (2006) Characterization of oxygen transfer conditions and their effects on Phaffia rhodozyma growth and carotenoid production in shake-flask cultures. **Biochemical Engineering Journal**, 27(3) Jan, pp.331-335.

Liu, Y. T. and Boone, D. R. (1991) EFFECTS OF SALINITY ON METHANOGENIC DECOMPOSITION. **Bioresource Technology**, 35(3), pp.271-273.

Lundquist, T. J., et al. (2010). **A Realistic Technology and Engineering Assessment of Algae Biofuel Production**, Energy Biosciences Inst: Berkeley, California.

Luo, L. J., et al. (2011) Hydrodynamics and mass transfer characteristics in an internal loop airlift reactor with different spargers. **Chemical Engineering Journal**, 175Nov, pp.494-504.

Lv, X. X., et al. (2010) Variations in lipid yields and compositions of marine microalgae during cell growth and respiration, and within intracellular structures. **Journal of Experimental Marine Biology and Ecology**, 391(1-2) Aug, pp.73-83.

Lynch, D. V. and Thompson, G. A. (1982) LOW TEMPERATURE-INDUCED ALTERATIONS IN THE CHLOROPLAST AND MICROSOMAL-MEMBRANES OF DUNALIELLA-SALINA. **Plant Physiology**, 69(6), pp.1369-1375.

MacKinney, G. (1941) Absorption of light by chlorophyll solutions. **Journal of Biological Chemistry**, 140(2) Aug, pp.315-322.

Madigan, M. T., et al. (2003) **Brock, biology of microorganisms**. Prentice Hall international editions.10th ed / ed. Upper Saddle River, N.J., Prentice Hall.

Mahmood, K. H., et al. (2011). **CO2 Mass Transfer Induced through an Airlift Loop by a Microbubble Cloud Generated by Fluidic Oscillation**. **American Chemical Society**, Ind. Eng. Chem. Res.

Markou, G., Angelidaki, I. and Georgakakis, D. (2013) Carbohydrate-enriched cyanobacterial biomass as feedstock for bio-methane production through anaerobic digestion. **Fuel**, 111Sep, pp.872-879.

Marrone, B. L., et al. **Concentrating biological particles from liquid suspension involves establishing uniform flow of liquid suspension extending along axis; applying acoustic field**

to the flow to concentrate particles; and separating them from suspension, Los Alamos Nat Security Llc.

Marshall, S. (2013) **Lipid Profiling of Three Substrains of Dunaliella Salina CCAP 19/18**. Molecular Biology and Biotechnology. University of Sheffield.

Mata, T. M., Martins, A. A. and Caetano, N. S. (2010) Microalgae for biodiesel production and other applications: A review. **Renewable & Sustainable Energy Reviews**, 14(1) Jan, pp.217-232.

Mathews, J. A. (2008) Carbon-negative biofuels. **Energy Policy**, 36(3) Mar, pp.940-945.

Mayzaud, P., Chanut, J. P. and Ackman, R. G. (1989) SEASONAL-CHANGES OF THE BIOCHEMICAL-COMPOSITION OF MARINE PARTICULATE MATTER WITH SPECIAL REFERENCE TO FATTY-ACIDS AND STEROLS. **Marine Ecology Progress Series**, 56(1-2) Aug 10, pp.189-204.

McCree, K. J. (1973) MEASUREMENT OF PHOTOSYNTHETICALLY ACTIVE RADIATION. **Solar Energy**, 15(1), pp.83-87.

McNichol, J., et al. (2012) Suitability of Soxhlet Extraction to Quantify Microalgal Fatty Acids as Determined by Comparison with In Situ Transesterification. **Lipids**, 47(2) Feb, pp.195-207.

Medina, A. R., et al. (1998) Downstream processing of algal polyunsaturated fatty acids. **Biotechnology Advances**, 16(3) May, pp.517-580.

Medley, G. (2009) **Microbubble generation for wastewater**. Chemical and Biological Engineering. University of Sheffield.

Melis, A. (2009) Solar energy conversion efficiencies in photosynthesis: Minimizing the chlorophyll antennae to maximize efficiency. **Plant Science**, 177(4) Oct, pp.272-280.

Mendoza Guzman, H., et al. (2010) Estimate by means of flow cytometry of variation in composition of fatty acids from Tetraselmis suecica in response to culture conditions. **Aquaculture International**, 18(2) Apr, pp.189-199.

Mendoza, H., et al. (1999) Oleic acid is the main fatty acid related with carotenogenesis in Dunaliella salina. **Journal of Applied Phycology**, 11(1), pp.15-19.

Merchuk, J. C., et al. (1990) ON THE 1ST-ORDER APPROXIMATION TO THE RESPONSE OF DISSOLVED-OXYGEN ELECTRODES FOR DYNAMIC KLA ESTIMATION. **Biotechnology and Bioengineering**, 35(11) May, pp.1161-1163.

Mertiri, T., et al. (2011) Optical Microplates for Photonic High Throughput Screening of Algal Photosynthesis and Biofuel Production. **2011 Annual International Conference of the Ieee Engineering in Medicine and Biology Society (Embc)**, pp.482-485.

Meseck, S. L., Alix, J. H. and Wikfors, G. H. (2005) Photoperiod and light intensity effects on growth and utilization of nutrients by the aquaculture feed microalga, Tetraselmis chui (PLY429). **Aquaculture**, 246(1-4) May, pp.393-404.

Metting, F. B. (1996) Biodiversity and application of microalgae. **Journal of Industrial Microbiology & Biotechnology**, 17(5-6) Nov-Dec, pp.477-489.

Meyer, M. and Griffiths, H. (2013) Origins and diversity of eukaryotic CO2-concentrating mechanisms: lessons for the future. **Journal of Experimental Botany**, 64(3) Jan, pp.769-786.

Millero, F. J., et al. (1980) A NEW HIGH-PRESSURE EQUATION OF STATE FOR SEAWATER. **Deep-Sea Research Part a-Oceanographic Research Papers**, 27(3-4) 1980, pp.255-264.

Miron, A. S., et al. (2002) Growth and biochemical characterization of microalgal biomass produced in bubble column and airlift photobioreactors: studies in fed-batch culture. **Enzyme and Microbial Technology**, 31(7) Dec 2, pp.1015-1023.

Miron, A. S., et al. (1999) Comparative evaluation of compact photobioreactors for large-scale monoculture of microalgae. **Journal of Biotechnology**, 70(1-3), pp.249-270.

Mishra, A., Mandoli, A. and Jha, B. (2008) Physiological characterization and stress-induced metabolic responses of Dunaliella salina isolated from salt pan. **Journal of Industrial Microbiology & Biotechnology**, 35(10) Oct, pp.1093-1101.

Mixson, S. M. and Burkholder, J. M. (2012) ENHANCING LIPID PRODUCTION IN THE MARINE MICROALGA DUNALIELLA THROUGH ENVIRONMENTAL STRESSORS. **Journal of Phycology**, 48Aug, pp.S43-S44.

Mohsenpour, S. F., Richards, B. and Willoughby, N. (2012) Spectral conversion of light for enhanced microalgae growth rates and photosynthetic pigment production. **Bioresource Technology**, 125Dec, pp.75-81.

Mohsenpour, S. F. and Willoughby, N. (2013) Luminescent photobioreactor design for improved algal growth and photosynthetic pigment production through spectral conversion of light. **Bioresource Technology**, 142Aug, pp.147-153.

Molina, E. M., et al. (2000) Scale-up of tubular photobioreactors. **Journal of Applied Phycology**, 12(3-5) Oct, pp.355-368.

Molina Grima, E., et al. (1999) Photobioreactors: Light regime, mass transfer, and scaleup. **Journal of Biotechnology**, 70(1-3) April 30, pp.231-247.

Montgomery, H. A. C., Thom, N. S. and Cockburn, A. (1964) DETERMINATION OF DISSOLVED OXYGEN BY WINKLER METHOD + SOLUBILITY OF OXYGEN IN PURE WATER + SEA WATER. **Journal of Applied Chemistry of the Ussr**, 14(7), pp.280-&.

Morweiser, M., et al. (2010) Developments and perspectives of photobioreactors for biofuel production. **Applied Microbiology and Biotechnology**, 87(4) Jul, pp.1291-1301.

Mouza, A. A., Dalakoglou, G. K. and Paras, S. V. (2005) Effect of liquid properties on the performance of bubble column reactors with fine pore spargers. **Chemical Engineering Science**, 60(5) Mar, pp.1465-1475.

Mus, F., et al. (2013) Physiological and molecular analysis of carbon source supplementation and pH stress-induced lipid accumulation in the marine diatom Phaeodactylum tricornutum. **Applied Microbiology and Biotechnology**, 97(8) Apr, pp.3625-3642.

Musvoto, E. V., et al. (2000) Integrated chemical-physical processes modelling - I. Development of a kinetic-based model for mixed weak acid/base systems. **Water Research**, 34(6) Apr, pp.1857-1867.

Mutanda, T., et al. (2011) Bioprospecting for hyper-lipid producing microalgal strains for sustainable biofuel production. **Bioresource Technology**, 102(1) Jan, pp.57-70.

Nagarajan, S., et al. (2013) An updated comprehensive techno-economic analysis of algae biodiesel. **Bioresource technology**, 1452013 Oct (Epub 2012 Dec, pp.150-6.

Naumann, T., et al. (2013) Growing microalgae as aquaculture feeds on twin-layers: a novel solid-state photobioreactor. **Journal of Applied Phycology**, 25(5) Oct, pp.1413-1420.

Nelson, D. and Cox, M. (2004). **Lehninger Principles of Biochemistry, Fourth Edition**, W. H. Freeman.

Nguyen, P. T., et al. (2012) The influence of gas velocity, salt type and concentration on transition concentration for bubble coalescence inhibition and gas holdup. **Chemical Engineering Research & Design**, 90(1A) Jan, pp.33-39.

Nunes, M. A. P., Fernandes, P. C. B. and Ribeiro, M. H. L. (2013) Microtiter plates versus stirred mini-bioreactors in biocatalysis: A scalable approach. **Bioresource Technology**, 136May, pp.30-40.

Ohlrogge, J. and Browse, J. (1995) LIPID BIOSYNTHESIS. **Plant Cell**, 7(7) Jul, pp.957-970.

Oki, T. and Kanae, S. (2006) Global hydrological cycles and world water resources. **Science**, 313(5790) Aug 25, pp.1068-1072.

Olmos, J., et al. (2009) DNA fingerprinting differentiation between beta-carotene hyperproducer strains of Dunaliella from around the world. **Saline systems**, 52009 Jun, pp.5-5.

Olmos, J., Paniagua, J. and Contreras, R. (2000) Molecular identification of Dunaliella sp utilizing the 18S rDNA gene. **Letters in Applied Microbiology**, 30(1) Jan, pp.80-84.

Oncel, S. and Sukan, F. V. (2008) Comparison of two different pneumatically mixed column photobioreactors for the cultivation of Artrospira platensis (Spirulina platensis). **Bioresource Technology**, 99(11) Jul, pp.4755-4760.

Oren, A. (2005) A hundred years of Dunaliella research: 1905-2005. **Saline systems**, 12005 Jul, pp.2-2.

Ortiz-Marquez, J. C. F., et al. (2013) Genetic engineering of multispecies microbial cell factories as an alternative for bioenergy production. **Trends in Biotechnology**, 31(9) Sep, pp.521-529.

Ozbek, H. (1977). **Viscosity of aqueous sodium chloride solutions from 0 - 150C**. **American Chemical Society 29th Southeast Regional Meeting, Tampa, FL, November 9-11, 1971**, Lawrence Berkeley National Laboratory.

Pal, D., et al. (2011) The effect of light, salinity, and nitrogen availability on lipid production by Nannochloropsis sp. **Applied Microbiology and Biotechnology**, 90(4) May, pp.1429-1441.

Park, S., Lee, Y. and Jin, E. (2013) Comparison of the responses of two Dunaliella strains, Dunaliella salina CCAP 19/18 and Dunaliella bardawil to light intensity with special emphasis on carotenogenesis. **Algae**, 28(2) Jun, pp.203-211.

Parkinson, L., et al. (2008) The terminal rise velocity of 10-100 mu m diameter bubbles in water. **Journal of Colloid and Interface Science**, 322(1) Jun, pp.168-172.

Parmar, R. and Majumder, S. K. (2013) Microbubble generation and microbubble-aided transport process intensification-A state-of-the-art report. **Chemical Engineering and Processing**, 64Feb, pp.79-97.

Parthasarathy, R. and Ahmed, N. (1996) Size distribution of bubbles generated by fine-pore spargers. **Journal of Chemical Engineering of Japan**, 29(6) Dec, pp.1030-1034.

Pate, R., Klise, G. and Wu, B. (2011) Resource demand implications for US algae biofuels production scale-up. **Applied Energy**, 88(10) Oct, pp.3377-3388.

Patil, P. D., et al. (2011) Optimization of direct conversion of wet algae to biodiesel under supercritical methanol conditions. **Bioresource Technology**, 102(1) Jan, pp.118-122.

Peeler, T. C., et al. (1989) LIPID CHARACTERIZATION OF AN ENRICHED PLASMA-MEMBRANE FRACTION OF DUNALIELLA-SALINA GROWN IN MEDIA OF VARYING SALINITY. **Plant Physiology**, 89(3) Mar, pp.970-976.

Perry, R. H., Green, D. W. and Maloney, J. O. (1997) **Perry's chemical engineers' handbook**. 7th ed. New York ; London, McGraw-Hill.

Petit, J. R., et al. (1999) Climate and atmospheric history of the past 420,000 years from the Vostok ice core, Antarctica. **Nature**, 399(6735) Jun, pp.429-436.

Pfleger, D., et al. (1999) Hydrodynamic simulations of laboratory scale bubble columns fundamental studies of the Eulerian-Eulerian modelling approach. **Chemical Engineering Science**, 54(21) Nov, pp.5091-5099.

Pfreundt, U., et al. (2012) Dinitrogen fixation in a unicellular chlorophyll d-containing cyanobacterium. **Isme Journal**, 6(7) Jul, pp.1367-1377.

Phycological Society Of, A. (1995) Meeting of the Phycological Society of America, Breckenridge, Colorado, USA, August 6-10, 1995. **Journal of Phycology**, 31(3 SUPPL.) 1995, pp.3-23.

Pick, U. and Rachutin-Zalogin, T. (2012) Kinetic anomalies in the interactions of Nile red with microalgae. **Journal of Microbiological Methods**, 88(2) Feb, pp.189-196.

Pokoo-Aikins, G., et al. (2010) Design and analysis of biodiesel production from algae grown through carbon sequestration. **Clean Technologies and Environmental Policy**, 12(3) Jun, pp.239-254.

Prabakaran, P. and Ravindran, A. D. (2011) A comparative study on effective cell disruption methods for lipid extraction from microalgae. **Letters in Applied Microbiology**, 53(2) Aug, pp.150-154.

Quicker, G., et al. (1981) COMPARISON OF MEASURED AND CALCULATED OXYGEN SOLUBILITIES IN FERMENTATION MEDIA. **Biotechnology and Bioengineering**, 23(3) 1981, pp.635-650.

Raja, R., Hemaiswarya, S. and Rengasamy, R. (2007) Exploitation of Dunaliella for beta-carotene production. **Applied Microbiology and Biotechnology**, 74(3) Mar, pp.517-523.

Ramirez-Duque, J.-L. and Ramos-Lucumi, M.-A. (2011) HYDRODYNAMIC COMPUTATIONAL EVALUATION IN SOLAR TUBULAR PHOTOBIOREACTORS BENDS WITH DIFFERENT CROSS SECTIONS. **Ct&F-Ciencia Tecnologia Y Futuro**, 4(4) Dec, pp.59-72.

Ramos, M. J., et al. (2009) Influence of fatty acid composition of raw materials on biodiesel properties. **Bioresource Technology**, 100(1) Jan, pp.261-268.

Ranjan, A., Patil, C. and Moholkar, V. S. (2010) Mechanistic Assessment of Microalgal Lipid Extraction. **Industrial & Engineering Chemistry Research**, 49(6) Mar 17, pp.2979-2985.

Rashid, N., Rehman, M. S. U. and Han, J. I. (2013) Recycling and reuse of spent microalgal biomass for sustainable biofuels. **Biochemical Engineering Journal**, 75Jun, pp.101-107.

Reba, I. (1966) APPLICATIONS OF COANDA EFFECT. **Scientific American**, 214(6), pp.84-&.

Reed, R. D. (1998) **Practical skills in biomolecular sciences**. Harlow, Prentice Hall.

RFA (2008). **The Gallagher Review of the indirect effects of biofuels production**. Agency, R. F.

Richmond, A. (2004) **Handbook of microalgal culture : biotechnology and applied phycology**. Oxford, Blackwell Science.

Riffat, R. and Krongthamchat, K. (2007) Anaerobic treatment of high-saline wastewater using halophilic methanogens in laboratory-scale anaerobic filters. **Water Environment Research**, 79(2) Feb, pp.191-198.

Rodolfi, L., et al. (2009) Microalgae for Oil: Strain Selection, Induction of Lipid Synthesis and Outdoor Mass Cultivation in a Low-Cost Photobioreactor. **Biotechnology and Bioengineering**, 102(1) Jan, pp.100-112.

Roessler, P. G. (1988) EFFECTS OF SILICON DEFICIENCY ON LIPID-COMPOSITION AND METABOLISM IN THE DIATOM CYCLOTELLA-CRYPTICA. **Journal of Phycology**, 24(3) Sep, pp.394-400.

Roleda, M. Y., et al. (2013) Effects of temperature and nutrient regimes on biomass and lipid production by six oleaginous microalgae in batch culture employing a two-phase cultivation strategy. **Bioresource technology**, 1292013 Feb (Epub 2012 Nov, pp.439-49.

Roncallo, O. P., et al. (2013) Comparison of Two Different Vertical Column Photobioreactors for the Cultivation of Nannochloropsis sp. **Journal of Energy Resources Technology-Transactions of the Asme**, 135(1) Mar, p.7.

Rubio, F. C., et al. (1999) Prediction of dissolved oxygen and carbon dioxide concentration profiles in tubular photobioreactors for microalgal culture. **Biotechnology and Bioengineering**, 62(1) Jan 5, pp.71-86.

Ruen-ngam, D., et al. (2008) Influence of salinity on bubble size distribution and gas-liquid mass transfer in airlift contactors. **Chemical Engineering Journal**, 141(1-3) Jul, pp.222-232.

Salim, S., Vermue, M. H. and Wijffels, R. H. (2012) Ratio between autoflocculating and target microalgae affects the energy-efficient harvesting by bio-flocculation. **Bioresource Technology**, 118, pp.49-55.

Sanchez-Garcia, D., et al. (2013) Effect of nitrate on lipid production by T-suecica, M-contortum, and C-minutissima. **Central European Journal of Biology**, 8(6) Jun, pp.578-590.

Sathish, A. and Sims, R. C. (2012) Biodiesel from mixed culture algae via a wet lipid extraction procedure. **Bioresource Technology**, 118, pp.643-647.

Savile, C. K. and Lalonde, J. J. (2011) Biotechnology for the acceleration of carbon dioxide capture and sequestration. **Current Opinion in Biotechnology**, 22(6) Dec, pp.818-823.

Schenk, P. M., et al. (2008) Second Generation Biofuels: High-Efficiency Microalgae for Biodiesel Production. **Bioenergy Research**, 1(1) Mar, pp.20-43.

Scholz, R. W., et al. (2013) Sustainable use of phosphorus: A finite resource. **Science of the Total Environment**, 461, pp.799-803.

Schumpe, A. (1993) THE ESTIMATION OF GAS SOLUBILITIES IN SALT-SOLUTIONS. **Chemical Engineering Science**, 48(1) Jan, pp.153-158.

Schumpe, A., Quicker, G. and Deckwer, W.-D. (1982). **Gas solubilities in microbial culture media**. Adv. Biochem, Eng., Springer Berlin Heidelberg: p.pp 1-38.

Sforza, E., et al. (2012) Adjusted Light and Dark Cycles Can Optimize Photosynthetic Efficiency in Algae Growing in Photobioreactors. **Plos One**, 7(6) Jun, p.10.

Shah, Y. T., et al. (1982) DESIGN PARAMETERS ESTIMATIONS FOR BUBBLE COLUMN REACTORS. **Aiche Journal**, 28(3), pp.353-379.

Sheehan, J., et al. (1998). **A Look Back at the U.S. Department of Energy's Aquatic Species Program: Biodiesel from Algae**. **Close-Out Report**, National Renewable Energy Laboratory.

Sheng, J., Vannela, R. and Rittmann, B. E. (2011) Evaluation of Cell-Disruption Effects of Pulsed-Electric-Field Treatment of Synechocystis PCC 6803. **Environmental Science & Technology**, 45(8) Apr 15, pp.3795-3802.

Sheng, J., Vannela, R. and Rittmann, B. E. (2012) Disruption of Synechocystis PCC 6803 for lipid extraction. **Water Science and Technology**, 65(3) 2012, pp.567-573.

Sialve, B., Bernet, N. and Bernard, O. (2009) Anaerobic digestion of microalgae as a necessary step to make microalgal biodiesel sustainable. **Biotechnology Advances**, 27(4) Jul-Aug, pp.409-416.

Silva, H. J., Cortinas, T. and Ertola, R. J. (1987) EFFECT OF HYDRODYNAMIC STRESS ON DUNALIELLA GROWTH. **Journal of Chemical Technology and Biotechnology**, 40(1) 1987, pp.41-49.

Singhal, A. K. and Spalding, D. B. (1981) PREDICTIONS OF TWO-DIMENSIONAL BOUNDARY-LAYERS WITH THE AID OF THE K-EPSILON-MODEL OF TURBULENCE. **Computer Methods in Applied Mechanics and Engineering**, 25(3), pp.365-383.

Skerratt, J. H., et al. (1991) THE PHOSPHOLIPID ESTER-LINKED FATTY-ACID COMPOSITION OF MEMBERS OF THE FAMILY HALOMONADACEAE AND GENUS FLAVOBACTERIUM - A CHEMOTAXONOMIC GUIDE. **Systematic and Applied Microbiology**, 14(1) Jan, pp.8-13.

Skoog, D. A., Holler, F. J. and Crouch, S. R. (2007) **Principles of instrumental analysis**. 6th ed. Belmont, C.A., Thomson/Brooks-Cole.

Smedes, F. and Askland, T. K. (1999) Revisiting the development of the Bligh and Dyer total lipid determination method. **Marine Pollution Bulletin**, 38(3) Mar.

Smith, J. L. (1908) On the simultaneous staining of neutral fat and fatty acid by oxazine dyes. **Journal of Pathology and Bacteriology**, 12.

Smith, J. L. (1911) The staining of fat by Nile-blue sulphate. **Journal of Pathology and Bacteriology**, 15.

Smith, P., et al. (2010) Competition for land. **Philosophical Transactions of the Royal Society B-Biological Sciences**, 365(1554) Sep, pp.2941-2957.

Soley, A., et al. (2012) Development of a simple disposable six minibioreactor system for suspension mammalian cell culture. **Process Biochemistry**, 47(4) Apr, pp.597-605.

Solovchenko, A. E. (2012) Physiological Role of Neutral Lipid Accumulation in Eukaryotic Microalgae under Stresses. **Russian Journal of Plant Physiology**, 59(2) Mar.

Spolaore, P., et al. (2006) Commercial applications of microalgae. **Journal of Bioscience and Bioengineering**, 101(2) Feb, pp.87-96.

Stephenson, P. G., et al. (2011) Improving photosynthesis for algal biofuels: toward a green revolution. **Trends in Biotechnology**, 29(12) Dec, pp.615-623.

Stern, N. (2007) **The economics of climate change : the Stern review**. Cambridge, Cambridge University Press.

Sukenik, A., Zmora, O. and Carmeli, Y. (1993) BIOCHEMICAL QUALITY OF MARINE UNICELLULAR ALGAE WITH SPECIAL EMPHASIS ON LIPID-COMPOSITION .2. NANNOCHLOROPSIS SP. **Aquaculture**, 117(3-4) Nov, pp.313-326.

Suzuki, T., et al. (1995) GAS-SPARGED BIOREACTORS FOR CO2 FIXATION BY DUNALIELLA-TERTIOLECTA. **Journal of Chemical Technology and Biotechnology**, 62(4) Apr, pp.351-358.

Takagi, M., Karseno and Yoshida, T. (2006) Effect of salt concentration on intracellular accumulation of lipids and triacylglyceride in marine microalgae Dunaliella cells. **Journal of Bioscience and Bioengineering**, 101(3) Mar, pp.223-226.

Tchobanoglous, G., et al. (2003) **Wastewater engineering : treatment and reuse**. The McGraw-Hill series in civil and environmental engineering.4th ed / ed. Boston ; London, McGraw-Hill.

Terry, K. L. and Raymond, L. P. (1985) SYSTEM-DESIGN FOR THE AUTOTROPHIC PRODUCTION OF MICROALGAE. **Enzyme and Microbial Technology**, 7(10), pp.474-487.

Thompson, G. A. (1996) Lipids and membrane function in green algae. **Biochimica Et Biophysica Acta-Lipids and Lipid Metabolism**, 1302(1) Jul, pp.17-45.

Thorpe, J. F. (1907) Reaction of certain colouring matters of the oxazine series. **Journal of the Chemical Society**, 911907.

Timmins, M., et al. (2009) Phylogenetic and molecular analysis of hydrogen-producing green algae. **Journal of Experimental Botany**, 60(6) Apr, pp.1691-1702.

Toh, P. Y., et al. (2012) Magnetophoretic removal of microalgae from fishpond water: Feasibility of high gradient and low gradient magnetic separation. **Chemical Engineering Journal**, 211Nov 15, pp.22-30.

Tonon, T., et al. (2002) Long chain polyunsaturated fatty acid production and partitioning to triacylglycerols in four microalgae. **Phytochemistry**, 61(1) Sep, pp.15-24.

Tredici, M. R. and Materassi, R. (1992) FROM OPEN PONDS TO VERTICAL ALVEOLAR PANELS - THE ITALIAN EXPERIENCE IN THE DEVELOPMENT OF REACTORS FOR THE MASS CULTIVATION OF PHOTOTROPHIC MICROORGANISMS. **Journal of Applied Phycology**, 4(3) Sep, pp.221-231.

Tredici, M. R. and Zittelli, G. C. (1998) Efficiency of sunlight utilization: Tubular versus flat photobioreactors. **Biotechnology and Bioengineering**, 57(2) Jan 20, pp.187-197.

Truesdale, G. A. and Downing, A. L. (1954) SOLUBILITY OF OXYGEN IN WATER. **Nature**, 173(4417), pp.1236-1236.

Tsonopoulos, C., Coulson, D. M. and Inman, L. B. (1976) IONIZATION-CONSTANTS OF WATER POLLUTANTS. **Journal of Chemical and Engineering Data**, 21(2) 1976, pp.190-193.

Ugwu, C. U., Ogbonna, J. C. and Tanaka, H. (2002) Improvement of mass transfer characteristics and productivities of inclined tubular photobioreactors by installation of internal static mixers. **Applied Microbiology and Biotechnology**, 58(5) Apr, pp.600-607.

UNFCCC (1998). **Kyoto protocol to the United Nations framework convention on climate change**.

UNFCCC (2009). **Report of the Conference of the Parties on its fifteenth session, held in Copenhagen from 7 to 19 December 2009.**

US-DOE (2013). **Bioenergy Technologies Office Multi-Year Program Plan**. DOE.

Vaara, M. (1992) AGENTS THAT INCREASE THE PERMEABILITY OF THE OUTER-MEMBRANE. **Microbiological Reviews**, 56(3) Sep, pp.395-411.

Van Vooren, G., et al. (2012) Investigation of fatty acids accumulation in Nannochloropsis oculata for biodiesel application. **Bioresource Technology**, 124Nov, pp.421-432.

Vandamme, D., et al. (2012) Flocculation of Chlorella vulgaris induced by high pH: Role of magnesium and calcium and practical implications. **Bioresource Technology**, 105Feb, pp.114-119.

Vanhandel, E. (1985) RAPID-DETERMINATION OF TOTAL LIPIDS IN MOSQUITOS. **Journal of the American Mosquito Control Association**, 1(3), pp.302-304.

Ventosa, A., Nieto, J. J. and Oren, A. (1998) Biology of moderately halophilic aerobic bacteria. **Microbiology and Molecular Biology Reviews**, 62(2) Jun, pp.504-+.

Versteeg, G. F. and Vanswaaij, W. P. M. (1988) SOLUBILITY AND DIFFUSIVITY OF ACID GASES (CO2, N2O) IN AQUEOUS ALKANOLAMINE SOLUTIONS. **Journal of Chemical and Engineering Data**, 33(1) Jan, pp.29-34.

Vial, C., et al. (2000) Study of hydrodynamic behaviour in bubble columns and external loop airlift reactors through analysis of pressure fluctuations. **Chemical Engineering Science**, 55(15) Aug, pp.2957-2973.

Vonshak, A., et al. (2001) Sub-optimal morning temperature induces photoinhibition in dense outdoor cultures of the alga Monodus subterraneus (Eustigmatophyta). **Plant Cell and Environment**, 24(10) Oct, pp.1113-1118.

Vreeland, R. H., Anderson, R. and Murray, R. G. E. (1984) CELL-WALL AND PHOSPHOLIPID-COMPOSITION AND THEIR CONTRIBUTION TO THE SALT TOLERANCE OF HALOMONAS-ELONGATA. **Journal of Bacteriology**, 160(3) 1984, pp.879-883.

Vreeland, R. H., et al. (1980) HALOMONAS-ELONGATA, A NEW GENUS AND SPECIES OF EXTREMELY SALT-TOLERANT BACTERIA. **International Journal of Systematic Bacteriology**, 30(2) 1980, pp.485-495.

Wang, B., Lan, C. Q. and Horsman, M. (2012) Closed photobioreactors for production of microalgal biomasses. **Biotechnology Advances**, 30(4) Jul-Aug, pp.904-912.

Wang, L. and You, X. (2013) Light-gradient Mixing Performance Improvement of the Flat Plate Photobioreactor with Waved Baffles. **Chemical and Biochemical Engineering Quarterly**, 27(2) Jun, pp.211-218.

Wang, L. K., et al. (2010) Gas Dissolution, Release, and Bubble Formation in Flotation Systems. In: Wang, L. K., Shammas, N. K., Selke, W. A.et al. (Eds.): **Flotation Technology**. Totowa, Humana Press Inc, pp.49-83

Watanabe, Y. and Hall, D. O. (1995) PHOTOSYNTHETIC CO2 FIXATION TECHNOLOGIES USING A HELICAL TUBULAR BIOREACTOR INCORPORATING THE FILAMENTOUS CYANOBACTERIUM SPIRULINA-PLATENSIS. **Energy Conversion and Management**, 36(6-9) Jun-Sep, pp.721-724.

Wegmann, K., Benamotz, A. and Avron, M. (1980) EFFECT OF TEMPERATURE ON GLYCEROL RETENTION IN THE HALOTOLERANT ALGAE DUNALIELLA AND ASTEROMONAS. **Plant Physiology**, 66(6) 1980, pp.1196-1197.

Weisenberger, S. and Schumpe, A. (1996) Estimation of gas solubilities in salt solutions at temperatures from 273 K to 363 K. **Aiche Journal**, 42(1) Jan, pp.298-300.

Weissman, J. C. and Goebel, R. P. (1987). **Design and Analysis of Microalgal Open Pond Systems for the Purpose of Producing Fuels - A Subcontract Report**. USDOE, Solar Energy Research Institute.

Weuster-Botz, D., Altenbach-Rehm, J. and Hawrylenko, A. (2001) Process-engineering characterization of small-scale bubble columns for microbial process development. **Bioprocess and Biosystems Engineering**, 24(1) Aug, pp.3-11.

Weyer, K. M., et al. (2010) Theoretical Maximum Algal Oil Production. **Bioenergy Research**, 3(2) Jun, pp.204-213.

Whipple, G. C. and Whipple, M. C. (1911) Solubility of oxygen in sea water. **Journal of the American Chemical Society**, 33Mar, pp.362-365.

Wijffels, R. H. and Barbosa, M. J. (2010) An Outlook on Microalgal Biofuels. **Science**, 329(5993) Aug 13, pp.796-799.

Williams, P. J. L. and Laurens, L. M. L. (2010) Microalgae as biodiesel & biomass feedstocks: Review & analysis of the biochemistry, energetics & economics. **Energy & Environmental Science**, 3(5), pp.554-590.

Wondraczek, L., et al. (2013) Solar spectral conversion for improving the photosynthetic activity in algae reactors. **Nature Communications**, 4Jun.

Wongluang, P., Chisti, Y. and Srinophakun, T. (2013) Optimal hydrodynamic design of tubular photobioreactors. **Journal of Chemical Technology and Biotechnology**, 88(1) Jan, pp.55-61.

Worden, R. M. and Bredwell, M. D. (1998) Mass-transfer properties of microbubbles. 2. Analysis using adynamic model. **Biotechnology Progress**, 14(1) Jan-Feb, pp.39-46.

Wu, H., et al. (2011) In vivo lipidomics using single-cell Raman spectroscopy. **Proceedings of the National Academy of Sciences of the United States of America**, 108(9) Mar 1, pp.3809-3814.

Xiao, M., Mathew, S. and Obbard, J. P. (2009) Biodiesel fuel production via transesterification of oils using lipase biocatalyst. **Global Change Biology Bioenergy**, 1(2) Apr, pp.115-125.

Xu, L., et al. (2012) Development of a draft-tube airlift bioreactor for Botryococcus braunii with an optimized inner structure using computational fluid dynamics. **Bioresource Technology**, 119Sep, pp.300-305.

Xu, L., et al. (2009) Microalgal bioreactors: Challenges and opportunities. **Engineering in Life Sciences**, 9(3) Jun, pp.178-189.

Xu, X. Q. and Beardall, J. (1997) Effect of salinity on fatty acid composition of a green microalga from an Antarctic hypersaline lake. **Phytochemistry**, 45(4) Jun, pp.655-658.

Xue, J., Grift, T. E. and Hansen, A. C. (2011) Effect of biodiesel on engine performances and emissions. **Renewable & Sustainable Energy Reviews**, 15(2) Feb, pp.1098-1116.

Yago, T., et al. (2012) Effects of flashing light from light emitting diodes (LEDs) on growth of the microalga Isochrysis galbana. **African Journal of Microbiology Research**, 6(30) Aug, pp.5896-5899.

Yang, J., et al. (2011) Life-cycle analysis on biodiesel production from microalgae: Water footprint and nutrients balance. **Bioresource Technology**, 102(1) Jan, pp.159-165.

Yasuno, M., et al. (2004) Monodispersed microbubble formation using microchannel technique. **Aiche Journal**, 50(12) Dec, pp.3227-3233.

Ye, Z. W., Jiang, J. G. and Wu, G. H. (2008) Biosynthesis and regulation of carotenoids in Dunaliella: Progresses and prospects. **Biotechnology Advances**, 26(4) Jul-Aug, pp.352-360.

Yeesang, C. and Cheirsilp, B. (2011) Effect of nitrogen, salt, and iron content in the growth medium and light intensity on lipid production by microalgae isolated from freshwater sources in Thailand. **Bioresource Technology**, 102(3), pp.3034-3040.

Yongmanitchai, W. and Ward, O. P. (1992) SEPARATION OF LIPID CLASSES FROM PHAEODACTYLUM-TRICORNUTUM USING SILICA CARTRIDGES. **Phytochemistry**, 31(10) Oct, pp.3405-3408.

Yoo, G., et al. (2012) Direct lipid extraction from wet Chlamydomonas reinhardtii biomass using osmotic shock. **Bioresource Technology**, 123Nov, pp.717-722.

Yu, G., et al. (2009) A novel method using CFD to optimize the inner structure parameters of flat photobioreactors. **Journal of Applied Phycology**, 21(6) Dec, pp.719-727.

Zahradnik, J., et al. (1997) Duality of the gas-liquid flow regimes in bubble column reactors. **Chemical Engineering Science**, 52(21-22) Nov, pp.3811-3826.

Zamboni, A., et al. (2011) Biofuels carbon footprints: Whole-systems optimisation for GHG emissions reduction. **Bioresource Technology**, 102(16) Aug, pp.7457-7465.

Zhang, G., Zhang, P. and Fan, M. (2009) Ultrasound-enhanced coagulation for Microcystis aeruginosa removal. **Ultrasonics Sonochemistry**, 16(3) Mar, pp.334-338.

Zhang, J. and Hu, B. (2012) A novel method to harvest microalgae via co-culture of filamentous fungi to form cell pellets. **Bioresource Technology**, 114Jun, pp.529-535.

Zhang, X., et al. (2010) Harvesting algal biomass for biofuels using ultrafiltration membranes. **Bioresource Technology**, 101(14) Jul, pp.5297-5304.

Zheng, H., et al. (2012) Harvesting of microalgae by flocculation with poly (gamma-glutamic acid). **Bioresource Technology**, 112May, pp.212-220.

Zheng, H., et al. (2011) Disruption of Chlorella vulgaris Cells for the Release of Biodiesel-Producing Lipids: A Comparison of Grinding, Ultrasonication, Bead Milling, Enzymatic Lysis, and Microwaves. **Applied Biochemistry and Biotechnology**, 164(7) Aug, pp.1215-1224.

Zhukova, N. V. and Aizdaicher, N. A. (1995) FATTY-ACID COMPOSITION OF 15 SPECIES OF MARINE MICROALGAE. **Phytochemistry**, 39(2) May, pp.351-356.

Zidan, H. M. and Abu-Elnader, M. (2005) Structural and optical properties of pure PMMA and metal chloride-doped PMMA films. **Physica B-Condensed Matter**, 355(1-4) Jan 31, pp.308-317.

Zimmerman, W. B., et al. (2010a) On the design and simulation of an airlift loop bioreactor with microbubble generation by fluidic oscillation. **International Sugar Journal**, 112(1334), pp.90-103.

Zimmerman, W. B., Tesar, V. and Bandulasena, H. C. H. (2011) Towards energy efficient nanobubble generation with fluidic oscillation. **Current Opinion in Colloid & Interface Science**, 16(4) Aug, pp.350-356.

Zimmerman, W. B., et al. (2007). **Microbubble Generation**. **Recent Patents on Engineering 2008**, Bentham Science Publishers: p.1-8.

Zimmerman, W. B., et al. (2010b). **Design of an airlift loop bioreactor and pilot scales studies with fluidic oscillator induced microbubbles for growth of a microalgae Dunaliella salina**.

Zimmerman, W. B., et al. (2011) Design of an airlift loop bioreactor and pilot scales studies with fluidic oscillator induced microbubbles for growth of a microalgae Dunaliella salina. **Applied Energy**, 88(10) Oct, pp.3357-3369.

Zimmerman, W. B. J. and Tesar, V. (2006). **Bubble generation for aeration and other purposes**. office, U. P. **GB 2443396 A**.

Zittelli, G. C., Pastorelli, R. and Tredici, M. R. (2000) A Modular Flat Panel Photobioreactor (MFPP) for indoor mass cultivation of Nannochloropsis sp under artificial illumination. **Journal of Applied Phycology**, 12(3-5), pp.521-526.

Zosel, J., et al. (2011) The measurement of dissolved and gaseous carbon dioxide concentration. **Measurement Science & Technology**, 22(7) Jul.

Zou, N. and Richmond, A. (1999) Effect of light-path length in outdoor flat plate reactors on output rate of cell mass and of EPA in Nannochloropsis sp. **Journal of Biotechnology**, 70(1-3) Apr 30, pp.351-356.

Appendix

A – Light source wavelengths

A-1 MBB Growth Room (H Floor) – Bottom Shelf

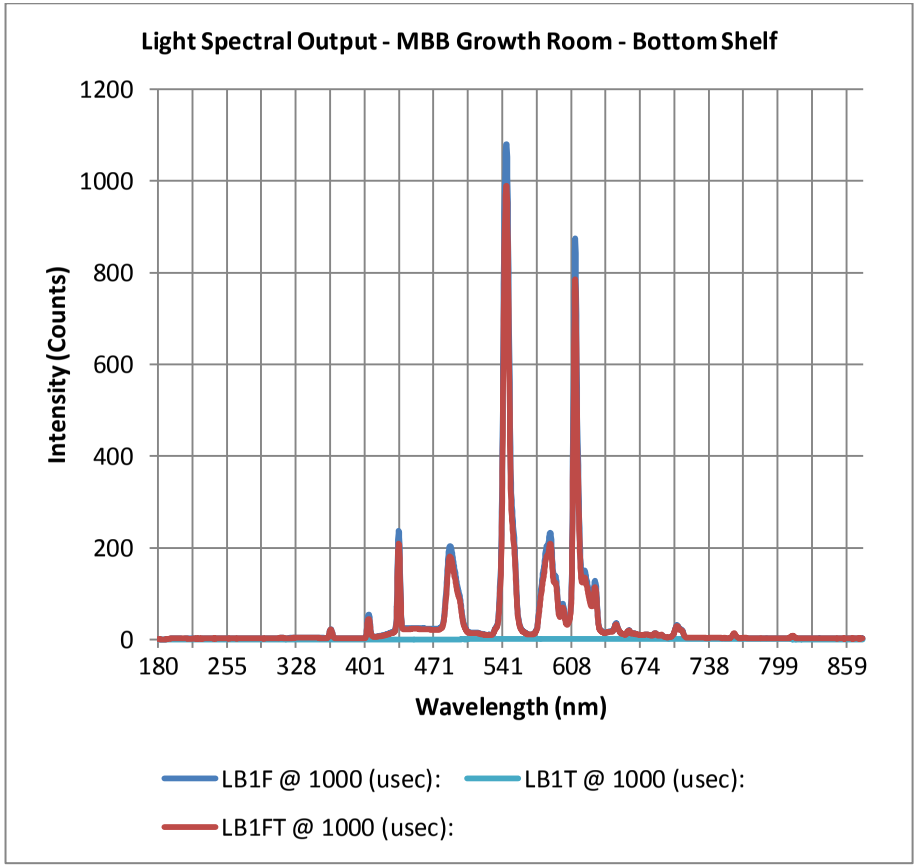

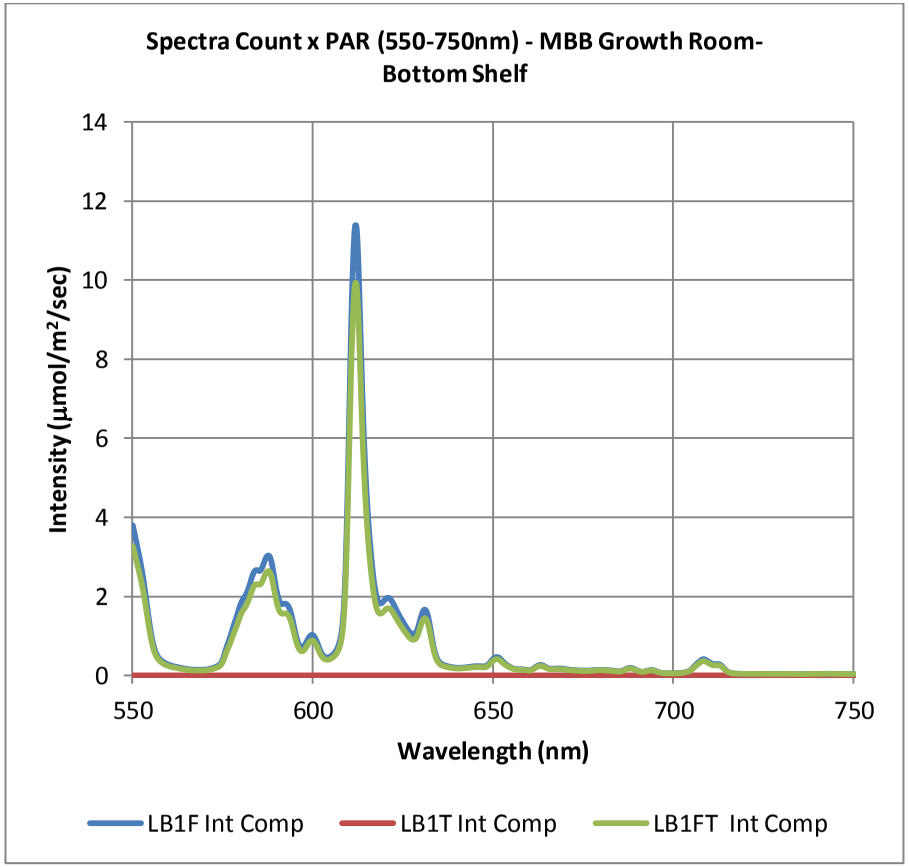

Reading Key:

L-Left stack of shelves, B-Bottom Shelf, 1 to 3 - Position along shelf, F - Fluorescent tubes on, T - Tungsten tubes on, **Example:**"LB1FT" = Left stack of shelves, Bottom Shelf, 1st Position, Both types of bulbs on.

A-2- MBB Growth Room (H Floor) – Middle Shelf

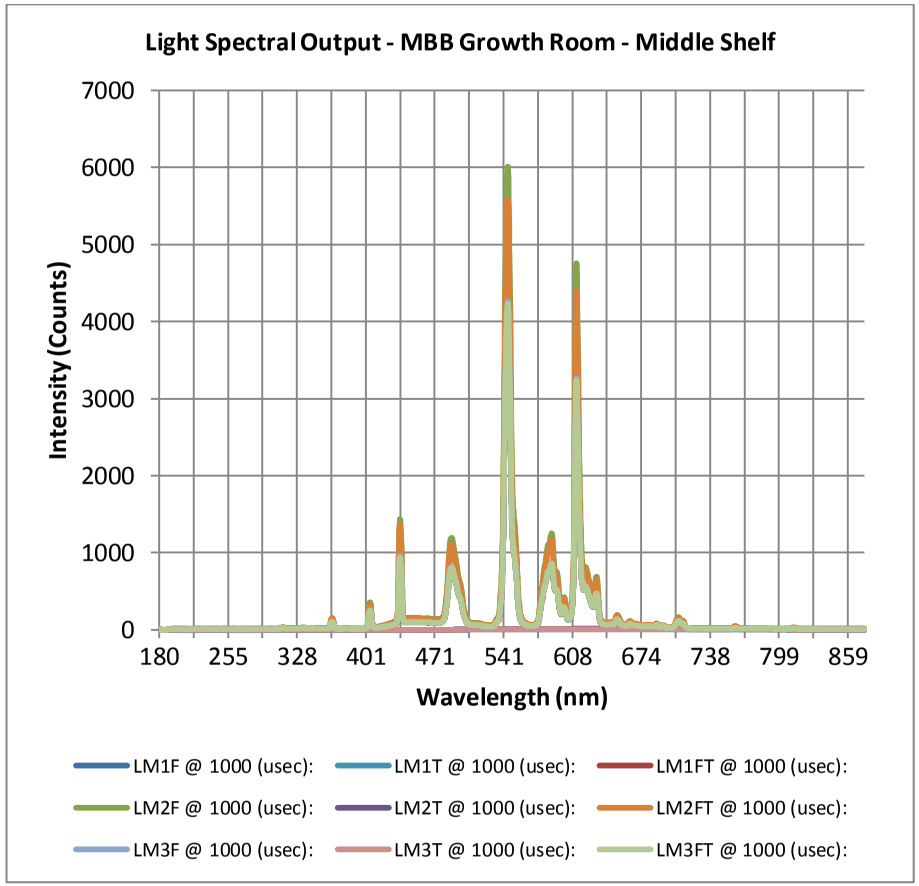

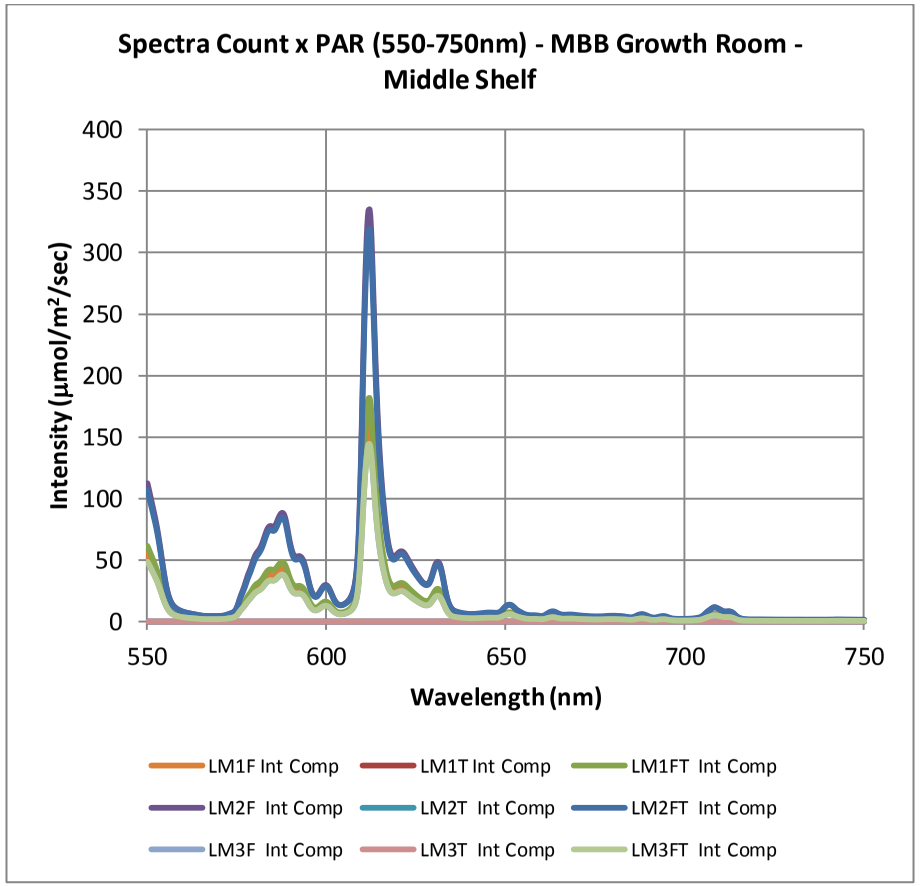

A-3 -MBB Growth Room (H Floor) – Top Shelf

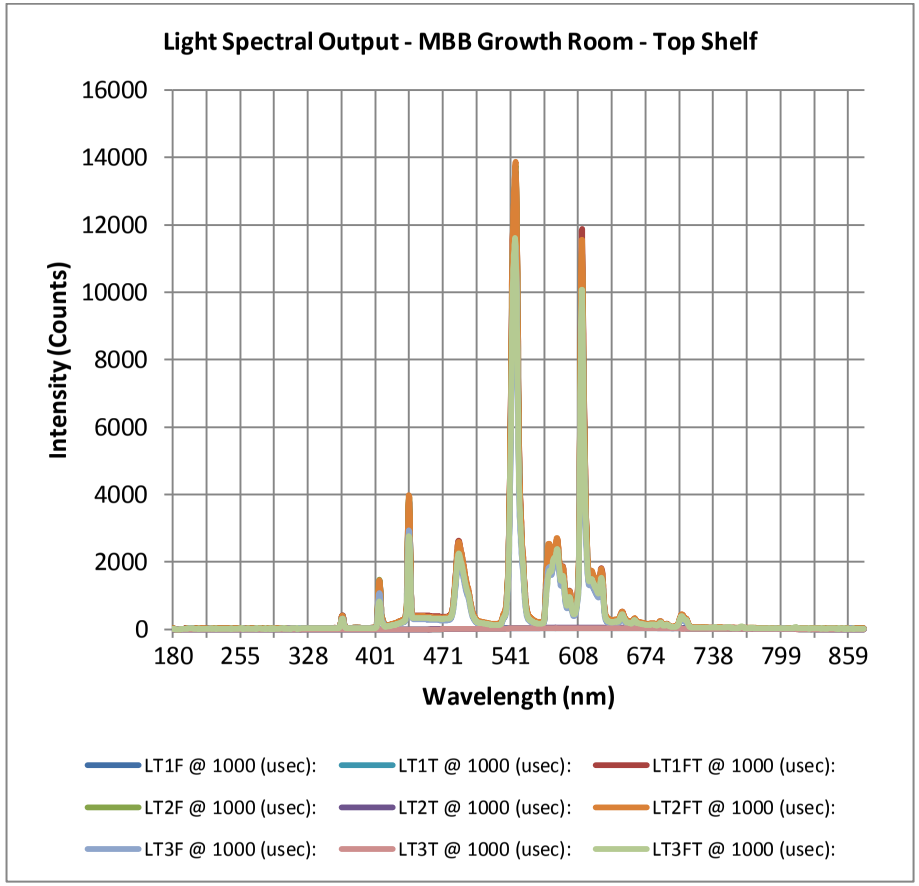

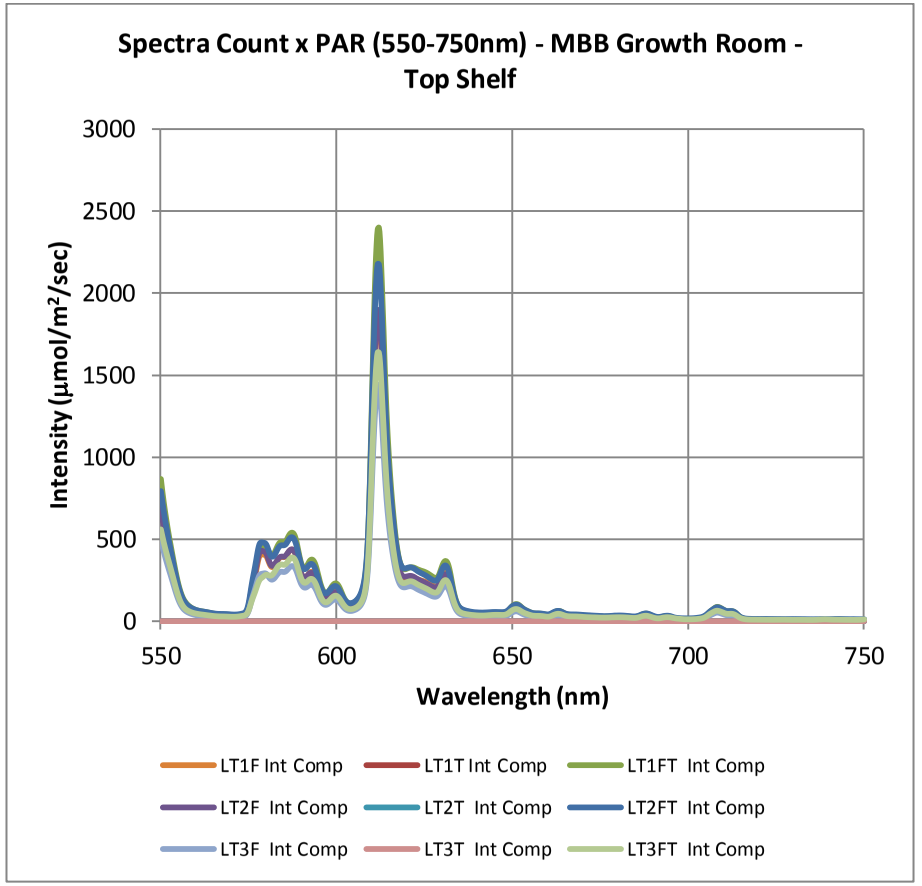

A-4-Annex Growth Unit 503 (APS) – Top Shelf

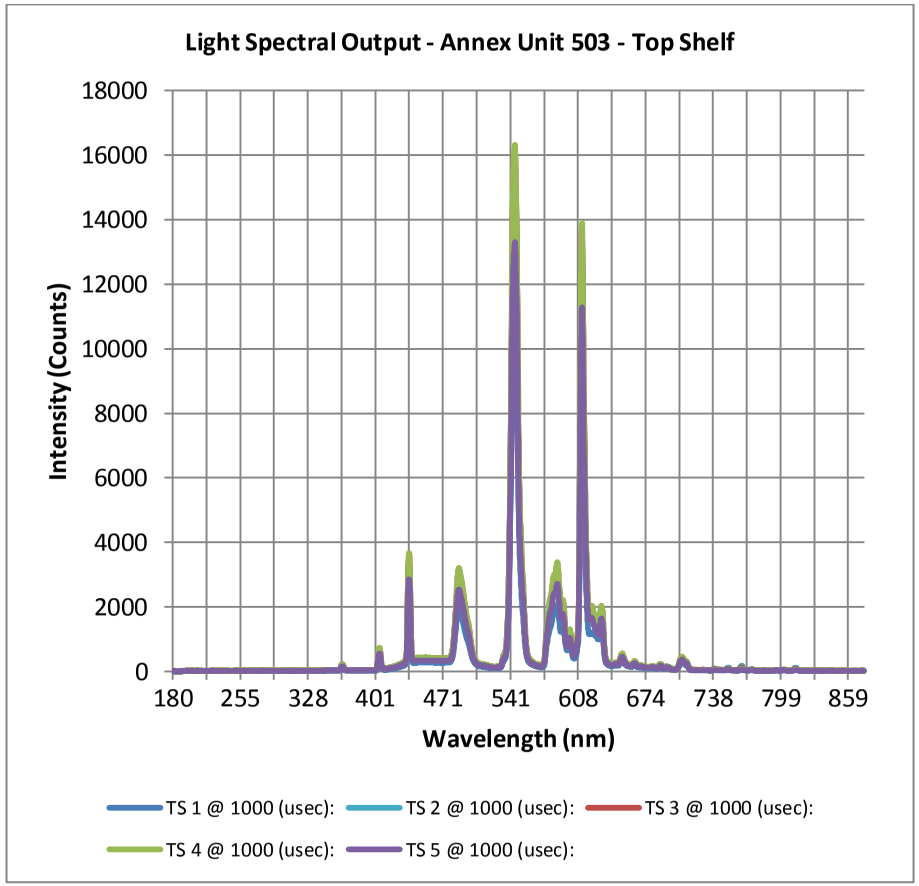

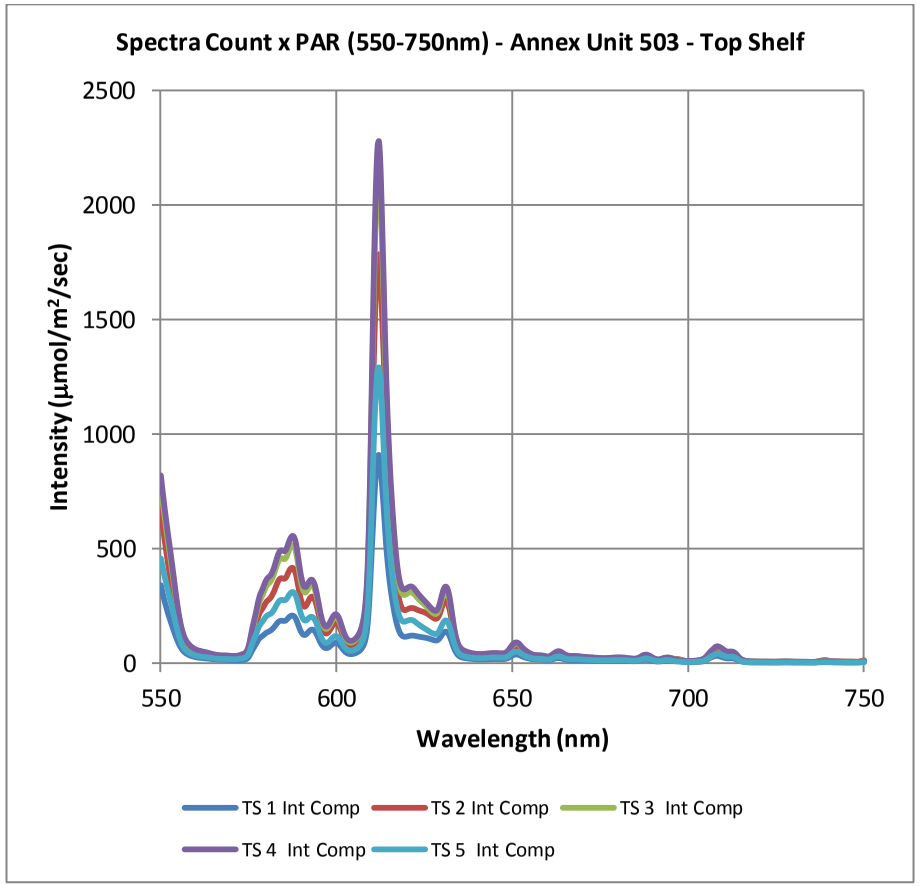

Reading Key: TS – Top Shelf, 1- 5- Position along shelf

A-5-Annex Growth Unit 503 (APS) – Bottom Shelf

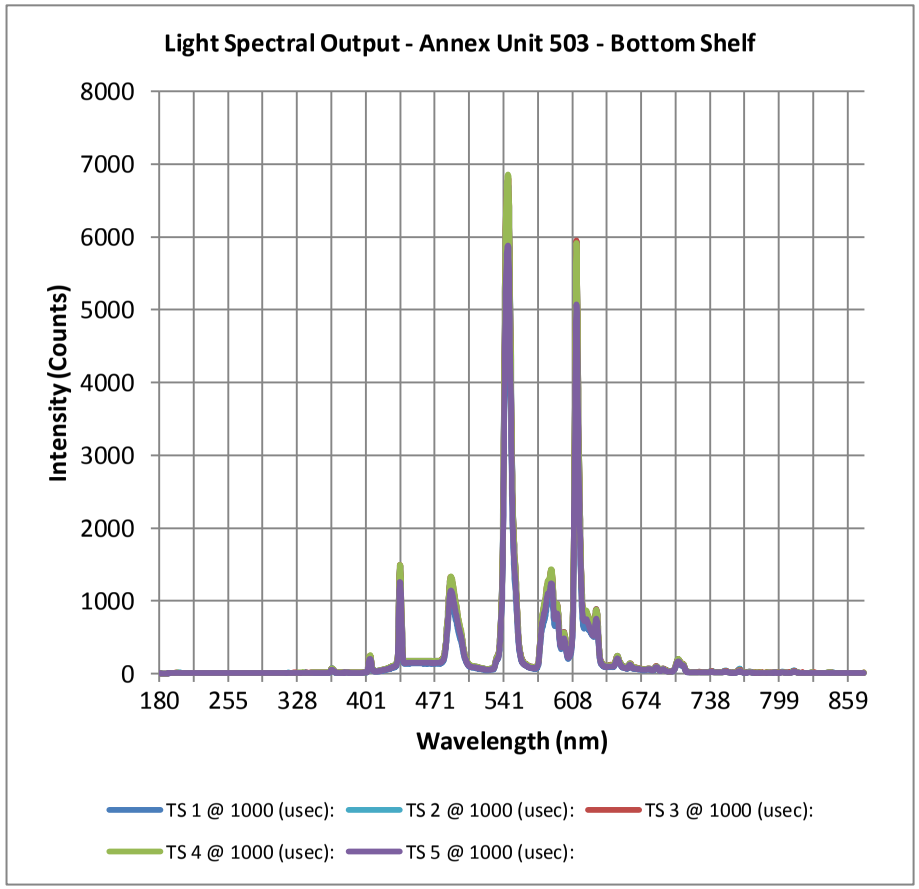

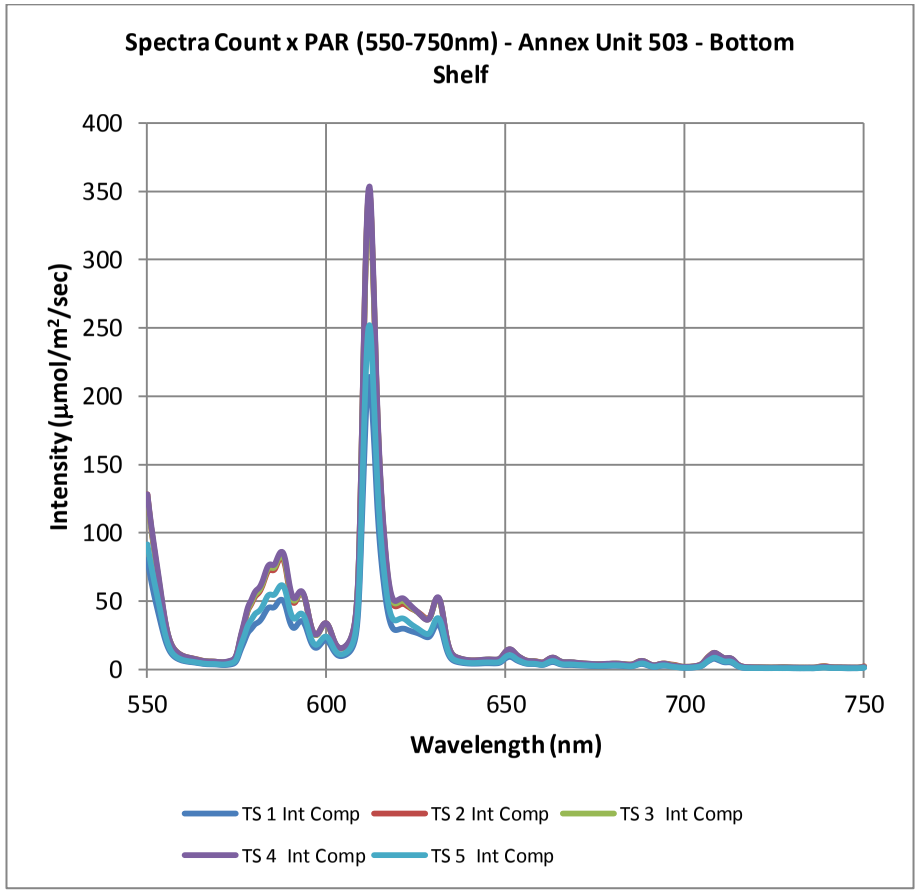

A-6-Fish Tank Lights (MBB Lab F3) – Top Lights

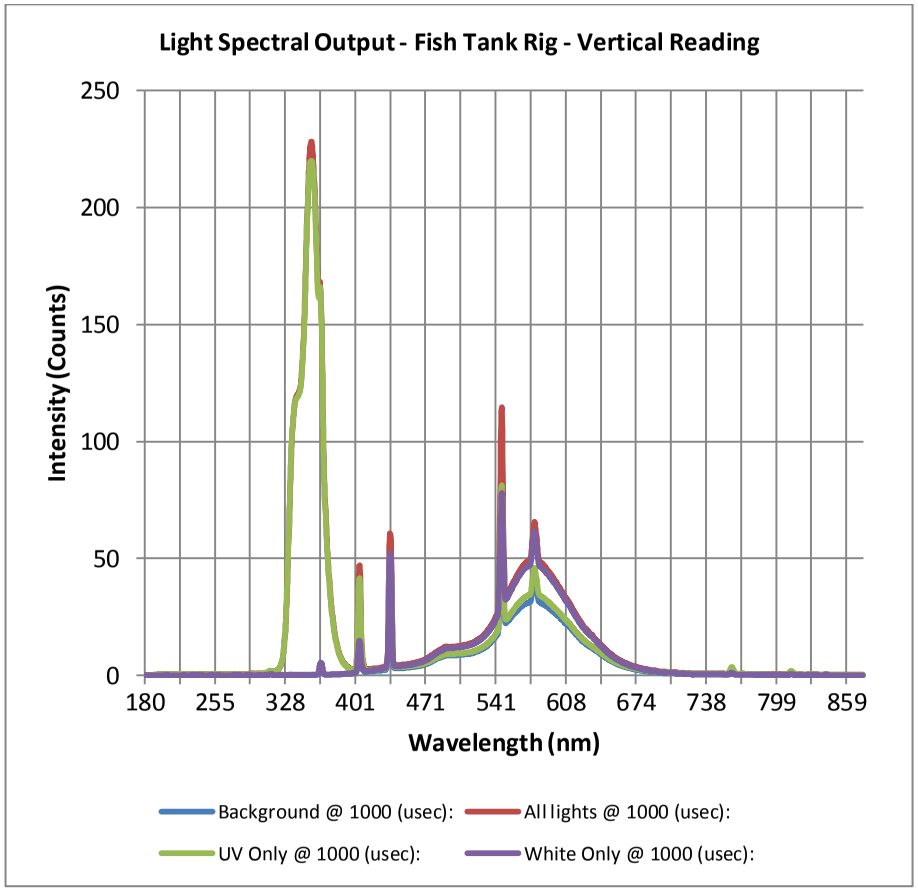

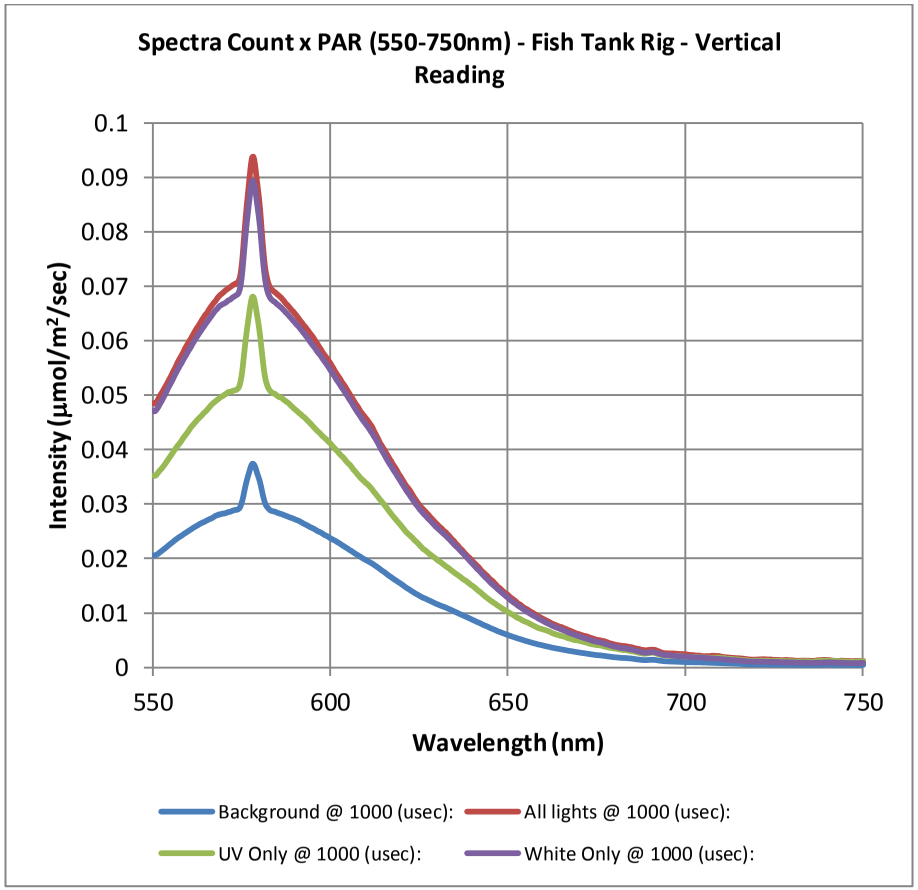

A-7-Fish Tank Lights (MBB Lab F3) – Side Lights

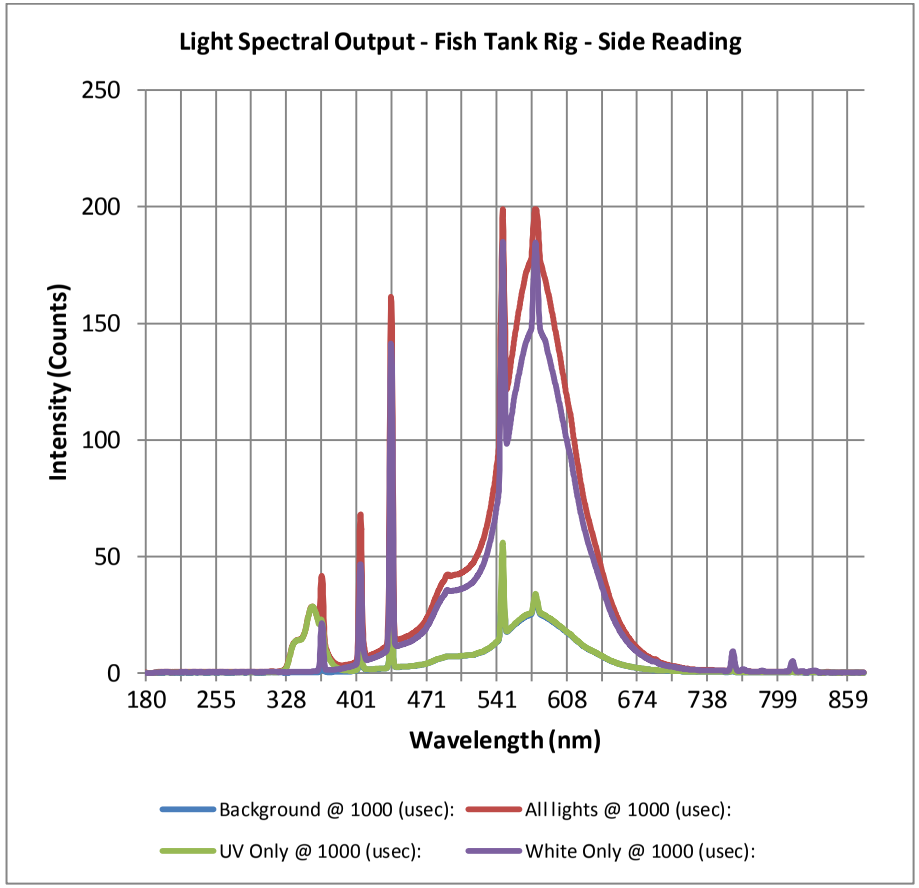

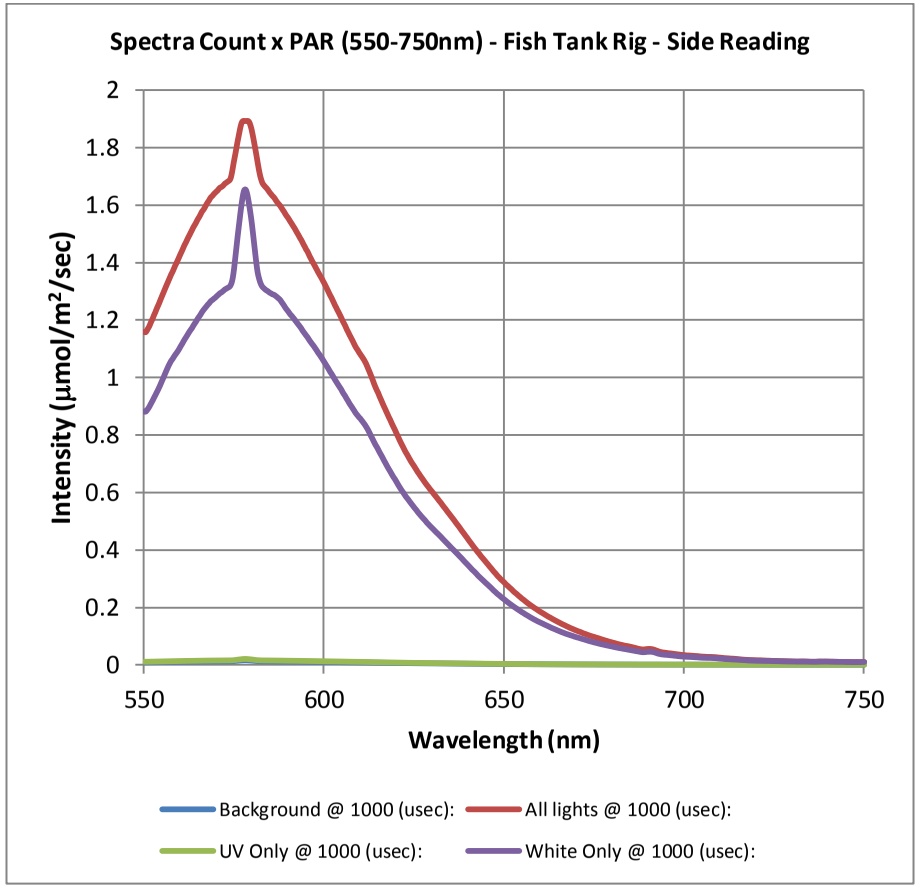

A-8-Trans-illuminator (MBB Lab F3)

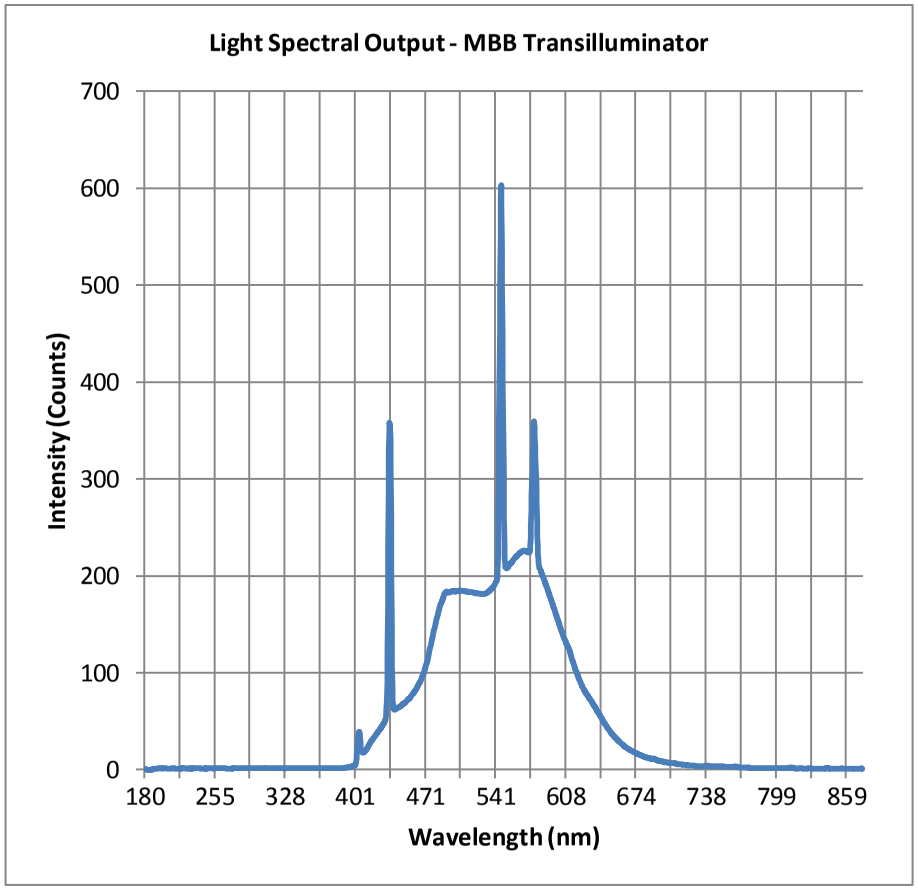

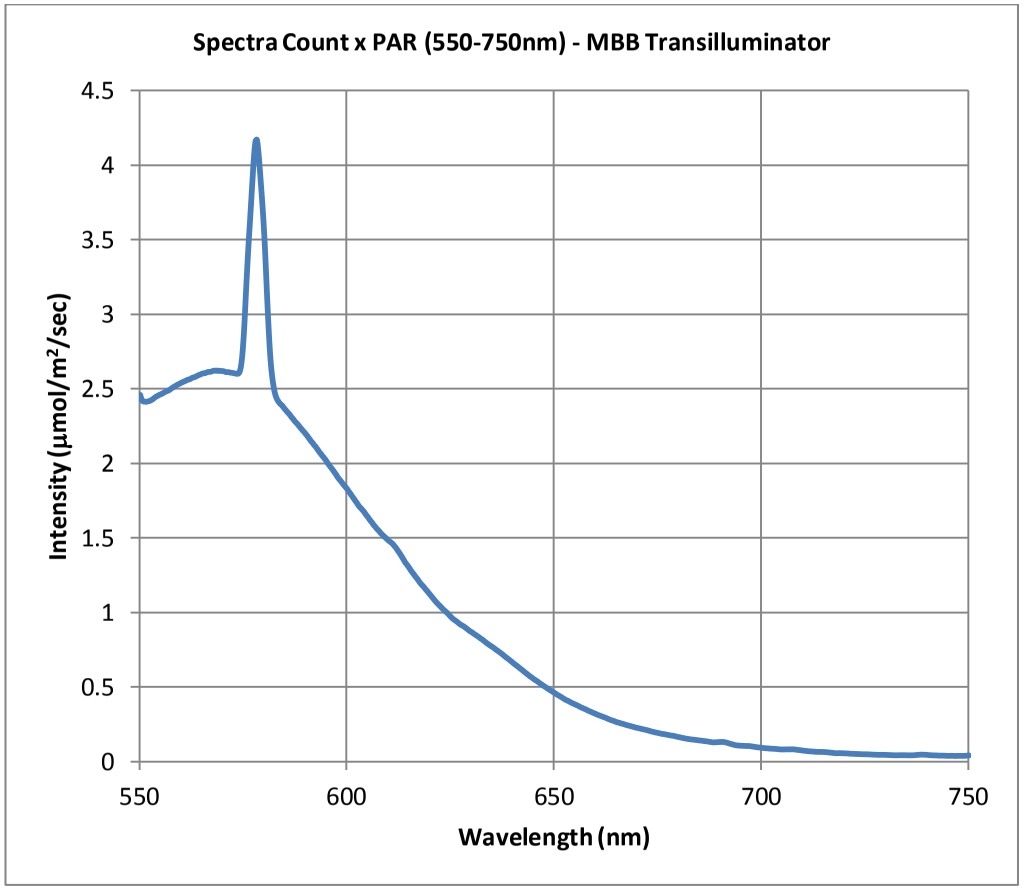

A-9-Ring Fluorescent Tube (MBB Lab F3)

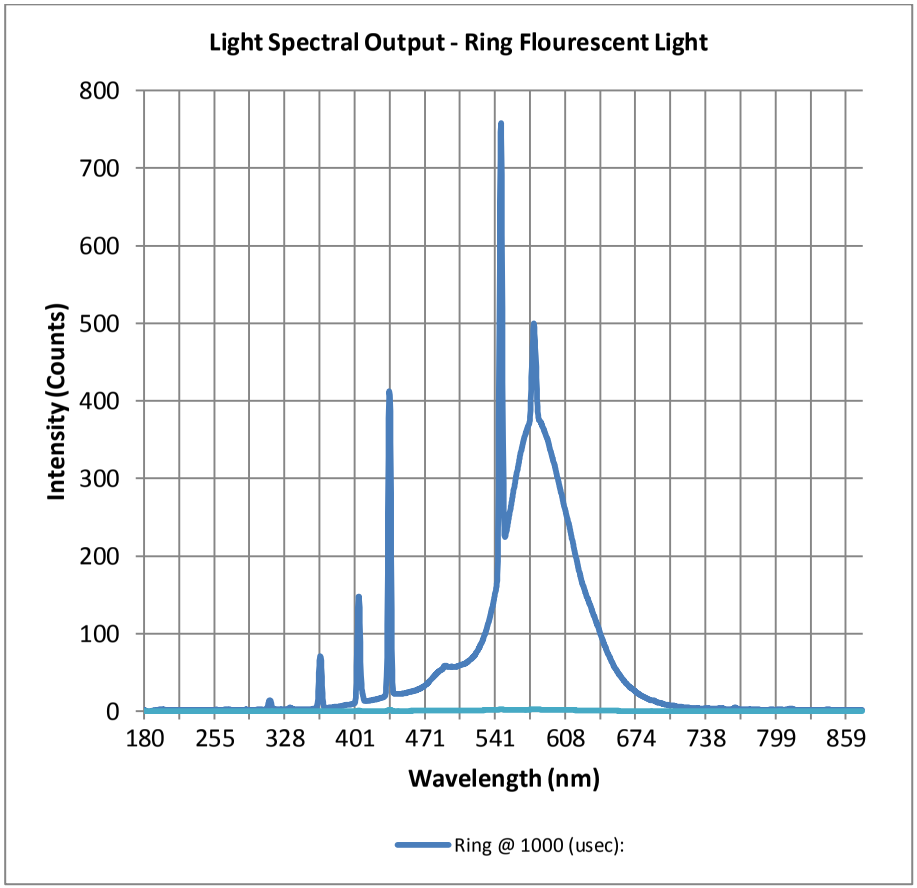

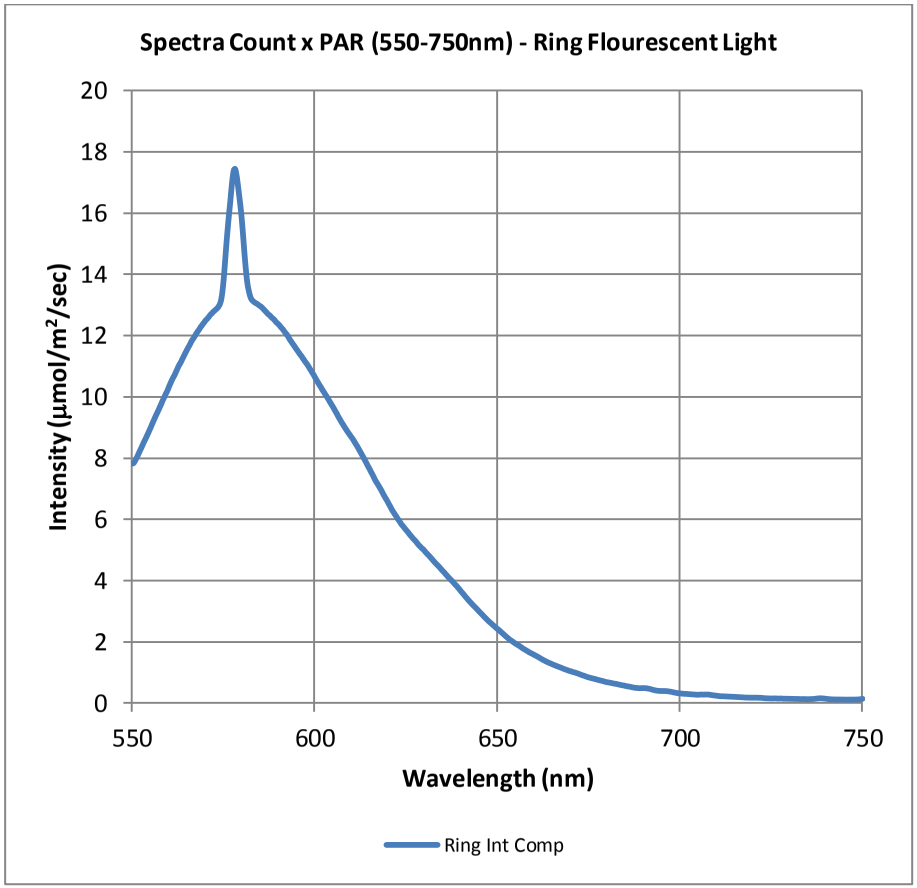

A-10-Thin Fluorescent Tube x2 (MBB Lab F3)

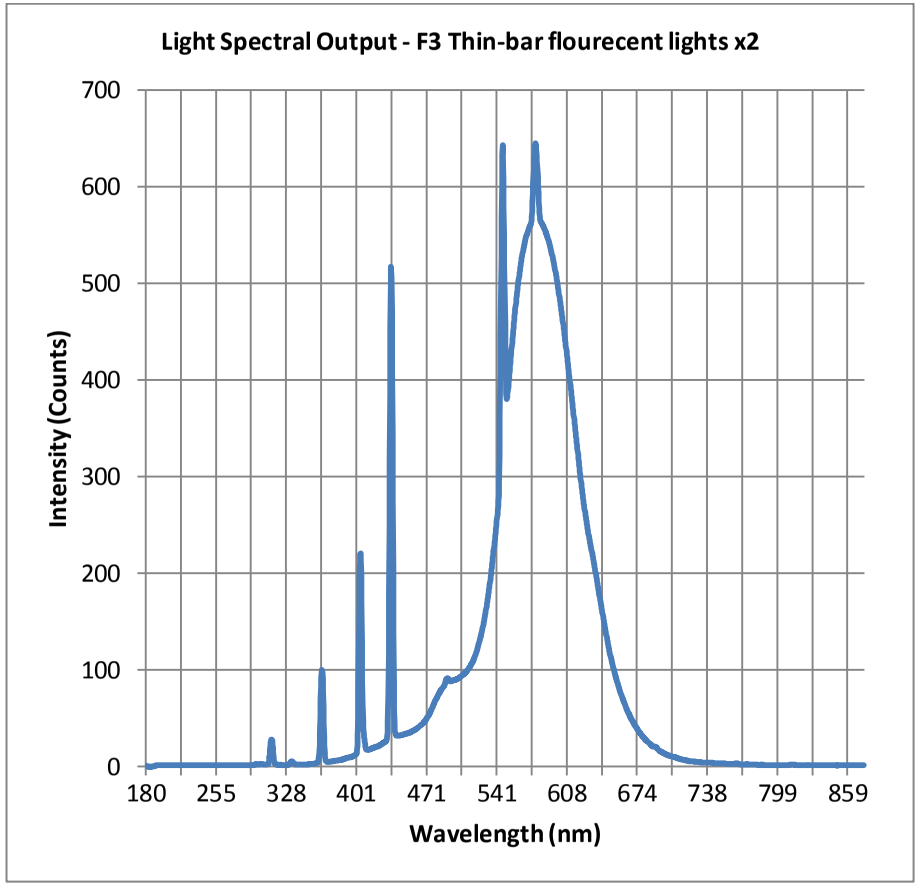

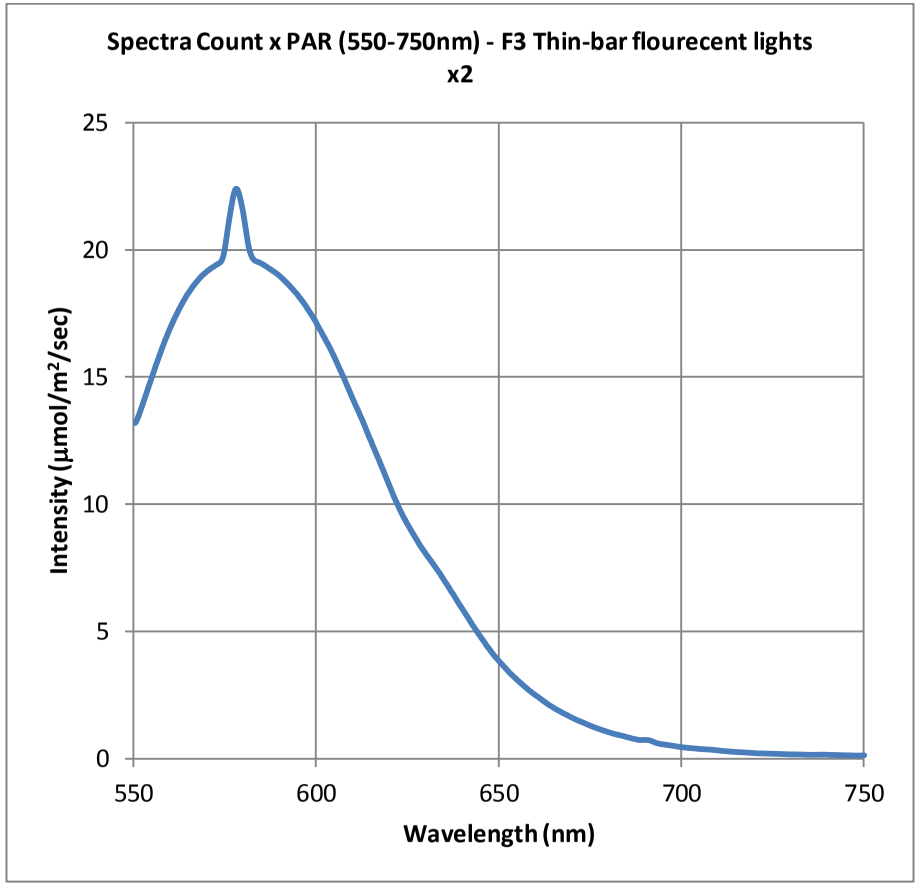

B - Coated slide measurement setup

The following setup for measuring slide absorbance and emission was used by project student David Hosking (Hosking, 2013) during the collaboration in chapter 5.The spectral properties of eachdye coated slide were measured and compared to a reference of a plain, uncoated glass slide with the relevant light source.

Absorbance setup

Absorbance readings were performed by mounting coated slides in an Ocean Optics 4-way cuvette holder. Light was guided to the samples from a Ocean Optics UV-VIS-NIR Deuterium Tungsten Halogen light source (Model DT-MINI-2-GS) using a series of fibre optic cables (Ocean Optics P600-1-SR). The source and receiver optical cables were connected at 180^{o}to each other in the cuvette holder. The light readings were detected using an Ocean Optics USB2000+UV-VIS-ES sensor connected to a computer via a USB. The Spectrasuite software was used to capture the data with the same settings as in section 2.9.2.

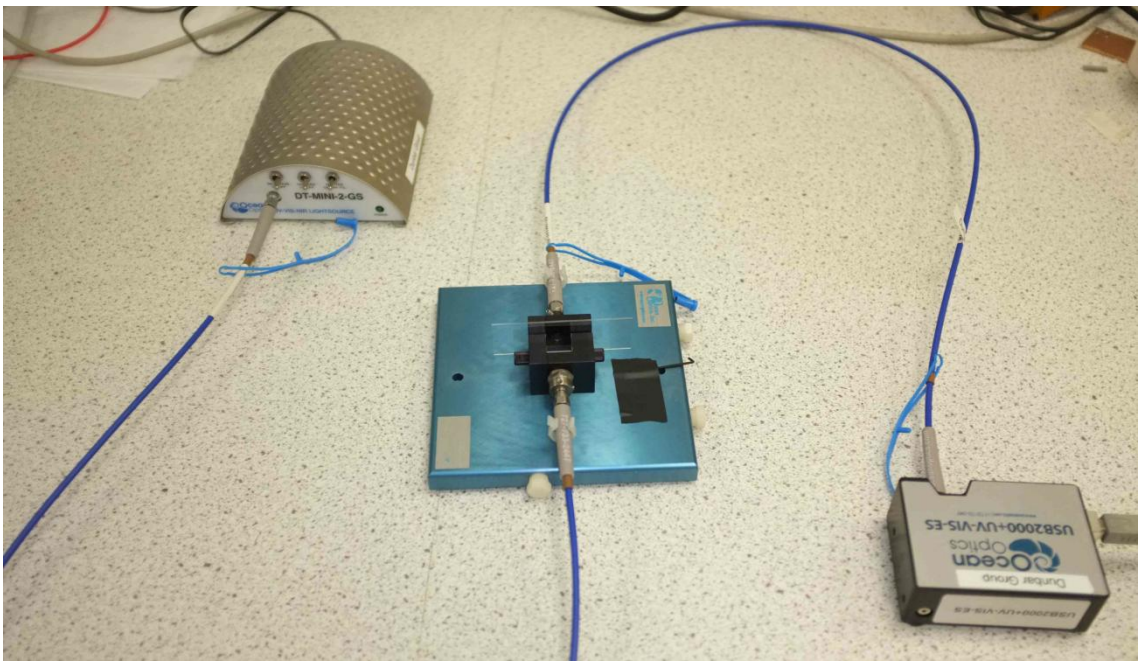

Emission setup

Emission readings were performed by mounting coated slides in an Ocean Optics 4-way cuvette holder at 45^{o} (to avoid light reflection to the detector). Excitation light was guided to the samples from a StellarNet Ltd SL1-LED light source (Model DT-MINI-2-GS, with variable wavelength LEDs) using a series of fibre optic cables (Ocean Optics P600-1-SR). The source and receiver optical cables were connected at 90^{o}to each other in the cuvette holder, to avoid any unabsorbed light entering the detector. A UV LED with a peak excitation of 402nm was used

for the Coumarin 1 tests and a Green LED with a peak excitation of 528nm was used for the Rhodamine B tests. The light readings were detected using an Ocean Optics USB2000+UV-VIS-ES sensor connected to a computer via a USB. The Spectrasuite software was used to capture the data with the same settings as in section 2.9.2.

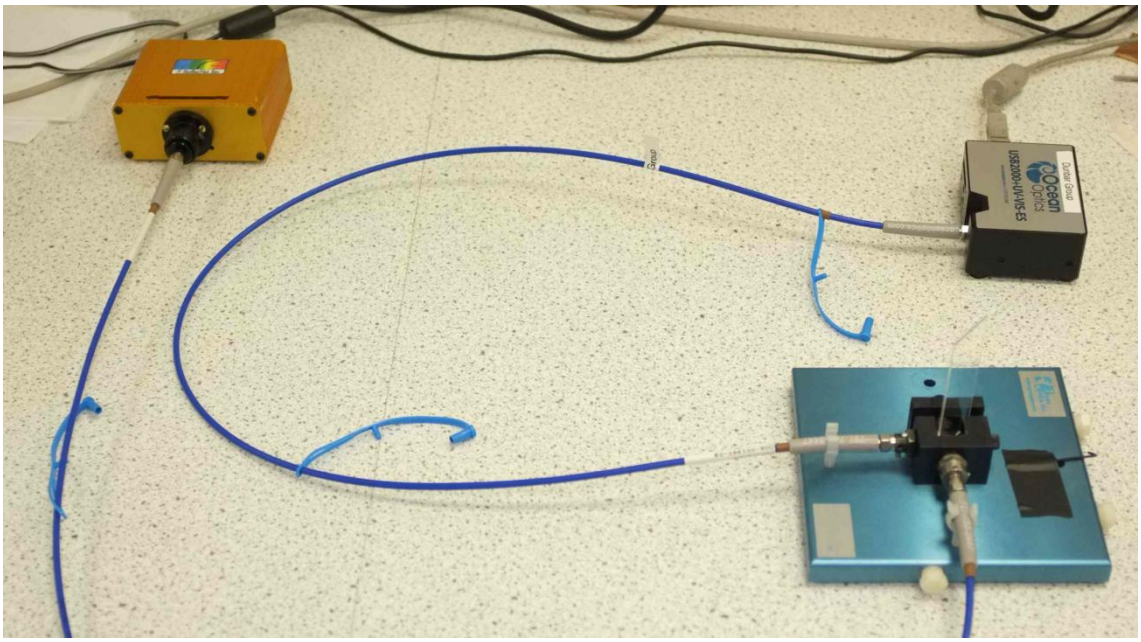

C - COMSOL Procedures

Batch processing, terminal and upload procedures

Standalone computer systems owned by Sheffield University were used to create 2D and 3D models in COMSOL multiphysics 4.1, under individual software licence agreements. These systems were not used to carry out the calculation work due to insufficient memory and processor resources. To perform this processing the relevant files were uploaded to the university supercomputer system directly or via the VPN (Virtual private network).

File upload

Files were uploaded using the Open Text Exceed 14 – Connection central FTP software. An account was set-up on the host server: eyrie.shef.ac.uk. Files to be processed were transferred to the user directory.

Batch File Setup

To enable the files to be run without a user interface (in batch mode), COMSOL was run remotely on the eyrie server via the Sun micro systems 'Sun Secure Global Desktop' hosted at the University (Note: This method was preferred due to the decreased lag issues, when running the software direct from the eyrie server). Once logged in, a 'General Applications' 'Xterm to remote server' 'remote_shh' terminal was started. The server address, user name and password were entered to log in to the command line on the server. The command "comsol41" was used to open the program and establish a remote user GUI (graphical user interface). Once the appropriate file was opened within the program, under the 'Model Builder' > "Study 1" right-click submenu, a 'Batch' function was added. This enables the program to be run remotely via the command line. Under the 'Batch' settings an output 'Filename' and the 'Directory' was specified, where the processed data file will be saved. Once this procedure had been completed, the File was saved with the alterations.

Executing Batch Function

A new Open Text Exceed Xterminal was opened directly to the eyrie server, using the username and password. Once the command line was displayed, the following commands could be used:

comsol41 batch -inputfile original_file_name.mph -outputfile output_file_name.mph >outfile 2>errfile &

The command targets the original file to be processed (original_file_name.mph) and specifies the new output file to be made when the study has finished processing (output_file_name.mph).

Note: The output_file_name filename, must match the 'Filename' specified in the 'Batch' functionmentionedin the previous section.

The other lines of code (">outfile 2>errfile &") are for monitoring the status of the file as is processed, any text that would have gone to the terminal screen, is redirected to files called outfile and errfile. All files are created in the output file directory, the "&" runs the entire process in the background. If "cat outfile" is typed into the command line, the progress of the job can be monitored, if for any reason the job stops an error message is sent to the errfile.Once the job has been completed, the "output_file_name.mph" will contain the processed data. The file can be then transferred via FTP to a standalone PC to view the results.

D - SEM Images

Dunaliella Salina 19/30

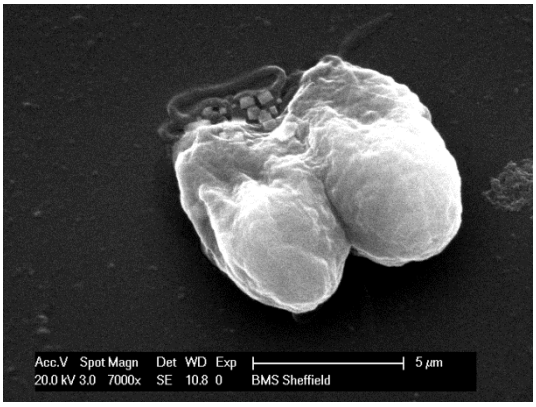

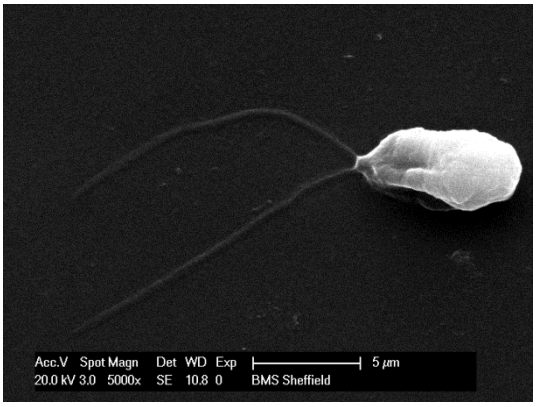

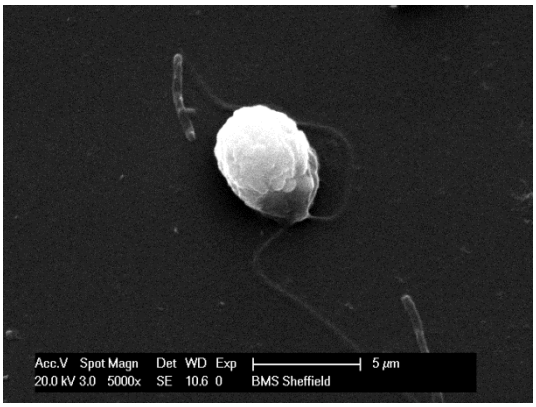

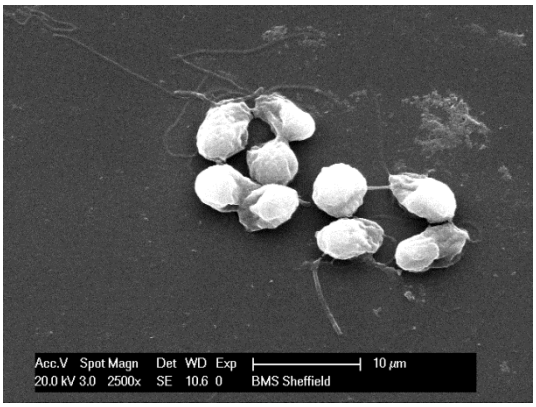

Dunaliella 'gamete' isolate

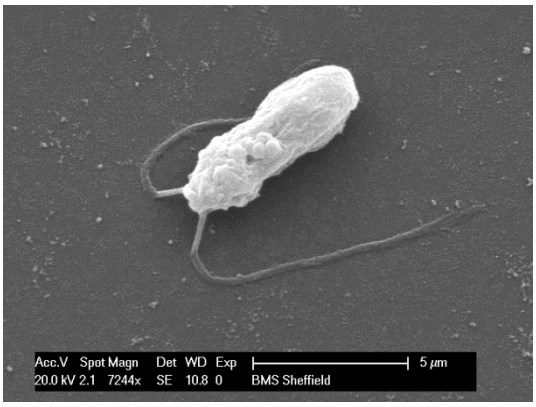

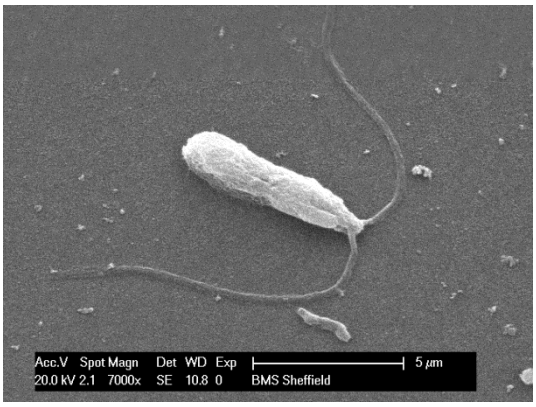

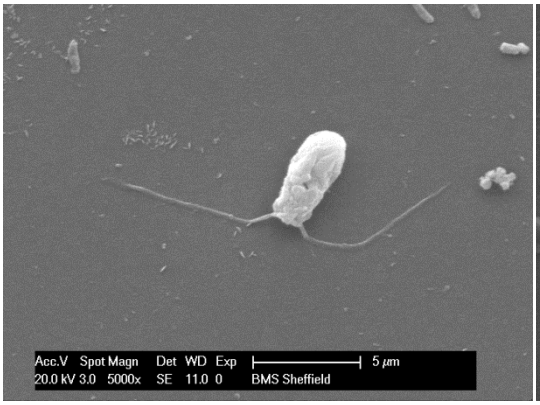
Acc.V Spot Magn Det WD Exp 5 µm
20.0 kV 3.0 5000x SE 11.0 0 BMS Sheffield

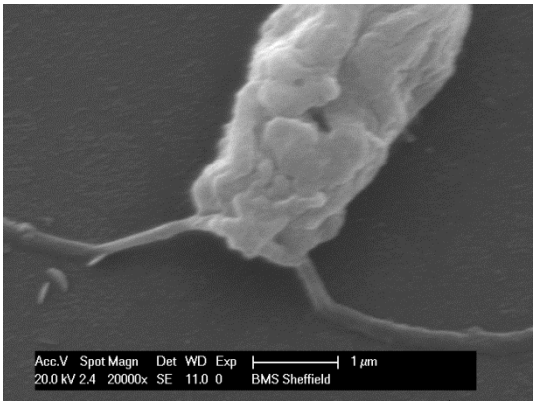
Acc.V Spot Magn Det WD Exp 1 µm
20.0 kV 2.4 20000x SE 11.0 0 BMS Sheffield

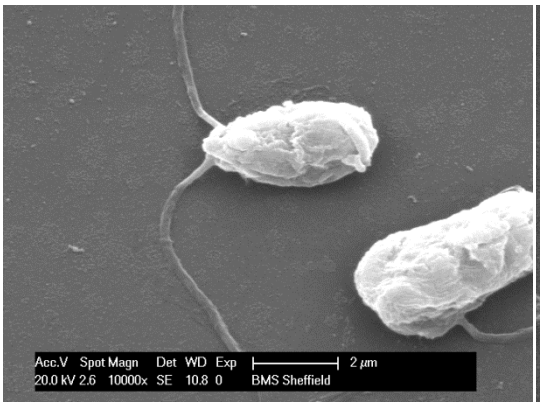
Acc.V Spot Magn Det WD Exp 2 µm
20.0 kV 2.6 10000x SE 10.8 0 BMS Sheffield

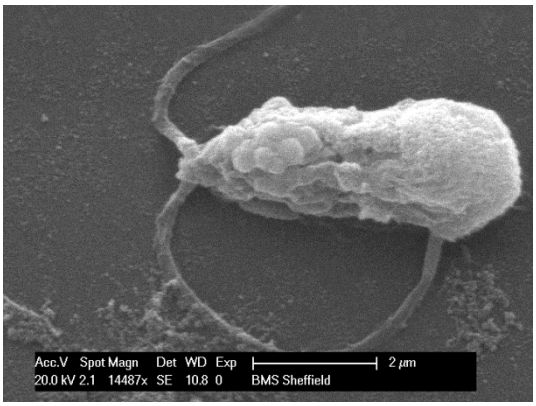
Acc.V Spot Magn Det WD Exp 2 µm
20.0 kV 2.1 14487x SE 10.8 0 BMS Sheffield

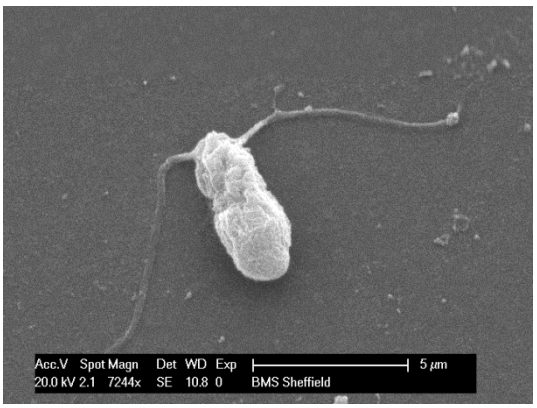
Acc.V Spot Magn Det WD Exp 5 µm
20.0 kV 2.1 7244x SE 10.8 0 BMS Sheffield

E - Supelco mix lipid calibration for GC-MS

Supelco 37 Component FAME Mix (47885-U) Specification					GC-MS Matches			
Comp No	Name in Supelco	Carbon, double bonds	Weight (%)	Weight (mg)	Match in NIST Library	Match Prob (%)	Time on column	M w
1	Butyric Acid Methyl ester	4,0	4	0.4	Not found		2.06	102
2	Caproic Acid Methyl ester	6,0	4	0.4	Hexanoic Acid Methyl ester (ion 74 int)	88	2.30	130
3	Caprylic Acid Methyl ester	8,0	4	0.4	Octanoic Acid Methyl ester	79	4.60	158
4	Capric Acid Methyl ester	10,0	4	0.4	Decanoic Acid Methyl ester	63.2	10.10	186
5	Undecanoic Acid Methyl ester	11,0	2	0.2	Undecanoic Acid Methyl ester	27.2	14.22	200
6	Lauric Acid Methyl ester	12,0	4	0.4	Dodecanoic Acid Methyl ester	42.2	19.00	214
7	Tridecanoic Acid Methyl ester	13,0	2	0.2	Tridecanoic Acid Methyl ester	74	23.99	228
9	Myrisoleic Acid Methyl ester	14,1	2	0.2	Methyl myristoleate	4.34	28.35	240
8	Myristic Acid Methyl ester	14,0	4	0.4	Methyl tetradecanoate	30.6	29.13	242
11	Cis-10-Pentadecanoic Acid Methyl ester	15,1	2	0.2	Pentadecanoic Methyl ester	45.9	33.37	254
10	Pentadecanoic Acid Methyl ester	15,0	2	0.2	Pentadecanoic Methyl ester	44.7	34.10	256
13	Palmitoleic Acid Methyl ester	16,1	2	0.2	9-Hexadecenoic Acid Methyl ester	62.8	37.83	268
12	Palmitic Acid Methyl ester	16,0	6	0.6	Hexadecanoic Acid Methyl ester	40.50	39.09	270
15	Cis - 10 - heptadecanoic Acid Methyl ester	17,1	2	0.2	Cis - 10 - heptadecanoic Methyl ester	25.8	42.57	282
14	Heptadecanoic Acid Methyl ester	17,0	2	0.2	Heptadecanoic Methyl ester	32	43.62	284
22	γ linolenic Acid Methyl ester	18,3 (n6)	2	0.2	γ linolenic Methyl ester	30.3	45.61	292
20	Linoleic Acid Methyl ester	18,2 (6 cis)	2	0.2	9,12-Octadecadienoic Acid Methyl ester	30	46.44	294
24	Linolenic Acid Methyl ester	18,3 (n3)	2	0.2	9,12,15-Octadecadienoic Acid Methyl ester	55.5	46.68	292
18	Oleic Acid Methyl ester	18,1 (9 Cis)	4	0.4	9-Octadecadienoic Acid Methyl ester	18.4	46.83	296
19	Linolelaidic Acid Methyl ester	18,2 (6 trans)	2	0.2	9,12-Octadecadienoic Acid Methyl ester	34.2	46.96	294
17	Elaidic Acid Methyl ester	18,1 (9 trans)	2	0.2	9-Octadecadienoic Acid Methyl ester	26.7	47.17	296

Supelco 37 Component FAME Mix (47885-U) Specification					GC-MS Matches			
Comp No	Name in Supelco	Carbon, double bonds	Weight (%)	Weight (mg)	Match in NIST Library	Match Prob (%)	Time on column	M w
16	Stearic Acid Methyl ester	18,0	4	0.4	Octadecanoic Acid Methyl ester	51.9	48.13	298
31	Arachidonic Acid Methyl ester	20,4	2	0.2	5,8,11,14-Eicosatetraenoic Acid Methyl ester	25.5	53.37	318
35	Cis - 5, 8, 11, 14, 17 - eicosapentaenoic Acid Methyl ester	20,5 (n3)	2	0.2	cis-5,8,11,14,17-Eicosapentaenoic Acid Methyl ester	34.5	53.57	316
28	Cis - 8, 11, 14 - eicosatrienoic Acid Methyl ester	20,3 (n6)	2	0.2	Cis - 8, 11, 14 - eicosatrienoic Methyl ester	8.01	54.23	320
26	Cis - 11, 14 - eicosadienoic Acid Methyl ester	20,2	2	0.2	Cis - 11, 14 - eicosadienoic Methyl ester	58.4	55.14	322
30	Cis - 11, 14, 17 - eicosatrienoic Acid Methyl ester	20,3 (n3)	2	0.2	Cis - 11, 14, 17 - Eicosatrienoic Acid Methyl ester	25.9	55.42	320
23	Cis - 11 - eicosenoic Acid Methyl ester	20,1	2	0.2	Cis - 11 - eicosenoic Methyl ester	12.4	55.59	324
21	Arachidic Acid Methyl ester	20,0	4	0.4	Eicosanoic Acid Methyl ester	49.9	56.84	326
25	Heneicosanoic Acid Methyl ester	21,0	2	0.2	Heneicosanoic Acid Methyl ester	62.1	60.67	340
37	Cis - 4, 7, 10, 13, 16, 19 - Docosahexaenoic Acid Methyl ester	22,6 (n3)	2	0.2	Cis - 4, 7, 10, 13, 16, 19 - Docosahexaenoic Methyl ester	17.9	61.2	342
33	Cis - 13, 16 - docoadienoic Acid Methyl ester	22,2	2	0.2	Cis - 13, 16 - Docoadienoic Acid Methyl ester	5.52	63.2	350
29	Erucic Acid Methyl ester	22,1 (n9)	2	0.2	13-Docosenoic Acid Methyl ester	13.3	63.43	352
27	Behenic Acid Methyl ester	22,0	4	0.4	Docosanoic Acid Methyl ester	50.2	64.56	354
32	Tricosanoic Acid Methyl ester	23,0	2	0.2	Tricosanoic Acid Methyl ester	35.4	68.28	368
36	Nervonic Acid Methyl ester	24,1	2	0.2	15-Tetracosenoic Acid Methyl ester	19.7	70.89	380
34	Lignoceric Acid Methyl ester	24,0	4	0.4	Tetracosanoic Acid Methyl ester	14	71.89	382

Internal Standard Calcs														
Comp No	Carbon, double bonds	Ratio area FAME to Int Std (y-axis)					Ratio conc FAME to Int Std (x-axis)					Linear Regression Analysis		
		0	2	4	6	8	0	2	4	6	8	Slope (m)	y-intcpt (c)	Corr (R2)
1	4,0	0	0	0	0	0	0	0.32	0.64	0.96	1.28	0	0	0
2	6,0	0	0.014439	0.034518	0.05835	0.082486	0	0.32	0.64	0.96	1.28	0.065276	-0.00382	0.990656
3	8,0	0	0.031758	0.080598	0.162128	0.213283	0	0.32	0.64	0.96	1.28	0.174042	-0.01383	0.97859
4	10,0	0	0.051434	0.156498	0.295709	0.342926	0	0.32	0.64	0.96	1.28	0.290664	-0.01671	0.97377
5	11,0	0	0.026184	0.084314	0.175835	0.189362	0	0.16	0.32	0.48	0.64	0.330234	-0.01054	0.952403
6	12,0	0	0.084926	0.235085	0.453974	0.510116	0	0.32	0.64	0.96	1.28	0.43415	-0.02104	0.969874
7	13,0	0	0.038533	0.129335	0.243186	0.257546	0	0.16	0.32	0.48	0.64	0.449841	-0.01023	0.954433
9	14,1	0	0.04137	0.125349	0.268773	0.279059	0	0.16	0.32	0.48	0.64	0.49095	-0.01419	0.943202
8	14,0	0	0.12038	0.313292	0.591857	0.601573	0	0.32	0.64	0.96	1.28	0.52332	-0.0095	0.94955
11	15,1	0	0.042525	0.150166	0.29428	0.294775	0	0.16	0.32	0.48	0.64	0.525816	-0.01191	0.935916
10	15,0	0	0.054614	0.16426	0.302835	0.337623	0	0.16	0.32	0.48	0.64	0.577167	-0.01283	0.969389
13	16,1	0	0.052522	0.179289	0.326884	0.356102	0	0.16	0.32	0.48	0.64	0.616604	-0.01435	0.961827
12	16,0	0	0.24185	0.666911	1.114478	1.209098	0	0.48	0.96	1.44	1.92	0.685588	-0.0117	0.968963
15	17,1	0	0.052944	0.181666	0.357049	0.394388	0	0.16	0.32	0.48	0.64	0.68305	-0.02137	0.960322
14	17,0	0	0.071633	0.224664	0.363016	0.391638	0	0.16	0.32	0.48	0.64	0.671662	-0.00474	0.963481
22	18,3 (n6)	0	0.052182	0.182958	0.354726	0.389909	0	0.16	0.32	0.48	0.64	0.676476	-0.02052	0.959746
20	18,2 (6 cis)	0	0.064256	0.204665	0.376652	0.406338	0	0.16	0.32	0.48	0.64	0.703171	-0.01463	0.961183
24	18,3 (n3)	0	0.066112	0.202812	0.366095	0.412348	0	0.16	0.32	0.48	0.64	0.702925	-0.01546	0.971773
18	18,1 (9 Cis)	0	0.189589	0.52586	0.946962	1.019637	0	0.32	0.64	0.96	1.28	0.873952	-0.02292	0.965354
19	18,2 (6 trans)	0	0.071203	0.210924	0.363573	0.404787	0	0.16	0.32	0.48	0.64	0.688715	-0.01029	0.972264
17	18,1 (9 trans)	0	0.077067	0.224709	0.413186	0.451305	0	0.16	0.32	0.48	0.64	0.774206	-0.01449	0.966298
16	18,0	0	0.200395	0.51708	0.865226	0.9358	0	0.32	0.64	0.96	1.28	0.792635	-0.00359	0.969923
31	20,4	0	0.065832	0.195611	0.347223	0.43001	0	0.16	0.32	0.48	0.64	0.713382	-0.02055	0.984743
35	20,5 (n3)	0	0.061028	0.180463	0.314572	0.393287	0	0.16	0.32	0.48	0.64	0.650073	-0.01815	0.986469

Internal Standard Calcs														
Comp No	Carbon, double bonds	Ratio area FAME to Int Std (y-axis)					Ratio conc FAME to Int Std (x-axis)					Linear Regression Analysis		
		0	2	4	6	8	0	2	4	6	8	Slope (m)	y-intcpt (c)	Corr (R2)
28	20,3 (n6)	0	0.062038	0.178366	0.34227	0.376654	0	0.16	0.32	0.48	0.64	0.645962	-0.01484	0.96567
26	20,2	0	0.089008	0.248425	0.464773	0.502865	0	0.16	0.32	0.48	0.64	0.863434	-0.01528	0.964476
30	20,3 (n3)	0	0.102682	0.295473	0.507559	0.613463	0	0.16	0.32	0.48	0.64	1.019877	-0.02253	0.985408
23	20,1	0	0.102682	0.295473	0.507559	0.613463	0	0.16	0.32	0.48	0.64	1.019877	-0.02253	0.985408
21	20,0	0	0.244392	0.671076	1.071047	1.278268	0	0.32	0.64	0.96	1.28	1.057247	-0.02368	0.987217
25	21,0	0	0.101264	0.299261	0.542008	0.645922	0	0.16	0.32	0.48	0.64	1.082868	-0.02883	0.980483
37	22,6 (n3)	0	0.051347	0.207471	0.386284	0.466709	0	0.16	0.32	0.48	0.64	0.792722	-0.03131	0.972106
33	22,2	0	0.087445	0.2963	0.559298	0.659066	0	0.16	0.32	0.48	0.64	1.11874	-0.03758	0.97307
29	22,1 (n9)	0	0.101215	0.307963	0.570616	0.676005	0	0.16	0.32	0.48	0.64	1.138382	-0.03312	0.977653
27	22,0	0	0.26158	0.731346	1.270909	1.448131	0	0.32	0.64	0.96	1.28	1.220497	-0.03873	0.977894
32	23,0	0	0.097041	0.338559	0.608284	0.701212	0	0.16	0.32	0.48	0.64	1.196042	-0.03371	0.972224
36	24,1	0	0.08416	0.285018	0.523065	0.687995	0	0.16	0.32	0.48	0.64	1.134309	-0.04693	0.980831
34	24,0	0	0.241937	0.702246	1.375804	1.521734	0	0.32	0.64	0.96	1.28	1.305417	-0.06712	0.964932

F - Nile red plate timing optimisation

A timed calibration experiment was performed to see how long the stained sections of a 96 well microplate (A1-D8) took to read with different integration times overall and the effect it has on background fluorescence (with no plate).

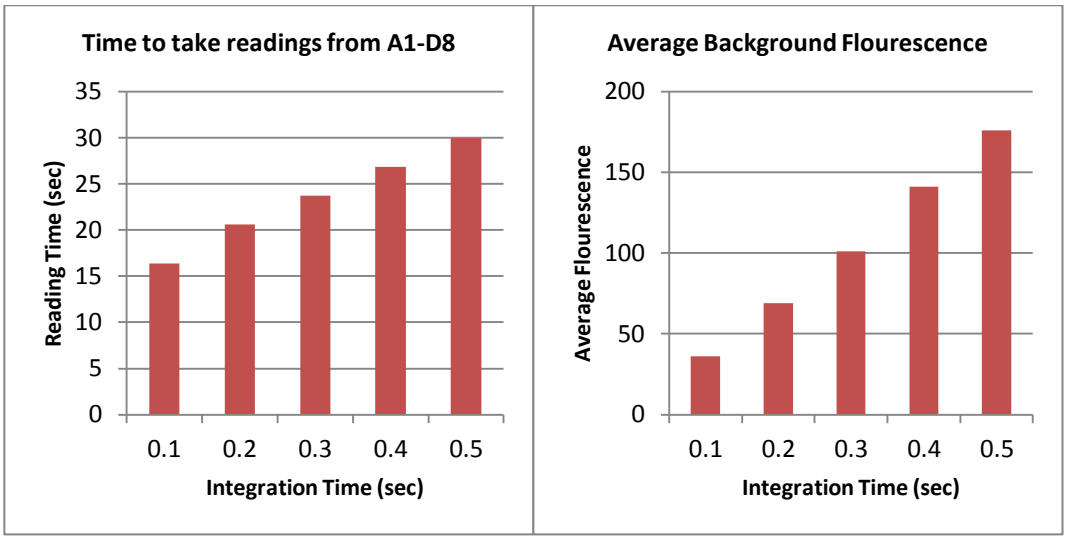

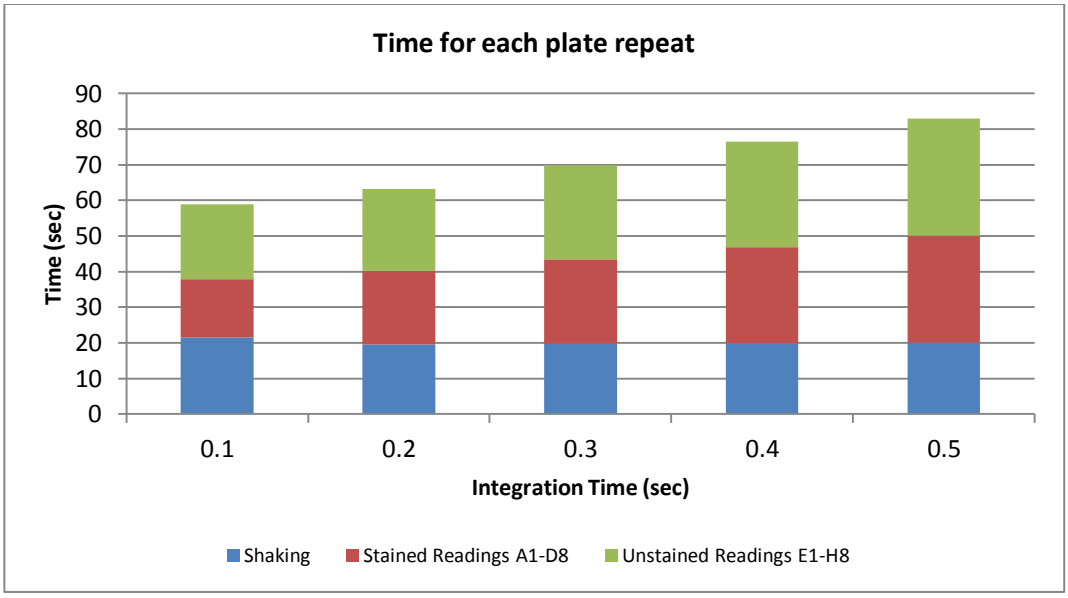

Based on this data, it can be seen that a lot of time is taken up per repeat from taking the readings of the unstained wells. This reading only needs to be taken once per experiment as a background standard, so effectively it is wasting time in the peak measurement experiment. If this background reading was taken at the end of the experiment, just leaving the stained readings to be repeated, each repeat would fall under one minute with an integration of 0.5 to maximise the fluorescence peak. From these findings, the plate protocols were written accordingly.

G - Experimental temperature, DO and pH logs

G1 - 4-5-1 3LPBR DS1918 W-WO MB 100cc Air

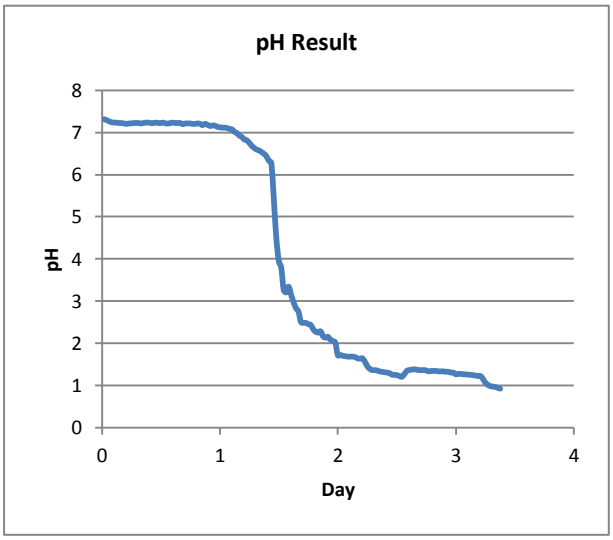

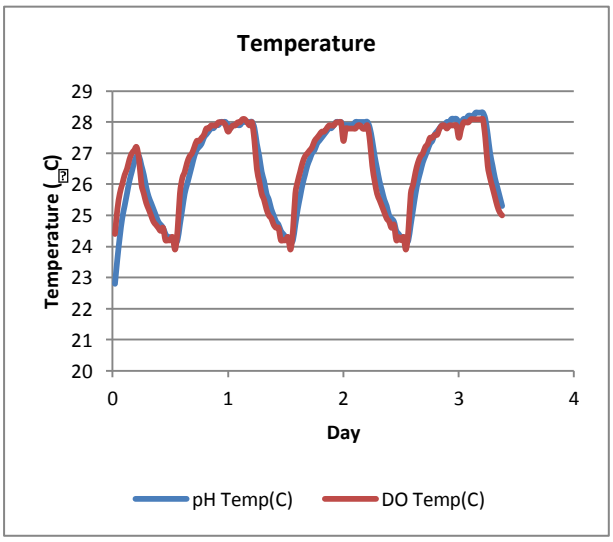

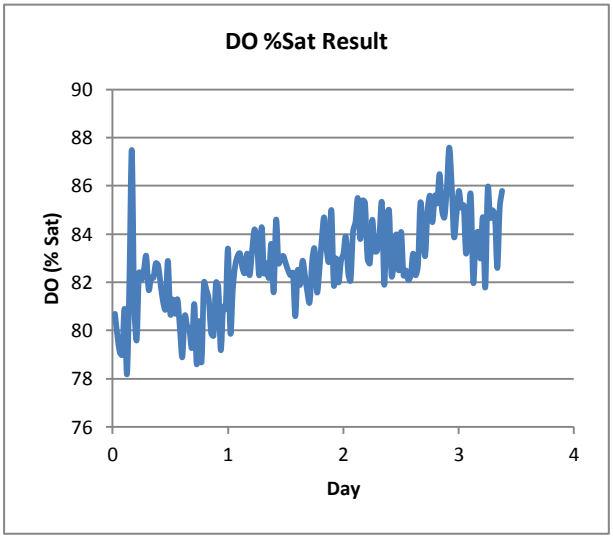

G2 - 4-5-2 3LPBR DS1930 W-WO MB 100cc Air

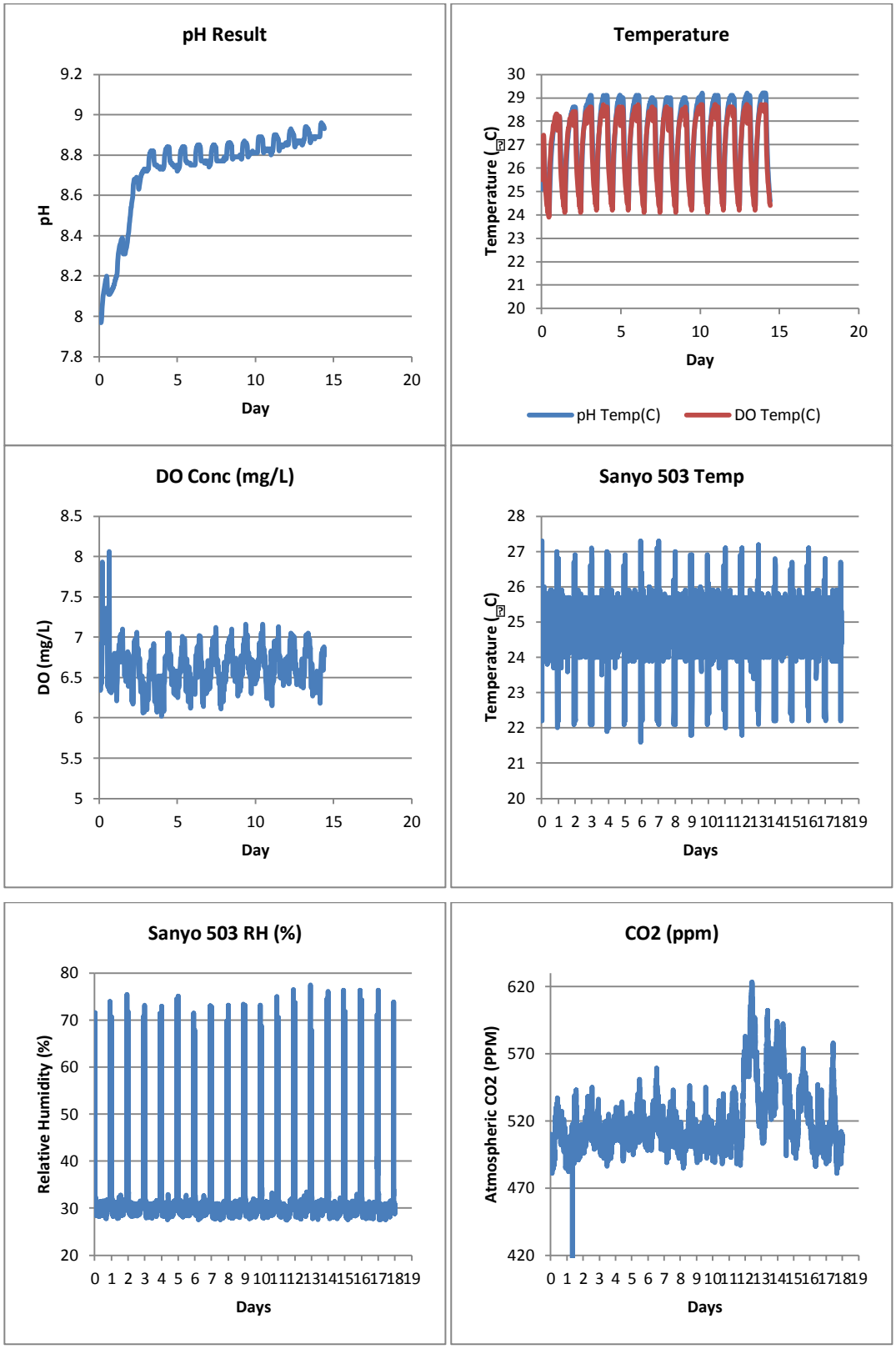

G3 - 4-5-3 3LPBR DS1930 No Air Ambient test

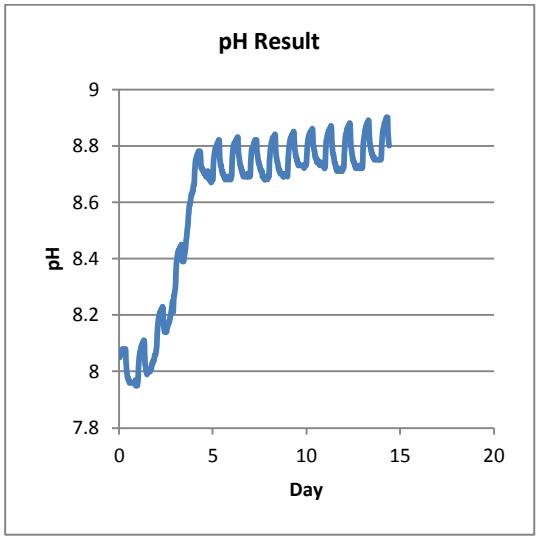

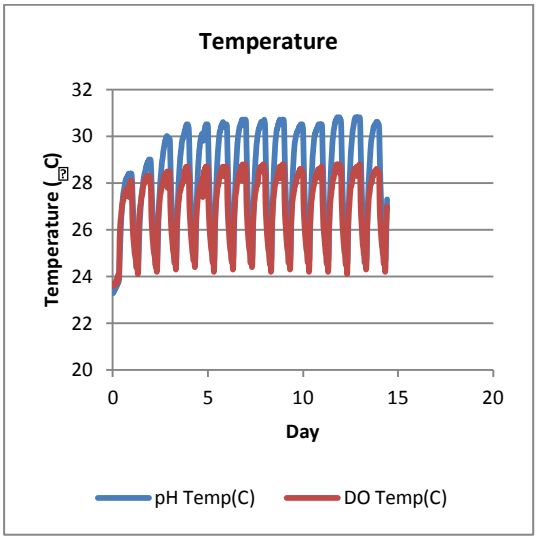

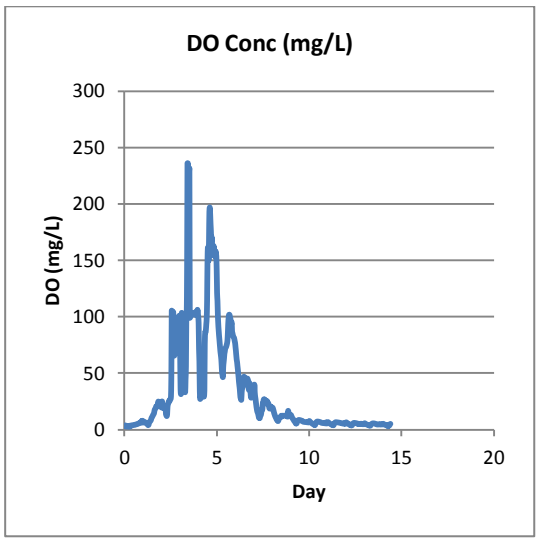

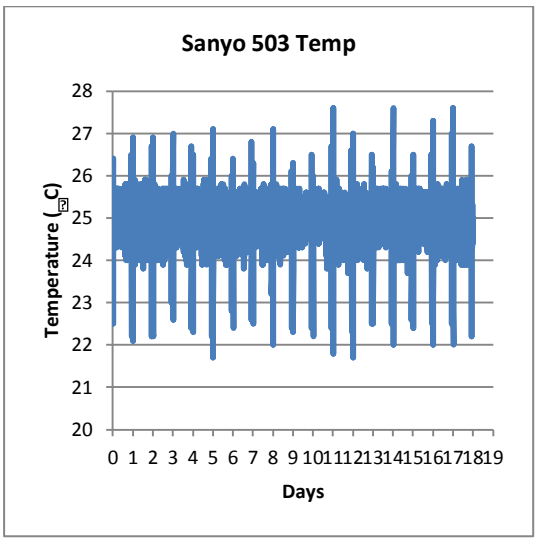

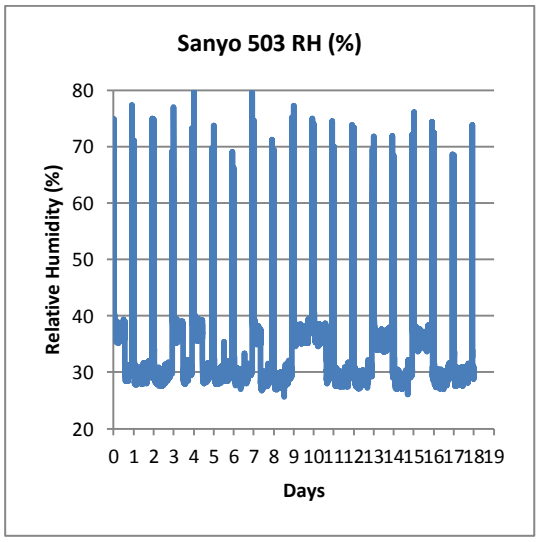

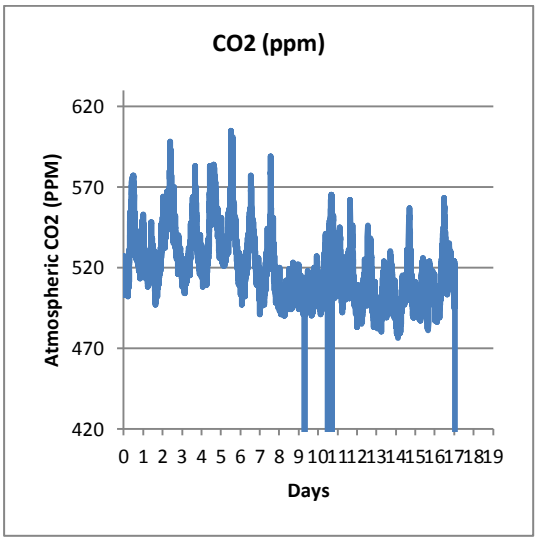

G4 - 4-5-5 3LPBR DS1930W-WO MB 100cc Air CO2

Reactor 1 - Non oscillated, then 100% CO2 at end

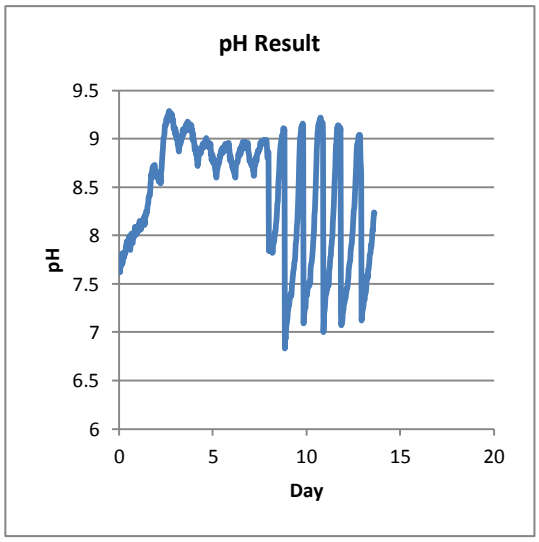

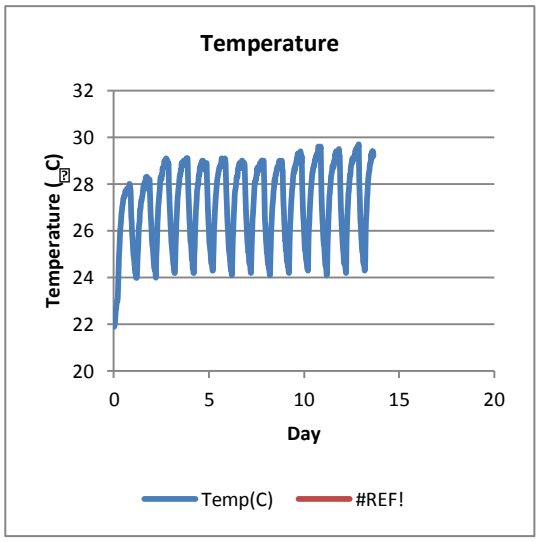

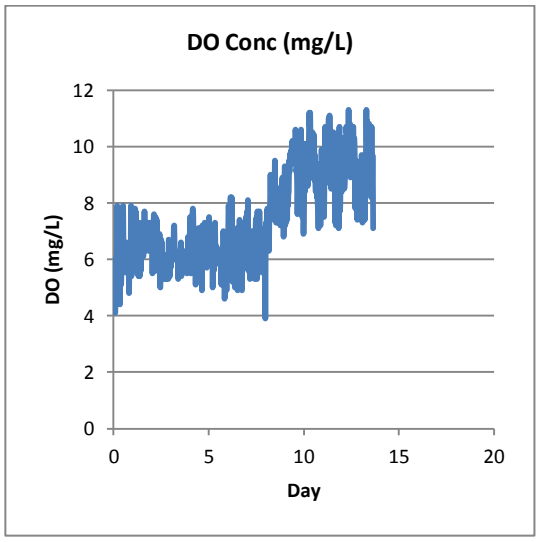

Reactor 2 - Oscillated

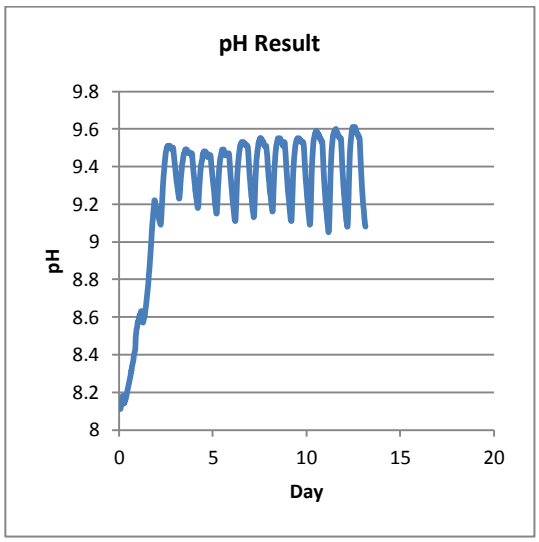

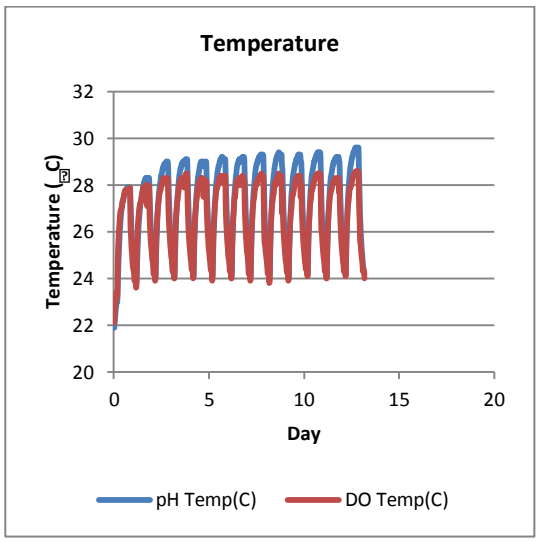

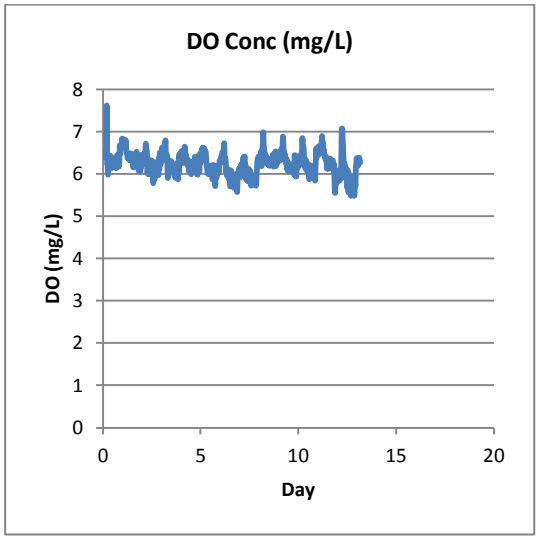
DO Conc (mg/L)
DO (mg/L)
0
1
2
3
4
5
6
7
8
0
5
10
15
20
Day

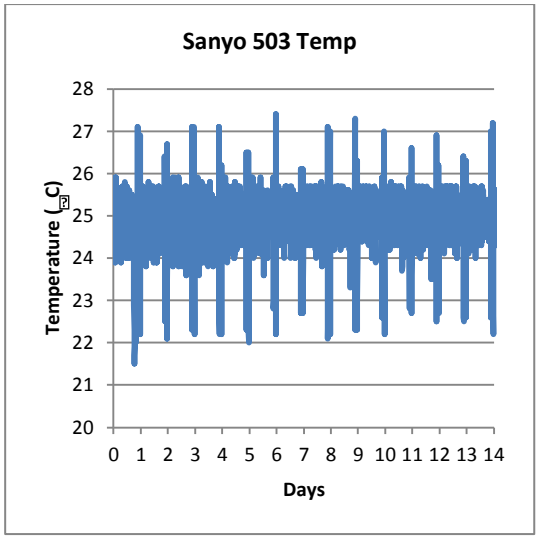
Sanyo 503 Temp
Temperature (_C)
20
21
22
23
24
25
26
27
28
0 1 2 3 4 5 6 7 8 9 10 11 12 13 14
Days

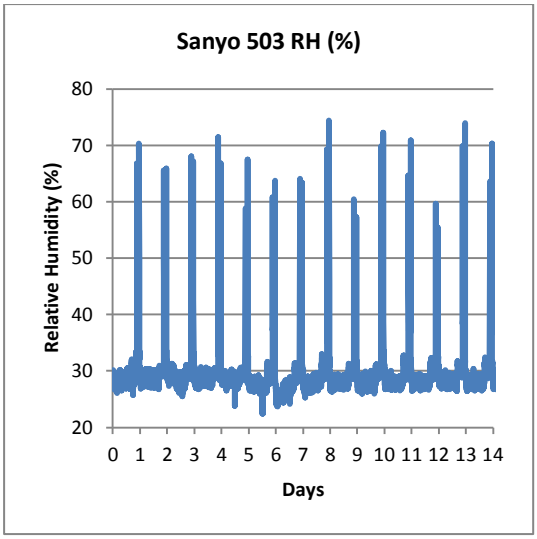
Sanyo 503 RH (%)
Relative Humidity (%)
20
30
40
50
60
70
80
0 1 2 3 4 5 6 7 8 9 10 11 12 13 14
Days

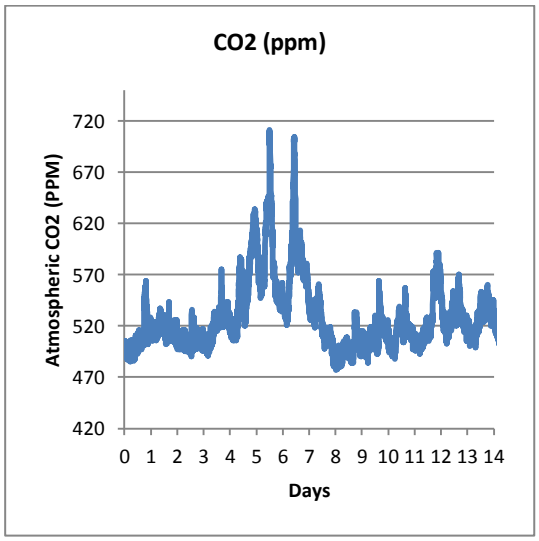
CO2 (ppm)
Atmospheric CO2 (PPM)
420
470
520
570
620
670
720
0 1 2 3 4 5 6 7 8 9 10 11 12 13 14
Days

G5 - 4-8-2 MKII MPBR DS1930 W-WO Air 2-5cc

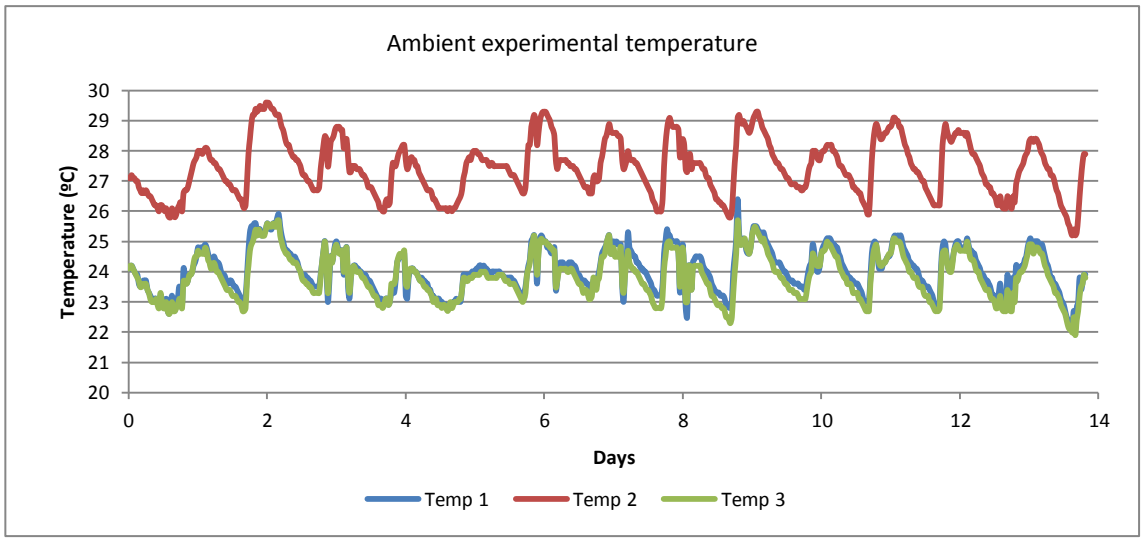

G6 - 4-8-3 MKII MPBR DS1930 0-20cc Air

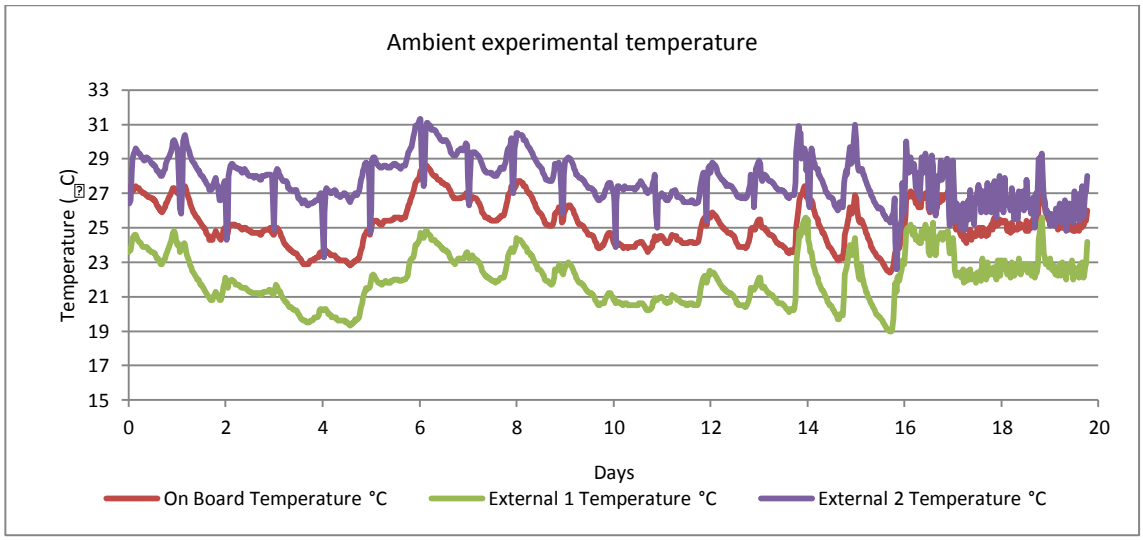

G7 - 4-8-4 MKII MPBR DS1930 0-20cc CO2

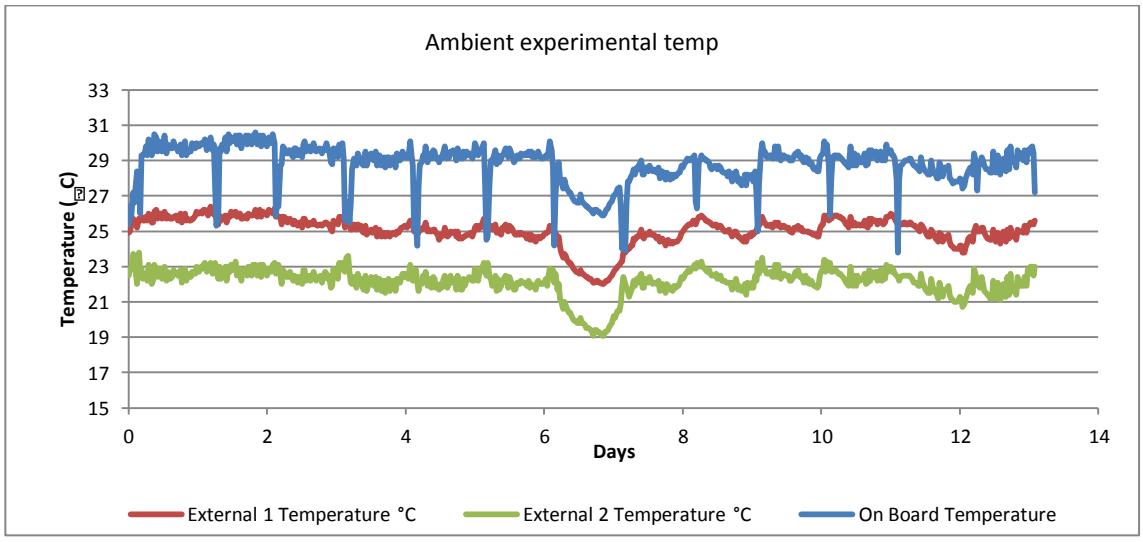

G8 - 4-8-5 MKII MPBR DS1930 10cc Air Osc vs Norm

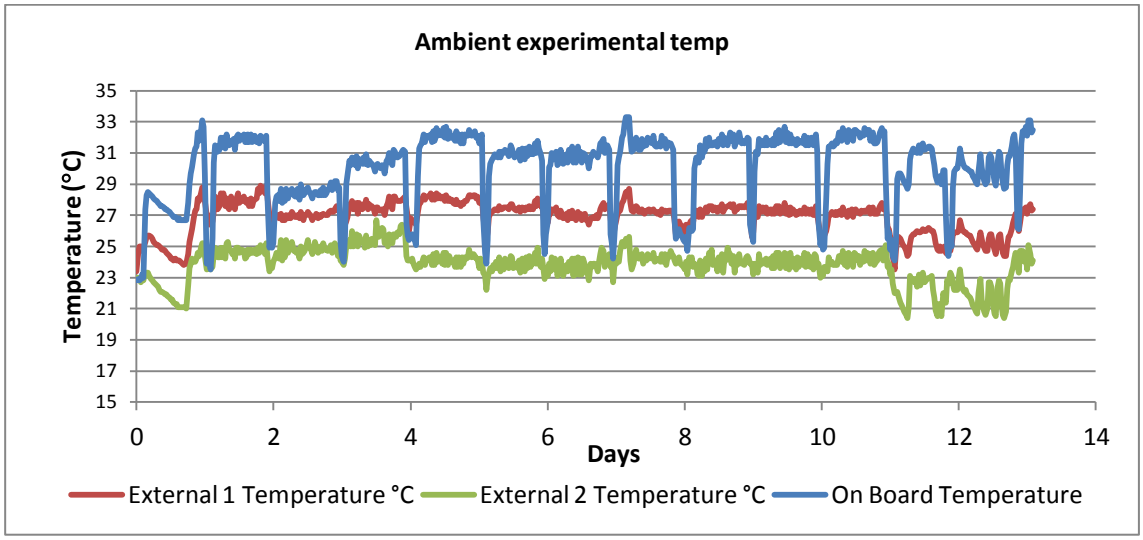

G9 - 4-8-6 MKII MPBR DS1930 5cc Air Osc vs Norm

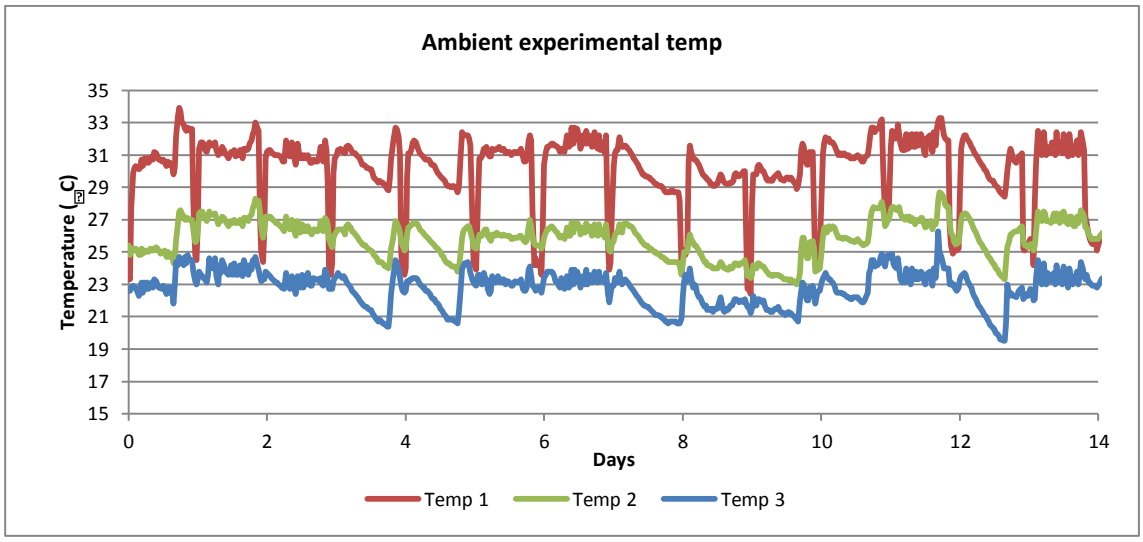

H - k_La graphs

H1 - DO Water

Non Oscillated

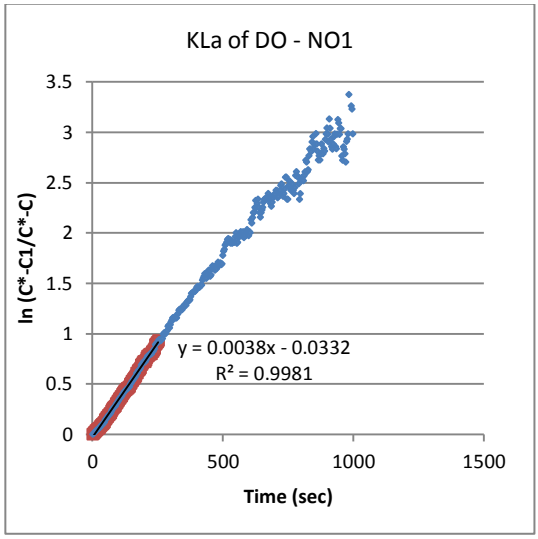

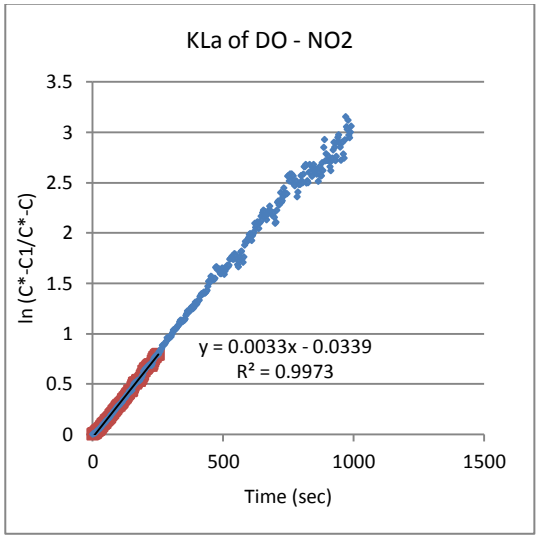

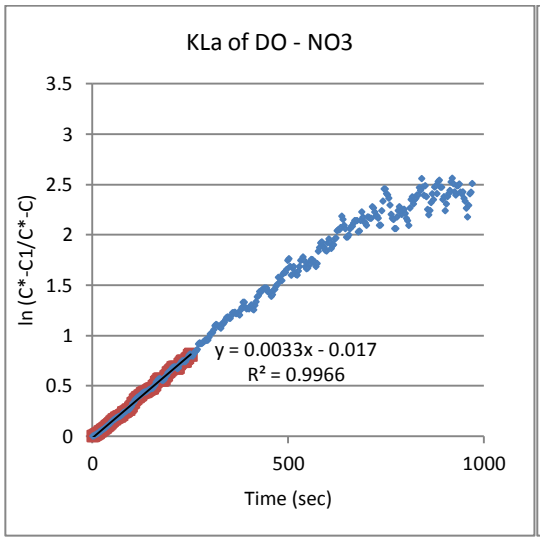

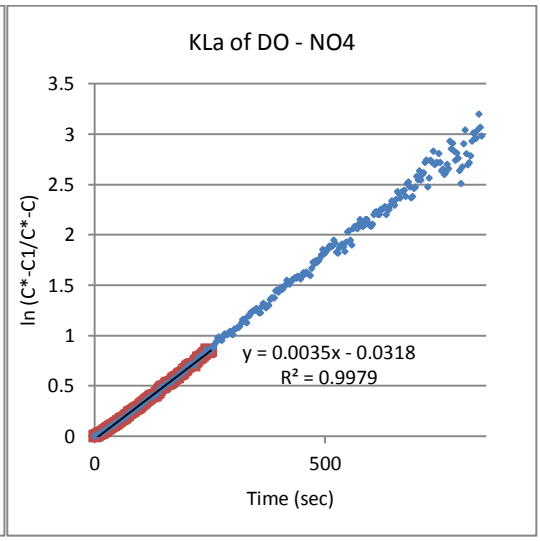

Oscillated

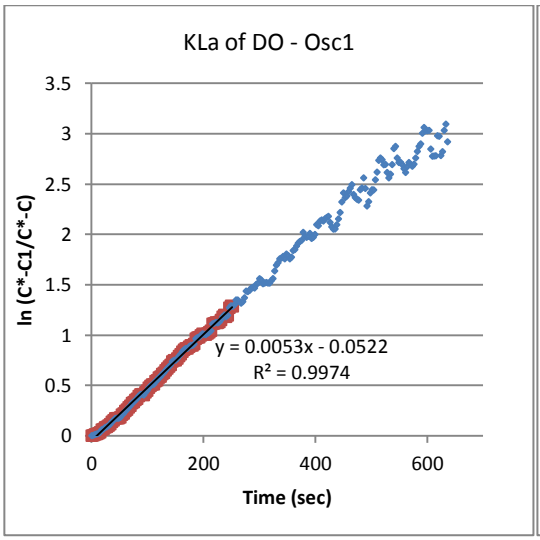

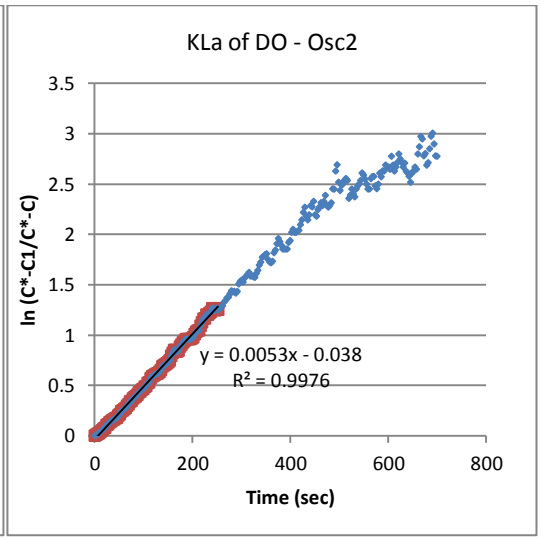

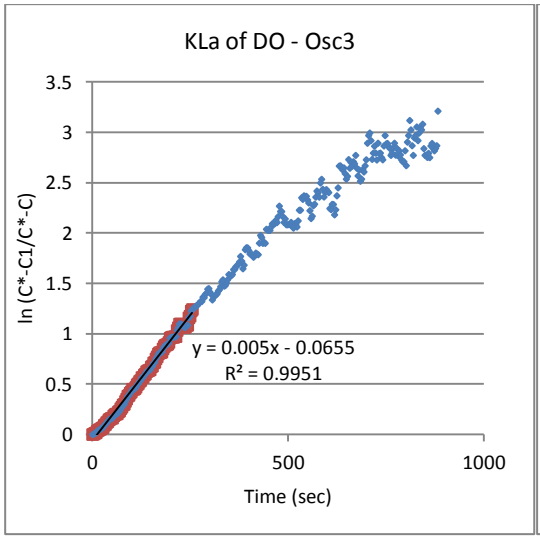

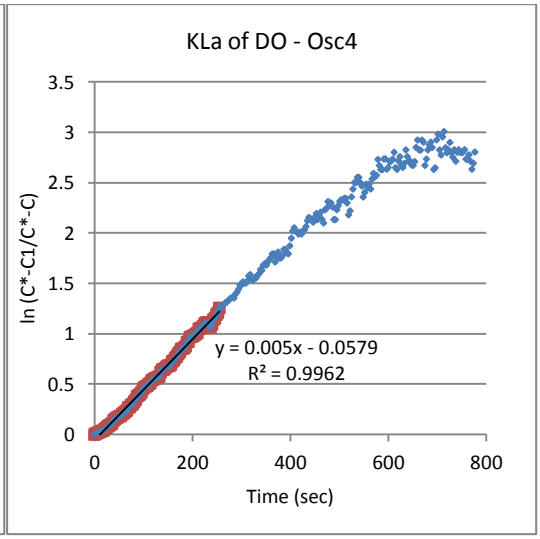

H2 - DO Water + 1M NaCl

Non Oscillated

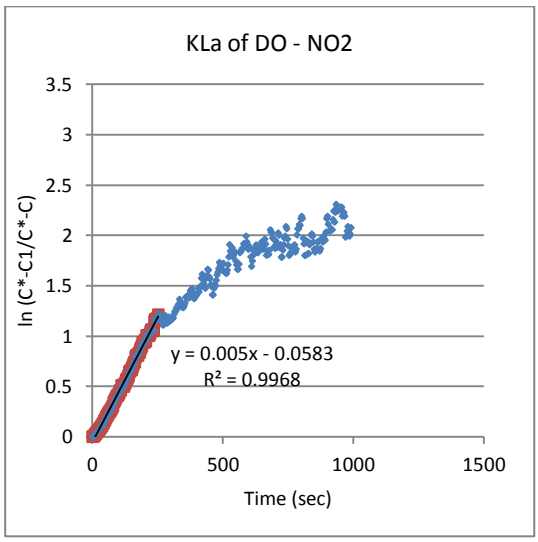

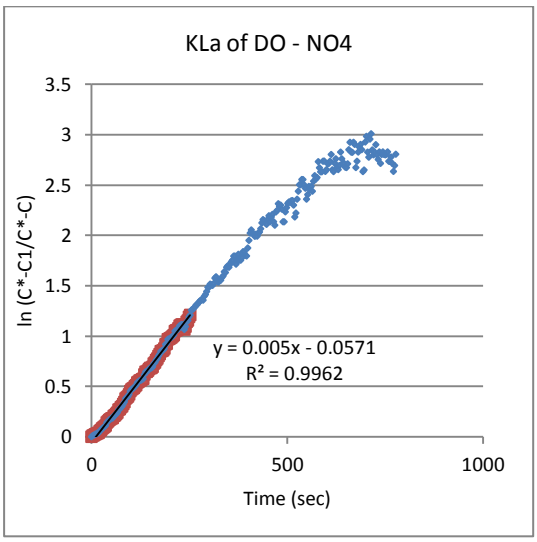

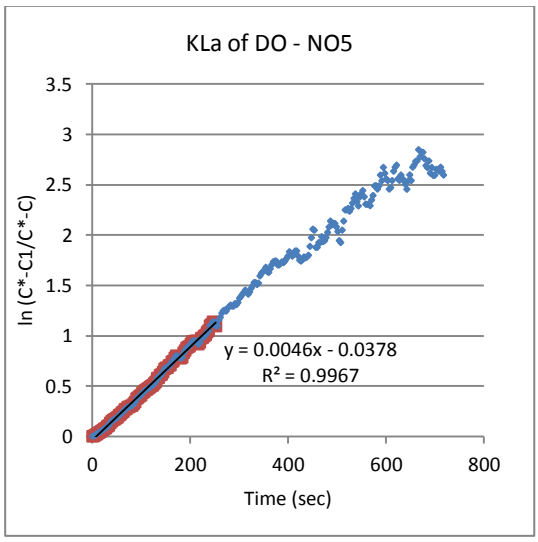

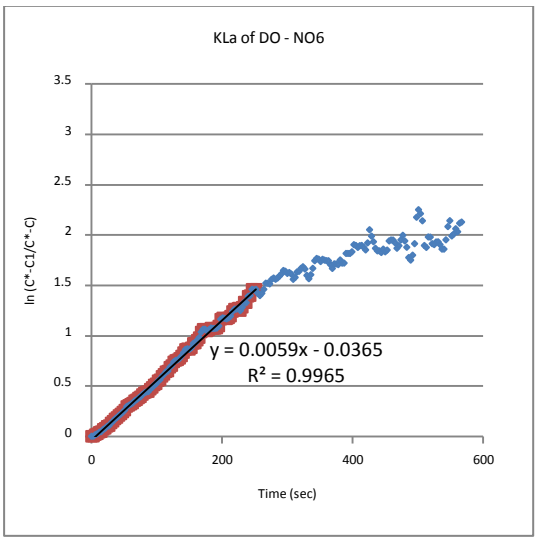

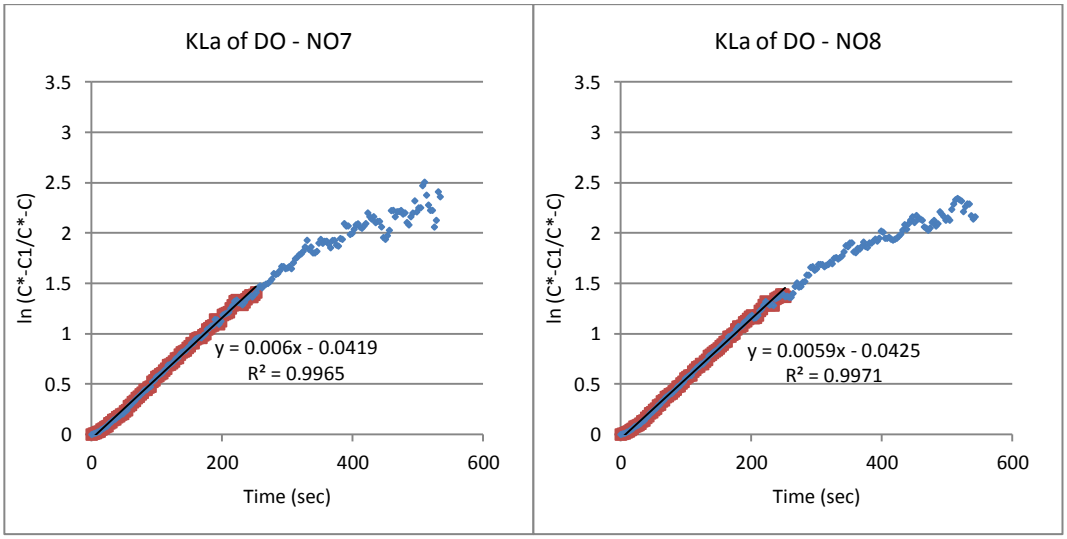
KLa of DO - NO7
ln (C*-C1/C*-C)
y = 0.006x - 0.0419
R² = 0.9965
Time (sec)
KLa of DO - NO8
ln (C*-C1/C*-C)
y = 0.0059x - 0.0425
R² = 0.9971
Time (sec)

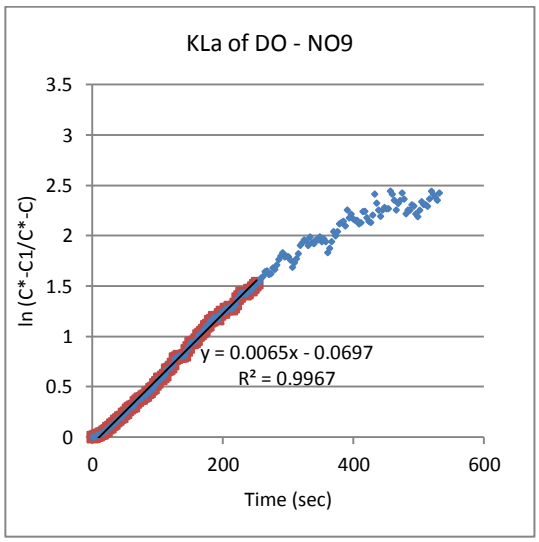
KLa of DO - NO9
ln (C*-C1/C*-C)
y = 0.0065x - 0.0697
R² = 0.9967
Time (sec)

Oscillated

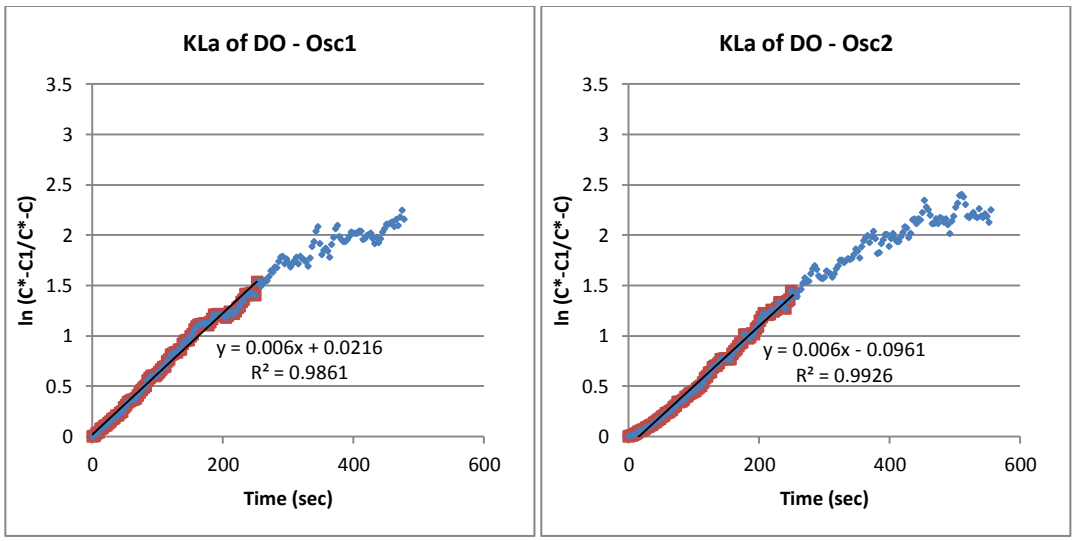
KLa of DO - Osc1
ln (C*-C1/C*-C)
y = 0.006x + 0.0216
R² = 0.9861
Time (sec)
KLa of DO - Osc2
ln (C*-C1/C*-C)
y = 0.006x - 0.0961
R² = 0.9926
Time (sec)

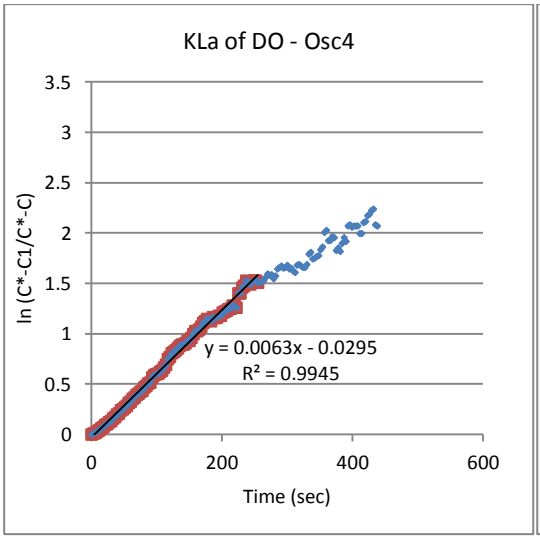
KLa of DO - Osc4
ln (C*-C1/C*-C)
Time (sec)
y = 0.0063x - 0.0295
R² = 0.9945

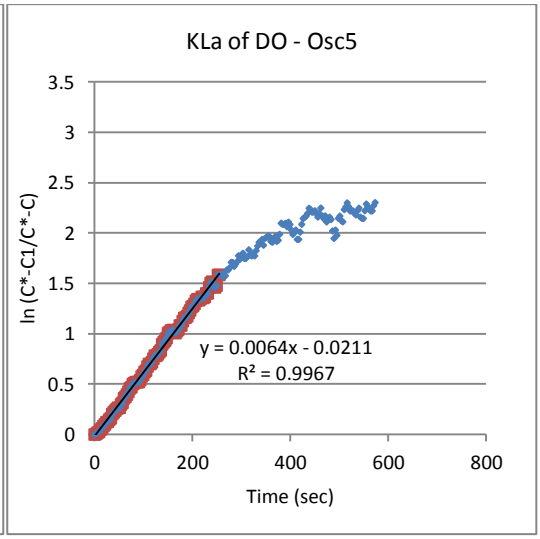
KLa of DO - Osc5
ln (C*-C1/C*-C)
Time (sec)
y = 0.0064x - 0.0211
R² = 0.9967

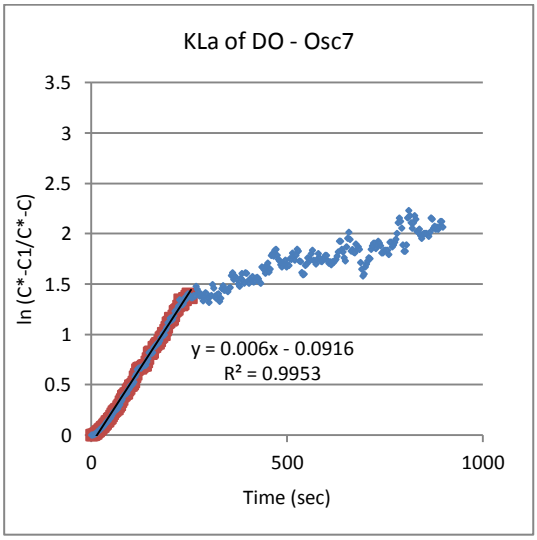
KLa of DO - Osc7
ln (C*-C1/C*-C)
Time (sec)
y = 0.006x - 0.0916
R² = 0.9953

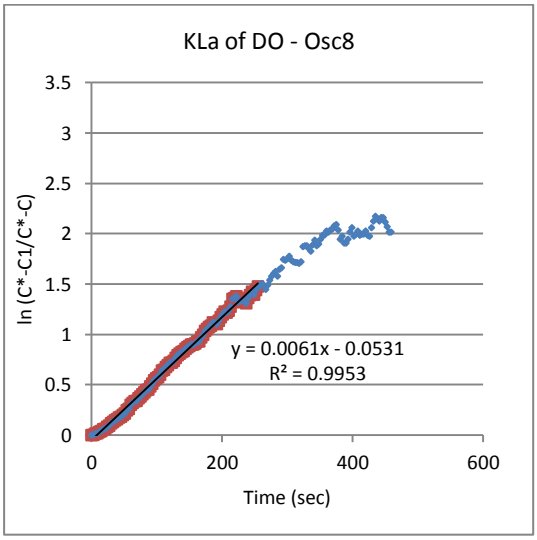
KLa of DO - Osc8
ln (C*-C1/C*-C)
Time (sec)
y = 0.0061x - 0.0531
R² = 0.9953

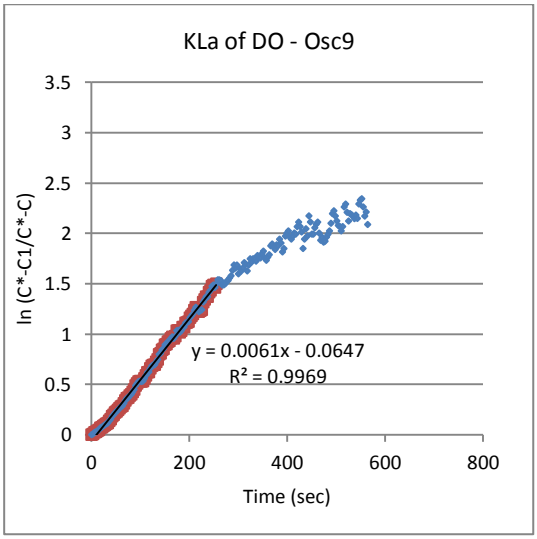
KLa of DO - Osc9
ln (C*-C1/C*-C)
Time (sec)
y = 0.0061x - 0.0647
R² = 0.9969

H3 - DO 1M NaCl Dunaliella Medium

Non Oscillated (NO), Oscillated(Osc)

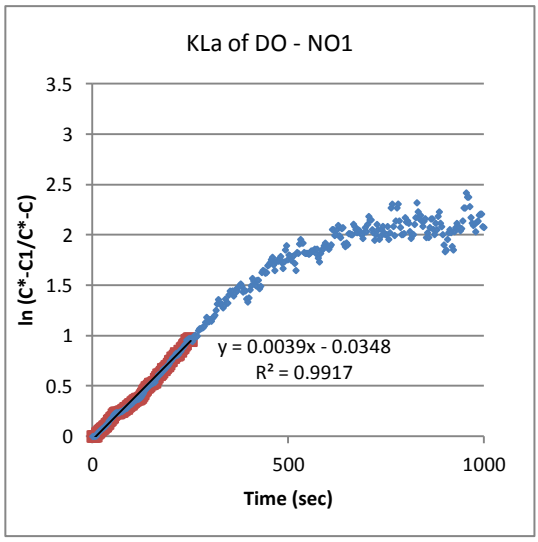

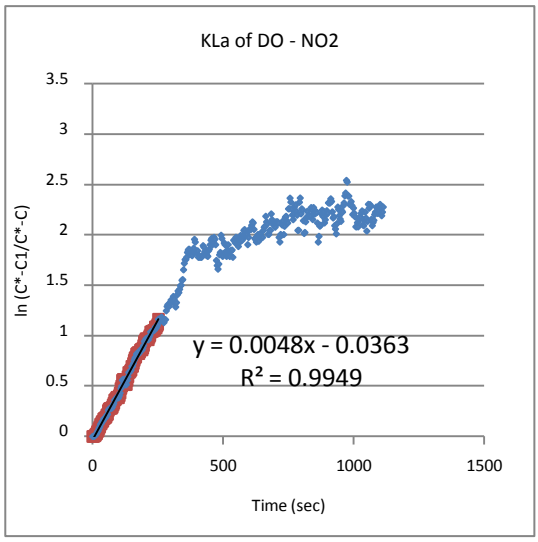

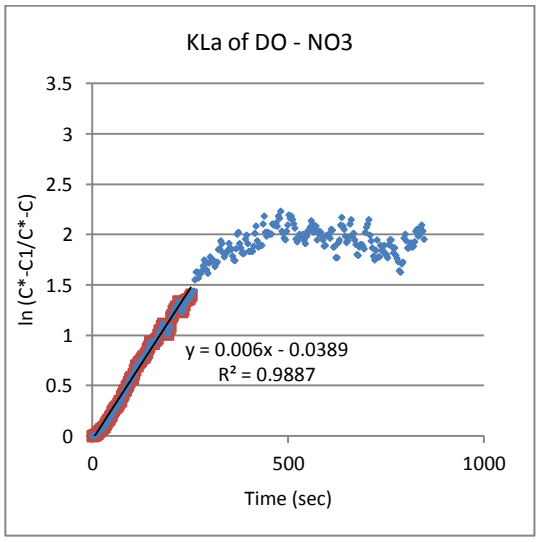

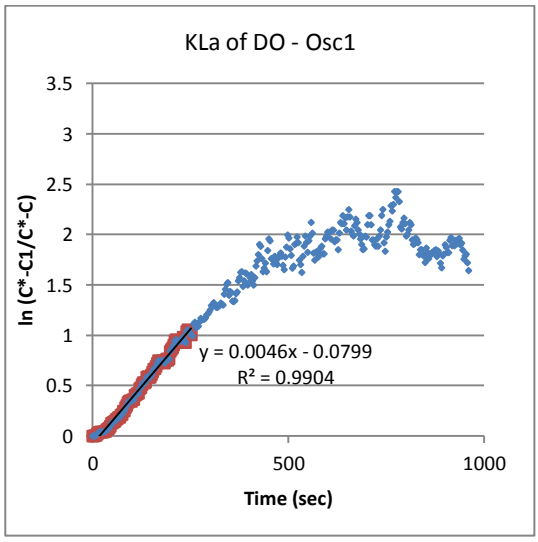

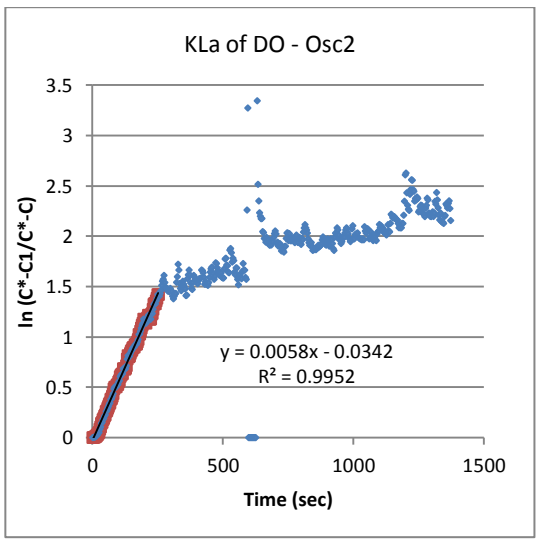

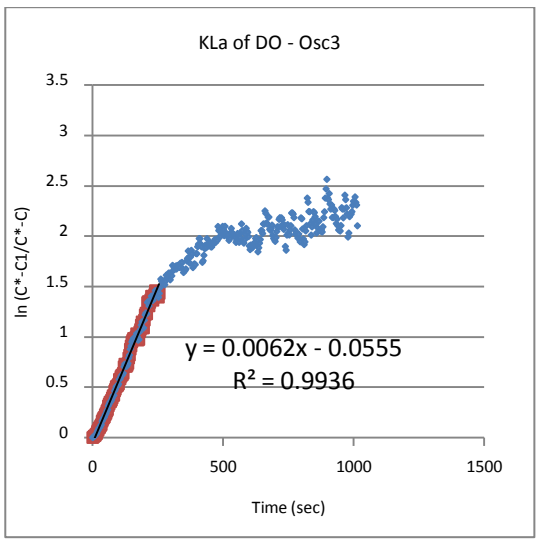

H4 - pHWater

Non Oscillated (NO), Oscillated(Osc)

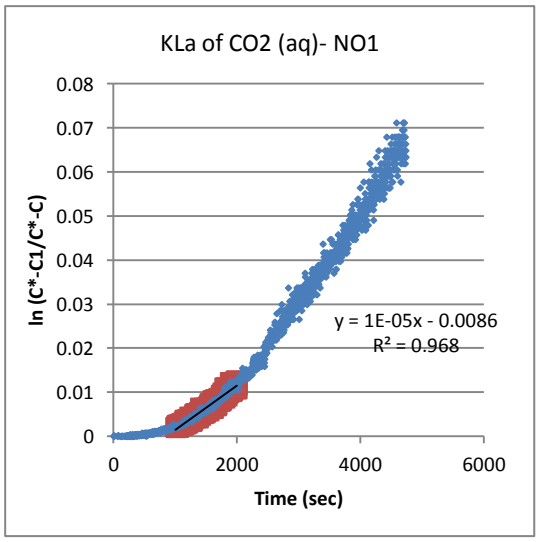

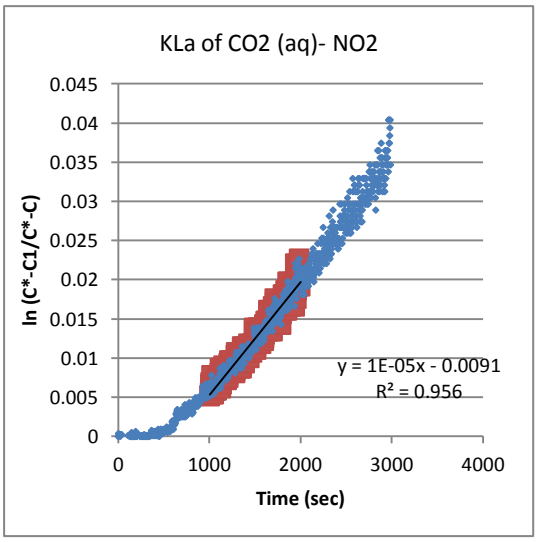

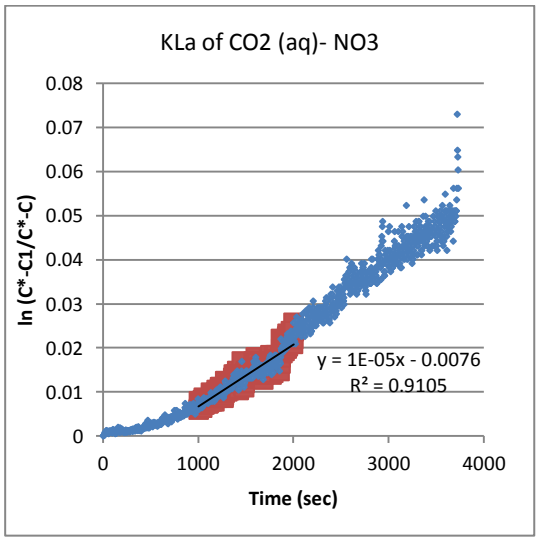

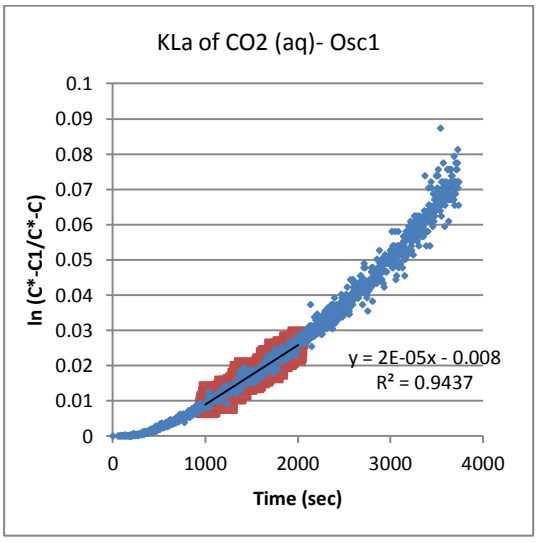

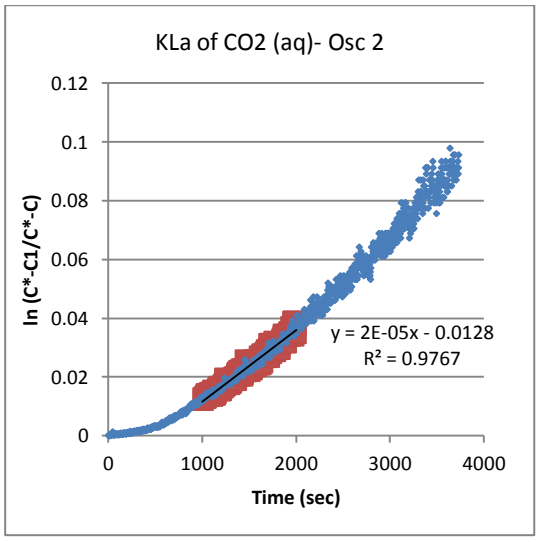

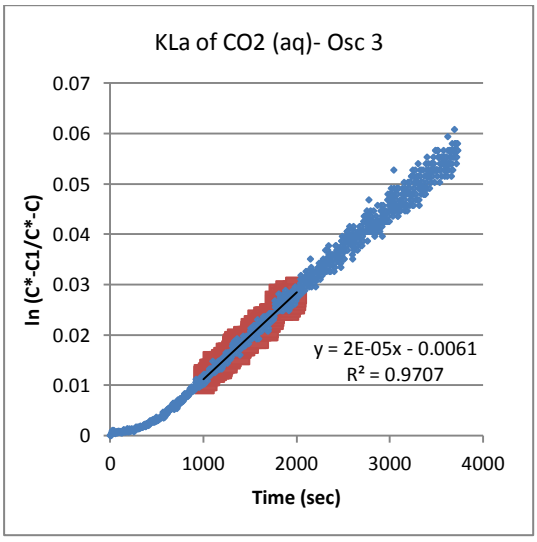

H5 - pHWater + 1M NaCl

Non Oscillated (NO), Oscillated(Osc)

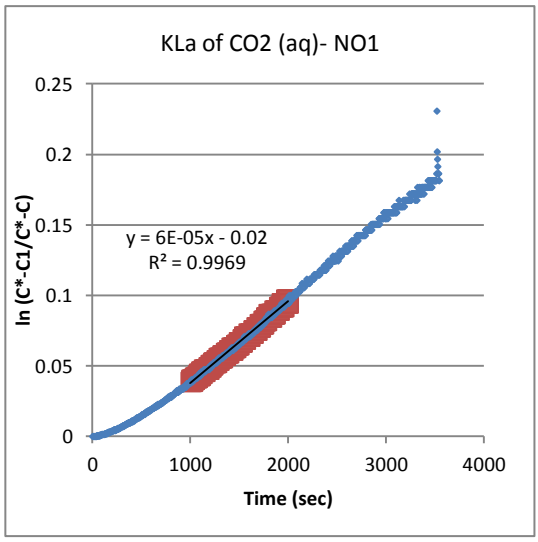

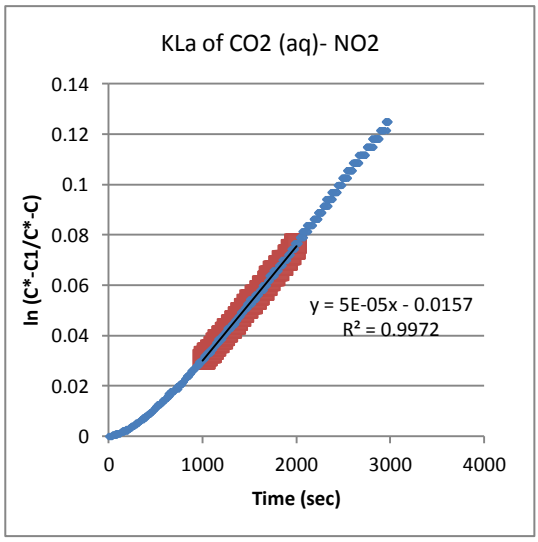

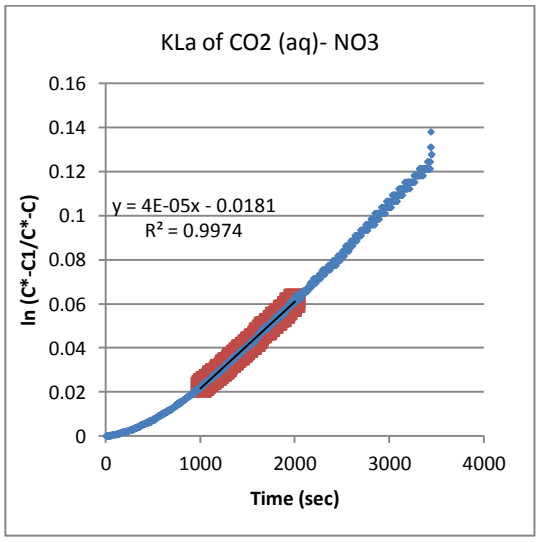

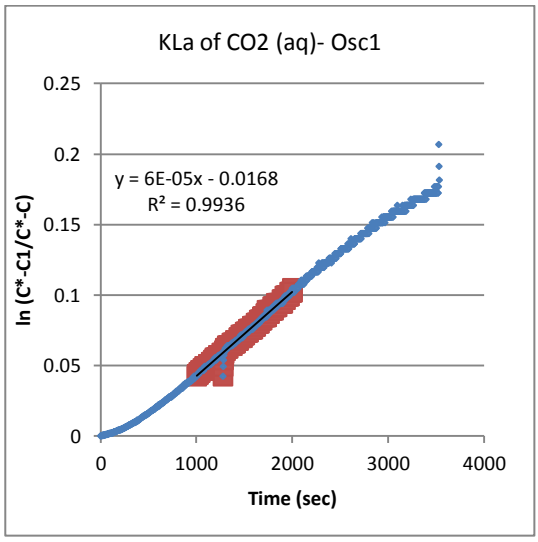

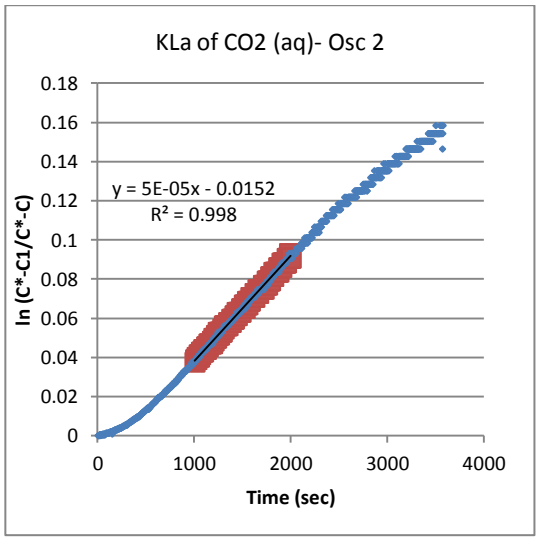

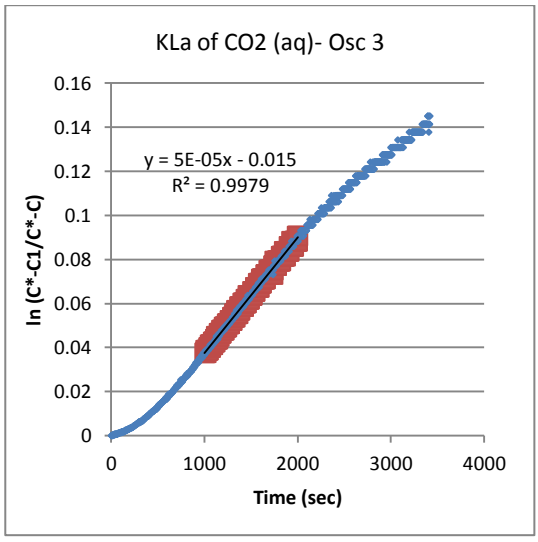

I - Previous Nile Red methodology

Sample Reading 96 Well: Monitoring of neutral lipid production in growing cultures using NR was performed in a 96 well plate format based on the work byAlonzo and Mayzaud (1999), Bertozzini, et al. (2011), Chen, et al. (2009), Cooksey, et al. (1987), Elsey, et al. (2007), Gardner, et al. (2011), Gardner, et al. (2012), Pick and Rachutin-Zalogin (2012).NR measurements were begun when *D. salina* cultures had reached a sufficient level of growth, to produce a clear fluorescence signal ($1x10^6$ cells /ml). For subsequent readings cultures were diluted to the same concentration to avoid self shading. 2 ml sampleswere removed from each growth vessel and added to a 2 ml Eppendorf tube. The culture was then centrifuged for 5 min at *3000*g and the supernatant was discarded immediately when finished. An equivalent volumeof fresh mediumwas then used to replace the discarded supernatant and the algal pellet was re-suspended. 3 x 200µL was then transferred from each 2ml tube and added to the plate as the 'unstained cells', labelled as the appropriate growth vessel/condition. 2 x 200µL was then discarded from each tube, leaving 1ml of culture. In the layout below, S1-1, S1-2 and S1-3 are separate growth vessels under the same conditions, each sample with the same condition is equally spaced to ensure any transient effects due to sequential reading delays on the plate are averaged:

Repeat Readings (R)		Nile Red Stained Samples (S)											
		S1-1	S2-1	S3-1	S4-1	S1-2	S2-2	S3-2	S4-2	S1-3	S2-3	S3-3	S4-3
		1	2	3	4	5	6	7	8	9	10	11	12
R1	A	200	200	200	200	200	200	200	200	200	200	200	200
R2	B	200	200	200	200	200	200	200	200	200	200	200	200
R3	C	200	200	200	200	200	200	200	200	200	200	200	200
	D	0	0	0	0	0	0	0	0	0	0	0	0
	E	0	0	0	0	0	0	0	0	0	0	0	0
R1	F	200	200	200	200	200	200	200	200	200	200	200	200
R2	G	200	200	200	200	200	200	200	200	200	200	200	200
R3	H	200	200	200	200	200	200	200	200	200	200	200	200
		S1-1	S2-1	S3-1	S4-1	S1-2	S2-2	S3-2	S4-2	S1-3	S2-3	S3-3	S4-3
		Un-Stained Samples (S)											

The optical density was measured at 595 nm, using a Wallac Victor 2 Multi-label Plate reader (see 'Shaken OD @ 595 (1.0s)' section 2.2.2.3) set at a fixed temperature of 25°C. 20 µL of optimised NR/acetone dye was then added to each 2 ml tube and the cultures were quickly whirlmixed. The timer was then started. The contents of the tubes were then transferred to a multi-pipette reservoir (1 tube per well), then the samples were then transferred to the corresponding 'Nile Red Stained Cells' using the multichannel pipette (3 x 200 µL, per concentration). At the appropriate time interval for peak fluorescence all wells were read using

an excitation wavelength of 490 nm and emission of 580 nm with a 0.1 s integration. All other original nile red procedures used the same mixing and transfer steps.

J - Solidworks CAD drawings

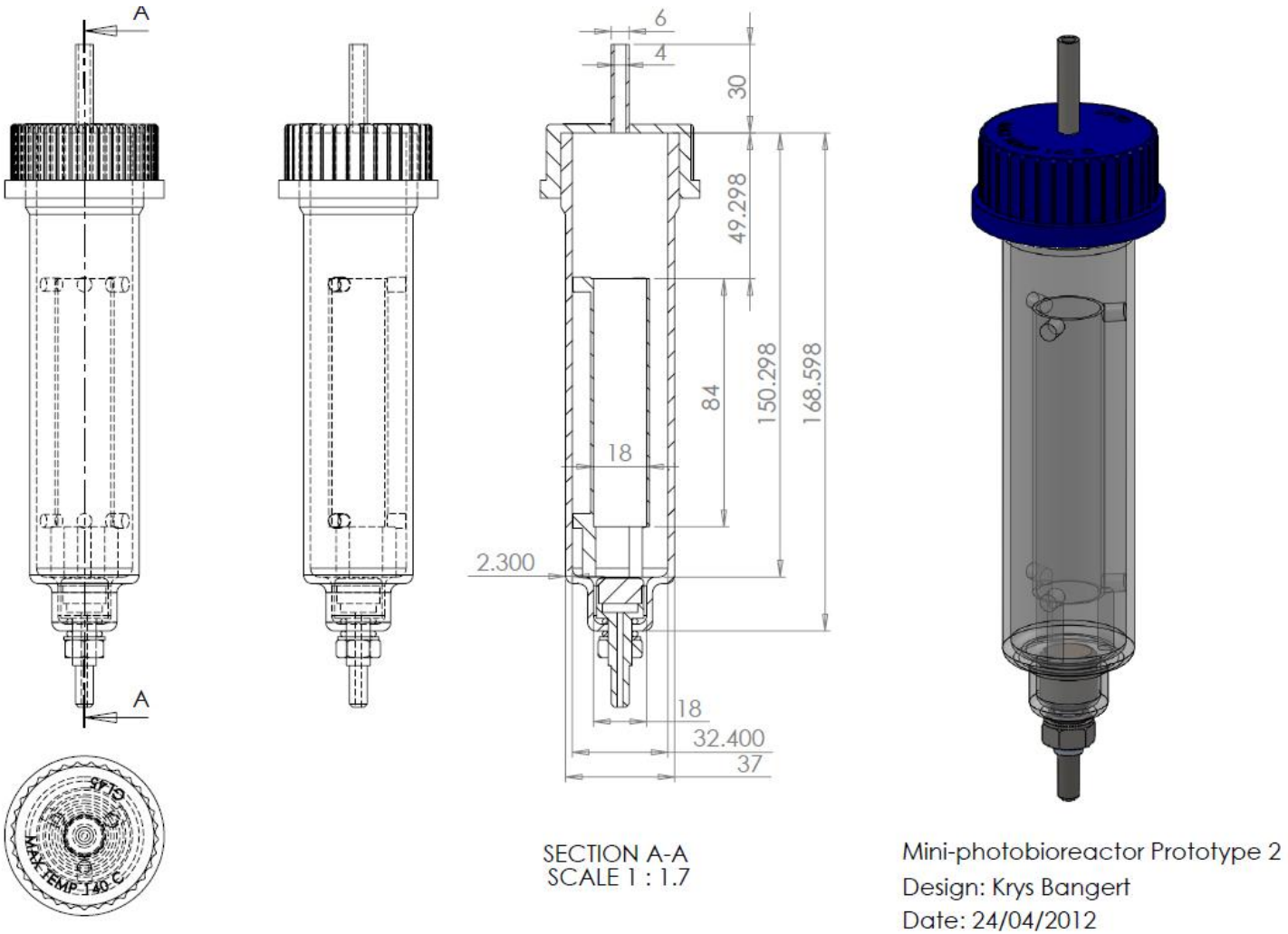

SECTION A-A
SCALE 1 : 1.7

Mini-photobioreactor Prototype 2
Design: Krys Bangert
Date: 24/04/2012

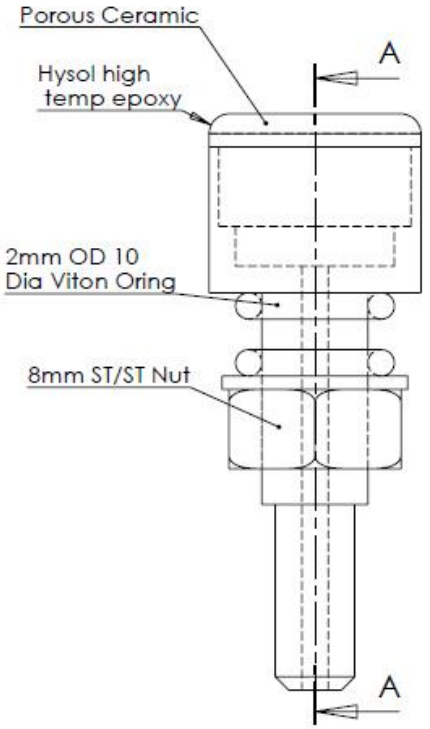

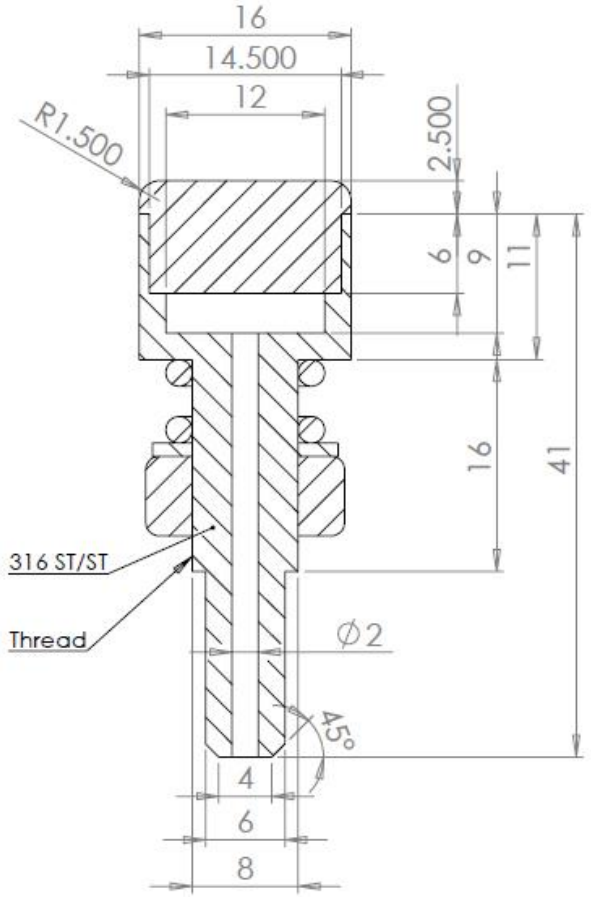

SECTION A-A
SCALE 2 : 1

Mini-sparger design v5

Krys Bangert & Andy Patrick

Jan 2012

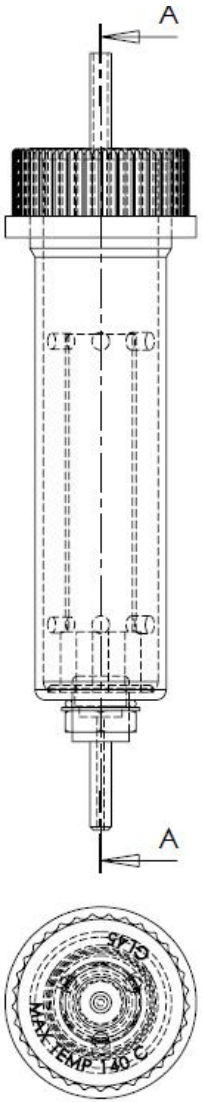

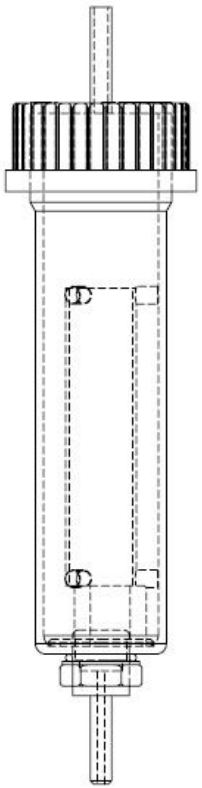

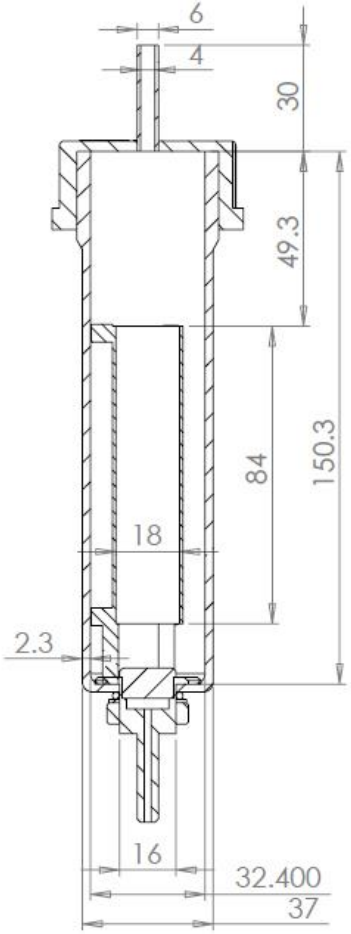

SECTION A-A
SCALE 1 : 1.7

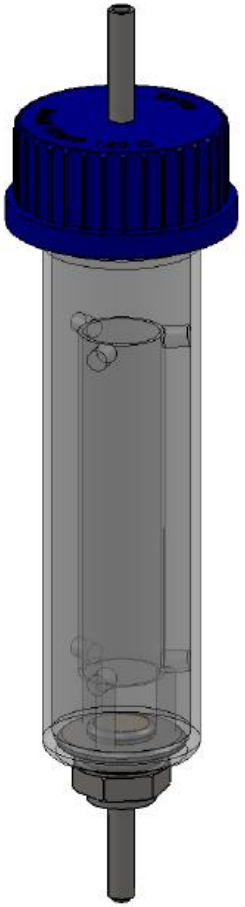

Mini-photobioreactor Prototype 3
Design: Krys Bangert
Date: 21/08/2013

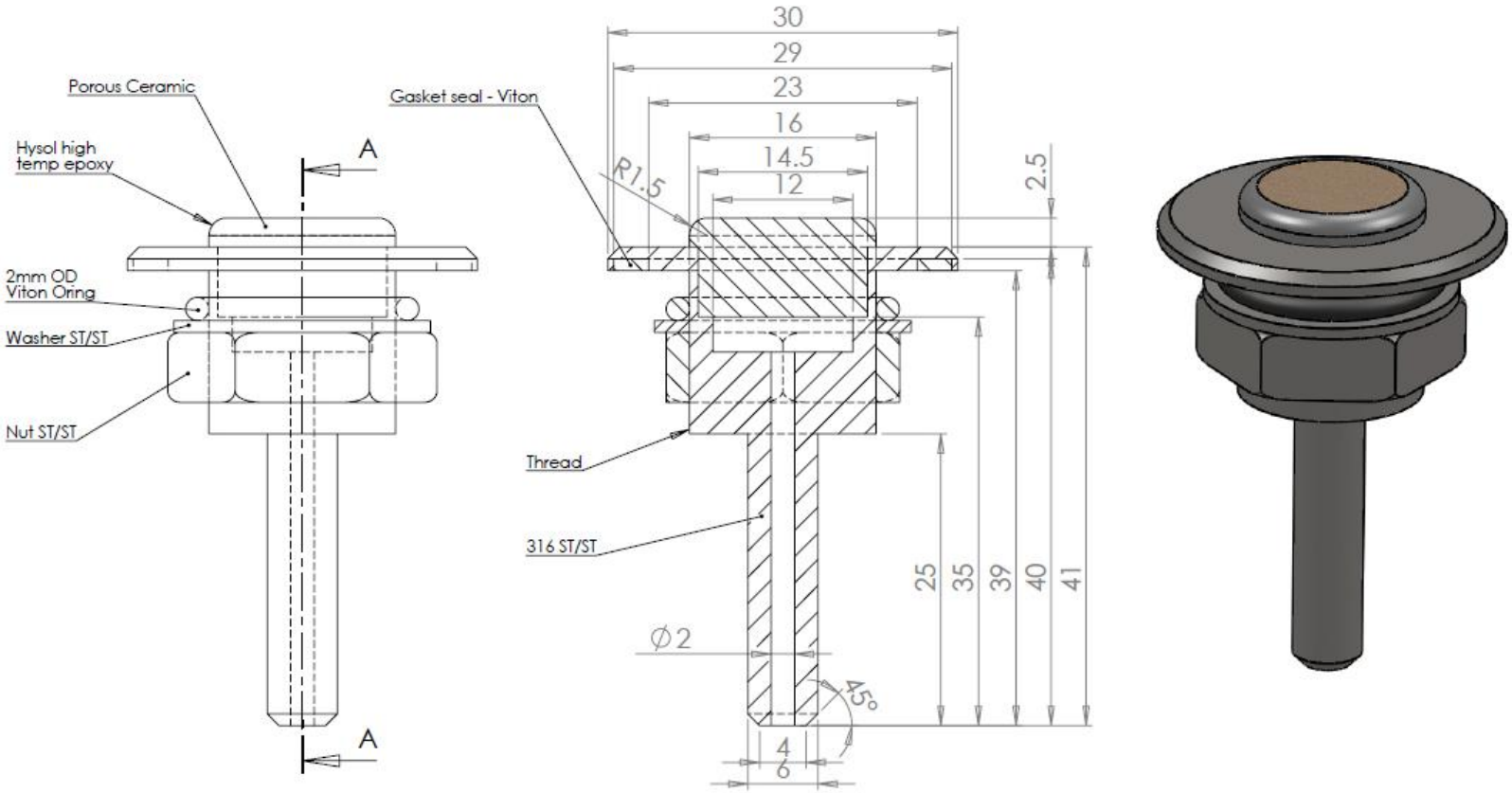

SECTION A-A
SCALE 2 : 1

Mini-sparger design v6

Krys Bangert

August 2013

K - COMSOL Mk II mini photo-bioreactor flow data

Data from 1M NaCl tests at four different flow rates, 2D liquid velocity surface colour profiles (m/s) with vector arrows.

K1 Fluid flow at 5 cc/min air with bubble sizes 0.2-1mm in water + 1M NaCl at 25°C

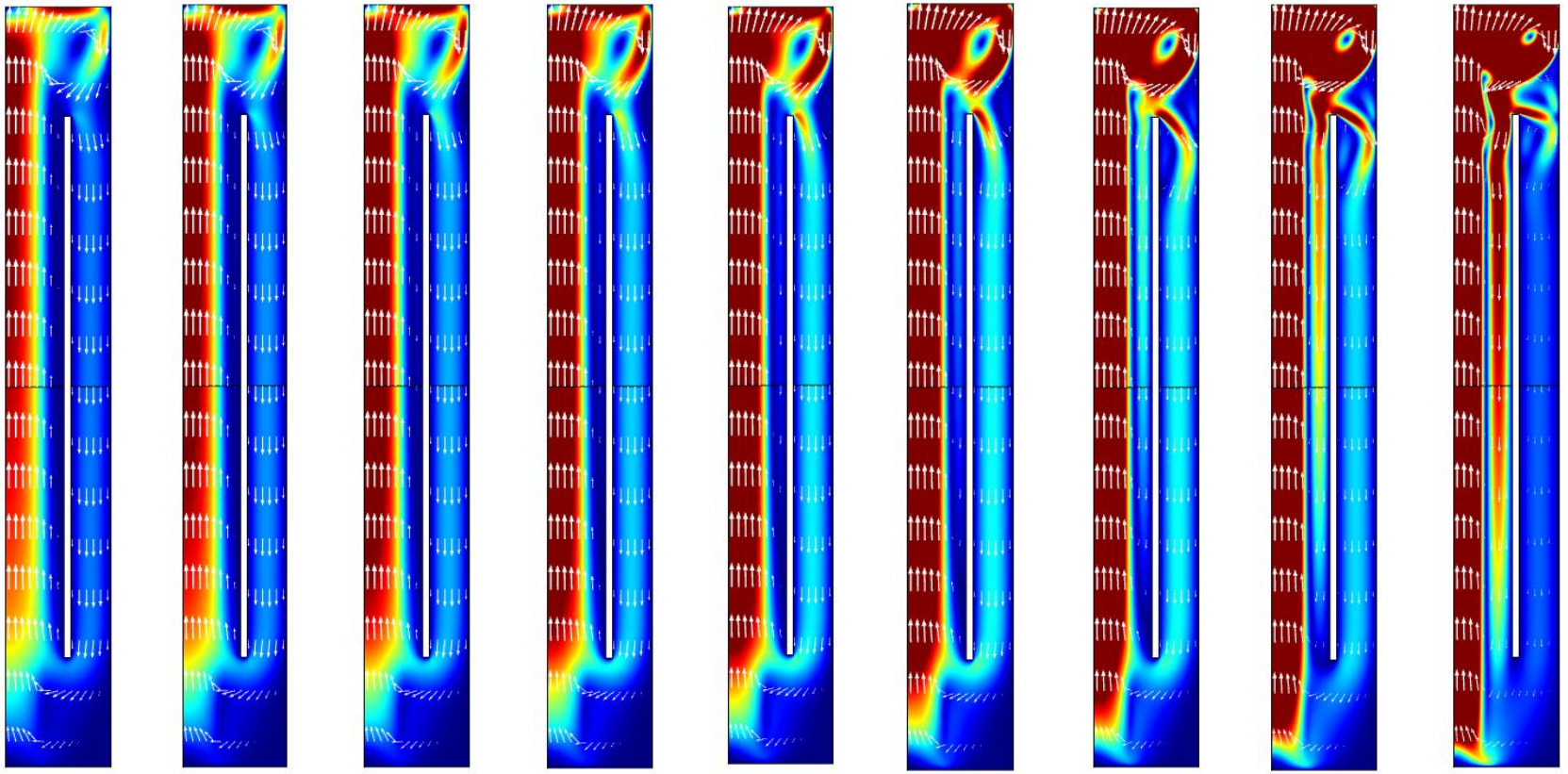

K2 Fluid flow at 10 cc/min air with bubble sizes 0.2-1mm in water + 1M NaCl at 25°C

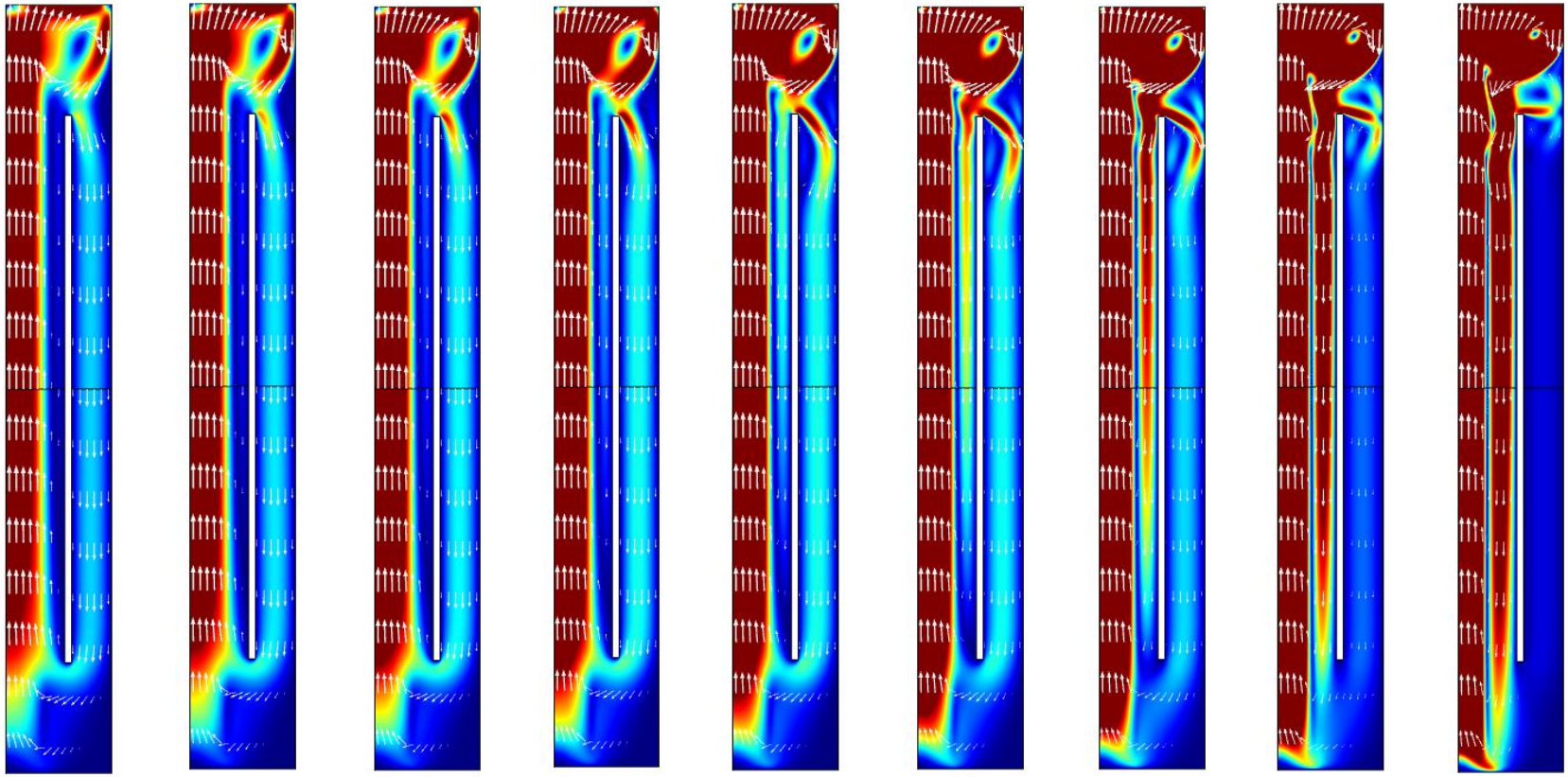

K3 Fluid flow at 15 cc/min air with bubble sizes 0.2-1mm in water + 1M NaCl at 25°C

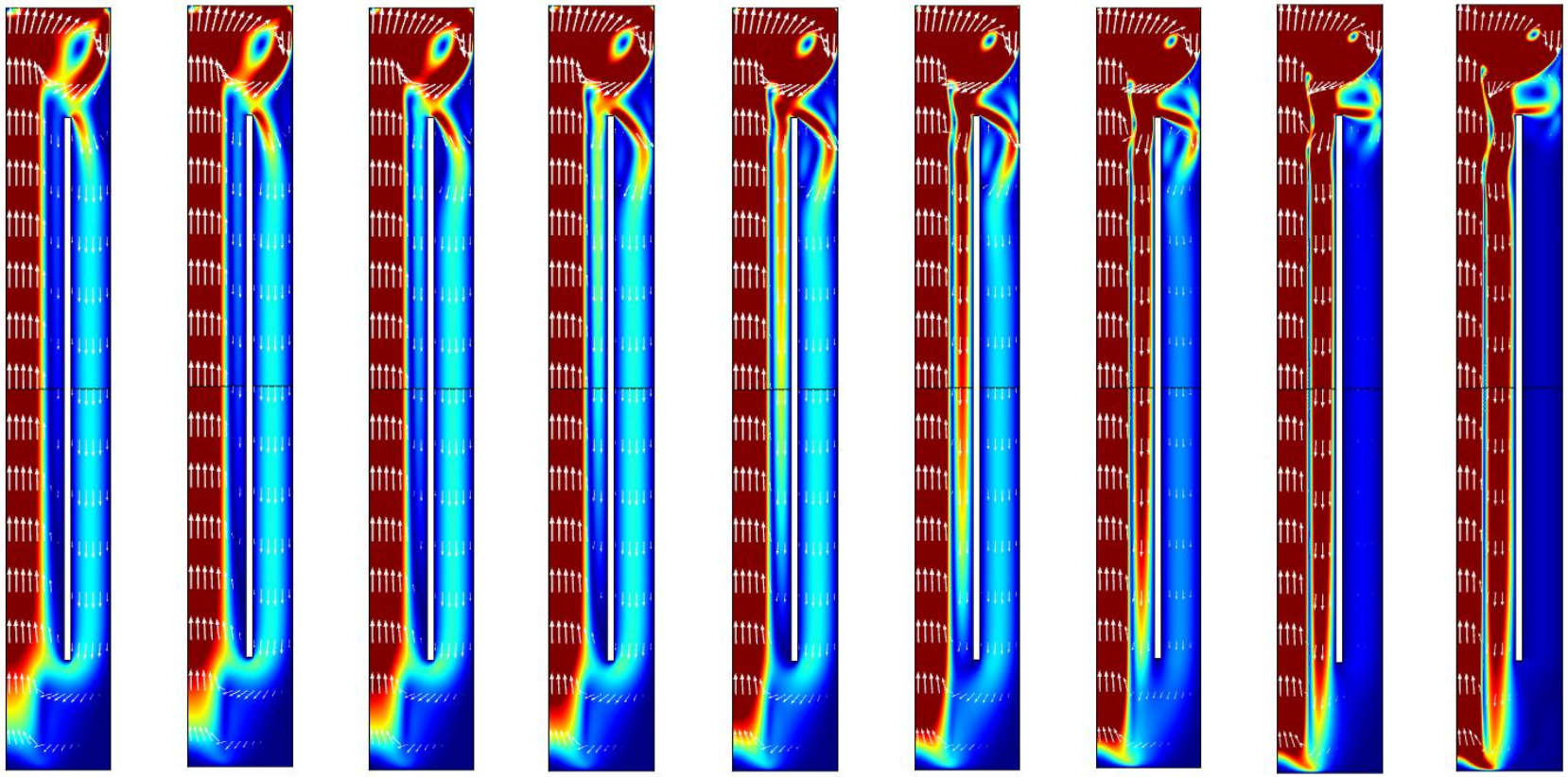

K4 Fluid flow at 20 cc/min air with bubble sizes 0.2-1mm in water + 1M NaCl at 25°C

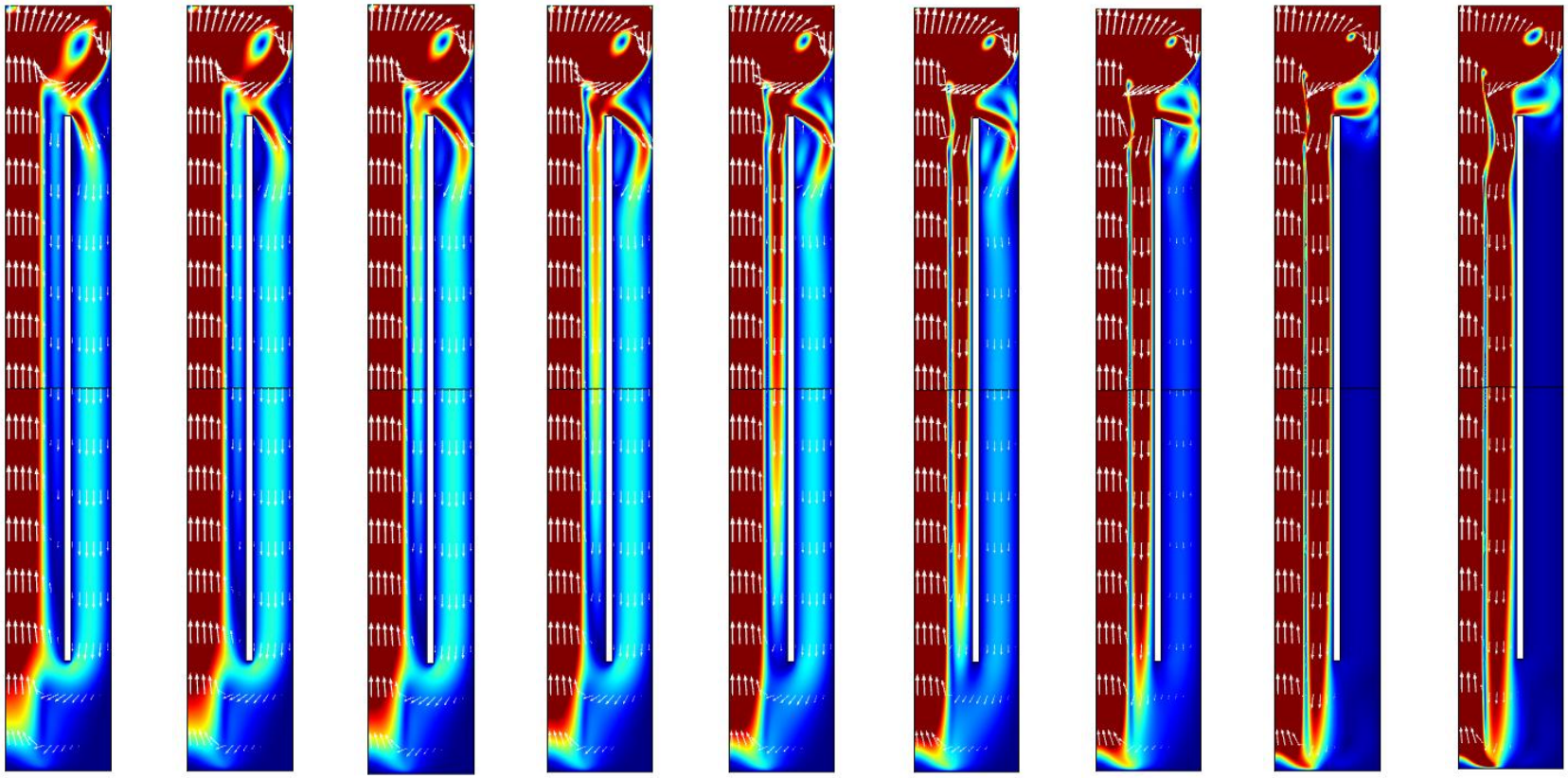

Isolation and culture of high lipid content substrains of *Dunaliella salina*CCAP 19/18 using flow cytometry

J.Shepherd[1], K. Bangert and D. J. Gilmour[2]

Department of Molecular Biology and Biotechnology

University of Sheffield,

Sheffield S10 2TN

[1] Present address:

[2] Corresponding Author: D.J.Gilmour@Sheffield.ac.uk

00 44 114 222 4412

Summary

The marine microalga *Dunaliella salina* CCAP19/18 is a promising candidate for the production of biodiesel, which can be used as an alternative to fossil fuels. Algae do not require agricultural land or fresh water and the production of biodiesel from algae does not introduce new hydrocarbons into the atmosphere. However, to be more economically viable, strains of algae must be used with the maximum potential for lipid production, along with features of rapid growth rates, tolerance of extreme physical conditions and ease of harvesting lipids. However, the maximum lipid content in this species is not as high as in other species which are albeit more difficult to handle or less hardy. We aimed to elucidate which growth conditions would provide maximal lipid accumulation per unit biomass of *D. salina*. We found that culture conditions of 1 M NaCl, 5 mM nitrogen and high light intensity provided maximum lipid accumulation in *D. salina*. We then isolated and cultured high-lipid producing substrains of *D. salina* using flow cytometry techniques to naturally select high lipid producing cells without the need for genetic manipulation.

Introduction

Algal biofuel, along with other renewable energy sources such as solar and wind power, is increasingly considered to be a viable alternative to fossil fuel. The culture of algae as feedstock for biodiesel has many advantages – it uses land unsuitable for agriculture, can use ocean and wastewater thereby not draining freshwater resources, and can be effectively a carbon neutral process. However, large scale production of algal biofuel is not currently an inexpensive method of fuel production due in part to high start up costs. More investment into basic research should provide an economically viable method of producing algal biodiesel on a

large scale. The lipids that accumulate in the algal cells used for biofuel production are the triacylglycerols (TAGs). After extraction of TAGs from the algae, TAGs undergo transesterification by reacting with an alcohol in the presence of a catalyst to form esters (biodiesel) and glycerol, also a potentially useful byproduct.

The marine microalga*Dunaliella* is a promising candidate for biofuel production. Most strains can grow at salinities of up to 4 M NaCl (approximately 8 times the salinity of seawater), making it ideal for growing in outdoor open ponds with minimal contamination from other organisms, which cannot withstand such high salinity. However, the maximum level of lipid accumulation in *Dunaliella* is generally shown to be about 20-30% of dry weight, which is not as high as some other potential algae, such as *Nannochloropsis oculata* or *Botryococcus braunii*, which have been demonstrated to accumulate ~50% and ~70% lipids respectively [Chiu, Wolf].

In this study, we wished to identify which growth conditions would induce the highest lipid accumulation in *D.salina* in relation to biomass productivity, and then identify, isolate and culture high lipid producing substrains, with tolerance of difficult physical conditions.

We established growth and survival ranges for *D.* salina 19/18 under a range of stress conditions including light, salinity and nitrogen deprivation. We then identified which stress conditions, or combination thereof, would lead to the highest lipid production per cell. We also demonstrated that Nile Red staining and Flow Cytometry could distinguish high lipid producing cells, and were able to use this technique to determine which stress conditions would lead to populations of cells within each sample with the highest lipid content to augment more traditional methods. Finally, we isolated single high-lipid producing cells from cultures of *D.salina* grown under optimum lipid accumulation conditions using flow cytometry, and cultured these to establish substrains with a high lipid content.

Materials and Methods

Algae

We acquired *D. salina* 19/18, algal class Chlorophycae, from the CCAP culture collection, SAMS, Oban, UK. Algae were cultured in *Dunaliella* growth medium in a constant temperature room at 25°C under continuous light, in 100ml cultures within 250ml flasks.Aseptic techniques were used during the culture of the algae, and samples of the cultures were examined regularly under light microscopy.

Stress conditions

D. salina was subjected to stress conditions either by culture under high irradiance ('high' light intensity = 279 μmol $m^{-2}s^{-1}$, 'low' light intensity = 155 μmol $m^{-2}s^{-1}$, measured with a Quantitherm light meter (Hansatech)), under nitrogen deprivation (0.5 mM N as opposed to the standard 5 mM N), high salinity (1-3 M NaCl) or combinations of the above (Table 1).

Extraction of genomic DNA

Genomic DNA was extracted from 10 ml samples of each algal strain using a Genomic-tip 20/G kit and genomic DNA buffer set (both QIAGEN). DNA pellets obtained were resuspended in 50 μl Tris-EDTA buffer (100 mM Tris-HCl pH 7.5 and 10 mM EDTA pH 8.0) and stored at -20°C

PCR amplification of 18S and 16s rDNA

A 5 μl template of each DNA sample was used in a 50 μl reaction which contained: 2.5 mM $MgCl_2$, 0.2 mM dNTPs, 0.5 units *Taq* polymerase, 1 x PCR buffer and 1 μM each of forward and reverse primers. The reaction mixture underwent an initial melting step at 94°C for 3 mins, followed by 30 cycles of melting at 94°C for 1 min, annealing at 50°C for 1 min, and extension at 72°C for 2 mins, prior to a final extension step at 72°C for 5 mins. Primer sequences were as follows: 18S Forward, 5' GTAGTCATATGCTTGTCTC 3' [Kong et al], 18S Reverse 5' CACCTACGGAAACCTTGTTACGACTT 3' [Maddison et al], 16S Forward 5'

CCGAATTCGTCGACAACAGAGTTTGATCCTGGCTCAG 3', 16S Reverse 5' CCCGGGATCCAAGCTTACGGCTACCTTGTTACGACTT 3' [Weisburg et al].

PCR products were visualised by running out 15 μl of each on a 1% TAE agarose gel. Products ranged from ~1750bp to ~2200bp in size.

Purification of PCR products

The remaining PCR products after running out (35 μl) were cleaned up using a quick PCR purification kit (Qiagen) resulting in 35 μl of each cleaned product, which were stored at 4°C until being sent for sequencing.

Sequencing of PCR products:

12 μl (** concn?) of each cleaned PCR product, along with 20 μl (** concn?) each of 18S forward and reverse primers used in the PCR reaction were sent to the University of Sheffield Core Genomics Facility for sequencing. Sequences were viewed using the software FinchTV v.1.4.0 (Geospiza).

Growth measurement

Algal growth was monitored by measuring optical density of 1 ml samples in disposable polystyrene cuvettes [Sartstedt] on a daily basis over a period of 21 days, at 600 nm. Absorbance was measured using a HEλIOS α spectrophotometer (Unicam). Chlorophyll was extracted from a 1ml sample of each culture using a solvent (acetone) and the absorbance read at 645nm and 663 nm. The following equation was used to determine the amount of chlorophyll present in each sample (in μg ml^{-1}):

OD_{645} x 202 = x

OD_{663} x 80.2 = y

(x + y)/2 = μg chlorophyll ml^{-1}

Nile Red staining

Sample OD was adjusted to 0.2 at 720 nm, then 10 μl of 250 μg ml^{-1} Nile Red solution added to 3 ml algal culture [Cooksey, Elsey].

Fluorescence Microscopy

Algae were viewed under oil immersion (100x objective) using a Nikon Eclipse E400 microscope with a Nikon DXM1200 camera and Lucia G image acquisition software (v.4.82, Laboratory Imaging Ltd.). Since lipid droplets stained with Nile Red are known to fluoresce around 528 nm on excitation at 450 -500 nm [Greenspan *et al.,* 1985], we examined results using the FITC fluorescence filters set (excitation 490 nm, emission 520 nm).

Flow cytometry

1 ml samples of both unstained and Nile Red stained samples were run though an LSR II flow cytometer (Becton Dickinson) and analysed using BD FACSDiva Software v6. Samples were excited at a wavelength of 488 nm, and we simultaneously collected fluorescence intensity data from several different emission filter sets; 530 nm, 575 nm, 730 nm and 780 nm. To isolate single cells using flow cytometry, a BD FACSAria cell sorter (Becton Dickinson) was used. Single cells were sorted into 96-well plates (one per well) which contained 100μl of media. The plates were then cultured at 25°C under constant illumination. Any evaporated media was replaced on a daily basis.

Measurement of total lipid content

30ml samples of algal culture were centrifuged for 10 mins at 3000 rpm.Each pellet was resuspended in 5 ml of distilled water and centrifuged again for 5 mins at 3000 rpm, the supernatant discarded, and each pellet re-suspended in 5 ml of distilled water.Samples were centrifuged again for 5 mins at 3000 rpm, supernatant discarded and each pellet re-suspended in 1 ml of distilled water. 1.5 ml Eppendorf tubes (one per sample) were labelled and weighed.

The 1 ml samples were transferred to the pre-weighed Eppendorf tubes. The tubes were sealed by cutting lids off extra Eppendorf tubes, making a hole in each lid, and using to seal the tubes containing samples. Samples were then frozen at minus 80 °C overnight, then freeze dried (lyophilized) for 24-48 hours. The Eppendorfs were re-weighed to estimate the weight of biomass. 500µl of methanol/chloroform (2:1 v/v) was added to each sample, then samples were sonicated for 1 min on ice. Samples were then centrifuged in the microfuge at full speed for 5 mins and transferred to a fresh Eppendorf.

The supernatant was composed of 2: 1 methanol:chloroform; chloroform and 1% NaCl were added to give 2:2:1 methanol:chloroform:water. Samples were then centrifuged in the microfuge for 2 minutes at full speed. Fresh Eppendorfs were labelled and weighed, and the chloroform phase transferred into the pre-weighed Eppendorfs. Samples were allowed to evaporate overnight or until dry.Eppendorfs were re-weighed and the weight of lipids recovered calculated

Results

Genetic identification of algae

To confirm the identification of our stock cultures, and then to provide a method of continuously monitoring the purity of the cultures as well as identifying substrains which have a high lipid-producing genotype, we carried out 18S ribosomal DNA gene sequencing on the unialgal cultures. Genomic DNA was extracted from our cultures of *D.salina*CCAP 19/18, and additionally from four other lab strains in our collection, *D. salina* CCAP 19/30, *Nannochloropsis oculata* CCAP 849/1*, Tetraselmis suecica* CCAP 66/4 and *D. primolecta* CCAP 11/34*,* which were used ascontrols to ensure the accuracy of the methodology. We then carried out a polymerase chain reaction (PCR) to specifically amplify the 18S rDNA gene, and sequenced the resulting DNA of the PCR product.

PCR products were visualised by running out 15 μl of each on a 1% TAE agarose gel. Products for all samples were ~1750bp in size, apart from that obtained for *D.salina* 19/18 which was larger at ~2200bp.

The remaining PCR products were purified and sequenced. Sequences returned were queried against sequences held by the National Center for Biotechnology Information (NCBI), using a BLASTn search. In each case the algal species was correctly identified using this method with at least 99% specificity.

Culture of D. salina under stress conditions

Growth of the algae under different conditions of salinity, nitrogen availability, and irradiation was monitored by measuring optical density and chlorophyll levels in 100 ml cultures over 21 days (Figure 1). From these results, it appears that *D.salina* 19/18 has an increased growth rate under conditions of high light and normal nitrogen availability (5mM), with 2M NaCl having the highest growth rate with respect to salinity. Limited nitrogen conditions were not as detrimental to growth rates as perhaps expected, particularly when combined with 3 M NaCl.

For cultures grown under each stress condition, we examined Nile Red stained algae under fluorescence microscopy to visualise lipid droplets within the cells. We then semi-quantified lipid content using flow cytometry techniques, then finally measured total lipid content as a percentage of dry biomass via the gravimetric method described by Chiu *et al* [Chiu].

Fluorescence microscopy of Nile-red stained cultures

Fluorescence microscopy images of the algae stained with Nile Red were acquired to visualise lipid droplets (Figure 2). From these qualitative results it appeared that conditions of 1 M NaCl combined with low nitrogen (0.5 mM N) or high light lead to the highest accumulation of lipid droplets in the cells. To examine this further, we investigated Nile Red stained samples from all culture conditions using flow cytometry.

Flow cytometry

Samples were cultured for three weeks in each set of conditions. 1 ml samples of both unstained and Nile Red stained samples were run though an LSR II flow cytometer (Becton Dickinson) and analysed using BD FACSDiva Software v6. Samples were excited at a wavelength of 488 nm, and we simultaneously collected fluorescence intensity data from several different emission filter sets; 530 nm, 575 nm, 730 nm and 780 nm.It became evident on analysis that we had two species present within our cultures, one composed of cells less granular and 5-10x smaller in size than the other (Figure 3). Under light microscopy, small cells of 1-2 μm diameter were abundant in the cultures, and PCR amplification of the 16S gene and subsequent sequencing revealed the cells to be to be *Halomonas* sp., a halotolerant bacterium. On analysis, it was clear that fluorescence of the stained cells had shifted from unstained. Analysis of flow cytometry data allows the investigator to 'gate', or select, subpopulations within the total population of the sample examined. We gated populations of cells to distinguish those which became fluorescent at an emission of 575 nm after staining with Nile Red from those which remained the same as unstained (Figure 3). We chose the arbitrary level of 10^2 for fluorescence at 575 nm as a gate point, since the vast majority of unstained cells were below this level. This allowed us to see what proportion of the total population had increased fluorescence (i.e., had taken up Nile Red within lipid droplets).To avoid confounding results from the bacteria, which also took up the Nile Red stain, we gated only the larger celled population for analysis.

We calculated the median fluorescence ratio for each sample at 575nm (Figure 4b). This gives the overall increase in fluorescence at that wavelength for the entire population. This is calculated as follows:

$$\frac{\text{Median fluorescence of stained sample}}{\text{Median fluorescence of unstained sample}} = \text{Median fluorescence ratio}$$

From these data it appears that the highest median fluorescence ratio, i.e., the highest overall increase in fluorescence for the whole population, was with *D. salina* grown in 1M NaCl with 5 mM N and high light.

We then examined the subpopulations with the highest fluorescence at 575 nm for each sample (Figure 4c). The analysis software provides results giving the percentage of the total population contained within any subpopulation. We compared the percentages of the total populations contained within 'P1' and a further subpopulation, 'P2' (see Figure 3). P2 contained all cells fluorescing above 10^3. This allowed us to compare which stress conditions provided cells with the very highest levels of fluorescence, and therefore contained the most lipid.

The flow cytometry data revealed that samples cultured under conditions of 1 M NaCl and high light proved to have the highest overall fluorescence (and by inference, highest amount of intracellular neutral lipids), and the subpopulation with the highest fluorescence, in broad agreement with both the qualitative fluorescence microscopy and lipid quantification data.

We then quantified total lipid content in the algal cultures grown under each stress condition using the gravimetric method (Figure 5). The quantification of total lipids broadly agreed with the flow cytometry data. After 21 days growth, the highest total lipid content was found in cultures grown in 1 M NaCl with 0.5 mM N and high light, closely followed by cultures grown in 1 M NaCl with 5 mM N and high light.

Given both growth curves and lipid content data, we chose to culture *D. salina* 19/18 in *Dunaliella* growth medium at 1M NaCl, 5mM N and high light conditions for 7 days to produce high lipid content substrains. We stained the culture with Nile Red and used FACSort flow cytometry to isolate single algal cells from the top 8% highest lipid producers (most fluorescent

at 575nm) in to a 96 well plate in 100ul medium (Figure 6?). We allowed the single cell cultures to grow under high light for *** days, after which time we examined the wells for signs of growth both visually and by reading absorbance of the plate.

Figure 6 – gates of population used for sorting

The 100ul samples were transferred into 2ml of culture in 15ml falcon tubes stoppered with cotton wool and again cultured in Dunaliella growth medium, 1M NaCl, 5mM N, high light for a further ** days. At this point cultures were examined microscopically to ensure Dunaliella **were present**

Cultures transferred into 10ml media

Into 100ml media and grown

Lipid contents measured.

Figure 7 – lipid contents of new substrains

Conclusions

We have successfully grown cultures of *D. salina*19/18 under a range of growth conditions with respect to salinity, light intensity, and nitrogen deprivation, and established growth curves for each set of conditions. Isolating genomic DNA from the algae and PCR amplification of the 18S gene were accomplished without complications, and we successfully attained DNA sequences from the PCR products for both of our model organism *D.salina* 19/18 and three further test organisms *Nannochloropsis*, *Tetraselmis* and *D.primolecta*. Whilst using BLASTn searches to align our sequences with known sequences held in the NCBI database (http://www.ncbi.nlm.nih.gov/) was able to correctly identify all species tested, the sequences attained did align with other algal species and so 18S rDNA sequencing alone may not be a

definitive method of species identification. The gene for 18S evolves relatively slowly and as such may not be the best gene to study in isolation. For example, two species of freshwater *Nannochloropsis*, *N.limnetica* and *Nannochloropsis* sp. 2 isolated in Germany and North Carolina respectively, differ in their 18S rDNA sequence by only 2 out of 1759 nucleotides [Andersen *et al.,*1998; Krienitz *et al.,*2000]. PCR amplification and sequence analysis of other genes to complement the 18S sequences may support our results. Other researchers have shown that sequencing of multiple genes aids in molecular identification of algae [Nozaki *et al*.,2000; Gontcharov *et al.,*2004]. We have begun studies using PCR amplification of the chloroplast gene rbcL, which encodes the large subunit of ribulose bisphosphate carboxylase (RuBisCo). Sequencing of this protein coding gene was demonstrated by Suda *et al.* [Suda] to provide around 3 times the variability of 18S rDNA for the molecular characterisation of *Nannochloropsis*, whilst Fawley and Fawley [Fawley] employed both 18S rDNA and rbcL sequencing in molecular identification of several freshwater *Nannochloropsis* species.

For our flow cytometry studies, 530 nm was used to simulate the wavelengths used in fluorescence microscopy. 575 nm was used asflow cytometric examination of the fluorescence of Nile Red-stained cells at wavelengths of ~570 nm preferentially detects thefluorescence of Nile Red interacting with extremely hydrophobicenvironments (i.e., neutral lipid droplets), whereas at this wavelength the fluorescence of Nile Red interacting with cellular membranes is minimized [Greenspan]. We inferred from this that results obtained at 575 nm would allow us to identify populations of cells with the highest neutral lipid content. 730 and 780 nm were used as controls; we did not expect to see any change in fluorescence emissions at these wavelengths.

We found that we had co-cultured the halotolerant bacterium *Halomona*s along with *D. salina*. This was not surprising, since *Halomonas* require conditions of high salinity to thrive, and indeed research has shown that a symbiotic relationship bacteria and algae may be necessary for the growth of some algal species [Croft].

Our data show that*D.salina* appears to favour conditions of high light with respect to growth, and fortunately high light also appears to be the key condition tested in lipid production as judged by fluorescence microscopy, flow cytometry and quantified by the gravimetric method. Our data suggested that 1 M NaCl with high light and 5 mM N produce the highest lipid content.

Following on from the initial culture and flow cytometry data, we set up 100 ml cultures of *D. salina* at the optimum growth/lipid content conditions. *D. salina* 19/18 is genetically heterogeneous, i.e. single cells within each strain will differ in their capacity for lipid production. We therefore then used those cultures to isolate individual cells with the highest lipid content using Nile Red staining and flow cytometry. We used Fluorescence Activated Cell Sorting (FACS), which uses flow cytometry principles to isolate single cells selected from a whole population. The single cells were cultured into high lipid content substrains, and we maintained those as pure substrains for further analysis.

We successfully isolated and cultured ** high-lipid producing substrains of *D.salina* 19/18 from our parent population, with an average increase of **% total lipid content as compared to the parent population. These substrains *appear to be stable?* and were achieved by natural selection, rather than by genetic modification of the organism.

References

Andersen R, Brett RW, Potter D and Sexton JP (1998). Phylogeny of the Eustigmatophyceae based upon 18S rDNA, with emphasis on *Nannochloropsis*. *Protist* 149: 61-74.

Fawley KP and Fawley MW (2007). Observations on the diversity and ecology of freshwater *Nannochloropsis* (Eustigmatophyceae), with descriptions of new taxa. *Protist* 158: 325-336.

Gontcharov AA, Marin B and Melkonian M (2004). Are combined analyses better than single gene phylogenies? A case study using SSU rDNA and rbcL sequence comparisons in the Zygnematophyceae (Streptophyta) *Mol. Biol. Evol*. 2:612–624.

Krienitz L, Hepperle D, Stich H-B, and Weiler W (2000). *Nannochloropsis limnetica* (Eustigmatophyceae), a new species of picoplankton from freshwater. *Phycologia* 39: 219-227.

Nozaki H, Misawa K, Kajita T, Kato M, Nohara S, and Watanabe MM (2000). Origin and evolution of the colonial Volvocales (Chlorophyceae) as inferred from multiple, chloroplast gene sequences. *Mol. Phylogenet. Evol*. 17:256–268.

Suda S, Atsumi M, Miyashita H (2002) Taxonomic characterization of a marine *Nannochloropsis* species, *N. oceanica* sp. nov. (Eustigmatophyceae). *Phycologia* 41: 273—279.

Chiu SY, Kao CY, Tsai MT, Ong SC, Chen CH, and Lin CS. (2009). Lipid accumulation and CO2 utilisation of *Nannochloropsis oculata* in response to CO2 aeration. (2009). *Bioresour Technol* 100:833-838.

Cooksey KE, Guckert JB, Williams SA, and Collis PR.(1987). Fluorometric determination of the neutral lipid content of microalgal cells using Nile Red. *J Microbiol Methods* 6:333-345

Elsey D, Jameson D, Raleigh B, and Cooney MJ. (2007). Fluorescent measurement of microalgal neutral lipids. *J Microb Methods* 68: 639-642

Greenspan P, Mayer EP and Fowler SD.(1985). Nile Red: A selective fluorescent stain for intracellular lipid droplets. *J Cell Biol* 100:965-973

POST SUBMISSION NOTE:

Subsequent to the submission of this thesis, it was found that the ceramic material used for the construction of the photo-bioreactor spargers in this work was actually hydrophobic, rather than hydrophilic as originally thought. This difference has no impact on the results and methodology of experimental work carried out, but has a minor bearing on some of the conclusions drawn from this data. Chiefly that, the attachment force during bubble formation is significant, rather than negligible as first assumed. This means that the oscillatory effect also has to overcome this force to produce smaller bubbles, which it did, but with only a marginal improvement. Given that the oscillation frequency was also not optimised, this could mean that if a different sparger material was utilised the positive bubble formation effects observed could be greatly enhanced in future work.